FELDSPAR PETROGRAPHY AND GEOCHEMISTRY: INSIGHTS INTO THE MAGMATIC-HYDROTHERMAL EVOLUTION OF IOCG SYSTEMS FROM SOUTH AUSTRALIA

ALKIVIADIS KONTONIKAS-CHAROS

This thesis is submitted for the degree of Doctor of Philosophy

in the

School of Physical Sciences, Department of Earth Sciences,

at

The University of Adelaide

THE UNIVERSITY of ADELAIDE

August 2017

TABLE OF CONTENTS

ABSTRACT ..... **viii**

DECLARATION ..... **x**

ACKNOWLEDGEMENTS ..... **xi**

PREFACE ..... **xiii**

CHAPTER 1: INTRODUCTION **1**

1.1 Feldspar nomenclature, phase equilibria and crystal structure 4

1.1.1 Nomenclature 4

1.1.2 Phase equilibria and strain-controlled exsolution 6

1.1.3 Crystal structure and Al, Si ordering 11

1.1.4 Accommodation of trace elements in feldspars 15

1.2 Feldspar replacement reactions 17

1.3 Iron-oxide copper-gold mineralization and the role of alteration 20

1.4 Olympic Cu-Au Province and local geology of case studies 24

1.4.1 Olympic Cu-Au Province 24

1.4.2 Olympic Dam (including Wirrda Well and Phillip's Ridge) 26

1.4.3 Moonta Wallaroo region 29

1.4.4 Hillside 30

1.4.5 Cape Donington 31

1.5 Research objectives and thesis structure 32

CHAPTER 2: METHODOLOGY 49

2.1 Sample selection and preparation 51

2.2 Optical microscopy 56

2.3 Scanning Electron Microscopy 57

2.4 Electron Probe Microanalysis 59

2.5 Laser Ablation Inductively-Coupled Plasma Mass Spectrometry 61

2.6 Focussed Ion Beam-Scanning Electron Microscopy 68

2.7 Transmission Electron Microscopy 71

CHAPTER 3: ALBITIZATION AND REDISTRIBUTION OF REE AND Y IN IOCG SYSTEMS: INSIGHTS FROM MOONTA-WALLAROO, YORKE PENINSULA, SOUTH AUSTRALIA..... 77

Abstract 80

3.1 Introduction 81

3.2 Geological background 82

3.2.1 IOCG mineralization and the Olympic Cu-Au Province 82

3.2.2 The Moonta-Wallaroo region 82

3.3 Approach and methodology 83

3.4 Petrography 83

3.4.1 Main rock types: primary and alteration features 83

3.4.1.1 Altered igneous rocks 83

3.4.1.2 Intensely altered igneous rocks 85

3.4.1.3 Metasedimentary rocks and Oorlano metasomatite 85

3.4.2 Accessory and REY-minerals 87

3.4.3 Key albitization textures 88

3.5 Trace element concentrations and distributions in feldspar and accessories: LA-ICP-MS 89
3.5.1 Trace element distributions: REY trends 90
3.5.1.1 Potassium feldspar 90
3.5.1.2 Plagioclase feldspar 91
3.5.1.3 Time-resolved depth spectra 91
3.5.1.4 Accessory minerals 92
3.5.2 Element mapping 92
3.5.3 Nanoscale investigations of plagioclase feldspars 93
3.6 Discussion 94
3.6.1 Trace element incorporation in feldspars and accessories 94
3.6.2 REY distributions 94
3.6.3 Alkali-metasomatism 97
3.6.3.1 Albitization of igneous rocks 98
3.6.3.2 Albitization of metasedimentary rocks 99
3.6.4 Implications for IOCG genesis and exploration methods 101
3.7 Conclusions 101
3.8 Acknowledgements 101
3.9 References 102

CHAPTER 4: FELDSPAR EVOLUTION IN THE ROXBY DOWNS GRANITE, HOST TO FE-OXIDE CU-AU-(U) MINERALIZATION AT OLYMPIC DAM, SOUTH AUSTRALIA 105

Abstract 108
4.1 Introduction 108
4.2 Background 109

4.2.1 Feldspar reactions and nomenclature 109
4.2.2 Olympic Dam geology 109
4.3 Approach and methodology 109
4.4 Results 110
4.4.1 Samples and whole-rock geochemistry 110
4.4.2 Petrography 111
4.4.2.1 Alkali feldspars in least-altered RDG 112
4.4.2.2 Plagioclase in least-altered RDG 116
4.4.2.3 Feldspars in sericite-hematite altered and mineralized RDG 116
4.5 Geothermobarometric estimates for least-altered RDG 117
4.5.1 Amphibole chemistry, geobarometry and geothermometry 117
4.5.2 Fe-Ti-mineral chemistry, geothermometry and fO_2 estimates 118
4.5.3 Feldspar geothermometry 120
4.6 Discussion 120
4.6.1 Plagioclase crystallization and significance of rapakivi texture 121
4.6.2 Alkali feldspars and deuteric coarsening 122
4.6.3 Albitization of plagioclase 123
4.6.4 Hydrothermal K-feldspar 126
4.6.5 Significance of feldspar evolution for IOCG mineralization 126
4.7 Conclusions 127
4.8 Acknowledgements 128
4.9 References 128

CHAPTER 5: RARE EARTH ELEMENT GEOCHEMISTRY OF FELDSPARS: EXAMPLES FROM FE-OXIDE CU-AU SYSTEMS IN THE OLYMPIC CU-AU PROVINCE, SOUTH AUSTRALIA 131

Abstract 134

5.1 Introduction 135
5.2 Background 137
5.2.1 Feldspar nomenclature 137
5.2.2 Trace element geochemistry and feldspar replacement reactions 137
5.2.3 Sample suite geology 140
5.3 Approach and methodology 144
5.4 Results 145
5.4.1 Sample suites 145
5.4.2 Petrography 149
5.4.3 Chondrite-normalized REY fractionation patterns for feldspars 156
5.5 Discussion 166
5.5.1 REY fractionation pattern comparison 166
5.5.2 Geochemical and genetic implications 168
5.5.3 Implications for IOCG systems and the Olympic Cu-Au Province 171
5.6 Conclusions 174
5.7 Acknowledgements 174
5.8 References 174

CHAPTER 6: FELDSPAR MINERALOGY AND RARE EARTH ELEMENT (RE)MOBILIZATION IN IRON-OXIDE COPPER GOLD SYSTEMS FROM SOUTH AUSTRALIA: A NANOSCALE STUDY .. 185

Abstract 189
6.1 Introduction 190
6.2 Background on IOCG deposits and feldspar alteration 193
6.3 Approach 195
6.4 Methods 199

6.5 Results 200

6.5.1 Perthites 200

6.5.2 Hydrothermal potassium feldspar - hyalophane 205

6.5.3 Red-stained potassium feldspar and advanced feldspar replacement:

Fe and REE metasomatism 209

6.5.4 Hillside - endoskarn 217

6.6 Discussion 220

6.6.1 Magmatic to hydrothermal feldspars – grain scale (re)mobilization 220

6.6.2 Broader scale zonation patterns: metasomatism and advance feldspar replacement 222

6.6.3 Rare earth element remobilization: the role of feldspars in defining IOCG mineral signatures 224

6.7 Implications and outlook 226

6.8 Acknowledgements 227

6.8 References 227

CHAPTER 7: SUMMARY, RECOMMENDATIONS AND IMPLICATIONS 235

7.1 Summary 237

7.1.1 Feldspar replacement reactions in magmatic-hydrothermal systems 237

7.2 Research gaps and recommendations 240

7.2.1 The role of alkali alteration in IOCG systems 240

7.2.2 Geochemical modelling: albitization of plagioclase 242

7.3 Implications 245

7.3.1 Evolution of the Olympic Dam deposit 245

7.3.2 The link between albitization and REE remobilization in IOCG systems 248

CHAPTER 8: SUPPLEMENTARY AND ADDITIONAL MATERIAL 261

SUPPLEMENTARY MATERIAL A: For Chapter 3 263

Electronic Appendix A for Chapter 3 264

Electronic Appendix B for Chapter 3 273

SUPPLEMENTARY MATERIAL B: For Chapter 5 276

Electronic Appendix A for Chapter 5 277

Electronic Appendix B for Chapter 5 283

SUPPLEMENTARY MATERIAL C: For Chapter 6 295

Electronic Appendix A for Chapter 6 296

ADDITIONAL MATERIAL D: Alteration at the Olympic Dam IOCG-U deposit: insights into distal to proximal feldspar and phyllosilicate chemistry from infrared reflectance spectroscopy 297

ADDITIONAL MATERIAL E: Apatite at Olympic Dam, South Australia: A petrogenetic tool 312

ADDITIONAL MATERIAL F: Deuteric coarsening and albitization in Hiltaba Suite granites from the Olympic Dam IOCG deposit, South Australia 329

ADDITIONAL MATERIAL G: Feldspar re-equilibration reactions in Hiltaba Suite granite from the Olympic Dam IOCG-(U) deposit, South Australia 334

ADDITIONAL MATERIAL H: Feldspar replacement reactions in IOCG systems: the Olympic Cu-Au Province 337

ADDITIONAL MATERIAL I: Rare earth element remobilization in feldspars: examples from IOCG systems in the Olympic Cu-Au Province 340

ADDITIONAL MATERIAL J: Remobilization of REE during feldspar replacement reactions in IOCG systems: examples from the Olympic Cu-Au Province, South Australia 342

ADDITIONAL MATERIAL K: The IOCG-IOA ore system at Olympic Dam and nearby prospects, South Australia 344

CHAPTER 9: REFERENCES 351

ABSTRACT

The iron-oxide copper-gold (IOCG) class of mineral deposits is characterized by, among other properties, widespread alkali alteration and an enrichment of multiple trace elements, including REE and U. The ability of feldspar replacement reactions to alter physical and chemical properties of host rocks invokes the idea that the early widespread alkali alteration stage within IOCG genesis may prove critical in the subsequent enrichment of trace elements within such magmatic-hydrothermal systems. Based on detailed petrographic investigations and geochemistry, the link between these two fundamental IOCG properties is tested in one of the largest IOCG metallogenic belts in the world, the Olympic Cu-Au Province.

Firstly, the temporal evolution of a deeper-style IOCG system (Moonta-Wallaroo) is tracked from protolith through to early and late mineralization stages using mineral reactions associated with regional alkali alteration (namely, albitization), their relative textures and chondrite-normalised REE+Y (hereafter REY) fractionation patterns. Different stages can be distinguished based on variation in REY-anomalies (e.g., Eu, Y), slope (LREE/HREE) and ∑REY concentration. The results also highlight how feldspar alteration is expressed across various lithologies within a single IOCG terrane, which is largely dependent on the style of fluid/rock interaction.

In contrast to Moonta-Wallaroo, mineralization at Olympic Dam is hosted largely within a single lithology; the Roxby Downs Granite. Thus, changes in feldspar textures and geochemistry from magmatic to hydrothermal stages within a single lithology can be tracked based on proximity to mineralization within the Olympic Dam Breccia Complex. From observations and analyses of cryptoperthitic alkali feldspars, patch perthite, plagioclase and albite, it is evident that feldspars preserve the major element exchange (loss of Na → gain of K and Fe → Cu-U-Au-Ag mineralization) occurring within the Olympic Dam deposit.

Moreover, results also highlight the ability of widespread feldspar replacement reactions (with a coupled dissolution-reprecipitation mechanism) to produce significant microporosity within the host rocks that facilitate subsequent fluid/rock interaction and mineralization.

The contribution and distribution of REE elements within the Roxby Downs Granite is also investigated and compared to other IOCG terranes within the Olympic Cu-Au province, as well as pre-Hiltaba Suite lithologies, such as the Donington Suite granite. Chondrite-normalized REY fractionation patterns obtained from magmatic and hydrothermal feldspars, show that feldspars in the Roxby Downs Granite are significantly enriched in lattice-bound REY relative to Donington Suite granite. Moreover, although it appears that hydrothermal albite and K-feldspar inherit REY concentrations from the respective parent phases, variation in ∑REE (~1-100 ppm) at Olympic Dam indicate an increase in mobility of REE from feldspars with proximity to the Olympic Dam Breccia Complex.

Nanoscale characterization is also undertaken on feldspars undergoing transformation from early post-magmatic to hydrothermal stages in the Roxby Downs Granite and the Hillside Granite. Numerous textures and phases are identified, including complex perthitic textures, anomalously Ba-, Fe-, or REE-rich compositions, and REE-fluorocarbonate + molybdenite assemblages which are observed to replace feldspars. Epitaxial orientations between cryptoperthite (magmatic), patch perthite (deuteric) and replacive albite (hydrothermal) support interface-mediated reactions between pre-existing alkali-feldspars and pervading fluid(s). In addition, nanoscale inclusions are observed within feldspars, such as epidote (Olympic Dam) and titanite + andradite (Hillside), which are strong hosts of REE and highlight the grain-scale remobilization of such elements during alkali alteration. Consequently, it appears that changes in REE fractionation trends can also be attributed to, and thus controlled by, sub-µm-scale inclusions within feldspars.

DECLARATION

I certify that this work, to the best of my knowledge, contains no material previously published or written by another person, except where due reference has been made in the text, and that, unless otherwise indicated, no material has been accepted for the award of any other degree or diploma in my name, in any university or other tertiary institution. In addition, I certify that no part of this work will, in the future, be used in a submission in my name, for any other degree or diploma in any university or other tertiary institution without the prior approval of The University of Adelaide and, where applicable, any partner institution responsible for the joint-award of this degree.

I acknowledge the support I have received for my research through the provision of an Australian Government Research Training Program Scholarship.

I give consent to this copy of my thesis, when deposited in the University Library, being made available for loan and photocopying, subject to the provisions of the Copyright Act 1968. I also give permission for the digital version of my thesis to be made available on the web, via the University's digital research repository, the Library Search and also through web search engines, unless permission has been granted by the University to restrict access for a period of time.

I acknowledge that copyright of published works contained within this thesis resides with the copyright holder(s) of those works.

Signed _____ Date 27/09/17

ACKNOWLEDGEMENTS

Firstly, I would like to express my deepest gratitude to my academic supervisors, and friends, Prof. Nigel Cook and Dr. Cristiana Ciobanu, for their tireless support, encouragement and wisdom over the last three years. Without you, none of this would be possible. Thank you for always believing in me and for providing invaluable guidance in matters of research as well as life. You have helped me develop into the researcher and person I am today. Nigel, your unwavering patience and staunch optimism have been a shining light and constant source of belief and positivity throughout the unpredictable roller-coaster of postgraduate studies. Cristi, I am forever indebted to you for sharing your experience and insights, and for always encouraging me to excel to new heights in the pursuit of knowledge. I hope what we achieved was "spicy" enough.

I would also like to express my appreciation for my external supervisor, Dr. Kathy Ehrig, for her unrelenting support, belief and interest in the project and myself. Thank you for always being available and open to new ideas. Your leadership and scientific curiosity are irreplaceable. I would also like to acknowledge the financial support of BHP Billiton and the hospitality of the Olympic Dam team for making this project possible.

I would like thank all the staff at Adelaide Microscopy, in particular, Mr. Angus Netting, Dr. Animesh Basak, Mr. Ken Neubauer, Ms. Aoife McFadden, and especially Dr. Benjamin Wade, for their willingness to train and assist me in various analytical techniques. Thank you also for the great chats and for creating a friendly and well-run workplace.

The last three years would not have been the same without the stimulating scientific discussions and late nights, as well as the interstate and international escapades, shared with my fellow PhD colleagues, Sasha, Luke and Matt. Thank you for the memories.

Finally, I would like to thank my close friends and family for their support over this journey. In particular, my Mother and Father, to whom I owe everything. I am very fortunate to have been raised by such wonderful and loving parents. Thank you for always believing in my abilities and for providing me with every opportunity to fulfil my dreams. I am proud to have you as parents, and hope that I have made you proud.

"The Cosmos is all that is or ever was or ever will be."

- Carl Sagan

"The known is finite, the unknown infinite; intellectually we stand on an islet in the midst of an illimitable ocean of inexplicability. Our business in every generation is to reclaim a little more land."

- T. H. Huxley

PREFACE

This thesis comprises of a portfolio of manuscripts which have been submitted, published, or accepted for publication, in international peer-reviewed journals. The journals in which these papers have been submitted, published and/or accepted are *'Lithos'* (Chapter 3, published), *'Ore Geology Reviews'* (Chapter 4, published), *'Mineralogy and Petrology'* (Chapter 5, accepted) and *'Mineralogical Magazine'* (Chapter 6, accepted, in press). All four manuscripts are closely related, and summarize key findings and interpretations of feldspar alteration and trace element geochemistry within iron-oxide copper-gold systems, that were made as part of this project. Recommendations have been made at the end of this thesis as a direct result of the key findings of this research, and it is hoped that these are explored at a later date.

The four papers which form the basis of this thesis are:

1. Kontonikas-Charos, A., Ciobanu, C.L., Cook, N.J., 2014. Albitization and redistribution of REE and Y in IOCG systems: Insights from Moonta-Wallaroo, Yorke Peninsula, South Australia. Lithos 208–209, 178-201. (*This paper builds on research undertaken during the candidate's honours year.)*

2. Kontonikas-Charos, A., Ciobanu, C.L., Cook, N.J., Ehrig, K., Krneta, S., Kamenetsky, V.S., 2017. Feldspar evolution in the Roxby Downs Granite, host to Fe-oxide Cu-Au-(U) mineralisation at Olympic Dam, South Australia. Ore Geology Reviews 80, 838-859.

3. Kontonikas-Charos, A., Ciobanu, C.L., Cook, N.J., Ehrig, K., Krneta, S. and Kamenetsky, V.S. (accepted) Rare earth element geochemistry of feldspars: Examples from Fe-oxide Cu-Au systems in the Olympic Cu-Au Province, South Australia. Mineralogy and Petrology (submitted 16th April 2017)

4. Kontonikas-Charos, A., Ciobanu, C.L., Cook, N.J., Ehrig, K., Ismail, R., Krneta, S., Basak, A. (in press) Feldspar mineralogy and rare earth element (re)mobilization in iron-oxide copper gold systems from South Australia: a nanoscale study. Mineralogical Magazine. https://doi.org/10.1180/minmag.2017.081.040.

Key findings and implications of this work, as well as future avenues of research, are summarized in Chapter 7.

Chapter 8 contains all supplementary material for the main papers outlined above, as well as additional conference abstracts, and other co-authored publications that have been generated during the PhD candidature. The additional material is as follows:

A. Supplementary material for Chapter 3 (Paper 1).

B. Supplementary material for Chapter 5 (Paper 3).

C. Supplementary material for Chapter 6 (Paper 4).

D. Mauger, A., Ehrig, K., Kontonikas-Charos, A., Ciobanu, C., Cook, N., Kamenetsky, V., 2016. Alteration at the Olympic Dam IOCG–U deposit: insights into distal to proximal feldspar and phyllosilicate chemistry from infrared reflectance spectroscopy. Australian Journal of Earth Sciences 63, 959-972.

E. Krneta, S., Ciobanu, C.L., Cook, N.J., Ehrig, K., Kontonikas-Charos, A., 2016. Apatite at Olympic Dam, South Australia: A petrogenetic tool. Lithos 262, 470-485.

F. Kontonikas-Charos, A., Ciobanu, C.L., Cook, N.J., Ehrig, K., Kamenetsky, V.S., 2015. Deuteric coarsening and albitization in Hiltaba granites from the Olympic Dam IOCG deposit, South Australia (Extended abstract). Proceedings, Mineral Resources in a Sustainable World, 13th Biennial SGA Meeting, 3:1099–1102.

G. Kontonikas-Charos, A., Ciobanu, C.L., Cook, N.J., Ehrig, K., Krneta, S., Kamenetsky, V.S., 2015. Feldspar re-equilibration reactions in Hiltaba Suite granite from the Olympic Dam IOCG-(U) deposit, South Australia (Poster). Society of Economic Geologists Conference 2015, 'World-Class Ore Deposits: Discovery to Recovery', Hobart, TAS, Australia, September 27th – 30th.

H. Kontonikas-Charos, A., Ciobanu, C.L., Cook, N.J., Ehrig, K., Kamenetsky, V.S., 2015. Feldspar replacement reactions in IOCG systems: The Olympic Cu-Au Province (Poster). The Institute for Geoscience Research Conference 2015, 'Key issues in fluid-rock interaction: From the nano to the macroscale', Curtin University, Perth, WA, Australia, 23-25th September 2015.

I. Kontonikas-Charos, A., Ciobanu, C.L., Cook, N.J., Ehrig, K., Krneta, S., 2015. Rare earth element remobilization in feldspars: Examples from IOCG systems in the Olympic Cu-Au Province (Abstract). 2nd European Mineralogical Conference, 'Minerals, rocks and fluids: Alphabet and words of planet Earth', Rimini, Italy, 11-15th September, 2016.

J. Kontonikas-Charos, A., Ciobanu, C.L., Cook, N.J., Ehrig, K., Kamenetsky, V.S., 2016. Remobilization of REE during feldspar replacement reactions in IOCG systems: Examples from the Olympic Cu-Au Province, South Australia (Abstract). Australian Earth Sciences Convention 2016 (On behalf of the Geological Society of Australia), 'Uncover Earth's past to discover our future', Adelaide Convention Centre, Adelaide SA, Australia, 26-30th June, 2016.

K. Ehrig, K., Kamenetsky, V.S., McPhie, J., Apukhtina, O., Ciobanu, C.L., Cook, N.J., Kontonikas-Charos, A., Krneta, S., 2017. The IOA-IOCG ore system at Olympic Dam and nearby prospects, South Australia (Accepted abstract). 'Mineral Resources to

Discover', Proceedings from the 14th Biennial SGA Meeting, Quebec City, Canada, August 20-23rd, 2017.

The final chapter of this thesis consists of a complete reference list of all publications cited within any of the manuscripts, chapters, supplementary and additional material submitted as a component this thesis.

CHAPTER 1

INTRODUCTION

CHAPTER 1: INTRODUCTION

Feldspars, as a mineral group, constitute the majority of the Earth's oceanic and continental crust (up to 60%), and are thus inherently involved in processes of petrogenesis, metamorphism and diagenesis. The superimposition of such processes often produces rocks containing systematic chemical, textural and mineralogical variability. Moreover, the resultant rocks may host anomalous concentrations of economically valuable elements and form part of a broader ore system. Studying the textural and chemical variability of minerals within ore systems, is thus imperative to improve our understanding of ore system genesis and, ultimately benefit future geological exploration and scientific knowledge.

As a major silicate phase in many plutonic rocks, feldspars have long since been utilized to unravel the thermal history of igneous rocks (e.g., Smith, 1974a, b, and references therein). This is in large part due to their tectosilicate crystal structure, which is able to accommodate various high and low temperature conversions. Moreover, their systematic behaviour and phase equilibria make them an invaluable resource for petrological studies (e.g., Parsons et al., 2015). However, in the context of large, economically significant magmatic-hydrothermal systems, a greater emphasis is often placed on ore-minerals, and thus feldspars as 'gangue' minerals are often overlooked due to their lack of extractive value. One such example is within the iron-oxide copper-gold (IOCG) deposit class (e.g., Hitzman et al., 1992; Groves et al., 2010; Barton, 2014), which host a significant portion of the world's Cu, Au, Ag and U (e.g., Olympic Dam, South Australia; BHP Billiton, 2016).

Despite feldspar alteration being recognized as a diagnostic property of the IOCG deposit class (e.g., Groves et al., 2010), the role they play in deposit genesis in the broadest sense remains poorly constrained. Numerous petrological studies of feldspars and their replacement

reactions highlight their ability to alter the physical and chemical properties of host rocks from the macro- down to the nanoscale during fluid-rock interaction (e.g., Putnis, 2002; Parsons and Lee, 2009; Plümper and Putnis, 2009). Applying this body of research in the context of IOCG systems and other magmatic-hydrothermal terranes provides a unique opportunity to investigate the function of feldspars during widespread fluid-rock interaction, and potentially invoke the idea that feldspar replacement reactions may even be a prerequisite for subsequent alteration stages and deposition of IOCG-style mineralization.

This chapter firstly provides a summary of background information on feldspar nomenclature, phase equilibria, crystal structure, replacement reactions and trace element geochemistry. In addition, it goes on to address IOCG systems, the Olympic Cu-Au Province, and the regional and local geology of each case study examined. Finally, it outlines the overarching objectives and individual goals of the research, and concludes with a chapter-by-chapter explanation of thesis structure.

1.1 Feldspar nomenclature, phase equilibria and crystal structure

1.1.1 Nomenclature

The feldspar mineral group comprises aluminosilicate minerals given by the chemical formula: MT_4O_8, where M can be Na^+, K^+ or Ca^{2+}, and T is a Al:Si ratio ranging from 3:1 to 1:1 where Al $\geq$1 and $\leq$2 (Smith, 1974a). Feldspars are classified primarily based on chemical composition, but are also differentiated by colour, fine-scale twinning, crystal structure and symmetry. They form part of a ternary solid solution series involving three end-member components: orthoclase (Or) - $KAlSi_3O_8$, albite (Ab) - $NaAlSi_3O_8$ and anorthite (An) - $CaAl_2Si_2O_8$. In addition, significant solid solution can exist between an additional component given by $BaAl_2Si_2O_8$ (Celsian - Cn), although this is typically grouped with the Or component (Smith, 1974a). The alkali feldspar series is defined by the solid solution between the Or and

Ab components, whereas the plagioclase feldspar series concerns Ab-An solid solution (Fig. 1.1). Although not shown on Figure 1.1, orthoclase and microcline, both given by the formula $KAlSi_3O_8$, are end-member minerals along the Or-Ab join, however they form at low temperatures (<500 °C), as well as via spinodal decomposition of alkali feldspar (see below), which is accompanied by formation of an Ab-rich counterpart (typically albite). Thus, albite is an end-member of both alkali and plagioclase feldspar. Sanidine and adularia (also not included on Fig. 1.1) are K-feldspar minerals ($KAlSi_3O_8$) which form at high (>700 °C) and low (<300 °C) temperatures, respectively, and are differentiated from other species in the series based on crystal structure and Al, Si ordering (see section 1.1.3).

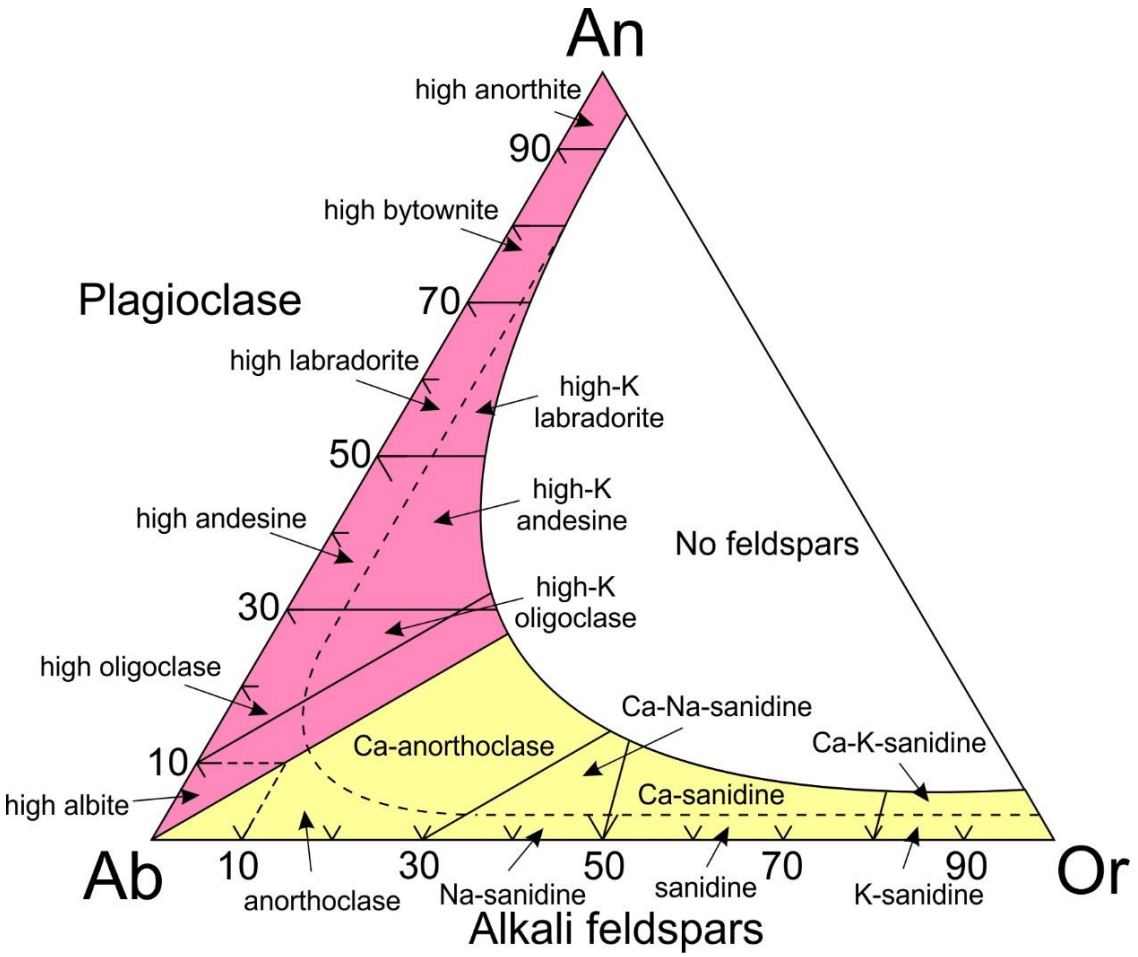

Figure 1.1: The maximum extent of feldspar solid solution at temperatures >1000 °C. The feldspar ternary system is defined by molecular components of orthoclase (Or) - $KAlSi_3O_8$, albite (Ab) - $NaAlSi_3O_8$ and anorthite (An) - $CaAl_2Si_2O_8$. Note the curvature of the line

within the ternary diagram, which is a result of extended solid solution at high temperatures allowing for high-K varieties in the plagioclase series, and Ca-Na-bearing varieties among alkali feldspars. Modified from Smith (1974a) and Parsons (2010).

1.1.2 Phase equilibria and strain-controlled exsolution

Feldspar phases existing in equilibrium, either through simultaneous growth from magma or through metamorphism, are defined by a ternary feldspar solvus (Or-Ab-An), given by a temperature-composition surface (Fig. 1.2). At high temperatures above the solvus (e.g., >700 °C), alkali feldspar exists as homogeneous crystals. However, as temperature decreases for a ternary feldspar crystal of a given bulk composition, it may drop below the coherent solvus (CS – Fig. 1.2), resulting in exsolution of Or- and Ab-rich phases in alkali feldspar (see below). Thus, the coherent solvus defines the bulk composition of both phases. If the crystal maintains the same framework structure (i.e., is coherent) during cooling, the Or- and Ab-rich phases will continue along the coherent solvus, becoming progressively K- and Na-rich, respectively. However, if the alkali feldspar crystal comes into contact with a fluid, it will recrystallize to a strain-free assemblage (e.g., patch perthite – see section 1.2) along the strain-free solvus (SFS – Fig. 1.2). The tie line between plagioclase and alkali feldspar (Fig. 1.2) defines the original bulk composition of feldspar components from a melt. If two crystals are deemed to have grown simultaneously from a melt, they may be labelled as feldspar ‘pairs’ and can be used for feldspar geothermometry. By using established isotherms to represent plagioclase and alkali feldspar tie lines, estimates of minimum crystallization temperatures can calculated. Such a method is useful for disordered feldspars (see below) formed at temperatures above ~700 °C, however problems arise due to the presence of An in the system for ordered alkali feldspars formed at low temperatures, which can drastically raise the ternary solvus. Nonetheless, reasonable estimates can be made in such a case (e.g., Parsons et al., 2009; Kontonikas-Charos et al., 2017).

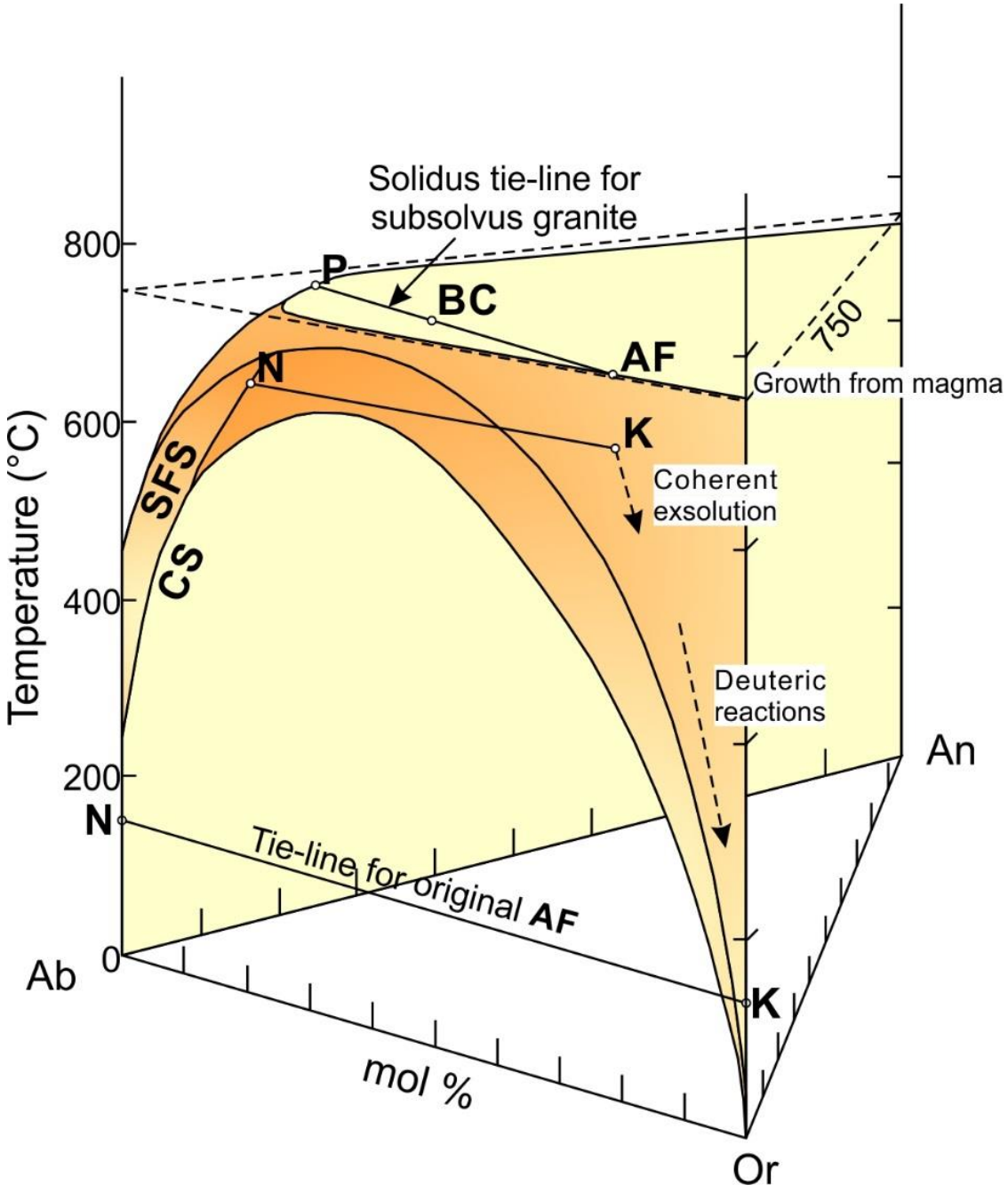

Figure 1.2: Temperature-composition prism for the ternary feldspar system at atmospheric pressure. AF – alkali feldspar, BC – bulk composition, CS – coherent solvus, N – Ab-rich phase in perthite, K – Or-rich phase in perthite, P – plagioclase, SFS – strain-free solvus. The solidus tie-line is an approximation used in geothermometry for plagioclase and alkali feldspar pairs. The tie-line for original alkali feldspar can be used to determine bulk composition of an initially homogenous alkali feldspar following recrystallization at lower temperatures. Modified from Parsons et al. (2005).

The process of exsolution occurs via spinodal decomposition which produces fine-scale lamellar intergrowths between Or- and Ab-rich phases. Such solid-state diffusion is driven by the strain on the Si-Al framework, a result of different ionic radii between Na^+ and K^+ which leads to structural clustering of alkali ions (Smith, 1974a). Depending on the dominant phase, the resultant intergrowths are classified as perthites (Or-rich host, Ab-rich exsolution) and antiperthites (Ab-rich host, Or-rich exsolution). Compositions which have roughly equal amounts of both components are termed mesoperthites. The composition of perthites is determined by the bulk chemistry of both the Ab-rich and Or-rich phases. Further classification may be required due optical properties and the scale of intergrowths. Depending on the thickness and periodicity of exsolution lamellae, the prefix micro- is added for optically visible intergrowths (on a petrographic microscope), whereas intergrowths below 1 μm in size are termed cryptoperthites. The bulk composition of perthites also influences feldspar speciation within the microstructure. In Ab-dominant alkali feldspar, the microperthitic intergrowths are likely to comprise microcline and albite (forming a 'braid' texture characterized by zig zag domains, which occur as a consequence of triclinic ordering of the dominant Ab-rich phase), while Or-dominant bulk compositions generally contain orthoclase (sometimes displaying a 'tweed' texture – see next section) and albite (with straight exsolution lamellae) (Parsons, 2010).

Although all natural feldspars are technically ternary feldspars, binary phase equilibria diagrams are often used to simplify and illustrate the behaviour of phases in the Or-Ab system (An-free) and the Ab-An system (Or-free) (e.g., Fig. 1.3). These diagrams include lines such as the solvus (defines the limit of solid solubility under equilibrium conditions), liquidus (defines the boundary between liquid and solid) and solidus (hypothetical area where solid and liquid are in equilibrium), which change depending on variables such as temperature, pressure and volatile content. An increase in pressure lowers the melting point, which may cause an

intersection between the liquidus and solidus, thus lowering the solvus and limiting solid solution (Fig. 1.4). The resultant system is referred to as subsolvus and produces two coexisting feldspars. A similar effect is seen if significant amounts of H_2O are present. In contrast, the system is referred to as hypersolvus if a single alkali feldspar crystallizes above the solvus, generally reflecting low pressures and H_2O content. Fractional crystallization may also affect solid solution by gradually changing the bulk composition of the system.

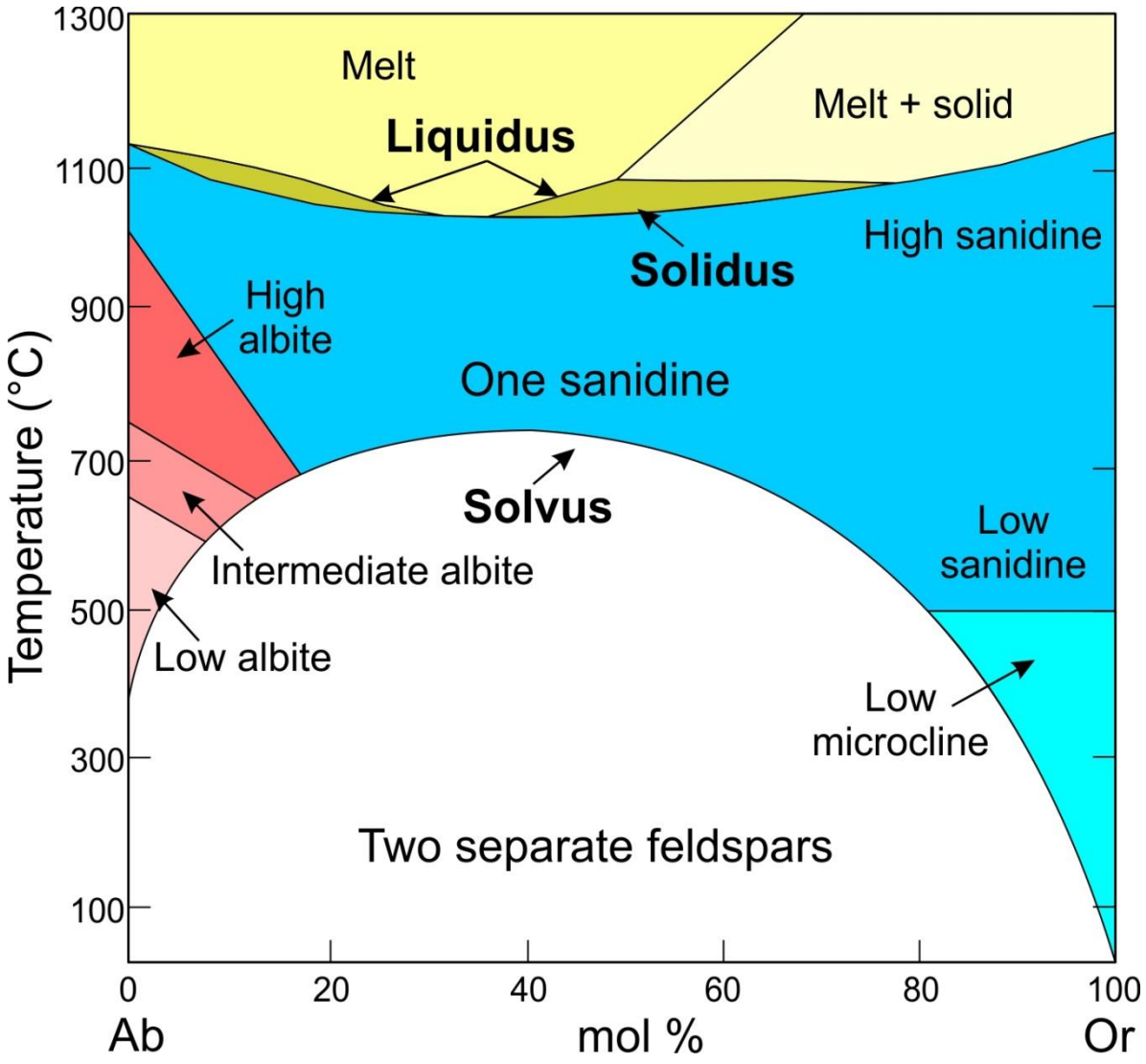

Figure 1.3: Stable equilibrium phase diagram for An-free plagioclase feldspars at atmospheric pressure. High, intermediate and low refer to Al, Si ordering of the phase. Adapted from Parsons (2010).

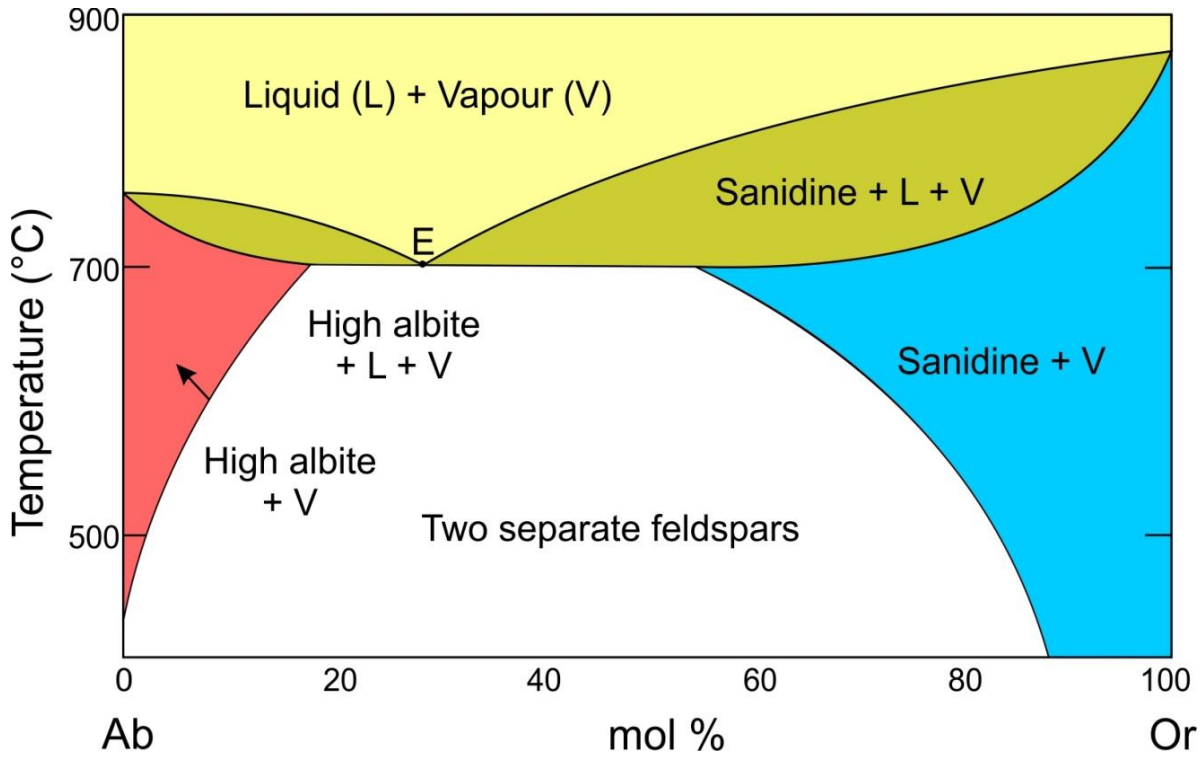

Figure 1.4: Phase diagram for disordered An-free alkali feldspars at P_{H2O} 500 MPa. Adapted from Parsons (2010).

Barring a few exceptions, the Ab-An system is generally at complete solid solution at both high and low temperatures. It involves the charge-balanced coupled exchange of Ca^{2+} and Al^{3+} for Na^{+} and Si^{4+} in the plagioclase crystal lattice. As the ionic radii of Na^{+} and Ca^{2+} are similar (227 pm and 231 pm, respectively), fine-scale exsolution is rarer than for the alkali feldspar system. Nonetheless, sub-solidus unmixing can occur during cooling and produce various exsolution textures dependent on miscibility gaps across certain composition intervals in the Ab-An system (Fig. 1.5). The Peristerite gap, extending over the ~An_{1-25} composition range, may cause exsolution of sub-microscopic domains/lamellae of albite and oligoclase, hundreds to thousands of Å in thickness (Gay and Smith, 1955; Fleet and Ribbe, 1965). The existence of miscibility gaps is driven by the free energy Al, Si ordering in albite relative to anorthite (Parsons, 2012). Similar to alkali feldspars, the resultant coherent microstructures are consistent with formation via spinodal decomposition. There also exist miscibility gaps for

composition ranges of ~An_{46-60} (Bøgglid gap) and ~An_{67-90} (Huttenlocher gap) which are dependent on transitions within the plagioclase crystal structure (see following section).

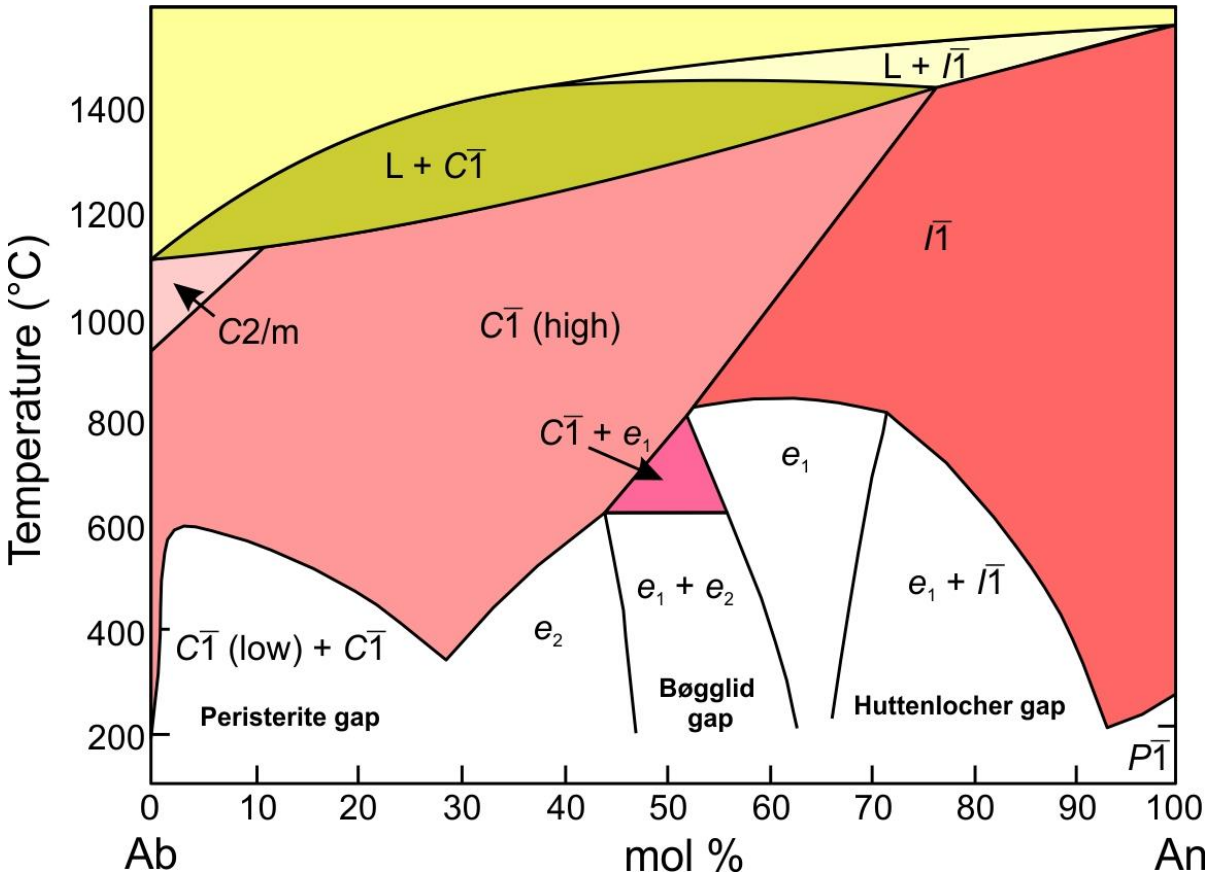

Figure 1.5: Phase diagram for Or-free plagioclase feldspars at atmospheric P. Area divisions are based on various phase transformations related to Al, Si ordering and An_x e.g., An_1 – 1:3 Al:Si ($C\bar{1}$space group), An_{100} – 1:1 Al:Si ($I\bar{1}$ space group). The *e* fields refer to e-plagioclase discussed in the next section. Note: The intersection of phase transition lines and miscibility gaps is still under debate, and thus should be used as a rough guide. Modified from Smith (1974a).

1.1.3 Crystal structure and Al, Si ordering

The feldspar tectosilicate structure consists of a continuous, negatively charged, three-dimensional framework of SiO_4 and AlO_4 tetrahedrons balanced by cations (Fig. 1.6). The

elasticity of this structure allows it to incorporate smaller cations (e.g., Na^{+}, Ca^{2+}) in triclinic symmetry, as well as relatively large cations (e.g., K^{+}), adjusting to monoclinic symmetry. Some general features of simple feldspar crystal structures are summarized in Table 1.1.

Table 1.1: General features of simple feldspar crystal structures at room temperature.

Name	End-member composition	Cell dimensions						Space Group	Tetrahedral order
		Nanometres			Degrees				
		a	***b***	***c***	***α***	***β***	***γ***		
Sanidine[1]	$KAlSi_3O_8$	0.860	1.303	0.718	90	116.0	90	*C*2/m	Disordered
Microcline[1]	$KAlSi_3O_8$	0.859	1.297	0.722	90.6	115.9	87.7	$C\bar{1}$	Ordered
High albite[1]	$NaAlSi_3O_8$	0.816	1.287	0.711	93.5	116.4	90.3	$C\bar{1}$	Disordered
Low albite[1]	$NaAlSi_3O_8$	0.814	1.279	0.716	94.3	116.6	87.7	$C\bar{1}$	Ordered
P-anorthite[1]	$CaAl_2Si_2O_8$	0.818	1.288	1.417	93.2	115.8	91.2	$P\bar{1}$	Ordered
Celsian[1]	$BaAl_2Si_2O_8$	0.864	1.305	1.440	90	115.1	90	*I* 2/c	Ordered
Orthoclase[2]	$KAlSi_3O_8$	0.856	1.299	0.719	90	116.0	90	*C*2/m	Partly ordered
Adularia[2]	$KAlSi_3O_8$	0.855	1.297	0.720	90	116.0	90	*C*2/m	Disordered
Intermediate Plagioclase[3]	$(Ca, Na)Al_{1-2}Si_{3-2}O_8$	0.818	1.288	0.711	93.4	116.2	90.2	$C\bar{1}$	Partly ordered

Sources: (1) Smith, 1974a; (2) Colville and Ribbe, 1968; (3) FitzGerald et al., 1986.

Structural distortions of the feldspar framework often occur in response to temperature changes. A decrease in temperature may cause the stable high temperature framework to collapse around the interstitial cation (Putnis, 1992). While larger cations are able to prevent this collapse, smaller cations allow for framework distortion (e.g., monoclinic to triclinic), producing variable symmetries and space groups (Putnis, 1992). At lower temperatures, Al, Si ordering involves the breaking of Si-O and Al-O bonds as a means to distribute atoms between the *T* sites (e.g., Fig. 1.6). Three distributions are commonly observed: ordered, partly order and disordered. An ordered distribution is typical for microcline (triclinic, $C\bar{1}$), which often indicates growth at low temperatures (e.g., diagenesis) or very slow cooling from high temperatures. Orthoclase (metastable, *C*2/m) is often partly ordered due to formation at intermediate temperatures or slow cooling from high temperatures (e.g., plutonic rocks). In contrast, sanidine (*C*2/m) has a disordered crystal structure, representing formation at high

temperatures followed by rapid cooling (e.g., volcanic rocks). Adularia (characterized by a distinctive {110} habit), forms at low temperatures but may either be highly ordered and untwinned, or highly disordered, indicating that triclinic untwinned microcline can also grow independent from a monoclinic transformation (Parsons, 2010).

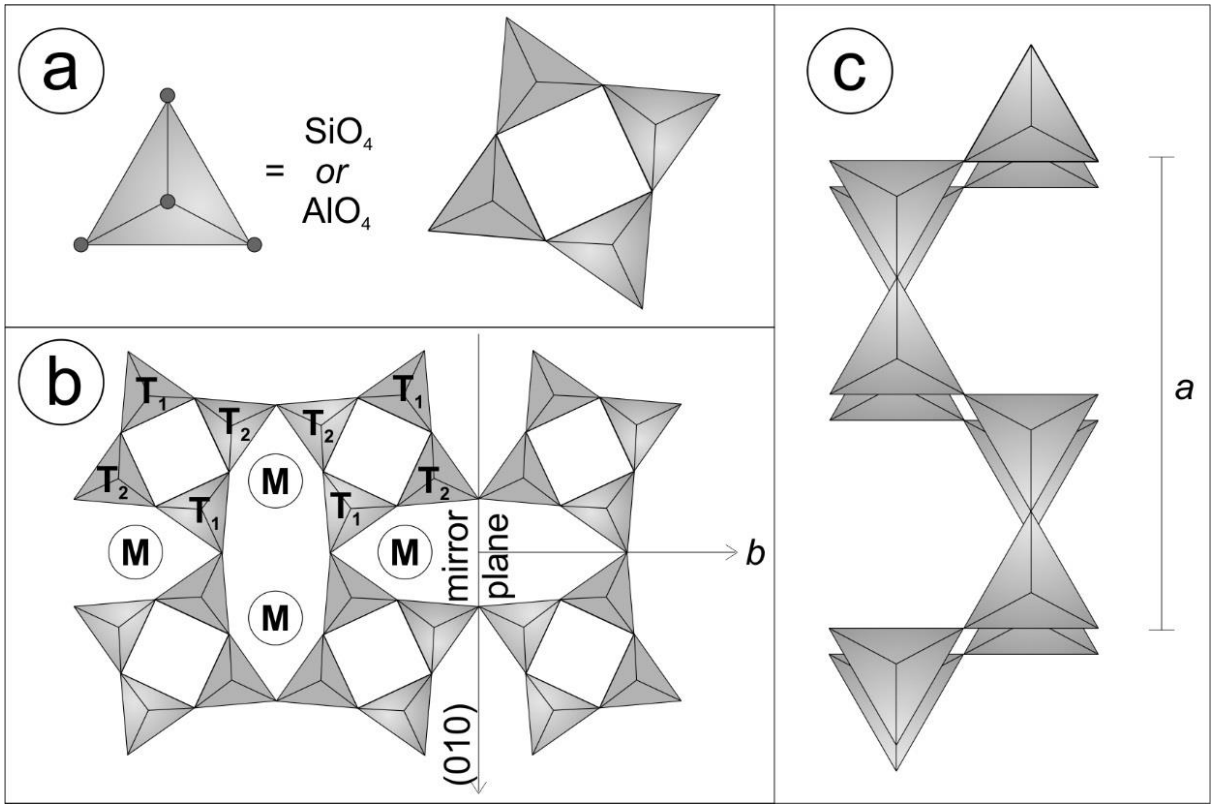

Figure 1.6: (a) The aluminosilicate tetrahedral structure of feldspars. The four-membered tetrahedra ring represents the basic building unit of the feldspar crystal structure consisting of one tetrahedra pair facing downwards and another tetrahedra pair facing upwards. (b) An example of connected tetrahedra rings forming a layer separated by the mirror plane at (010), perpendicular to the *b* axis. Large cations occupy the oval-shaped spaces in between sets of rings. *T* sites are related to one another by symmetry. (c) Tetrahedra ring sets shown parallel to the *a* axis. (Modified from Putnis, 1992).

Plagioclase has four known commensurate structures (space groups $C2/m$, $C\bar{1}$, $I\bar{1}$ and $P\bar{1}$) which change relative to composition and Al, Si ordering. Due to charge balance in Ca-rich

plagioclase, the Al/Si ratio increases and results in a change in *T*-site ordering. Consequently, the *c* dimension of anorthite in the $P\bar{1}$ unit cell becomes ~ 14 Å, compared to ~ 7 Å for albite. This complicates the crystal structure for intermediate plagioclase. In general, plagioclase below ~An_{60} will develop an overall albite-like $C\bar{1}$ structure with X-ray diffractions along the *a* lattice plane, whereas the crystal structure of plagioclase above ~An_{60} are anorthite-like with X-ray diffractions along the *a*, *b*, *c* and *d* lattice planes of the unit cell (Smith, 1974a). An incommensurate superstructure (e-plagioclase) has also been recognized in intermediate plagioclase, based on the presence of *e* diffractions (sometimes termed 'split-*b*' diffractions as they occur as pairs approximately along the *b* lattice plane), typically in association with unmixing microtextures across the miscibility gaps for the Ab-An system (Grove et al., 1983; Fig. 1.5).

Moreover, crystal structure influences the characteristic microscopic twinning observed in many feldspars. Due to the high pseudosymmetry of the feldspar crystal structure, there exist around 20 twin laws, of which five are commonly observed (Parsons, 2010). Twinning structures form during growth, often in response to applied stresses and changes in symmetry (e.g., from monoclinic to triclinic). Common simple twins are the Carlsbad law (parallel, occurring along the {010} composition plane and coinciding with the *c* axis) typical in orthoclase and occasionally in plagioclase, Baveno law (normal, occurring along the {021} composition plane, often at the contact between two crystals) and Manebach law (normal, along the {001} composition plane). Simple twinning is observed in both monoclinic and triclinic symmetries. Repeated twinning or polysynthetic twinning is typical for plagioclase, and, in conjunction with symmetrical extinction angles of Albite twins and Carlsbad-Albite twins (see below), can be used to deduce plagioclase composition. The most common polysynthetic twin laws are the Albite law (normal, along the {010} composition plane) and Pericline law (occurring along an irrational plane that contains the *b* axis and intersects {010}). The

intersection of the Albite and Pericline twins, common for microcline, form due to convergent ordering and produce the characteristic 'cross-hatch' or 'tartan' twinning (Parsons, 2010). Another twinning texture often encountered is 'tweed' orthoclase, which is the result of triclinic nanodomains formed within the monoclinic orthoclase structure during transformation to triclinic microcline (Smith and Brown, 1988).

1.1.4 Accommodation of trace elements in feldspars

The ideal MT_4O_8 feldspar chemical formula assumes all atomic sites are occupied within the ionic model for crystal structure; *T* sites are occupied by small, highly-charged cations (including high field strength elements - HFSE), whereas *M* sites are occupied by large, weakly charged cations (large ion lithophile elements – LILE) (e.g., Smith, 1974b). Deviations from this formula may be explained by unit cell modifications, such as site vacancies and/or trace element site affinities. Principles for element substitution and partitioning are dependent upon similarities in ionic radii and charge between elements (e.g., Goldschmidt, 1937). As such, in feldspars, any cations entering the *T* site must have ionic radii small enough to enter the tetrahedral interstices, and be highly charged to balance the oxygen anions, whereas cations entering the *M* site must be large enough to avoid any distortions within the feldspar lattice, and weakly charged to maintain overall charge balance (Smith, 1974b). Major element partitioning generally obeys these conditions, however, for minor and trace elements, a coupled substitution mechanism is required which allows for relative expansion and contraction of the feldspar framework while maintaining charge balance between the *M* and *T* sites.

A variety of chemical substitutions have been established in both natural and synthesized feldspars. Experiments on natural feldspars have shown that Fe^{3+} and Ti^{4+} can substitute for Al^{3+}, while Rb^{2+}, Cs^{2+} and Ba^{2+} for K^+ and Na^+, and Mg^{2+}, Fe^{2+}, Sr^{2+} and Mn^{2+} for Ca^{2+} in plagioclase (Papike, 1988; Pun et al., 1997). In addition, numerous feldspar synthesis

experiments indicate that B^{3+}, P^{5+}, Fe^{3+}, Ga^{3+} and Ge^{4+} are able to enter the *T* site (Fleet, 1988; Bychkov et al., 1989; London et al., 1990), and Rb^{2+}, Sr^{2+}, Ba^{2+}, Tl^{+}, Pb^{2+}, Eu^{2+} and REE^{3+} prefer the *M* site (D'Arco and Piriou, 1989; Kneip and Liebau, 1994) based on couple substitutions resulting from ionic radii similarities. In addition, Stix and Gorton (1990) suggest that light rare earth elements (LREE), ranging from La-Gd, are more effective than heavy rare earth elements (HREE), including Tb-Lu, Y and Sc, in entering the *M* sites of the feldspar crystal lattice. This is further substantiated by studies of trace element partitioning between alkali feldspar and silicic melts (e.g., Ren, 2004), and plagioclase and melts (e.g., Bindeman and Davis, 2000), which have shown that the partition coefficients of REE for feldspar decrease from La-Lu (i.e., with increase in atomic radius). The incorporation of some minor and trace elements results cell dimension modifications for certain end-member feldspars (Table 1.2).

Table 1.2: Modified cell dimensions of exotic end-member feldspars formed through synthesis experiments. Sourced from Smith (1974b) and references therein.

Formula	Feldspar Type	Cell dimensions					
		Nanometres			Degrees		
		a	***b***	***c***	***α***	***β***	***γ***
$PbAl_2Si_2O_8$	Celsian	0.839	1.305	1.433	90	115.2	90
$SrAl_2Si_2O_8$	Celsian	0.838	1.297	1.426	90	115.4	90
$RbFeGe_3O_8$	High sanidine	0.919	1.370	0.756	90	116.7	90
$RbGaGe_3O_8$	High sanidine	0.919	1.363	0.757	90	117.1	90
$RbAlGe_3O_8$	High sanidine	0.913	1.357	0.747	90	116.7	90
$RbGaSi_3O_8$	High sanidine	0.892	1.310	0.725	90	116.4	90
$RbAlSi_3O_8$	High sanidine	0.884	1.303	0.718	90	116.3	90
$RbAlSi_3O_8$	Low microcline	0.884	1.296	0.725	90.5	116.1	88.1
$KFeGe_3O_8$	High Sanidine	0.889	1.370	0.754	90	115.9	90
$KGaGe_3O_8$	High Sanidine	0.887	1.363	0.749	90	115.9	90
$KAlGe_3O_8$	High Sanidine	0.882	1.356	0.745	90	115.9	90
$KFeSi_3O_8$	High Sanidine	0.869	1.312	0.732	90	116.1	90
$KFeSi_3O_8$	Low microcline	0.868	1.310	0.734	90.7	116.1	86.2
$KGaSi_3O_8$	High Sanidine	0.867	1.309	0.721	90	116.1	90
$KGaSi_3O_8$	Low microcline	0.866	1.305	0.727	91.1	116.0	87.2
$NaGaGe_3O_8$	High albite	0.845	1.337	0.737	94.4	116.2	90.8
$NaAlGe_3O_8$	High albite	0.84	1.329	0.734	94.4	116.2	90.9
$NaGaSi_3O_8$	High albite	0.821	1.297	0.714	93.6	116.3	90.2
$NaGaSi_3O_8$	Low albite	0.817	1.286	0.720	94.4	116.5	87.2
$NaBSi_3O_8$	Low albite	0.783	1.236	0.680	93.3	116.4	92.1

1.2 Feldspar replacement reactions

With the exception of some rapakivi granites, larvikites and charnockites, alkali feldspars within plutonic rocks generally show evidence of recrystallization and areas of turbidity (related to microscale porosity). As mentioned previously, following crystallization, a homogeneous alkali feldspar crystal will undergo solid-state diffusion to form regular and coherent strain-controlled intergrowths (e.g., perthites). However, if such a crystal (at temperatures near the strain-free solvus) comes into contact with a fluid, it will recrystallize to some degree, coarsening the perthitic intergrowths and increasing turbidity. The resultant texture occurs as irregular and incoherent mosaics of Ab-rich and Or-rich subgrains, ranging in thickness from nm-mm (e.g., Fig. 1.7a, b; Parsons and Lee, 2009). This process is termed 'deuteric coarsening' (after Parsons and Brown, 1984) in relation to it occurring during the circulation of post-magmatic (e.g., deuteric) fluids, and the resultant texture is referred to as 'patch perthite', although nomenclature may vary dependent on texture morphology (e.g., 'vein perthite', which occurs as anastomosing veins across whole alkali feldspar crystals). Deuteric coarsening is generally considered to be isochemical with respect to bulk composition, although some minor and trace elements may be lost to the fluid (Parsons et al., 2009). Textural features observed in patch perthite are consistent with a coupled dissolution-reprecipitation reaction (CDRR), summarized by Putnis (2002) following previous work by Wang et al. (1995) and others. This type of replacement reaction couples dissolution of a pre-existing mineral with the rate of precipitation of new products at the site of reaction. Such reactions are typified by sharp interface reaction fronts between the parent and product phase, transient porosity development in the product phase and preservation of the original external volume of the parent phase (e.g. pseudomorphic replacement). A study on the Klokken intrusion in Greenland by Parsons et al. (2009) concluded that the patch perthite likely proceeded through thin fluid films which advanced as fronts through the initial coherent perthite texture.

Feldspar replacement reactions are not always isochemical. Albitization, for example, involves the non-isochemical replacement of pre-existing feldspar by Na-rich feldspar (albite), and is one of the most common hydrothermal aluminosilicate reactions in the Earth's upper crust (Perez and Boles, 2005). It is also associated with several other alteration types including scapolitization, sassuritization, sericitization and K-feldspathization (e.g., Garcia et al., 1996; Conor et al., 2010; Morad et al., 2010). Albitization may occur *in-situ* within plutonic rocks, typically affecting the original igneous plagioclase (although not restricted to), and also within sedimentary rocks during diagenesis, involving the replacement of clastic feldspars (e.g., Parsons et al., 2005). The texture albite varies dependent on reaction mechanism, precursor mineral/fluid chemistry and fluid/rock ratio. Albite replacing plagioclase in plutonic rocks is often observed to be fine-grained, highly porous and host to numerous co-precipitate minerals such as sericite, epidote, K-feldspar and hematite (e.g., Fig. 1.7c; Engvik et al., 2008). Features of this texture are consistent with CDRR (e.g., Fig. 1.7d; Plümper and Putnis, 2009). Pure albite (Ab_{99}), devoid of inclusions and micropores, has been observed in plutonic rocks, typically along rims of igneous plagioclase at the boundary between differently orientated alkali feldspar (summarized in detail by Smith, 1974a). Recent work has interpreted this texture to form as a result of deuteric coarsening or replacement of the adjacent alkali feldspar (e.g., Rong and Wang, 2016; Kontonikas-Charos et al., 2017). In contrast, high pressure or temperature and/or high fluid/rock ratios, can result in the formation of anomalous vein albite (e.g., eclogite facies metamorphism; Barnicoat, 1988) and granoblastic albite (e.g., greenschist metasediments; Kontonikas-Charos et al., 2014). Such textures differ significantly from the above albite. Albite veins are more commonplace within sedimentary sequences, and, in some cases, play a key role in remobilization of valuable elements (e.g., uraninite-albite veins from the Mistamisk Valley, Quebec, Canada; Kish and Cuney, 1981).

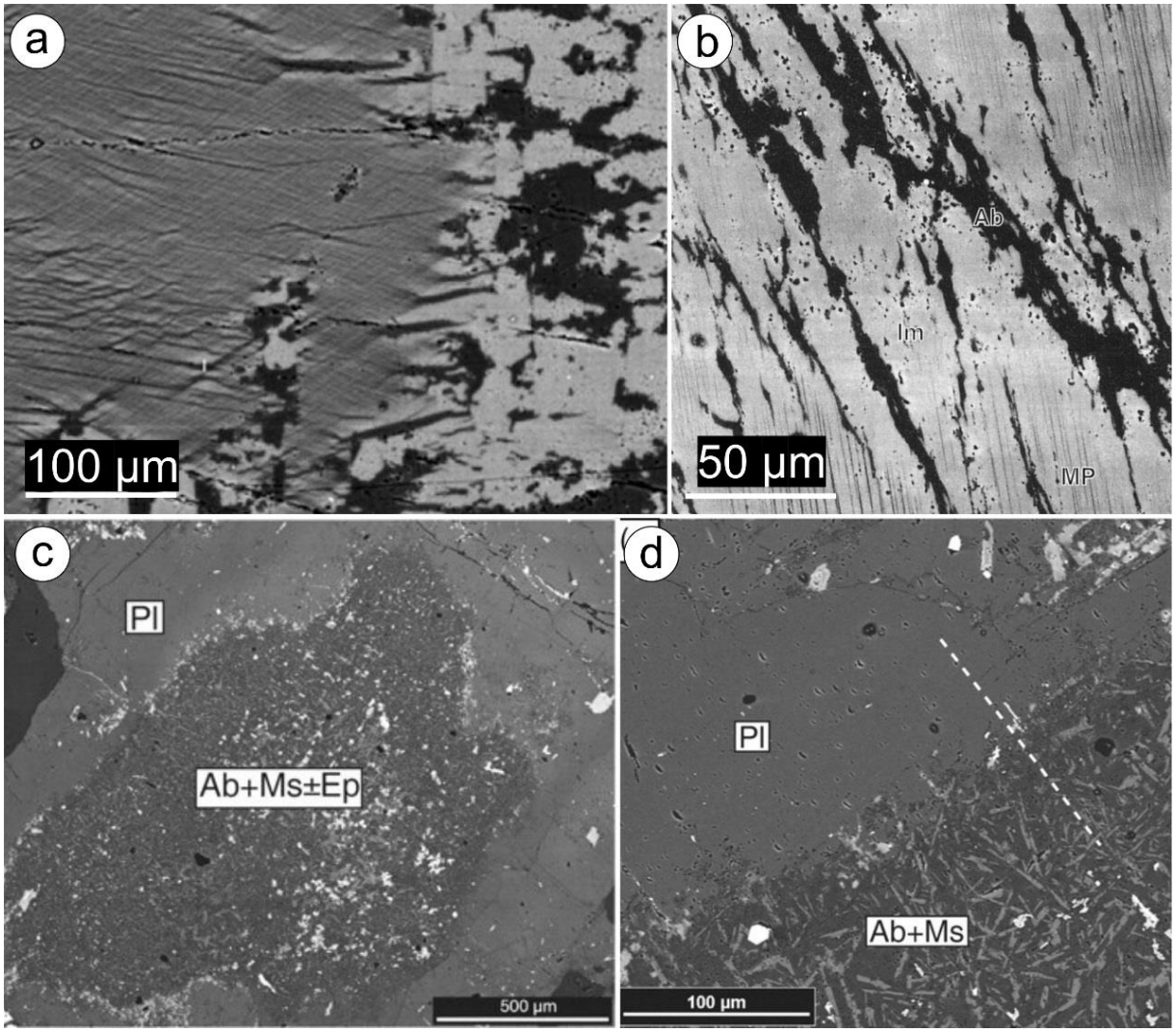

Figure 1.7: Back scatter electron images highlighting classic examples of feldspar replacement reactions compiled from the literature. (a) Braid cryptoperthite (grey) partially replaced by patch perthite mosaics as a result of deuteric coarsening in the Klokken syenite, Greenland (Parsons et al., 2009). (b) Replacement of microperthite (MP) by vein patch perthite (given by IM – intermediate microcline and Ab - albite) in the Shap granite, England (Lee and Parsons, 1997). Note the increased microporosity associated with the reaction. (c) Albitized core of igneous plagioclase (Pl) from a granitoid within the Scandinavian Igneous Belt (Plumper and Putnis, 2009). Albite (Ab) is accompanied by coprecipitation of muscovite (Ms) and epidote (Ep). (d) High magnification image of the reaction front between

plagioclase (Pl) and albite + muscovite (Ab + Ms) from the same granitoid in (c), supporting a coupled dissolution reprecipitation reaction (Plumper and Putnis, 2009).

The albitization of plagioclase involves a coupled substitution of (Ca^{2+} + Al^{3+}) by (Na^{+} + Si^{4+}). Hydrothermal replacement experiments of Hövelmann et al. (2010), in which oligoclase and labradorite crystals were re-equilibrated with aqueous sodium silicate solutions at 600 °C and 2 kbars, demonstrate that albitization of plagioclase is also accompanied by remobilization of REE and other trace elements, including Mg, Ti, Fe, Sr, Ba, Rb and Pb. Hövelmann et al. (2010) also found that released REE are dissolved in the fluid and potentially transported away from the site of dissolution to form discrete REE-minerals elsewhere within the system. Thus, CDRR can play an effective role in the (re)-distribution of minor/trace elements during fluid-rock interaction.

Combining observations of various feldspar replacement reactions can yield important geochemical implications. The initial coherent, strain-controlled alkali feldspar perthite textures, which only form during continuous and coherent exsolution, can be used as robust bulk chemical markers separating the later incoherent, irregular and strain-free patch perthite and albite, which often form via CDRR.

1.3 Iron-oxide copper-gold mineralization and the role of alteration

Iron-oxide copper-gold (IOCG) mineralization is presently considered part of a broad group of deposit types that form within ore systems spanning from the Archean to the Phanerozoic (Hitzman et al., 1992; Williams et al., 2005; Groves et al., 2010; Barton, 2014). Genetic models for these deposits are still much debated, particularly regarding the role of igneous rocks, the sources of metals and fluids, geodynamic settings (e.g., Barton and Johnson, 2004; Williams

et al., 2005; Chiaradia et al., 2006; Pollard, 2006; Groves et al., 2010), and relationship between IOCG, iron-oxide apatite (IOA) and iron-oxide alkali-altered (IOAA) deposits (Corriveau et al., 2016; Montreuil et al., 2016).

The discovery of the Olympic Dam deposit in 1975 provoked interest in a style of mineralization that appeared distinct from other deposit styles, and subsequently led to the conceptualization of IOCG systems (e.g., Hitzman et al., 1992). However, since then, the incorporation of numerous other deposits within the IOCG class has led to a broader range of defining characteristics. The latest and most comprehensive review of IOCG systems is given by Barton (2014). In general, the IOCG deposit class contain at least 10% of low-Ti Fe oxides (either hematite or magnetite) and elevated concentrations of Cu, Au, REE, P, U, Ag and Co (Barton, 2014). Moreover, they are temporally and spatially associated with Na-Ca-K metasomatism and are often typified by zoned, broad alteration haloes comprising early, barren albite, and, in most cases, a late, ore-hosting type of alteration (Barton, 2014). Albite-bearing alteration is part of a broader sodic (-calcic) alteration spectrum with various mineralogical expressions (Barton, 2014). The late ore-hosting alteration can be subdivided into deeper potassic (K-feldspar ± biotite) and upper hydrolytic (sericite ± chlorite ± carbonate) alteration, where magnetite and hematite are the dominant Fe-oxides, respectively. Sericitic alteration, in this case, may result from the breakdown of pre-existing potassium feldspars via interaction with an acidic fluid. Systems dominated by carbonate-rich protoliths are generally characterized by calc-silicate alteration (e.g., epidote + actinolite + clinopyroxene + calcic garnet) with the ore hosted within skarn lithologies. Based on gains or losses of different components, skarn formation is considered distinct from the Na-Ca alteration of aluminous igneous or sedimentary protoliths which can also produce calc-silicates, and is referred to as carbonate-hosted alteration (Barton, 2014). Table 1.3 compares and contrasts key metals and alteration types of selected IOCG deposits.

Table 1.3: Summary of metals, dominant Fe-oxide and alteration types for selected IOCG deposits

IOCG District	Deposit(s)	Key metals	Dominant Fe-oxide	Alteration assemblages				
				Na (-Ca)	Ca-Fe	K-Sk	Fe-K (L*T*)	Fe-K (H*T*)
Olympic Cu-Au Province (north)	Olympic Dam	Cu-Au-Ag-U-REE±Co	Hm-rich (±Mt)	x*	x		X	
	Prominent Hill, Carrapateena	Cu-Au-Ag±U±Co	Hm-rich (±Mt)				X	
Olympic Cu-Au Province (south)	Moonta-Wallaroo	Cu-Au-Ag	Hm + Mt	x	X			X
	Hillside	Cu-Au-Ag	Mt + Hm			x		x
Cloncurry	Ernest Henry	Cu-Au-Ag±U±Co	Mt-rich (±Hm)	X				X
Great Bear Magmatic Zone	NICO	Fe-Cu-Co-Au-Bi-W	Mt-rich (±Hm)	x	X			X
Kiruna	Kiruna	Fe(±Cu-Co)	Mt + Hm		X			
Andes	El Laco, Marcona, El Romeral	Fe(±Cu-Co)	Mt-rich (±Hm)		x		X	
	Raul-Condestable, Mina Justa	Cu-Au-Ag±U±Co	Mt + Hm	x	x			x
Carajas	Salobo, Alemao, Cristalino, La Candelaria	Cu-Au-Ag±U±Co	Mt + Hm	x				X
Missouri	Pea Ridge, Pilot Knob	Fe (±Cu-Co)	Mt + Hm		x			

Na (-Ca): albite-actinolite, Ca-Fe: amphibole-magnetite-apatite, K-Sk: K-feldspar-garnet skarn, Fe-K(L*T*): hematite-K-feldspar-sericite-carbonate-chlorite, Fe-K(H*T*): magnetite-biotite-K-feldspar. X – intense alteration, x – minor alteration. Data compiled from Harlov et al. (2002); (2016); Sillitoe (2003) and references therein; Williams et al. (2005) and references therein; Mark et al. (2006); Belperio et al. (2007); Xavier et al. (2010); Conor et al. (2010); Barton (2014) and references therein; Corriveau et al. (2016); Day et al. (2016). *see Kontonikas-Charos et al., 2017; Chapter 4.

Although regional Na-Ca-K metasomatism is a diagnostic property of IOCG deposits, it is also observed in other non-IOCG terranes. For example, widespread albitization is common in seafloor hydrothermal systems, and can also reflect regional-scale metasomatism related to metamorphic reactions involving evaporite-derived fluids (e.g., Alt, 1999). In addition, albitization of continental crust is recognized as a product of fluid-rock interaction with crustal fluids, sometimes producing regional-scale albitite terranes, e.g., Bamble Sector, SE Norway (e.g., Engvik et al., 2008; Plümper and Putnis, 2009). Moreover, Na-Ca alteration of gneisses, migmatites and granites relating to crustal-scale shear zones, can reconcentrate significant amounts of uranium, e.g., central Ukraine (Cuney et al., 2012). These examples clearly show that localized intense alkali alteration is independent of IOCG systems.

The role of sodic alteration in the formation of IOCG deposits has been addressed in the Eastern Mt. Isa Block, Australia (Oliver et al., 2004). Their results show that widespread alkali alteration (albitization in particular) can be modelled in terms of simple fluid-rock mixing, via small shifts in the K-feldspar/albite equilibrium curve. In addition, with increasing amounts of fluid-rock interaction, fluids became increasingly enriched in K, Fe and Ca. They also concluded that precipitation of Cu-Au mineralization was the result of mixing Cu-bearing brines of magmatic origin, modified by albitization, with S-bearing fluids or due to reaction between the brine and S-bearing rocks. Such studies highlight the importance of early, pre-mineralization alteration, during which feldspars are replaced by albite, mafic silicates by chlorite, and Fe-Ti-oxides by rutile (e.g., Barton, 2014), representing the initial stages of major element exchange during IOCG genesis.

1.4 Olympic Cu-Au Province and local geology of case studies

1.4.1 Olympic Cu-Au Province

The Olympic Cu-Au Province is one of the archetypal Mesoproterozoic examples of giant IOCG provinces, spanning 700 km across the eastern Gawler Craton, South Australia (Fig. 1.8a) and containing numerous deposits and prospects including Olympic Dam, Prominent Hill, Carrapateena, Cairn Hill, Hillside and Moonta-Wallaroo (Skirrow et al., 2002, 2007; Hayward and Skirrow, 2010). The Paleo- to Mesoproterozoic basement of the Olympic Cu-Au Province is attributed to one of the mobile belts that surround the Late Archean granulite facies core of the Gawler Craton. Two orogenic events are recognized: one associated with emplacement of the Donington granitoid suite at ~1850 Ma; and the Kimban orogeny at ~1730-1690 Ma (e.g., Hand et al., 2007). These affected the basinal rocks of the Hutchison Group (~2000-1850 Ma) and the Wallaroo Group (~1760-1740 Ma), respectively. Although deformation is considered to have largely ceased with the Kimban orogeny (e.g., ~1690 Ma), evidence for subsequent greenschist and lower amphibolite facies metamorphism is recognized in rocks of the Wallaroo Group within the Moonta-Wallaroo region. This metamorphic event, broadly termed the Kararan orogeny (e.g., Hand et al., 2007), is considered synchronous with emplacement of the Hiltaba Suite (HS) around 1598 ± 7 to 1575 ± 7 Ma (Cowley et al., 2003). It also produced regional-scale volcanism (Gawler Range Volcanics - GRV) and resulted in the formation of a silicic large igneous province covering 25,000 km^2 of the central Gawler Craton (e.g., Allen et al., 2008; Wade et al., 2012). Both intrusive and extrusive rocks include felsic and mafic components. The HS is comprised of both I- and A-type granitic batholiths (Flint, 1993) and is of similar composition to the GRV (Agangi et al., 2012).

The igneous rocks of the HS are considered to be temporally associated with Cu-Au mineralization throughout the Olympic Cu-Au Province, based on dating of magmatic and hydrothermal minerals (e.g., Johnson and Cross, 1995, Jagodzinski, 2005; Skirrow et al., 2007; Ciobanu et al., 2013; Reid et al., 2013). Alteration ranges from the 'end-member' sericite-hematite-breccia hosted type (e.g., Olympic Dam, Prominent Hill, Carrapateena), to skarn-hosted mineralization in the Punt Hill district (Reid et al., 2013), and strongly potassic- and/or sodic-altered and minor skarn-hosted mineralization at Moonta-Wallaroo and Hillside (Conor et al., 2010; Ismail et al., 2014). Unlike in other IOCG terranes in Australia (e.g., Cloncurry District), the Olympic Cu-Au Province also stands out with characteristic REE and U enrichment, irrespective of alteration style (e.g., Skirrow et al., 2007).

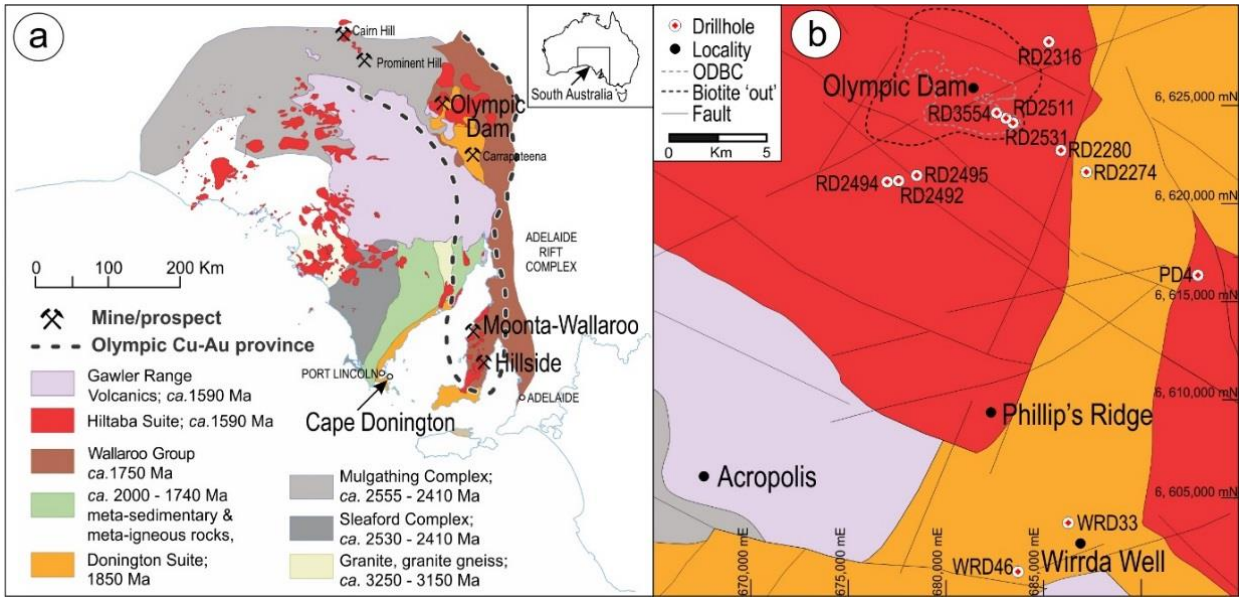

Figure 1.8: (a) Simplified regional geological map outlining various lithologies and deposits/prospects within the Gawler Craton and Olympic Cu-Au Province, South Australia. Larger font indicates sample suite areas. (b) Geological sketch map of bedrock in the Olympic Dam region displaying sampled drillholes and other prospects and localities within the area. From Kontonikas-Charos et al., (in review).

1.4.2 Olympic Dam (including Wirrda Well and Phillip's Ridge)

The Olympic Dam Cu-U-Au-Ag deposit (OD; 10,400 Mt tonnes @ 0.77 % Cu, 250 ppm U_3O_8, 0.32 ppm Au, 1 ppm Ag; BHP Billiton, 2016) is located in the north of the Olympic Cu-Au Province. Rocks of the Hutchison Group (~2000-1860 Ma), Donington Suite (~1845-1810 Ma) and Wallaroo Group equivalents (~1750 Ma) form the Paleoproterozoic basement of the Olympic Dam region (Creaser, 1989; Ferris et al., 2002; Jagodzinski, 2005). These units are unconformably overlain and intruded by felsic and mafic-ultramafic lithologies of the HS and GRV.

The HS intrusives are grouped together within the larger Burgoyne batholith, which makes up the basement of the northern Stuart Shelf (Creaser, 1989). The batholith is separated into two granitoid suites: the Wirrda Suite and the White Dam Suite, both of which comprise rocks varying from quartz monzodiorite to granite (Creaser, 1989). The Roxby Downs Granite (RDG) and Horn Ridge Quartz Monzonite (HRQM) are affiliated to the Wirrda Suite, which is situated on the western side of the Burgoyne batholith (Creaser, 1996). Creaser (1989) had earlier stressed the fundamental meta- to peraluminous, I-type character of the Wirrda Suite granitoid complex but also noted geochemical and mineralogical similarities with A-type granites (enrichment in K_2O, high FeO/MgO, and low H_2O content).

The GRV are comprised of a lower sequence, 0.5-3 km-thick, ranging in composition from basalt to rhyolite and minor volcaniclastic facies (e.g., ignimbrites), while the upper GRV succession is 250-300 m thick, of primarily rhyolitic and dacitic lava units (McPhie et al., 2008). The GRV is also intruded by porphyritic rhyolitic dykes and granites belonging to the HS (McPhie et al., 2008). In addition to Mesoproterozoic mafic-ultramafic units, weakly altered basaltic to doleritic dykes of the Gairdner Dyke Swarm (U-Pb apatite dated at 825±18 Ma; Huang et al., 2015) are also observed within the Olympic Dam area.

Deposition of Cu-U-Au-Ag mineralization at Olympic Dam is considered contemporaneous with the ~1590 Ma event (e.g., Johnson and Cross, 1995; Jagodzinski, 2005; Skirrow et al., 2007; Ciobanu et al., 2013; Courtney-Davies et al., 2016). Hydrothermal breccias of the Olympic Dam Breccia Complex (ODBC) host the Cu-U-Au-Ag mineralization and are contained within the RDG. Compositions and textures within the ODBC are gradational, and comprise a continuum from sericite-hematite-altered granite through mineralized, hematite-rich breccias to barren hematite-quartz breccias in the deposit centre (Ehrig et al., 2012). The majority of mineralization is closely associated with the hematite-rich breccias (Fe > 20 wt. %) and occasionally within the granite-rich breccias (Fe ~5 wt. %; Ehrig et al., 2012). Principal Cu-bearing minerals are chalcopyrite, bornite and chalcocite (including djurleite-digenite and other Cu-sulphides; Ciobanu et al., 2017), along with minor native copper, covellite and tenorite/cuprite (Ehrig et al., 2012). Uranium is mainly present as uraninite/pitchblende, coffinite and brannerite. Recent work has shown numerous uraninite crystallization events, as well as multiple stages of U dissolution and reprecipitation within the Olympic Dam deposit (Macmillan et al., 2016a, b; c, in press). Moreover, widespread U-rich hematite has been identified at Olympic Dam (Ciobanu et al., 2013), and may prove useful as a future geochronological tool for Fe-ore mineralization in the Olympic Cu-Au Province and elsewhere. Rare earth element mineralization is typically in the form of bastnäsite and florencite, but synchysite, monazite and xenotime are also recognized (Ehrig et al., 2012).

Despite the complexity and variable intensity of brecciation and alteration within the ODBC, there appears to be significant mineralogical and geochemical zonation. From periphery to centre, several sulphide zones are recognized: chalcopyrite-pyrite, chalcopyrite-bornite, bornite-chalcocite and chalcocite (Ehrig et al., 2012). In addition, polymetallic (Zn-Pb) mineralization is also recognized at the ODBC margins and siderite, fluorite and barite are zoned across the deposit (Ehrig et al., 2012).

Found within a large concentric gravity and magnetic anomaly, the Wirrda Well prospect is located approximately 20 km SSE of Olympic Dam (Fig. 1.8b). Mineralization is primarily hosted within a sheared, variably mylonized, K-feldspar megacrystic Donington Suite granite and deformed mafic dykes of the same age (Ehrig, 2013). A significant portion of the brecciation and mineralization is concentrated along the contacts of the intrusive rocks. In addition, volcanic sequences, attributed to the GRV, occur within a faulted block of possible post-mineralization origin within the northern zone. Mafic dykes occur throughout the prospect and are recognized as pre-, syn- and post-mineralization in age (Huang et al., 2016).

Mineralization within the Wirrda Well prospect consists of breccias and vein networks containing magnetite, apatite (± hematite ± carbonate ± quartz ± sulphides) accompanied by widespread chlorite-sericite alteration. Hematite + magnetite are the dominant iron-oxides, whereas chalcopyrite + pyrite ± bornite ± chalcocite are the main Cu-(Fe)-sulphides. Magnetite + pyrite + apatite + chlorite assemblages are dominant at depth and grade upwards into minor zones of bornite-chalcocite mineralization with increased abundance of hematite.

The Phillip's Ridge prospect is located 17 Km SE of Olympic Dam (Fig. 1.8b), near the contact between the HS and Donington Suite granite. Quartz monzodiorite is the dominant lithology in the area, and is interpreted as the equivalent rock reported in Granite Suite #3 in Creaser (1989). Widespread sodic-calcic alteration has been recognized across the area, resulting in alteration assemblages consisting of albite + epidote (± allanite) + actinolite + titanite ± garnet (hydrogarnet with composition ~$Adr_{56}Grs_{44}$) (Kontonikas-Charos et al., in review). This mineralogical association is similar to early, deep sodic-calcic alteration preserved within numerous IOCG systems across the Olympic Cu-Au Province.

1.4.3 Moonta Wallaroo region

The Moonta-Wallaroo region, located in the north-west of the Yorke Peninsula, contains IOCG mineralization (with hematite/magnetite and chalcopyrite, pyrite, bornite as the characteristic minerals) hosted within felsic porphyry rocks associated with K-Fe-metasomatism (Morales-Ruano et al., 2002; Conor et al., 2010). The region is an example of an IOCG-hosting terrane in which regional-scale alkali alteration is recognized in different lithologies (e.g., Cowley et al., 2003; Conor et al., 2010; Kontonikas-Charos et al., 2014). Copper-Au mineralization is contained within the Moonta Porphyry Member; a variably altered rhyolite-rhyodacite (U-Pb zircon age 1737±5 Ma; Fanning et al., 1988), and the Doora Member; a schistose, Fe-rich unit with varying hornfels, amphibolite and silicate facies (Parker, 1993; Cowley et al., 2003). Both units are constituents of the ~1750 Ma Wallaroo Group; a suite of siltstone-dominated metasedimentary, felsic and mafic metavolcanic rock packages, including the variably metamorphosed, plagioclase-phyric rhyolitic-rhyodacitic Wardang Volcanics Member, and minor dolomitic/limestone sequences attributed to the New Cornwall Member (Conor, 1995; Cowley et al., 2003; Conor et al., 2010). The Wallaroo Group has been intruded by the Arthurton and Tickera granitoids (variable monzogranites, quartz monzonites and leucotonalites) and the Curramulka Gabbronorite (metamorphosed to amphibolite facies), all affiliated with the HS (Cowley et al., 2003). Both the Arthurton and Tickera granitoids show evidence of alkali alteration, in this case albitization (e.g., Kontonikas-Charos et al., 2014). The Oorlano Metasomatite (a Fe-rich, skarn-like unit composed primarily of calc-silicates and feldspars) is found along the boundary of the Tickera Granite and Wallaroo Group, and is interpreted to reflect metasomatism related to the intrusion of the HS in the Moonta Wallaroo region (Cowley et al., 2003). Regional-scale alkali alteration in the Moonta-Wallaroo area is postulated to be sourced from evaporitic sediments, observed in various parts of the Wallaroo Group (Conor et al., 2010).

1.4.4 Hillside

The Hillside Cu-Au deposit, located within the N-S-striking Pine Point Fault Zone along the eastern coast of the Yorke Peninsula, South Australia, is defined by a sequence of highly deformed metasediments of the ~1750 Ma Wallaroo Group intruded by granites, micro- and porphyritic gabbros and gabbro-diorites, attributed to the HS (Conor et al., 2010). Structurally, Cu-Au-(U) mineralization is hosted within steeply-dipping, N-S trending skarn and associated breccia bodies of varying dimensions (Conor et al., 2010). As in the Moonta-Wallaroo area, the magnetite-dominant mineralization and skarn-type alteration at Hillside (Conor et al., 2010; Ismail et al., 2014) is thought to represent hydrothermal activity at a relatively deep crustal level, thus contrasting with shallower (?), brecciated hematite-sericite-dominant mineralization at Olympic Dam. Evidence of early high temperature potassic alteration, expressed as a K-feldspar ± biotite + magnetite ± bornite ± chalcocite assemblage, is commonly displayed in gabbroic rocks from the Hillside area (Conor et al., 2010; Ismail, 2016), whereas partial chloritization and sericitization of mafics are common in the Hillside granite. In addition, late-stage K-feldspar alteration is observed to replace pre-existing plagioclase within the host rocks (Conor et al., 2010; Ismail et al., 2014). Such alteration styles are characteristic of HS granites at Olympic Dam and Moonta-Wallaroo (e.g., Kontonikas-Charos et al., 2014; 2017). The typical skarn assemblage comprises garnet, pyroxene and epidote-group minerals (Ismail et al., 2014). They are predominantly fine grained, however coarser grained, almost monomineralic garnet skarns (garnetites) are also present (Ismail et al., 2014). Characteristically, these skarns are extremely rich in a variety of trace elements, of which REE, Y, Sn and other HFSE are particularly abundant in andradite skarn (Y up to several wt. %; Ismail et al., 2014; Ismail 2016). Magnetite, hematite, pyrite and Cu–(Fe)-sulphides (chalcopyrite, chalcocite and bornite) are widespread within the Hillside skarns and less so in the granitic and gabbroic rocks (Ismail et al., 2014; Ismail 2016). Chalcopyrite is the main Cu-Fe-sulphide in the ore and

increases in abundance during the prograde to retrograde skarn transition, which is marked by replacement of primary magnetite by hematite (Ismail, 2016).

Uranium-Pb dating of hydrothermal titanite and allanite (1601 ± 16 Ma to 1584 ± 7 Ma) indicates that alteration at Hillside is broadly contemporaneous with the emplacement of Hiltaba suite granites (Gregory et al., 2011). This, along with a magnetic-gravity anomaly, prominent structural control and Cu-(Fe)-sulphide assemblage, highlights Hillside's significance in the overall understanding of the Olympic Cu-Au Province.

1.4.5 Cape Donington

The basement suite at Cape Donington (Eyre Peninsula) comprises Archean orthogneisses, granite and granodiorites, as well as felsic and mafic volcanics of the Archean-Paleoproterozoic Sleaford complex (2560-2420 Ma; Fanning, 2002; Jagodzinski et al., 2012). Following deposition of the Hutchison Group metasediments (~2000-1850 Ma), Donington Suite intrusive rocks (varying in composition from gabbronorite to leucogranite) were emplaced around 1850 Ma (U-Pb zircon ages; Fanning, 1997). Following emplacement of the Donington Suite, transpressional convergence during the Kimban Orogeny (~1740-1700 Ma) resulted in regional metamorphism at amphibolite to granulite facies, and associated syn-metamorphic deformation of the Archean-Proterozoic crust, as well as the formation of the Kalinjala Mylonite Zone (KMZ), which separates the Donington Suite from the Hutchison Group (Ferris et al., 2002). Local geology at Cape Donington, to the east of the KMZ, consists of outcropping coarse-grained, porphyritic, orthopyroxene-bearing granitoids (attributed to the Donington Suite), crosscutting metabasaltic and doleritic dykes, and biotite-hornblende-quartz-feldspathic gneisses (Mortimer, 1984).

1.5 Research objectives and thesis structure

Conceptualization of this study was tied to results from the 'Hypogene alteration in IOCG systems' research project within the Deep Exploration Technologies Cooperative Research Centre (DET CRC). This project invoked the idea that feldspar alteration can track REE behaviour, mobility and relative enrichment throughout alteration stages in magmatic-hydrothermal systems, particularly IOCGs. The aim was to link feldspar alteration and replacement mechanisms to REE enrichment, based on fractionation patterns in feldspars during evolution from magmatic to hydrothermal stages in IOCGs. Gaining access to Olympic Dam and other IOCG systems within South Australia provided a unique opportunity to test this idea within one of the largest metallogenic belts in the world, the Olympic Cu-Au-Province.

A combination of hand specimens, polished blocks and thin sections were used for this research. In some cases, drillcore logging and sampling was necessary to target specific intervals of interest. Following preparation, samples were analyzed using a range of qualitative and quantitative microanalytical techniques capable of characterization at different scales of observation. These included microscopy (optical, scanning electron and transmission), electron probe microanalysis, laser-ablation inductively coupled plasma mass spectrometry and focussed ion beam scanning electron microscopy, and are summarized in **Chapter 2**.

The IOCG deposit class remains rather contentious due to the misclassification of some systems, which barely meet the requirements for IOCGs (e.g., magnetite-bearing porphyry Cu-Au deposit; Williams, 2010). Consequently, some fundamental properties of IOCG systems are notably absent in many deposits. Copper-Au mineralization in the Moonta-Wallaroo region is hosted by multiple lithologies and occurs at greater depths than the typical sericite-hematite-breccia IOCG mineralization style hosted in shallower terranes (e.g., Olympic Dam, Prominent Hill). Therefore, any geochemical interpretations must account for diversity in host rock

lithology. **Chapter 3** focusses on tracking the temporal evolution of the deeper-style IOCG system at Moonta-Wallaroo, from protolith through to early-late mineralization stages using mineral reactions associated with regional alkali alteration (namely, albitization), their relative textures and REY fractionation patterns. The study showed how feldspar alteration is expressed across various lithologies within a single IOCG system, and that different styles of fluid/rock interaction and resultant mineral textures can have a direct impact on trace element partitioning in minerals (e.g., granoblastic albite accounting for the whole-rock REE budget in the absence of other mineral hosts).

Although, regional alkali alteration is a diagnostic property of the IOCG deposit class, it has yet to be reported from Olympic Dam; the deposit which defines the IOCG *sensu stricto*. Given that mineralization is hosted within the RDG at Olympic Dam, changes in feldspar textures and geochemistry from magmatic to hydrothermal stages within a single lithology can be tracked based on proximity to mineralization. This is covered by a comprehensive summary of feldspar mineralogy, geochemistry and alteration at Olympic Dam given in **Chapter 4**. The results of this study show how the major element exchange (loss of Na → gain of K and Fe → Cu-Au-REE-Mo-U mineralization) occurring within the Olympic Dam deposit is expressed in the form of systematic changes in feldspar textures and chemistry. Moreover, they highlight the ability of widespread feldspar replacement reactions (with a coupled-dissolution re-precipitation mechanism) to produce significant microporosity within the host rocks to facilitate subsequent fluid/rock interaction and mineralization. A combination of geothermometry (from feldspars) and geobarometry (plagioclase-amphibole) estimates provided constraints on minimum crystallization temperatures (~765 °C) and emplacement depth (2.2 kbar corresponding to ~6 km) for the RDG.

The presence of significant albitization is also reported from the RDG in **Chapter 4**, previously unrecognized at Olympic Dam, which subsequently led to a deposit-scale investigation on feldspar alteration via hyperspectral techniques that confirmed albitization preserved at depth and to the periphery of the ODBC (Mauger et al., 2016).

A follow-up study on feldspars was undertaken to constrain the contribution and distribution of REE elements within the Roxby Downs Granite, and compare this to other IOCG terranes within the Olympic Cu-Au province and pre-Hiltaba suite lithologies, such as the Donington Suite granite (**Chapter 5**). This was achieved by analyzing igneous and hydrothermal feldspars from across Olympic Dam and other terranes to produce fractionation patterns allowing for a visual representation of REE behaviour. Although feldspars are not often considered good hosts of REE, the results of this study show variation in ∑REE (~1-100 ppm) and indicate an increase in mobility of REE from feldspars with proximity to the ODBC. In addition, results indicate that feldspars in the RDG are significantly enriched in lattice-bound REE relative to Donington Suite granite (from both Wirrda Well and Cape Donington).

Feldspars containing anomalous concentrations of REE and Fe in solid solution were reported from **Chapters 3 and 4**. This was based on nanoscale investigations, which are critical in linking macro- to sub-microscale observations for a holistic understanding of mineral-chemistry relationships (e.g., Ciobanu et al., 2016, and references therein). It is thus imperative to understand whether crystal-structure modifications or lattice-scale disorder are responsible for incorporation of trace elements and their subsequent release from a host mineral (e.g., REE from feldspars), and if so, to identify the mechanisms and timing of this, and to assess how such crystal structural modification will be expressed texturally at different scales. **Chapter 6** focusses on these issues from several representative feldspar and REE-mineral (e.g., REE-fluorocarbonates) textures across the Olympic Dam and Hillside deposits. The study linked

feldspar alteration from post-magmatic to hydrothermal stages at the nanoscale to constrain the behaviour of REE associated with latter Fe-metasomatism at Olympic Dam. Results revealed that in many cases, the changes in REE fractionation patterns were controlled by sub-μm scale inclusions within feldspars, such as epidote (Olympic Dam) and titanite + andradite (Hillside), rather than crystal structure modifications.

Chapter 7 provides a summary of key findings and implications of this research, as well as identifying areas for future investigation. Additional material, such as conference contributions, co-authored publications and appendices, are given in **Chapter 8.** A full reference list is provided in **Chapter 9**.

Agangi, A., Kamenetsky, V.S., McPhie, J., 2012. Evolution and emplacement of high fluorine rhyolites in the Mesoproterozoic Gawler silicic large igneous province, South Australia. Precambrian Research 208, 124-144.

Allen, S., McPhie, J., Ferris, G., Simpson, C., 2008. Evolution and architecture of a large felsic igneous province in western Laurentia: the 1.6 Ga Gawler Range Volcanics, South Australia. Journal of Volcanology and Geothermal Research 172, 132-147.

Alt, J.C., 1999. Hydrothermal alteration and mineralization of oceanic crust: mineralogy, geochemistry and processes. Reviews in Economic Geology 8, 133–155.

Barnicoat, A., 1988. The mechanism of veining and retrograde alteration of Alpine eclogites. Journal of Metamorphic Geology 6, 545-558.

Barton, M., 2014. Iron oxide (–Cu–Au–REE–P–Ag–U–Co) systems. Treatise on Geochemistry (second edition, volume 13): Amsterdam, Elsevier, 515-541.

Barton, M.D., Johnson, D.A., 2004. Footprints of Fe-oxide (-Cu-Au) systems. University of Western Australia Special Publication 33, 112-116.

Belperio, A., Flint, R., Freeman, H., 2007. Prominent Hill: A hematite-dominated, iron oxide copper-gold system. Economic Geology 102, 1499-1510.

BHP Billiton, 2016. http://www.bhpbilliton.com/home/investors/annualreporting2016.pdf

Bindeman, I. N., Davis, A. M., 2000. Trace element partitioning between plagioclase and melt: investigation of dopant influence on partition behavior. Geochimica et Cosmochima Acta 64:2863-2878.

Bychkov, A., Kotelnikov, A., Romanenko, I., Senderov, E., 1989. Effect of isomorphic replacement of silicon by phosphorus on structural peculiarities of feldspars. Rossiiskaya Akademiya Nauk Savelevskii Per., Moscow, Russia, pp. 310-313.

Chiaradia, M., Banks, D., Cliff, R., Marschik, R., De Haller, A., 2006. Origin of fluids in iron oxide–copper–gold deposits: constraints from $\delta^{37}Cl$, $^{87}Sr/^{86}Sr_i$ and Cl/Br. Mineralium Deposita 41, 565-573.

Ciobanu, C.L., Wade, B.P., Cook, N.J., Mumm, A.S., Giles, D., 2013. Uranium-bearing hematite from the Olympic Dam Cu–U–Au deposit, South Australia: a geochemical tracer and reconnaissance Pb–Pb geochronometer. Precambrian Research 238, 129-147.

Ciobanu, C.L., Cook, N.J., Maunders, C., Wade, B.P., Ehrig, K. 2016. Focused ion beam and advanced electron microscopy for minerals: Insights and outlook from bismuth sulphosalts. Minerals, 6(4), 112.

Ciobanu, C.L., Cook, N.J., Ehrig, K., 2017. Ore minerals down to the nanoscale: Cu-(Fe)-sulphides from the iron oxide copper gold deposit at Olympic Dam, South Australia. Ore Geology Reviews, 81, 1218-1235.

Colville, A.A., Ribbe, P.H., 1968. The crystal structure of an adularia and a refinement of the structure of orthoclase. American Mineralogist 53, 25-37.

Conor, C., 1995. Moonta-Wallaroo region: an interpretation of the geology of the Maitland and Wallaroo 1: 100 000 sheet areas. Mines and Energy South Australia, Open File Envelope 8886.

Conor, C., Raymond, O., Baker, T., Teale, G., Say, P., Lowe, G., 2010. Alteration and Mineralisation in the Moonta-Wallaroo Cu-Au Mining Field Region, Olympic Domain, South Australia. In Porter, T.M. (Ed.), Hydrothermal Iron Oxide Copper-Gold and Related Deposits: A Global Perspective 3, PGC Publishing, Adelaide, 1-24.

Corriveau, L., Montreuil, J.-F., Potter, E., 2016. Alteration facies linkages among iron oxide copper-gold, iron oxide-apatite, and affiliated deposits in the Great Bear magmatic zone, Northwest Territories, Canada. Economic Geology 111, 2045-2072.

Courtney-Davies, L., Zhu, Z., Ciobanu, C.L., Wade, B.P., Cook, N.J., Ehrig, K., Cabral, A.R., Kennedy, A., 2016. Matrix-matched iron-oxide laser ablation ICP-MS U–Pb geochronology using mixed solution standards. Minerals 6, 85.

Cowley, W., Conor, C., Zang, W., 2003. New and revised Proterozoic stratigraphic units on northern Yorke Peninsula. MESA Journal 29, 46-58.

Creaser, R.A., 1989. The geology and petrology of Middle Proterozoic felsic magmatism of the Stuart Shelf, South Australia. La Trobe University, Melbourne.

Creaser, R.A., 1996. Petrogenesis of a Mesoproterozoic quartz latite-granitoid suite from the Roxby Downs area, South Australia. Precambrian Research 79, 371-394.

Cuney, M., Emetz, A., Mercadier, J., Mykchaylov, V., Shunko, V., Yuslenko, A., 2012. Uranium deposits associated with Na-metasomatism from central Ukraine: a review of some of the major deposits and genetic constraints. Ore Geology Reviews 44, 82-106.

D'Arco, P., Piriou, B., 1989. Fluorescence spectra of Eu^{3+} in synthetic polycrystalline anorthite: Distribution of Eu^{3+} in the structure. The American mineralogist 74, 191-199.

Day, W.C., Slack, J.F., Ayuso, R.A., Seeger, C.M., 2016. Regional geologic and petrologic framework for iron oxide ± apatite ± rare earth element and iron oxide copper-gold deposits of the Mesoproterozoic St. Francois Mountains terrane, southeast Missouri, USA. Economic Geology 111, 1825-1858.

Ehrig, K., 2013. Geology of the Wirrda Well IOCG deposit. Powerpoint presentation, 10th Annual SA Exploration and Mining Conference, Adelaide. http://www.saexplorers.com.au

Ehrig, K., McPhie, J., Kamenetsky, V., 2012. Geology and mineralogical zonation of the Olympic Dam Iron Oxide Cu-U-Au-Ag deposit, South Australia. In: Hedenquist J.W., Harris, M., Camus, F., (Eds.), Geology and Genesis of Major Copper Deposits and Districts of the World: A Tribute to Richard H. Sillitoe, 16. SEG Special Publication, 237–267.

Engvik, A.K., Putnis, A., Gerald, J.D.F., Austrheim, H., 2008. Albitization of granitic rocks: the mechanism of replacement of oligoclase by albite. The Canadian Mineralogist 46, 1401-1415.

Fanning, C.M., 1997. Geochronological synthesis of southern Australia. Part II. The Gawler Craton. South Australian Department of Mines and Energy, Open file envelope 8918 (unpubl.)

Fanning, C.M., 2002. Gawler Craton: synthesis of recent SHRIMP U–Pb geochronology. In: Gawler Craton 2002: State of Play. Department of Primary Industries and Resources Workshop Proceedings (CD). Office of Minerals and Energy Resources, South Australia.

Fanning, C., Flint, R., Parker, A., Ludwig, K., Blissett, A., 1988. Refined Proterozoic evolution of the Gawler craton, South Australia, through U-Pb zircon geochronology. Precambrian Research 40, 363-386.

Ferris, G.M., Schwarz, M.P., Heithersay, P., 2002. The geological framework, distribution, and controls of Fe-oxide Cu–Au mineralisation in the Gawler Craton, South Australia: Part 1—Geological and tectonic framework. In Porter, T.M. (Ed.), Hydrothermal iron oxide copper–gold and related deposits: a global perspective 2, PGC Publishing, Adelaide, 9-32.

FitzGerald, J.D., Parise, J.B., Mackinnon, I.D.R., 1986. Average structure of an An_{48} plagioclase from the Hogarth Ranges. American Mineralogist 71, 1399-1408.

Fleet, M.E., 1988. Tetrahedral-site occupancies in reedmergnerite and synthetic boron albite ($NaBSi_3O_8$). American Mineralogist 77, 76-84.

Fleet, S., Ribbe, P., 1965. An electron-microscope study of peristerite plagioclases. Mineralogical Magazine 35, 165-176.

Flint, R., 1993. Hiltaba suite. The Geology of South Australia 1, 127-131.

Garcia, D., Pascal, M.-L., Roux, J., 1996. Hydrothermal replacement of feldspars in igneous enclaves of the Velay granite and the genesis of myrmekites. European Journal of Mineralogy 8, 703-718.

Gay, P., Smith, J., 1955. Phase relations in the plagioclase felspars: composition range An_0 to An_{70}. Acta Crystallographica 8, 64-65.

Goldschmidt, V.M., 1937. The principles of distribution of chemical elements in minerals and rocks. The seventh Hugo Müller Lecture, delivered before the Chemical Society on March 17th, 1937. Journal of the Chemical Society (Resumed), 655-673.

Grove, T.L., Ferry, J.M., Spear, F.S., 1983. Phase transitions and decomposition relations in calcic plagioclase. American Mineralogist 68, 41-59.

Groves, D.I., Bierlein, F.P., Meinert, L.D., Hitzman, M.W., 2010. Iron Oxide Copper-Gold (IOCG) Deposits through Earth History: Implications for Origin, Lithospheric Setting, and Distinction from Other Epigenetic Iron Oxide Deposits. Economic Geology 105, 641-654.

Hand, M., Reid, A., Jagodzinski, L., 2007. Tectonic framework and evolution of the Gawler Craton, southern Australia. Economic Geology 102, 1377-1395.

Harlov, D.E., Andersson, U.B., Förster, H.-J., Nyström, J.O., Dulski, P., Broman, C., 2002. Apatite–monazite relations in the Kiirunavaara magnetite–apatite ore, northern Sweden. Chemical Geology 191, 47-72.

Harlov, D.E., Meighan, C.J., Kerr, I.D., Samson, I.M., 2016. Mineralogy, chemistry, and fluid-aided evolution of the Pea Ridge Fe oxide-(Y+ REE) deposit, southeast Missouri, USA. Economic Geology 111, 1963-1984.

Hitzman, M.W., Oreskes, N., Einaudi, M.T., 1992. Geological characteristics and tectonic setting of Proterozoic iron oxide (Cu-U-Au-REE) deposits. Precambrian Research 58, 241-287.

Hövelmann, J., Putnis, A., Geisler, T., Schmidt, B.C., Golla-Schindler, U., 2010. The replacement of plagioclase feldspars by albite: observations from hydrothermal experiments. Contributions to Mineralogy and Petrology 159, 43-59.

Huang, Q., Kamenetsky, V.S., McPhie, J., Ehrig, K., Meffre, S., Maas, R., Thompson, J., Kamenetsky, M., Chambefort, I., Apukhtina, O., 2015. Neoproterozoic (ca. 820–830 Ma) mafic dykes at Olympic Dam, South Australia: Links with the Gairdner Large Igneous Province. Precambrian Research 271, 160-172.

Huang, Q., Kamenetsky, V.S., Ehrig, K., McPhie, J., Kamenetsky, M., Cross, K., Meffre, S., Agangi, A., Chambefort, I., Direen, N.G., 2016. Olivine-phyric basalt in the Mesoproterozoic Gawler silicic large igneous province, South Australia: Examples at the Olympic Dam Iron Oxide Cu–U–Au–Ag deposit and other localities. Precambrian Research 281, 185-199.

Ismail, R., 2016. Spatial-Temporal Evolution of Skarn Alteration in IOCG Systems: Evidence from Petrography, Mineral Trace Element Signatures and Fluid Inclusion Studies at Hillside, Yorke Peninsula, South Australia. Unpublished Ph.D. thesis, The University of Adelaide.

Ismail, R., Ciobanu, C.L., Cook, N.J., Teale, G.S., Giles, D., Mumm, A.S., Wade, B., 2014. Rare earths and other trace elements in minerals from skarn assemblages, Hillside iron oxide–copper–gold deposit, Yorke Peninsula, South Australia. Lithos 184–187, 456-477.

Jagodzinski, E., 2005. Compilation of SHRIMP U-Pb geochronological data, Olympic Domain, Gawler Craton. South Australia, 2001-2003. Geoscience Australia Record 2005/020

Jagodzinski, E.A., Reid, A.J., Hand, M., 2012. SHRIMP U-Pb geochronology of Archaean to Palaeoproterozoic rocks from southern Eyre Peninsula. Report book 2012/00015,

Department of Manufacturing, Trade, Innovation, Resources and Energy, South Australia, Adelaide.

Johnson, J.P., Cross, K.C., 1995. U-Pb geochronological constraints on the genesis of the Olympic Dam Cu-U-Au-Ag deposit, South Australia. Economic Geology 90, 1046-1063.

Kish, L., Cuney, M., 1981. Uraninite-albite veins from the Mistamisk Valley of the Labrador Trough, Quebec. Mineralogical Magazine 44, 471-483.

Kneip, H.-J., Liebau, F., 1994. Feldspars with trivalent non-tetrahedral cations: Experimental studies in the system $NaAlSi_3O_8$-$CaAl_2Si_2O_8$-$LaAl_3SiO_8$. European Journal of Mineralogy 6, 87-98.

Kontonikas-Charos, A., Ciobanu, C.L., Cook, N.J., 2014. Albitization and redistribution of REE and Y in IOCG systems: Insights from Moonta-Wallaroo, Yorke Peninsula, South Australia. Lithos 208–209, 178-201.

Kontonikas-Charos, A., Ciobanu, C.L., Cook, N.J., Ehrig, K., Krneta, S., Kamenetsky, V.S., 2017. Feldspar evolution in the Roxby Downs Granite, host to Fe-oxide Cu-Au-(U) mineralisation at Olympic Dam, South Australia. Ore Geology Reviews 80, 838-859.

Kontonikas-Charos, A., Ciobanu, C.L., Cook, N.J., Ehrig, K., Krneta, S. and Kamenetsky, V.S. (in review) Rare earth element geochemistry of feldspars: Examples from Fe-oxide Cu-Au systems in the Olympic Cu-Au Province, South Australia. Mineralogy and Petrology.

London, D., Černý, P., Loomis, J.L., Pan, J.J., 1990. Phosphorus in alkali feldspars of rare-element granitic pegmatites. Canadian Mineralogist, 28(4), 771-786.

Macmillan, E., Cook, N.J., Ehrig, K., Ciobanu, C.L., Pring, A., 2016a. Uraninite from the Olympic Dam IOCG-U-Ag deposit: Linking textural and compositional variation to temporal evolution. American Mineralogist 101, 1295–1320.

Macmillan, E., Ciobanu, C.L., Ehrig, K., Cook, N.J., Pring, A., 2016b. Chemical zoning and lattice distortion in uraninite from Olympic Dam, South Australia. American Mineralogist 101, 2351-2354.

Macmillan, E., Ciobanu, C.L., Ehrig, K., Cook, N.J., Pring, A., 2016c. Replacement of uraninite by bornite via coupled dissolution-reprecipitation: Evidence from texture and microstructure. The Canadian Mineralogist 54, 1369-1383.

Macmillan, E., Cook, N.J., Ehrig, K., Pring, A. Chemical and textural interpretation of late-stage coffinite and brannerite from the Olympic Dam IOCG-Ag-U deposit. Mineralogical Magazine (in press).

Mark, G., Oliver, N.H., Williams, P.J., 2006. Mineralogical and chemical evolution of the Ernest Henry Fe oxide–Cu–Au ore system, Cloncurry district, northwest Queensland, Australia. Mineralium Deposita 40, 769-801.

McPhie, J., DellaPasqua, F., Allen, S., Lackie, M., 2008. Extreme effusive eruptions: palaeoflow data on an extensive felsic lava in the Mesoproterozoic Gawler Range Volcanics. Journal of Volcanology and Geothermal Research 172, 148-161.

Montreuil, J.-F., Corriveau, L., Potter, E., De Toni, A., 2016. On the relationship between alteration facies and metal endowment of iron oxide-alkali-altered systems, southern Great Bear magmatic zone (Canada). Economic Geology 111, 2139-2168.

Morad, S., El-Ghali, M., Caja, M., Sirat, M., Al-Ramadan, K., Mansurbeg, H., 2010. Hydrothermal alteration of plagioclase in granitic rocks from Proterozoic basement of SE Sweden. Geological Journal 45, 105-116.

Morales-Ruano, S., Both, R., Golding, S., 2002. A fluid inclusion and stable isotope study of the Moonta copper–gold deposits, South Australia: evidence for fluid immiscibility in a magmatic hydrothermal system. Chemical Geology 192, 211-226.

Mortimer, G.E., 1984. Early to middle Proterozoic granitoids, basaltic dykes and associated layered rocks of SE Eyre Peninsula, South Australia. Unpublished PhD thesis, University of Adelaide.

Oliver, N.H., Cleverley, J.S., Mark, G., Pollard, P.J., Fu, B., Marshall, L.J., Rubenach, M.J., Williams, P.J., Baker, T., 2004. Modeling the role of sodic alteration in the genesis of iron oxide-copper-gold deposits, Eastern Mount Isa block, Australia. Economic Geology 99, 1145-1176.

Papike, J.J., 1988. Chemistry of the rock-forming silicates: Multiple-chain, sheet, and framework structures. Reviews of Geophysics, 26(3), 407-444.

Parker, A., 1993. Gawler craton. Cleve and Moonta subdomains: South Australian Geological Survey Bulletin 54, 51-68.

Parsons, I., 2010. Feldspars defined and described: a pair of posters published by the Mineralogical Society. Sources and supporting information. Mineralogical Magazine 74, 529-551.

Parsons, I., Brown, W.L., 1984. Feldspars and the thermal history of igneous rocks, Feldspars and feldspathoids. Springer, 317-371.

Parsons, I., Thompson, P., Lee, M.R., Cayzer, N., 2005. Alkali feldspar microtextures as provenance indicators in siliciclastic rocks and their role in feldspar dissolution during transport and diagenesis. Journal of Sedimentary Research 75, 921-942.

Parsons, I., Lee, M.R., 2009. Mutual replacement reactions in alkali feldspars I: microtextures and mechanisms. Contributions to Mineralogy and Petrology 157, 641-661.

Parsons, I., Magee, C.W., Allen, C.M., Shelley, J., Lee, M.R., 2009. Mutual replacement reactions in alkali feldspars II: trace element partitioning and geothermometry. Contributions to Mineralogy and Petrology 157, 663-687.

Parsons, I., Gerald, J.D.F., Lee, M.R., 2015. Review. Routine characterization and interpretation of complex alkali feldspar intergrowths. American Mineralogist 100, 1277-1303.

Perez, R.J., Boles, J.R., 2005. An empirically derived kinetic model for albitization of detrital plagioclase. American Journal of Science 305, 312-343.

Plümper, O., Putnis, A., 2009. The complex hydrothermal history of granitic rocks: multiple feldspar replacement reactions under subsolidus conditions. Journal of Petrology 50, 967-987.

Pollard, P.J., 2006. An intrusion-related origin for Cu–Au mineralization in iron oxide–copper–gold (IOCG) provinces. Mineralium Deposita 41, 179-187.

Pun, A., Papike, J., Layne, G., 1997. Subsolidus REE partitioning between pyroxene and plagioclase in cumulate eucrites: An ion microprobe investigation. Geochimica et Cosmochimica Acta 61, 5089-5097.

Putnis, A., 1992. An introduction to mineral sciences. Cambridge University Press.

Putnis, A., 2002. Mineral replacement reactions: from macroscopic observations to microscopic mechanisms. Mineralogical Magazine 66, 689-708.

Reid, A., Smith, R.N., Baker, T., Jagodzinski, E.A., Selby, D., Gregory, C.J., Skirrow, R.G., 2013. Re-Os dating of molybdenite within hematite breccias from the Vulcan Cu-Au prospect, Olympic Cu-Au province, South Australia. Economic Geology 108, 883-894.

Ren, M., 2004. Partitioning of Sr, Ba, Rb, Y, and LREE between alkali feldspar and peraluminous silicic magma. American Mineralogist 89, 1290-1303.

Rong, J., Wang, F., 2016. Metasomatic Textures in Granites: Evidence from Petrographic Observation. Springer.

Sillitoe, R.H., 2003. Iron oxide-copper-gold deposits: an Andean view. Mineralium Deposita 38, 787-812.

Skirrow, R., Bastrakov, E., Davidson, G., Raymond, O., Heithersay, P., 2002. The geological framework, distribution and controls of Fe-oxide Cu-Au mineralisation in the Gawler Craton, South Australia. Part II-alteration and mineralisation. In Porter, T.M. (Ed.), Hydrothermal Iron Oxide Copper-Gold and Related Deposits: A Global Perspective 2, PGC Publishing, Adelaide, 33-47.

Skirrow, R.G., Bastrakov, E.N., Barovich, K., Fraser, G.L., Creaser, R.A., Fanning, C.M., Raymond, O.L., Davidson, G.J., 2007. Timing of iron oxide Cu-Au-(U) hydrothermal activity and Nd isotope constraints on metal sources in the Gawler craton, South Australia. Economic Geology 102, 1441-1470.

Smith, J.V., 1974a. Feldspar Minerals. Volume 1. Crystal structure and physical properties. Springer-Verlag.

Smith, J.V., 1974b. Feldspar Minerals. Volume 2. Chemical and Textural Properties. Springer-Verlag.

Smith, J.V., Brown, W.L., 1988. Feldspar Minerals, 2nd, Springer, New York, pp 828

Stix, J., Gorton, M.P., 1990. Variations in trace element partition coefficients in sanidine in the Cerro Toledo Rhyolite, Jemez Mountains, New Mexico: Effects of composition, temperature, and volatiles. Geochimica et Cosmochimica Acta 54, 2697-2708.

Wade, C.E., Reid, A.J., Wingate, M.T., Jagodzinski, E.A., Barovich, K., 2012. Geochemistry and geochronology of the c. 1585Ma Benagerie Volcanic Suite, southern Australia: Relationship to the Gawler Range Volcanics and implications for the petrogenesis of a Mesoproterozoic silicic large igneous province. Precambrian Research 206, 17-35.

Wang, Y., Wang, Y., Merino, E., 1995. Dynamic weathering model: constraints required by coupled dissolution and pseudomorphic replacement. Geochimica et Cosmochimica Acta 59, 1559-1570.

Williams, P.J., 2010. Classifying IOCG Deposits. Short Course Notes, vol. 20, pp. 23–38. Canada: Geological Association of Canada.

Williams, P.J., Barton, M.D., Johnson, D.A., Fontboté, L., De Haller, A., Mark, G., Oliver, N.H., Marschik, R., 2005. Iron oxide copper-gold deposits: Geology, space-time distribution, and possible modes of origin. Economic Geology 100, 371-405.

Xavier, R., Monteiro, L., Moreto, C., Pestilho, A., Melo, G., Silva, M.d., Aires, B., Ribeiro, C., Silva, F., 2010. The Iron Oxide Copper-Gold systems of the Carajás Mineral Province, Brazil: an Updated and Critical Review. In Porter T M, (Ed), Hydrothermal Iron Oxide Copper-Gold and Related Deposits: A Global Perspective 3, PGC Publishing, Adelaide, 285-306.

CHAPTER 2

METHODOLOGY

CHAPTER 2: METHODOLOGY

This chapter provides an overview of samples investigated, sample selection criteria and sample preparation. This is followed by detailed descriptions of microanalytical techniques used, instrumentation, set-up conditions and reference standards. Techniques include optical microscopy, Scanning Electron Microscopy (SEM), Electron Probe Microanalysis (EPMA), Laser Ablation Inductively-Coupled Plasma Mass Spectrometry (LA-ICP-MS), Focussed Ion Beam (FIB)-SEM and Transmission Electron Microscopy (TEM). All microanalysis was performed at Adelaide Microscopy, The University of Adelaide.

2.1 Sample selection and preparation

A combination of 86 polished block and accompanying polished thin sections were studied (Table 2.1). With the exception of the Cape Donington sample suite (which was hand-selected from *in-situ* outcrop), each polished block and polished thin section was prepared from samples sourced from diamond drillcore. The Moonta-Wallaroo and Hillside sample suites were made prior to this study, and derive from the B.Sc. (Hons.) study of Kontonikas-Charos (2014), and Ph.D. study of Ismail (2016), respectively. In addition, many of the Olympic Dam samples were also received prepared from Dr. Kathy Ehrig (BHP Billiton Olympic Dam), having been used in other prior research projects, however around 36 samples from Olympic Dam were selected and prepared specifically for this study (Sample ID beginning with 'AKC').

Ready-made samples were initially selected based on how representative they were of the main lithologies and alteration stages of each case study, and further qualified by their mineralogical associations, geochemistry (whole-rock assays) and the presence of feldspars, and textures thereof. The main purpose here was to be able to compare and contrast changes in mineralogy (including feldspars) with whole-rock geochemistry across the sample suites.

Following a general characterization of the ready-made samples from Olympic Dam, site visits (September 2015 and August 2016) provided an opportunity to view complete drillcores, assess their macroscale features (see Fig. 2.1 for hand specimens), and directly select suitable samples. This was achieved via a combination of drillcore logging and whole-rock assay targeting. As alteration throughout the Roxby Downs Granite (RDG) is widespread in the Olympic Dam area, the primary aim was to select intervals of drillcore which would be most representative of the least-altered RDG, as to be able to compare this with altered and mineralized samples. Selection criteria was based on macroscale features (pink colouration of feldspars, preservation of mafic phases and rapakivi textures) and geochemistry (K_2O:Na_2O ratios between 1-3 and FeO > 4 wt. %). Drillcore samples were subsequently prepared for microanalysis at Adelaide Petrographics (formerly Pontifex & Associates Pty Ltd.), Adelaide. Corresponding assay data was provided by BHP Billiton Olympic Dam was performed by a combination of four-acid digestion and inductively coupled plasma – optical emission spectroscopy (ICP-OES) for Cu, Ag, As, Co, Ni, Pb, and Zn; lithium metaborate/tetraborate fusion and ICP-OES for Ba, Al, Ca, Ce, Fe, K, La, Mg, Mn, Na, P, Si, Sr, Ti, Y, and Zr; and lithium metaborate/tetraborate fusion and ICP-MS for U, Bi, Sb, and Mo; induction furnace - infrared spectrometry (IF-IS) for C and S; and fire assay - flame atomic absorption spectrometry (FA-AAS) for Au (Ehrig et al. 2012).

Table 2.1: List of samples used in this study.

Locality	Sample ID	Drillhole	Depth/interval (-mRL)	Lithology	Chapter
Cape Donington	PL6	N/A	N/A	Leucogranite	5
	PL11	N/A	N/A	Donington Suite granite	5
	PL12	N/A	N/A	Leucogranite	5
	PL13	N/A	N/A	Donington Suite granite	5
Hillside	GT30a	HDD407	582.3*	Altered alkali granite	6
	HS26	Unknown	Unknown	Hillside granite	5
Moonta-Wallaroo	33DDH1	DDH33	See description	Undefined Hiltaba Suite granite	3, 5

	33PBD1	PBD33		Tickera granite	3, 5
	33PBD2			Tickera granite	3, 5
	38PBD1	PBD38		Oorlano Metasomatite	3
	38PBD2			Oorlano Metasomatite	3
	158DDH1	DDH158		Wanderah Formation schist	3
	175DDH1	DDH175		Doora Member schist	3
	190DDH1	DDH190		New Cornwall Member limestone	3
	190DDH2			New Cornwall Member limestone	3
	193DDH1	DDH193		Arthurton granite	3, 5
	197DDH1	DDH197		Moonta Porphyry rhyodacite	3
	212DDH1	DDH212		Wardang Volcanic rhyodacite	3
	212DDH2			Wardang Volcanic rhyodacite	3
	227DDH1	DDH227		Arthurton granite	3, 5
	227DDH2			Arthurton granite	3, 5
Olympic Dam	AKC1	RD2531	315.6 - 316.6	Ser-Hm-altered RDG	4, 5
	AKC2		423.4 - 424.4		4
	AKC3		619.1 - 620.1		4
	AKC5		718.8 - 719.8		4
	AKC8	RD2511	274.7 - 275.7	Ser-Hm-altered RDG	4
	AKC9		295.1 - 296.1		4, 5
	AKC10		338.7 - 339.7		4
	AKC11		510.5 - 515.5		4
	AKC12		510.5 - 515.5		4
	AKC13		664.6 - 665.6		4
	AKC16	RD2280	244.9 - 249.9	Least-altered RDG	4, 5
	AKC17		259.9 - 264.9		4, 5
	AKC18		294.9 - 299.9	Ser-Hm-altered RDG	4
	AKC19		294.9 - 299.9		4
	AKC20		299.9 - 304.9		4
	AKC21		309.9 - 314.9	Least-altered RDG	4, 5
	AKC22		314.9 - 319.9		4
	AKC23		324.9 - 329.9	Ser-Hm-altered RDG	4
	AKC24		354.9 - 359.9		4
	AKC25		369.9 - 374.9		4
	AKC26		369.9 - 374.9		4
	AKC27	RD2274	214.9 - 217.9	Least-altered RDG	4
	AKC28		232.9 - 237.9	RDG-HRQM contact	5
	AKC29		247.9 – 252.9	HRQM	5
	RX6685	RD2316	481.8 - 482.8	Mineralized RDG	4
	RX6686		489.8 - 490.8		4
	RX6687		489.8 490.8		4, 6
	RX6690		545.8 - 546.8		4
	RX6691		546.8 - 547.8		4
	RX6693		576.8 - 577.8		4

	RX6694		599.7 - 600.7		4
	RX6698		634.7 - 635.7	Ser-Hm-altered RDG	4, 5, 6
	RX6700		662.7 - 663.7		4, 5
	RX6702		664.7 - 665.7		4
	RX6703		664.7 - 665.7		4
	RX6704		670.7 - 671.7		4
	RX6706		674.7 - 675.7		4, 5
	RX7307	RD3554	261.3 - 262.3	Mineralized RDG	4
	RX7315		341.3 - 342.3		4
	RX7321		392.9 - 393.9		4
	RX7322		491.3 - 492.3	Ser-Hm-altered RDG	4
	RX7323		513.8 - 514.8		4
	RX7324		520.4 - 521.4	Mineralized RDG	4
	RX7325		524.1 - 525.1		4
	RX7326		527.9 - 528.9		4, 5
	RX7327		535.4 - 536.4		4
	RX7328		561.6 - 562.6		4
	RX7329		585.9 - 586.9		4
	RX7331		764.3 - 765.3	Ser-Hm-altered RDG	4, 5
	RX7332		823.8 - 824.8	Mineralized RDG	4, 5
	RX7860	RD2494	480.3 - 485.3	Least-altered RDG	4, 5
	RX7864	RD2492	653.1 658.1	Least-altered RDG	4, 5
	RX7865	RD2495	448.1 - 453.1	Least-altered RDG	4, 5, 6
	RX7866		483.1 - 488.1		4
	RX8751	RD2488	680.8	Least-altered RDG	5
	RX8752		680.8		5
Phillip's Ridge	PD4.1B	PD4	262	Quartz monzodiorite	5
	PD4.2B		282		5
	PD4.3B		289		5
	PD4.4B		594		5
	PD4.5B		622		5
Wirrda Well	AKC33	WRD33	1889.9	Altered Donington Suite granite	5
	AKC34		1916.9		5
	WW-46.1	WRD46	536.4	Donington Suite granite	5
	WW-46.2		548.4		5

Note: Cape Donington samples obtained from *in-situ* outcrop. All Moonta-Wallaroo samples from the drillhole contact between basement and cover sequence. *corresponds to depth of drillhole, rather than mRL. Abbreviations: RDG – Roxby Downs Granite, HRQM – Horn Ridge Quartz Monzodiorite, Hm – hematite, Ser – sericite.

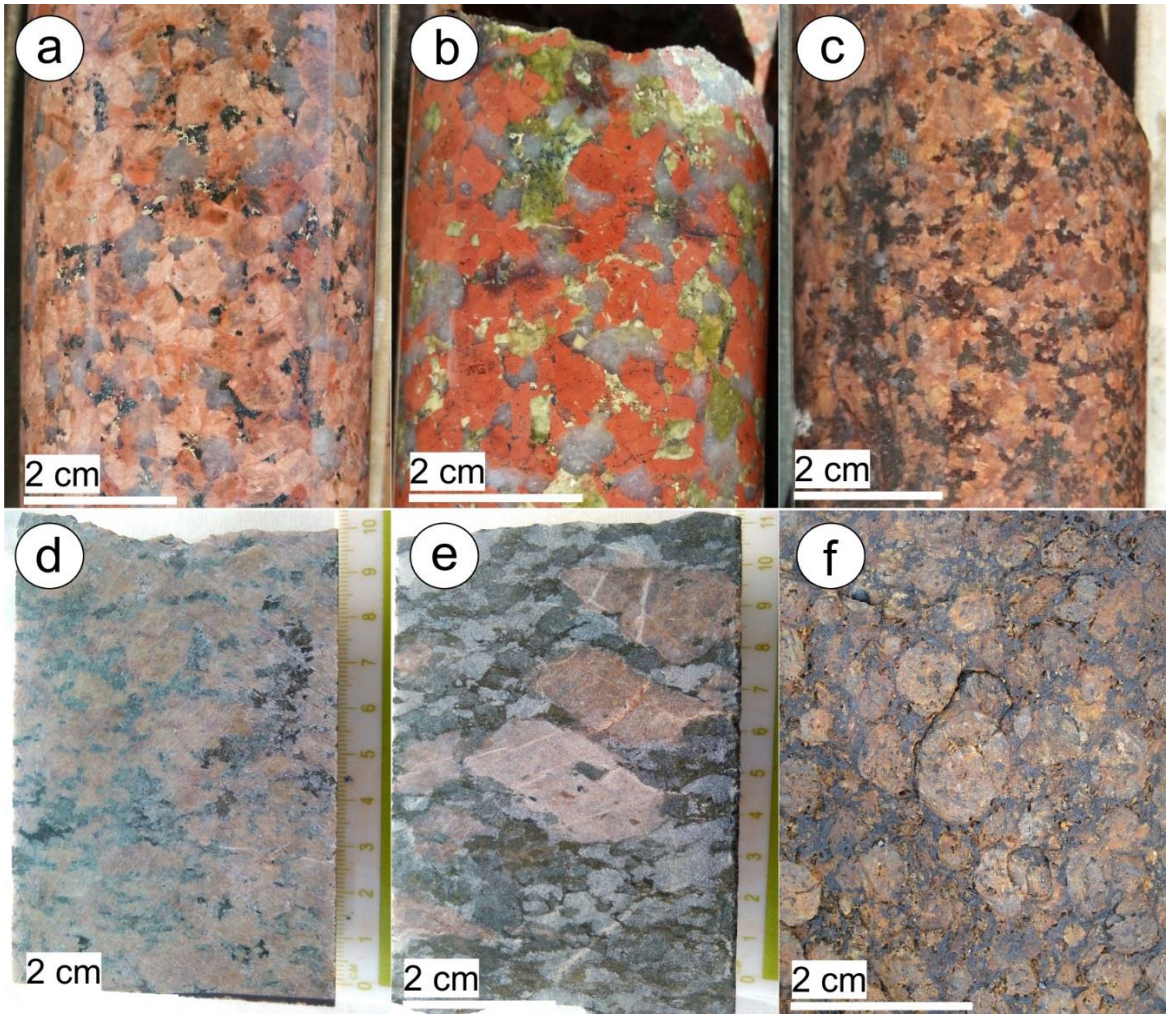

Figure 2.1: Hand specimen photographs displaying differences between sample colouration and textures at the macroscale. (a) Least altered RDG. Note the pink colouration of feldspars and preservation of mafic minerals. (b) Sericite-hematite-altered RDG. Note the change from pink to red in feldspars and green/yellow of sericite. (c) Horn Ridge Quartz Monzonite (HRQM). Note relatively greater abundance of mafic minerals as well as minor red staining of feldspars. (d) Phillip's Ridge quartz monzonite. The rock displays zones of pink reflecting sodic-calcic alteration, otherwise similar in appearance to the HRQM. (e) Donington Suite granite from Wirrda Well. This is very coarse-grained and contains large angular K-feldspar phenocrysts. (f) Donington Suite granite from Cape Donington. Coarse grained, rounded K-feldspar phenocrysts within a fine-grained silicate matrix. From Kontonikas-Charos et al. (in review).

2.2 Optical Microscopy

Prior to microanalysis, all polished blocks were first characterized by reflected light optical microscopy, and all polished thin sections by transmitted light microscopy, using a Nikon Eclipse LV100 POL Petrographic Microscope. This technique was used to identify dominant mineral assemblages and textures, major silicate phases (feldspars, amphiboles etc.) and determine areas of the section for further investigation at higher magnification (e.g., by SEM). In particular, optical microscopy was crucial for distinguishing feldspar speciation and features (e.g., twinning, turbidity/microporosity – Fig. 2.2) and paragenesis of primary and secondary phases using extinction angles (e.g., interstitial polycrystalline quartz, feldspar regrowth/recrystallization textures).

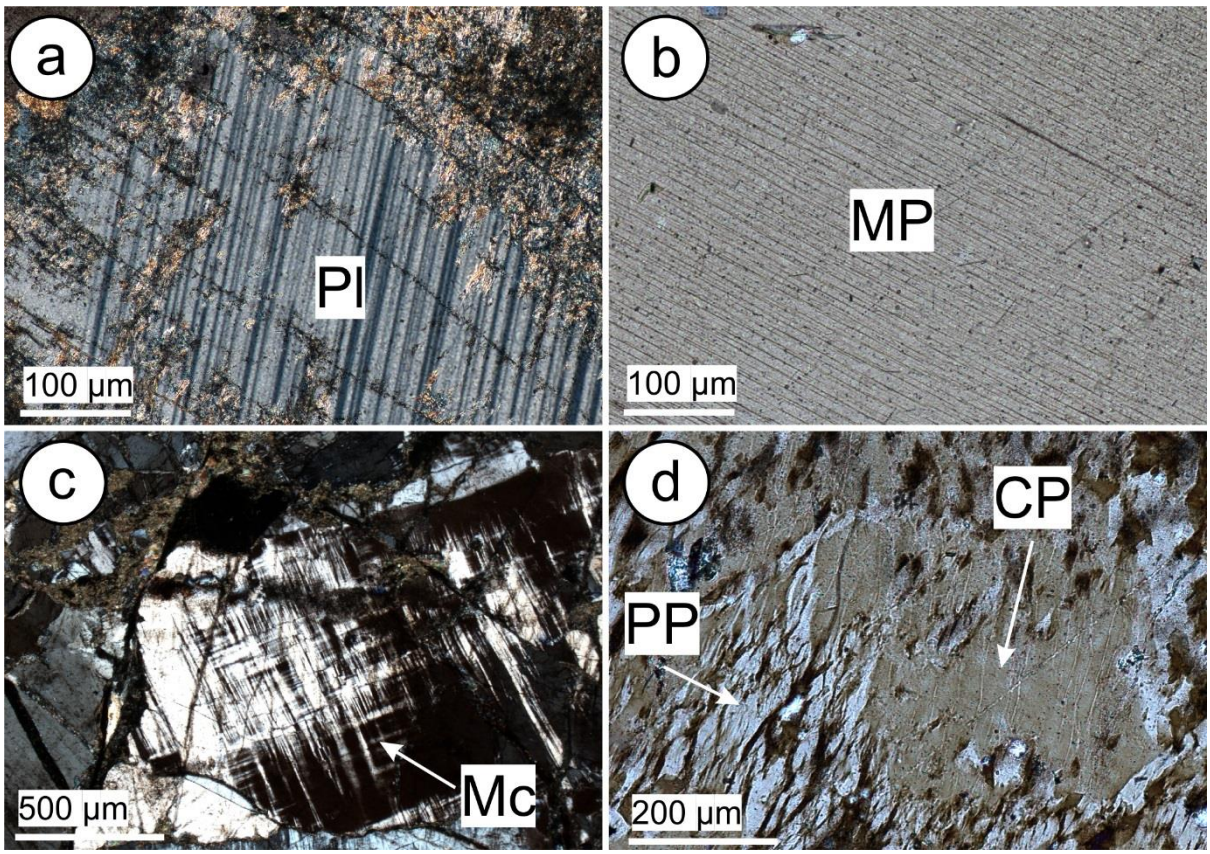

Figure 2.2: Transmitted light microscopy images (crossed polars). (a) Twinning features in plagioclase (Pl) partially replaced by extremely turbid phase (albite + sericite) in quartz

monzodiorite from Phillip's Ridge (PD4.4B). (b) Microperthite (MP) texture displaying semi-coherent Ab-rich exsolution lamellae from Donington Suite granite, Cape Donington (PL13). Scale of exsolution visible in optical microscopy, hence micro- prefix rather than crypto-. (c) Characteristic 'tartan' twinning of microcline (Mc) observed in the alkaline Hillside granite (HS26). (d) Vein patch perthite (PP) replacing cryptoperthite (CP) in least-altered RDG, Olympic Dam (RX8751).

2.3 Scanning Electron Microscopy

Scanning electron microscopy (SEM) was performed using a FEI Quanta 450 Field Emission Gun (FEG) Scanning Electron Microscope with SDD energy-dispersive X-ray spectrometry (EDS) and back-scatter electron (BSE) imaging capabilities. Prior to analysis, all samples were coated with a ~15 nm thick layer of carbon applied by a Quorum Q150TE vacuum evaporator, carried out at Adelaide Microscopy. Polished blocks and thin sections were attached to a 12 mm-diameter aluminium sample holder using double-sided conductive carbon tape which extended to the sample surface area. Samples were then inserted into the vacuum chamber in high-vacuum mode for high resolution imagery of conductive samples. Operating conditions were at a constant accelerating voltage of 20 kV, beam current of 10 nA, 4 µm spot size, 10 mm working distance, 0° stage tilt and 130 Pa chamber pressure. Sample characterization and imaging was carried out in BSE mode, supported by semi-quantitative compositional analyses which were obtained from the EDS detector.

The primary aim of SEM was to characterize the dominant mineralogy and textures of each sample, as well as to further investigate areas of interest determined by optical microscopy. In addition, SEM was used to determine whether any minerals were characterized by features unnoticeable via optical microscopy alone, and also to identify sample areas for subsequent LA-ICP-MS analysis and FIB-SEM investigations. The EDS capabilities of SEM allowed for

preliminary mineral identification, particularly within certain mineral groups, and for documenting textural and compositional changes (e.g., replacement reactions, or grain-scale oscillatory zoning – Fig. 2.3a, b). Moreover, the high magnification (maintaining high resolution up to a 5 μm^2 area) and contrast capabilities were useful for examining the presence of any microscale structures and inclusions within minerals of interest (e.g., Fig. 2.3c, d). This is crucial for interpretations of subsequent quantitative compositional data collected via EPMA and LA-ICP-MS. As such, relatively clean and homogeneous feldspar grains or areas within grains were targeted for microanalysis.

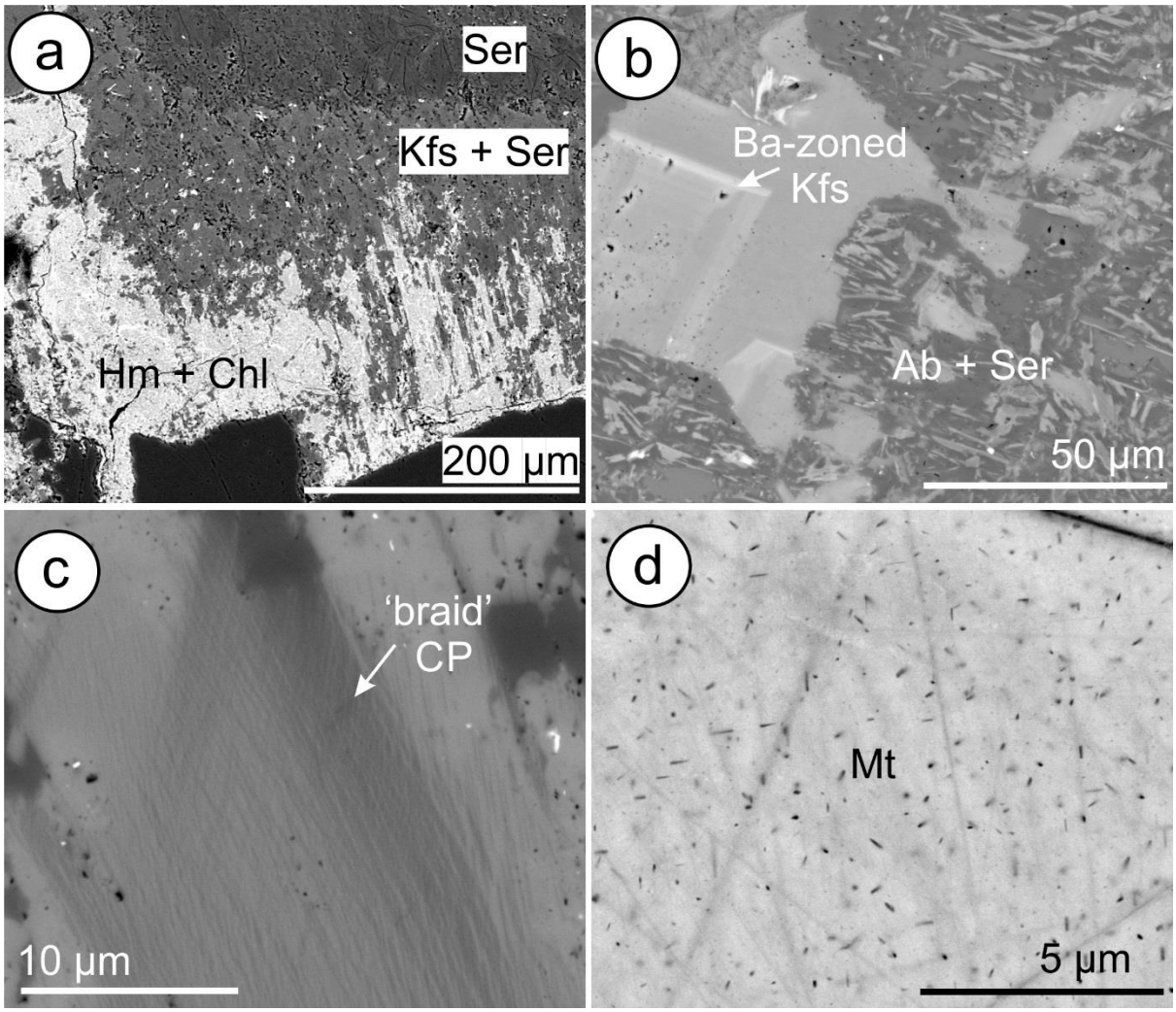

Figure 2.3: Backscatter electron (BSE) images of various mineral textures and features. (a) Replacement reaction progressing from core to rim, sericite (Ser) followed by sericite + K-

feldspar (Kfs), and hematite (Hm) + chlorite (Chl) in sericite-hematite-altered RDG (AKC24). (b) Variably Ba-zoned K-feldspar forming in association with albitization of plagioclase (Ab-albite) in quartz monzodiorite from Phillip's Ridge (PD4.5B). (c) High magnification image displaying cross-hatching Ab-rich lamellae of 'braid' cryptoperthite (CP) texture in least-altered RDG, Olympic Dam (AKC16). (d) High magnification image of magnetite (Mt) containing disseminated Al-spinel inclusions in least-altered RDG, Olympic Dam (RX8751).

2.4 Electron Probe Microanalysis

Quantitative concentrations of major and minor elements for feldspars, amphiboles, micas, epidote, garnet and Fe-Ti-oxides (ilmenite, titanite, rutile, hematite and magnetite) were determined using a Cameca SX-Five Electron Probe Microanalyzer. The instrument is fitted with five wavelength-dispersive spectrometers (WDS) for EPMA analysis, as well as an EDS, SEM and optical microscope. The diffraction crystal arrangement for spectrometers 1 and 3 were large area pentaerythritol (LPET) crystals, spectrometer 2 was a W-Si pseudocrystal (PC0), spectrometer 4 was a thallium hydrogen phthalate (TAP) crystal, and spectrometer 5 was a large area lithium fluoride (LLIF) crystal.

All analyses were carried out under constant beam operating conditions of 20 keV, 20 nA and a take-off angle of 40°. Beam size and element packages varied with minerals analyzed. Feldspars were analyzed for Si, Al, Na, K, Ca, Sr, Ba, Fe, Mg and Mn. Rubidium could not be analyzed quantitatively due to the lack of a suitable reference standard. Generally, a spot size of 5 µm was used, however bulk compositional analysis of perthitic feldspars required larger spot sizes (> 20 µm) to account for both the Or-rich and Ab-rich phases of the texture. In addition, linear transects were often used to gauge the compositional variation in zoned plagioclase. The element suite analyzed for other silicates (amphiboles, micas, epidote, garnet)

consisted of Si, Al, Na, K, Ca, Ba, Fe, Mg, Mn, P, Ti, Cr, V, Zn, Zr, Cl and F, with a spot size of 1 µm. Iron- and Fe-Ti-oxides were analyzed for Fe, Mg, Mn, Ti, Nb, W, Zn, V, Cr, Si and Al, with a spot size of 1 µm. Certified natural and synthetic standards for probe analysis were supplied by Astimex Ltd. and P & H Associates. Calibration and reduction of data was completed using Probe for EPMA software (Donovan, 2014). Table 2.2 provides relevant information for EPMA analysis. Element maps for feldspars were carried out with beam settings at 20 keV, 224 nA, and a step size between 1-5 µm depending on the dimensions of the selected area.

Table 2.2: List of EPMA X-ray lines, standards, spectrometers, count times (in seconds) and average minimum detection limits

Element /Line	**Standard**	**Spectrometer**	**Count Time unknown/back ground**	**Typical minimum detection limits (ppm)**
Si Kα	Astimex Albite	4 TAP	20/10	150
Al Kα	Astimex Albite	4 TAP	20/10	100
Na Kα	Astimex Albite	4 TAP	20/10	170
K Kα	Sanidine	1 LPET	20/10	110
Ca Kα	Plagioclase	1 LPET	20/10	110
Sr Lα	Celestite	4 TAP	20/10	210
Ba Lα	Barite	1 LPET	20/10	340
Fe Kα	Astimex Almandine	5 LLIF	20/10	270
Mg Kα	Astimex Almandine	4 TAP	20/10	120
Mn Kα	Rhodonite	5 LLIF	20/10	270
P Kα	Astimex Apatite	3 LPET	20/10	150
Ti Kα	Rutile	3 LPET	20/10	150
Nb Lα	Niobium	3 LPET	20/10	350
W Lα	Tungsten	5 LLIF	20/10	1300
Cr Kα	Synthetic Cr_2O_3	5 LLIF	20/10	300
V Kα	Vanadium	5 LLIF	20/10	320
Zn Kα	Willemite	5 LLIF	20/10	700
Zr Lα	Zircon	3 LPET	20/10	600
F Kα	Astimex Apatite	2 PC0	30/15	540
Cl Kα	Tugtupite	1 LPET	30/15	160

2.5 Laser Ablation Inductively-Coupled Plasma Mass Spectrometry

Laser-Ablation Inductively-Coupled Mass Spectrometry (LA-ICP-MS) was used to provide quantitative trace element data for silicates, oxides and phosphates in selected samples. Spot analysis and element mapping was primarily performed on a Resonetics M-50-LR 193-nm Excimer laser microprobe coupled to an Agilent 7700cx Quadrupole ICP-MS, a relatively new-generation laser system that offers excellent spatial resolution coupled with sub-ppm level sensitivity for most trace elements. Spot analysis was also carried out on an ASI M-50-LR-193 nm Excimer laser equipped to an Agilent 7700cx Quadrupole ICP-MS. A relatively large spot size ranging from 30-50 μm was used for feldspars in order to generate increased counts during ablation, whereas a comparatively smaller 20-25 μm spot size was used for oxides and phosphates. In addition, sweep times on heavier elements, including REE, were increased to reduce signal disturbance. Both laser systems were operated at pulse rates of 10 Hz and power levels of 50% power level; laser energy was typically 6-9 J/cm-2, giving an ablation rate of approximately 1.5 μm/s-1.

The following basic set of isotopes were monitored: ^{23}Na, ^{24}Mg, ^{27}Al, ^{29}Si, ^{31}P, ^{39}K, ^{43}Ca, ^{45}Sc, ^{47}Ti, ^{48}Ti, ^{49}Ti, ^{51}V, ^{53}Cr, ^{55}Mn, ^{57}Fe, ^{58}Fe, ^{59}Co, ^{60}Ni, ^{65}Cu, ^{66}Zn, ^{69}Ga, ^{75}As, ^{85}Rb, ^{88}Sr ^{89}Y, ^{90}Zr, ^{93}Nb, ^{95}Mo, ^{118}Sn, ^{133}Cs, ^{137}Ba, ^{139}La, ^{140}Ce, ^{141}Pr, ^{146}Nd, ^{147}Sm, ^{153}Eu, ^{157}Gd, ^{159}Tb, ^{163}Dy, ^{165}Ho, ^{166}Er, ^{169}Tm, ^{172}Yb, ^{175}Lu, ^{178}Hf, ^{181}Ta, ^{182}W, ^{206}Pb, ^{207}Pb, ^{208}Pb, ^{232}Th and ^{238}U. Dwell times of 0.05 seconds were used for Y, REEs, Pb, Th and U to achieve a lower detection limit, whereas 0.01 seconds was used for other elements. Multiple isotopes of Fe and Ti were measured to test for data consistency. Acquisition time for each spot was a uniform 60 seconds, comprising a 30-second measurement of background (laser-off), and 30-second analysis of the unknown (laser-on). In order to provide the best estimation of mean trace element

concentrations, values recorded below the detection limit were given an artificial value of mdl/2. Table 2.3 provides typical minimum detection limits (99% confidence) and 1σ errors for feldspars. Errors are typically <10 % for most elements, particularly for elements at concentrations >1 ppm in feldspars, and thus data accuracy may be considered sufficient.

Table 2.3: Typical minimum detection limits (ppm) and 1σ errors for all elements analyzed in plagioclase and alkali feldspar

Plagioclase						Alkali feldspar					
Element	**MDL**	**1σ Error**	**Element**	**MDL**	**1σ Error**	**Element**	**MDL**	**1σ Error**	**Element**	**MDL**	**1σ Error**
Na	1.35	1634	Mo	0.27	0.07	Na	1.17	438	Mo	0.23	0.07
Mg	0.07	0.69	Sn	0.31	0.18	Mg	0.06	0.36	Sn	0.26	0.19
Al	0.45	3858	Cs	0.04	0.02	Al	0.41	3124	Cs	0.04	0.66
Si	160	12003	Ba	0.41	2.47	Si	142	17577	Ba	0.33	185
P	11.4	8.89	La	0.02	0.50	P	9.95	9.68	La	0.02	0.14
K	1.82	77.1	Ce	0.02	0.50	K	1.54	6319	Ce	0.01	0.08
Ca	94.1	2032	Pr	0.01	0.08	Ca	84.1	158	Pr	0.01	0.02
Sc	0.11	0.16	Nd	0.10	0.34	Sc	0.09	0.21	Nd	0.10	0.09
^{49}Ti	0.90	3.22	Sm	0.10	0.11	^{49}Ti	0.78	11.2	Sm	0.09	0.06
V	0.06	0.03	Eu	0.03	0.19	V	0.05	0.02	Eu	0.03	0.25
Cr	0.81	0.42	Gd	0.10	0.09	Cr	0.72	0.41	Gd	0.09	0.04
Mn	0.50	0.85	Tb	0.01	0.01	Mn	0.43	0.56	Tb	0.01	0.01
^{57}Fe	9.22	57.4	Dy	0.07	0.05	^{57}Fe	7.51	49.6	Dy	0.06	0.03
Co	0.09	0.04	Ho	0.02	0.01	Co	0.07	0.03	Ho	0.02	0.01
Ni	0.34	0.17	Er	0.04	0.03	Ni	0.36	0.29	Er	0.05	0.02
Cu	0.42	0.21	Tm	0.02	0.01	Cu	0.44	0.28	Tm	0.01	0.01
Zn	0.70	1.17	Yb	0.07	0.03	Zn	0.63	0.55	Yb	0.07	0.03
Ga	0.09	2.11	Lu	0.02	0.01	Ga	0.08	5.06	Lu	0.01	0.01
As	0.78	0.58	Hf	0.06	0.02	As	0.65	0.69	Hf	0.06	0.04
Rb	0.07	0.13	Ta	0.02	0.01	Rb	0.07	29.7	Ta	0.01	0.04
Sr	0.05	13.4	W	0.06	0.03	Sr	0.04	17.9	W	0.06	0.08
Y	0.05	0.05	^{208}Pb	0.06	1.19	Y	0.04	0.04	^{208}Pb	0.04	4.19
Zr	0.09	0.06	Th	0.04	0.03	Zr	0.09	0.06	Th	0.02	0.01
Nb	0.06	0.04	U	0.02	0.01	Nb	0.05	0.07	U	0.01	0.01

Data calculated by using individual spot means from each sample and determining the median of the sample mean.

The standard reference material used for all mineral matrices was NIST-610, using coefficients given by Pearce et al. (1997). Standards were run after each 20-24 unknowns; detection limits were calculated for each element in each spot analysis. Calibration was achieved by assuming ideal stoichiometry of the mineral analyzed, using the internal standard element for quantification (see Table 2.4). Data reduction was performed using Glitter software (Van Achterbergh et al., 2001), which requires the internal element standard to be entered as

an oxide wt. % value. The software also calculates error using counting statistics for internal uncertainties (e.g., ablation signal and background), as well as external uncertainties (e.g., laser induced elemental fractionation (LIEF) and instrument drift). A 1% relative uncertainty is given to element concentrations within the standard (e.g., NIST-610), while a 3% relative uncertainty is given to the internal element standard (e.g., Al for feldspars). Internal uncertainties were reduced by increasing dwell times and method run time to the optimal values. External uncertainties were minimized by maintaining consistency of spot sizes, frequency and output energy between the unknown and standard. Rather than ignoring below minimum detection limits (providing an over estimation of the mean), or treating them as zero values (leading to underestimation of the mean), they were given artificial values of mdl/2 at an attempt to best represent the actual mean for the dataset (e.g., Winderbaum et al., 2012; Cook et al., 2016). Analyses in which the majority or all values were below detection limits were ignored and no mean was calculated. In general, data which was within 1σ of the mean was retained (e.g., 95% confidence intervals for data). Significant outliers in the dataset often occurred due to contamination from underlying inclusions (see below).

Table 2.4: Internal calibration elements used for quantification of LA-ICP-MS data

Mineral analyzed	Internal calibration element	Element weight %	Oxide weight %
Albite	Al	10.77	20.35
Andesine	Al	14.06	26.57
Apatite	Ca	39.36	55.07
Calcite	Ca	40.04	56.03
Oligoclase	Al	12.20	23.05
Orthoclase	Al	9.69	18.32
Rutile	^{49}Ti	59.94	100.00
Sanidine*	Al	9.84	18.59
Titanite	Ca	19.25	26.94
Zircon	Zr	43.14	58.27

*Used for bulk compositions of perthitic alkali feldspars

The aim of LA-ICP-MS spot analysis was to obtain representative trace element data from multiple minerals across multiple samples. Depending on grain size, an average of 10-20 spots per grain were collected, typically from up to 5 grains per sample. As highlighted previously,

some minerals may host microscale inclusions which can potentially contaminate and influence trace element data. Aside from microscale SEM investigation and nanoscale techniques (see next section), LA-ICP-MS time-resolved downhole profiles can be checked for the signal smoothness of each spot analysis. Generally, the signal profiles for elements hosted in solid solution within a mineral will appear smooth (Fig. 2.4a), whereas nanoscale or sub-surface inclusions may form sporadic peaks along signal profiles (Fig. 2.4b). In some cases, the presence of these inclusions may be systematically hosted within the mineral (Fig. 2.4c – see also Chapter 6), however if an inclusion was accidentally ablated, the analysis was removed. In cases where an inclusion was hit towards the end of the ablation run, the analysis could be retained by removal of the 'contaminated' interval from integration using GLITTER (Fig. 2.4d).

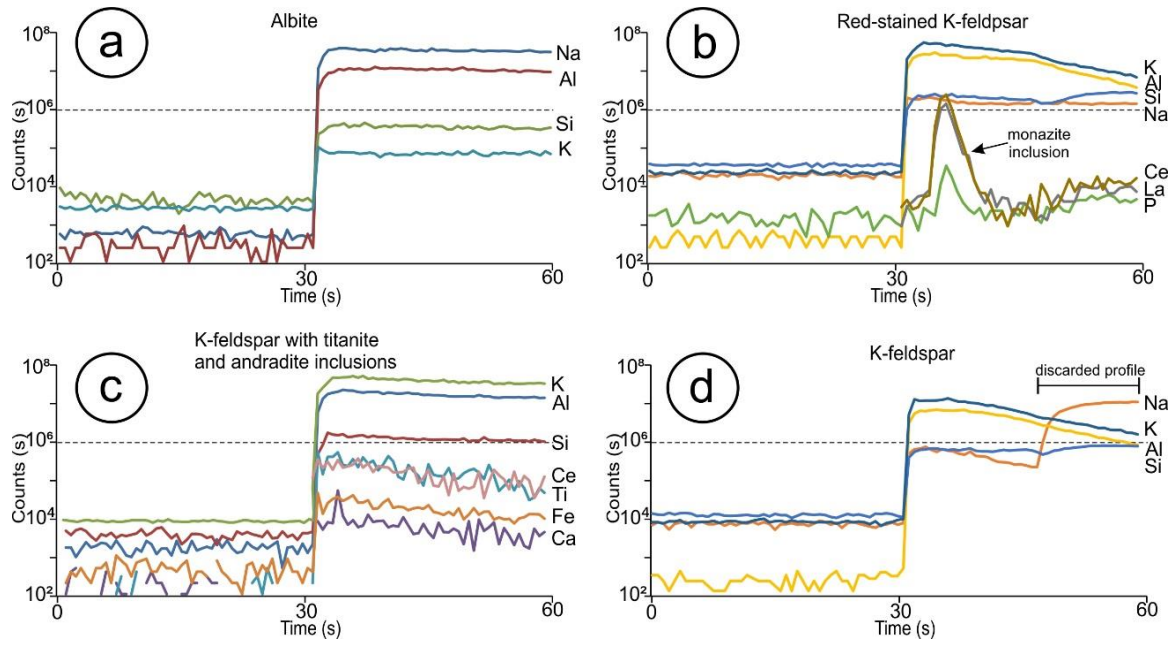

Figure 2.4: Examples of LA-ICP-MS spot analysis downhole profiles for feldspars. (a) Smooth profiles from analysis of albite, indicating the elements are within solid solution. (b) Sporadic peaks of Ce, La and P highlight the presence of monazite inclusions within red-stained K-feldspar. (c) Consistently sporadic profiles of Ce, Ti, Fe and Ca indicate the high

abundance of titanite and andradite inclusions within the host K-feldspar. (d) Example of data reduction applied to profile of K-feldspar analysis which was contaminated towards the end of ablation.

As data was calibrated based on ideal stoichiometry of an internal element standard (e.g., Table 2.4), EPMA was used to check the precision of LA-ICP-MS analyses, particularly for major elements. Figure 2.5 gives a visual representation bi-element variation in EPMA and LA-ICP-MS spot analyses. In each case, the LA-ICP-MS data is reproducible and plots relatively close to EPMA data indicating high precision.

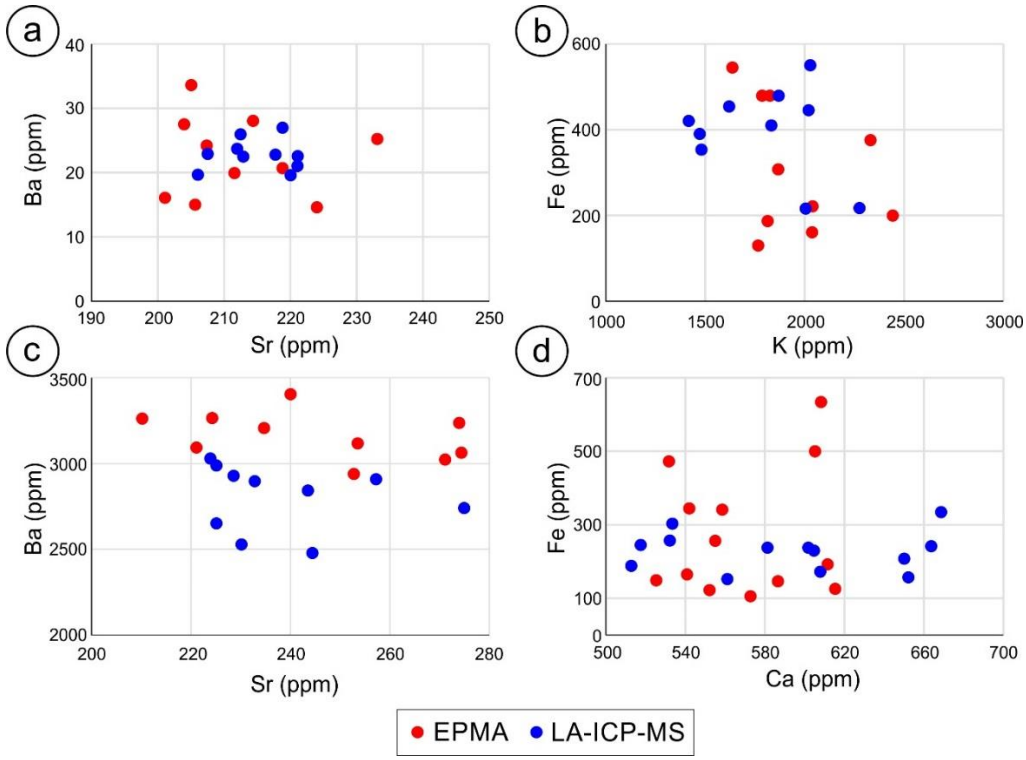

Figure 2.5: Scatter plots showing the precision of LA-ICP-MS data relative to EPMA data for elements within plagioclase (a-b) and microperthite (c-d).

A visual representation of trace element distribution was able to be produced by LA-ICP-MS element mapping of selected feldspar grains (Fig. 2.6). Mapping was conducted using the same Resonetics M-50-LR instrument as above. The M-50 instrument utilizes a two-volume

small volume ablation cell (Laurin Technic Pty designed for excellent trace element sensitivity, e.g., Müller et al., 2009). Ablation was performed in an atmosphere of UHP He (0.7 l/min), and upon exiting the cell the aerosol cell is mixed with Ar (0.93 l/min) immediately after the ablation cell, after which the mix is passed through a pulse-homogenizing device or "squid" prior to direct introduction into the torch. The ICP-MS was optimized daily to maximize sensitivity on isotopes of the mass range of interest, while keeping production of molecular oxide species (i.e., $^{232}Th^{16}O/^{232}Th$) and doubly charged ion species (i.e., $^{140}Ce^{2+}/^{140}Ce^{+}$) as low as possible, and usually below 0.2%.

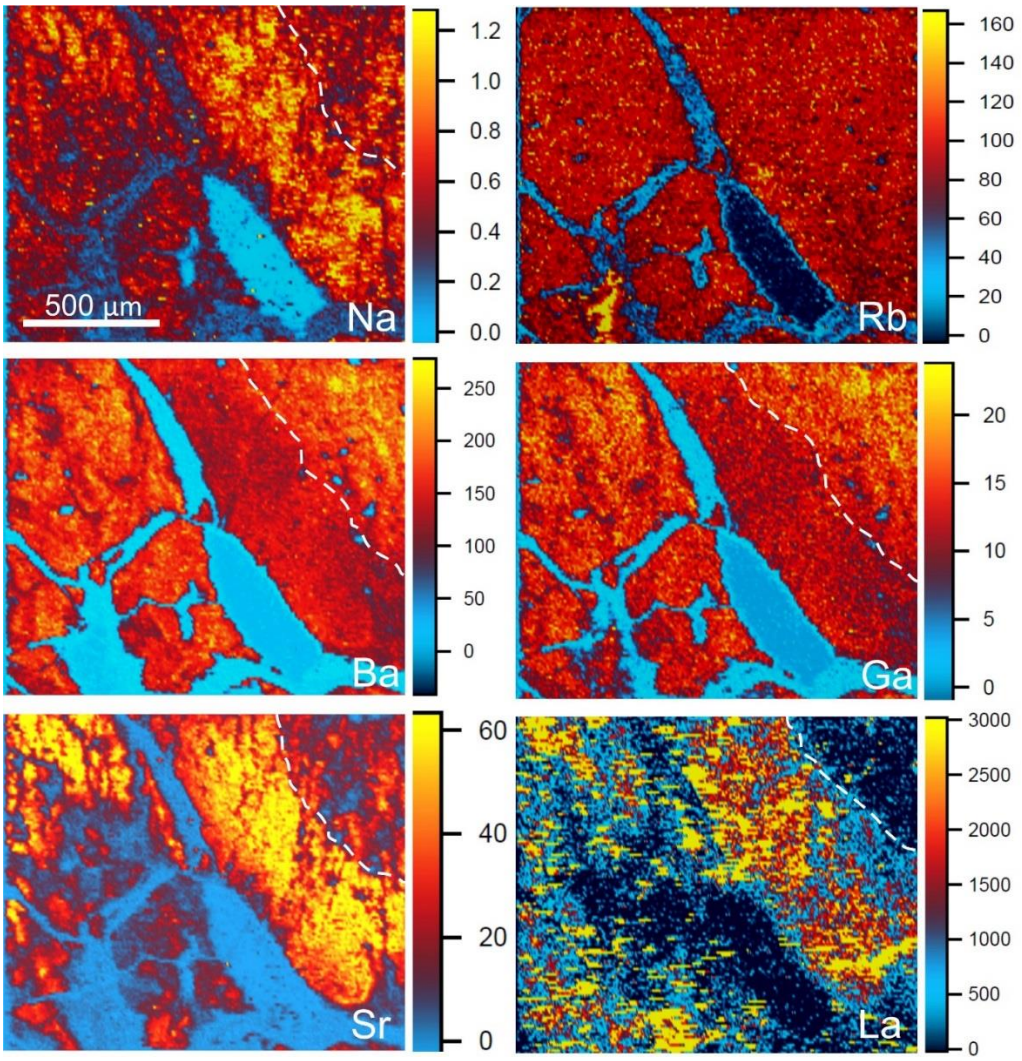

Figure 2.6: Element maps produced by LA-ICP-MS displaying element distributions within partially albitized K-feldspar from the Arthurton granite, Moonta-Wallaroo. Note positive

correlation between Na, Sr and La, as well as between Ba and Ga. Scale bar represents counts per second (cps) for La; 10^3 cps for Rb, Ba, Ga, Sr; 10^6 cps for Na. Figure from Kontonikas-Charos et al. (2014).

Imaging of grains was performed by ablating sets of parallel line rasters in a grid across the sample. A beam size of 6–22 μm (depending on specified resolution and counts) and a scan speed of 1.5 x beam size (μm/s) were chosen which resulted in the desired sensitivity of elements of interest, and adequate spatial resolution for the study. To ensure the lines covered the entire selected area, spacing between lines was always equal to the beam size. The effect of redeposition during mapping was minimized by pre-ablating each line prior to its main data collection run. A laser repetition of 10 Hz was selected at a constant energy output of 100 mJ, resulting in an energy density of ≈6 J/cm^2 at the target. Using these beam conditions, depth of ablation during mapping was around 5-10 μm. A set of 21 elements were analyzed with dwell time for all masses set to 0.003 seconds, resulting in a total sweep time of ~0.07 seconds. A 30 second background acquisition was acquired at the start of every raster, and to allow for cell wash-out, gas stabilization, and computing processing, a delay of 20 seconds was used after each line. Identical rasters were done on USGS reference glasses NIST SRM 610 at the start and end of a mapping run. Further details of practices used in the University of Adelaide LA-ICP-MS laboratory, particularly with respect to generation of trace element maps, are given by Cook et al. (2013, 2016).

Element maps were compiled and processed using the program Iolite developed by the Melbourne Isotope Group at Melbourne University (e.g., Woodhead et al., 2007). Iolite is an open source software package for processing ICP-MS data, and is an add-in for the data analysis program Igor developed by WaveMetrics. A typical mapping run was analyzed over a 6-7 hour-long session, in which significant instrument drift could occur. To correct for this,

standards were analyzed immediately before and after the run to assess drift and if present, was corrected for by applying a linear fit between the two sets of standards. Following this, for each raster and every element, the average background was subtracted from its corresponding raster, and the rasters were compiled into a two-dimensional image displaying combined background/drift corrected intensity for each element.

2.6 Focussed Ion Beam-Scanning Electron Microscopy

The aim of using FIB-SEM was firstly, to characterize feldspar replacement reaction areas with respect to porosity, sub-micron fractures and mineral inclusions (e.g., Lee et al., 2007), and secondly, to prepare thinned foils of selected areas for further investigation by TEM. Table 2.5 summarizes all foils prepared for TEM study.

Table 2.5: Overview of foils for TEM investigation prepared via FIB-SEM.

Locality	Foil description	Sample ID (no. of foils)	Drillhole	Chapter used
Olympic Dam	Cryptoperthite and patch perthite	RX7865 (2)	RD2495	4, 6
	Andesine + oligoclase	RX7865 (1)	RD2495	-
	Oligoclase + albite	RX7865 (1)	RD2495	-
	Albite + sericite	RX7865 (1)	RD2495	-
		RX6700 (1)	RD2316	-
	Red-stained K-feldspar	RX6698 (4)	RD2316	6
	Hyalophane + albite	RX7865 (1)	RD2495	6
	REE-mineral intergrowth + molybdenite	RX6687 (2)	RD2316	6
Moonta-Wallaroo	Albite + inclusions	33PBD1 (1)	PBD33	3
		175DDH1 (2)	DDH175	3
	Oligoclase	33PBD1 (1)	PBD33	3
Hillside	K-feldspar + inclusions	GT30a (2)	HDD407	6

A Dual Beam FEI Helios Nanolab 600 platform equipped with SEM and EDS capabilities was used for high-resolution imaging and *in-situ* preparation of TEM foils (following

procedures outlined in Ciobanu et al., 2011). This system incorporates a Ga-source Focussed Ion Beam (FIB) column aligned at 52° angle to a field-emission SEM column, allowing for cross-section imaging, as well as cutting, extraction and thinning of TEM foils. In addition, this system also comprises a solid-state Scanning Transmission Electron Microscopy (STEM) detector allowing for high resolution imaging of textures and element mapping.

Following thorough sample characterization via microanalytical techniques mentioned previously, selected areas from carbon-coated polished blocks and thin sections were targeted to prepare thin foils necessary for TEM study. Operating conditions for the electron beam were at an accelerating voltage of 10 kV, beam current of 0.69 nA and working distance at 4 mm. Once inserted within the FIB chamber, the stage was tilted to 52°, as to be directly perpendicular to the ion beam, and a 1-2 μm thick layer of platinum (*X*: 15-20 μm, *Y*: 2 μm) was deposited across the sample area (Fig. 2.7a). The purpose of the platinum layer is to, firstly, protect the foil from damage during milling (see below) and, secondly, to allow for the extraction of the foil via attachment to a tungsten needle. Following Pt deposition, 'trenches' were milled with Ga ions at high voltage (30 kV) and current (~9.7 pA) as regular cross sections (multiscan mode, *Z*: 20 μm) above, below and to the left of Pt layer to produce sufficient space for extraction (Fig. 2.7b). Due to the high current used during this process, curtaining effects (uneven surface artefacts) may be visible along the wall surfaces of the trenches (typical for 'softer' minerals), and some excess material may accumulate at the base of the trenches. Subsequently, a low current cleaning cross section was applied to the top (stage tilted to 50.5°) and bottom (stage tilted to 53.3°) trench walls to negate these phenomena and allow for documentation of gradual layer-by-layer textural changes and the approximate depth of pores and inclusions (Fig. 2.7c). Imaging at this point was carried out using the electron beam in 'field free' mode (20 kV) and the high resolution 'immersion' mode (5 kV).

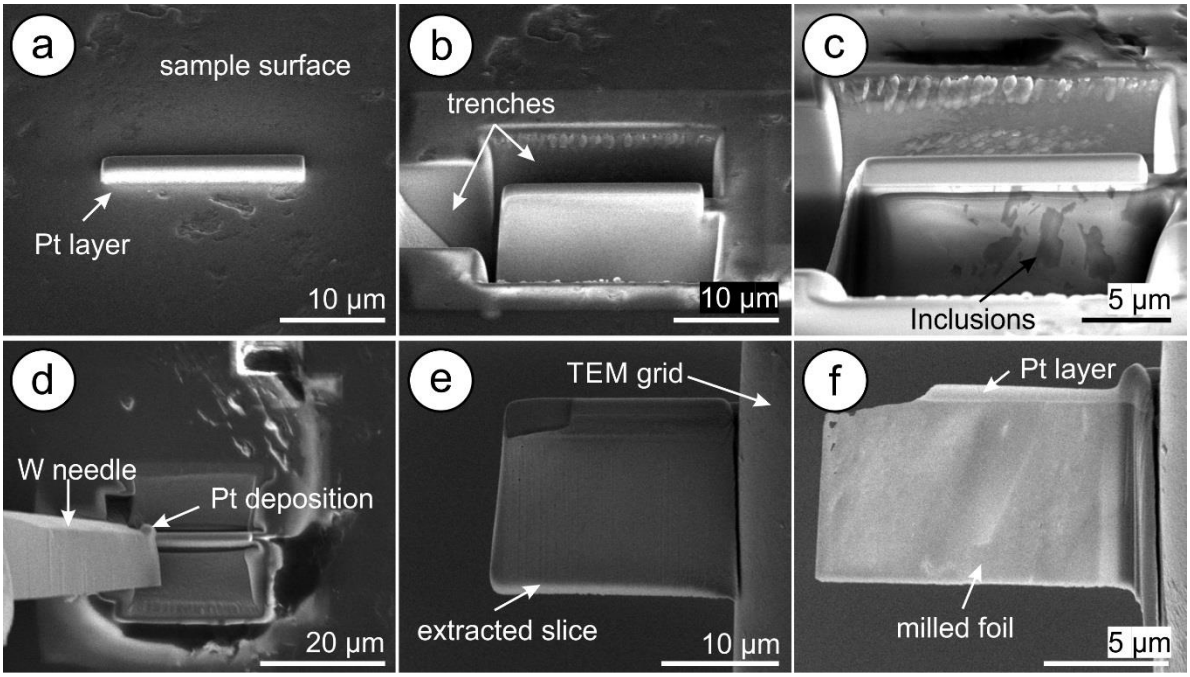

Figure 2.7: Secondary Electron (SE) images outlining FIB-TEM foil procedures used in this study. (a) Initial platinum (Pt) layer deposited at the area of interest on the sample surface. (b) Trenches milled around the foil area in order to allow sufficient space for extraction. (c) Documentation of various inclusions and foil features following cleaning cross sections. (d) Attachment of tungsten needle to Pt layer of foil via Pt deposition. (e) Unmilled foil attached to TEM grid. (f) Final product of milling, foil ready for TEM investigation.

Once the foil was ready to be extracted, the stage was tilted to 7° to allow for a high current (> 6.5 nA) rectangle cut to be made along the bottom of the foil, leaving the right limb as the remaining attachment to the sample. The stage was then reset to 0°, and a tungsten needle was brought into the field for foil attachment, extraction and transportation to the TEM grid holder. The needle was attached by depositing another Pt layer to the top of the foil (Fig. 2.7d), the remaining right limb cut with a high current, and the foil extracted, transported and attached to the grid holder (via Pt deposition) for further milling (Fig. 2.7e). Once the needle was detached from the foil, the stage was tilted back to 52° and milling of both sides was carried out at 2.8 nA (*Z*: foil length). Following this, the current was reduced to 0.92 and 0.46 nA and stage tilted

to 50.5° and 53.5° for finer milling and to reduce the possibility of curtaining. The aim of this process was to mill the foil to an ideal thickness between 60-100 nm, as to be transparent for TEM analysis (Fig. 2.7f). A final cleaning cross section was applied at 5 kV to remove any excess material deposited on the surface. Ongoing imaging throughout the milling process was critical to avoid any unwanted damage to the foil, which may occur as the foil becomes thinner and drifts due to exposure to accelerated Ga ions.

2.7 Transmission Electron Microscopy

The aim of the TEM study was to characterize the feldspars, from magmatic to hydrothermal stages, down to the nanoscale. Main topics included: (i) identification of feldspars in cryptoperthites; (ii) orientation between perthitic feldspars – to understand whether they are epitaxial (formed via CDRR), or random; (iii) presence of Fe-oxide inclusions in red-stained K-feldspar – address the relationships between feldspar transformation and Fe-metasomatism; (iv) high-REE albite – REE in solid solution or as inclusions; (v) hydrothermal Ba-rich K-feldspar associated with albitization – the presence of other mineral inclusions, particularly good hosts for REE incorporation. In addition, intergrowths of REE-fluorocarbonates with molybdenite, found in association with red-stained K-feldspar, were studied to establish the dominant stacking sequences and corresponding polytypes present, as well as to ascertain whether these are coherent and ordered/disordered at the nanoscale.

High Angle Annular Dark Field - Scanning Transmission Electron Microscopy (HAADF STEM) imaging and EDS measurements were performed on an ultra-high resolution, probe-corrected, FEI Titan Themis S/TEM. This instrument is equipped with the X-FEG Schottky source and Super-X EDS geometry. The Super-X detector provides geometrically symmetric EDS detection with an effective solid angle of 0.8 sr. Probe correction delivered sub-Ångstrom spatial resolution and an inner collection angle greater than 50 mrad were used for HAADF

experiments using the Fischione HAADF detector. This was used for obtaining EDS spectra from phases <10 nm width (e.g., cryptoperthites, nm-scale inclusions).

High-Resolution (HR)-TEM imaging in Bright Field mode (BF) and electron diffractions were performed using a Philips CM200 TEM. This instrument is equipped with a LaB6 source and was operated at 160 and 200 kV. In addition, it utilizes a double-tilt holder (allowing for greater tilt) and a Gatan Orius digital camera. Energy-dispersive X-Ray spectra (EDS) were acquired using an Oxford Instruments X-Max 65T SDD detector running Aztec software. Diffraction measurements were performed using DigitalMicrograph™ 3.11.1 and Winwulff© 1.4.0 software. Publicly available data from the American Mineralogist Crystal Structure Database (http://rruff.geo.arizona.edu/AMS/amcsd.php) were used for indexing of the electron diffractions.

Once inserted within the chamber and located with the beam, low magnification images were taken using the objective aperture (for sharper contrast) to provide an overview of the foil (Fig. 2.8a). High resolution imaging and EDS analysis was carried out in areas of interest, such as inclusions, pores and grain boundaries (Fig. 2.8b). The diffraction aperture was then inserted, replacing the objective aperture, and electron diffraction patterns were produced. The mineral zone axes were located by adjusting the tilt of the double-tilt sample holder (angles ranging from A: ±60° and B: ±30°). Foil preparation was crucial for the production of representative electron diffraction patterns, which may be unattainable in thicker foils due to double diffraction occurring from underlying structures. Conversely, EDS analysis (Fig. 2.8c) performs better on thicker foils which provide higher counts for the detector. Most foils, however, comprised areas which varied in thickness, nonetheless, it was critical to carry out sufficient EDS analyses during prior FIB procedures.

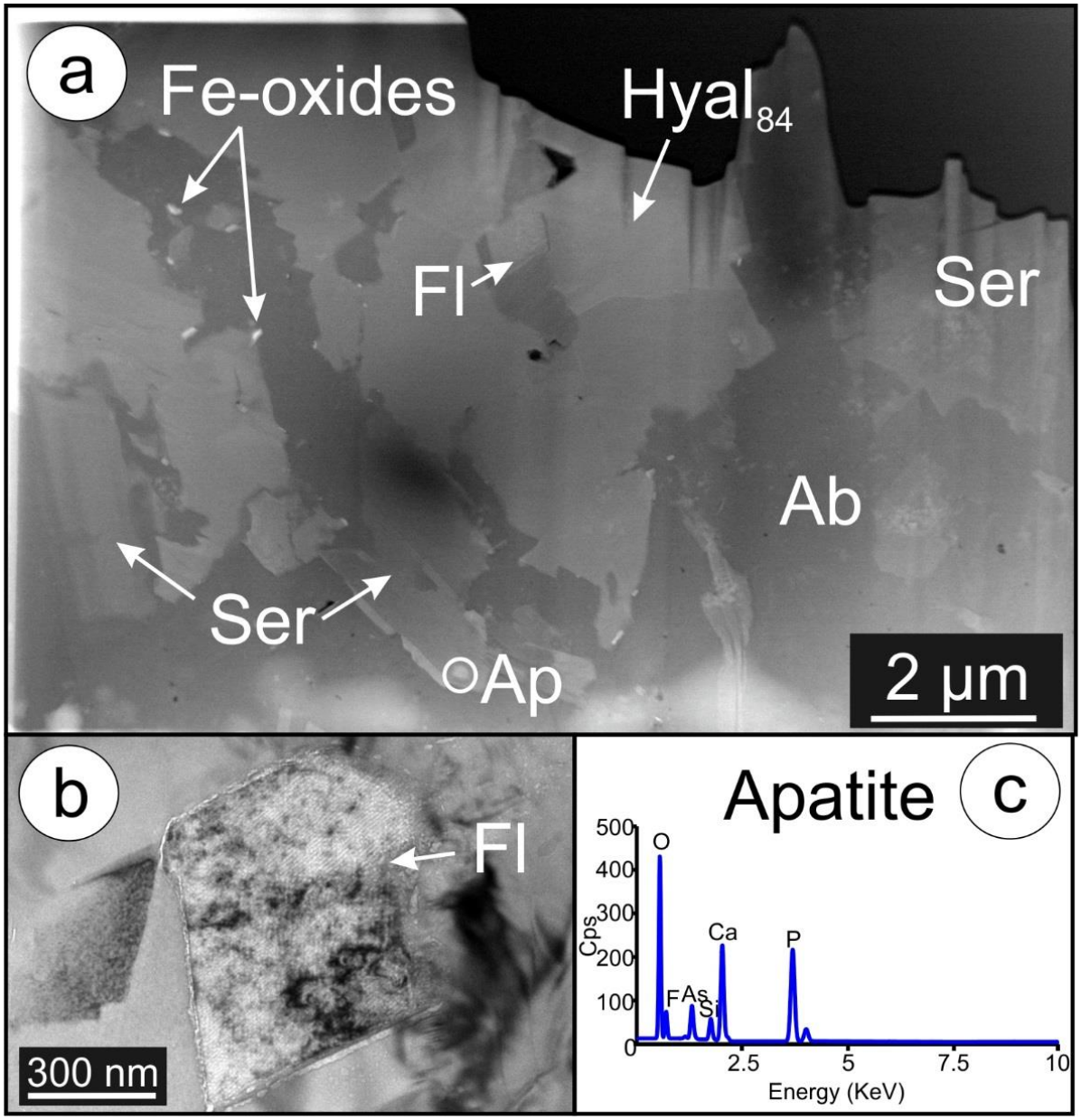

Figure 2.8: Transmission electron microscope images taken using the Phillips CM200 and EDS spectra acquired on the Titan Themis. (a) Low magnification image displaying the relationship between albite (Ab), sericite (Ser), hyalophane (Hyal) and other disseminated inclusions, Fe-oxides, apatite (Ap) and fluorite (Fl), within an albitized area of plagioclase. (b) BF image of the fluorite (Fl) inclusion from (a). (c) EDS spectra of apatite from (a). Compiled from Kontonikas-Charos et al. (2014); (in press).

Ciobanu, C.L., Cook, N.J., Utsunomiya, S., Pring, A., Green, L., 2011. Focussed ion beam transmission electron microscopy applications in ore mineralogy: bridging micro and nanoscale observations. Ore Geology Reviews 42, 6–31.

Cook, N.J., Ciobanu, C.L., Meria, D., Silcock, D., Wade, B., 2013. Arsenopyrite-pyrite association in an orogenic gold ore: tracing mineralization history from textures and trace elements. Economic Geology, 108, 1273-1283.

Cook, N., Ciobanu, C.L., George, L., Zhu, Z.Y., Wade, B., Ehrig, K., 2016. Trace element analysis of minerals in magmatic-hydrothermal ores by laser ablation inductively-coupled plasma mass spectrometry: Approaches and opportunities. Minerals, 6(4), 111, doi:10.3390/min6040111

Donovan, J.J., 2014. Probe for EPMA: Acquisition, automation and analysis. Ver. 10.3.5 Xtreme Edition, Probe Software, Inc., Oregon, United States of America

Ismail, R., 2016. Spatial-Temporal Evolution of Skarn Alteration in IOCG Systems: Evidence from Petrography, Mineral Trace Element Signatures and Fluid Inclusion Studies at Hillside, Yorke Peninsula, South Australia. Unpublished Ph.D. thesis, The University of Adelaide.

Kontonikas-Charos, A., 2014. Albitization and REE-U enrichment in IOCG systems: Insights from Moonta-Wallaroo, Yorke Peninsula, South Australia. Unpublished Honours thesis, The University of Adelaide.

Kontonikas-Charos, A., Ciobanu, C.L., Cook, N.J., 2014. Albitization and redistribution of REE and Y in IOCG systems: Insights from Moonta-Wallaroo, Yorke Peninsula, South Australia. Lithos 208–209, 178-201.

Kontonikas-Charos, A., Ciobanu, C.L., Cook, N.J., Ehrig, K., Ismail, R., Krneta, S., Basak, A. (in press) Feldspar mineralogy and rare earth element (re)mobilization in iron-oxide copper

gold systems from South Australia: a nanoscale study. Mineralogical Magazine. https://doi.org/10.1180/minmag.2017.081.040

Kontonikas-Charos, A., Ciobanu, C.L., Cook, N.J., Ehrig, K., Krneta, S. and Kamenetsky, V.S. (in review) Rare earth element geochemistry of feldspars: Examples from Fe-oxide Cu-Au systems in the Olympic Cu-Au Province, South Australia. Mineralogy and Petrology.

Lee, M.R., Brown, D.J., Smith, C.L., Hodson, M.E., MacKenzie, M., Hellmann, R., 2007. Characterization of mineral surfaces using FIB and TEM: A case study of naturally weathered alkali feldspars. American Mineralogist, 92(8-9), 1383-1394.

Müller, W., Shelley, M., Miller, P., Broude, S., 2009. Initial performance metrics of a new custom-designed ArF excimer LA-ICPMS system coupled to a two-volume laser-ablation cell. Journal of Analytical Atomic Spectrometry 24, 209–214.

Pearce, N.J.G., Perkins, W.T., Westgate, J.A., Gorton, M.P., Jackson, S.E., Neal, C.R., Chenery, S.P., 1997. A compilation of new and published major and trace element data for NIST SRM 610 and NIST SRM 612 glass reference material. Geostandards Newsletter 21, 115–144.

Van Achterbergh, E., Ryan, C.G., Jackson, S.E., Griffin, W.L., 2001. LA-ICP-MS in the Earth Sciences - Appendix 3, data reduction software for LA-ICP-MS. In: Sylvester, P.J. (Ed.), Mineralogical Association of Canada Short Course vol. 29, 239-243.

Winderbaum, L., Ciobanu, C.L., Cook, N.J., Paul, M., Metcalfe, A., Gilbert, S., 2012. Multivariate analysis of an LA-ICP-MS trace element dataset for pyrite. Mathematical Geosciences 44, 823–842.

Woodhead, J.D., Hellstrom, J., Hergt, J.M., Greig, A., Maas, R., 2007. Isotopic and elemental imaging of geological materials by laser ablation inductively coupled plasma-mass spectrometry. Geostandards and Geoanalytical Research 31, 331–3

CHAPTER 3

ALBITIZATION AND REDISTRIBUTION OF REE AND Y IN IOCG SYSTEMS: INSIGHTS FROM MOONTA-WALLAROO, YORKE PENINSULA, SOUTH AUSTRALIA

Alkis Kontonikas-Charos[1], Cristiana L. Ciobanu[2], Nigel J. Cook[2]

[1]*School of Physical Sciences, The University of Adelaide, Adelaide, SA, 5005, Australia*

[2]*School of Chemical Engineering, The University of Adelaide, Adelaide, SA, 5005, Australia*

Article published in Lithos 208-209, 178-201

Statement of Authorship

Title of Paper	Albitization and redistribution of REE and Y in IOCG systems: Insights from Moonta-Wallaroo, Yorke Peninsula, South Australia
Publication Status	☑ Published ☐ Accepted for Publication ☐ Submitted for Publication ☐ Unpublished and Unsubmitted w ork w ritten in manuscript style
Publication Details	Kontonikas-Charos, A., Ciobanu, C.L., Cook, N.J., 2014. Albitization and redistribution of REE and Y in IOCG systems: Insights from Moonta-Wallaroo, Yorke Peninsula, South Australia. Lithos 208–209, 178-201.

Principal Author

Name of Principal Author (Candidate)	Alkis Kontonikas-Charos		
Contribution to the Paper	Performed analytical work, carried out data processing and interpretation, oversaw development of work and wrote manuscript.		
Overall percentage (%)	75		
Certification:	This paper reports on original research I conducted during the period of my Higher Degree by Research candidature and is not subject to any obligations or contractual agreements with a third party that would constrain its inclusion in this thesis. I am the primary author of this paper.		
Signature		Date	11/07/17

Co-Author Contributions

By signing the Statement of Authorship, each author certifies that:

i. the candidate's stated contribution to the publication is accurate (as detailed above);

ii. permission is granted for the candidate in include the publication in the thesis; and

iii. the sum of all co-author contributions is equal to 100% less the candidate's stated contribution.

Name of Co-Author	Cristiana L. Ciobanu		
Contribution to the Paper	Helped define direction of research, supervised development of work, assisted with data interpretation and contributed to manuscript preparation.		
Overall percentage (%)	15		
Signature		Date	10 July 2017

Name of Co-Author	Nigel J. Cook		
Contribution to the Paper	Helped define direction of research, supervised development of work, assisted with data interpretation and contributed to manuscript preparation.		
Overall percentage (%)	10		
Signature		Date	10/7/17

Lithos 208–209 (2014) 178–201

Contents lists available at ScienceDirect

Lithos

journal homepage: www.elsevier.com/locate/lithos

Albitization and redistribution of REE and Y in IOCG systems: Insights from Moonta-Wallaroo, Yorke Peninsula, South Australia

Alkis Kontonikas-Charos, Cristiana L. Ciobanu *, Nigel J. Cook

Centre for Tectonics, Resources and Exploration, School of Earth and Environmental Sciences, University of Adelaide, 5005 SA, Australia

ARTICLE INFO

Article history:
Received 2 November 2013
Accepted 1 September 2014
Available online 16 September 2014

Keywords:
Albitization
Rare earth elements
IOCG deposits
Feldspar
Moonta-Wallaroo
Olympic Province

ABSTRACT

Trace element concentrations, particularly rare earth elements and yttrium (REY) in feldspars and accessory minerals, have been determined in a suite of albitized igneous, metasedimentary and metasomatite rocks from the Moonta-Wallaroo district, Olympic Cu–Au Province, South Australia. Results show that changes in REY-fractionation trends and concentrations in feldspars and common accessories are associated with key textures in albite-bearing associations from different lithologies. In granitic rocks, pseudomorphic replacement of pre-existing feldspars is typified by porous albite with cleavage-oriented intergrowths of sericite and pore-attached hematite. These observations are comparable with albitization features of granitic terranes elsewhere. A mineral association (albite-sericite ± chlorite), similar to that from granitoids, is observed as pervasive spots in limestone, inferring prograde skarnoid reactions at low fluid/rock ratio in an impure carbonate. In metasedimentary and metasomatite rocks with comparable Na_2O content (~5–6 wt.%), fine-grained granoblastic albite suggests growth under high fluid/rock ratios irrespective of lithology. In such cases, albite with the highest REY content (ΣREY ~ 200 ppm) accounts for the entire REY budget, e.g., in albite–biotite-schist with the lowest abundance of accessory minerals. Nanoscale investigation confirms this albite to be a REY carrier (elements incorporated within the crystal lattice); no pore-attached inclusions are observed. In contrast, albite with the lowest REY-concentration (~14 ppm) is encountered in the metasomatite. In such rocks, recording the highest ΣREY (~1000 ppm) in whole-rock, partitioning of REY is favoured among the abundant accessories (titanite, apatite) and calc-silicates (actinolite, clinozoisite) rather than albite. Comparable low-REY albite is also found in granitoid-derived albitite (Na_2O ~5 wt.%), in which abundant accessories and discrete REY-minerals formed during albitization account for the high ΣREY content (~700 ppm) in whole rock.

The role of coupled dissolution–reprecipitation reactions (CDRR) is critical for REY (re)distribution within albitized igneous rocks, where REY-release from early magmatic accessories and/or feldspars assists REY-enrichment into late albite. The presence of abundant nanopore-attached inclusions in plagioclase demonstrates the nanoscale nature of CDRR-driven albitization in granitoids, consistent with published experimental work on altered granites. Such porosity offers sites for REY entrapment seen within discrete REY-minerals in new-formed K-feldspar. Similarly, release and uptake of REY, concurrent with albitization, is seen in formation of coarser REY-minerals (xenotime, bastnäsite, synchysite) during CDRR-driven replacement of accessory Fe–Ti-oxides by symplectites of chlorite and hematite.

Based on the differences identified between the albitization pathways in igneous and metasedimentary rocks, we discuss how albitization proceeds via a series of complex fluid–mineral reactions, each involving the redistribution, accumulation and retention of REY. These reactions are critical for defining the endowment and deportment of REY in rocks that have undergone sodic alteration. Contrary to previous models, albitization appears controlled by pH rather than redox conditions. Despite regional differences in local geological environment and alteration style across the Olympic Cu–Au Province, albitization, the initiation of hydrothermal alteration, is a pre-requisite stage for REY-enrichment in Iron-Oxide–Copper–Gold (IOCG) systems. REY distribution patterns in feldspars may thus have value in mineral exploration as criteria enabling alteration associated with mineralization to be distinguished from the regional background. Strong albitization without superposition of later potassic alteration may not, however, be automatically linked to the formation of giant IOCG deposits. Albitization enhances rock permeability and in a strongly faulted structural environment without a suitable trap, hydrothermal fluids may be more readily lost from the system.

© 2014 Elsevier B.V. All rights reserved.

* Corresponding author.
E-mail address: cristiana.ciobanu@adelaide.edu.au (C.L. Ciobanu).

http://dx.doi.org/10.1016/j.lithos.2014.09.001
0024-4937/© 2014 Elsevier B.V. All rights reserved.

1. Introduction

Iron oxide copper-gold (IOCG) mineralization is presently considered part of a broad group of deposit types that form within ore systems spanning from the Archean to the Phanerozoic (Barton, 2014; Groves et al., 2010; Hitzman et al., 1992; Williams, 2010; Williams et al., 2005). Formation models for these deposits are still much debated, particularly regarding the role of igneous rocks, the sources of metals and fluids, and geodynamic settings (e.g., Barton and Johnson, 2004; Chiaradia et al., 2006; Groves et al., 2010; Pollard, 2006; Williams et al., 2005).

IOCG systems are typified by zoned, broad alteration haloes comprising early, barren albite, and, in most cases, a late, ore-hosting type of alteration. Albite-bearing alteration is part of a broader sodic(-calcic) alteration spectrum with various mineralogical expressions. The late ore-hosting alteration can be broadly subdivided into deeper potassic (K-feldspar ± biotite) and upper hydrolytic (sericite ± chlorite ± carbonate) alteration, where magnetite and hematite are dominant Fe-oxides, respectively. The sericitic alteration may result from breakdown of pre-existing potassium feldspars, e.g., in granitic rocks or their volcanic equivalents, by interaction with acidic fluids (e.g., Hitzman et al., 1992). Other systems, associated with carbonate-rich protoliths, feature instead calc-silicate alteration and in this case the ore is hosted within skarn assemblages. Based on gains or losses of different components, Barton (2014) considers skarn formation (referred to as carbonate-hosted alteration) as distinct from the Na–Ca alteration of aluminous igneous or sedimentary protoliths which can also result in formation of calc-silicates. A comprehensive account of variation in alteration styles in IOCG systems worldwide, and how they differ from those in other types of hydrothermal deposits, is given by Barton (2014).

Albitization, by itself, does not define an IOCG system. For example, widespread regional expression of albitization (Na–Ca-alteration) is also recognized in seafloor hydrothermal systems (e.g., Alt, 1999), or can reflect regional-scale metasomatism related to metamorphic reactions involving evaporite-derived fluids (e.g., Oliver et al., 2004). Large-scale metasomatic albitization of continental crust is recognized as a product of fluid–rock interaction with crustal fluids, sometimes resulting in regional-scale albitite terranes, e.g., Bamble, SE Norway (e.g., Engvik et al., 2008; Plümper and Putnis, 2009). Moreover, sodium metasomatism of gneisses, migmatites and granites relating to crustal-scale shear zones can result in concentration of uranium, as for example, central Ukraine (Cuney et al., 2012) and also in IOCG-hosting terranes elsewhere (Montreuil et al., in press).

Modelling the role of sodic alteration in the formation of IOCG deposits has been addressed in the Eastern Mt. Isa Block, Australia (Oliver et al., 2004). This is considered a landmark study as it provides a comprehensive approach (whole-rock geochemistry, stable isotopes, fluid inclusions and numerical modelling) aimed at understanding gains and losses of various elements and processes associated with fluid–rock interaction during sodic metasomatism. Oliver et al. (2004) studied the behaviour of a broad range of major and minor elements (Na, Fe, K, Ba, Rb, Ca, Pb, Zn, Cu etc.) but did not include either rare earth elements and yttrium (hereafter REY) or uranium (U). The marked enrichment in REY and U relative to average crustal values is, however, a defining characteristic of the IOCG deposit class, for which any genetic model must account (Hitzman et al., 1992). This is despite the fact that some IOCG terranes do not contain accumulations of these elements at the levels seen in >9000 Mt Olympic Dam Cu–Au–U deposit, South Australia (0.26 kg/t U_3O_8, ~0.17 wt.% La and 0.25 wt.% Ce; Ehrig et al., 2013). The conceptualization of IOCG deposits (large tonnages, low Cu and Au grades and abundance of Fe-oxides in the breccia host for the Cu–Au–U ore) is based on Olympic Dam (Hitzman et al., 1992), which contains the largest known resource of U on Earth (Cuney, 2010; Hitzman and Valenta, 2005).

The Olympic IOCG Province, eastern Gawler Craton, South Australia (Skirrow et al., 2002, 2007), including the Olympic Dam deposit, is one of the archetypal Mesoproterozoic examples of giant IOCG provinces. Whereas Olympic Dam stands out by being hosted within a large body of brecciated granite with multiple deposit-scale mineral and geochemical zoning (e.g., Ehrig et al., 2013), other deposits and prospects in the province feature a range of alteration styles and metal endowments (e.g., Hayward and Skirrow, 2010; Skirrow et al., 2002, 2007). Alteration ranges from the 'end-member' sericite–hematite–breccia hosted type such as Olympic Dam and Prominent Hill, in the northern part of the province (Fig. 1a), with transition to skarn-hosted mineralization in the Punt Hill district, in the central part of the province (Reid et al., 2011), and mineralization on the Yorke Peninsula in the south with Hillside as the best characterized example (Conor et al., 2010; Ismail et al., 2014). Unlike in other IOCG terranes in Australia (e.g., Cloncurry District), the Olympic Province also stands out by a

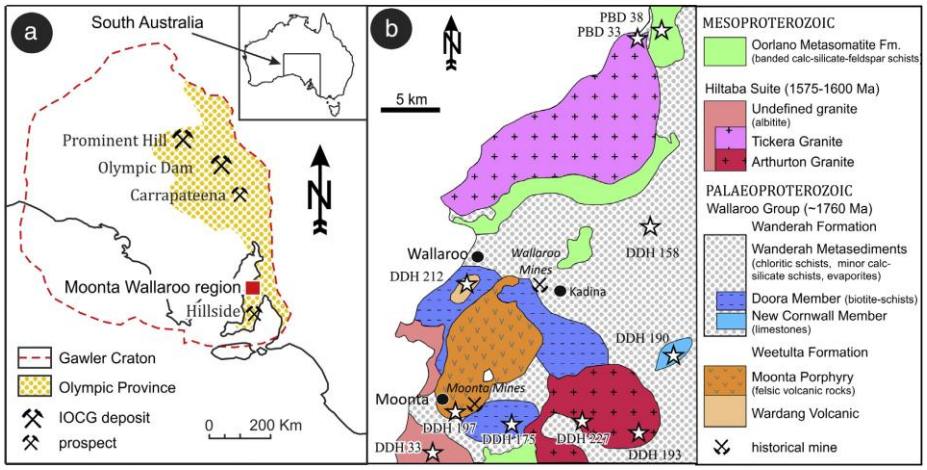

Fig. 1. a) Location of Moonta-Wallaroo region and IOCG deposits/prospects within the Olympic IOCG Province, Gawler Craton (adapted from Conor et al., 2010). Inset: Location of South Australia. b) Geological sketch of basement stratigraphy and location of drill hole locations in the Moonta-Wallaroo region (adapted from Forbes, 2012).

characteristic REE and U enrichment, irrespective of alteration style (e.g., Skirrow et al., 2007).

The Moonta-Wallaroo area in the north-west of the Yorke Peninsula is known for past exploitation of small Cu–Au veins (Fig. 1). Mineralization in the Moonta and Wallaroo Mines is hosted within felsic porphyry rocks displaying potassic alteration (biotite–magnetite ± K-feldspar ± albite; e.g., Conor et al., 2010). The area is considered prospective for new, large-tonnage, lower-grade resources. The region is also an example of an IOCG-hosting terrane in which regional-scale alkali alteration is recognized in different lithologies (e.g., Conor et al., 2010; Cowley et al., 2003), ranging from igneous to metasedimentary rocks. These include distinctive calc-silicate-bearing lithologies such as the Oorlano Metasomatite Formation (Conor, 1995), a descriptor for distinctive, highly-altered bodies of rock for which the sedimentary or granitic precursor identity cannot be readily determined, as well as units within the Wandearah Formation of the Wallaroo Group comprising banded feldspar + calc-silicates and carbonate-rich units (Fig. 1b). Rocks of the Wallaroo Group are also recognized in the Punt Hill district and at Hillside where they are likely protoliths for skarn formation.

Skirrow et al. (2002) suggested that the Moonta-Wallaroo district represents a deeper crustal level of IOCG hydrothermal activity than the Olympic Dam district. Given the extreme REY-U-enrichment in sericite-altered granitic rocks at Olympic Dam, we raise the question of whether the initiation of such an event can be recognized in deeper, less altered rocks of the Moonta-Wallaroo district in which granitic and felsic volcanic rocks are abundant and albitization is present. The applicability of REY fractionation trends in minerals to track the temporal evolution of an IOCG system from protolith through early and late mineralization stages has been demonstrated at Hillside (Ismail et al., 2014). Using the Moonta-Wallaroo area as a study case, our aim is to use this highly sensitive tool to track those mineral reactions associated with initiation of hydrothermal activity (albitization) relative to mineral textures and their REE geochemistry in both granitic and sedimentary rocks. Given the close paragenetic and geochemical correlation between REY and U, this work also carries implications for the distribution of U in IOCG systems.

2. Geological background

2.1. IOCG mineralization and the Olympic Cu–Au Province

The Olympic Cu–Au Province (Hayward and Skirrow, 2010; Skirrow et al., 2002, 2007; Fig. 1a) is located in the Olympic Domain (Ferris et al., 2002) and extends for over 700 km, encompassing numerous prospects alongside the Olympic Dam and Prominent Hill deposits (Ferris et al., 2002; Hayward and Skirrow, 2010; Skirrow et al., 2002, 2007). The Paleo- to Mesoproterozoic basement of the Olympic Domain belongs to one of the mobile belts that surround the Late Archean granulite facies core of the Gawler Craton. Two orogenic events are recognized: one associated with emplacement of the Donington granitoid suite at 1.85 Ga; and the Kimban orogeny at 1.73–1.69 Ga (e.g., Hand et al., 2007; Reid and Hand, 2012). These affected the basinal rocks of the (2.0–1.85 Ga) Hutchinson Group and the (1.76–1.74 Ga) Wallaroo Group, respectively.

Major magmatism, interpreted as a Large Igneous Province by some authors (e.g., Allen et al., 2008; Wade et al., 2012) took place at ~1.6 Ga. This comprised emplacement of the Hiltaba Intrusive Suite (HIS) and large-scale volcanism (Gawler Range Volcanics; GRV). Both intrusive and extrusive rocks include felsic and mafic components. Although deformation is considered to have largely ceased with the Kimban orogeny, evidence for subsequent greenschist- to lower amphibolite facies metamorphism is recognized in Wallaroo Group rocks in the Moonta region. This, broadly termed the Kararan orogeny (Hand et al., 2007; Reid and Hand, 2012), is considered synchronous with emplacement of the Tickera Granite at 1598 ± 7 to 1575 ± 7 Ma (Conor, 1995; Fanning et al., 2007; Fig. 1). Recognition of this metamorphic overprint has been taken as an argument against the proposed anorogenic setting for LIP magmatism, with implications for generation of IOCG systems (Skirrow, 2008).

Deposition of Cu–Au mineralization is considered to be contemporaneous with the ~1.6 Ga magmatic event, based on dating of igneous and hydrothermal minerals (e.g., Ciobanu et al., 2013; Jagodzinski, 2005; Johnson and Cross, 1995; Reid et al., 2013; Skirrow et al., 2007).

The region is unconformably overlain by sequences of Neoproterozoic, Cambrian, Permian and Cenozoic sediments (e.g., Conor et al., 2010; Morales Ruano et al., 2002).

2.2. The Moonta-Wallaroo region

The Wallaroo Group is a diverse suite of siltstone-dominated metasedimentary, felsic and mafic metavolcanic rock packages, including the Wandearah and Weetulta Formations (Conor et al., 2010; Cowley et al., 2003). The Wandearah Formation comprises metasediments, and a range of feldspathic, calc-silicate and carbonaceous members, including the Doora and New Cornwall Members, whereas the rhyodacitic Moonta Porphyry Member and ~1740 Ma Wardang Volcanic Member form the Weetulta Formation (Cowley et al., 2003; Fig. 1).

The Hiltaba Suite comprises granites of which the Tickera and 1583 ± 7 Ma Arthurton Granites are the largest in the Moonta-Wallaroo district (Conor et al., 2010), as well as mafic–ultramafic intrusive rocks, e.g., the 1583 ± 3 Ma Curramulka Gabbronorite to the west of the study area (Zang et al., 2007). Zang et al. (2007) defined both the Tickera and Arthurton Granites as composite batholiths, with compositions ranging from monzogranite and granodiorite to tonalite. Granitoids of the Tickera Granite are stated as I- and S-type, whereas the Arthurton Granite is described as A-type (Cowley et al., 2003).

Alteration is widespread throughout a varied range of rocks across the northern Yorke Peninsula (Conor et al., 2010). The link between district- to regional-scale alteration and IOCG mineralization in the Gawler Craton was first stressed by Conor (1995) in the Moonta-Wallaroo district. A summary of the current view on alteration stages across the Olympic Province (Hayward and Skirrow, 2010), comprising four different types of alteration, highlights the Moonta-Wallaroo district in the overall context of the Olympic IOCG Province.

Early albite ± calc-silicate (actinolite-diopside) ± magnetite alteration (*alias* Na-Ca-Fe alteration) is recognized as km-scale zones in the Moonta-Wallaroo district and in the Mt. Woods Inlier. Geophysical models infer large-scale magnetite alteration at deeper levels in the Olympic Dam district. Calc-silicate (actinolite-clinopyroxene ± titanite) or scapolite-bearing assemblages occur locally and are considered part of this alteration stage. This first alteration stage is comparable to Na-Ca alteration seen in other IOCG domains in Australia (e.g., in the Cloncurry district; Williams et al., 2005) and worldwide. The second type of alteration (biotite-magnetite or Fe-K) is characteristic of the Moonta-Wallaroo district and Mt. Woods Inlier. It is also considered a regional alteration signature in the deeper part of the Olympic Dam district based on aeromagnetic data (Raymond, 2003). Albite is considered to be stable during this alteration. Although only weak Cu-mineralization is generally associated with this stage, such alteration can also host high-grade vein Cu-Au ores as seen by the mineralization character of the Moonta and Wallaroo Mines (Conor et al., 2010).

The third type of alteration (magnetite-K-feldspar ± actinolite ± carbonate), although a similar type of Fe–K metasomatism as the biotite–magnetite, has a distinct mineralogy and is typical of the Olympic Dam district, in particular satellite prospects such as Acropolis, Wirrda Well and Murdie Murdie (e.g., Davidson et al., 2007). Relicts of similar assemblages are observed in many IOCG systems. As in the biotite-magnetite alteration, the magnetite-K-feldspar ± actinolite ± carbonate alteration may be associated with low-grade Cu-mineralization. This is also suggested to be the equivalent of hydrothermal magnetite-siderite in deeper and outer parts of the Olympic Dam deposit (Haynes et al., 1995; Reeve et al., 1990).

The fourth style of alteration (sericite–hematite–chlorite–carbonate) is not characteristic of the Moonta-Wallaroo district but is the dominant alteration style at Olympic Dam and also at Prominent Hill (Belperio et al., 2007). Hayward and Skirrow (2010) attribute deposition of the main Cu–Au–U ores and REE-phosphates to this stage. Sericite is interpreted to replace igneous and metamorphic K-bearing phases such as K-feldspar whereas chlorite replaces Fe–Mg-silicates (amphiboles, biotite). In cases where no precursor minerals are evident, such alteration is considered to form in vein and breccia matrices. This alteration is interpreted as a form of H_2O–CO_2 metasomatism involving strong oxidation. The latter is inferred from the change in mineral assemblage from one containing ferrous iron (e.g., magnetite, amphibole) to another containing ferric iron (hematite, clinozoisite). This alteration type is interpreted (Hayward and Skirrow, 2010) as the equivalent of 'hydrolytic alteration' in IOCG districts elsewhere (see above) but argue against use of this term since it has a strong genetic connotation.

Based on dating in the Moonta-Wallaroo district and elsewhere in the Yorke Peninsula, Conor et al. (2010) states that the main ingredients in this sub-domain are a suite of HIS granites, regional greenschist facies metamorphism, Na–K–Ca–Fe metasomatism and polymetallic mineralization. This convergence is optimally seen at contacts with the Wallaroo Group, where intensely partitioned deformation and metasomatism have produced high-grade ores. There is, however, difficulty in constraining the relative timing of metasomatism, intrusion and regional metamorphism.

3. Approach and methodology

Fifteen drillcore samples (Fig. 1, Table 1) previously collected from 10 drillcores in the Moonta-Wallaroo region were studied.

An FEI Quanta 450 scanning electron microscope (SEM) with energy dispersive X-ray spectrometry and back-scatter electron (BSE) imaging capabilities (Adelaide Microscopy, University of Adelaide) was used. BSE imaging (accelerating voltage, 20 kV, and beam current of 10 nA) allowed for characterization of each sample in terms of significant textures and mineralogical relationships, and identification of suitable areas for further microanalysis.

Quantitative compositions of feldspars and accessory minerals within representative samples were determined using a Cameca SX-Five Electron Probe Microanalyser (EPMA). Standards, X-ray lines, count times, typical minimum detection limits (mdl) are given in Appendix B.

Laser-Ablation Inductively-Coupled Mass Spectrometry (LA-ICP-MS) was used on selected samples to provide quantitative trace element data (as spot analyses and element maps) for potassium feldspar, albite, rutile, titanite, apatite, zircon and calcite. This was performed on a Resonetics M-50-LR 193-nm Excimer laser microprobe coupled to an Agilent 7700cx Quadrupole ICP-MS at Adelaide Microscopy, University of Adelaide. Full details of the analytical methods are given in Electronic Appendix B.

Focussed ion beam-scanning electron microscopy (FIB-SEM) work was carried out on a Dual Beam FEI Helios Nanolab 600 platform (Adelaide Microscopy) allowing for cross-section imaging, as well as cutting, extraction and thinning of foils for transmission electron microscopy (TEM) study at site-specific locations in the sample. Procedures for cutting, extraction and thinning of TEM foils followed Ciobanu et al. (2011). Working on polished blocks, grain areas were selected immediately adjacent to LA-ICP-MS craters of interest. Slices removed for TEM sample preparation were attached to a tungsten needle and transported to the grid holder. Each slice was then sequentially thinned from both sides until it became sufficiently transparent for TEM analysis. Final thinning (to <60–100 nm) is done at 30 kV and (maximum) 93 pA, and then cleaned at 5 kV or lower to remove material deposited onto the surface.

The TEM study was performed on Philips 200CM and FEI Tecnai G2 Spirit instruments operated at 200 and 120 kV, respectively (Adelaide Microscopy). Both instruments are equipped with a Gatan digital camera and energy-dispersive X-ray analysis (EDAX) capabilities.

4. Petrography

Of the lithologies in the Moonta area illustrative of early regional alkali metasomatism (albite ± K-feldspar), particularly albitization (Conor et al., 2010), three types have been studied here: altered felsic igneous rocks, intensively altered rocks of igneous origin and rocks of metasedimentary origin from the Wandearah Formation and Oorlano Metasomatite (Fig. 1). Key textures and mineral relationships are depicted in BSE images in Figs. 2–5. Compositional data (EPMA) for feldspars are given as Tables 2a and 2b. Data for actinolite, clinozoisite, accessory and REY-minerals are given as Appendix A, Tables 1–5.

4.1. Main rock types: primary and alteration features

4.1.1. Altered igneous rocks

Igneous rocks studied include two granitoids (Tickera Granite and Arthurton Granite) and a felsic volcanic (rhyodacite; Wardang Volcanic). The Tickera Granite is intensely deformed and maybe older than the Arthurton Granite, even though ages overlap (Cowley et al., 2003).

Table 1
Index of samples studied.

Sample ID	Stratigraphy	Rock type	Main mineralogy				Accessory minerals				Minor/trace minerals	
			Kfs	Ab	Qz	Chl	Ap	Rt	Ttn	Zrc	Other	REEm
227DDH1	Arthurton Granite	Alkali monzogranite	**xx**	**x**	**xx**	**xx**	x	x		x	Hm, Chl	Xn, Bast,
227DDH2	Arthurton Granite	Alkali monzogranite	**xx**	**xx**	**xx**	**x**	x	x		x	Hm, Chl	Xen, Bast,
193DDH1	Arthurton Granite	Alkali monzogranite	**xx**	**x**	**xx**	**xx**		x		x	Hm, Chl	Xen, Mon
33PBD1	Tickera Granite	Variable monzogranite and quartz monzonite	**xx**	**xx**	**x**	**x**	x	x	x	x	Hm, Chl, Cp	Bast, Mon
33PBD2	Tickera Granite	Variable monzogranite and quartz monzonite	**xx**	**xx**	**x**	**x**	x	x		x	Hm, Chl, Cal	Bast, Xen
212DDH1	Wardang Volcanic	Rhyodacite felsic volcanic	**xxx**	**x**	**xx**	**x**	x	x			Hm, Chl	Bast, Mon
212DDH2	Wardang Volcanic	Rhyodacite felsic volcanic	**xxx**	**x**	**xx**	**x**	x	x		x	Hm, Chl	
33DDH1	Undefined Hiltaba Suite	Highly albitised granite (albitite)	**x**	**xxx**	**xx**	**xx**	x	x		x	Hm, Chl	Bast, Xen, Syn
197DDH1	Moonta Porphyry	Highly altered rhyodacite	**xxx**	**x**	**xx**	**xx**	x	x		x	Hm, Chl,	Xen, Mon
175DDH1	Doora Member	Albitebiotite- schist	**xx**	**xx**	**x**	**x**		x			Bt, Mu, Hm, Chl, Mgh, Cp	
158DDH1	Wanderah Formation	Chloritic schist	**xx**	**x**	**xx**	**xx**	x	x			Hm, Chl	
190DDH1	New Cornwall Member	Limestone		**x**	**x**	**x**	x				Dol, Chl,	
190DDH2	New Cornwall Member	Limestone		**x**	**x**	**x**	x	x			Dol, Chl,	Bast,
38PBD1	Oorlano Metasomatite	Calc-silicate feldspar schist	**x**	**xx**	**x**	**x**	x		x		Clz, Act, Hm, Chl, , Cp, Cal	Bast,
38PBD2	Oorlano Metasomatite	Calc-silicate feldspar schist	**x**	**xx**		**x**	x		x	x	Clz, Act, Hm, Chl, Cp	Mon

Abbreviations: Ab — albite, Act — actinolite, Ap — apatite, Bast — bastnasite, Bt — biotite, Cal — calcite, Chl — chlorite, Clz — clinozoisite, Cp — chalcopyrite, Dol — dolomite, Hm — hematite, Ilm — ilmenite, Kfs — K-feldspar, Mgh — maghemite, Mon — monazite, Mt — magnetite, Mu — muscovite, Plag — plagioclase, Rt — rutile, Ser — sericite, Syn — synchysite, Ttn — titanite, Xen — xenotime, Zrc — zircon, REEm — REE minerals. Note on compositions: xxx = >50%, xx = 20–50%, x = 5–20%, x = <5%.

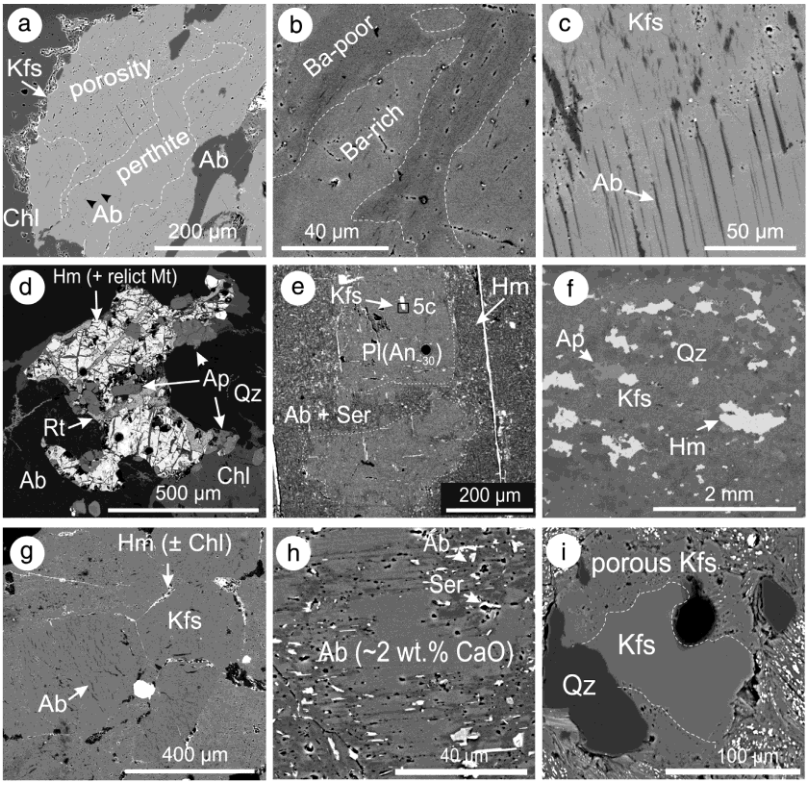

Fig. 2. Back-scatter electron (BSE) images showing petrographic aspects of igneous rocks: Arthurton and Tickera Granites (a–e); felsic rhyodacite, Wardang Volcanics (f–g); albitite (h); Moonta Porphyry (i). (a) Coarse, xenoblastic orthoclase displaying varying degrees of porosity and domains of perthite. (b) Zonation with respect to Ba content in the K-feldspar. (c) 'Exsolution-like' lamellae of albite preserved within K-feldspar. (d) Accessory apatite clustered around pockets of Fe–Ti-oxides. (e) Large relict plagioclase (~An_{30}) containing small inclusions of K-feldspar and replaced by an intergrowth of albite and sericite. (f) Porphyritic and flow banding fabrics in felsic volcanic. Note abundant hematite and apatite. (g) Potassium feldspar aggregates with minor perthitic domains, varying degrees of porosity with rims of hematite. (h) Ca-richer domains within porous albite; note cleavage-oriented sericite lamellae. (i) Corroded, relict K-feldspar surrounded by an overgrowth of second-generation K-feldspar characterized by more abundant pores. Abbreviations: Ab — albite; Ap — apatite; Chl — chlorite; Hm — hematite; Kfs — K-feldspar; Mt — magnetite; Qz — quartz; Rt — rutile; Ser — sericite; Mt — magnetite; Zrc — zircon.

Both granitoids are coarse-grained and consist of K-feldspar, low-Ca plagioclase ($An_{0.8-8}$; Tables 2a and 2b), quartz and chlorite (mostly replacing hornblende ± biotite) as main components, minor Fe- and Ti-oxides, as well as abundant accessory minerals such as zircon and apatite. Although albite is presently the dominant plagioclase feldspar in both rocks, andesine ($An_{\sim 32}$), an intermediate member of the plagioclase series, is also present as relicts in the Tickera Granite (Tables 2a and 2b). Large (>2 mm) xenoblastic K-feldspar (orthoclase) of igneous origin commonly displays zonation with respect to Ba content, areas of sericitization, and varying degrees of porosity (Fig. 2a, b). In addition, 'exsolution-like' lamellae of albite are preserved at various scales within this K-feldspar, forming perthitic textures (Fig. 2a, c). Such perthitic textures could be an end product of feldspar crystallization from granitic melts. In the Tickera Granite, perthites are more abundant and also show changes in the albite morphology from lamellar to lens-shaped. Such modification can be attributed to diffusion and/or syn-deformational (re)crystallization of pre-existing exsolution perthites. Accessory minerals such as apatite and zircon are clustered around pockets of Fe-Ti-oxides (Fig. 2d).

Superimposed hydrothermal alteration is expressed in three assemblages resulting from pseudomorphic replacement of pre-existing minerals within the two granitoids. Firstly, igneous feldspars are replaced by widespread coarse albite displaying characteristic porosity. The andesine in the Tickera Granite occurs as relicts (Fig. 2e), illustrating replacement of igneous plagioclase by albite. The hydrothermal nature of the albite can be inferred from its textures such as the presence of abundant pores in both granitoids, as well as nucleation of sericite, hematite and discrete REY-U-minerals within such pores. Formation of albite + sericite on behalf of pre-existing andesine is also marked by the appearance of a new K-feldspar generation (Fig. 2e; see below). Comparable replacement among feldspars is seen in granitic rocks elsewhere (Engvik et al., 2008; Plümper and Putnis, 2009). Secondly, pre-existing mafic minerals are replaced by chlorite + hematite assemblages. Thirdly, accessory Fe- and Fe–Ti-oxides (ilmenite and magnetite) are replaced by hematite (Fig. 2d) and symplectites consisting of rutile + chlorite ± hematite. The coarser REY-minerals are found within such symplectites (see below). In the Tickera Granite, relict ilmenite is preserved within the symplectite, and is more abundant. This is consistent with the relatively reduced character of the Tickera Granite relative to the Arthurton Granite (e.g., Cowley et al., 2003).

The rhyodacitic Wardang Volcanic is predominantly composed of K-feldspar, quartz, minor albite, and contains abundant hematite and

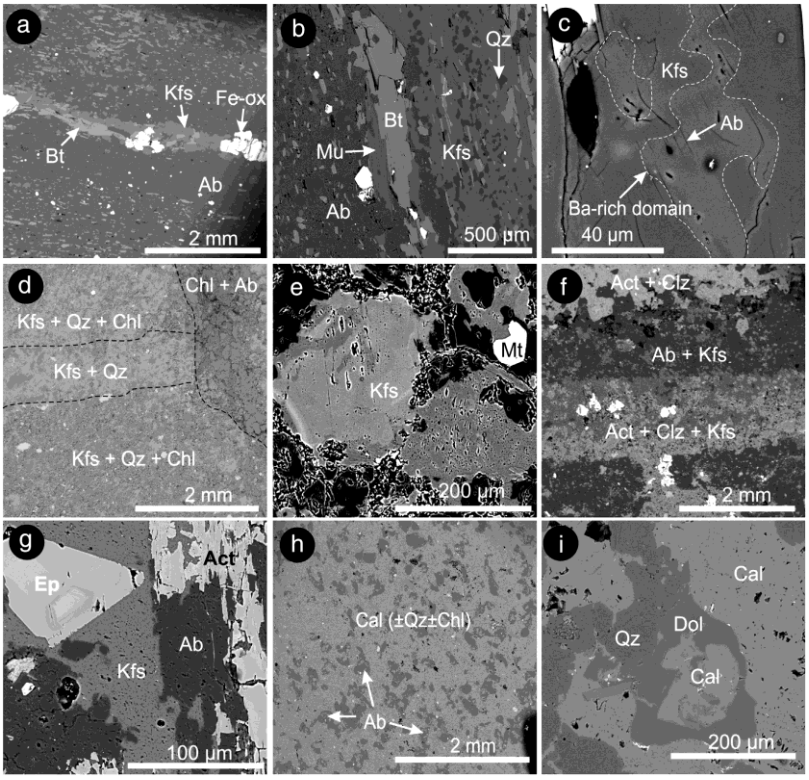

Fig. 3. BSE images showing petrographic aspects of the albite–biotite-schist (a–c), chlorite-schist (d–e), Oorlano Metasomatite (f–i) and limestone (j–l). (a and b) Fine- to medium-grained laminar layers of albite + biotite ± muscovite + K-feldspar + quartz defining a schistose fabric. Note disseminations of Fe-oxides. (c) Distinctive Ba-zonation and domains of fine perthitic textures. (d) Banding in the chlorite-schist expressed by differing proportions of chlorite; note albite in crosscutting vein. (e) K-feldspar porphyroblast showing domains suggestive of multiple stages of syn-deformational growth (variation in the intensity of porosity and Ba-content). (f) Alternating bands in the Oorlano Metasomatite dominated by feldspars (both albite and K-feldspar) or calc-silicates (actinolite and clinozoisite). (g) Disequilibrium replacement textures between K-feldspar, albite and calc-silicates. Note oscillatory zoning in clinozoisite. (h) Pervasive albite as spots in impure limestone. (i) Dolomite + quartz-bearing domains within the limestone. Abbreviations: Ab — albite; Act — actinolite; Bt — biotite; Cal — calcite; Chl — chlorite; Dol — dolomite; Ep — epidote; Kfs — K-feldspar; Mt — magnetite; Mu — muscovite; Qz — quartz; Rt — rutile.

accessory apatite. This rock has an overall fine-grained, porphyritic and flow-banded texture (Fig. 2f). Potassium feldspar aggregates commonly display minor perthitic domains and varying degrees of porosity (Fig. 2g). In addition, K-feldspar grain boundaries are also rimmed by hematite. In contrast to the granites, albitization is relatively minor and advanced hematite alteration prevails.

4.1.2. Intensely altered igneous rocks

Two pervasively altered igneous rocks were studied: an albitite from an undefined Hiltaba Suite granite; and a porphyritic felsic volcanic (rhyodacite) attributed to the Moonta Porphyry. These are representative of distinct alteration sub-types, i.e., intense albitization and K-feldspar + silicification, respectively. Although relict textures are still recognisable, the dominant feldspar within each is of replacement origin (see below).

The albitite is mainly composed of albite (An_1; Tables 2a and 2b), quartz, K-feldspar and chlorite, and contains abundant accessory minerals clustering Fe-Ti-oxides. The albite hosts homogeneous, Ca-richer (1–2 wt.% CaO) domains enclosed by areas of increased porosity and intergrowths with sericite (Fig. 2h). This feature is comparable to plagioclase relationships in the Arthurton Granite.

The highly altered felsic volcanic representing the Moonta Porphyry is similar to the aforementioned rhyodacite with respect to fine-grain size, flow banding, and porphyritic texture (Fig. 2i). The Moonta Porphyry, however, features strong silicification, which is seen as layering within the K-feldspar-rich domains. Importantly, albite is only present in trace amounts. In both rocks, Fe-oxides (magnetite and hematite), are significant components, either as dusty inclusions underlining the breakdown of mafic minerals to chlorite, or as large, fractured porphyroblasts. The latter texture suggests precipitation within strain shadows of larger K-feldspar. The cores of relict igneous K-feldspar are surrounded by pore-bearing overgrowths with mutual boundaries suggesting inwards-directed corrosion and replacement (Fig. 2i).

4.1.3. Metasedimentary rocks and Oorlano metasomatite

Three banded rocks were studied: albite–biotite-schist (Doora Member); chlorite-schist (Wandearah Formation); and calc–silicate-schist (Oorlano Metasomatite Formation). In addition to the three schists, a limestone (New Cornwall Member) with incipient but pervasive dolomitization and albitization was also studied. The banded rocks all contain feldspars as major components but differ in terms of mafic

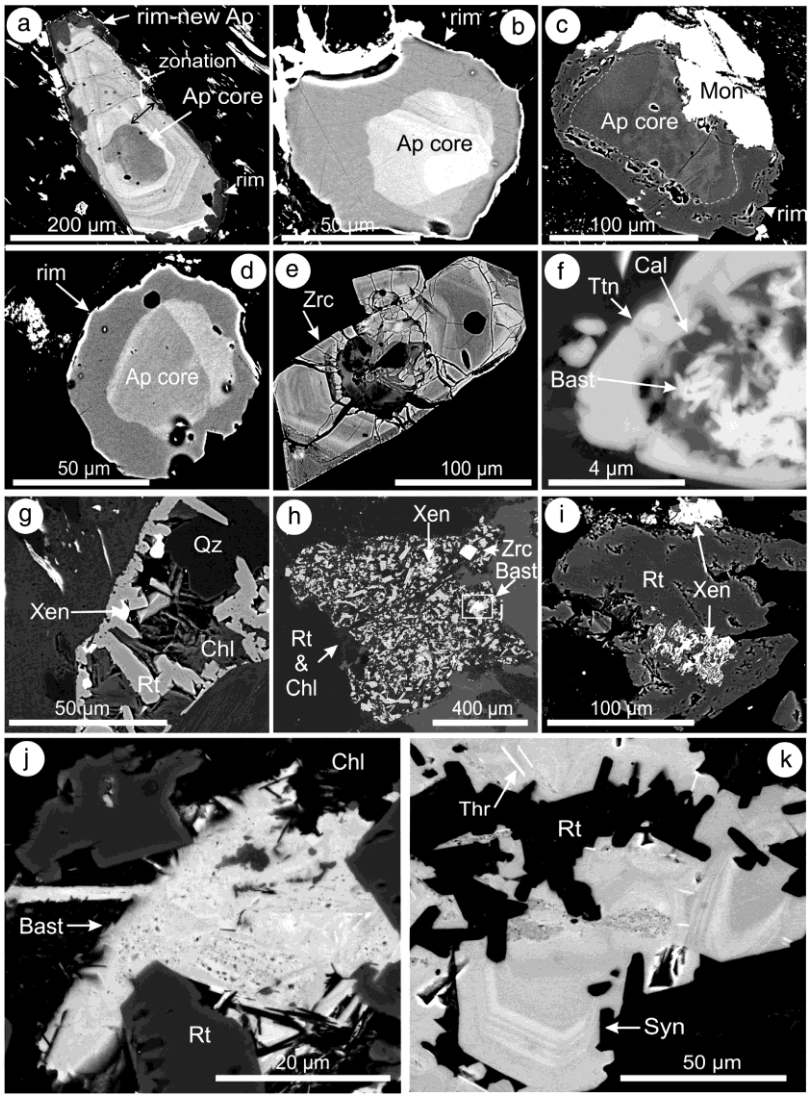

Fig. 4. BSE images showing accessory and REY-minerals. (a and b) Oscillatory zonation in apatite from granitoids showing inverse core-to-rim patterns; bright and dark shades correspond to higher- and lower-REY concentrations. (c) Patchy zones in apatite core with porous margin marked by REY-depletion (darker on figure); note monazite partially replacing the apatite margin. (d) Typical texture of apatite in the chlorite–schist comprising a rounded, deformed REE-rich core surrounded by a REE-poor rim suggestive of multiple stages of growth. (e) Highly fractured, metamict zircon with oscillatory zoning typical of the granitoids. (f) Pseudomorphic replacement of titanite by bastnäsite and calcite, Oorlano Metasomatite. (g) Cavities rimmed by rutile; note inclusions of xenotime, albitite. (h) Typical pseudomorphic replacement of accessory ilmenite by rutile–chlorite symplectites in granitoids. Note abundant REY-minerals (xenotime and bastnäsite) as well as zircon. (i) Coarse, corroded rutile in the rhyodacite hosting xenotime. (j) Detail of bastnäsite within rutile (Fig. 4h) showing compositional variation and fields of dusty inclusions and pores. (k) Synchysite-(Ce) displaying oscillatory zoning; note lamellar exsolutions of thorite. Abbreviations: Ap — apatite; Bast — bastnäsite; Cal — calcite; Chl — chlorite; Mon — monazite; Qz — quartz; Rt — rutile; Syn — synchysite; Thr — thorite; Ttn — titanite; Xen — xenotime; Zrc — zircon.

minerals, i.e., mica, dominantly biotite (albite–biotite-schist), chlorite (chlorite-schist), and actinolite + clinozoisite (Oorlano Metasomatite). Whereas in the albite–biotite-schist, albite is the dominant mineral (~50%), the proportion of K-feldspar to albite, and feldspars to calc-silicates varies with banding in the Oorlano Metasomatite; albite is very minor in the chlorite-schist. With the exception of the Oorlano Metasomatite, the banded rocks are considered to be of sedimentary origin and are relatively poor in accessory minerals.

The albite–biotite-schist (Fig. 3a, b) comprises fine- to medium-grained laminated layers of albite + biotite + K-feldspar + quartz ±

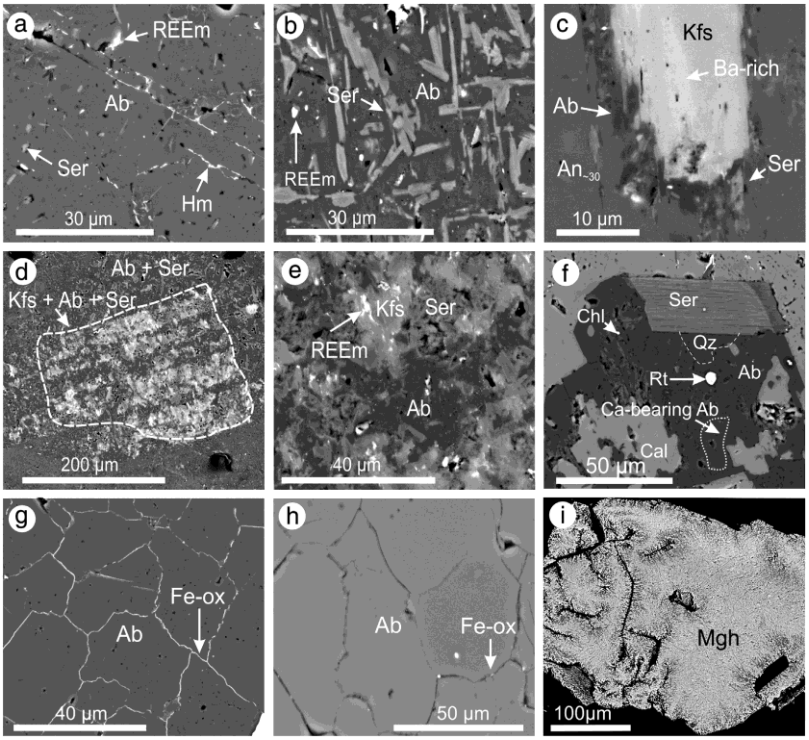

Fig. 5. BSE images showing key albitization textures in the Arthurton Granite (a), Tickera Granite (b–e), limestone (f), Oorlano Metasomatite (g–h) and albite–biotite-schist (i). (a) Thin, cleavage films of sericite and dusty inclusions of K-feldspar ± hematite ± REY-minerals attached to pores. (b) Coarsening of cleavage-oriented sericite in albite surrounding relict andesine as in Fig. 2e. (c–d) Detail of Fig. 2e showing new K-feldspar (note Ba-zonation) grains (c) and as mesh-domains interspersed with sericite and albite (d). (e) Abundant, sub-μm-sized REY-minerals in such meshes. (f) Typical albite spot within impure carbonate; note Ca-richer domains and phyllosilicates. (g, h) Fine-grained, granoblastic albite, with films of Fe-oxides and/or irregular dusty inclusions along grain boundaries. (i) Pseudomorphism of magnetite by maghemite; textures suggest volume decrease during alteration. Abbreviations: Ab — albite; Cal — calcite; Chl — chlorite; Hm — hematite; Kfs — K-feldspar; REEm — REY-minerals; Ser — sericite.

muscovite ± chlorite which define the schistose fabric. Accessory minerals include rutile ± ilmenite and trace apatite, zircon and monazite. Maghemite, pseudomorphing magnetite, is widespread throughout the rock but forms coarse porphyroblastic aggregates within the coarser layers. The K-feldspar displays some common features with the granitoids: distinctive Ba-zonation; and domains of fine perthitic textures (Fig. 3c). Minor alteration is also expressed by patchy chlorite replacing biotite and breakdown of ilmenite to rutile.

The chlorite-schist is also a fine- to medium-grained rock. Banding is expressed by changes in the relative proportions of chlorite (Fig. 3d). Minor magnetite and more abundant apatite occur throughout. Albite is mostly observed in crosscutting chlorite veinlets. K-feldspar displays porphyroblast development (<200 μm) with domains suggestive of multiple stages of syn-deformational growth, as seen by variation in the intensity of porosity and Ba-content (Fig. 3e).

The Oorlano Metasomatite is composed of alternating bands dominated by either feldspars (both albite and K-feldspar) or calc-silicates (actinolite and clinozoisite) (Fig. 3f). In contrast to the other banded rocks, the Oorlano Metasomatite contains abundant titanite, apatite and Fe–(Ti)-oxides. Euhedral clinozoisite [Fe/(Fe + Al) ~0.3] and actinolite [Fe/(Fe + Mg) = 0.3–0.4] commonly display internal chemical zoning and occasional overgrowth textures. Some of the calc-silicates are overgrown by feldspars; disequilibrium textures between K-feldspar and albite are recognized at the finer scale (Fig. 3g).

The limestone is porous, calcite-dominant, and also contains pervasive quartz, dolomite, feldspar (mainly albite), chlorite, sericite and minor apatite (Fig. 3h). Some coarser domains within the otherwise fine-grained rock tend to be dolomite-rich (Fig. 3i). The albite contains patchy domains enriched in Ca (up to 1–2 wt.%), as seen in the albitite above.

4.2. Accessory and REY-minerals

As mentioned above, all rocks contain variable amounts of accessory minerals. These include zircon, apatite, rutile, titanite and REY-minerals (bastnäsite, xenotime, synchysite, monazite) (Fig. 4). Such minerals are most widespread in the igneous rocks and Oorlano Metasomatite. Based on textures, the observed REY-minerals relate to the package of mineral reactions involving albite formation rather than magmatic crystallization. In the Oorlano Metasomatite, they are also paragentically tied to an overprint of pre-existing accessory minerals.

Apatite retains textures indicating superimposed alteration and is always characterized by chemical zoning observable on BSE images (Fig. 4a-d). EPMA data indicates fluorapatite throughout all lithologies, with higher F in igneous rocks relative to the chlorite-schist and limestone (~4.5 and ~3.5 wt.%, respectively). EPMA data shows no minor elements that would explain the observed zoning; these are instead attributed to REY variation as measured by LA-ICP-MS spot

Table 2a
Electron probe microanalytical data for albite.

	Arthurton granite	Tickera granite			Felsic volcanic	Albitite	Chlorite schist	Limestone	Calc-silicate schist	Biotite-schist							
	227DDH2	33PBD1*		33PBD1	212DDH2	33DDH1	158DDH1	190DDH2	38PBD1a	175 DDH1							
	(n = 5)	Albite	Andesine (n = 10)	(n = 4)	(n = 5)	(n = 5)	(n = 8)	(n = 9)	(n = 15)	(individual analyses of Ca-bearing plagioclase feldspar)							
F	0.02			0.80	0.07	0.18	0.03	0.06	0.23								
Na_2O	10.89	8.75	6.98	9.12	10.89	8.87	11.50	10.16	10.74	13.09	12.48	13.30	12.73	13.60	13.13	13.10	13.47	13.50
SiO_2	67.29	68.01	62.03	64.44	65.31	73.98	68.81	67.54	68.84	66.45	65.59	67.53	67.76	68.08	67.37	67.14	68.03	67.42
MgO	0.25			0.50	0.03			1.17	0.07		0.12							
Al_2O_3	20.52	20.79	25.02	22.96	19.62	16.42	19.57	20.96	20.72	18.82	18.45	20.20	19.93	19.89	20.01	20.09	19.76	20.24
P_2O_5	0.03						0.02	0.02										
Cl				0.19		0.03		0.12	0.10		0.04			0.02				
K_2O	0.49			0.90	0.26	0.07	0.02	0.29	0.11	0.09	0.12	0.06	0.05	0.05	0.08	0.06	0.05	0.08
CaO	0.16	1.39	5.90	1.33	0.44	0.17	0.04	0.68	0.28	0.83	0.96	1.15	1.12	0.89	1.02	1.17	0.84	1.08
FeO	0.09			0.26	0.55	0.16	0.08	0.33	0.47		0.63	0.11	0.06	0.07		0.08	0.09	0.03
Total	99.72	98.94	99.93	100.51	97.20	99.88	100.07	101.35	101.55	99.28	98.38	102.35	101.66	102.60	101.61	101.64	102.23	102.36
		* SEM-EDAX data																
%Ab	96.4	91.9	68.3	87.3	96.3	98.4	99.7	94.7	97.9	96.2	95.3	95.2	95.1	96.3	95.5	95.0	96.5	95.4
%An	0.8	8.1	31.7	7.0	2.1	1.1	0.2	3.5	1.4	3.4	4.1	4.5	4.6	3.5	4.1	4.7	3.3	4.2
%KFsp	2.8			5.7	1.5	0.5	0.1	1.8	0.6	0.4	0.6	0.3	0.3	0.2	0.4	0.3	0.2	0.4

Table 2b
Electron probe microanalytical data for K-feldspar.

	Arthurton granite	Tickera granite	Felsic volcanic		Albitite	Calc-silicate schist
	227DDH2	33PBD1	212DDH2	212DDH1	33DDH1	38PBD1a
	(n = 5)	(n = 13)	(n = 5)	(n = 5)	(n = 4)	(n = 21)
F			0.07	0.31	0.24	0.12
Na_2O	0.76	1.06	0.29	0.31	0.42	0.64
SiO_2	63.24	64.30	61.06	62.46	63.78	63.24
MgO				0.12		0.05
Al_2O_3	17.65	18.28	17.38	17.88	17.90	18.13
Cl	0.05	0.03	0.04	0.03	0.05	0.13
K_2O	15.39	14.68	15.37	15.86	16.17	15.52
CaO	0.03	0.06	0.08	0.54		0.03
TiO_2	0.02		0.02			
FeO	0.04	0.17	0.07	0.25	0.08	0.13
Total	97.19	98.59	94.39	97.76	98.64	97.99
%Ab	7.0	9.9	2.8	2.8	3.8	5.9
%An	0.1	0.3	0.4	2.7	0.0	0.1
%KFsp	92.8	89.8	96.8	94.5	96.2	93.9

analysis (see below). Oscillatory zonation in apatite shows variation in the core-to-rim patterns, e.g., inverse trends in terms of REY abundance (Fig. 4a, b). Distinct zones are underlined by porosity and corrosion, particularly at the outer overgrowth margin (Fig. 4a–c). In the altered volcanic rocks, the corroded overgrowth margin is further marked by REY-depletion in apatite and incorporation of released REY to form monazite (Fig. 4c). Comparable textures in apatite, also with monazite formation, have been reported for the Hillside granite (Ismail et al., 2014). Apatite from the chlorite-schist displays multiple stages of growth (Fig. 4d), corresponding to similar patterns shown above for K-feldspar (Fig. 3e).

Zircon is only abundant within the two granitoids and albitite. It commonly displays intense fracturing, metamict cores and oscillatory zoning (Fig. 4e). Zircon recrystallization likely took place during hydrothermal alteration. Compositional data show little variation in terms of Hf (1.2–1.6 wt.% HfO_2) or U content (hundreds to thousands of ppm).

Hydrothermal titanite (Oorlano Metasomatite) and rutile (igneous rocks) are typically associated with formation of discrete REY-bearing minerals. Both Ti-minerals contain measurable amounts of Nb, Ta, V, REE, and Y. We note the presence of F in both rutile (in the albitite), and titanite, as well as Sr in the latter. In the Oorlano Metasomatite, coarser euhedral grains of titanite host fine aggregates of acicular bastnäsite intergrown with calcite (Fig. 4f), clearly indicating pseudomorphic replacement. In the albitite, large cavities, rimmed by rutile and filled by chlorite + quartz, contain fine-grained xenotime (Fig. 4g). The most characteristic occurrence of discrete REY-minerals (xenotime, bastnäsite and synchysite) in the igneous rocks is, however, within the rutile-bearing symplectites forming during pseudomorphic replacement of Fe-Ti-oxides (Fig. 4h). Coarser rutile, resulting from similar symplectites, also hosts REY-minerals in the rhyodacite (Fig. 4i, j). In detail, some of the REY-minerals display oscillatory zoning or fields of dusty inclusions and pores (Fig. 4j, k). Synchysite-(Ce) displays particularly stunning oscillatory zoning and thin lamellae of thorite (Fig. 4k). Compositional data for synchysite-(Ce) and bastnäsite-(Ce) are given in Electronic Appendix A, Table 5.

4.3. Key albitization textures

All studied rocks show various degrees of albitization. Lithology, mineralogy and inherited textures of each play a role in how albitization is expressed. A striking aspect is that albite formation is always accompanied by formation of other minerals at finer scales (Fig. 5).

Such minerals are seen as thin cleavage films or dusty inclusions of sericite ± K-feldspar ± hematite ± REY-minerals attached to pores (Fig. 5a). Coarsening of sericite is observed in the Tickera Granite and felsic volcanic rocks, as well as regular, cleavage-oriented lamellar

intergrowths of sericite and albite surrounding relict andesine (Fig. 5b). There is clear evidence that albite and new K-feldspar are both formed at this stage. The latter occurs either as irregular, subhedral grains (<50 μm; Fig. 5c), or as mesh-domains interspersed with sericite and albite within host albite (Fig. 5d). Importantly, sub-μm sized REY-minerals are abundant in such meshes (Fig. 5e).

The same type of sericite nucleation also surrounds albite cores richer in Ca (Fig. 2h) in both albitite and limestone (Fig. 5f). In contrast, the Oorlano Metasomatite and albite–biotite-schist both host fine-grained (<40 μm), granoblastic albite, with films of Fe-oxides and/or irregular dusty inclusions nucleating along grain boundaries (Fig. 5g, h). The conspicuous pseudomorphism of magnetite by maghemite throughout the albite–biotite-schist (Fig. 5i), and textures suggesting volume decrease rather than typical weathering, suggest such transformation relates to albitization.

All these aspects point to the scale of albitization as a complex phenomenon tied to sub-micron-scale mineral reaction/nucleation, and an overall chemistry that involves not only Na, but also K, Ca, Fe, REY and U.

5. Trace element concentrations and distributions in feldspar and accessories: LA-ICP-MS

Seven minerals within representative samples were analysed by LA-ICP-MS to provide concentrations of REY and other trace elements. Results are given for feldspars in Tables 3 and 4, and for apatite, zircon, rutile, titanite and calcite in Electronic Appendix A, Tables 6–8. Chondrite-normalized REY trends for each mineral and individual time-resolved depth spectra (Figs. 6 and 7) allow comparative analysis of patterns for each mineral. Normalization to chondrite follows McDonough and Sun (1995). In addition, element maps of feldspars (Figs. 8 and 9) provide further insights into element distributions and partitioning from grain to nanoscale.

For the purpose of constraining and defining the early albitization, the majority of analyses were carried out on feldspars (K-feldspar and albite). The REY fractionation trends of these minerals are useful for characterizing inherited magmatic and hydrothermal signatures (e.g., as shown for the Hillside deposit, Yorke Peninsula; Ismail et al., 2014). Moreover, individual time-resolved depth spectra, showing

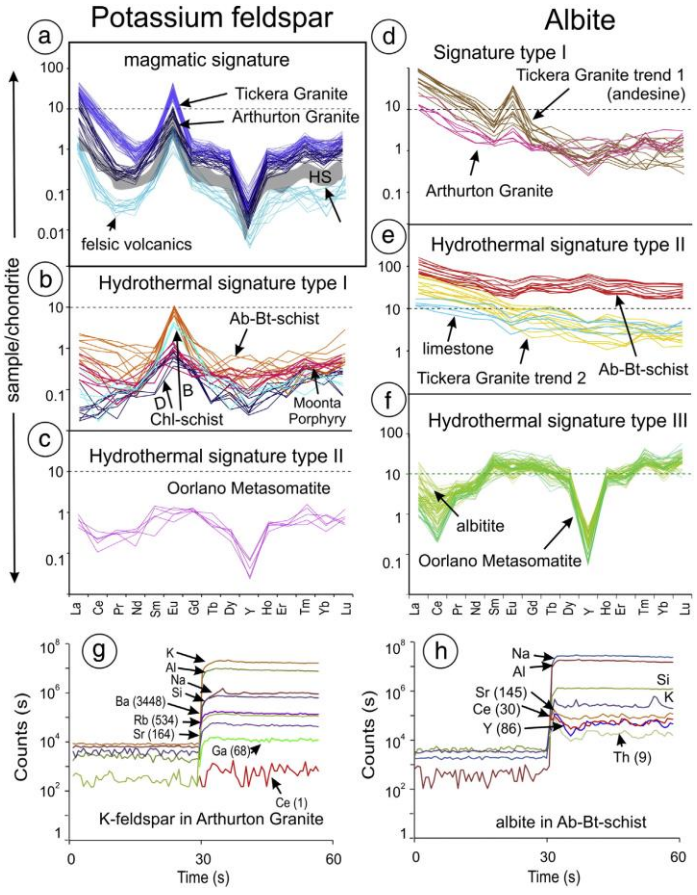

Fig. 6. Chondrite-normalized REY fractionation trends in K-feldspar (a–c) and albite (d–f). LA-ICP-MS time-resolved depth spectra for K-feldspar (g) and albite (h) showing representative signal morphologies for trace elements of interest. See text for additional explanation.

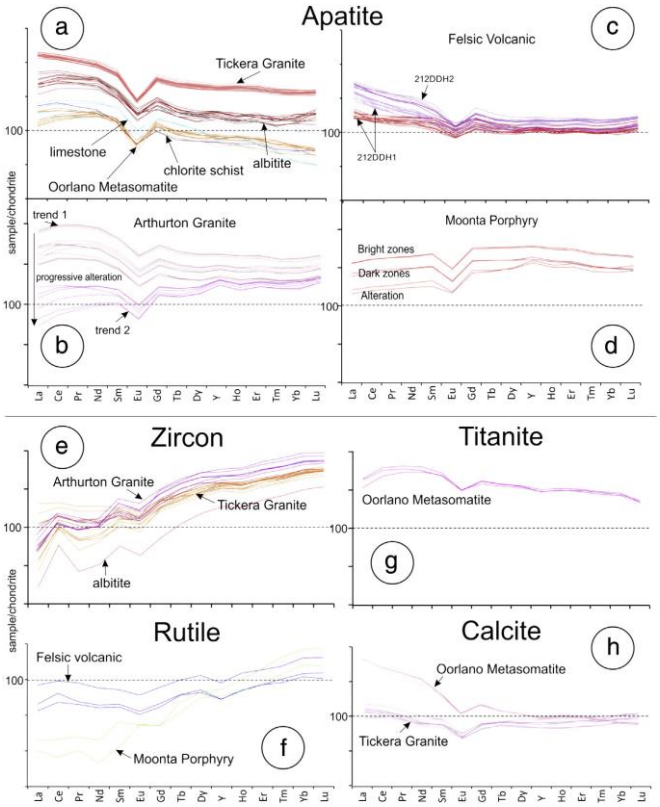

Fig. 7. Chondrite-normalized REY fractionation trends in apatite (a–d), zircon (e), rutile (f), titanite (g) and calcite (g) in studied lithologies. Note that two samples of felsic volcanic (c) show diverging fractionation trends. See text for additional explanation.

signal flatness for each element during ablation, allow a first assessment of whether inclusions (possibly at the nanoscale) or elements in solid solution are responsible for the presence of these elements. This can, however, be challenging when dealing with elements at low concentrations. Accessories such as apatite, titanite, zircon, rutile and calcite were analysed due to their ability to host significant amounts of REY. Interpreting the trends in feldspars is contingent upon understanding the distribution of REY among all minerals, either inherited from pre-existing lithologies or due to alteration. Apatite is of particular interest since it is present within almost all lithologies, as well as in rocks from across the Olympic IOCG Province.

5.1. Trace element distribution: REY trends

5.1.1. Potassium feldspar

ΣREY concentrations in K-feldspar are the lowest among the analysed minerals, varying from <1 ppm to tens of ppm in the chlorite-schist and Tickera Granite, respectively (Tables 3a and 3b). Three types of reproducible REY fractionation trends (Fig. 6a–c) are distinguished by differences in REY slope, as well as the size and strength of Eu- and Y-anomalies.

Spot analyses of K-feldspar from altered igneous rocks (Hiltaba Suite granitoids and felsic volcanics) illustrate a trend characterized by La-enrichment, a strong downward-sloping trend in the La-Pr interval, and sharp positive Eu-, and negative Y-anomalies (Fig. 6a). The trends for different lithologies are, however, distinct from one another in terms of absolute ΣREY concentrations, which span two orders of magnitude (ΣREY = 1–14 ppm). Such trends are consistent with the K-feldspar trend shown by the relatively fresh Hillside granite (Ismail et al., 2014) shown as HS on Fig. 6a. Potassium feldspar giving such trends displays similar textures to those at Hillside (presence of perthite, zonation with respect to Ba concentration, and little porosity; Fig. 2a–c, g). Importantly, as at Hillside, REY concentrations in individual spot analyses do not vary relative to the Ba-zoning in the K-feldspar. Based on such similarities, and knowing that the three granitoids belong to HIS, this trend is considered to represent a typical magmatic signature of the K-feldspar in this igneous suite. The fact that K-feldspar in the felsic volcanics (Wardang Volcanic) mimics the same pattern probably underlines the communality of REY-partitioning processes in feldspar in felsic melts. The strong negative Y-anomaly can be attributed to depletion of Y in the melt due to early crystallization of accessories such as Fe–Ti-oxides, zircon and apatite.

Contrasting with the above, the intensely altered igneous rocks and metasedimentary rocks, as well as the Oorlano Metasomatite (Fig. 6b, c) show considerably different REY fractionation trends. These K-feldspars are interpreted as hydrothermal based on the textural features described above. Measured ΣREY concentrations are much lower for such hydrothermal K-feldspar, ranging from 0.1 to 4 ppm.

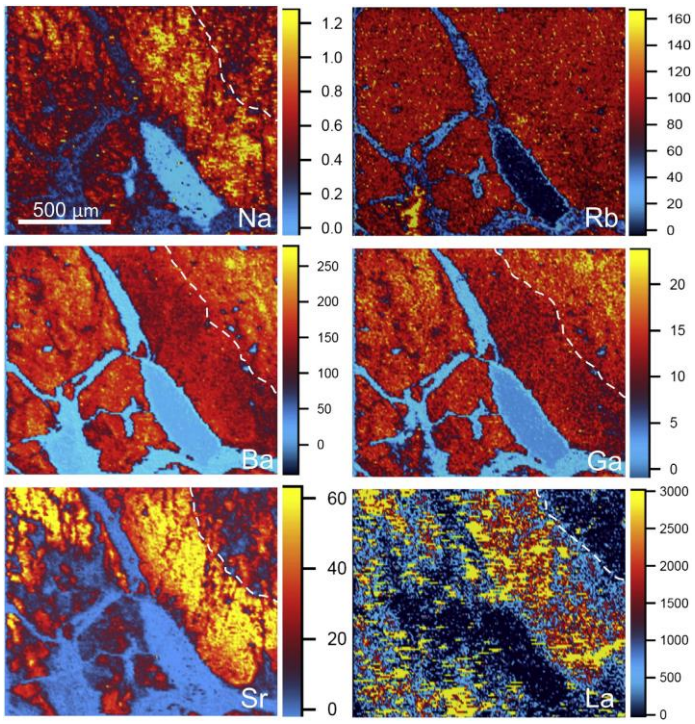

Fig. 8. LA-ICP-MS elemental maps displaying distributions within brecciated K-feldspar in the Arthurton Granite. Note white line representing onset of albitization and brecciation. Scale for La in counts-per-second (cps); 10^3 cps for Rb, Ba, Ba, Sr; 10^6 cps for Na.

These are separated into two types of trends. Trend type I (Fig. 6b), representing K-feldspar in albite–biotite- and chlorite-schists and Moonta Porphyry, is characterized by varying slopes of the La–Pr interval from one rock type to another. They share, however, a gradual, slight HREE-enrichment. This trend is also characterized by a positive Eu-anomaly but with variable height from one rock to another, and importantly no Y-anomaly. Such trends are comparable with K-feldspar in skarn protoliths at Hillside (Ismail et al., 2014). In contrast to the granitoids and felsic volcanics, K-feldspar within the chlorite-schist shows a positive correlation between strength of Eu anomaly, ΣREY and Ba concentration (Fig. 6b). Trend type II (Fig. 6c), obtained for K-feldspar in the Oorlano Metasomatite, is characterized by slight LREE-depletion relative to the above, and a pronounced negative Y-anomaly. Ismail et al. (2014) observe a similar trend in K-feldspar from calcic skarn at Hillside.

5.1.2. Plagioclase feldspar

Unlike K-feldspar, albite shows higher ΣREY, ranging between 14 and 198 ppm (Tables 4a and 4b). Three types of REY fractionation trends are observed (Fig. 6d-f). Trend type I, obtained from albite within the Arthurton Granite (Fig. 5a), and andesine and early albite in the Tickera Granite (trend 1 on Fig. 6d) is downwards-sloping and characterized by a positive Eu-anomaly of variable size; average ΣREY concentrations are 49 in albite from the Arthurton Granite and 107 and 39 ppm in andesine and early albite in the Tickera Granite, respectively.

Trend type II (Fig. 6e), representing albite in the albite–biotite-schist, limestone, and the albite from the Tickera Granite with more abundant, coarser intergrowths with sericite (trend 2 on Fig. 6e), is defined by a slight LREE-enrichment, and a relatively flat pattern, with small differences in the slope from one rock type to another. Interestingly, this trend includes albite with the lowest and highest average ΣREY: albite–biotite-schist (ΣREY = 198 ppm), Tickera Granite T2 (ΣREY = 91 ppm) and the limestone (ΣREY = 26 ppm). The textures representing trend type II are very different from one another, however: homogenous, fine-grained granoblastic albite in the albite–biotite-schist (Fig. 5i); intergrowths with sericitized, K-feldspar and REY-minerals in Tickera trend 2 (Fig. 5d, e); and Ca-richer domains in albite from the limestone (Fig. 4f).

Trend type III (Fig. 6f) represents albite in the albitite and Oorlano Metasomatite and corresponds to the lowest ΣREY measured in albite (15 and 4 ppm, respectively). The REY fractionation trend shows slight LREE-depletion and negative Ce- and Y-anomalies. Similarly to trend II, the albite textures differ significantly, i.e., Ca-richer domains and sericite inclusions in the albitite (Fig. 2h), and granoblastic fine-grained aggregates (Fig. 5h) in the Oorlano Metasomatite.

5.1.3. Time-resolved depth spectra

Individual time-resolved depth spectra for the K-feldspar in the Arthurton Granite, as well as the other altered igneous rocks, show smooth signals for Ba, Rb, Sr and Ga, whereas Ce shows a relatively ragged signal during the ablation interval (Fig. 6g). This can be interpreted to indicate the presence of Ba, Rb, Sr and Ga in solid solution but may suggest that Ce and other REY occur, at least in part, as nano-scale inclusions of discrete REY-minerals. However, variation in the signal could also be caused by the low count-per-second rate at sub-ppm concentration values.

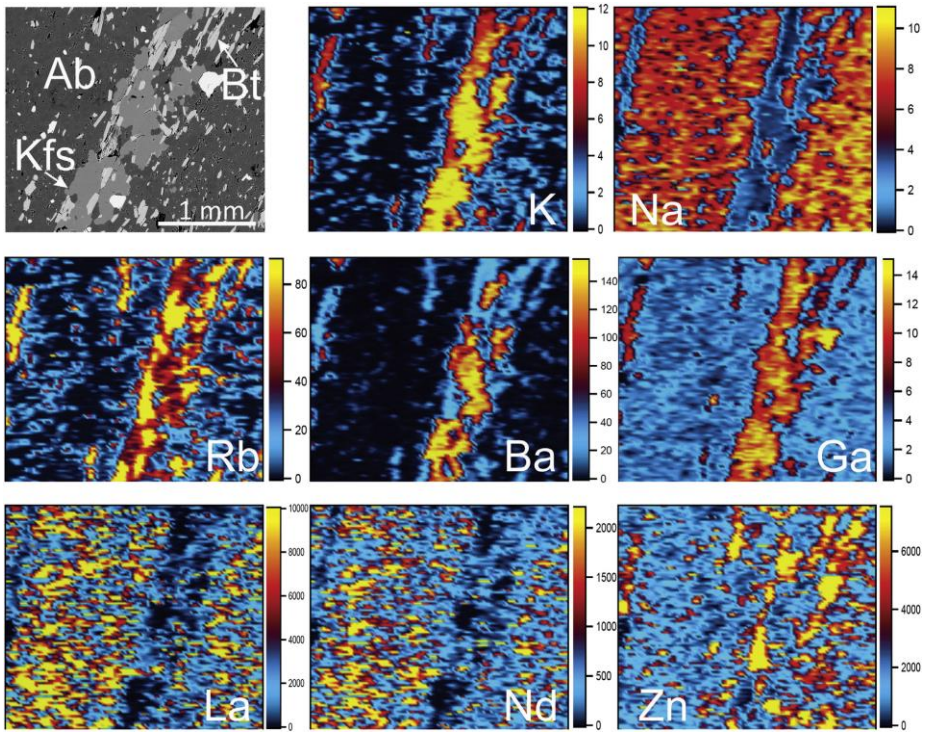

Fig. 9. BSE image and LA-ICP-MS element maps for albite and K-feldspar in the albite–biotite-schist. Scales for Cs, Nb, La, Nd, Zn in cps; 10^3 cps for Rb, Ba, Ga, Ti; 10^6 cps for K and Na.

Individual time-resolved depth spectra for the REY-rich trend in albite from the albite–biotite-schist (Fig. 6h) shows parallel, ragged but relatively low amplitude variations in the signals for Ce, Y and Th during ablation. This may be considered evidence for presence of widespread and pervasively distributed nanoscale inclusions of discrete REY- and/or Th-bearing minerals. As seen however, from the comparable raggedness of the Sr signal on the same figure, an element normally considered to occur in solid solution in albite (see Discussion), such a hypothesis needs to be checked by further study (see Section 5.3).

5.1.4. Accessory minerals

Apatite shows two distinct REY fractionation trends. A downwards-sloping trend is representative of all rock types except the Moonta Porphyry and one of the two trends (trend 2) from the Arthurton Granite (Fig. 7a-d). All analysed apatite displays a negative Eu-anomaly. Measured ΣREY concentrations differ in the different lithologies: up to 1–2 wt.% in the granitoids and thousands of ppm in all the others, except the limestone (~500 ppm). The Arthurton Granite (Fig. 7b) shows variation with progressive alteration from magmatic cores (trend 1) to rims (trend 2), coupled with a marked decrease of ΣREY (1.7 wt.% to 620 ppm) and change in slope. Similarly, the felsic volcanic shows a change in the slope with alteration (Fig. 7c). In the Moonta porphyry (Fig. 7d), the pattern is flat but with a distinct, upwards-sloping REY fractionation trend with alteration.

Zircon analyses from the two granitoids and albitite show REY fractionation trends dominated by a positive Ce-anomaly, negative Eu-anomaly and HREE-enrichment (Fig. 7e). Measured ΣREY concentrations are lower than those in apatite: up to 7000 ppm for the Tickera Granite, 3300 ppm in the Arthurton Granite and 2900 ppm in albitite. In addition, the dataset for zircon shows a positive correlation between U (hundreds of ppm) and ΣREY.

REY fractionation trends for (hydrothermal) rutile in the felsic volcanic and Moonta Porphyry show an upwards-sloping pattern (Fig. 7f). Measured ΣREY concentrations are 200 and 280 ppm, respectively, still lower than zircon and apatite. Both datasets consistently show >7000 ppm Nb, and up to 1000 ppm Ta.

ΣREY concentrations in titanite from the Oorlano Metasomatite are significantly higher (1.5 wt.%) than those in rutile. The REY fractionation trend is flat, slightly downwards-sloping and with a negative Eu-anomaly. Data for late-stage vein calcite show it to be a significant LREE-host. ΣREY exceeds 3000 ppm in calcite from the Oorlano Metasomatite. Concentrations of Fe, Mn, Mg and Sr are also high.

5.2. Element mapping

LA-ICP-MS mapping allows a visual assessment of changes in trace element distributions during alteration. Element maps of a fractured igneous orthoclase from the Arthurton Granite (Fig. 8) show patterns of trace element redistribution during progressive albitization propagated via fractures. The maps demonstrate that an increase in Na due to albitization is positively correlated with an increase in Sr and LREE (La shown as a proxy on the maps). In the areas displaying Na-enrichment, Ba and Ga are markedly depleted. Notably, the element map for Rb shows a homogeneous distribution, indicating it is neither enriched nor depleted.

Table 3a
Summary of LA-CP-MS data for K-feldspar: REE, Pb, Th and U (ppm).

	Y	La	Ce	Pr	Nd	Sm	Eu	Gd	Tb	Dy	Ho	Er	Tm	Yb	Lu	ΣREY	^{206}Pb	^{207}Pb	^{208}Pb	Th	U
Altered magmatic rocks																					
Tickera granite 33PBD1																					
Mean (n = 49)	0.07	6.4	4.3	0.20	0.37	0.23	1.5	0.21	0.03	0.16	0.03	0.10	0.04	0.16	0.04	14	2.5	2.4	2.4	0.06	0.05
S.D.	0.04	1.8	1.2	0.06	0.12	0.06	0.49	0.07	0.01	0.05	0.01	0.04	0.01	0.06	0.01	3.2	1.1	1.2	1.1	0.03	0.02
Maximum	0.19	11	8.1	0.35	0.74	0.35	2.7	0.36	0.05	0.30	0.06	0.17	0.06	0.28	0.07	22	5.6	5.5	4.8	0.20	0.11
Minimum	0.02	3.4	2.6	0.09	0.20	0.09	0.51	0.10	0.01	0.08	0.02	0.02	0.02	0.07	0.01	8.8	0.71	0.60	0.65	0.03	0.02
Arthurton granite 193DDH1																					
Mean (n = 26)	0.04	2.5	0.78	0.03	0.12	0.16	0.31	0.12	0.02	0.09	0.02	0.07	0.02	0.11	0.02	4.4	3.7	3.8	3.6	0.15	0.03
S.D.	0.02	1.6	0.37	0.01	0.03	0.06	0.16	0.04	0.01	0.03	0.01	0.02	0.01	0.04	0.01	2.0	1.4	1.3	1.1	0.56	0.01
Maximum	0.11	6.3	1.4	0.04	0.19	0.31	0.64	0.21	0.04	0.17	0.04	0.13	0.04	0.26	0.04	9.0	5.9	6.3	5.7	3.0	0.06
Minimum	0.02	0.44	0.21	0.01	0.06	0.08	0.12	0.07	0.01	0.04	0.01	0.04	0.01	0.05	0.01	1.6	0.16	0.57	0.65	0.02	0.02
Felsic volcanic 212DDH1																					
Mean (n = 12)	1.6	0.41	0.15	0.01	0.05	0.04	0.16	0.07	0.01	0.03	0.01	0.03	0.00	0.02	0.01	1.0	0.62	0.54	0.54	0.01	0.02
S.D.	4.3	0.11	0.05	0.00	0.02	0.01	0.06	0.02	0.00	0.02	0.00	0.01	0.00	0.01	0.00	0.16	0.20	0.19	0.21	0.01	0.02
Maximum	16	0.67	0.24	0.01	0.09	0.07	0.25	0.12	0.01	0.06	0.01	0.04	0.01	0.04	0.01	1.3	0.94	0.91	0.88	0.02	0.08
Minimum	0.01	0.22	0.08	0.01	0.03	0.03	0.07	0.04	0.01	0.01	0.01	0.01	0.01	0.01	0.01	0.67	0.32	0.18	0.21	0.01	0.01
Intensely altered magmatic rocks																					
Moonta porphyry 197DDH1																					
Mean (n = 7)	0.17	0.07	0.10	0.01	0.04	0.05	0.05	0.06	0.01	0.03	0.01	0.03	0.01	0.04	0.01	0.66	1.3	0.68	0.99	0.69	0.31
S.D.	0.13	0.04	0.06	<0.01	0.02	0.02	0.02	0.03	<0.01	0.02	<0.01	0.01	<0.01	0.02	<0.01	0.17	0.48	0.53	0.79	1.47	0.56
Maximum	0.43	0.16	0.22	0.01	0.08	0.07	0.08	0.11	0.01	0.06	0.01	0.04	0.01	0.06	0.02	0.88	2.0	1.9	2.8	4.28	1.68
Minimum	0.02	0.03	0.03	0.01	0.01	0.02	0.02	0.03	0.01	0.01	0.01	0.01	0.01	0.01	0.01	0.46	0.67	0.32	0.36	0.02	0.03
Metamorphic rocks																					
Biotite-feldspar schist 175DDH1																					
Mean (n = 12)	0.33	0.19	0.35	0.04	0.13	0.06	0.55	0.13	0.01	0.05	0.01	0.04	0.01	0.07	0.02	2.0	4.9	3.8	4.9	0.15	0.11
S.D.	0.35	0.12	0.29	0.03	0.13	0.03	0.11	0.07	0.01	0.04	0.01	0.05	0.01	0.10	0.02	0.69	1.1	0.85	1.0	0.21	0.08
Maximum	1.3	0.44	0.83	0.10	0.41	0.12	0.67	0.27	0.02	0.14	0.05	0.17	0.03	0.37	0.06	3.1	6.3	5.2	6.2	0.83	0.27
Minimum	0.05	0.07	0.05	<0.01	<0.01	<0.01	0.35	0.04	<0.01	<0.01	0.01	<0.01	<0.01	<0.01	<0.01	1.0	3.4	2.5	3.1	0.02	0.02
Chlorite-schist B 158DDH1 (Ba-bearing)																					
Mean (n = 4)	0.12	0.03	0.04	0.01	0.01	0.05	0.19	0.22	0.01	0.03	0.01	0.02	<0.01	0.02	<0.01	0.76	7.0	6.0	6.4	0.13	0.02
S.D.	0.04	0.02	0.03	0.01	0.02	0.01	0.03	0.07	<0.01	0.01	<0.01	0.01	<0.01	0.01	<0.01	0.15	0.80	0.77	1.2	0.08	0.01
Maximum	0.17	0.08	0.09	0.02	0.04	0.06	0.23	0.27	0.01	0.04	0.01	0.02	0.01	0.03	0.01	0.97	8.1	7.0	8.4	0.25	0.04
Minimum	0.06	0.02	0.01	<0.01	<0.01	0.04	0.15	0.10	<0.01	0.01	0.01	<0.01	<0.01	<0.01	<0.01	0.55	6.0	5.2	5.5	0.04	0.01
Chlorite-schist D 158DDH1																					
Mean (n = 8)	0.05	0.01	0.02	0.01	0.04	0.03	0.04	0.06	0.00	0.02	<0.01	0.02	0.01	0.02	0.01	0.33	2.2	1.4	1.6	0.05	0.05
S.D.	0.02	0.01	0.01	<0.01	0.02	0.02	0.01	0.01	<0.01	0.01	<0.01	<0.01	<0.01	0.02	<0.01	0.05	0.56	0.46	0.42	0.07	0.06
Maximum	0.09	0.03	0.03	0.01	0.05	0.05	0.06	0.08	0.01	0.04	0.01	0.02	0.01	0.04	0.01	0.39	3.1	2.2	2.4	0.21	0.21
Minimum	0.04	<0.01	0.01	<0.01	<0.01	<0.01	0.02	0.04	<0.01	0.01	<0.01	0.01	<0.01	<0.01	<0.01	0.25	1.5	0.86	1.1	<0.01	<0.01
Calc-silicate schist 38PBD1																					
Mean (n = 5)	0.07	0.15	0.13	0.03	0.14	0.14	0.06	0.23	0.02	0.08	0.03	0.08	0.03	0.10	0.02	1.3	0.56	0.56	0.68	0.04	0.02
S.D.	0.03	0.04	0.05	0.01	0.04	0.06	0.01	0.02	0.01	0.02	<0.01	0.02	0.01	0.04	0.01	0.12	0.33	0.23	0.34	0.01	0.01
Maximum	0.11	0.22	0.21	0.04	0.18	0.22	0.08	0.27	0.04	0.10	0.03	0.10	0.04	0.15	0.03	1.5	1.2	0.85	1.1	0.06	0.04
Minimum	0.04	0.10	0.06	0.02	0.07	0.04	0.03	0.21	0.02	0.05	0.02	0.04	0.01	0.06	0.01	1.2	0.24	0.18	0.25	0.03	<0.01

A map of a K-feldspar band contained within a granoblastic albite zone of the albite–biotite-schist (Fig. 9) shows enrichment in Rb, Ba and Ga corresponding to the K-feldspar, whereas LREE are enriched in albite. Other elements, notably Zn and Nb (not shown), are enriched in the small inclusions of biotite. This map clearly shows that, of the two feldspars, albite incorporates more LREE — either as sub-microscopic mineral inclusions or in solid solution (see below).

5.3. Nanoscale investigation of plagioclase feldspars

In order to test the significance of the down-hole profiles for REY trends in feldspars, nanoscale investigation was undertaken on granoblastic albite from the albite–biotite-schist that carried the highest ΣREY (~200 ppm). *In-situ* FIB-SEM slicing followed by TEM investigation on FIB-prepared foils is a useful petrological tool to solve such problems (Ciobanu et al., 2011). Slicing was performed around two LA-ICP-MS holes (e.g., Fig. 10a) typified by down-hole profiles such as Fig. 6h.

Cross-section FIB imaging on slice walls shows the presence of oriented sets of lamellae within each albite grain (Fig. 10b) and rare inclusions and pores. EPMA data across such grains indicated variation in anorthite component ($An_{3.3–4.7}$). These compositions may, however, be averages, given the sub-μm scale of the lamellae. Un-mixing of two plagioclases in this compositional range (termed peristerite) is known from granites. Electron diffraction studies have shown that such peristerites consist of sub-microscopic domains of An_3 and An_{23} composition, hundreds to thousands of Å in thickness (Fleet and Ribbe, 1965; Gay and Smith, 1955) attributable to sub-solidus un-mixing. Inclusions (Fe-oxides, apatite and zircon) are concentrated along or close to grain boundaries (Fig. 10c). Low-magnification TEM imaging of albite (Fig. 10d), shows the lamellae with bright-dark contrast suggestive of twinning. The orientation of the lamellae is along the b^* axis, as indicated by electron diffractions down to zone axis [-101] (Fig. 10e). The albite is free of inclusions or porosity although cross-cutting defects associated with microfractures are observed. Similar lamellar twin domains and defects have been shown for oligoclase–albite relationships in granitic rocks undergoing albitization elsewhere (Engvik et al., 2008). Based on these observations, we conclude that the measured REY concentrations in albite from the albite–biotite-schist are attributable to incorporation of these elements in solid solution rather than nanoscale inclusions of REY-minerals.

Nanoscale investigation was also performed on andesine and albite from the Tickera granitoid, displaying progressive sericitization (Fig. 10f). Scanning transmission electron microscopy (STEM) imaging shows fields of nanopores and attached inclusions even in the more homogeneous andesine (Fig. 10g) as well as slivers of phyllosilicates such as sericite and chlorite, the latter also hosting fluorite inclusions, ~200 nm in size (Fig. 10h). Chlorite is also identified within the albite,

Table 3b
Summary of LA-CP-MS data for K-feldspar: other elements (ppm).

	Na	Mg	P	Ca	Sc	Ti	Mn	Fe	Cu	Zn	Ga	Rb	Sr	Zr	Cs	Ba	Ta
Altered magmatic rocks																	
Tickera granite 33PBD1																	
Mean (n = 49)	6745	45	14	729	2.6	80	20	931	–	3.7	39	595	127	0.27	1.2	1302	–
S.D.	3261	164	3.9	410	1.1	21	22	690	–	9.5	6.4	51	35	0.81	0.24	411	–
Maximum	16,358	880	26	2971	6.1	154	122	5220	–	68	56	719	249	5.7	1.9	2324	–
Minimum	2909	0.45	8.7	272	0.96	41	0.63	525	–	0.61	31	483	42	0.02	0.80	788	–
Arthurton granite 193DDH1																	
Mean (n = 26)	5029	4.7	9.7	375	1.2	49	15	483	–	2.2	66	512	183	0.08	2.8	3287	–
S.D.	2194	7.2	4.1	111	0.15	40	21	203	–	1.8	5.4	25	57	0.12	0.58	416	–
Maximum	14,813	31	19	575	1.6	147	101	1053	–	9.1	76	566	264	0.62	3.5	4139	–
Minimum	2483	0.46	5.5	220	0.96	15	1.4	225	–	0.93	53	466	28	0.01	0.38	2525	–
Felsic volcanic 212DDH1																	
Mean (n = 12)	2964	6.1	11	463	1.8	54	4.5	813	–	1.7	127	359	162	0.05	0.91	3868	0.08
S.D.	514	11	3.2	99	0.18	73	5.0	1417	–	1.5	7.1	17	42	0.02	0.07	169	0.07
Maximum	4070	43	18	575	2.1	295	18	5468	–	5.0	138	394	215	0.08	1.1	4093	0.36
Minimum	2221	0.74	5.1	248	1.5	16	0.30	177	–	0.69	118	335	80	0.02	0.82	3540	0.01
Intensely altered magmatic rocks																	
Moonta porphyry 197DDH1																	
Mean (n = 7)	2529	401	8.8	382	1.7	95	6.4	1421	38	3.0	90	333	45	2.5	1.3	2723	0.19
S.D.	693	474	3.4	194	0.22	147	4.2	981	46	2.0	27	37	27	3.5	0.39	888	0.14
Maximum	3784	1416	17	819	2.0	439	14	3442	136	6.2	124	370	88	9.6	1.8	3827	0.46
Minimum	1827	29	6.1	208	1.3	8.5	2.0	427	4.2	0.83	34	266	9.0	0.01	0.74	946	0.03
Metamorphic rocks																	
Biotite-feldspar schist 175DDH1																	
Mean (n = 12)	5818	105	690	504	1.9	46	2.3	1766	3.6	2.7	120	308	180	12	1.4	4246	0.07
S.D.	1591	157	499	80	0.38	57	1.8	1992	2.4	1.9	7.5	24	46	20	0.23	289	0.07
Maximum	10,579	602	1300	673	3.0	228	7.1	6829	7.2	6.8	139	352	248	51	1.9	5001	0.31
Minimum	4115	3.4	73	371	1.4	12	0.54	166	0.36	0.86	110	265	107	0.05	0.94	3897	0.02
Chlorite-schist B 158DDH1 (Ba-bearing)																	
Mean (n = 4)	4621	2758	9.1	722	6.3	59	104	3051	16	14	284	313	114	1.4	0.88	5233	0.08
S.D.	2721	4322	3.0	106	1.1	44	156	4220	15	13	31	62	21	0.76	0.16	496	0.00
Maximum	7969	10,242	12	884	7.6	114	375	10,357	41	33	328	401	135	2.5	1.1	5898	0.09
Minimum	1829	153	5.5	622	5.0	8.5	6.1	495	3.4	2.0	241	228	90	0.55	0.68	4516	0.08
Chlorite-schist D 158DDH1																	
Mean (n = 8)	2062	1714	7.2	423	5.2	33	78	2397	13	4.5	50	537	22	0.72	0.90	930	0.07
S.D.	1454	1952	2.5	43	0.43	63	81	2255	12	3.1	6.4	57	5.8	0.70	0.31	111	0.03
Maximum	5826	4910	12	506	6.1	199	208	6553	32	9.6	63	630	32	2.0	1.5	1064	0.13
Minimum	1195	19	3.0	374	4.6	4.0	5.0	251	1.9	1.7	40	444	14	0.12	0.49	762	0.04
Calc-silicate schist 38PBD1																	
Mean (n = 5)	3455	18	11	284	1.6	3.5	7.9	748	2.3	1.1	33	754	8.7	0.06	0.71	1001	0.06
S.D.	2480	4.6	2.1	121	0.24	0.91	6.1	151	2.6	0.66	5.6	72	3.7	0.03	0.22	205	0.02
Maximum	7580	24	15	500	2.0	5.2	18	958	7.6	2.5	43	862	15	0.10	0.95	1353	0.09
Minimum	1282	11	8.5	183	1.3	2.7	2.9	529	0.69	0.66	28	661	3.9	0.03	0.37	812	0.03

and, in this case, the coarser intergrowths with sericite are observed to go down to nanoscale (Fig. 10i). Fields of pores and attached inclusions are also characteristic of this replacement texture.

Erratic inclusions of minerals at the nanoscale, particularly fluorite, may explain the raggedness of some REY-fractionation trends. This also proves that the micron-scale textures shown for albite persist to the nanoscale in the granitoids but not in the albite–biotite-schist.

6. Discussion

6.1. Trace element incorporation in feldspars and accessories

We have shown that K-feldspar and albite display a range of trace element concentrations and REY-anomalies. Alkali ions in these framework silicates are readily substituted by, for example, K, Ba, Rb, Cs, Pb, Sr and REE. Mineral chemistry is dependent on the affinity for, and crystallographic site preferences of, particular elements. LREE are suggested to be more effective than HREE in competing for the K^+ and Na^+ sites in feldspars (Stix and Gorton, 1990). Ba^{2+} and Rb^+ ions have a similar ionic radius to K^+, but are much larger than the Na^+ ion, thus readily explaining enrichment of these elements in K-feldspar relative to albite.

Apatite-group minerals, in this case fluorapatite [$Ca_5(PO_4)_3$ F], are a recognized repository for REE. Substitution of REE^{3+} for Ca^{2+} is compensated in charge by replacement of P^{5+} by Si^{4+} (Fleet and Pan, 1994). Similarly, zircon ($ZrSiO_4$) hosts substantial concentrations of REY, incompatible LILE and High Field Strength Elements (HFSE). Due to the resistant nature and ability of both apatite and zircon to host trace elements, they are widely used as petrogenetic indicators (e.g., Belousova et al., 2002a,b). Moreover, apatite analysed in this study frequently displays REY-depleted hydrothermal rims relatively to magmatic cores in the igneous rocks, and can thus be used to further constrain trace element remobilization during hydrothermal alteration.

This study shows that other hydrothermal accessory minerals formed during albitization such as rutile, titanite and calcite can also carry significant concentrations of trace elements (Fig. 7f–h).

6.2. REY distributions

REY fractionation within minerals is predominantly governed by the systematic decrease in atomic radius with increased atomic number (e.g., Smith et al., 2004). However, hydrothermal processes, such as albitization, are accompanied by changes in fluid characteristics (e.g., redox conditions, pH, temperature and salinity), which can assist partitioning of REE from one another (Bau, 1991). Europium and Ce can change oxidation states to Eu^{2+} and Ce^{4+}, creating measurable anomalies relative to other REE. In addition, the anomalous behaviour of Y relative to lanthanide REE, i.e., Dy and Ho, in hydrothermal systems has shown promise as a petrogenetic indicator (Smith et al., 2009). REY

Table 4a
Summary of LA-CP-MS data for albite: REE, Pb, Th and U (ppm).

	Y	La	Ce	Pr	Nd	Sm	Eu	Gd	Tb	Dy	Ho	Er	Tm	Yb	Lu	ΣREY	^{206}Pb	^{207}Pb	^{208}Pb	Th	U
Altered magmatic rocks																					
Tickera 33PBD1 (trend 1, andesine)																					
Mean (n = 5)	1.8	37	48	3.8	10	1.1	3.3	0.91	0.10	0.46	0.09	0.20	0.02	0.17	0.02	107	4.0	2.4	2.8	0.03	0.04
S.D.	0.84	2.7	4.5	0.45	1.4	0.32	0.32	0.40	0.04	0.17	0.04	0.12	0.01	0.09	0.01	12	0.10	0.07	0.24	0.03	0.03
Maximum	3.1	40	53	4.3	12	1.7	3.6	1.5	0.15	0.73	0.15	0.35	0.04	0.33	0.03	121	4.2	2.5	3.0	0.08	0.07
Minimum	1.1	34	43	3.4	8.6	0.90	2.8	0.63	0.07	0.29	0.05	0.10	0.01	0.12	0.01	79	3.9	2.3	2.4	0.01	0.01
Tickera 33PBD1 (trend 1, albite)																					
Mean (n = 10)	1.1	13	17	1.4	4.3	0.60	0.63	0.47	0.06	0.25	0.06	0.20	0.04	0.20	0.04	39	1.7	0.53	1.2	0.07	0.10
S.D.	0.64	4.9	6.0	0.64	2.1	0.28	0.34	0.18	0.03	0.14	0.02	0.10	0.01	0.07	0.01	14	0.67	0.17	0.48	0.02	0.06
Maximum	2.9	22	28	2.7	8.5	1.3	1.2	0.86	0.14	0.56	0.11	0.42	0.07	0.33	0.05	65	2.9	0.80	2.0	0.11	0.26
Minimum	0.44	6.0	7.9	0.54	1.8	0.23	0.24	0.27	0.03	0.10	0.04	0.08	0.01	0.11	0.02	19	0.80	0.29	0.46	0.04	0.04
Tickera 33PBD1 (trend 2)																					
Mean (n = 11)	4.9	20	39	4.3	15	2.9	0.56	1.9	0.30	1.5	0.22	0.48	0.09	0.39	0.06	91	2.1	0.64	1.4	0.28	0.12
S.D.	2.2	9.2	19	1.9	6.4	1.1	0.27	0.94	0.18	0.86	0.16	0.29	0.04	0.19	0.02	42	1.5	0.42	0.88	0.37	0.07
Maximum	8.4	36	77	8.2	30	5.2	1.0	3.4	0.61	2.8	0.53	1.1	0.17	0.76	0.10	174	6.8	1.8	3.6	1.3	0.28
Minimum	1.9	10	18	2.2	7.6	1.4	0.20	0.37	0.07	0.36	0.04	0.16	0.04	0.15	0.03	43	0.71	0.26	0.43	0.03	0.06
Arthurton 227DDH2																					
Mean (n = 6)	0.73	3.6	5.5	0.28	0.82	0.14	0.10	0.13	0.03	0.12	0.04	0.10	0.03	0.16	0.03	49	1.1	0.84	1.1	0.86	0.35
S.D.	0.74	1.4	3.9	0.12	0.31	0.02	0.03	0.02	0.01	0.06	0.02	0.04	0.01	0.11	0.01	18	0.49	0.35	0.56	0.76	0.26
Maximum	2.3	6.6	14	0.52	1.3	0.17	0.15	0.17	0.04	0.24	0.08	0.20	0.05	0.40	0.06	88	2.0	1.4	1.8	2.0	0.91
Minimum	0.14	2.4	2.3	0.16	0.43	0.10	0.06	0.11	0.02	0.07	0.02	0.06	0.01	0.08	0.02	32	0.66	0.47	0.51	0.06	0.14
Intensely altered magmatic rocks																					
Albitite 33DDH1																					
Mean (n = 66)	0.42	1.1	1.1	0.36	2.4	2.7	0.78	3.3	0.43	1.8	0.47	1.6	0.50	2.2	0.54	15	3.8	3.5	2.4	0.79	0.78
S.D.	0.15	0.96	0.69	0.12	0.64	0.86	0.26	0.81	0.12	0.60	0.12	0.47	0.13	0.53	0.17	3.0	1.5	1.1	1.9	0.25	0.43
Maximum	0.75	4.6	3.0	0.64	4.5	5.1	1.4	5.5	0.80	3.7	0.74	2.8	0.98	3.5	1.1	24	7.9	6.9	10	1.5	2.5
Minimum	0.15	0.27	0.21	0.13	1.1	1.3	0.32	2.1	0.21	0.77	0.25	0.71	0.34	1.0	0.26	10	1.7	1.7	0.51	0.29	0.29
METAMORPHIC ROCKS																					
Bt-Fds schist 175DDH1																					
Mean (n = 12)	69	23	43	5.0	21	5.0	1.5	7.8	1.3	8.2	1.8	5.4	0.67	4.2	0.66	198	2.9	1.1	2.2	11	1.9
S.D.	20	7.2	12	1.4	5.4	1.7	0.46	2.0	0.36	2.3	0.52	1.5	0.21	1.4	0.17	50	0.70	0.48	0.45	3.2	0.55
Maximum	103	38	66	7.3	31	8.2	2.5	12	2.1	12	2.7	7.7	1.00	6.5	0.96	288	4.0	2.3	3.0	16	3.2
Minimum	48	16	30	3.3	13	3.0	0.97	5.3	0.83	5.8	1.2	3.5	0.43	2.7	0.43	138	2.0	0.74	1.6	7.4	1.2
Calc-silicate schist 38PBD2																					
Mean (n = 16)	0.31	0.46	0.30	0.23	1.9	2.1	0.74	2.7	0.34	1.1	0.37	0.97	0.32	2.0	0.44	14	4.5	3.7	2.9	2.2	1.5
S.D.	0.23	0.17	0.22	0.16	1.3	1.00	0.44	0.94	0.22	0.92	0.20	0.69	0.27	1.1	0.23	2.8	2.6	0.98	1.9	2.1	0.94
Maximum	0.97	0.80	0.64	0.47	4.5	3.5	1.5	4.4	0.77	2.4	0.70	2.0	0.71	3.2	0.87	20	11	6.4	8.8	7.3	4.1
Minimum	0.00	0.00	0.00	0.00	0.00	0.00	0.00	0.00	0.00	0.00	0.00	0.00	0.00	0.00	0.00	10	2.0	2.2	1.1	0.00	0.51
Limestone 190DDH2a																					
Mean (n = 4)	4.3	3.6	8.2	1.1	3.8	1.1	0.18	1.0	0.21	0.95	0.17	0.45	0.06	0.31	0.07	26	1.4	0.65	0.72	2.0	1.6
S.D.	1.3	0.76	2.9	0.44	1.5	0.57	0.07	0.47	0.11	0.46	0.06	0.14	0.02	0.06	0.02	8.5	0.18	0.15	0.13	0.92	0.97
Maximum	5.7	4.8	13	1.7	6.2	2.1	0.28	1.8	0.38	1.6	0.25	0.59	0.09	0.38	0.10	39	1.7	0.84	0.82	3.6	3.2
Minimum	2.6	2.9	4.9	0.57	2.2	0.64	0.08	0.46	0.08	0.51	0.09	0.24	0.04	0.24	0.04	16	1.2	0.45	0.51	1.2	0.66

trends of magmatic-hydrothermal systems can thus be discriminated by variations in Eu-, Ce- and Y-anomalies (Eu/Eu*, Ce/Ce* and Y/Y*) and changes in REY-slopes, with specific minerals such as feldspar showing greater sensitivity than whole-rock analyses.

K-feldspar from igneous rocks is characterized by a pronounced positive Eu-anomaly and negative Ce-anomaly, whereas hydrothermal K-feldspar is quite variable in terms of these anomalies. K-feldspar compositions from the Tickera and Arthurton Granites cluster in Fig. 11a. The Moonta Porphyry, in which K-feldspar is strongly affected by alteration, is shifted towards the centre of the diagram relative to the two granitoids. The felsic volcanic overlaps with both granites and Moonta Porphyry. Overall, K-feldspar in the igneous rocks from Moonta defines a conspicuous field on Fig. 11a, which, interestingly, is separated from the field for Hillside granite (Ismail et al., 2014). This indicates both regional and local differences among HIS granitoids, possibly relating to variations in the oxidation state of magmas, as also shown by differences in Fe–Ti-oxide mineralogy, as well as the relative proportions of potassium and plagioclase feldspar.

Hydrothermal K-feldspar in the metasedimentary rocks and Oorlano Metasomatite (Fig. 11b) shows distinct fields for the albite–biotite-schist relative to the chlorite-schist (and Oorlano Metasomatite), despite the fact that they share a common REY-fractionation trend on Fig. 6b. K-feldspar in the albite–biotite-schist has a pronounced positive Eu-anomaly relative to the chlorite-schist. Fig. 11b thus may indicate changes in fluid conditions from the greenschist facies (chlorite-schist) to lower amphibolite facies (albite–biotite-schist). Considering that the two rocks are broadly comparable, and that magnetite is stable in both, such a change could be attributable to temperature increase rather than fO_2 variation. The chlorite-schist shows a large spread with respect to Ce-anomaly, reflecting Ba-rich ($Ce/Ce^* > 1$) to Ba-poor domains ($Ce/Ce^* < 1$), as shown in Fig. 3e. This is attributable to local changes in fO_2 during syn-deformational porphyroblast growth.

The Y/Y^* vs. Ce/Lu_{CN} (a measure of LREE/HREE fractionation) plot for K-feldspar (Fig. 11c) separates the granitoids from felsic volcanic and Moonta Porphyry. This suggests equilibrium partitioning of REE into early accessory minerals, particularly abundant zircon, in the granitoids relative to the others. Such an interpretation is supported by the observed clustering of zircon with early magmatic Fe–Ti-oxides. The same plot for the metasedimentary rocks and Oorlano Metasomatite (Fig. 11d) shows that K-feldspar in the Oorlano Metasomatite plots in a comparable position on the diagram as the granitoids. Considering the abundance of titanite and apatite in this rock, REY may be partitioned into these minerals at the expense of K-feldspar.

The La/Nd_{CN} vs. $(La + Ce + Pr)/\Sigma REY$ plot for K-feldspar shows a separation of igneous from hydrothermal signatures, whereby the latter shows no particular discrimination by lithology (Fig. 11e). This diagram clearly indicates the shift from LREE- to HREE-enrichment during transition from igneous to hydrothermal signature.

Table 4b
Summary of LA-CP-MS data for albite: other elements (ppm).

	Mg	P	K	Ca	Sc	Ti	V	Mn	Fe	Cu	Zn	Ga	Rb	Sr	Zr	Nb	Sn	Cs	Ba
Altered magmatic rocks																			
Tickera 33PBD1 (trend 1, andesine)																			
Mean (n = 5)	4165	21	15,011	37,626	17	100	1.4	121	2538	3.4	14	40	101	267	0.04	0.03	0.17	3.7	433
S.D.	4521	7.7	4044	4981	0.28	10.0	1.3	49	1174	3.8	8.5	0.96	28	8.6	0.02	0.02	0.07	1.0	131
Maximum	12,240	30	21,143	42,002	17	111	3.5	167	4566	8.9	29	41	134	276	0.07	0.06	0.22	5.2	645
Minimum	1839	10	11,258	31,649	17	85	0.39	57	1645	0.64	6.7	39	70	258	0.02	0.01	0.12	2.6	327
Tickera 33PBD1 (trend 1, albite)																			
Mean (n = 10)	2339	15	22,517	4966	2.7	67	5.7	101	6360	1.6	8.2	29	363	105	0.21	0.06	0.46	1.4	156
S.D.	819	3.9	3014	1653	0.87	29	1.9	22	933	1.7	1.9	3.0	81	25	0.21	0.04	0.24	0.41	58
Maximum	3587	21	27,301	8732	4.7	137	8.5	150	7965	6.7	12	33	497	165	0.70	0.18	0.99	2.3	314
Minimum	1433	11	15,809	2777	1.8	32	2.2	80	5061	0.77	5.6	24	212	80	0.05	0.01	0.19	0.98	109
Tickera 33PBD1 (trend 2)																			
Mean (n = 11)	2087	41	23,266	4560	3.9	82	9.4	88	6367	2.2	8.1	30	414	104	0.45	0.15	1.2	1.8	279
S.D.	1061	28	3458	3505	1.2	33	5.2	21	967	1.9	4.0	4.5	107	66	0.73	0.14	0.98	0.65	168
Maximum	4976	91	27,374	11,719	5.8	152	17	133	8345	7.2	19	38	616	211	2.7	0.45	3.6	2.8	693
Minimum	930	10	16,410	1164	2.6	22	1.6	64	4920	0.70	2.7	22	242	41	0.05	0.03	0.10	0.90	149
Arthurton 227DDH2																			
Mean (n = 6)	1048	8.8	3188	3385	5.0	12	8.5	30	3398	4.3	2.3	13	20	44	1.6	0.09	0.67	0.25	26
S.D.	1909	3.5	1927	2341	5.0	8.6	11	23	3039	2.9	2.5	2.6	8.3	6.2	1.8	0.10	0.77	0.19	8.5
Maximum	5311	16	6610	8373	15	30	32	78	8760	9.2	7.9	16	29	56	5.1	0.29	2.0	0.59	35
Minimum	109	5.6	1234	1749	1.5	5.2	1.1	11	761	1.1	0.78	9.9	8.5	37	0.06	0.02	0.08	0.11	14
Intensely altered magmatic rocks																			
Albitite 33DDH1																			
Mean (n = 66)	647	61	9509	4203	2.7	32	1.1	47	2901	5.1	8.1	30	105	80	1.9	0.48	1.9	0.64	67
S.D.	899	8.6	5074	2225	1.1	89	0.78	24	1700	2.2	4.0	6.2	73	32	3.7	0.68	0.72	0.62	60
Maximum	7264	91	27,908	10,213	6.4	742	3.1	101	9771	14	20	49	309	148	28	4.7	4.7	4.7	346
Minimum	21	47	1784	1138	1.7	6.8	0.29	4.6	345	2.8	2.9	17	4.4	28	0.36	0.16	0.95	0.22	9.8
Metamorphic rocks																			
Bt-Fds schist 175DDH1																			
Mean (n = 12)	481	371	2742	6085	3.6	267	4.6	8.4	2364	14	6.7	16	14	174	51	0.65	<mdl	0.20	63
S.D.	714	67	2325	266	1.2	451	4.9	9.8	2393	5.4	2.6	2.8	14	35	48	1.1	<mdl	0.28	85
Maximum	2514	535	9084	6478	6.5	1709	16	35	9635	27	14	22	50	262	154	4.2	<mdl	1.1	341
Minimum	27	274	717	5647	2.6	10	1.2	1.3	1001	7.3	4.1	13	2.0	139	7.2	0.07	<mdl	0.01	15
Calc-silicate schist 38PBD2																			
Mean (n = 16)	196	63	478	1470	4.0	22	2.6	14	3444	<mdl	<mdl	27	3.0	7.9	3.4	<mdl	<mdl	<mdl	6.6
S.D.	180	13	96	552	1.6	12	4.4	8.0	3638	<mdl	<mdl	4.6	2.2	4.3	3.3	<mdl	<mdl	<mdl	3.5
Maximum	750	90	545	3174	7.4	51	19	31	16,229	<mdl	<mdl	39	8.5	21	13	<mdl	<mdl	<mdl	14
Minimum	5.9	47	131	938	1.8	11	0.41	2.9	500	<mdl	<mdl	20	0.67	4.8	0.00	<mdl	<mdl	<mdl	0.00
Limestone 190DDH2a																			
Mean (n = 4)	8588	13	8204	50,082*	3.0	297	11	942	5838	25	5.7	18	51	46	36	0.42	<mdl	1.7	133
S.D.	5383	0.99	6445	25,113	0.45	459	7.1	397	3496	13	2.0	3.7	53	28	16	0.49	<mdl	2.6	122
Maximum	15,476	14	19,345	74,305*	3.5	1092	22	1278	10,245	46	7.9	25	143	94	57	1.3	<mdl	6.2	339
Minimum	627	11	3829	10,172	2.4	8.0	1.8	278	677	11	2.5	16	15	26	15	0.05	<mdl	0.22	25

* These high concentrations could not be confirmed by SEM-EDAX-mixture with calcite at the scale of the LA-ICP-MS spot is suspected.

Eu/Eu* vs. Ce/Lu_{CN} for albite (Fig. 12a) efficiently discriminates the three REY-fractionation trends (types I, II and III; Fig. 6d–f). The Tickera Granite shows a spread from positive to negative Eu-anomaly for albite type-I and type-II, respectively. These trends reflect progressive albitization from albite + sericite + hematite (Fig. 5a, b) to albite + K-feldspar ± sericite (Fig. 5c, d) assemblages. Considering that formation of sericite from pre-existing K-feldspar involves H^+ (i.e., acidic fluids), and the formation of new K-feldspar from sericite effectively reverses this reaction, the trend on Fig. 11a can be interpreted as a change in pH from acidic to neutral conditions. Analogous, complex feldspar replacement reactions involving albitization (of K-feldspar and/or plagioclase as shown above), which also result in sericite formation, and subsequent formation of new K-feldspar replacing that sericite, have been shown by Plümper and Putnis (2009).

The position of albite in the albite–biotite-schist on Fig. 12a is markedly different to K-feldspar in the same rock (Fig. 11b) with respect to Eu-anomaly. If we assume that biotite + K-feldspar alteration is distinct from, and follows early albite alteration (Hayward and Skirrow, 2010), this discrepancy, in the absence of other minerals that can take in REY, means that there is an evolution in fluid conditions from one alteration stage to the other, as discussed for the igneous rocks above. This explanation is rejected, however, as the same temporal association involving albite and K-feldspar would be expressed by an opposite change in Eu-anomaly, driven by pH. An alternative scenario is that the two feldspars co-crystallize in the albite–biotite-schist, and the difference in Eu-anomaly simply reflects competition among the minerals; although albite is richer in ΣREY, Eu is preferentially incorporated into K-feldspar (Henderson, 1984). A further possibility, with implications for the direct comparison of granitoids with metasedimentary rocks, is that K-feldspar (and biotite?) in the latter is an inherited metamorphic assemblage resulting from metamorphism of an arkose at low amphibolite facies, and thus is implicitly superposed by albitization. The commonality of albitizing fluids affecting the metasedimentary rocks is seen from the overlap of albite in the limestone with the albite–biotite-schist on Fig. 12a. The distinctive, high HREE/LREE signature of type III albite in the albitite and Oorlano Metasomatite reflects their characteristic REY fractionation trend and presence of a greater number of accessory minerals competing for LREE. The large spread of Eu/Eu* may reflect the variety of local conditions relative to co-crystallization of REY-minerals at this very intense stage of alteration. The same grouping of the albitite and Oorlano Metasomatite is seen on the Y/Y* vs. Ce/Lu_{CN} plot for albite (Fig. 12b), again indicating the important role of co-crystallization of Y-bearing accessory minerals at this stage (xenotime, rutile and titanite).

Anomalies in REY fractionation trends displayed by magmatic apatite have been used to infer variation in the oxidation state of

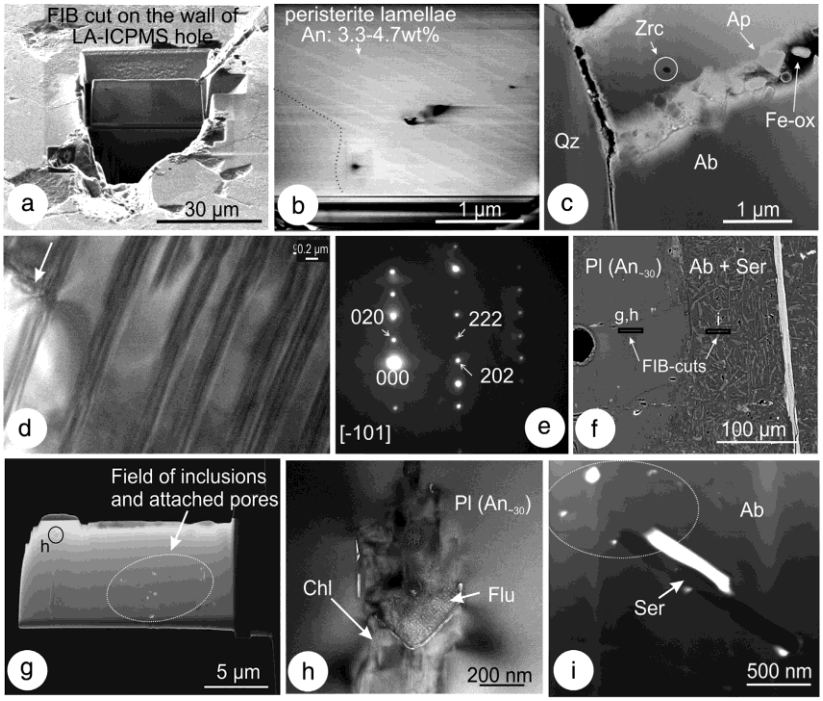

Fig. 10. Micron- to nanoscale aspects of feldspars: (a–e) albite–biotite-schist; (f–i) Tickera Granite. (a) Secondary electron (SE) image showing FIB-slice cut from high-REY albite attached to tungsten needle for lifting to grid for thinning as TEM foil. (b, c) SE images obtained during FIB-cross-sectioning showing peristerite lamellae in albite grains (b) and minor inclusions along grain boundaries (c). (d) Low-magnification bright-field (BF) TEM image showing detail of peristerite lamellae with contrast suggestive of twinning. Arrow shows cross-cutting defects. (e) SAED down to zone axis [−101] showing the orientation of the peristerite lamellae along the b^* axis. (f) SE image showing location of FIB-cuts in andesine and albite with coarse, cleavage-oriented sericite. (g) STEM image showing fields of nanopores and attached inclusions in andesine. (h) Low-magnification BF-TEM image showing an inclusion of fluorite within chlorite sliver. (i) Low-magnification BF-TEM image showing pore-attached inclusions surrounding a sericite sliver within the albite. Abbreviations as in Fig. 5; Flu — fluorite; Zrc — zircon.

magma (e.g., Cao et al., 2012). Eu/Eu^* vs. Ce/Lu_{CN} and Eu/Eu^* vs. Ce/Ce^* plots for apatite here show magmatic apatite in granitoids as tighter clusters when compared to apatite from felsic volcanic or other rocks (Fig. 13a, b). On both diagrams, Tickera Granite apatite shows larger negative Eu-anomalies and lower Ce/Ce^* relative to apatite in the Arthurton Granite. This clearly correlates with the interpretations above, indicating the more reduced magma character of the Tickera Granite. The Y/Y^* vs. Ce/Lu_{CN} plot (Fig. 13c) shows apatite in the Tickera and Arthurton Granites sharing a common inverse relationship between the two variables. Tickera apatite has a small negative Y-anomaly and is LREE-enriched relative to Arthurton, which displays a positive Y-anomaly. Apatite from felsic volcanics are clearly separated from apatite from all the other rocks on the La/Nd_{CN} vs. $(La + Ce + Pr)/\Sigma REY$ plot (Fig. 13d). Their positions at higher La/Nd_{CN} ratios suggest fluids with variable and high volatile concentration during albitization development. The scattered trends shown by apatite from the felsic volcanic on all four diagrams in Fig. 13 emphasize their complex multi-stage evolution (e.g. Fig. 4c).

REY distributions in zircon justify the interpretation of magma oxidation state reflected by apatite in the granitoids. The observed increase in Ce-anomaly for zircon in samples of Arthurton Granite relative to the Tickera Granite can be attributed to an fO_2 increase, as documented in experimental studies with hydrous silicate melts at 10 kbar and 800–1300 °C (Trail et al., 2012).

6.3. Alkali-metasomatism

Figs. 14–16 show, schematically, the range of mineral reactions, textural variety and REY-signatures associated with regional alkali-metasomatism in the Moonta-Wallaroo area. The anomalous concentration of REE in IOCG systems (Hitzman, 2000) can be linked to albitization if either albite itself, or the package of minerals formed during albitization, accounts for the REY budget in a given rock considered to be REY-enriched. Whole-rock data for the rocks studied (Fig. 14, data from Forbes, 2012) shows ΣREY concentrations for the granitoids and other igneous rocks are some hundreds of ppm, with Na_2O content up to 2.7 wt.% (4.9 wt.% in the albitite). In the case of the Oorlano Metasomatite (up to 6.8 wt.% Na_2O), concentrations may exceed those of the granitoids. ΣREY concentrations in what we term metasedimentary rocks, including the albite–biotite-schist, which Conor et al. (2010) consider as a rock accounting for 'alteration and metasomatism', are in the same concentration range. The chlorite-schist and limestone, in which we have identified albitization (2.7–2.9 and 1.4–2.3 wt.% Na_2O, respectively), also contain ~100–150 ppm REY and are therefore in the same range as the albite–biotite-schist, placing them in the same 'alteration and metasomatism' category. The whole rock REY fractionation trends of all lithologies (Fig. 14) are also broadly similar, showing LREE-enrichment and consistent negative Eu-anomalies. Moreover, the fact that albite, a major component (~50%)

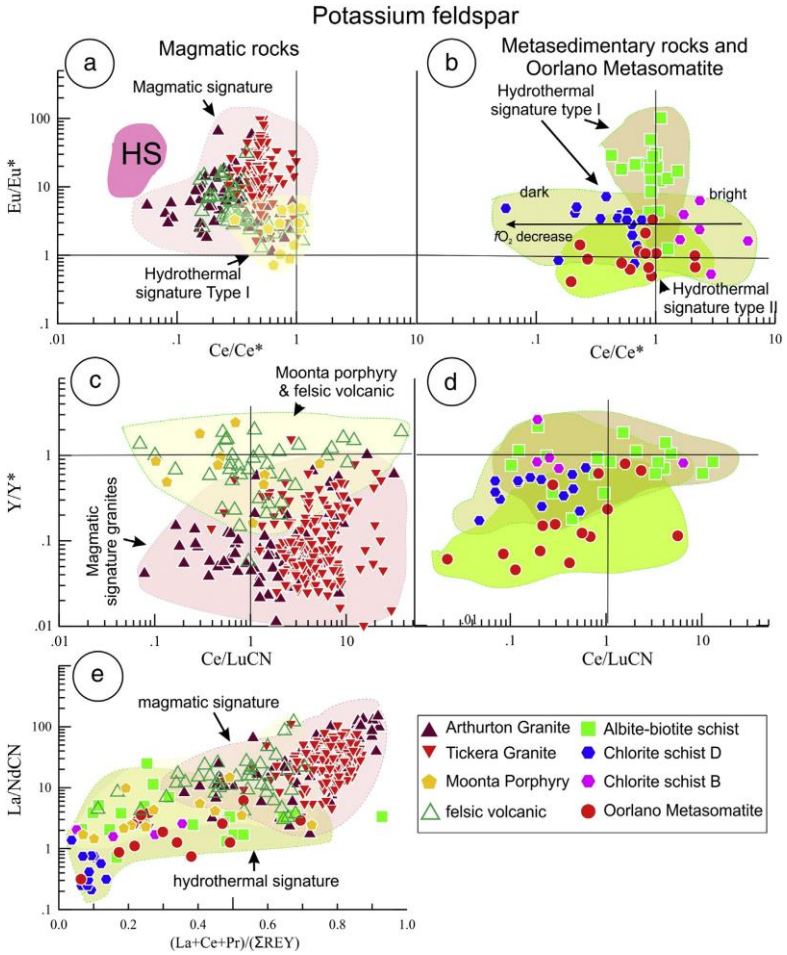

Fig. 11. Plots representing REY distributions in K-feldspar in studied lithologies. (a and b) Eu/Eu* vs. (c and d) Y/Y* vs. Ce/Lu_{CN}. (e) La/Nd_{CN} vs. (La + Ce + Pr)/ΣREY. $Eu/Eu^* = Eu_{CN}/[(Sm_{CN} + Gd_{CN})/2]$; $Ce/Ce^* = Ce_{CN}/[(La_{CN} + Pr_{CN})/2]$; $Y/Y^* = Y_{CN}/[(Dy_{CN} + Ho_{CN})/2]$.

of the albite–biotite-schist (5 wt.% Na_2O), also contains ~200 ppm ΣREY, and the REY fractionation trend mimics that of the whole-rock REY pattern, reinforces the conclusion that albite accounts for the entire, anomalous REY budget in this rock.

6.3.1. Albitization of igneous rocks

Based on the pseudomorphic character of replacement reactions accompanying direct albitization in the igneous rocks (Fig. 15), albitization proceeds via REY-release (from magmatic Fe-Ti-oxides, apatite and zircon, as well as from andesine), and uptake of REY (by new-formed albite + hematite + sericite ± chlorite, followed by K-feldspar + discrete REY-(U) minerals). The fact that albite resulting from albitization of pre-existing perthite, orthoclase or andesine is characterized by lower ΣREY (compare trends I and II for albite in the Tickera Granite; Fig. 6d, e), shows that the albite loses REY that are incorporated within discrete REY-minerals at the stage of new K-feldspar formation. The low ΣREY in albite and abundance of discrete REY-minerals in the albitite is further evidence of REY mobility during albitization. The onset of this process requires destabilization of K-feldspar under acidic fluid conditions to form albite + sericite, but reverts to more neutral conditions, as evidenced by pH-controlled formation of new K-feldspar from sericite. Chloritization of pre-existing, magmatic biotite may also contribute to an increase in fluid K^+/H^+. The presence of hematite with albite + sericite, and replacement of magmatic magnetite suggests the fluid is oxidized (hematite-stable). This observation contradicts the contention that albitization always occurs at magnetite-stable conditions (Conor et al., 2010; Hayward and Skirrow, 2010). The association of hematite with albite-sericite during replacement of granitic feldspars is, however, not restricted to the observations here but appears to be a common phenomenon in albitization of granitic rocks (Plümper and Putnis, 2009).

Hövelmann et al. (2010) provide experimental evidence for pseudomorphic replacement of oligoclase and labradorite by albite, and suggest that albitization proceeds via an interface-coupled-dissolution-

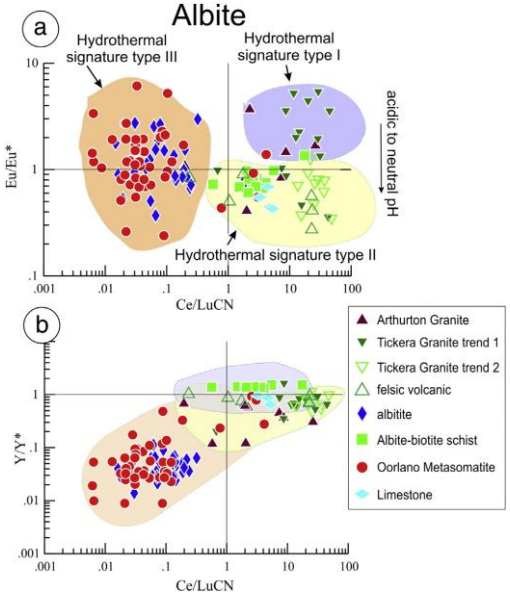

Fig. 12. Plots representing REY distributions in albite in studied lithologies. (a) Eu/Eu* vs. Ce/Lu_{CN}. Y/Y* vs. Ce/Lu_{CN}. $Eu/Eu^* = Eu_{CN}/[(Sm_{CN} + Gd_{CN})/2]$; $Y/Y^* = Y_{CN}/[(Dy_{CN} + Ho_{CN})/2]$.

(re)-precipitation mechanism, during which increased porosity drives pervasive fluid flow. This type of replacement reaction couples dissolution of a pre-existing mineral with the rate of (re)precipitation of new products at the site of reaction (CDRR), and thus can effectively play a role in (re)distribution of minor/trace elements during fluid-rock interaction. The experiments of Hövelmann et al. (2010) demonstrate that albitization is accompanied by remobilization of REY and other trace elements often considered as relatively immobile during alteration. Furthermore, they found that released REY are lost to fluid and are thus available for formation of discrete REY-minerals. CDRR is also identified as playing a major role in albitization of K-feldspar (Norberg et al., 2014), again with mobilization of minor components.

Although the andesine in the Tickera Granite may be considered to be a primary igneous mineral, it could also be an intermediate product of K-feldspar replacement, as shown by Plümper and Putnis (2009). In our case, the necessary Ca to form an intermediate plagioclase rather than end-member albite could be explained by uptake of Ca released from mafic minerals during chlorite formation prior to albitization *sensu stricto*. A hydrothermal origin for the andesine is supported by nanoscale inclusions of sericite and chlorite (Fig. 10f-h). The co-presence of fluorite in the same grain (Fig. 10h) is concordant with an acidic fluid at this stage.

The question of whether albitization was 'self-sourced' by post-magmatic hydrothermal fluids or required a net input of fluids is difficult to answer. The fact that the albitite shows an approximate doubling of Na_2O content relative to the granitoids but is directly comparable in terms of mineral reactions and ΣREY with the other two granitoids suggests input of Na but not necessarily of REY.

6.3.2. Albitization of metasedimentary rocks

In contrast to the igneous rocks, no evidence for CDRR is seen in the albitized metasedimentary rocks (Fig. 16). Although albitization of limestone involves formation of sericite and chlorite as seen in the igneous rocks, the mineral reactions have a prograde, pervasive and localized character resembling skarnoid development (e.g., Meinert, 1992). Sodic metasomatism of carbonate protoliths containing impurities released under thermal gradients, and reaction with pervading fluids accounts for the observed features. In the albite–biotite-schist and Oorlano Metasomatite, development of granoblastic albite indicates

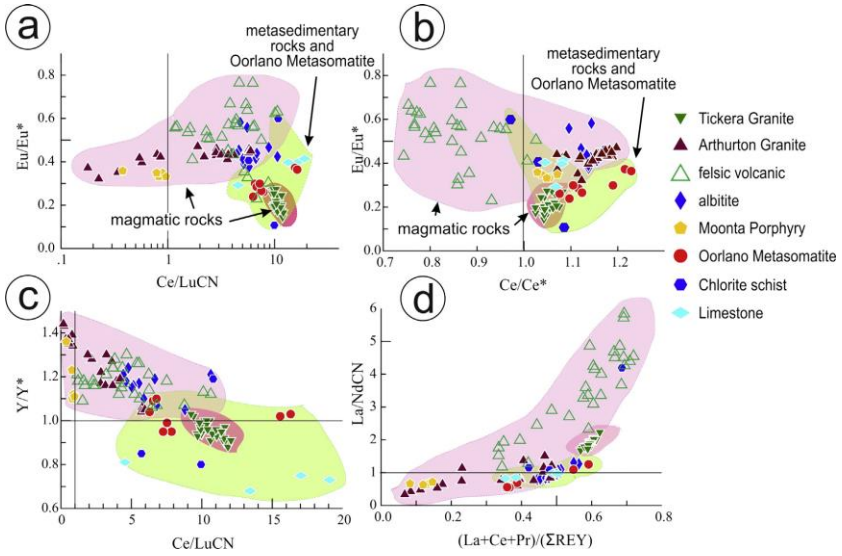

Fig. 13. Plots representing REY distributions in apatite in studied lithologies. (a) Eu/Eu* vs. Ce/Lu_{CN}. (b) Eu/Eu* vs. Ce/Ce*. (c) Y/Y* vs. Ce/Lu_{CN}. (d) La/NdCN vs. (La + Ce + Pr)/ΣREY. $Eu/Eu^* = Eu_{CN}/[(Sm_{CN} + Gd_{CN})/2]$; $Ce/Ce^* = Ce_{CN}/[(La_{CN} + Pr_{CN})/2]$; $Y/Y^* = Y_{CN}/[(Dy_{CN} + Ho_{CN})/2]$.

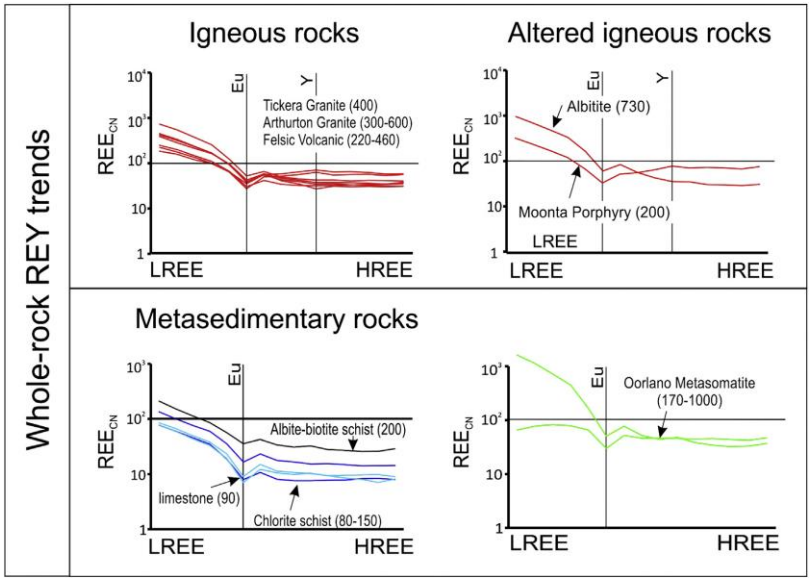

Fig. 14. Chondrite-normalized REY-fractionation trends in whole-rock for the analysed igneous and metasedimentary rocks and the Oorlano Metasomatite. Numbers in brackets are ΣREY ranges in ppm. Data from Forbes (2012).

high fluid/rock ratio infiltration-driven fluid flow. In the absence of competing minerals, such as calc-silicates or accessories as in the Oorlano Metasomatite, albite in the albite–biotite-schist accounts for the majority of the REY budget in the rock. Pseudomorphic replacement of magnetite by maghemite may have accompanied albite formation in the presence of acidic fluids. Maghemite formation, an intermediate stage in the conversion of magnetite to hematite, has been shown to be pH- rather than fO_2-driven (Otake et al., 2010).

Alteration in the metasedimentary rocks requires a protolith and an external source of fluids. Evaporite and/or Na–(Ca)–(K) bearing units within the Wallaroo Group could have readily provided Na, and carbonate/volcanic units would have provided Ca as a protolith to form calc-silicates or K-minerals rich rocks (biotite-K-feldspar-schist) but neither evaporites nor carbonates are likely to directly account for the REY endowment in the albitized rocks. Scapolite is reported from the Moonta-Wallaroo area (Skirrow et al., 2007) but is more likely to be a product of sodic alteration rather than a source.

In the absence of obvious sources within the rock sequence, we suggest involvement of mantle REY transported as magmatic volatiles, as proposed for Cu at Olympic Dam (Johnson and McCulloch, 1995).

The fact that albitization is followed by incipient potassic alteration is shown in the igneous rocks as new-formed K-feldspar. Progressive

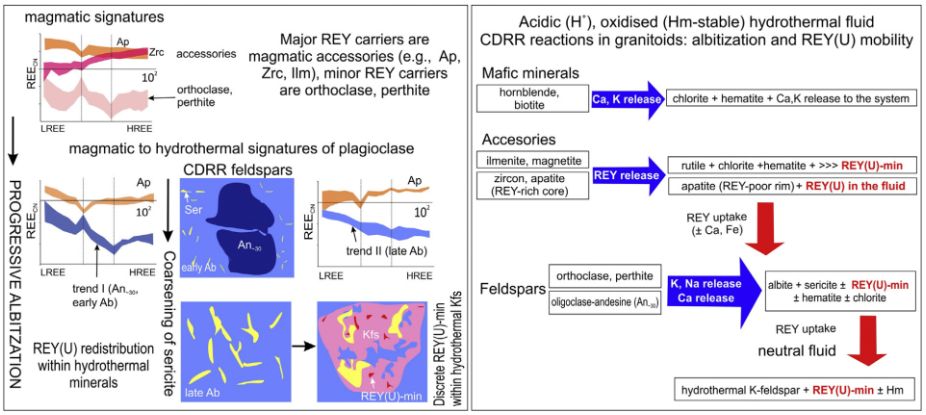

Fig. 15. Schematic diagram showing key textures and REY fractionation trends (left panel), and REY-pathways (right panel) during CDRR-driven albitization of igneous rocks. See text for additional explanation. Abbreviations: Ab — albite; Ap –apatite; An — anorthite; Hm — hematite; Ilm — ilmenite; Kfs — K-feldspar; REY(U)-min — discrete REY-(U)-bearing minerals; Ser — sericite; Zrc — zircon.

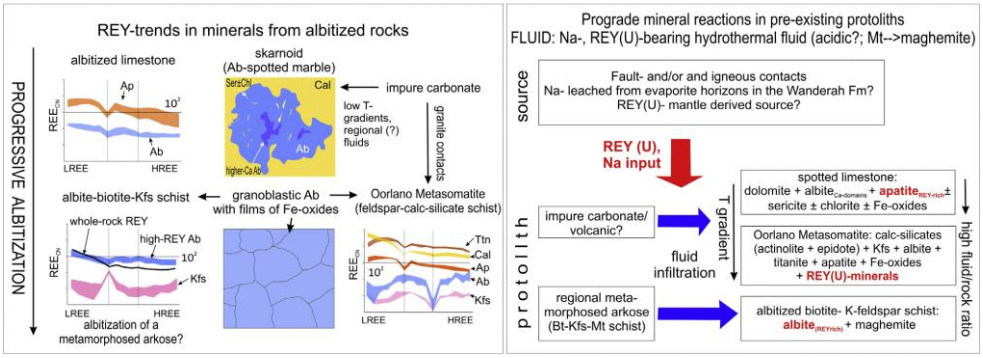

Fig. 16. Schematic diagram showing key textures and REY fractionation trends (left panel), and REY-pathways (right panel) during progressive albitization of the metasedimentary rocks and Oorlano Metasomatite. See text for additional explanation. Abbreviations: Ab — albite; Ap — apatite; Bt — biotite; Cal — calcite; Chl — chlorite; Kfs — K-feldspar; Mt — magnetite; REY(U)-min — discrete REY-(U)-bearing minerals; Ser — sericite; Ttn — titanite.

alteration with higher fluid/rock ratios may obliterate albite, leading to a dominance of K-feldspar, as seen in the Moonta Porphyry. Analogous to this, the dominance of K-feldspar in the chlorite-schist would account for the comparable REY fractionation trends in the new, hydrothermal K-feldspar. We have insufficient data to support a relationship between this alteration and high-grade vein mineralization but it may be an intermediate link between albitization and hydrolytic alteration is required to form sericite-hematite-bearing breccias at upper levels.

6.4. Implications for IOCG genesis and exploration models

The findings of this study have several implications in terms of constraints of IOCG genetic models and their application in exploration.

Albitization, in particular when driven via CDRR, is shown to increase the overall porosity of rocks during initial stages of alteration. This may promote higher rates of fluid flow through the mineralizing system during subsequent stages. This makes albitization, and resultant trace element redistribution, a key process in development of the characteristic alteration patterns present in IOCG-hosting terranes. The question of how much metal endowment follows intense albitization is, however, yet to be resolved.

The significance of feldspar trace element signatures has also been highlighted. The process of albitization redistributes a range of trace elements – all of which are recorded in mineral signatures – clearly validating its use for interpretation of complex petrogenetic histories in analogous terranes.

Trace element signatures in feldspars can reflect the transition from magmatic to hydrothermal stages within an evolving IOCG system. The low-REY concentration in magmatic K-feldspar of the Hiltaba Suite granitoids provides a regional background signature for the Moonta-Wallaroo area, which should be tested across the entire Olympic IOCG Province.

Strong albitization may not, however, be automatically linked to the formation of giant IOCG ore deposits. In fact, albitized rocks that display little or no superposition by later potassic alteration may actually be poor hosts for large IOCG systems. Albitization via CDRR not only enhances rock permeability but also provides a medium for trapping REY(U) as discrete minerals within the same area of reaction. In the presence of fluids focused and confined within the same granitic body undergoing repeated brecciation, such REY(U)-minerals will be further recycled as subsequent alteration stages obliterate evidence of albitization. At Olympic Dam, elevated REY(U)-concentrations are associated with zones where Fe > 40% (Ehrig et al., 2013). In a strongly faulted structural environment, hydrothermal fluids may be more readily focused but are unlikely to lead to REY(U) concentration in the absence of a suitable structural/lithological trap.

7. Conclusions

This study allows several conclusions to be made. Firstly, the various processes involved in albitization are shown to be critical in determining the endowment and deportment of REY in rocks that have undergone alteration.

Secondly, REY signatures of feldspars and accessory minerals are shown to be valuable geochemical tracers of alteration stages within IOCG systems.

Albitization reactions involve the redistribution, accumulation and retention (locking-in) of REY via complex fluid–rock reactions that are dependent on the pre-existing mineral assemblages and fluid characteristics. However, the igneous rocks display a communality of albitization reactions, traceable to the nanoscale. These reactions carry implications for the distribution of U, with which REY are closely related.

There are significant differences in the albitization pathways followed in the igneous and metasedimentary rocks. In the former, CDRR is shown to be important as a driver of increased rock porosity, consistent with published experimental data. In the metasedimentary rocks, however, we see evidence for large-scale fluid infiltration and higher fluid/rock ratios.

We show the importance of small-scale observation in understanding alteration as, for example, the recognition of new-formed K-feldspar within albitized rocks, emphasizing how potassic alteration follows sodic alteration. Future work at the micron- to nanoscale should aim to further constrain reactants and products and write balanced chemical equations for each of the reactions involved. These can, in turn, serve as a basis for numerical modelling of REY partitioning trends.

Acknowledgments

The Deep Exploration Technologies Cooperative Research Centre (Project 3.2, Hypogene alteration in IOCG systems) is acknowledged for financial support of the analytical work. CLC acknowledges Caroline Forbes who provided samples and whole-rock geochemistry datasets for the studied samples. Roniza Ismail assisted with data collection. Adelaide Microscopy is thanked for assistance with microanalysis. We thank AMMRF for access to the Dual Beam FEI Helios Nanolab 600 platform. We appreciate the comments of two anonymous reviewers and *Lithos* Editor-in-Chief, Nelson Eby, which helped us clarify many of the ideas expressed. This is TRaX contribution no. 293.

Appendix A. Supplementary data

Supplementary data (electron probe and LA-ICP-MS data for minerals) to this article can be found online at http://dx.doi.org/10.1016/j.lithos.2014.09.001.

Appendix B. Analytical methods

Complete details of analytical methodology in this article can be found online at http://dx.doi.org/10.1016/j.lithos.2014.09.001.

References

Allen, S.R., McPhie, J., Ferris, G., Simpson, C., 2008. Evolution and architecture of a large felsic igneous province in western Laurentia: the 1.6 Ga Gawler Range Volcanics, South Australia. Journal of Volcanology and Geothermal Research 172, 132–147.

Alt, J.C., 1999. Hydrothermal alteration and mineralization of oceanic crust: mineralogy, geochemistry and processes. Reviews in Economic Geology 8, 133–155.

Barton, M.D., 2014. Iron oxide(-Cu-Au-REE-P-Ag-U-Co) systems, Treatise on Geochemistry2nd edition. Elsevier, pp. 515–541.

Barton, M.D., Johnson, D.A., 2004. Footprints of Fe-oxide (-Cu-Au) systems. University of Western Australia Special Publication 33, 112–116.

Bau, M., 1991. Rare-earth element mobility during hydrothermal and metamorphic fluid–rock interaction and the significance of the oxidation state of europium. Chemical Geology 93, 219–230.

Belousova, E.A., Griffin, W.L., O'Reilly, S.Y., Fisher, N.I., 2002a. Apatite as an indicator mineral for mineral exploration: trace-element compositions and their relationship to host rock type. Journal of Geochemical Exploration 76, 45–69.

Belousova, E.A., Griffin, W.L., O'Reilly, S.Y., Fisher, N.I., 2002b. Igneous zircon: trace element composition as an indicator of source rock type. Contributions to Mineralogy and Petrology 143, 602–622.

Belperio, A., Flint, R., Freeman, H., 2007. Prominent Hill: a hematite-dominated, iron oxide copper-gold system. Economic Geology 102, 1499–1510.

Cao, M., Li, G., Qin, K., Seitmuratova, E.Y., Liu, Y., 2012. Major and trace element characteristics of apatites in granitoids from Central Kazakhstan: implications for petrogenesis and mineralization. Resource Geology 62, 63–83.

Chiaradia, M., Banks, D., Cliff, R., Marschik, R., De Haller, A., 2006. Origin of fluids in iron oxide–copper–gold deposits: constraints from δ^{37}Cl, $^{87}Sr/^{86}Sr$ and Cl/Br. Mineralium Deposita 41, 565–573.

Ciobanu, C.L., Cook, N.J., Utsunomiya, S., Pring, A., Green, L., 2011. Focussed ion beam - transmission electron microscopy applications in ore mineralogy: bridging micron- and nanoscale observations. Ore Geology Reviews 42, 6–31.

Ciobanu, C.L., Wade, B., Cook, N.J., Schmidt Mumm, A., Giles, D., 2013. Uranium-bearing hematite from the Olympic Dam Cu-U-Au deposit, South Australia; a geochemical tracer and reconnaissance Pb-Pb geochronometer. Precambrian Research 238, 129–147.

Conor, C.H.H., 1995. Moonta-Wallaroo region: an interpretation of the geology of the Maitland and Wallaroo 1:100 000 sheet areas. Mines and Energy South Australia, Open File Envelope 8886, DME 588/93.

Conor, C., Raymond, O.L., Baker, T., Teale, G., Say, P., Lowe, G., 2010. Alteration and mineralisation in the Moonta-Wallaroo Copper-Gold Mining Field Region, Olympic Domain, South Australia. In: Porter, T.M. (Ed.), Hydrothermal Iron Oxide Copper-Gold & Related Deposits: A Global Perspective vol. 3–4. PGC Publishing, Adelaide, pp. 1–24.

Cowley, W., Conor, C., Zang, W., 2003. New and revised Proterozoic stratigraphic units on northern Yorke Peninsula. MESA Journal 29, 46–58.

Cuney, M., 2010. Evolution of uranium fractionation processes through time: driving the secular variation of uranium deposit types. Economic Geology 105, 553–569.

Cuney, M., Emetz, A., Mercadier, J., Mykchaylov, V., Shunko, V., Yuslenko, A., 2012. Uranium deposits associated with Na-metasomatism from central Ukraine: a review of some of the major deposits and genetic constraints. Ore Geology Reviews 44, 82–106.

Davidson, G.J., Paterson, H., Meffre, S., Berry, R.F., 2007. Characteristics and origin of the Oak Dam East breccia-hosted, iron oxide Cu-U-(Au) deposit: Olympic Dam region, Gawler craton, South Australia. Economic Geology 102, 1471–1498.

Ehrig, K., McPhie, J., Kamenetsky, V., 2013. Geology and mineralogical zonation of the Olympic Dam iron oxide Cu–U–Au–Ag deposit, South Australia. In: Hedenquist, J.W., Harris, M., Camus, F. (Eds.), Geology and Genesis of Major Copper Deposits and Districts of the World, a Tribute to Richard Sillitoe. Society of Economic Geologists Special Publication 16, pp. 237–268.

Engvik, A.K., Putnis, A., Fitzgerald, J.D., Austrheim, H., 2008. Albitization of granitic rocks: The mechanism of replacement of oligoclase by albite. Canadian Mineralogist 46, 1401–1415.

Fanning, C.M., Reid, A.J., Teale, G.S., 2007. A geochronological framework for the Gawler craton, South Australia. Bulletin 55. Primary Industries and Resources South Australia, Adelaide.

Ferris, G.M., Schwarz, M.P., Heithersay, P., 2002. The geological framework, distribution and controls of Fe-oxide and related alteration, and Cu–Au mineralisation in the Gawler Craton, South Australia. Part I, Geological and tectonic framework. In: Porter, T.M. (Ed.), Hydrothermal Iron Oxide Copper-Gold & Related Deposits: A Global Perspective vol. 2, pp. 9–31.

Fleet, M.E., Pan, Y., 1994. Site preference of Nd in fluorapatite [Ca_{10} (PO_4)$_6$ F_2]. Journal of Solid State Chemistry 112, 78–81.

Fleet, S.G., Ribbe, P.H., 1965. An electron-microscope study of peristerite plagioclases. Mineralogical Magazine 35, 165–176.

Forbes, C., 2012. Report on production of first version of top of basement solid geology map for the central Yorke Peninsula. Project 3.2/3.3: Yorke Peninsula Project. Unpublished internal report, DET CRC (http://detcrc.com.au/publications/research/)

Gay, P., Smith, J.V., 1955. Phase relations in the plagioclase feldspars: composition range An_0 to An_{70}. Acta Crystallographica 8, 64–65.

Groves, D.I., Bierlein, F.P., Meinert, L.D., Hitzman, M.W., 2010. Iron oxide copper-gold (IOCG) deposits through earth history: implications for origin, lithospheric setting, and distinction from other epigenetic iron oxide deposits. Economic Geology 105, 641–654.

Hand, M., Reid, A., Jagodzinski, L., 2007. Tectonic framework and evolution of the Gawler craton, southern Australia. Economic Geology 102, 1377–1395.

Haynes, D.W., Cross, K.C., Bills, R.T., Reed, M.H., 1995. Olympic Dam ore genesis: a fluid mixing model. Economic Geology 90, 281–307.

Hayward, N., Skirrow, R., 2010. Geodynamic setting and controls on iron oxide Cu-Au (±U) ore in the Gawler craton, South Australia. In: Porter, T.M. (Ed.), Hydrothermal Iron Oxide Copper-Gold & Related Deposits: A Global Perspective vol. 3–4. PGP Publishing, Adelaide, pp. 105–131.

Henderson, P. (Ed.), 1984. Rare Earth Element Geochemistry, Developments in Geochemistry vol. 2. Elsevier (510 pp.).

Hitzman, M.W., 2000. Iron oxide–Cu–Au deposit: what, where, when, and why? In: Porter, T.M. (Ed.), Hydrothermal iron oxide copper-gold and related deposits a global perspective. Australian Mineral Foundation, pp. 9–26.

Hitzman, M.W., Valenta, R.K., 2005. Uranium in iron oxide-copper-gold (IOCG) systems. Economic Geology 100, 1657–1661.

Hitzman, M.W., Oreskes, N., Einaudu, M.T., 1992. Geological characteristics and tectonic setting of Proterozoic iron oxide (Cu-U-Au-REE) deposits. Precambrian Research 58, 241–287.

Hövelmann, J., Putnis, A., Geisler, T., Schmidt, B.C., Golla-Schindler, U., 2010. The replacement of plagioclase feldspars by albite: observations from hydrothermal experiments. Contributions to Mineralogy and Petrology 159, 43–59.

Ismail, R., Ciobanu, C.L., Cook, N.J., Teale, G.S., Giles, D., Schmidt Mumm, A., Wade, B., 2014. Rare Earths and other trace elements in minerals from skarn assemblages, Hillside iron oxide-copper-gold deposit, Yorke Peninsula, South Australia. Lithos 184–187, 456–477.

Jagodzinski, E.A., 2005. Compilation of SHRIMP U-Pb geochronological data, Olympic Domain, Gawler Craton, South Australia, 2001-2003. Geoscience Australia, Record 2005/20. .

Johnson, J.P., Cross, K.C., 1995. U-Pb geochronological constraints on the genesis of Olympic Dam Cu-U-Au-Ag deposit, South Australia. Economic Geology 88, 1046–1063.

Johnson, J.P., McCulloch, M.T., 1995. Sources of mineralising fluids for the Olympic Dam deposit (South Australia): Sm–Nd isotopic constraints. Chemical Geology 121, 177–199.

McDonough, W.F., Sun, S.-s, 1995. The composition of the Earth. Chemical Geology 120, 223–253.

Meinert, L.D., 1992. Skarns and skarn deposits. Geoscience Canada 19, 145–162.

Montreuil, J.-F., Corriveau, L., Potter, E.G., 2014. Formation of albitite-hosted uranium within IOCG systems: the Southern Breccia, Great Bear magmatic zone, Northwest Territories, Canada. Mineralium Deposita, http://dx.doi.org/10.1007/s00126-014-0530-7 (in press).

Morales Ruano, S.M., Both, R.A., Golding, S.D., 2002. A fluid inclusion and stable isotope study of the Moonta copper-gold deposits, South Australia: evidence for fluid immiscibility in a magmatic hydrothermal system. Chemical Geology 192, 211–226.

Norberg, N., Harlov, D., Neusser, G., Wirth, R., Rhede, D., 2014. Element mobilization during feldspar metasomatism: an experimental study. European Journal of Mineralogy 26, 71–82.

Oliver, N.H.S., Cleverley, J.S., Mark, G., Pollard, P.J., Fu, B., Marshall, L.J., Rubenach, M.J., Williams, P.J., Baker, T., 2004. Modeling the role of sodic alteration in the genesis of iron oxide–copper–gold deposits, Eastern Mount Isa Block, Australia. Economic Geology 99, 1145–1176.

Otake, T., Wesolowski, D.J., Anovitz, L.M., Allard, L.F., Ohmoto, H., 2010. Mechanisms of iron oxide transformations in hydrothermal systems. Geochimica et Cosmochimica Acta 74, 6141–6156.

Plümper, O., Putnis, A., 2009. The complex hydrothermal history of granitic rocks: multiple feldspar replacement reactions under subsolidus conditions. Journal of Petrology 50, 967–987.

Pollard, P.J., 2006. An intrusion-related origin for Cu–Au mineralization in iron oxide–copper–gold (IOCG) provinces. Mineralium Deposita 41, 179–187.

Raymond, O., 2003, Yorke Peninsula (Moonta Subdomain), Geophysical Interpretation of Pre-NeoProterozoic Basement Geology 1:250 000 scale map (2nd edition). Geoscience Australia, Canberra.

Reeve, J.S., Cross, K.C., Smith, R.N., Oreskes, N., 1990. Olympic Dam copper-uranium-gold-silver deposit. In: Hughes, F.E. (Ed.), Geology of the Mineral Deposits of Australia and Papua New GuineaMonograph 14. Australasian Institute of Mining and Metallurgy, pp. 1009–1035.

Reid, A., Hand, M., 2012. Mesoarchean to Mesoproterozoic evolution of the southern Gawler Craton, South Australia. Episodes 35, 216–225.

Reid, A.J., Swain, G.S., Mason, D., Maas, R., 2011. Nature and timing of Cu-Au-Zn-Pb mineralisation at Punt Hill, eastern Gawler craton. MESA Journal 60, 7–17.

Reid, A., Smith, R.N., Baker, T., Jagodzinski, E.A., Selby, D., Gregory, C.J., Skirrow, R.G., 2013. Re-Os dating of molybdenite within hematite breccias from the Vulcan Cu-Au prospect, Olympic Cu-Au province, South Australia. Economic Geology 108, 883–894.

Skirrow, R., 2008. "Hematite-group" IOCG ± U ore systems: tectonic settings, hydrothermal characteristics, and Cu–Au and U mineralising processes. In: Corriveau, L., Mumin, A.H. (Eds.), Exploring for Iron Oxide Copper-gold Deposits: Canada and Global Analogues. Geological Association of Canada, Short Course Notes vol. 20, pp. 39–57.

Skirrow, R.G., Bastrakov, E., Davidson, G.J., Raymond, O.L., Heithersay, P., 2002. The geological framework, distribution and controls of Fe-oxide Cu–Au mineralisation in the Gawler Craton, South Australia. Part II-alteration and mineralisation. In: Porter, T.M. (Ed.), Hydrothermal Iron Oxide Copper–Gold and Related Deposits: A Global Perspective vol. 2. PGC Publishing, Adelaide, pp. 33–47.

Skirrow, R.G., Bastrakov, E., Evgeniy, N., Barovich, K., Fraser, G.L., Creaser, R.A., Fanning, C.M., Raymond, O.L., Davidson, G.J., 2007. Timing of iron oxide Cu–Au–(U) hydrothermal activity and Nd isotope constraints on metal sources in the Gawler craton, South Australia. Economic Geology 102, 1441–1470.

Smith, M., Henderson, P., Jeffries, T.E., Long, J., Williams, C.T., 2004. The rare earth elements and uranium in garnets from the Beinn an Dubhaich Aureole, Skye, Scotland, UK: constraints on processes in a dynamic hydrothermal system. Journal of Petrology 45, 457–484.

Smith, M., Storey, C.D., Jeffries, T.E., Ryan, C., 2009. In situ U–Pb and trace element analysis of accessory minerals in the Kiruna district, Norrbotten, Sweden: new constraints on the timing and origin of mineralization. Journal of Petrology 50, 2063–2094.

Stix, J., Gorton, M.P., 1990. Variations in trace element partition coefficients in sanidine in the Cerro Toledo Rhyolite, Jemez Mountains, New Mexico: effects of composition, temperature, and volatiles. Geochimica et Cosmochimica Acta 54, 2697–2708.

Trail, D., Watson, E.B., Tailby, N.D., 2012. Ce and Eu anomalies in zircon as proxies for the oxidation state of magmas. Geochimica et Cosmochimica Acta 97, 70–87.

Wade, C.E., Reid, A.J., Wingate, M.T.D., Jagodzinski, E.A., Barovich, K., 2012. Geochemistry and geochronology of the c. 1585 Ma Benagerie Volcanic Suite, southern Australia: relationship to the Gawler Range Volcanics and implications for the petrogenesis of a Mesoproterozoic silicic large igneous province. Precambrian Research 206–207, 17–35.

Williams, P.J., 2010. Classifying IOCG deposits. In: Corriveau, L., Mumin, H. (Eds.), Exploring for Iron Oxide Copper–Gold Deposits: Canada and Global Analogues. Geological Association of Canada Short Course Notes vol. 20, pp. 23–38.

Williams, P.J., Barton, M.D., Johnson, D.A., Fontbote, L., De Haller, A., Mark, G., Oliver, N.H.S., Marschik, R., 2005. Iron oxide copper–gold deposits: geology, space-time distribution, and possible modes of origin. Economic Geology 100th Anniversary Volume. pp. 371–405.

Zang, W.L., Fanning, G.M., Purvis, A.C., Raymond, O.L., Both, R.A., 2007. Early Mesoproterozoic bimodal plutonism in the southeastern Gawler Craton, South Australia. Australian Journal of Earth Sciences 54, 661–674.

CHAPTER 4

FELDSPAR EVOLUTION IN THE ROXBY DOWNS GRANITE, HOST TO FE-OXIDE CU-AU-(U) MINERALISATION AT OLYMPIC DAM, SOUTH AUSTRALIA

Alkis Kontonikas-Charos[1], Cristiana L. Ciobanu[2], Nigel J. Cook[2], Kathy Ehrig[3], Sasha Krneta[1], Vadim S. Kamenetsky[4]

[1]*School of Physical Sciences, The University of Adelaide, Adelaide, SA, 5005, Australia*

[2]*School of Chemical Engineering, The University of Adelaide, Adelaide, SA, 5005, Australia*

[3]*BHP Billiton Olympic Dam, Adelaide, SA, 5000, Australia*

[4]*School of Physical Sciences, University of Tasmania, Hobart, TAS, 7001, Australia*

Article published in Ore Geology Reviews 80, 838-859.

Statement of Authorship

Title of Paper	Feldspar evolution in the Roxby Downs Granite, host to Fe-oxide Cu-Au-(U) mineralisation at Olympic Dam, South Australia
Publication Status	☑ Published ☐ Accepted for Publication ☐ Submitted for Publication ☐ Unpublished and Unsubmitted w ork w ritten in manuscript style
Publication Details	Kontonikas-Charos, A., Ciobanu, C.L., Cook, N.J., Ehrig, K., Krneta, S., Kamenetsky, V.S., 2017. Feldspar evolution in the Roxby Downs Granite, host to Fe-oxide Cu-Au-(U) mineralisation at Olympic Dam, South Australia. Ore Geology Reviews 80, 838-859.

Principal Author

Name of Principal Author (Candidate)	Alkis Kontonikas-Charos		
Contribution to the Paper	Performed analytical work, carried out data processing and interpretation, oversaw development of work and wrote manuscript.		
Overall percentage (%)	75		
Certification:	This paper reports on original research I conducted during the period of my Higher Degree by Research candidature and is not subject to any obligations or contractual agreements with a third party that would constrain its inclusion in this thesis. I am the primary author of this paper.		
Signature		Date	11/07/17

Co-Author Contributions

By signing the Statement of Authorship, each author certifies that:

i. the candidate's stated contribution to the publication is accurate (as detailed above);

ii. permission is granted for the candidate in include the publication in the thesis; and

iii. the sum of all co-author contributions is equal to 100% less the candidate's stated contribution.

Name of Co-Author	Cristiana L. Ciobanu		
Contribution to the Paper	Helped define direction of research, supervised development of work, assisted with data interpretation and contributed to manuscript preparation.		
Overall percentage (%)	7.5		
Signature		Date	10. July 2017

Name of Co-Author	Nigel J. Cook		
Contribution to the Paper	Helped define direction of research, supervised development of work, assisted with data interpretation and contributed to manuscript preparation.		
Overall percentage (%)	7.5		
Signature		Date	10/7/17

Name of Co-Author	Kathy Ehrig		
Contribution to the Paper	Provided sample material and helped to evaluate and edit manuscript.		
Overall percentage (%)	5		
Signature		Date	10 July 2017

Name of Co-Author	Sasha Krneta		
Contribution to the Paper	Helped to evaluate and edit manuscript.		
Overall percentage (%)	2.5		
Signature		Date	11/7/2017

Name of Co-Author	Vadim S. Kamenetsky		
Contribution to the Paper	Helped to evaluate and edit manuscript.		
Overall percentage (%)	2.5		
Signature		Date	11/7/17

Ore Geology Reviews 80 (2017) 838–859

Contents lists available at ScienceDirect

Ore Geology Reviews

journal homepage: www.elsevier.com/locate/oregeorev

Feldspar evolution in the Roxby Downs Granite, host to Fe-oxide Cu-Au-(U) mineralisation at Olympic Dam, South Australia

Alkis Kontonikas-Charos [a,*], Cristiana L. Ciobanu [b], Nigel J. Cook [b], Kathy Ehrig [c], Sasha Krneta [a], Vadim S. Kamenetsky [d]

[a] School of Physical Sciences, University of Adelaide, Adelaide, SA 5000, Australia
[b] School of Chemical Engineering, University of Adelaide, Adelaide, SA 5000, Australia
[c] BHP Billiton Olympic Dam, Adelaide, SA 5000, Australia
[d] School of Physical Sciences, University of Tasmania, Hobart, TAS, 7001, Australia

ARTICLE INFO

Article history:
Received 14 March 2016
Received in revised form 8 August 2016
Accepted 20 August 2016
Available online 24 August 2016

Keywords:
Feldspars
Albitisation
Iron-oxide copper-gold mineralisation
Olympic dam

ABSTRACT

The textural relationships and geochemistry of feldspars from least-altered to sericite-hematite altered and mineralised ~1.595 Ga Roxby Downs Granite (RDG) at Olympic Dam, South Australia, were examined. The sample suite is representative of RDG both distal (>5 km) and proximal (<1 km) to the hydrothermal breccias of the Olympic Dam Breccia Complex (ODBC), which host Fe-oxide Cu-Au-(U) mineralisation at Olympic Dam. Microscopic observations and quantitative analyses indicate that a range of feldspar reactions have taken place within the RDG hosting the Olympic Dam deposit. An early phase of igneous plagioclase (~$An_{27–34}$) is recognised, along with a more abundant, less-calcic plagioclase (~$An_{12–20}$) both displaying rapakivi and anti-rapakivi textures with alkali feldspar. Alkali feldspars (~$Or_{55}Ab_{43}An_2$) record post-magmatic evolution from cryptoperthite to patch perthite. Subsequent patch perthite is overprinted by highly porous, near end-member albite and K-feldspar, while plagioclase undergoes replacement by albite + sericite ± Ba-rich K-feldspar. In sericite-hematite altered and mineralised RDG along the margin of the ODBC, sericite replaces all plagioclase, whereas red-stained, Fe-rich K-feldspar persists. Sulphide-uranium-rare earth element mineralisation is observed in association with hydrothermal feldspars, and increases in abundance with proximity to the orebody. Petrographic observations and whole-rock geochemistry illustrate the transformation of plagioclase and alkali feldspar from igneous to hydrothermal processes, and indicate that hydrothermal albite and K-feldspar formed within the RDG without the need for an external source of alkalis. Feldspar geothermometry indicates a minimum crystallisation temperature of 765 °C at 2.2 kbar for alkali feldspar (pressure estimate obtained using plagioclase-amphibole geobarometry) followed by a range of lower temperature transformations. Late-stage magma mixing/contamination is postulated from supportive temperature and pressure estimates along with feldspar and mafic mineral relationships.
© 2016 Elsevier B.V. All rights reserved.

1. Introduction

The presence of feldspar replacement reactions has long been recognised as a diagnostic property of iron-oxide copper-gold (IOCG) systems (*e.g.*, Groves et al., 2010); however the exact role they play in the genesis of such deposits remains poorly constrained. Detailed studies of deuteric coarsening (e.g., Parsons and Lee, 2009) and albitisation (*e.g.*, Putnis, 2002; Plümper and Putnis, 2009) have highlighted the ability of such reactions to alter the physical and chemical properties of the host rocks from the macro- down to the nanoscale during fluid-rock interaction. This invokes the idea that feldspar replacement reactions might be more important than once thought, and may even be a required stage for deposition of IOCG mineralisation.

The Olympic Dam IOCG-U deposit, South Australia, is widely regarded as the archetype of the IOCG *sensu stricto* deposit class (*e.g.*, Hitzman et al., 1992; Groves et al., 2010). At Olympic Dam, all IOCG mineralisation is localised within the ~1.595 Ga Roxby Downs Granite (RDG) (*e.g.*, Reeve et al., 1990; Johnson and Cross, 1995). Therefore, Olympic Dam provides an outstanding opportunity to understand the relationship between magmatism, alteration and mineralisation. New insights into the formation of Olympic Dam can be obtained by constraining the major mineralogical changes preserved in the host rocks, which cannot be unambiguously interpreted on the basis of whole rock geochemistry alone. In this contribution, changes in feldspar textures and chemistry in the RDG from magmatic to hydrothermal stages are documented at various (sub-μm to dm) scales.

* Corresponding author.
E-mail address: alkiviadis.kontonikas-charos@adelaide.edu.au (A. Kontonikas-Charos).

http://dx.doi.org/10.1016/j.oregeorev.2016.08.019
0169-1368/© 2016 Elsevier B.V. All rights reserved.

2. Background

2.1. Feldspar reactions and nomenclature

Feldspar microtextures provide a valuable tool for understanding subsolidus re-equilibration in slowly cooled igneous rocks (*e.g.*, Parsons et al., 2015). As fluid-feldspar interaction readily occurs during cooling, feldspars are often subject to post-crystallisation modification (Brown and Parsons, 1989). This typically involves circulation of a deuteric fluid (post-magmatic, internally exsolved), and results in the formation of highly porous, strain-free regions of albite- and orthoclase-rich subgrains within perthitic feldspars (Lee and Parsons, 1997). This process is known as 'deuteric coarsening' (Brown and Parsons, 1984), and the resultant intergrowth texture is termed 'patch perthite' (Parsons, 1978).

Deuteric coarsening is generally considered isochemical (*e.g.*, Parsons et al., 2005) but albitisation, one of the most common metasomatic aluminosilicate reactions in the Earth's upper crust (Perez and Boles, 2005), involves non-isochemical replacement of feldspar by albite. Regional-scale albitisation has been documented from a number of igneous-metamorphic terranes including the Bamble Sector, Norway (Engvik et al., 2008), the Cloncurry District, Queensland, Australia (*e.g.*, Oliver et al., 2004), and recently from the southern part of the Gawler Craton, South Australia (Conor et al., 2010; Ismail et al., 2014; Kontonikas-Charos et al., 2014). Albitisation is also spatially and temporally associated with iron-oxide copper-gold (IOCG) mineralisation (Barton, 2014; and references therein). In this case, albitisation typically forms a broad halo surrounding the deposit, and results in an assemblage dominated by albite (replacing feldspars), chlorite (replacing mafic minerals) and rutile (replacing Fe-Ti-oxides). In extreme cases, almost monomineralic albitites can result (Barton, 2014).

Previous authors (*e.g.*, Engvik et al., 2008; Plümper and Putnis, 2009) have concluded that albitisation occurs through a coupled dissolution-precipitation mechanism (Putnis, 2002), whereby porosity generated is crucial for advancement of the replacement interface between the parent and product phases. It is clear that feldspar reactions are capable of altering the physical properties and chemistry of rocks by significantly enhancing rock permeability (*e.g.*, Putnis, 2002), allowing for subsequent element remobilisation (*e.g.*, Parsons et al., 2009; Hövelmann et al., 2010; Kontonikas-Charos et al., 2014).

2.2. Olympic Dam geology

The Olympic Dam deposit (10,100 Mt @ 0.78% Cu, 250 ppm U_3O_8, 0.3 ppm Au, 1 ppm Ag; BHP Billiton, 2015) is situated within the Olympic Cu-Au Province, a large metallogenic belt which strikes roughly N-S for over 500 km along the eastern margin of the Gawler Craton. The Olympic Cu-Au province also encompasses numerous other IOCG deposits and prospects, including Prominent Hill, Carrapateena, Hillside and Moonta-Wallaroo (Hayward and Skirrow, 2010). The province comprises Palaeo- to Mesoproterozoic sediments, granites, volcanics and conglomerates (Ferris et al., 2002). Rocks of the Hutchison Group (~2 Ga), Donington Granitoid Suite (~1845–1810 Ma) and Wallaroo Group equivalents (~1.75 Ga) form the Palaeoproterozoic basement of the Olympic Dam region (Creaser, 1989; Ferris et al., 2002; Jagodzinski, 2005). These units are unconformably overlain and intruded by felsic and mafic lithologies of the Hiltaba Intrusive Suite (HIS) and Gawler Range Volcanics (GRV); both are the products of a regional-scale magmatic event at ~1.6 Ga (*e.g.*, Skirrow et al., 2007).

Deposition of Cu-Au mineralisation has been considered contemporaneous with the ~1.6 Ga event, based on dating of hydrothermal minerals at Olympic Dam and other prospects (*e.g.*, Johnson and Cross, 1995, Jagodzinski, 2005; Skirrow et al., 2007; Ciobanu et al., 2013; Reid et al., 2013). The hydrothermal breccias of the Olympic Dam Breccia Complex (ODBC), which host the Olympic Dam deposit, are contained within the RDG, which is unconformably overlain by Neoproterozoic to Cambrian sediments of the Stuart Shelf (Reeve et al., 1990). Compositions and textures within the ODBC are gradational, and comprise a continuum from sericite-altered granite through mineralised hematite-rich breccias to barren hematite-quartz breccias in the centre of the deposit (Ehrig et al., 2012). Such changes can be expressed by Fe-Si relationships of whole rock compositions (Fig. 3 in Ehrig et al., 2012). Sericite and hematite, as well as quartz, chlorite, siderite, fluorite, barite and minor magnetite, are the dominant minerals within the complex. Degree of alteration and intensity of brecciation increase from the edges of the ODBC towards the deposit centre (Haynes et al., 1995; Ehrig et al., 2012).

The RDG is relatively undeformed, equigranular and medium- to coarse-grained. It is primarily composed of alkali feldspar (~50%), quartz (21–25%), plagioclase (17–23%) and minor biotite, amphibole and opaques/accessories (5–7%) (Creaser, 1989). The latter include magnetite (containing exsolution of relic ilmenite, which is altered to hematite and rutile), titanite, apatite, zircon, as well as allanite, fluorite, tourmaline, ankerite, uranothorite, synchysite and trace sulphides (Creaser, 1989; Ehrig et al., 2012). Plagioclase forms euhedral grains with core-to-rim compositional zoning ($An_{34–20}$). Alkali feldspars are coarsely perthitic and may be mantled by plagioclase ('rapakivi' texture); occasionally, granophyric textures with quartz are also observed (Creaser, 1989). Alteration of feldspars to an assemblage of sericite and hematite, and to a lesser extent chloritisation of mafic minerals, is seen throughout the RDG (Creaser, 1989; Oreskes and Einaudi, 1990).

Despite its prominence elsewhere throughout the Gawler Craton (*e.g.*, Yorke Peninsula; Conor et al., 2010; Ismail et al., 2014; Kontonikas-Charos et al., 2014), sodic alteration (particularly albitisation) has not been considered to be significant at Olympic Dam (*e.g.*, Hayward and Skirrow, 2010). Furthermore, hydrothermal K-feldspar has not been previously recognised at Olympic Dam.

3. Approach and methodology

A mineralogical and petrological study was carried out on representative granite samples from various parts of the Olympic Dam region. Drillholes RD2492, -2494 and -2945, ~3 km SW of the deposit ('Area 1' on Fig. 1), were sampled for granite to investigate the chemical and mineralogical homogeneity of the RDG around the Olympic Dam deposit. Drillholes along a 5 km-long NW-SE transect (from RD2274 to RD2511; 'Area 2' on Fig. 1) were also selected to understand feldspar modifications in granite towards the margin of the deposit. In addition, the sample suite includes mineralised granites located both proximal (Drillhole RD3554), and distal (Drillhole RD2316), relative to the ODBC. All samples were obtained from drill core which had been previously assayed by BHP Billiton (see Ehrig et al., 2012 for assay methodology). Initial mineral identification and sample characterisation was made on thin sections and polished blocks by optical microscopy.

All instruments used for analytical characterisation of thin sections and polished blocks are hosted at Adelaide Microscopy, University of Adelaide. A FEI Quanta 450 scanning electron microscope (SEM) with energy-dispersive X-ray spectrometry and back-scatter electron (BSE) imaging capabilities was used at an accelerating voltage of 20 kV and beam current of 10 nA.

Quantitative compositions of feldspars within representative samples were determined using a Cameca SX-Five electron probe microanalyser (EPMA). All feldspars, amphibole and Fe-Ti-minerals were analysed in samples from least-altered RDG (drillholes RD2492, RD2494, RD2495, RD2280 and RD2774), whereas only albite and red-stained K-feldspar were analysed from sericite-hematite altered and mineralised RDG (drillholes RD2531, RD2511, RD3554 and RD2316). Appendix A provides further details of EPMA methodology, including standards, wavelengths, count times and minimum detection limits (mdl).

Transmission electron microscopy (TEM) was performed on foils prepared using the focussed ion beam (FIB)-SEM technique for

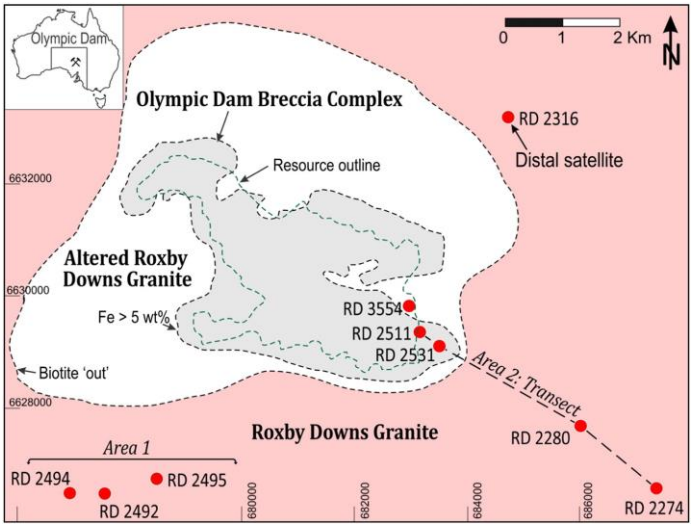

Fig. 1. Sketch map outlining the Olympic Dam deposit and sampled drillhole locations. The map is representative of geology 350 m below the surface, which is overlain by metasediments of the Stuart Shelf. For simplicity, geological structures are ignored. Note that the 3D morphology of the deposit is variable and drillholes marked within the ODBC may cross over respective zones at various depths. For a detailed 3D outline see Ehrig et al. (2012). The white area represents weakly hematite–sericite altered RDG, whereas the area within the Fe >5 wt.% contour contains granite-breccias, hematite-breccias and barren hematite-quartz breccias towards the centre.
Sketch map was modified after Ehrig et al. (2012).

characterisation of feldspars in cryptoperthites. FIB-SEM work was carried out on a Dual Beam FEI Helios Nanolab 600 platform allowing for cross-section imaging, as well as cutting, extraction and thinning of foils for TEM study. Procedures for cutting, extraction and thinning of TEM foils followed Ciobanu et al. (2011). High-resolution (HR)-TEM images in bright field mode (BF) and electron diffractions were obtained using a Philips CM200 TEM equipped with LaB6 source, double-tilt holder and Gatan digital camera, operated at 200 kV. Diffraction measurements were performed using DigitalMicrograph™ 3.11.1 Winwulff© 1.4.0 (JCrystalSoft) software. Publicly available data from the American Mineralogist Crystal Structure Database (http://rruff.geo.arizona.edu/AMS/amcsd.php) were used for indexing of electron diffractions. Energy-dispersive X-ray spectra (EDS) for cryptoperthite analysis were performed on an ultra-high resolution, probe-corrected, FEI Titan Themis S/TEM operated at 200 kV, with an EDS spot size ~5 nm. The Titan Themis is equipped with a FEI Super-X and Fischione HAADF detector. The Super-X detector provides geometrically symmetric EDS detection with an effective solid angle of 0.8 Sr Probe correction delivering sub-Angstrom-scale spatial resolution.

4. Results

4.1. Samples and whole-rock geochemistry

The ubiquitous pink-red colouration of the RDG throughout the sample suite indicates that it is not completely free of alteration. There are, however, important differences in the intensity of alteration. This variability makes it imperative to outline the mineralogical differences between samples from individual drillholes or areas within the Olympic Dam region. This was achieved *via* a combination of macroscopic observation of drillcores and whole-rock geochemistry. Least-altered RDG is most abundant in drillholes >3 km outside the ODBC and is primarily recognised by the pink colouration of feldspars, preservation of mafic minerals and rapakivi textures (Fig. 2). Least-altered RDG is typically characterised by K_2O:Na_2O ratios between 1 and 3 (this varies with degrees of hydrothermal alteration), FeO <4 wt.%, and trace amounts (~25 ppm) of Cu (Table 1a).

In hand specimen, red-staining of alkali feldspar, yellow-green coloration of plagioclase (sericite replacement) and destruction of mafic minerals are diagnostic of alteration in the RDG (Fig. 2), which is more intense and abundant in drillholes proximal to the ODBC. A low Na_2O content (<0.5 wt.%) and Fe content of ~7 wt.% are also characteristic (Table 1b). Such properties define the 'sericite-hematite altered RDG' sample suite. Mineralised RDG (Table 1c) is typical within drillholes closest to the ODBC, and features elevated Fe (>10 wt.%), a drop in K_2O (from ~7 to ~5.5 wt.%), and Cu concentrations exceeding 1 wt.%. Note, however, that the data in Table 1c is restricted to intervals in the drillhole from which samples were collected for this study. Fig. 3 depicts the progressive alteration and mineral replacement of the RDG associated with mineralisation, using whole-rock analyses over an ~300 m-thick section from drillhole RD2316. In this drillhole the mineralisation (Cu, Mo, LREE and U) strongly correlates with depletion in Na_2O and increase in FeO. Mineralogical changes taking place along this downhole profile are discussed in more detail in the next section. Based on characteristics outlined in this section, three sample suites are defined: (1) least altered RDG; (2) sericite-hematite altered RDG; and (3) mineralised RDG.

Whole-rock analyses for least-altered RDG (Table 1a), show values for the main oxides (*e.g.*, SiO_2 ~ 70%; Al_2O_3 ~ 13%; K_2O ~ 5%, Na_2O ~ 3–4%; FeO ~ 3–4, CaO < 1%, P_2O_5 < 1% and MgO + Ti_2O < 1.5%; LOI ~ 1–2.2%) close to those of granites. Such analyses are used to discriminate among different types of granitoids and their geochemical affiliation (Fig. 4). Two diagrams based on CIPW normative calculations are used, QAP (Streckeisen, 1976; LeMaitre et al., 1989) and Ab-An-Or (Barker, 1979), to show the differences in terms of rock types within the least-altered RDG (Fig. 4a, b). The QAP diagram is modified by dividing the albite (Ab) norm between the orthoclase (Or + Ab ∗ 0.33) and plagioclase (An + Ab ∗ 0.66) apexes, which is based on EPMA spot analyses of cryptoperthite in the least-altered RDG. This approximation is checked by the petrographic study (see below). Least-altered RDG

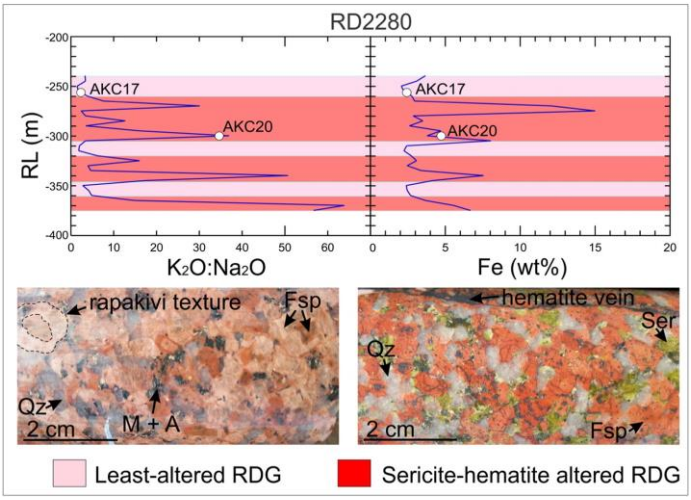

Fig. 2. Binary plots of whole-rock analyses for drillhole RD2280 and hand specimen photographs showing differences in appearance between least-altered and altered RDG. Pink sections represent least-altered RDG (low K_2O:Na_2O ratios and low Fe content), whereas red sections represent altered RDG (high K_2O:Na_2O ratios and high Fe content). Note the change from pink to red colouration of feldspars and the yellow-green colour of sericite in altered RDG. Abbreviations: Fsp — feldspar, M + A — mafic and accessory minerals, Qz — quartz, RL — relative depth of drillhole, Ser — sericite. (For interpretation of the references to colour in this figure legend, the reader is referred to the web version of this article.)

plots as a tight cluster on both the QAP and Ab-An-Or diagrams (Fig. 4a, b), however some of the data begins to extend towards the 'alkali feldspar granite' field and the Or-apex, respectively. Fig. 4c indicates the least-altered RDG ranges from weakly metaluminous to moderately peraluminous. The sample suite is further discriminated by the modified alkali-lime index (Fig. 4d). The least-altered RDG plots between the alkalic and alkali calcic fields due to high Na_2O and K_2O relative to CaO. It also straddles the fields for A- and I-type granitoids, as defined by published data (*e.g.*, Frost et al., 2001).

4.2. Petrography

The petrographic and mineralogical differences between the sample suites are summarised in Table 2. Importantly, although RDG from Area 2 retains the geochemical hallmarks of the least-altered RDG outlined above, it is more altered than RDG from Area 1. Feldspars are more extensively altered and markedly microporous, while all igneous mafic minerals are altered to chlorite + rutile. Thus, Area 2 represents a transition between the least-altered and altered RDG categories. Subsequent feldspar descriptions and interpretations regarding the magmatic history of the RDG hinge primarily on observations from the Area 1 sample suite.

Despite differences in degrees of alteration, least-altered RDG from both Areas 1 and 2 display many petrographic similarities. Feldspars are characterised by various textural overprints (see below) and also form rapakivi and anti-rapakivi textures, while quartz occurs interstitial to other minerals as small groundmass crystals, as well as larger grains (>2 mm). Large microgranular mafic enclaves (>2 mm), consisting of amphibole, biotite and Fe-Ti-minerals (ilmenite, titanite and magnetite), are also found throughout the RDG and have been partially (Area 1) and completely altered (Area 2). In this case, amphibole and biotite are altered to chlorite + hematite ± rutile ± albite, whereas ilmenite breaks down to hematite + rutile symplectites, titanite is replaced by rutile + quartz and magnetite is replaced by hematite. Photomicrographs (Fig. 5) highlight some textural characteristics of minerals in least-altered RDG.

Sericite-hematite altered RDG occurs irregularly throughout all drillholes along the transect (Fig. 1), increasing in abundance and intensity with proximity to the ODBC. Dominant minerals are K-feldspar, quartz, sericite, Fe-oxides (both magnetite and hematite), chlorite,

Table 1a
Sample list and whole-rock assay data for least-altered RDG.

Sample	Drillhole	Depth (mRL)	Whole rock assay data															
			SiO_2	TiO_2	Al_2O_3	FeO	MnO	MgO	CaO	BaO	Na_2O	K_2O	P_2O_5	Total	LOI	K_2O: Na_2O	Cu (ppm)	U_3O_8 (ppm)
RX7860	RD2494	−480.3 to 485.3	71.2	0.48	13.5	3.07	0.05	0.90	0.94	0.10	3.81	5.36	0.07	99.48	1.18	1.41	<50	14
RX7864	RD2492	−653.1 to 658.1	69.3	0.42	13.5	3.36	0.06	0.73	0.76	0.10	3.24	5.55	0.09	97.11	1.40	1.72	<50	8
RX7865	RD2495	−448.1 to 453.1	68.7	0.48	13.1	3.05	0.08	0.99	0.85	0.09	3.73	5.30	0.09	96.46	1.27	1.42	<50	12
RX7866		−483.1 to 488.1	69.7	0.43	13.3	3.06	0.06	0.81	0.88	0.10	3.71	5.36	0.07	97.48	1.04	1.45	<50	12
AKC16	RD2280	−244.9 to 249.9	70.8	0.45	13.8	3.98	0.04	0.83	0.42	0.11	2.16	6.53	0.09	99.21	1.92	3.03	200	<4
AKC17		−259.9 to 264.9	71.4	0.43	13.7	3.56	0.05	1.19	0.57	0.09	1.91	6.59	0.05	99.54	2.24	3.44	<50	5
AKC21		−309.9 to 314.9	70.0	0.45	13.7	3.11	0.05	0.76	0.59	0.09	3.15	5.64	0.09	97.63	1.64	1.79	350	15
AKC22		−314.9 to 319.9	70.6	0.42	13.9	2.88	0.06	0.86	0.76	0.09	3.41	5.57	0.07	98.62	1.62	1.63	200	20
AKC27	RD2274	−214.9 to 217.9	69.1	0.27	12.7	4.80	0.03	0.63	0.14	0.16	1.02	7.05	0.01	95.91	1.55	6.88	<50	<4

Note: 'Total' column only refers to elements given in tables, which are used for rock classification diagrams in Fig. 4. All values given are in wt.% aside from Cu and U_3O_8. Intervals for whole-rock assay data are 5 m. Depth (mRL) is relative to sea level.

Table 1b
Sample list and whole-rock assay data for sericite-hematite altered RDG.

Sample	Drillhole	Depth (mRL)	Whole rock assay data															
			SiO_2	TiO_2	Al_2O_3	FeO	MnO	MgO	CaO	BaO	Na_2O	K_2O	P_2O_5	Total	LOI	K_2O: Na_2O	Cu (ppm)	U_3O_8 (ppm)
AKC1	RD2531	−315.6 to 316.6	62.0	0.37	12.2	12.4	0.63	0.45	0.07	0.04	0.12	5.65	0.12	94.05	5.89	47.1	850	50
AKC2		−423.4 to 424.4	67.0	0.33	12.5	7.08	0.37	0.38	0.08	0.36	0.12	6.13	0.07	94.42	4.09	51.1	200	40
AKC3		−619.1 to 620.1	66.3	0.40	12.8	5.70	0.23	0.32	0.21	0.11	0.18	8.00	0.07	94.32	3.42	44.4	100	25
AKC5		−718.8 to 719.8	65.9	0.40	12.7	7.17	0.31	0.43	0.31	0.07	0.13	6.58	0.14	94.14	4.08	50.6	700	35
AKC8	RD2511	−274.7 to 275.7	65.7	0.35	11.8	7.74	0.04	0.46	0.59	0.61	0.16	6.65	0.07	94.17	2.27	41.6	2400	72
AKC9		−295.1 to 296.1	65.5	0.40	12.9	7.00	0.19	0.33	0.62	0.12	0.19	7.81	0.07	95.13	3.26	41.1	3350	145
AKC10		−338.7 to 339.7	67.8	0.35	12.1	8.45	0.09	0.38	0.21	0.09	0.15	6.38	0.07	96.07	2.62	42.5	2200	38
AKC11		*−510.5 to 515.5*	69.7	0.38	13.5	3.80	0.08	0.81	0.34	0.09	0.16	7.90	0.07	96.83	4.56	49.4	450	26
AKC12		*−510.5 to 515.5*	69.7	0.38	13.5	3.80	0.08	0.81	0.34	0.09	0.16	7.90	0.07	96.83	4.56	49.4	450	26
AKC13		−664.6 to 665.6	67.6	0.38	13.5	6.69	0.05	0.35	0.11	0.17	0.13	6.34	0.07	95.39	2.70	48.8	450	32
AKC18	RD2280	*−294.9 to 299.9*	68.5	0.42	13.2	6.05	0.04	0.83	0.31	0.07	0.47	6.75	0.12	96.76	2.13	14.4	<50	<4
AKC19		*−294.9 to 299.9*	68.5	0.42	13.2	6.05	0.04	0.83	0.31	0.07	0.47	6.75	0.12	96.76	2.13	14.4	<50	<4
AKC20		*−299.9 to 304.9*	70.2	0.45	13.4	4.86	0.03	0.68	0.21	0.09	0.23	7.56	0.05	97.76	1.95	32.9	<50	<4
AKC23		*−324.9 to 329.9*	70.8	0.47	14.4	3.96	0.03	0.60	0.18	0.09	0.54	7.73	0.09	98.89	1.81	14.3	250	10
AKC24		*−354.9 to 359.9*	67.4	0.40	12.6	3.16	0.23	1.38	1.72	0.07	1.70	6.32	0.07	95.05	3.80	3.7	<50	10
AKC25		*−369.9 to 374.9*	66.3	0.42	13.2	8.59	0.01	0.36	0.06	0.04	0.13	6.83	0.05	95.99	1.73	52.5	3800	10
AKC26		*−369.9 to 374.9*	66.3	0.42	13.2	8.59	0.01	0.36	0.06	0.04	0.13	6.83	0.05	95.99	1.73	52.5	3800	10
RX6698	RD2316	−634.7 to 635.7	52.2	0.30	8.0	20.9	0.22	3.10	2.36	0.19	0.85	3.85	0.37	92.34	5.20	4.53	1800	330
RX6700		−662.7 to 663.7	68.2	0.35	12.9	5.84	0.09	0.71	0.49	0.09	2.87	5.72	0.07	97.33	1.67	1.99	300	50
RX6702		−664.7 to 665.7	60.8	0.27	10.3	13.5	0.28	1.74	1.89	0.08	1.62	4.38	0.16	95.02	4.79	2.70	1400	110
RX6703		−664.7 to 665.7	60.8	0.27	10.3	13.5	0.28	1.74	1.89	0.08	1.62	4.38	0.16	95.02	4.79	2.70	1400	110
RX6704		−670.7 to 671.7	61.8	0.30	10.9	13.6	0.14	1.19	0.94	0.08	1.33	5.07	0.16	95.51	3.19	3.81	1400	74
RX6706		−674.7 to 675.7	68.2	0.35	13.0	6.06	0.17	0.83	0.94	0.08	2.78	5.67	0.07	98.15	2.04	2.04	1800	76
RX7322	RD3554	−491.3 to 492.3	71.7	0.32	13.3	3.15	0.01	0.15	0.06	0.27	0.18	7.26	0.02	96.42	2.63	40.3	890	50
RX7323		−−513.8 to 514.8	68.5	0.32	11.9	5.85	0.21	0.27	0.10	0.11	0.15	6.04	0.02	93.47	3.61	40.3	4500	65
RX7331		−764.3 to 765.3	64.2	0.35	12.9	7.42	0.15	0.18	0.87	0.36	0.27	8.37	0.09	95.16	3.82	31.0	4500	35

Note: 'Total' column only refers to elements given in tables, which are used for rock classification diagrams in Fig. 4. All values given are in wt.% aside from Cu and U_3O_8. Italics indicates whole-rock assay data intervals of 5 m, whereas others are 1 m. Depth (mRL) is relative to sea level.

sulphides (chalcopyrite, pyrite, sphalerite, galena and molybdenite), rutile, REE- and U-minerals, as well as minor albite. In terms of major mineralogical changes, sericite replaces all igneous plagioclase, while the abundance of hematite and minor, disseminated Cu-Fe-sulphides increases compared to least-altered RDG. Primary mafic minerals are not preserved in sericite-hematite altered RDG. Accessory minerals are generally sparse; however metamict zircon is occasionally preserved. Hydrothermal rutile contains measurable concentrations of Nb and W, and is also morphologically distinct from the rutile forming symplectites with hematite. Samples of mineralised RDG contain a greater abundance of Cu-Fe-sulphides (chalcopyrite, minor chalcocite and bornite) and hematite, which predominates over sericite. Albite is still preserved at depth in both sericite-hematite altered and mineralised RDG.

4.2.1. Alkali feldspars in least-altered RDG

The majority of alkali feldspars observed in least-altered RDG display perthitic textures. Due to their complexity, textural characterisation of alkali feldspars requires a careful systematic approach. Categorisation of feldspar textures follows terminology outlined by Parsons et al. (2005), with compositional data obtained by EPMA. A total of four textural categories are preserved within the least-altered RDG: cryptoperthite; patch perthite; film perthite and highly porous albite and K-feldspar. Their features and compositions are summarised in Tables 3 and 4, respectively. Optical properties routinely used to discriminate between feldspar phases are not apparent using transmitted light microscopy alone, even in the least-altered samples. Thus, SEM was primarily used in feldspar characterisation.

Table 1c
Sample list and whole-rock assay data for mineralised RDG.

Sample	Drillhole	Depth (mRL)	Whole rock assay data															
			SiO_2	TiO_2	Al_2O_3	FeO	MnO	MgO	CaO	BaO	Na_2O	K_2O	P_2O_5	Total	LOI	K_2O: Na_2O	Cu (ppm)	U_3O_8 (ppm)
RX7307	RD3554	−261.3 to 262.3	65.9	0.20	10.4	7.46	0.06	0.51	0.50	0.40	0.12	4.60	0.01	90.16	3.53	38.3	36,800	20
RX7315		−341.3 to 342.3	59.7	0.25	10.3	14.4	0.27	0.20	0.17	0.27	0.11	3.25	0.14	89.06	3.58	29.5	25,800	235
RX7321		−392.9 to 393.9	41.5	0.18	7.4	28.3	0.87	0.28	0.15	0.22	0.08	2.34	0.23	81.55	8.18	29.3	16,900	495
RX7324		−520.4 to 521.4	66.5	0.28	11.9	5.71	0.13	0.33	0.15	0.09	0.16	6.08	0.01	91.34	2.63	38.0	28,500	175
RX7325		−524.1 to 525.1	64.6	0.28	12.2	4.57	0.01	0.18	0.06	0.33	0.16	5.36	0.01	87.76	2.43	33.5	45,000	100
RX7326		−527.9 to 528.9	61.4	0.30	12.3	3.86	0.01	0.18	0.04	0.09	0.13	5.66	0.01	83.98	3.52	43.5	83,700	80
RX7327		−535.4 to 536.4	67.0	0.30	11.2	5.67	0.01	0.17	0.04	0.29	0.16	5.24	0.02	90.10	5.30	32.8	33,800	185
RX7328		−561.6 to 562.6	35.3	0.13	4.7	45.4	0.01	0.05	0.03	0.11	0.05	1.92	0.12	87.82	1.92	38.4	45,400	600
RX7329		−585.9 to 586.9	64.8	0.28	11.7	9.94	0.01	0.13	0.04	0.31	0.23	6.40	0.07	93.91	1.75	27.8	13,800	225
RX6685	RD2316	−481.8 to 482.8	47.5	0.20	7.2	29.6	0.06	0.45	0.22	0.06	0.07	4.35	0.16	89.87	6.72	62.1	7300	155
RX6686		−489.8 to 490.8	64.6	0.32	10.5	11.7	0.06	0.48	0.28	0.10	0.12	7.20	0.14	95.50	2.13	60.0	3900	155
RX6687		−489.8 to 490.8	64.6	0.32	10.5	11.7	0.06	0.48	0.28	0.10	0.12	7.20	0.14	95.50	2.13	60.0	3900	155
RX6690		−545.8 to 546.8	49.4	0.25	8.4	23.5	0.25	1.79	1.39	0.08	0.09	4.35	0.18	89.68	5.46	48.3	11,500	490
RX6691		−546.8 to 547.8	39.6	0.15	5.1	34.6	0.22	1.56	1.76	0.03	0.05	1.99	0.28	85.34	8.73	39.8	26,800	950
RX6693		−576.8 to 577.8	44.9	0.20	6.2	29.9	0.18	1.41	1.79	0.40	0.07	2.83	0.37	88.25	6.77	40.4	15,000	650
RX6694		−599.7 to 600.7	48.3	0.18	5.6	28.4	0.23	1.18	1.53	0.03	0.07	2.61	0.34	88.47	7.31	37.3	5400	550

Note: 'Total' column only refers to elements given in tables, which are used for rock classification diagrams in Fig. 4. All values given are in wt.% aside from Cu and U_3O_8. Depth (mRL) is relative to sea level.

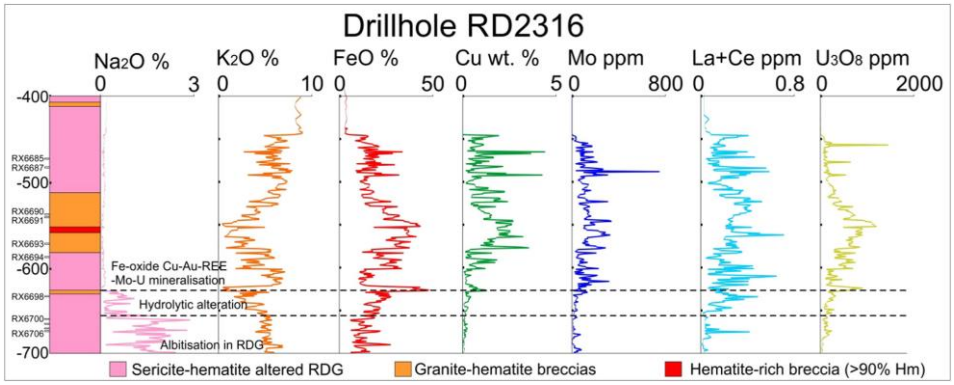

Fig. 3. Down-hole profile of drillhole RD2316 illustrating major elemental changes in whole-rock analyses. Note the transition in alteration and subsequent mineralisation styles in the RDG across an ~80 m section. There is a clear positive correlation between FeO, Cu, Mo, La + Ce and U_3O_8 in mineralised RDG.

Cryptoperthite, more frequently preserved in Area 1 than in Area 2, occurs as fields of fully coherent, sub-μm-sized Ab-rich lamellae with sub-μm periodicities within Or-rich feldspar (Fig. 6a). Depending on grain orientation, it may also form a braid texture. Measured bulk compositions of cryptoperthite vary from ~$Or_{68.3}Ab_{30.1}An_{1.6}$ to $Or_{48.3}Ab_{50.1}An_{1.6}$ (mean values given in Table 4), while individual analyses indicate that the interiors of cryptoperthite are more Ab-rich and Or-poor relative to the rims. In addition, it is apparent that this change in composition coincides with a loss in lamellar coherency at field boundaries. Micropores are extremely scarce.

Cryptoperthites have been partially overprinted by clusters of incoherent, Or-rich (~$Or_{85.1}$) and Ab-rich (~$Ab_{83.3}$) subgrains which are noticeably microporous near subgrain junctions, and may also be associated with sub-μm-sized hematite inclusions (Fig. 6b). Depending upon the viewing plane, this 'patch perthite' may appear as sets of intragranular anastomosing veinlets occurring along, or crosscutting Ab-rich lamellae within the cryptoperthite.

Film perthite is very scarce and typically only preserved towards the centres of some Or-rich grains of patch perthite. It is characterised by semi-coherent, <500 nm-thick Ab-rich lamellae with a sub-μm

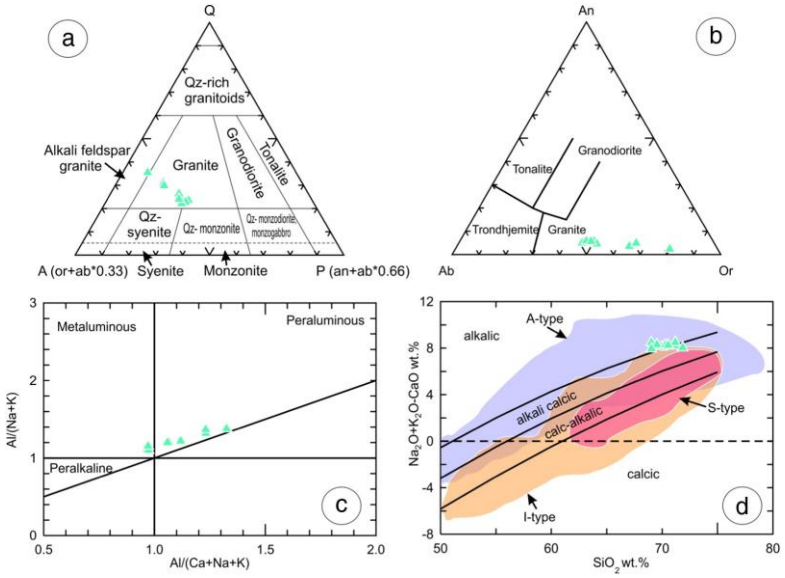

Fig. 4. Ternary and binary plots of whole-rock analytical data used for least-altered RDG classification at Olympic Dam. (a) QAP diagram (Streckeisen, 1976; LeMaitre et al., 1989) from CIPW normalised whole-rock data. The diagram is modified for the proportions of Ab in A and P which is based on the presence of normative albite within the alkali feldspars of the least-altered RDG. (b) CIPW normalised data plotted on a Ab-An-Or diagram after Barker (1979). See text for explanation. (c) Alumina saturation index diagram after Shand (1943), using ratios of molecular Al, Ca, K and Na. (d) Binary plot of the modified alkali-lime index, ($Na_2O + K_2O$-CaO)/SiO_2, and approximate fields for the alkalic, alkali calcic, calc-alkalic and calcic rock series. Granite field types are based on existing data from plutonic rocks in various terranes (see Frost et al., 2001 and references therein).

Table 2
Summary of mineralogy and geochemistry for the RDG.

Lithology	Drillholes	Texture	Mineralogy	Whole-rock geochemistry
Least-altered RDG (Area 1)	RD2492, RD2494, RD2495	Medium- to coarse-grained, granitic, equigranular-porphyritic	Alkali feldspar (40%), plagioclase (25%), quartz (20%), amphibole and biotite (10%), and accessories (5%) — zircon, apatite, magnetite, Fe-Ti-minerals (ilmenite, titanite), REE-U-minerals (synchysite, uraninite, uranothorite). Mafic minerals are partially altered. (Amphibole and biotite to chlorite, magnetite to hematite, ilmenite to rutile + hematite and titanite to rutile + quartz)	K_2O:Na_2O ~ 1–2, FeO < 4 wt.%, Cu < 50 ppm
Least-altered RDG (Area 2)	RD2280, RD2274	Medium- to coarse-grained, granitic, equigranular	Alkali feldspar (40%), plagioclase (25%), quartz (20%), amphibole and biotite (10%) and accessories (5%) — zircon, apatite, magnetite, Fe-Ti-minerals, REE-U-minerals (synchysite, uraninite, uranothorite). All mafic minerals are completely altered (see above).	K_2O:Na_2O ~ 1–3.5, FeO < 4 wt.%, Cu ~ <50–350 ppm
Sericite-hematite altered RDG	RD2280, RD2531, RD2511, RD2316, RD3554	Coarse-grained, highly-fractured,	K-feldspar (35%), sericite (25%), quartz (20%), chlorite (10%), variable amounts (up to 10%) of magnetite, hematite, rutile, carbonates (calcite, siderite, ankerite), disseminated sulphides (chalcopyrite, pyrite, sphalerite, galena, molybdenite), REE-U-minerals (synchysite, bastnäsite, uraninite, florencite). Trace amounts of albite.	Na_2O < 0.5 wt.%, FeO ~ 7 wt.%
Mineralised RDG (distal)	RD2316	Coarse-grained, brecciated	K-feldspar (25%), sericite (25%), quartz (25%), variable amounts (up to 25%) of magnetite, hematite, chlorite, rutile, carbonates (calcite, siderite, ankerite), sulphides (chalcopyrite, bornite, chalcocite, pyrite, sphalerite, galena, molybdenite), REE-U minerals (bastnäsite, uranothorite, brannerite, coffinite, florencite). Albite preserved at depth.	FeO > 10 wt.%, K_2O ~ 5.5 wt.%, Cu > 1 wt.%, (Na_2O ~ 1–2 wt.% at depth)
Mineralised RDG (proximal)	RD3554	Coarse-grained, brecciated	K-feldspar (25%), sericite (25%), quartz (25%), variable amounts (up to 25%) of magnetite, hematite, chlorite, rutile, carbonates (calcite, siderite, ankerite), sulphides (chalcopyrite, bornite, chalcocite, pyrite, sphalerite, galena, molybdenite), REE-U minerals (bastnäsite, uranothorite, brannerite, coffinite, florencite).	FeO > 10 wt.%, K_2O ~ 5.5 wt.%, Cu > 1 wt.%

periodicity (Fig. 6c). Measured bulk compositions of film perthite vary from $Or_{78}Ab_{21.4}An_{0.6}$ to $Or_{88.4}Ab_{11.3}An_{0.3}$, likely due to variability in lamellae size, and thus the initial composition of the Or-rich phase.

All feldspar microtextures have been extensively overprinted by highly porous, incoherent, near-end member albite and K-feldspar (Fig. 6d). As with the cryptoperthites, the overprinted feldspars are more abundant in RDG from Area 2, but are also quite widespread in Area 1. Initially coherent and semi-coherent lamellae of cryptoperthite and film perthite may be irregularly thickened, or feature trails of micropores. These highly porous feldspars have similar composition to the feldspars they replace; however some grains are almost entirely comprised of highly porous K-feldspar. The Ab-rich phase of patch perthite is typically overprinted by highly porous albite which may also contain sub-μm inclusions of sericite. This albite is compositionally similar to

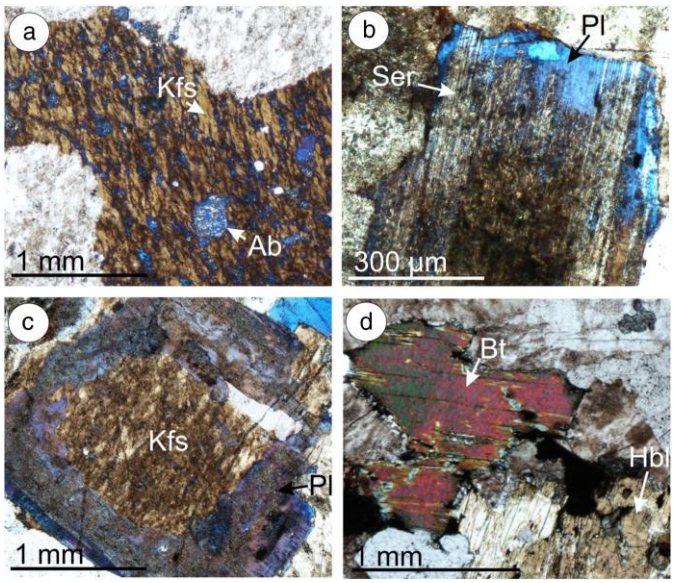

Fig. 5. Photomicrographs in transmitted light (crossed polars) showing primary minerals in the least-altered RDG. (a) Large perthitic alkali feldspar grain displaying various turbid areas related to recrystallisation. (b) Typical appearance of plagioclase; note the zonation and sericite alteration along polysynthetic twins. (c) Alkali feldspar grain mantled by plagioclase. (d) Cluster of variably altered hornblende and biotite. Abbreviations: Ab — albite, Bt — biotite, Hbl — hornblende, Kfs — K-feldspar, Pl — plagioclase, Ser — sericite.

Table 3
Summary of feldspar textures and bulk compositions in the RDG.

Microtexture	Phases	Description	Composition range (bulk)	Textural relationships	Figures
Plagioclase	Andesine–oligoclase	Large (>2 mm) phenocrysts, displaying typical calcic-sodic core to rim compositional zoning. Only preserved within least-altered RDG from Area 1.	~$An_{27–34}$	Phenocrysts are extremely altered and overprinted by replacive albite and highly porous K-feldspar.	8a
Plagioclase	Oligoclase	Forms individual grains and rims on pre-existing feldspars. Hosts inclusions of worm-like quartz, fluorite and alkali feldspar.	~$An_{12–20}$	Forms mantles around alkali feldspars (rapakivi), and discontinuous rims around andesine-oligoclase.	8a, b, d, 9a, 15
Cryptoperthite	Ab- and Or-rich feldspar	Fully coherent intergrowth of sub-μm sized Ab-rich lamellae with sub-μm periodicities in Or-rich feldspar. Micropores are scarce.	~$Or_{42-74}Ab_{25-55}An_{1–3}$	Preserved as regions within feldspar grains.	6a, d, 7a–d, 14
Patch perthite	Subgrains of Ab- and Or-rich feldspar	Incoherent clusters of Ab- and Or-rich subgrains, highly porous near subgrain boundaries, may be associated with sub-μm-sized hematite inclusions.	~$Ab_{84}An_{14}Or_2$ ~$Or_{85}Ab_{14}An_1$	Forms mosaics or veins, depending upon viewing plane, which crosscut cryptoperthite.	6a, b, d, 8a, 14
Film perthite	Ab- and Or-rich feldspar	Semi-coherent, <500 nm-thick Ab-rich lamellae with a sub-μm periodicity within Or-rich phase of patch perthite.	~$Or_{83}Ab_{16}An_1$	Only partially preserved towards the centre of the Or-rich phase of patch perthite.	6b, c
Replacive albite, highly porous albite	Albite ± sericite	Highly porous, incoherent, near-end member albite.	~$Ab_{97}An_1Or_2$	Crosscuts and partially replaces all pre-existing alkali and plagioclase feldspars.	6d, 8c, d, 9a, b, 10a, 15
Highly porous K-feldspar	K-feldspar ± Ba-rich K-feldspar	Highly porous, incoherent, near-end member K-feldspar. Variably red-stained.	~$Or_{98}Ab_2$	Crosscuts and partially replaces all pre-existing alkali and plagioclase feldspars.	6b–d, 9a–d, 10a, b, 17

albite directly replacing plagioclase grains (discussed below). In addition, both highly porous feldspars are intimately associated with sub-μm-sized inclusions of hematite.

Nanoscale characterisation of the cryptoperthite is shown in Fig. 7. Low-resolution TEM imaging shows typical cryptoperthite appearance with albite lamellae tens to hundreds of nm in width, generally parallel to one another but with variation in thickness and branching (Fig. 7a, b). High-resolution TEM imaging shows coherent lattice fringes between host orthoclase and exsolved albite, both down to the same [1 − 12] zone axis (Fig. 7c). The spinodal and slightly disordered character of the exsolution is seen on selected areas of electron diffraction (SAED) as distortion of main reflections, with streaks along $(hk0)^*$ directions (Fig. 7d). Based on several zero- and second-order SAEDs obtained from perthites, the host is orthoclase rather than microcline; the latter interpretation is concordant with the lack of typical tartan twinning. The composition of both host and lamellae was checked using EDS

Table 4
Mean electron probe microanalyses of alkali feldspars in the RDG.

	Cryptoperthite ($n = 61$)	Ab-rich phase of patch perthite ($n = 11$)	Or-rich phase of patch perthite ($n = 18$)	Film perthite ($n = 17$)	Highly porous albite ($n = 18$)	Highly porous K-feldspar ($n = 39$)	Ba-rich K-feldspar ($n = 21$)	Red-stained areas of K-feldspar ($n = 52$)
Sample wt.%								
SiO_2	65.89 (0.28)	64.31 (0.61)	64.21 (0.65)	65.41 (0.27)	68.86 (1.72)	65.21 (0.51)	55.82 (1.57)	63.29 (1.06)
Al_2O_3	18.71 (0.12)	21.69 (0.32)	18.39 (0.39)	18.20 (0.17)	20.04 (0.36)	18.17 (0.47)	20.51 (0.52)	17.71 (0.37)
FeO	0.16 (0.02)	0.22 (0.04)	0.12 (0.14)	0.12 (0.02)	0.12 (0.91)	0.19 (0.25)	0.06 (0.12)	1.42 (1.33)
CaO	0.38 (0.07)	3.16 (0.37)	0.08 (0.05)	0.07 (0.09)	0.24 (0.1)	<mdl	0.01 (0.03)	0.04 (0.11)
SrO	0.33 (0.01)	0.25 (0.02)	0.35 (0.10)	0.35 (0.02)	<mdl	<mdl	0.25 (0.02)	<mdl
BaO	0.31 (0.07)	0.03 (0.01)	1.03 (0.30)	0.25 (0.30)	<mdl	0.27 (0.05)	10.81 (1.73)	0.24 (0.15)
Na_2O	5.18 (0.44)	10.19 (0.25)	1.67 (0.47)	1.85 (0.44)	11.85 (0.49)	0.23 (0.11)	0.21 (0.12)	0.23 (0.06)
K_2O	9.64 (0.30)	0.31 (0.08)	14.57 (1.05)	14.79 (0.69)	0.27 (0.08)	16.12 (0.95)	12.09 (0.63)	16.71 (0.32)
Total	100.69 (0.30)	100.11 (0.49)	100.45 (0.70)	101.12 (0.16)	101.26 (1.22)	100.11 (0.73)	99.59 (0.51)	99.89 (0.98)
a.p.f.u.								
Ca	0.02	0.15	0.00	0.00	0.02	0.00	0.00	0.00
Sr	0.01	0.01	0.01	0.01	0.00	0.00	0.01	0.00
Ba	0.01	0.00	0.02	0.00	0.00	0.00	0.21	0.00
Na	0.45	0.87	0.15	0.16	0.98	0.02	0.02	0.02
K	0.56	0.02	0.86	0.86	0.01	1.01	0.77	1.00
Total	1.06	1.05	1.04	1.05	1.02	1.03	1.00	1.02
Al	1.00	1.13	1.01	0.98	1.02	0.99	1.21	0.98
Si	2.98	2.84	2.98	2.99	2.97	3.00	2.79	2.97
Fe	0.01	0.01	0.00	0.01	0.01	0.01	0.00	0.06
mol.%								
Ab %	43.51 (3.54)	83.29 (1.81)	14.51 (0.94)	15.61 (3.70)	97.41 (0.83)	2.17 (0.45)	2.03 (1.26)	2.02 (0.48)
An %	1.74 (0.31)	14.31 (1.68)	0.39 (0.20)	0.35 (0.40)	1.10 (0.55)	0	0.06 (0.18)	0.18 (0.54)
Or %	54.89 (3.67)	1.71 (0.42)	85.09 (1.14)	82.89 (3.89)	1.15(0.43)	97.79 (0.54)	97.39 (1.45)	96.79 (0.65)
Feldspar geothermometry (Fuhrman and Lindsley, 1988)								
Minimum T (°C)	765	430	430	<430	*	*	*	*

Note: figures in parentheses represent standard deviations. <mdl indicate values below the minimum detection limits. Geothermometry uncertainties of ±40 °C.
Analyses represent transects of cryptoperthite grains from interior to rim. For maximums and minimums see Appendices.
* No reliable estimates calculated.

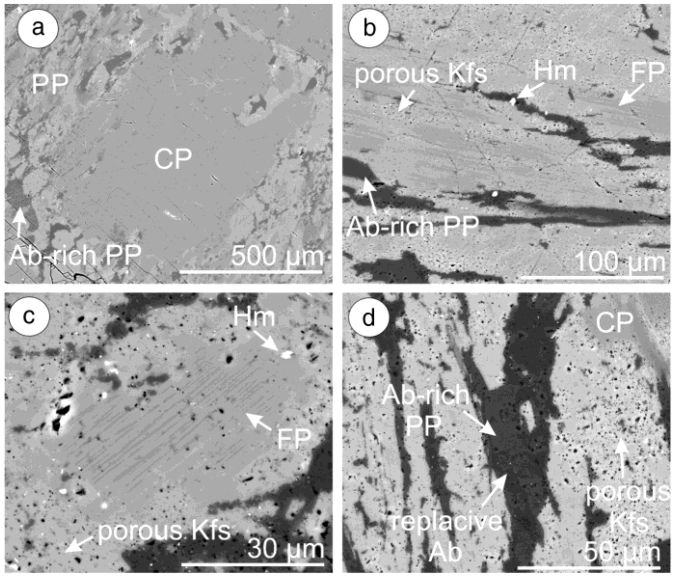

Fig. 6. Back scatter electron images detailing important features of alkali feldspar microtextures in least-altered RDG. (a) Large fields of cryptoperthite (CP) cross-cut by patch perthite (PP). Note the anastomosing nature of the patch perthite. (b) Area of alkali feldspar phenocryst displaying exsolution lamellae of film perthite (FP) crosscut by highly porous albite and K-feldspar. Note the presence of hematite (Hm). (c) High-magnification image of film perthite surrounded by porous K-feldspar. (d) Albite-rich subgrain of patch perthite overprinted by replacive albite (Ab).

spectra with a spot size of ~5 nm (Fig. 7e, f). Although the sample is sensitive to beam damage, the data clearly shows the lack of Na in the host potassium feldspar.

4.2.2. Plagioclase in least-altered RDG

Two distinct compositions of igneous plagioclase are identified in the RDG: andesine-oligoclase (~$An_{27–34}$); and oligoclase (~$An_{12–20}$). Similar to the alkali feldspars, plagioclase commonly exhibits complex overprints.

In Area 1, andesine-oligoclase (~$An_{27–34}$) forms the cores of plagioclase grains surrounded by oligoclase ($An_{12–20}$) mantles (Fig. 8a). These andesine-oligoclase cores have been extensively altered and are only partially preserved in Area 1. In both areas, oligoclase with a lower An component (~$An_{12–20}$) occurs as rapakivi mantles and as individual grains without andesine cores. Irrespective of textural type, this oligoclase is characterised by high K_2O content (~0.73 wt.%, Table 5) and often contains worm-like quartz, fluorite (<20 µm-sized) and irregular alkali feldspar (cryptoperthite and patch perthite) inclusions (Fig. 8b).

Alteration of plagioclase is predominantly in the form of albitisation, where the replacive albite is typically concentrated within grain cores (*e.g.*, Figs. 5b and 8a). This replacement can be seen to extend from core to margin along polysynthetic twins (*e.g.*, Fig. 5b), and eventually form completely albitised pseudomorphs. In detail, replacive albite is extremely porous and forms fine-grained intergrowths with sericite ± hematite (Fig. 8c). Due to the presence of sub-µm-scale sericite, K_2O (from *in-situ* EPMA spot analysis) may be overestimated. Inclusions of dolomite and calcite may also occur within this albite. In addition to pervasive albitisation, a thin layer of homogenous albite commonly forms rims around oligoclase, which is in direct contact with recrystallised alkali feldspar. This rim is devoid of micropores and is superposed by replacive albite (Fig. 8d).

Importantly, Ba-bearing K-feldspar is observed within RDG from both areas, even in samples preserving the mafic minerals. Such K-feldspar occurs along twin planes and compositional zones of albitised plagioclase (Fig. 9a, b) to which it is restricted. This K-feldspar varies widely with respect to Ba content, ranging from <1 wt.% BaO up to as much as ~15 wt.% BaO. In detail, this K-feldspar is very fine-grained (<10 µm) and highly porous (Fig. 9c, d).

4.2.3. Feldspars in sericite-hematite altered and mineralised RDG

As documented above, sericite-hematite altered RDG occurs irregularly throughout all drillholes along the transect (Fig. 1), however the intensity of alteration increases with proximity to the ODBC. The only feldspars preserved in sericite-hematite altered and/or mineralised granite are replacive albite and porous K-feldspar, described above. There are, however, significant differences in the abundance of feldspars between sericite-hematite altered and mineralised RDG. This can be observed in the ~300 m-thick profile from drillhole RD2316 (Fig. 3). The deeper part retains significant replacive albite and porous K-feldspar. Importantly, this K-feldspar displays heterogeneous zones of intense red-staining (Fig. 10a), averaging ~1.5 wt.% FeO (Table 4). In detail, dusty sub-µm sized Fe-oxide inclusions (hematite) are observed, likely contributing to the characteristic red-staining (Fig. 10b). The abundance of these red-stained zones increases upwards, over ~100 m, as replacive albite is progressively destroyed by sericite and Cu-Au mineralisation starts to predominate.

The stability of sericite over albite at this stage is not only evident from whole-rock analyses (Table 1a, 1b, 1c), but also from textural observations of mm-sized grains of sericite resembling plagioclase pseudomorphs (Fig. 10c). Importantly, some of these pseudomorphs are partially replaced by hematite ± chlorite. In addition, some rapakivi textures survive; however they are now defined by porous, red-stained, K-feldspar cores rimmed by fine-grained sericite (Fig. 10d). Granophyric textures between quartz and K-feldspar (partially replaced by

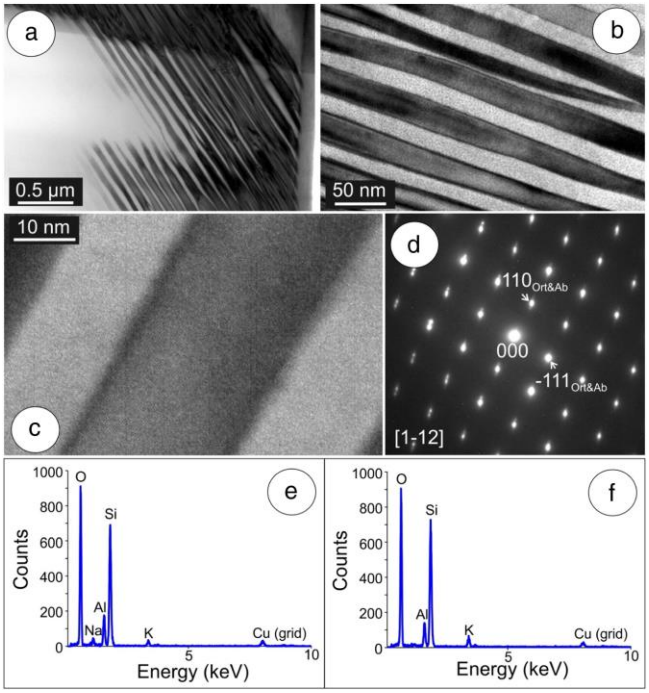

Fig. 7. Transmission electron microscope images of cryptoperthite from least-altered RDG. (a, b) Low-resolution images of albite lamellae (dark) within orthoclase host (light). Note the varying thickness of lamellae. (c) High-resolution image displaying coherent lattice fringes between both albite and orthoclase along a zone axis of cryptoperthite. (d) Selected Area of Electron Diffraction (SAED) along zone axis from (c). (e, f) TEM-EDX spectra obtained from Ab lamellae and Or host in cryptoperthite, respectively. A spot size of 5 nm was used.

sericite) are also occasionally observed along the margin of the ODBC (*e.g.*, drillhole RD2511). Such textures are characteristic of sericite-hematite altered RDG from drillhole RD2316 and from drillholes along the transect in Area 2 (RD2274, RD2280, RD2511, RD2531 and RD3554).

Mineralised RDG within drillholes RD2316 and RD3554 contains variable amounts of chalcopyrite, bornite, chalcocite, sphalerite, galena, native gold and molybdenite, but is devoid of replacive albite, whereas red-stained K-feldspar becomes more abundant. A spatial association between the porous, red-stained K-feldspar and sulphides (*e.g.*, sphalerite, chalcopyrite and galena) is notable throughout all RDG sample suites. Remarkably, some feldspar grains are pervasively replaced by intimate intergrowths of sericite + synchysite + bastnäsite + parisite (not previously recognised at Olympic Dam) + molybdenite (Fig. 11). Discrete uranium minerals (uraninite, coffinite and brannerite) are also present within reaction zones at the margins of sulphide disseminations. In addition, W- and Nb-zoned rutile is also abundant.

5. Geothermobarometric estimates for least-altered RDG

Compositional variation among amphiboles, amphibole-plagioclase pairs, magnetite-ilmenite pairs and feldspars can be used to place constraints on the T-P-fO_2 conditions of crystallisation from the magmatic to early hydrothermal stage. This was achieved by analysing distinct zones and mineral associations within feldspar phenocrysts from the RDG, principally from Area 1. Such phenocrysts (*e.g.*, Fig. 12) were found to contain feldspars representative of all stages of evolution from magmatic to hydrothermal (see Discussion), and also to host abundant magmatic amphibole (edenite), biotite and Fe-(Ti)-oxides. In addition, the phenocrysts contain discrete areas of alteration also containing sulphides (galena, sphalerite, and pyrite as inclusions in apatite), and coarse REE-minerals such as synchysite.

5.1. Amphibole chemistry, geobarometry and geothermometry

A common method to estimate pressures for granitic rocks is Al-in-hornblende geobarometry (Hammarstrom and Zen, 1986; Hollister et al., 1987; Schmidt, 1992). The geobarometer has been experimentally calibrated, and is suitable for an assemblage of quartz + alkali feldspar + + plagioclase + hornblende + biotite + Fe-Ti-oxide + titanite + melt + fluid. It is assumed that following solidification and cooling, the equilibration of hornblende with the above assemblage would eventually cease, and thus the Al content would reflect the final crystallisation depth of the magma. The Al content in hornblende is also affected by temperature, addressed by Blundy and Holland (1990) who propose an amphibole-plagioclase thermometer. It is recommended to apply this to rocks equilibrated between 500 and 1000 °C, plagioclase with $<An_{92}$ and amphiboles containing <7.8 a.p.f.u. However, the geothermometer requires pressure information, thus using the Al-in-hornblende method of Schmidt (1992) and correcting for the effects of temperature and fO_2 (Anderson and Smith, 1995) was necessary.

Compositional data for amphibole from three locations contained within a phenocryst from sample RX7865 are compared with amphibole in the groundmass from sample RX7860 (Table 6). The amphibole shows bright and dark areas on BSE images, corresponding to differences in Fe/(Fe + Mg). The brighter areas are compositionally similar to amphibole in the rock groundmass, and on the rapakivi margin of the phenocryst. This suggests that the darker areas represent retrogression followed by chlorite alteration (also observed to replace coexisting

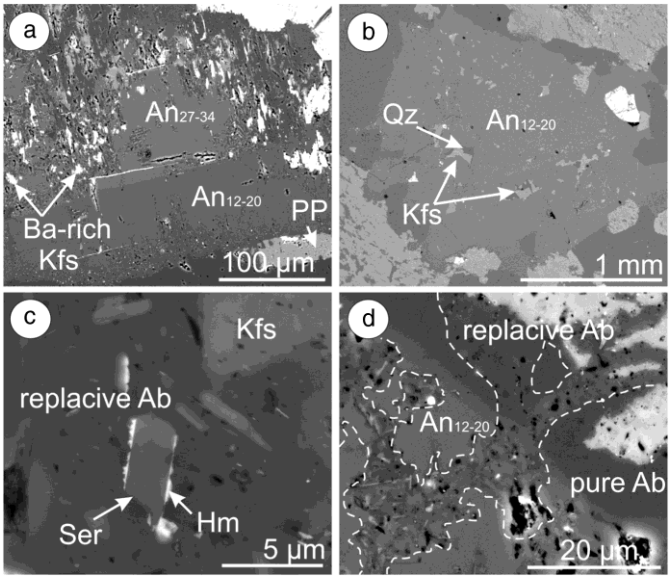

Fig. 8. Back scatter electron images outlining features of plagioclase and associated alteration textures. (a) Typical andesine–oligoclase core sharing a discontinuous boundary with low-An oligoclase. Note the Ba-rich K-feldspar and patch perthite (PP). (b) Large low-An oligoclase grain with random, irregularly-shaped perthitic K-feldspar and quartz (Qz) inclusions. (c) High-magnification image of the replacive albite ± sericite intergrowth texture. Note the rim of hematite (Hm) around sericite (Ser). (d) BSE image showing the homogeneous albite rim on low-An oligoclase superposed by the replacive albite ± sericite texture.

biotite). The compositions of biotite co-existing with amphibole in the same samples (Table 6) are broadly comparable with one another. However, biotite replacing amphibole in sample RX7860 is slightly Mg-richer, consistent with the loss of Fe during overprinting described for amphibole above.

Table 5
Mean electron probe microanalyses of plagioclase feldspar in the RDG.

	Andesine-oligoclase cores	Rapakivi oligoclase	Replacive albite
	($n = 25$)	($n = 47$)	($n = 63$)
wt.%			
SiO_2	59.71 (0.48)	63.59 (0.51)	68.56 (1.11)
Al_2O_3	24.48 (0.28)	22.10 (0.27)	19.84 (0.23)
FeO	0.41 (0.11)	0.25 (0.04)	0.11 (1.37)
CaO	6.61 (0.41)	3.86 (0.34)	0.19 (0.15)
SrO	0.22 (0.01)	0.24 (0.02)	<mdl
BaO	0.05 (0.03)	0.04 (0.03)	<mdl
Na_2O	7.89 (0.21)	9.42 (0.43)	11.88 (0.76)
K_2O	0.44 (0.21)	0.73 (0.36)	0.43 (0.29)
TOTAL	99.92 (0.21)	100.30 (0.23)	101.26 (1.58)
a.p.f.u.			
Ca	0.32	0.18	0.01
Sr	0.01	0.00	0.00
Ba	0.00	0.00	0.00
Na	0.69	0.81	1.00
K	0.03	0.04	0.02
TOTAL	1.04	1.04	1.03
Al	1.30	1.16	1.02
Si	2.68	2.82	2.98
Fe	0.02	0.01	0.00
mol.%			
Ab %	66.21 (1.58)	77.71 (3.21)	96.80 (0.90)
An %	30.60 (1.91)	17.60 (1.59)	0.86 (0.33)
Or %	2.52 (1.20)	4.04 (1.99)	2.31(0.78)

Note: figures in parentheses represent standard deviations.

Application of the Al-in-hornblende geobarometer based on total Al content (Schmidt, 1992) gives pressure estimates between 2.08 and 2.85 kbar. However, these estimates are not corrected for temperature. Applying the modified geobarometer of Anderson and Smith (1995), using temperatures derived from the amphibole-plagioclase geothermometer of Blundy and Holland (1990; Table 7), a fit is obtained at pressures of ~2.2 kbar (corresponding to a final crystallisation depth of 6–8 km) and minimum crystallisation temperatures of 710 and 731 °C for the assemblages within the rapakivi mantle and groundmass, respectively. Overprinted assemblages in the phenocryst core and rapakivi mantle give temperature ranges of 703 to 657 °C, and 710 to 700 °C, respectively, at the same pressure; the lower estimate in each case being for the darker amphibole. Overprinting during uplift is unlikely since, on the basis of the measured compositions, this would infer an unrealistic temperature increase. Instead, a fit between temperature decrease at constant pressure (~2.2 kbar) is reasonable. Creaser (1996) also applied Al-in-hornblende geobarometry to a quartz-monzodiorite from the same pluton as the RDG (following Schmidt, 1992) using the average composition of hornblende. A pressure estimate of 200 MPa (2 kbar) was obtained, corresponding to a final crystallisation at a depth of approximately 6–8 km.

5.2. Fe-Ti-mineral chemistry, geothermometry and fO_2 estimates

The association of Fe-(Ti)-minerals is variable throughout the least-altered RDG samples, from magnetite to magnetite-ilmenite-titanite. All these associations can be present in samples where amphibole is preserved (*e.g.*, sample RX7860). In samples where no mafic silicates survive, ilmenite commonly breaks down to rutile + hematite, while magnetite is replaced by hematite. Magnetite displays skeletal exsolution of other spinels that vary from extremely dense to scattered (whether coexisting with ilmenite or not). Moreover, trellis exsolution of ilmenite in magnetite is observed, particularly in areas where

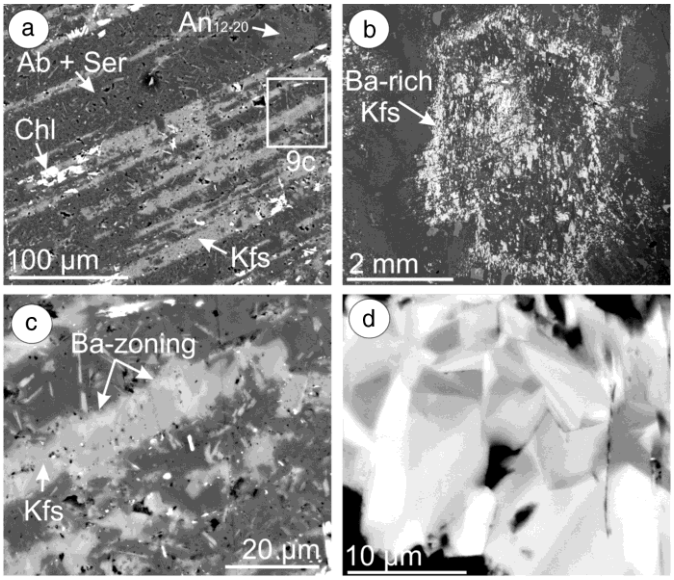

Fig. 9. Back scatter electron images of K-feldspar textures associated with altered plagioclase. (a) K-feldspar forming along twins of albitized low-An oligoclase. Note the presence of chlorite. (b) Large pseudomorph of albitized oligoclase rimmed and dominated by Ba-rich K-feldspar. (c) High-magnification image of (a), revealing Ba-zoning and porosity of the K-feldspar. (d) High-magnification image of complex Ba-zonation in fine-grained, Ba-rich K-feldspar found within a large albitised andesine core. BaO concentration varies from 5 to 14 wt.% in dark and bright areas, respectively. Abbreviations: Ab — albite, Chl — chlorite, Kfs — K-feldspar, Olg — oligoclase, Ser — sericite.

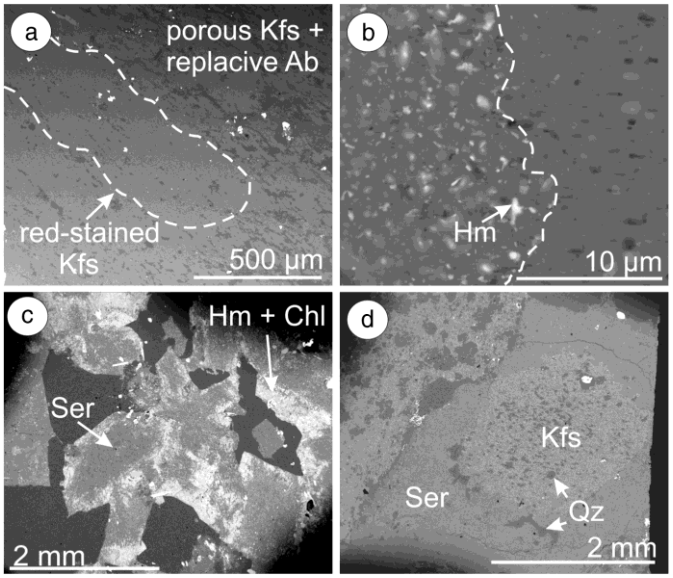

Fig. 10. Back scatter electron images highlighting important features of feldspars in sericite-hematite altered and mineralised RDG. (a) Typical perthitic K-feldspar (Kfs) observed in sericite-hematite altered RDG at depth or to the peripheries of the ODBC. Note the destruction of perthitic texture by red-stained K-feldspar. (b) High-magnification image illustrating the presence of sub-µm-sized hematite (Hm) corresponding to the red-stained areas of K-feldspar. (c) Large sericite pseudomorph grains being replaced by fine-grained hematite ± chlorite. (d) Altered rapakivi texture. Plagioclase mantle has been completely replaced by sericite, whereas the core, although similar in appearance to patch perthite, is comprised of porous K-feldspar with quartz. (For interpretation of the references to colour in this figure legend, the reader is referred to the web version of this article.)

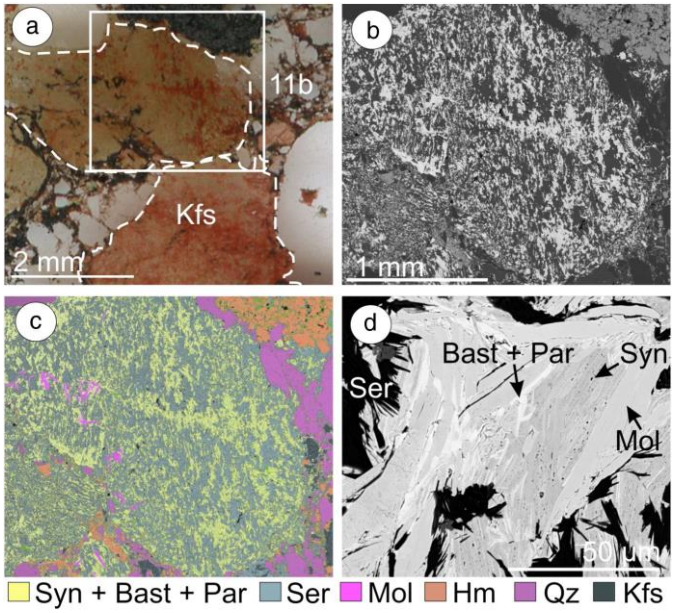

Fig. 11. Back scatter electron and scanned images of REE-mineral + molybdenite association overprinting K-feldspar in mineralised RDG within drillhole RD2316. (a) Scanned area of polished thin section from drillhole RD2316, highlighting the preserved shape of perthitic K-feldspar grains. (b) Low-magnification BSE image of area in (a). (c) False colour BSE map of the image in (b), showing the various minerals within the texture. (d) BSE image, and highlighting rhythmic interlayering of fine-grained molybdenite + synchysite + bastnäsite + sericite overprint. Abbreviations: Bast — bastnäsite, Hm — hematite, Kfs — K-feldspar, Mol — molybdenite, Qz — quartz, Ser — sericite, Syn — synchysite. (For interpretation of the references to colour in this figure legend, the reader is referred to the web version of this article.)

sulphides occur, such as on the rapakivi mantle of the phenocryst in Fig. 12. The TiO_2 content of magnetite (Table 8) varies from 0.34 (associated with hematite) to 3.17 wt.% (dense exsolution of spinels). Ilmenite contains ~10 wt.% MnO along with measurable Nb_2O_5 (thousands of ppm). The Nb content increases when associated with titanite. Both magnetite and ilmenite contain measurable V_2O_5, and magnetite with trellis exsolution or from the groundmass also contains ZnO.

Table 8 also shows estimates of re-equilibration temperatures from pairs of coexisting magnetite-ilmenite in the phenocryst and in sample RX7860, following routines developed by Lepage (2003). Temperature-fO_2 estimates based on the calibrations of Andersen and Lindsley (1985), that acknowledge the effect of minor elements such as Mn, Mg and Cr, are in the range 567–624 °C and −20.6 to −18.5 logfO_2. The higher temperature range (611 to 624 °C), consistent with amphibole-plagioclase geothermometry (654 °C from areas where amphibole has been overprinted), is from magnetite-ilmenite pairs in sample RX7860 in which the magnetite contains dense exsolutions. Such a temperature is close to that obtained from magnetite-ilmenite pairs in the andesine-oligoclase core of the phenocryst (609 °C). The lowest temperature estimates are from magnetite-ilmenite pairs in the same core (567 °C) and from the rapakivi mantle (577 °C), in both cases associated with amphibole. The fO_2 estimate is consistent with the stability field of magnetite at temperatures of 550–650 °C. The discrepancy between the lowest temperatures from magnetite-ilmenite pairs (567–577 °C, taken to reflect solid-state Fe-Ti re-equilibration) and magmatic temperatures derived from amphibole-plagioclase geothermometry can be explained by the much faster compositional re-equilibration in Fe-Ti-oxide system (*e.g.*, presence of trellis exsolution of ilmenite) down-temperature after crystallisation of the amphibole-plagioclase assemblage.

5.3. Feldspar geothermometry

Temperature estimates were obtained using SOLVCALC software following the ternary feldspar model of Fuhrman and Lindsley (1988) based on phase equilibria for disordered feldspars. Minimum temperature estimates for crystal growth can be obtained from ternary solvus isotherms. Using the average An composition of cryptoperthite (0.174 mol.%; Table 4), along with a reasonable pressure of 2.2 kbar (see above), a minimum temperature estimate for crystal growth of 765 °C was obtained. Following crystallisation, subsequent exsolution, ordering and coarsening likely occurred *via* similar mechanisms outlined by Brown and Parsons (1984) whereby processes such as spinodal decomposition and diffusion occurred around 700 °C to form cryptoperthite.

Exsolution likely continued down temperature until fluid-feldspar interaction resulted in formation of patch perthite. Application of the Fuhrman and Lindsley (1988) feldspar geothermometer using the average compositions of Ab- and Or-rich phases within patch perthite from Table 4 yields a temperature of 430 °C for formation at 2.2 kbar. A secondary stage of coherent exsolution took place following patch perthite formation, leading to development of film perthite within the Or-rich phase of the patch perthite, at some temperature range below 430 °C.

6. Discussion

Plagioclase and alkali feldspar textures and chemistry both define a transition from magmatic to hydrothermal processes within the RDG. The following sections and Fig. 13 summarise and discuss each stage within this evolutionary sequence.

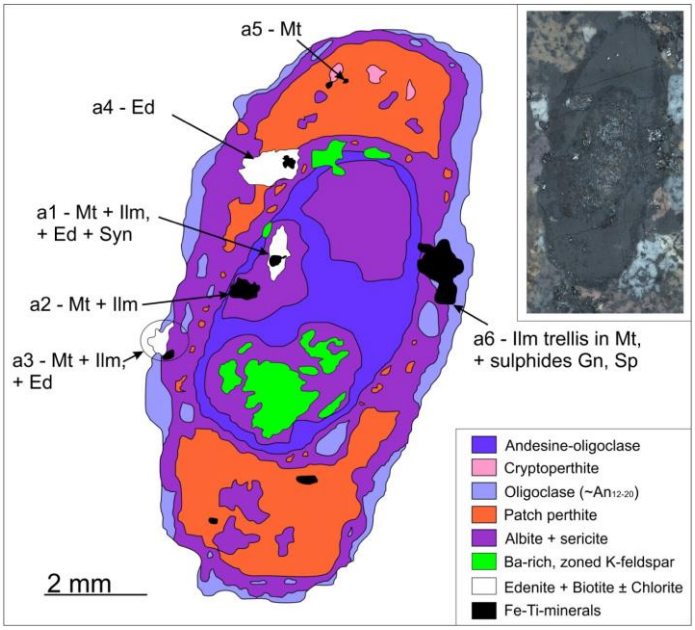

Fig. 12. Inset: reflected light image of a large feldspar phenocryst from least-altered RDG in Area 1. Schematic of the large feldspar phenocryst showing all stages within feldspar evolution. Highlighted areas indicate mafic and Fe-Ti-mineral locations used for geobarometry and geothermometry. Abbreviations: Ed — edenite, Gn — galena, Ilm — ilmenite, Mt — magnetite, Sp — sphalerite, Syn — synchysite.

6.1. Plagioclase crystallisation and significance of rapakivi texture

The timing of plagioclase crystallisation relative to other feldspars is critical to understand the magmatic evolution of the RDG. Compositions and textural observations indicate the presence of at least two generations of igneous plagioclase in the RDG. The first generation is defined by the andesine-oligoclase cores (~$An_{27–34}$), which show calcic-sodic core to rim compositional zoning. The low-An oligoclase is interpreted as a second generation based on the fact that it forms rapakivi mantles and discontinuous rims around andesine-oligoclase cores. Commonalities in textural features between all low-An oligoclase (*e.g.*, inclusions of alkali feldspar, fluorite and quartz), suggest that they are contemporaneous. Moreover, this low-An plagioclase shows evidence of replacing pre-existing alkali feldspar. Such an interpretation is based on the continuity of lamellae within the perthitic alkali feldspar inclusions.

Previous authors (*e.g.*, Plümper and Putnis, 2009) have attributed the replacement of microcline by oligoclase in granites to a late-stage alkali ion exchange process (Orville, 1963), in which Na^+ and K^+ preferentially partition to feldspars and a post-magmatic fluid, respectively. This interpretation was based on the marked microporosity in the oligoclase relative to microcline, which is consistent with fluid-feldspar interaction. However, in the RDG, low-An oligoclase is relatively porosity-free, and is also implied to have crystallised prior to fluid-rock interaction. This requires a physical and/or chemical change in melt conditions which would alter the stability of feldspars to the point where plagioclase would nucleate on K-feldspar, and vice versa. Decreases in pressure and/or temperature, or an increase in Ca and mafic components in the melt, are the preferred catalysts (*e.g.*, Müller et al., 2008). Feldspar resorption textures in the RDG, interpreted to have occurred prior to deuteric coarsening, are supportive of late-stage magma mixing/contamination and/or ascent (*e.g.*, Emslie, 1991; Wark and Stimac, 1992; Dempster et al., 1994; Rämö and Haapala, 1995). Such processes would increase the degree of crustal melting and can also initiate magma convection, explaining the partial (rapakivi mantles) and complete resorption of some alkali feldspars observed in the RDG. The coexistence of mantled and non-mantled alkali feldspars along with the heterogeneity in rapakivi mantle morphology (*e.g.*, tabular, ovoid) may be explained by the relative timing of crystallisation among other factors. Alkali feldspars which have ovoid morphologies or have undergone complete resorption would likely have crystallised early in the magma chamber (*e.g.*, Ryan, 1991) or could be evidence for incomplete mingling between magmas (Hibbard, 1981). Crystal migration has been proposed as an alternative explanation for the presence of mantled feldspars in the past (*e.g.*, Słaby and Goetze, 2004; Słaby et al., 2011). In this case, feldspar phenocryst chemistry would reflect the different magma conditions under which each feldspar mantle formed, making it difficult to relate this to the surrounding groundmass. Regardless, feldspar textures and geochemistry, in conjunction with the presence of microgranular mafic enclaves, two generations of igneous magnetite (Ti-rich and Ti-poor) and magmatic apatite textures (see Krneta et al., 2016), point towards late-stage magma mixing/contamination in the RDG. In addition, this is supported by geobarometric estimates along with amphibole-plagioclase geothermometry (Tables 6 and 7) which indicate that formation of the rapakivi mantle occurred at the same depth *via* a change in temperature rather than through magma ascent.

The presence of fluorite inclusions within low-An oligoclase has significant implications. Firstly, this suggests that the melt was at least supersaturated with respect to F at the time of rapakivi formation. Fluorine has been demonstrated to greatly increase the alkali ion interdiffusion rates in alkali feldspars (Snow and Kidman, 1991), and has also been reported from other rapakivi granites (Troeng, 1982; Wilson and

Table 6
EPMA compositional data for amphibole and biotite in least-altered RDG and Al-in-hornblende geobarometry.

	Amphibole: edenite							Biotite		
	RX7865					RX7860		RX7865	RX7860 (groundmass)	
	Phenocryst							Phenocryst	Magmatic	Hydrothermal
	a3	a1 'bright'	a1 'dark'	a4 'bright'	a4 'dark'	a4		a4	a5	a4
	n = 4	n = 4	n = 4	n = 4	n = 4	n = 12		n = 4	n = 19	n = 15
SiO_2	42.94	44.06	45.29	43.29	44.04	42.87	SiO_2	36.73	36.70	37.06
TiO_2	1.13	1.18	0.77	1.42	1.37	0.94	TiO_2	2.14	2.56	1.77
Al_2O_3	6.48	6.17	5.92	6.68	6.40	6.60	Al_2O_3	11.32	11.35	10.84
FeO	20.64	19.44	15.29	18.87	17.50	21.19	FeO	20.84	20.34	20.03
MnO	0.45	0.48	0.46	0.43	0.43	0.49	MnO	0.16	0.26	0.16
MgO	9.29	10.18	13.30	10.48	11.50	9.30	MgO	12.74	12.81	13.43
CaO	10.88	11.13	11.51	10.90	11.12	10.97	CaO	0.02	0.01	0.03
Na_2O	2.19	2.04	2.06	2.37	2.23	2.19	Na_2O	0.18	0.26	0.17
K_2O	1.10	1.04	1.01	1.12	1.08	1.18	K_2O	9.42	9.65	9.50
P_2O_5	0.01	0.01	0.01	0.01	0.01	0.01	P_2O_5	0.01	0.01	0.02
Cl	0.20	0.17	0.14	0.23	0.18	0.23	Cl	0.29	0.27	0.29
F	1.40	1.42	1.93	1.57	1.78	1.53	F	2.50	2.89	2.66
Total	96.72	97.32	97.69	97.37	97.64	97.51	Total	93.84	94.23	93.31
Amphibole: formulae based on: $Ca_2(Mg,Fe^{2+},Fe^{3+},Mn,Al^{vi})_5(Si,Al^{iv})_8O_{22}(OH,F,Cl)_2$							Biotite: formulae based on $K(Mg,Fe,Mn)_3AlSi_3O_{10}(OH,F,Cl)_2$			
Si	6.811	6.884	6.937	6.775	6.828	6.779	Si	2.93	2.92	2.97
Al (iv)	1.189	1.116	1.063	1.225	1.172	1.221	Al	1.07	1.06	1.02
Total (T)	8.000	8.000	8.000	8.000	8.000	8.000	Total (T)	4.00	3.98	3.99
Al (vi)	0.023	0.020	0.006	0.007	0.000	0.010	Ti	0.13	0.16	0.11
Ti	0.135	0.139	0.089	0.167	0.160	0.112	Mn	0.01	0.02	0.01
Fe (iii)	0.274	0.254	0.196	0.247	0.227	0.281	Mg	1.52	1.52	1.60
Fe (ii)	2.737	2.539	1.958	2.469	2.268	2.802	Fe	1.39	1.35	1.34
Mn	0.060	0.063	0.059	0.057	0.056	0.066	Total (M)	4.13	4.13	4.09
Mg	2.197	2.371	3.034	2.443	2.658	2.190	Na	0.03	0.04	0.03
Total (C)	5.426	5.387	5.342	5.391	5.369	5.460	K	0.96	0.98	0.97
Ca	1.849	1.864	1.889	1.828	1.847	1.858	Ca	0.00	0.00	0.00
Na	0.674	0.619	0.612	0.718	0.671	0.673	Total (I)	0.99	1.02	1.00
K	0.222	0.207	0.198	0.223	0.213	0.239	F	0.63	0.73	0.67
Total (A + B)	2.745	2.689	2.699	2.769	2.730	2.770	Cl	0.04	0.04	0.04
F	0.704	0.703	0.936	0.778	0.871	0.764	OH	1.33	1.24	1.29
Cl	0.055	0.045	0.035	0.061	0.048	0.061	Total (A)	2.000	2.000	2.000
OH*	1.241	1.252	1.028	1.161	1.080	1.175	Mg/(Fe + Mg + Mn)	0.520	0.526	0.542
Total (W)	2.000	2.000	2.000	2.000	2.000	2.000				
Fe/(Fe + Mg + Mn)	0.56	0.52	0.40	0.51	0.47	0.57				
Al-in-hornblende geobarometry (kbar)										
	1.67	1.35	1.06	1.75	1.49	1.74	Johnson and Rutherford (1989)			
	2.18	1.79	1.46	2.28	1.97	2.27	Hammarstrom and Zen (1986)			
	2.76	2.40	2.08	2.85	2.56	2.84	Schmidt (1992)			
	1.84	1.52	1.23	1.93	1.66	1.92	Anderson and Smith (1995) @ 750 °C			
	2.11	1.77	1.46	2.20	1.92	2.19	Mean of all estimates			

Note: compositions for amphibole are based on 24 oxygens. Compositions for biotite are based on 11 oxygens.

Åkerblom, 1982). Moreover, experimental work (Manning, 1981) indicates that interaction between F- and H_2O-saturated granitic melts can reduce the minimum temperature of the melt, and also shift the eutectic point in the Qz-Ab-Or ternary system. Given that F would likely concentrate towards the later stages of crystallisation, plagioclase crystallising at this point is expected to be more sodic. High F concentrations would shift the Qz-Ab-Or eutectic point towards the Ab-apex and thus the melt composition would enter the quartz field. Following crystallisation of quartz at this stage, the melt composition would subsequently enter the quartz-alkali feldspar cotectic and both quartz and alkali feldspar would crystallise. Finally, as the melt composition reaches the new eutectic point, sodic plagioclase would crystallise together with quartz and alkali feldspar. This behaviour explains the presence of both rapakivi (plagioclase mantling alkali feldspar) and anti-rapakivi (alkali feldspar mantling plagioclase-calcic in this case) textures observed throughout the RDG.

6.2. Alkali feldspars and deuteric coarsening

Textural observations of cryptoperthite are consistent with interpretations and models proposed by previous authors (*e.g.*, Parsons et al., 2015; references therein), involving continuous interdiffusion of Na and K in the aluminosilicate tetrahedral framework during cooling from the solvus. Conversely, the incoherency and microporosity of

Table 7
Results of amphibole-plagioclase geothermometry.

Ed-Plag	Phenocryst (RX7865)					RX7860
	Core-overprinted		Rapakivi mantle overprinted			Edenite-Ads-Olig
Amphibole (from Table 6)	a1 bright	a1 dark	a4 bright	a4 dark	a3	a4
Plag X_{Ab}	0.66	0.97	0.85	0.85	0.75	0.66
Pressure estimate (kbar)	2.2	2.2	2.2	2.2	2.2	2.2
T (°C)	731	657	710	700	703	754

Calibration of Blundy and Holland (1990). Uncertainties of ±75 °C.

Table 8
EPMA compositional data for selected magnetite-ilmenite pairs and geothermometric estimates.

	Phenocryst (RX7865)								RX7860								
	a1		a2		a3		a5	a6	Dense inclusions (a3)				Scarce inclusions (a1)			Hm-associated	
	Mt	Ilm	Mt	Ilm	Mt	Ilm	Mt		Mt	Ilm	Mt	Ilm	Mt			Mt	
SiO_2	0.01	0.10	0.01	1.17	0.01	0.32	0.02	0.06	<mdl	0.04	0.03	0.04	0.06	<mdl	0.02	0.03	<mdl
TiO_2	1.13	48.97	1.42	48.16	1.13	48.92	0.89	1.27	3.17	49.54	2.45	49.54	1.27	1.37	0.56	0.69	0.34
Al_2O_3	0.33	0.05	0.52	0.28	0.45	0.13	0.27	0.44	0.36	<mdl	0.33	<mdl	0.44	0.24	0.14	0.17	0.07
Fe_2O_3	63.79	3.63	63.0	4.83	64.23	3.99	65.50	63.49	60.81	4.50	62.23	4.50	63.49	64.97	66.41	65.81	66.62
FeO	30.92	34.08	31.2	33.9	31.11	33.49	29.47	31.13	33.17	33.97	32.39	33.97	31.13	31.66	30.98	31.05	30.66
MnO	0.17	9.70	0.13	9.30	0.14	10.07	0.11	0.15	0.20	9.83	0.31	9.83	0.15	0.25	0.07	0.05	<mdl
MgO	<mdl	0.12	0.03	0.19	0.02	0.25	0.02	0.04	0.02	0.02	0.02	0.02	0.04	0.01	0.02	0.02	<mdl
CaO	0.01	0.03	<mdl	0.81	0.07	0.20	<mdl	<mdl	0.01	0.50	0.01	0.50	<mdl	0.02	0.02	<mdl	0.02
Cr_2O_3	0.02	0.03	0.02	<mdl	0.02	<mdl	<mdl	<mdl	0.02	0.02	0.02	0.02	<mdl	0.02	<mdl	0.02	<mdl
ZnO	<mdl	<mdl	<mdl	<mdl	<mdl	<mdl	<mdl	0.06	<mdl	<mdl	0.04	<mdl	0.06	<mdl	<mdl	<mdl	<mdl
V_2O_5	0.21	0.25	0.22	0.27	0.18	0.27	0.18	0.17	0.18	0.27	0.18	0.27	0.17	0.18	0.18	0.13	0.11
Nb_2O_5	<mdl	<mdl	<mdl	0.11	<mdl	<mdl	<mdl	<mdl	<mdl	<mdl	<mdl	<mdl	<mdl	<mdl	<mdl	<mdl	<mdl
Total	96.60	96.95	96.58	99.04	97.36	97.64	96.45	96.82	97.95	98.69	98.01	98.69	96.82	98.73	98.39	97.97	97.84
Cation proportions (Carmichael, 1967)																	
Si	0.000	0.003	0.001	0.030	0.001	0.008	0.001	0.003	0.000	0.001	0.001	0.001	0.003	0.000	0.001	0.001	0.000
Ti	0.034	0.958	0.042	0.917	0.033	0.948	0.027	0.038	0.093	0.953	0.072	0.953	0.038	0.040	0.017	0.020	0.010
Al	0.015	0.002	0.024	0.008	0.021	0.004	0.013	0.021	0.017	0.000	0.015	0.000	0.021	0.011	0.006	0.008	0.003
Fe^{3+}	1.909	0.071	1.882	0.092	1.905	0.077	1.927	1.893	1.790	0.087	1.832	0.087	1.893	1.902	1.954	1.944	1.973
Fe^{2+}	1.028	0.742	1.037	0.718	1.025	0.722	1.023	1.032	1.085	0.726	1.060	0.726	1.032	1.030	1.013	1.019	1.009
Mn	0.006	0.214	0.004	0.199	0.005	0.220	0.004	0.005	0.007	0.213	0.010	0.213	0.005	0.008	0.002	0.002	0.000
Mg	0.000	0.005	0.002	0.007	0.001	0.009	0.001	0.002	0.001	0.001	0.001	0.001	0.002	0.001	0.001	0.001	0.000
Ca	0.001	0.001	0.000	0.022	0.003	0.006	0.000	0.000	0.000	0.014	0.000	0.014	0.000	0.001	0.001	0.000	0.001
Cr	0.001	0.001	0.001	0.000	0.001	0.000	0.000	0.000	0.001	0.000	0.001	0.000	0.000	0.001	0.000	0.001	0.000
Zn	0.000	0.000	0.000	0.000	0.000	0.000	0.000	0.002	0.000	0.000	0.001	0.000	0.002	0.000	0.000	0.000	0.000
V	0.007	0.005	0.007	0.006	0.006	0.006	0.006	0.006	0.006	0.005	0.006	0.005	0.006	0.006	0.005	0.004	0.004
Nb	0.000	0.000	0.000	0.001	0.000	0.000	0.000	0.000	0.000	0.000	0.000	0.000	0.000	0.000	0.000	0.000	0.000
Total	3.000	2.000	3.000	2.000	3.000	2.000	3.000	3.000	3.000	2.000	3.000	2.000	3.000	3.000	3.000	3.000	3.000

Calc. methods:	mol.% Usp	mol.% Ilm	mol.% Usp	mol.% Ilm	mol.% Usp	mol.% Ilm	mol.% Usp	mol.% Ilm	mol.% Usp	mol.% Ilm
Carmichael (1967)	3.4%	96.1%	4.3%	94.6%	3.4%	95.7%	9.3%	95.4%	7.2%	95.4%
Anderson (1968)	3.1%	95.3%	4.1%	93.4%	3.1%	94.7%	9.1%	95.2%	6.6%	95.2%
Lindsley and Spencer (1982)	3.4%	95.3%	4.3%	93.5%	3.4%	94.8%	9.4%	95.2%	7.2%	95.2%
Stormer (1983)	3.4%	96.0%	4.4%	94.6%	3.4%	95.5%	9.5%	95.0%	7.2%	95.0%

Geothermobarometer by Andersen and Lindsley (1985)

X'Usp & X'Ilm from:	*T* (°C)	$\log fO_2$	*T* (°C)	$\log fO_2$	*T* (°C)	$\log fO_2$	*T* (°C)	$\log fO_2$	*T* (°C)	$\log fO_2$
Carmichael (1967)	559		600		569		620		609	
Anderson (1968)	573	−20.3	617	−18.1	584	−19.6	622	−19.3	608	−19.6
Lindsley and Spencer (1982)	576	−20.3	618	−18.2	586	−19.6	624	−19.3	612	−19.5
Stormer (1983)	562	−21.2	601	−19.2	572	−20.5	629	−19.1	616	−19.3
Average:	567	−20.6	609	−18.5	577	−19.9	624	−19.2	611	−19.5

patch perthite support formation through fluid-feldspar interaction. Recrystallisation of cryptoperthite, at this stage, is generally isochemical with respect to major elements. Fig. 14 illustrates the behaviour of alkali elements during this process. The Ca and Na contents positively correlate with one another; both elements appear to be concentrated within the cryptoperthite grain interiors. In contrast, K increases towards the rims.

Trails of micropores observed to replace Ab-rich lamellae of cryptoperthite point to direct removal of Na. This is supported by interpretations in Walker et al. (1995), who conclude that the microporosity in patch perthite cannot be fully accounted for by molar volume reduction, and that some feldspar components are inevitably lost to the fluid. Such an observation may in fact represent an initial stage of Na remobilisation, leading to subsequent albitisation observed in the RDG. In addition, it may explain the homogeneous albite rim observed in plagioclase adjacent to recrystallised alkali feldspar in the RDG.

The generation of microporosity in feldspars has also been discussed by Putnis (2002), who concludes that pores may form due to differences in solubility and/or molar volume between the parent (cryptoperthite) and product (patch perthite) phases. In addition, microporosity development in patch perthite has long been documented (*e.g.*, Worden et al., 1990). Given the intragranular nature of deuteric coarsening, microporosity in patch perthite opens up the possibility of elements entering the mineral from adjacent grains. In the RDG, nearby biotite alteration of amphibole and/or re-equilibration of high Fe/low Mg igneous biotite may provide a source of Fe (*e.g.*, Brimhall et al., 1985), and explain the presence of sub-μm-sized hematite associated with patch perthite. Moreover, generation of microporosity in patch perthite, critical for the advancement of the replacement reaction interface (Putnis, 2002), could also promote subsequent fluid-feldspar interaction (Lee and Parsons, 1997). Consequently, the majority of patch perthite reported here has been altered by the highly porous albite and K-feldspar.

6.3. Albitisation of plagioclase

Albitisation of plagioclase is a ubiquitous feature of the RDG. The resultant albite + sericite texture is mostly localised within the plagioclase cores; however, it may also progress along cleavage planes to form pseudomorphs of albitised plagioclase. The pseudomorphic character and sharp boundaries between plagioclase and replacive albite are consistent with coupled dissolution-precipitation reactions (*e.g.*, Putnis, 2002). Such reactions proceed from grain boundaries inwards, and thus plagioclase cores with albite rims would be expected. However, the opposite is commonly observed throughout the RDG, inferring that fluids were able to access plagioclase cores. Such a mechanism was discussed by Que and Allen (1996), who postulated that hydrothermal fluids penetrated plagioclase cores *via* microfractures, which formed prior to hydraulic fracturing in the Rosses granite complex, Ireland. Element maps in Fig. 15 illustrate this core to rim albitisation process in the RDG. The grain interior comprises replacive albite (dark

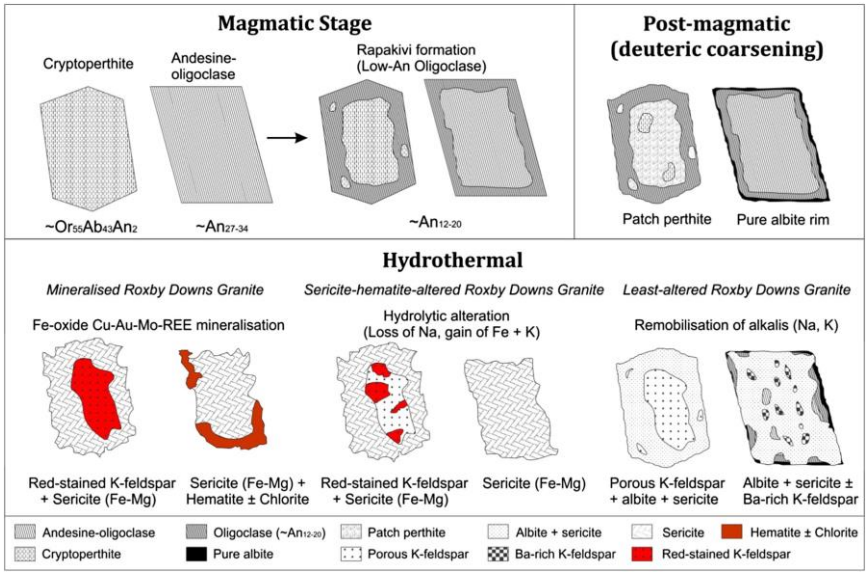

Fig. 13. Schematic diagram outlining the evolutionary sequence of feldspars in the RDG. Relationships between zones preserve magmatic, post-magmatic and hydrothermal feldspar replacement reactions. See text for detailed explanation.

blue) ± sericite (light blue), with oligoclase relicts observed along the grain boundary. In addition, a homogeneous albite rim can be seen between the grain boundary and oligoclase relicts on the Ca and K maps. This feature is observed in all plagioclase grains adjacent to patch perthite (see also Fig. 8d), and is interpreted to represent liberation of Na during recrystallisation of cryptoperthite (deuteric coarsening stage). The circled areas on the BSE image represent K-feldspar inclusions and are thus depleted in both Ca and Na.

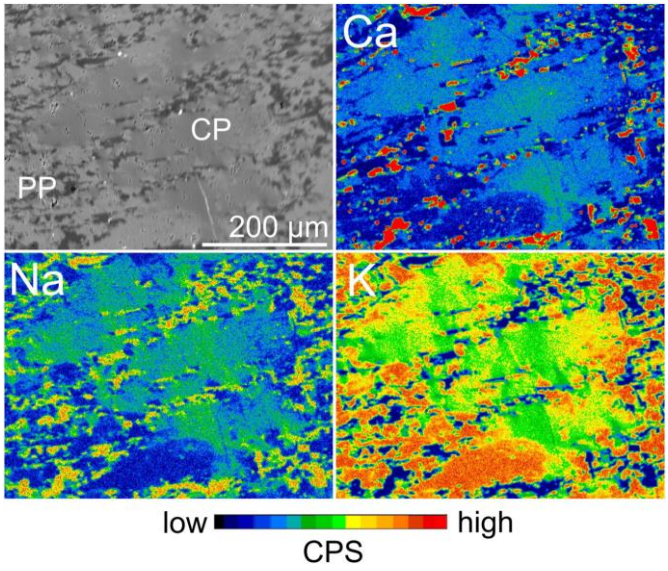

Fig. 14. Back scatter electron image (top left) and EPMA major element maps of cryptoperthite (CP) and patch perthite (PP). See text for explanation. Counts per second scales range from 0 to 92 (Ca), 0 to 52 (Na) and 0 to 245 (K).

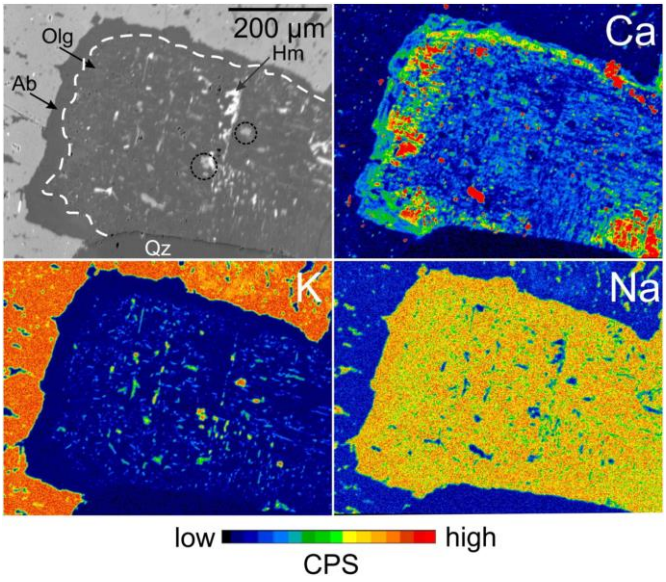

Fig. 15. Back scatter electron image (top left) and EPMA major element maps for an albitized oligoclase grain in the RDG. Circled areas on BSE image represent K-feldspar. See text for explanation. Counts per second scales range from 0 to 158 (Ca), 0 to 52 (Na) and 0 to 248 (K).

Previous authors have attempted to constrain the chemical reactions that best represents the albitisation of plagioclase. Applying the equations proposed by Merino (1975); Boles (1982) and Engvik et al. (2008), replacement of plagioclase by albite in the RDG may be given by:

$$Na_{0.8}Ca_{0.2}Al_{1.2}Si_{2.8}O_8(\text{oligoclase}) + 0.2Na^+(\text{aq.}) + 0.2H_4SiO_4(\text{aq.}) \rightarrow NaAlSi_3O_8(\text{albite}) + 0.2Ca^{2+}(\text{aq.}) + 0.2Al^{3+}(\text{aq.}) + 0.8OH^-(\text{aq.}) \quad (1)$$

$$Na_{0.8}Ca_{0.2}Al_{1.2}Si_{2.8}O_8(\text{oligoclase}) + 0.4Na^+(\text{aq.}) + 0.8H_4SiO_4(\text{aq.}) \rightarrow 1.2NaAlSi_3O_8(\text{albite}) + 0.2Ca^{2+}(\text{aq.}) + 1.6H_2O(\text{aq.}) \quad (2)$$

Eq. (1) implies mobility of Al^{3+}, which, given the close association of sericite with replacive albite, may in fact be released from plagioclase and incorporated in sericite. This hypothesis is preferred in the case of the RDG due to the close association with sericite. Eq. (2) conserves Al within the product albite, and may be more relevant for the formation of the pure albite rim discussed above. Regardless of which equation is most suitable, the albitisation of plagioclase principally involves consumption of Na^+, Si^{-4} and H^+, and the release of Ca^{2+} and Al^{3+}. Whole-rock analyses of least-altered RDG do not show a gain of Na, which indicates that Na for albitisation was locally sourced from within the RDG. A potential source is the widespread replacement of patch perthite by highly porous albite and K-feldspar. Observed textures indicate the grain-scale removal of Na from alkali feldspar (collectively patch perthite) at this later stage. Moreover, the alteration of edenite to chlorite involves liberation of Na from the sodic amphibole. Beyond these potential sources, a seminal study by Orville (1963) showed that Na-rich fluids are not necessarily required for albitisation, and that a fluid simply has to be of suitable temperature to facilitate exchange between Na^+ and K^+. The source of Si for albitisation in the RDG is also of importance. Previous authors (Plümper and Putnis, 2009) interpreted nearby corroded quartz as a source of Si for albitisation in granitoids of the Trans-Scandinavian Igneous Belt in SE Sweden. However, no corroborative textures have been observed in the RDG and thus an alternative source of Si for the albitisation reaction is required. A potential source may be the chloritisation of biotite in the RDG, based on the cogenetic precipitation of hydrothermal quartz with chlorite (*e.g.*, Parry and Downey, 1982).

Using EPMA spot analyses of plagioclase and albite, an isocon plot (Gresens, 1967; Grant, 1986) was constructed to observe the behaviour of elements during the albitisation of low-An oligoclase in the RDG (Fig. 16). Assuming constant volume or mass, Al is slightly mobile, and K increases in the resultant albite. This may represent contamination of sub-µm-sized inclusions of sericite in albite. Variations in albite:sericite ratio may reflect local fluctuations in a_{K+} in the fluids, or a decrease in temperature, since sericite is more stable at lower temperatures than albite (Johnson et al., 1992). Despite the high K content of plagioclase in the RDG (Table 6), sericite would still require K from an external source. Similarly to Si, the chloritisation of biotite typically releases K^+ (Parry and Downey, 1982), and thus might represent such a potential source.

In addition to sericite, sub-µm-sized inclusions of hematite are also associated with replacive albite. This is highlighted in the isocon, which shows an increase of Fe in albite. A likely source of Fe in this case might be the hydrothermal conversion of amphibole to biotite (Brimhall et al., 1985), a phenomenon seen throughout the RDG, and possibly also from plagioclase, even if FeO is well below 0.5 wt.%.

Calcite and dolomite inclusions are also observed within albitised plagioclase and have likely sourced Ca from the igneous plagioclase. However, such inclusions are not ubiquitously present, indicating grain-scale removal of Ca during albitisation, as well as CO_2 within the albitising fluid. Dissolution experiments (Słaby, 1995), in which oligoclase was dissolved in K_2CO_3 solution, produced a similar assemblage consisting of K-feldspar + albite + calcite + dolomite, and may indicate a similar environment for the alteration of plagioclase in the RDG.

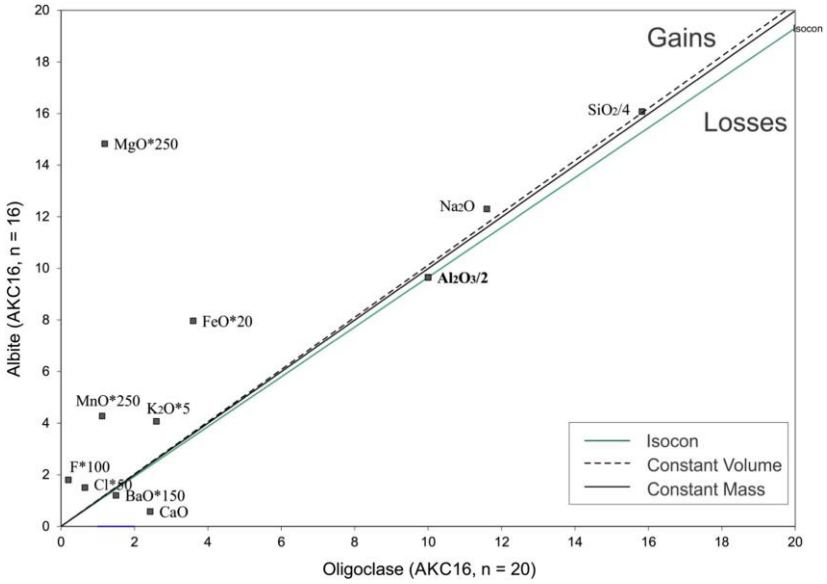

Fig. 16. Isocon plot (Gresens, 1967; Grant, 1986) showing elemental gains and losses during albitization of low-An oligoclase. This plot assumes the immobility of Al^{3+}, which may be incorporated into sericite (see text).

6.4. Hydrothermal K-feldspar

Hydrothermal K-feldspar has not previously been reported from Olympic Dam. However, a change in physico-chemical conditions from albite- to K-feldspar-stable is apparent in even the least-altered RDG. This is evident from a compositionally and texturally distinct K-feldspar which is restricted to previously albitised zones of plagioclase (Fig. 8; Table 2). Fluctuation in Ba content of this K-feldspar could reflect the initial composition of plagioclase, but is more likely related to differential flow of hydrothermal fluids. Similar Ba-zoned K-feldspar was associated with albitisation in granites from Proterozoic terranes in the Fennoscandian Shield (*e.g.*, Morad et al., 2010). This type of feldspar is also reported from Hiltaba suite granites in the Moonta-Wallaroo region (Kontonikas-Charos et al., 2014).

Similarly to plagioclase, alkali feldspar is also affected by hydrothermal K-feldspar formation. This highly porous, near end-member K-feldspar is the most common form of hydrothermal K-feldspar observed in the RDG. Analogous to replacive albite, sub-μm hematite inclusions in the red-stained areas of this K-feldspar are related to Fe release *via* local mineral reactions (*e.g.*, breakdown of primary mafic minerals). A similar mechanism has been suggested for rocks containing red-stained K-feldspar and contemporaneous alteration of biotite and hornblende (*e.g.*, Putnis et al., 2007; Drake et al., 2008). Moreover, the increased FeO content in between hematite inclusions of red-stained K-feldspar (*e.g.*, Fig. 17) indicates that Fe could be present as either nm-scale inclusions, or incorporated within the feldspar crystal lattice. The heterogeneous distribution of hematite throughout the red-stained areas of K-feldspar could relate to porosity generation and locally variable rates of nucleation in the RDG. Putnis et al. (2007) concluded that such red-staining, characteristic of many granitic rocks, is a direct product of fluid-feldspar interaction rather than solid-state exsolution.

The decrease in Na_2O and increase in K_2O between least-altered and sericite-hematite altered RDG observed in whole-rock analyses (*e.g.*, Fig. 2) likely reflects Na/K exchange of the type typical for IOCG systems (*e.g.*, Barton, 2014). Similar to patch perthite, the generation of porosity in hydrothermal albite and K-feldspar likely promotes further fluid-feldspar interaction, and would thus partly influence the apparent shift of alteration style.

The association of red-stained K-feldspar with various sulphides, gold and REE-(U)-minerals strongly implies a genetic relationship between them. Moreover, the replacement of red-stained K-feldspar by interlayered sericite + molybdenite + REE-minerals (Fig. 10d) further emphasises the link between mineralisation and K-feldspar at this hydrothermal stage. All the evidence presented here highlights the ability of feldspars to preserve distinct stages within an evolving magmatic-hydrothermal system.

6.5. Significance of feldspar evolution for IOCG mineralisation

The magmatic evolution of feldspars supports late-stage magma mixing/contamination, a critical component of crustal continuum models for generation of fertile IOCG systems (*e.g.*, Groves et al., 2010). The present study also highlights the preservation of alteration styles, from the grain- to cm-scale that occurs as the granite cools from >750 °C (see Table 9 for summary of geothermobarometry). Post-crystallisation uplift and brecciation of the RDG likely contributed to hydrothermal alteration of feldspars at Olympic Dam. An increase in abundance of hematite and sulphides progressively obliterates the features described for the RDG. Evidence for remobilisation of Na and subsequent albitisation and formation of hydrothermal K-feldspar, are nevertheless preserved within the granite immediately adjacent to the ODBC.

The results collectively point to a process in which initial fluids exsolved from the melt and evolved through cooling and subsequent convection within the granitoid pluton. The abundant microporosity and presence of additional phases (*e.g.*, hematite and sericite) associated with feldspar replacement reactions indicate that each feldspar grain represents an open system, which at least extends to adjacent grains.

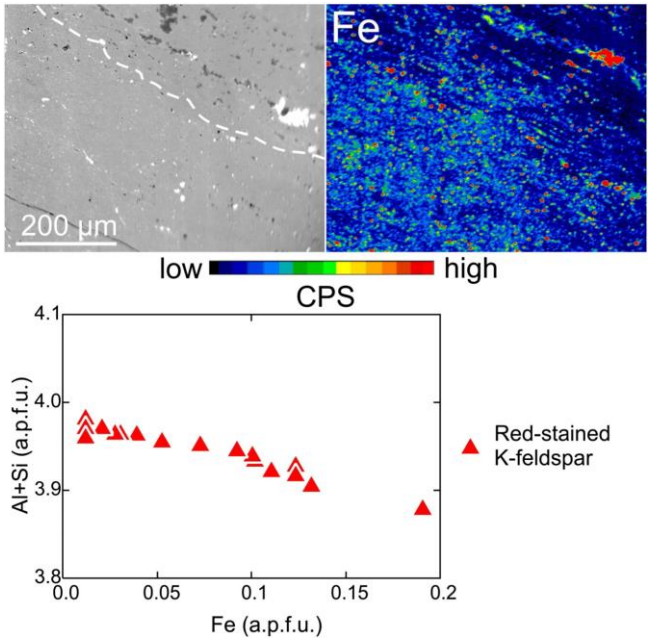

Fig. 17. Back scatter electron image, EPMA Fe element map and binary plot of variably red-stained K-feldspar within altered RDG. See text for explanation. Counts per second scales range from 0 to 155. (For interpretation of the references to colour in this figure legend, the reader is referred to the web version of this article.)

Microfracturing and repeated fracture reactivation could be effective mechanisms by which multiple open systems link up. Whole-rock analyses of least-altered RDG at one-metre intervals (Table 1a) are consistent with existing data for granites (*e.g.*, Frost et al., 2001; references therein). In addition, the data plots in the same area on the modified QAP and Ab–An–Or diagrams, irrespective of textures and mineralogy suggesting that Area 2 is more altered than Area 1. Thus, regardless of the extent of feldspar replacement textures in the least-altered RDG samples, the rock still maintains its overall granitic composition at the m-scale. Such evidence further supports recycling of feldspar components within the RDG and implies that hydrothermal albite and K-feldspar can form *in-situ* without the need for an external source of alkalis (*e.g.*, evaporites; Barton and Johnson, 1996, 2000; Conor et al., 2010).

The presence of albite at depth within the ODBC is concordant with proposed models for IOCG systems, in which deep sodic alteration transitions to intermediate potassic alteration followed by shallower hydrolytic alteration (*e.g.*, Hitzman et al., 1992; Barton, 2014). This telescoping of alteration assemblages is supported by higher $a\mathrm{Na}^{+}$ than $a\mathrm{K}^{+}$ at higher temperatures (Orville, 1963). However, it is important to highlight that in the case of the RDG, albitisation does not produce the barren, monomineralic albitites as reported from other IOCG terranes, *e.g.*, from Cloncurry, Queensland (Mark, 1998; Bertelli and Baker, 2010). There is a clear remobilisation of Na from the host RDG, which indeed leads to local albitisation; and may also lead to albitisation elsewhere in the Olympic Dam area. Nevertheless, the preservation of albitisation at depth and to the peripheries of the ODBC is an important observation and one which reflects the critical role that successive alteration events play in the formation of giant orebodies such as Olympic Dam. In addition, the significant geochemical and textural changes related to feldspar recrystallisation in the RDG clearly played a role in facilitating fluids and subsequent or synchronous hydrothermal alteration/mineralisation at Olympic Dam.

7. Conclusions

The results of this study allow the following conclusions:

- Major element exchange occurring at Olympic Dam can be tracked from feldspar textures in the surrounding RDG. There is a remobilisation and eventual loss of Na occurring in the least-altered RDG and a gain of Fe and K in sericite-hematite altered and mineralised RDG. This corresponds to observed albitisation, sericite-hematite alteration and

Table 9
Summary of geothermobarometric estimates for the RDG.

Technique	Minerals	*P* (kbar)	*T* (°C)	Implications
Al-in-hornblende geobarometry	Edenite	2.2	N/A	Corresponds to crystallisation depths of ~8 km
Feldspar geothermometry	Cryptoperthite	2.2	~765	Minimum crystallisation *T* for ternary feldspars
Amphibole-plagioclase geothermometry	Edenite, plagioclase	2.2	700–710	Minimum crystallisation *T* for rapakivi mantles
Magnetite-ilmenite geothermometry	Magnetite, ilmenite	N/A	574–624	Minimum re-equilibration *T* of Fe-Ti-oxides
Feldspar geothermometry	Patch perthite	2.2	~430	*T* for onset of deuteric coarsening
	Film perthite	2.2	<430	Secondary exsolution in Or-rich phase of patch perthite

subsequent Fe-oxide Cu-Au-REE-Mo-U mineralisation. In addition, there is a significant association between increased red-staining of K-feldspar and abundance of sulphide mineralisation.

- Textural relationships and geochemistry of feldspars and mafic minerals in the least-altered RDG point to late-stage magma mixing/contamination.
- Geothermometry indicates minimum crystallisation temperatures of 765 °C for ternary feldspar at a pressure of ~2.2 kbar (using Al-in-hornblende geobarometry corrected for temperature by amphibole-plagioclase geothermometry), followed by re-equilibration of Fe-Ti-minerals and feldspars at ~550–650 °C and ~430 °C, respectively. Pre-existing feldspars have been extensively overprinted by highly porous albite and K-feldspar.
- The presence of hydrothermal albite and K-feldspar at Olympic Dam illustrate the ability for these forms of alteration, characteristic of IOCG systems, to be internally sourced from within the host rock (granite). Such widespread physical and chemical changes resulting from these reactions may indeed facilitate subsequent mineralisation.

Acknowledgements

We thank BHP Billiton for financial support and access to Olympic Dam samples and facilities. We also thank Adelaide Microscopy for assistance with microanalysis, in particular Animesh Basak for assistance operating the Titan Themis TEM and Benjamin Wade for assistance with various software packages. We acknowledge the insightful comments of Ewa Słaby and two anonymous reviewers. Constructive comments from Ian Parsons on an earlier version of this manuscript are greatly appreciated and helped us present our ideas with greater clarity. We also acknowledge support from the 'FOX' project (Trace elements in iron oxides), supported by BHP Billiton and the South Australian Mining and Petroleum Services Centre of Excellence.

References

Andersen, D.J., Lindsley, D.H., 1985. New (and final!) models for the Ti-magnetite/ilmenite geothermometer and oxygen barometer. AGU Spring Meeting. Eos 66 (18), p. 416.
Anderson, A.T., 1968. The oxygen fugacity of alkaline basalt and related magmas. Am. J. Sci. 266, 704–727.
Anderson, J.L., Smith, D.R., 1995. The effects of temperature and fO_2 on the Al-in-hornblende barometer. Am. Mineral. 80, 549–559.
Barker, F., 1979. Trondhjemite: definition, environment and hypotheses of origin. Trondhjemites, dacites and related rocks. 1-12, Elsevier, Amsterdam, p. 659.
Barton, M., 2014. Iron oxide (-Cu-Au-REE-P-Ag-U-Co) systems. Treatise on Geochemistry, second edition vol. 13. Elsevier, Amsterdam, pp. 515–541.
Barton, M.D., Johnson, D.A., 1996. Evaporitic-source model for igneous-related Fe oxide-(REE-Cu-Au-U) mineralisation. Geology 24, 259–262.
Barton, M.D., Johnson, D.A., 2000. Alternative brine sources for Fe-oxide (-Cu-Au) systems: implications for hydrothermal alteration and metals. Hydrothermal Iron Oxide Copper-Gold & Related Deposits: A Global Perspective. vol. 1, pp. 43–60.
Bertelli, M., Baker, T., 2010. A fluid inclusion study of the Suicide Ridge Breccia Pipe, Cloncurry district, Australia: implication for breccia genesis and IOCG mineralisation. Precambrian Res. 179, 69–87.
BHP Billiton, 2015. http://www.bhpbilliton.com/home/investors/annualreporting2015.pdf.
Blundy, J.D., Holland, T.J.B., 1990. Calcic amphibole equilibria and a new amphibole-plagioclase geothermometer. Contrib. Mineral. Petrol. 104, 208–224.
Boles, J.R., 1982. Active albitization of plagioclase, Gulf Coast Tertiary. Am. J. Sci. 282, 165–180.
Brimhall, G.H., Agee, C., Stoffregen, R., 1985. The hydrothermal conversion of hornblende to biotite. Can. Mineral. 23, 369–379.
Brown, W., Parsons, I., 1984. Exsolution and coarsening mechanisms and kinetics in an ordered cryptoperthite series. Contrib. Mineral. Petrol. 86, 3–18.
Brown, W.L., Parsons, I., 1989. Alkali feldspars: ordering rates, phase transformations and behaviour diagrams for igneous rocks. Mineral. Mag. 53, 25–42.
Carmichael, I.S.E., 1967. The iron-titanium oxides of salic volcanic rocks and their associated ferromagnesian silicates. Contrib. Mineral. Petrol. 14, 36–64.
Ciobanu, C.L., Cook, N.J., Utsunomiya, S., Pring, A., Green, L., 2011. Focussed ion beam-transmission electron microscopy applications in ore mineralogy: bridging micro- and nanoscale observations. Ore Geol. Rev. 42, 6–31.
Ciobanu, C.L., Wade, B.P., Cook, N.J., Schmidt Mumm, A., Giles, D., 2013. Uranium-bearing hematite from the Olympic Dam Cu–U–Au deposit, South Australia: a geochemical tracer and reconnaissance Pb–Pb geochronometer. Precambrian Res. 238, 129–147.
Conor, C., Raymond, O., Baker, T., Teale, G., Say, P., Lowe, G., 2010. Alteration and mineralisation in the Moonta-Wallaroo Cu–Au mining field region, Olympic domain, South Australia. Hydrothermal Iron Oxide Copper–Gold and Related Deposits: A Global Perspective. vol. 3, pp. 1–24.
Creaser, R.A., 1989. The Geology and Petrology of Middle Proterozoic Felsic Magmatism of the Stuart Shelf, South Australia. La Trobe University, Melbourne.
Creaser, R.A., 1996. Petrogenesis of a Mesoproterozoic quartz latite-granitoid suite from the Roxby Downs area, South Australia. Precambrian Res. 79, 371–394.
Dempster, T., Jenkin, G., Rogers, G., 1994. The origin of rapakivi texture. J. Petrol. 35, 963–981.
Drake, H., Tullborg, E.-L., Annersten, H., 2008. Red-staining of the wall rock and its influence on the reducing capacity around water conducting fractures. Appl. Geochem. 23, 1898–1920.
Ehrig, K., McPhie, J., Kamenetsky, V., 2012. Geology and mineralogical zonation of the Olympic Dam iron oxide Cu-U-Au-Ag deposit, South Australia. In: Hedenquist, J.W., Harris, M., Camus, F. (Eds.), Geology and Genesis of Major Copper Deposits and Districts of the World: A Tribute to Richard H. Sillitoe vol. 16. Society of Economic Geologists Special Publication, pp. 237–267.
Emslie, R., 1991. Granitoids of rapakivi granite-anorthosite and related associations. Precambrian Res. 51, 173–192.
Engvik, A.K., Putnis, A., Gerald, J.D.F., Austrheim, H., 2008. Albitization of granitic rocks: the mechanism of replacement of oligoclase by albite. Can. Mineral. 46, 1401–1415.
Ferris, G.M., Schwarz, M.P., Heithersay, P., 2002. The geological framework, distribution, and controls of Fe-oxide Cu–Au mineralisation in the Gawler Craton, South Australia: Part 1—Geological and tectonic framework. Hydrothermal Iron Oxide Copper–Gold and Related Deposits: A Global Perspective. vol. 2, pp. 9–32.
Frost, B.R., Barnes, C.G., Collins, W.J., Arculus, R.J., Ellis, D.J., Frost, C.D., 2001. A geochemical classification for granitic rocks. J. Petrol. 42, 2033–2048.
Fuhrman, M.L., Lindsley, D.H., 1988. Ternary-feldspar modeling and thermometry. Am. Mineral. 73, 201–215.
Grant, J.A., 1986. The isocon diagram; a simple solution to Gresens' equation for metasomatic alteration. Econ. Geol. 81, 1976–1982.
Gresens, R.L., 1967. Composition–volume relationships of metasomatism. Chem. Geol. 2, 47–65.
Groves, D.I., Bierlein, F.P., Meinert, L.D., Hitzman, M.W., 2010. Iron oxide copper-gold (IOCG) deposits through earth history: implications for origin, lithospheric setting, and distinction from other epigenetic iron oxide deposits. Econ. Geol. 105, 641–654.
Hammarstrom, J.M., Zen, E., 1986. Aluminium in hornblende: an empirical geobarometer. Am. Mineral. 71, 1297–1313.
Haynes, D.W., Cross, K.C., Bills, R.T., Reed, M.H., 1995. Olympic Dam ore genesis; a fluid-mixing model. Econ. Geol. 90, 281–307.
Hayward, N., Skirrow, R., 2010. Geodynamic setting and controls on iron oxide Cu-Au (±U) ore in the Gawler Craton, South Australia. Hydrothermal Iron Oxide Copper-Gold and Related Deposits: A Global Perspective. vol. 3, pp. 105–131.
Hibbard, M.J., 1981. The magma mixing origin of mantled feldspars. Contrib. Mineral. Petrol. 76, 158–170.
Hitzman, M.W., Oreskes, N., Einaudi, M.T., 1992. Geological characteristics and tectonic setting of proterozoic iron oxide (Cu-U-Au-REE) deposits. Precambrian Res. 58, 241–287.
Hollister, L.S., Grissom, G.C., Peters, E.K., Stowell, H.H., Sisson, V.B., 1987. Confirmation of the empirical correlation of aluminium in hornblende with pressure of solidification of calcalkaline plutons. Am. Mineral. 72, 231–239.
Hövelmann, J., Putnis, A., Geisler, T., Schmidt, B.C., Golla-Schindler, U., 2010. The replacement of plagioclase feldspars by albite: observations from hydrothermal experiments. Contrib. Mineral. Petrol. 159, 43–59.
Ismail, R., Ciobanu, C.L., Cook, N.J., Teale, G.S., Giles, D., Schmidt Mumm, A., Wade, B., 2014. Rare earths and other trace elements in minerals from skarn assemblages, Hillside iron oxide–copper–gold deposit, Yorke Peninsula, South Australia. Lithos 184–187, 456–477.
Jagodzinski, E.A., 2005. Compilation of SHRIMP U-Pb geochronological data. Geoscience Australia Record 2005/20.
Johnson, J.P., Cross, K.C., 1995. U-Pb geochronological constraints on the genesis of the Olympic Dam Cu-U-Au-Ag deposit, South Australia. Econ. Geol. 90, 1046–1063.
Johnson, M.C., Rutherford, M.J., 1989. Experimental calibration of the aluminium-in-hornblende geobarometer with application to Long Valley caldera (California). Geology 17, 837–841.
Johnson, J.W., Oelkers, E.H., Helgeson, H.C., 1992. SUPCRT92: a software package for calculating the standard molal thermodynamic properties of minerals, gases, aqueous species, and reactions from 1 to 5000 bar and 0 to 1000 °C. Comput. Geosci. 18, 899–947.
Kontonikas-Charos, A., Ciobanu, C.L., Cook, N.J., 2014. Albitization and redistribution of REE and Y in IOCG systems: insights from Moonta-Wallaroo, Yorke Peninsula, South Australia. Lithos 208–209, 178–201.
Krneta, S., Ciobanu, C.L., Cook, N.J., Ehrig, K., Kontonikas-Charos, A., 2016. Apatite at Olympic Dam, South Australia: a petrogenetic tool. Lithos 262, 470–485.
Lee, M.R., Parsons, I., 1997. Dislocation formation and albitization in alkali feldspars from the Shap granite. Am. Mineral. 82, 557–570.
LeMaitre, R.W., Streckeisen, A., Zanettin, B., Le Bas, M.J., Bonin, B., Bateman, P. (Eds.), 1989. A Classification of Igneous Rocks and Glossary of Terms: Recommendations of the International Union of Geological Sciences Subcommission on the Systematics of Igneous Rocks. Blackwell Scientific, Oxford (193 pp.).
Lepage, L.D., 2003. ILMAT: an Excel worksheet for ilmenite-magnetite geothermometry and geobarometry. Comput. Geosci. 29, 673–678.
Lindsley, D.H., Spencer, K.J., 1982. Fe-Ti oxide geothermometry: reducing analyses of coexisting Ti-magnetite (Mt) and ilmenite (Ilm). EOS Trans. Am. Geophys. Union 63, 471.
Manning, D., 1981. The effect of fluorine on liquidus phase relationships in the system Qz-Ab-Or with excess water at 1 kb. Contrib. Mineral. Petrol. 76, 206–215.

Mark, G., 1998. Albitite formation by selective pervasive sodic alteration of tonalite plutons in the Cloncurry district, Queensland. Aust. J. Earth Sci. 45, 765–774.

Merino, E., 1975. Diagenesis in Tertiary sandstones from Kettleman North Dome, California: I. Diagenetic mineralogy. J. Sediment. Petrol. 45, 320–336.

Morad, S., El-Ghali, M., Caja, M., Sirat, M., Al-Ramadan, K., Mansurbeg, H., 2010. Hydrothermal alteration of plagioclase in granitic rocks from Proterozoic basement of SE Sweden. Geol. J. 45, 105–116.

Müller, A., Seltmann, R., Kober, B., Eklund, O., Jeffries, T., Kronz, A., 2008. Compositional zoning of rapakivi feldspars and coexisting quartz phenocrysts. Can. Mineral. 46, 1417–1442.

Oliver, N.H., Cleverley, J.S., Mark, G., Pollard, P.J., Fu, B., Marshall, L.J., Rubenach, M.J., Williams, P.J., Baker, T., 2004. Modeling the role of sodic alteration in the genesis of iron oxide-copper-gold deposits, Eastern Mount Isa block, Australia. Econ. Geol. 99, 1145–1176.

Oreskes, N., Einaudi, M.T., 1990. Origin of rare earth element-enriched hematite breccias at the Olympic Dam Cu-U-Au-Ag deposit, Roxby Downs, South Australia. Econ. Geol. 85, 1–28.

Orville, P.M., 1963. Alkali ion exchange between vapor and feldspar phases. Am. J. Sci. 261, 201–237.

Parry, W., Downey, L., 1982. Geochemistry of hydrothermal chlorite replacing igneous biotite. Clay Clay Miner. 30, 81–90.

Parsons, I., 1978. Feldspars and fluids in cooling plutons. Mineral. Mag. 42, 1–17.

Parsons, I., Thompson, P., Lee, M.R., Cayzer, N., 2005. Alkali feldspar microtextures as provenance indicators in siliciclastic rocks and their role in feldspar dissolution during transport and diagenesis. J. Sediment. Res. 75, 921–942.

Parsons, I., Lee, M.R., 2009. Mutual replacement reactions in alkali feldspars I: microtextures and mechanisms. Contrib. Mineral. Petrol. 157 (5), 641–661.

Parsons, I., Magee, C.W., Allen, C.M., Shelley, J., Lee, M.R., 2009. Mutual replacement reactions in alkali feldspars II: trace element partitioning and geothermometry. Contrib. Mineral. Petrol. 157, 663–687.

Parsons, I., Fitz Gerald, J.D., Lee, J.K.W., Ivanic, T., Golla-Schindler, U., 2010. Time-temperature evolution of microtextures and contained fluids in a plutonic alkali feldspar during heating. Contrib. Mineral. Petrol. 160, 155–180.

Parsons, I., Gerald, J.D.F., Lee, M.R., 2015. Review. Routine characterization and interpretation of complex alkali feldspar intergrowths. Am. Mineral. 100, 1277–1303.

Perez, R.J., Boles, J.R., 2005. An empirically derived kinetic model for albitization of detrital plagioclase. Am. J. Sci. 305, 312–343.

Plümper, O., Putnis, A., 2009. The complex hydrothermal history of granitic rocks: multiple feldspar replacement reactions under subsolidus conditions. J. Petrol. 50, 967–987.

Putnis, A., 2002. Mineral replacement reactions: from macroscopic observations to microscopic mechanisms. Mineral. Mag. 66, 689–708.

Putnis, A., Hinrichs, R., Putnis, C.V., Golla-Schindler, U., Collins, L.G., 2007. Hematite in porous red-clouded feldspars: evidence of large-scale crustal fluid–rock interaction. Lithos 95, 10–18.

Que, M., Allen, A.R., 1996. Sericitization of plagioclase in the Rosses granite complex, Co. Donegal, Ireland. Mineral. Mag. 60, 927–936.

Rämö, O., Haapala, I., 1995. One hundred years of rapakivi granite. Mineral. Petrol. 52, 129–185.

Reeve, J., Cross, K., Smith, R., Oreskes, N., 1990. Olympic Dam copper-uranium-gold-silver deposit. Geology of the Mineral Deposits of Australia and Papua New Guinea vol. 2. AusIMM, Melbourne, pp. 1009–1035.

Reid, A., Smith, R.N., Baker, T., Jagodzinski, E.A., Selby, D., Gregory, C.J., Skirrow, R.G., 2013. Re-Os dating of molybdenite within hematite breccias from the Vulcan Cu-Au prospect, Olympic Cu-Au province, South Australia. Econ. Geol. 108, 883–894.

Ryan, B., 1991. Makhavinekh Lake pluton, Labrador, Canada: geological setting, subdivisions, mode of emplacement, and a comparison with Finnish rapakivi granites. Precambrian Res. 51, 193–225.

Schmidt, M.W., 1992. Amphibole composition in tonalite as a function of pressure: an experimental calibration of the Al-in-hornblende barometer. Contrib. Mineral. Petrol. 110, 304–310.

Shand, S.J., 1943. The Eruptive Rocks. 2nd edition. John Wiley, New York.

Skirrow, R.G., Bastrakov, E.N., Barovich, K., Fraser, G.L., Creaser, R.A., Fanning, C.M., Raymond, O.L., Davidson, G.J., 2007. Timing of iron oxide Cu-Au-(U) hydrothermal activity and Nd isotope constraints on metal sources in the Gawler craton, South Australia. Econ. Geol. 102, 1441–1470.

Słaby, E., 1995. TAS classification — how to overcome problems with post-magmatic feldspar formation in Permian volcanic rocks. Zbl. Geol. Paläontol. 5, 541–552.

Słaby, E., Goetze, J., 2004. Feldspar crystallization under magma-mixing conditions shown by cathodoluminescence and geochemical modelling — a case study from the Karkonosze pluton (SW Poland). Mineral. Mag. 68, 561–577.

Słaby, E., Śmigielski, M., Śmigielski, T., Domonik, A., Simon, K., Kronz, A., 2011. Chaotic three-dimensional distribution of Ba, Rb and Sr in feldspar megacrysts grown in an open magmatic system. Contrib. Mineral. Petrol. 162, 909–927.

Snow, E., Kidman, S., 1991. Effect of fluorine on solid-state alkali interdiffusion rates in feldspar. Nature 349, 231–233.

Stormer, J.C., 1983. The effects of recalculation on estimates of temperature and oxygen fugacity from analyses of multicomponent iron-titanium oxides. Am. Mineral. 68, 586–594.

Streckeisen, A.L., 1976. Classification and nomenclature of igneous rocks. Earth-Sci. Rev. 12, 1–35.

Troeng, B., 1982. Uranium-rich granites in the Olden Window, Sweden. Mineral. Mag. 46, 217–226.

Walker, F.D.L., Lee, M.R., Parsons, I., 1995. Micropores and micropermeable texture in alkali feldspars: geochemical and geophysical implications. Mineral. Mag. 59, 505–534.

Wark, D.A., Stimac, J.A., 1992. Origin of mantle (rapakivi) feldspars: experimental evidence of a dissolution- and diffusion-controlled mechanism. Contrib. Mineral. Petrol. 111, 345–361.

Wilson, M., Åkerblom, G., 1982. Geological setting and geochemistry of uranium-rich granites in the Proterozoic of Sweden. Mineral. Mag. 46, 233–245.

Worden, R.H., Walker, F.D.L., Parsons, I., Brown, W.L., 1990. Development of microporosity, diffusion channels and deuteric coarsening in perthitic alkali feldspars. Contrib. Mineral. Petrol. 104, 507–515.

CHAPTER 5

RARE EARTH ELEMENT GEOCHEMISTRY OF FELDSPARS: EXAMPLES FROM FE-OXIDE CU-AU SYSTEMS IN THE OLYMPIC CU-AU PROVINCE, SOUTH AUSTRALIA

Alkis Kontonikas-Charos[1], Cristiana L. Ciobanu[2], Nigel J. Cook[2], Kathy Ehrig[3], Sasha Krneta[1], Vadim S. Kamenetsky[4]

[1]*School of Physical Sciences, The University of Adelaide, Adelaide, SA, 5005, Australia*

[2]*School of Chemical Engineering, The University of Adelaide, Adelaide, SA, 5005, Australia*

[3]*BHP Billiton Olympic Dam, Adelaide, SA, 5000, Australia*

[4]*School of Physical Sciences, University of Tasmania, Hobart, TAS, 7001, Australia*

Article submitted for publication in Mineralogy and Petrology 16 April 2017

Accepted 10 August, 2017

Statement of Authorship

Title of Paper	Rare earth element geochemistry of feldspars: Examples from Fe-oxide Cu-Au systems in the Olympic Cu-Au Province, South Australia
Publication Status	☐ Published ☐ Accepted for Publication ☑ Submitted for Publication ☐ Unpublished and Unsubmitted w ork w ritten in manuscript style
Publication Details	Kontonikas-Charos, A., Ciobanu, C.L., Cook, N.J., Ehrig, K., Krneta, S. and Kamenetsky, V.S. (in review) Rare earth element geochemistry of feldspars: Examples from Fe-oxide Cu-Au systems in the Olympic Cu-Au Province, South Australia. Mineralogy and Petrology.

Principal Author

Name of Principal Author (Candidate)	Alkis Kontonikas-Charos		
Contribution to the Paper	Performed analytical work, carried out data processing and interpretation, oversaw development of work and wrote manuscript.		
Overall percentage (%)	85		
Certification:	This paper reports on original research I conducted during the period of my Higher Degree by Research candidature and is not subject to any obligations or contractual agreements with a third party that would constrain its inclusion in this thesis. I am the primary author of this paper.		
Signature		Date	11/07/17

Co-Author Contributions

By signing the Statement of Authorship, each author certifies that:

i. the candidate's stated contribution to the publication is accurate (as detailed above);

ii. permission is granted for the candidate in include the publication in the thesis; and

iii. the sum of all co-author contributions is equal to 100% less the candidate's stated contribution.

Name of Co-Author	Cristiana L. Ciobanu		
Contribution to the Paper	Helped define direction of research, supervised development of work, assisted with data interpretation and contributed to manuscript preparation.		
Overall percentage (%)	7		
Signature		Date	10 July 2017

Name of Co-Author	Nigel J. Cook		
Contribution to the Paper	Helped define direction of research, supervised development of work, assisted with data interpretation and contributed to manuscript preparation.		
Overall percentage (%)	4		
Signature		Date	10/7/17

Name of Co-Author	Kathy Ehrig		
Contribution to the Paper	Provided sample material and helped to evaluate and edit manuscript.		
Overall percentage (%)	2		
Signature		Date	10 July 2017

Name of Co-Author	Sasha Krneta		
Contribution to the Paper	Helped to evaluate and edit manuscript.		
Overall percentage (%)	1		
Signature		Date	11/7/2017

Name of Co-Author	Vadim S. Kamenetsky		
Contribution to the Paper	Helped to evaluate and edit manuscript.		
Overall percentage (%)	1		
Signature		Date	11/7/17

Abstract

Rare earth element (REE) fractionation patterns in feldspars are reported from Olympic Dam (including Wirrda Well and Phillip's Ridge) and Cape Donington (Port Lincoln), for comparison with two other igneous-metamorphic regions within the Gawler Craton: Moonta-Wallaroo and Hillside. The case studies were selected as they represent ~1590 Ma Hiltaba Suite and/or ~1845-1810 Ma Donington Suite granites, and, aside from Cape Donington, are associated with Mesoproterozoic iron-oxide copper gold (IOCG)-type mineralization. Both plagioclase and alkali feldspar were analyzed within selected samples with the purpose of constraining and linking changes in REE concentrations and fractionation patterns in feldspars to local and whole-rock textures and geochemistry. Two unique, reproducible fractionation trends were obtained for igneous plagioclase and alkali feldspars, distinguished from one another by light rare earth element enrichment, Eu-anomalies and degrees of fractionation (e.g. La/Lu slopes). Results for hydrothermal albite and K-feldspar indicate that REE concentrations and fractionation patterns are generally inherited from igneous predecessors, however in some instances, significant amounts of REE appear to have been lost to the fluid. These results may have critical implications for the formation of world-class IOCG systems, in which widespread alkali metasomatism plays a key role by altering the physical and chemical properties of the host rocks during early stages of IOCG formation, as well as trapping trace elements (including REE).

5.1 Introduction

The application of rare earth element (REE) geochemistry to support petrogenetic models for igneous rocks has long been established (e.g., Schilling and Winchester, 1967; Gast, 1968). The petrological applicability of such studies is based on the systematic decrease in atomic radius with increased atomic number within the lanthanide series, principles outlined by Goldschmidt (1937). More recent work has shown the anomalous behaviour of certain multivalent REEs (e.g. Ce, Eu), relative to adjacent lanthanides, in aqueous solutions due to variations in pH, temperature, salinity, redox conditions and fluid composition (e.g., Bau, 1991; Haas et al., 1995; Migdisov and Williams-Jones, 2014; Migdisov et al., 2016). The chondrite-normalized REE fractionation patterns, and systematic changes thereof, in individual component minerals can thus be used as geochemical tracers in hydrothermal systems (e.g., Smith et al., 2004; Brugger et al., 2008). Petrogenetic interpretation of such patterns hinge strongly on an adequate understanding of the geological and geochemical characteristics of rocks hosting REE-bearing minerals.

Recent studies (Ismail et al., 2014; Kontonikas-Charos et al., 2014, 2017, in press) have combined microanalysis with observations at the macro- to nanoscopic scales to document changes in the textures and geochemistry of feldspars from fresh to altered and mineralized host rocks in different settings within the Olympic Cu-Au Province. The province extends over 500 km along the eastern margin of the Gawler Craton, South Australia, and encompasses numerous Fe-oxide Cu-Au (IOCG) deposits and prospects (e.g., Hayward and Skirrow, 2010). These studies have highlighted the applicability of feldspars as geochemical tracers of various alteration stages within giant magmatic-hydrothermal systems, for understanding the effects which *in-situ* feldspar replacement reactions have on the host rocks, and the implications which these reactions carry for ore formation.

This study aims to constrain variation in REE + Y (hereafter REY) fractionation using chondrite-normalized patterns for both igneous and hydrothermal feldspars from Olympic Dam – including the adjacent prospects of Wirrda Well and Phillip's Ridge; to compare and contrast with existing data from two other IOCG deposits within the Olympic Cu-Au Province: Moonta-Wallaroo and Hillside (Fig. 1). In addition, feldspar REY-fractionation patterns are also obtained from pre-Hiltaba Suite lithologies located at Cape Donington (Lincoln National Park) in the southernmost Eyre Peninsula, for a comparison with a non-mineralized terrane. Subsequent interpretations provide insight as to whether certain REY fractionation patterns and anomalies are diagnostic of particular alteration stages within the case studies and IOCG systems.

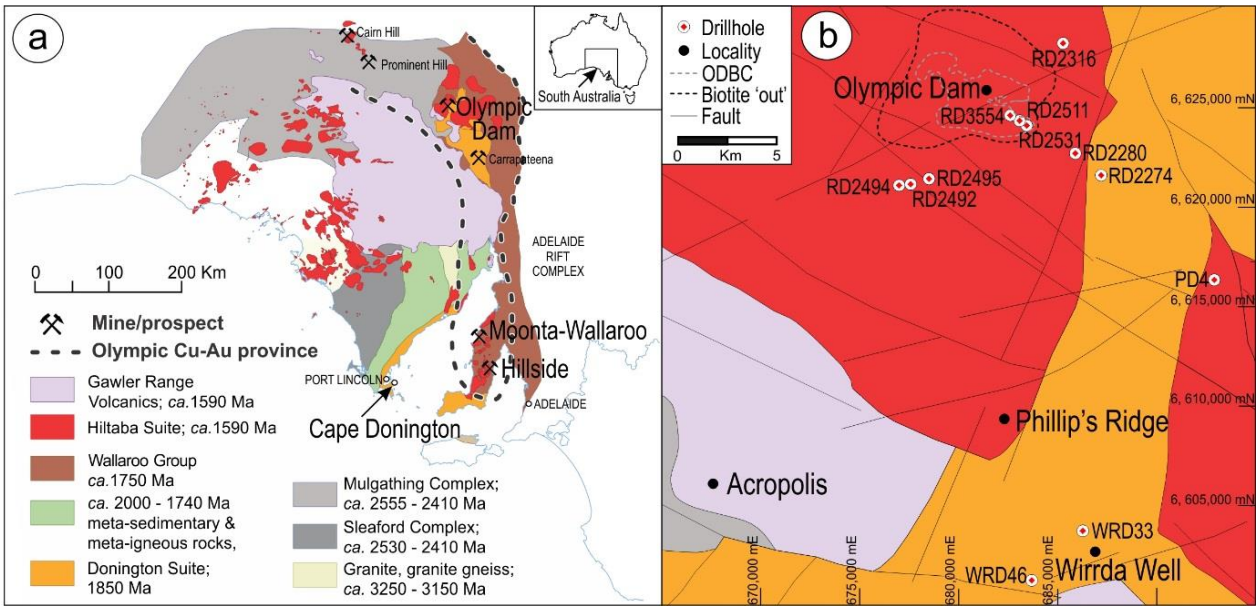

Figure 1: (a) Simplified regional geological map outlining various lithologies and deposits/prospects within the Gawler Craton and Olympic Cu-Au Province, South Australia. Larger font indicates case studies. Modified from Reid and Fabris (2015). (b) Geological sketch map of bedrock in the Olympic Dam region displaying sampled drillholes and other prospects and localities within the area

5.2 Background

5.2.1 Feldspar nomenclature

Alkali feldspars form part of a ternary solid solution series involving three end-member components: albite (Ab) - $NaAlSi_3O_8$, orthoclase (Or) - $KAlSi_3O_8$ and anorthite (An) - $CaAl_2Si_2O_8$. Celsian (Csn), $BaAl_2Si_2O_8$, may be an additional component. Below magmatic temperatures, alkali feldspars will undergo solid-state exsolution during which alkali ions diffuse through the aluminosilicate crystal lattice, resulting in the formation of two separate feldspar phases (Or-rich and Ab-rich phase), often termed perthite. The present study deals with certain feldspar intergrowth textures that are defined as follows. A perthite refers to a texture comprising Ab-rich lamellae enclosed within the Or-rich phase, where the bulk composition is a mixture of both components (Or>Ab). Dependent on the scale of lamellae, the prefix micro- is added for optically visible intergrowths (e.g., on a petrographic microscope), whereas intergrowths below 1 μm in size are termed cryptoperthites. Deuteric coarsening refers to the recrystallization of alkali feldspar via the circulation of post-magmatic fluids. Albitization is one of the most common hydrothermal aluminosilicate reactions in the Earth's upper crust (Perez and Boles, 2005) and involves replacement of pre-existing feldspar by Na-rich feldspar, which may be associated with scapolitization, saussuritization, sericitization and K-feldspathization (e.g., Garcia et al., 1996; Conor et al., 2010; Morad et al., 2010). For a comprehensive summary of alkali feldspar nomenclature, the reader is referred to Parsons et al. (2005).

5.2.2 Trace element geochemistry and feldspar replacement reactions

The ideal MT_4O_8 feldspar chemical formula assumes all atomic sites are occupied within the ionic model for crystal structure; *T* sites are occupied by small, highly-charged cations (including high field strength elements - HFSE), whereas *M* sites are occupied by large, weakly

charged cations (large ion lithophile elements – LILE) (e.g., Smith, 1974). Deviations from this formula may be explained by unit cell modifications, such as site vacancies and/or trace element site affinities. Principles for element substitution and partitioning are dependent upon similarities in ionic radii and charge between elements (e.g., Goldschmidt, 1937). As such, in feldspars, any cations entering the *T* site must have ionic radii small enough to enter the tetrahedral interstices, and be highly charged to balance the oxygen anions, whereas cations entering the *M* site must be large enough to avoid any distortions within the feldspar lattice, and weakly charged to maintain overall charge balance (Smith, 1974). Major element partitioning generally obeys these conditions, however, for minor and trace elements, a coupled substitution mechanism is required which allows for relative expansion and contraction of the feldspar framework while maintaining charge balance between the *M* and *T* sites.

A variety of chemical substitutions have been established in both natural and synthesized feldspars. Experiments on natural feldspars have shown that Fe^{3+} and Ti^{4+} can substitute for Al^{3+}, while Rb^{2+}, Cs^{2+} and Ba^{2+} for K^{+} and Na^{+}, and Mg^{2+}, Fe^{2+}, Sr^{2+} and Mn^{2+} for Ca^{2+} in plagioclase (Papike, 1988; Pun et al., 1997). In addition, numerous feldspar synthesis experiments indicate that B^{3+}, P^{5+}, Fe^{3+}, Ga^{3+} and Ge^{4+} are able to enter the *T* site (Fleet, 1988; Bychkov et al., 1989; London et al., 1990), and Rb^{2+}, Sr^{2+}, Ba^{2+}, Tl^{+}, Pb^{2+}, Eu^{2+} and REE^{3+} prefer the *M* site (D'Arco and Piriou, 1989; Kneip and Liebau, 1994) based on couple substitutions resulting from ionic radii similarities. In addition, Stix and Gorton (1990) suggest that light rare earth elements (LREE), ranging from La-Gd, are more effective than heavy rare earth elements (HREE), including Tb-Lu, Y and Sc, in entering the *M* sites of the feldspar crystal lattice. Based on such synthesis studies, Bindeman and Davis (2000) summarized possible substitution mechanisms for REE in plagioclase based on substitution for Ca:

(1) $2Ca^{2+} = REE^{3+} + Na^{+}$

(2) $3Ca^{2+} = 2REE^{3+} + \text{vacancy}$

Equation (1) is deemed as feasible due to the solid-solution produced between REE and Ca in plagioclase, whereas the feasibility of equation (2) is complimented by work done on synthesized REE-bearing feldspar, in which site vacancies were identified (Kimata, 1988; Kneip and Liebau, 1994).

Fractionation of REE within minerals follows the same principles as for other trace elements, and similarly, their distributions are affected by phase composition, temperature, pressure and fO_2 (see Henderson, 1984). Moreover, the solubility of REE have been highlighted in more recent work (e.g., Haas et al., 1995; Migdisov and Williams-Jones, 2014; Migdisov et al., 2016), indicating that certain aqueous REE-complexes are sensitive to pH, temperature, salinity, redox conditions and fluid composition. Thus, hydrothermal processes can influence partitioning of REE from one another (e.g., Bau, 1991; Lottermoser, 1992; Smith et al., 2004). Europium and Ce can change oxidation states to Eu^{2+} (Towell et al., 1965) and Ce^{4+} (Elderfield and Greaves, 1982), respectively, causing decoupling relative to other REE and creating measurable anomalies. The anomalous behavior of Y relative to lanthanide REE, notably Dy and Ho (Bau and Dulski, 1995), has also shown promise as a petrogenetic indicator in hydrothermal systems (e.g., Smith et al., 2004). The REY fractionation patterns for minerals from magmatic-hydrothermal systems can thus be discriminated by variations in Eu-, Ce- and Y-anomalies, and changes in REY-slopes (LREE/HREE ratio). Previous studies have highlighted the applicability of REY fractionation patterns in feldspars (e.g., Kontonikas-Charos et al., 2014) to visually represent alteration stages in magmatic-hydrothermal systems, as well as from resistate minerals such as apatite (Krneta et al., 2016) and zircon (Belousova et al., 2006).

Albitization may be spatially and temporally associated with iron-oxide copper-gold (IOCG) mineralization (Barton, 2014; and references therein). This type of replacement reaction couples dissolution of a pre-existing mineral with the rate of precipitation of new

products at the site of reaction (coupled dissolution-reprecipitation reaction – CDRR; Wang et al., 1995; Putnis, 2002). In the case of the albitization of plagioclase, the reaction involves coupled substitution of (Ca^{2+}+Al^{3+}) by (Na^{+}+Si^{4+}). CDRR can play an effective role in the redistribution of minor/trace elements during fluid-rock interaction. The experiments of Hövelmann et al. (2010) demonstrate that albitization of plagioclase likely proceeds via the CDRR mechanism, and is accompanied by a remobilization of REE and other trace elements from the precursor plagioclase, including Mg, Ti, Fe, Sr, Ba, Rb and Pb. Hövelmann et al. (2010) also found that released REE are dissolved in the fluid and potentially transported away from the site of dissolution to form discrete REE-minerals elsewhere within the system.

5.2.3 Sample suite geology

The **Olympic Dam Cu-U-Au-Ag deposit** (OD; 10,400 Mt tonnes @ 0.77 % Cu, 250 ppm U_3O_8, 0.32 ppm Au, 1 ppm Ag; BHP Billiton, 2016) is located in the north of the Olympic Cu-Au Province. Rocks of the Hutchison Group (~2000-1860 Ma), Donington Suite (~1845-1810 Ma) and Wallaroo Group equivalents (~1750 Ma) form the Paleoproterozoic basement of the Olympic Dam region (Creaser, 1989; Ferris et al., 2002; Jagodzinski, 2005). These units are unconformably overlain and intruded by felsic and mafic-ultramafic lithologies of the Mesoproterozoic Hiltaba Suite (HS) and Gawler Range Volcanics (GRV); both are the products of a crustal-scale magmatic event at ~1590 Ma, interpreted as a silicic large igneous province, covering more than 25,000 km^2 of the central part of the Gawler Craton (e.g., Skirrow et al., 2007; McPhie et al., 2008). The HS intrusives are grouped together within the larger Burgoyne batholith, which makes up the basement of the northern Stuart Shelf (Creaser, 1989). The batholith is separated into two granitoid suites: the Wirrda Suite and the White Dam Suite, both of which comprise rocks varying from quartz monzodiorite to granite (Creaser, 1989). The Roxby Downs Granite (RDG) and Horn Ridge Quartz Monzonite (HRQM) are affiliated

to the Wirrda Suite, which is situated on the western side of the Burgoyne batholith (Creaser, 1996).

The GRV are comprised of a lower sequence, 0.5-3 km-thick, ranging in composition from basalt to rhyolite and minor volcaniclastic facies (e.g., ignimbrites), while the upper GRV succession is 250-300 m thick, of primarily rhyolitic and dacitic lava units (McPhie et al., 2008). The GRV is also intruded by porphyritic rhyolitic dykes and granites belonging to the HS (McPhie et al., 2008). In addition to Mesoproterozoic mafic-ultramafic units, weakly altered basaltic to doleritic dykes of the Gairdner Dyke Swarm (U-Pb apatite dated at 825±18 Ma; Huang et al., 2015) are also observed within the Olympic Dam area.

Deposition of Cu-Au-U mineralization at Olympic Dam has been considered contemporaneous with the ~1590 Ma event, based on dating of hydrothermal minerals within the ODBC and other prospects (e.g., Johnson and Cross, 1995; Jagodzinski, 2005; Skirrow et al., 2007; Ciobanu et al., 2013; Courtney-Davies et al., 2016). Hydrothermal breccias of the Olympic Dam Breccia Complex (ODBC) host Cu-U-Au-Ag mineralization and are contained within the RDG, which is unconformably overlain by Neoproterozoic to Cambrian sediments of the Stuart Shelf (Reeve et al., 1990). Compositions and textures within the ODBC are gradational, and comprise a continuum from sericite-hematite-altered granite through mineralized, hematite-rich breccias to barren hematite-quartz breccias in the deposit centre (Ehrig et al., 2012). Degree of alteration and intensity of brecciation increase from the edges of the ODBC towards the deposit centre (Haynes et al., 1995; Ehrig et al., 2012). The impact of increasing alteration on feldspar compositions and textures has been detailed in Mauger et al. (2016) and Kontonikas-Charos et al. (2017).

Found within a large concentric gravity and magnetic anomaly, the **Wirrda Well** prospect is located approximately 20 km SSE of Olympic Dam. Mineralization is primarily hosted within a sheared, variably mylonized, K-feldspar megacrystic Donington Suite granite and

deformed mafic dykes of the same age (Ehrig, 2013). A significant portion of the brecciation and mineralization is concentrated along the contacts of the intrusive rocks. In addition, volcanic sequences, attributed to the GRV, occur within a faulted block of possible post-mineralization origin within the northern zone.

The **Phillip's Ridge** prospect is located 17 Km SE of Olympic Dam, near the contact between the HS and Donington Suite granite. Quartz monzodiorite is the dominant lithology in the area, and is interpreted as the equivalent reported in Granite Suite #3 in Creaser (1989).

The **Moonta-Wallaroo region**, located in the north-west of the Yorke Peninsula, contains Cu-Au mineralization hosted within felsic porphyry rocks associated with K-Fe metasomatism (biotite ± K-feldspar ± magnetite) (Morales-Ruano et al., 2002; Conor et al., 2010). The region is an example of an IOCG-hosting terrane in which regional-scale alkali alteration is recognized in different lithologies (e.g., Cowley et al., 2003; Conor et al., 2010; Kontonikas-Charos et al., 2014). Copper-Au mineralization is hosted within the Moonta Porphyry Member; a variably altered rhyolite-rhyodacite (U-Pb zircon age 1737±5 Ma; Fanning et al., 1988), and the Doora Member; a schistose, Fe-rich unit with varying hornfels, amphibolite and silicate facies (Parker, 1993; Cowley et al., 2003). Both units are constituents of the ~1750 Ma Wallaroo Group; a suite of siltstone-dominated metasedimentary, felsic and mafic metavolcanic rock packages. The Wallaroo Group has been intruded by, and subsequently altered by fluids related to the Arthurton and Tickera granitoids (variable monzogranites, quartz monzonites and leucotonalites) and the Curramulka Gabbronorite (metamorphosed to amphibolite facies), all affiliated with the younger, ~1590 Ma HS, widespread throughout the Gawler Craton (Cowley et al., 2003). Both the Arthurton and Tickera granitoids show evidence of alkali alteration, in this case albitization (e.g., Kontonikas-Charos et al., 2014). The Oorlano Metasomatite (a skarn-like Fe-rich metasomatite containing calc-silicates and feldspars) is found along the boundary of the Tickera Granite and Wallaroo Group, and is interpreted to reflect

metasomatism related to the intrusion of the HS in the Moonta Wallaroo region (Cowley et al., 2003). Regional-scale alkali alteration in the Moonta-Wallaroo area has been postulated to be sourced from evaporitic sediments, which have been observed in various parts of the Wallaroo Group (Conor et al., 2010).

Local geology around the **Hillside Cu-Au deposit**, located within the N-S-striking Pine Point Fault Zone along the eastern coast of the Yorke Peninsula, South Australia, is defined by a sequence of highly deformed metasediments of the ~1750 Ma Wallaroo Group intruded by granites, micro- and porphyritic gabbros and gabbro-diorites, presumed to be part of the HS (Conor et al., 2010). Structurally, Cu-Au-(U) mineralization is hosted within steeply-dipping, N-S trending skarn and associated breccia bodies of varying dimensions (Conor et al., 2010). As in the Moonta-Wallaroo area, the magnetite-dominant mineralization and skarn-type alteration at Hillside (Conor et al., 2010; Ismail et al., 2014) is thought to represent hydrothermal activity at a relatively deep crustal level, thus contrasting with shallower, brecciated hematite-sericite-dominant mineralization at Olympic Dam. Evidence of early high temperature potassic alteration, expressed as a K-feldspar + biotite + magnetite ± bornite assemblage, is commonly displayed in gabbroic rocks from the Hillside area (Conor et al., 2010).

The basement suite at **Cape Donington** (Eyre Peninsula) comprises Archean orthogneisses, granite, granodiorites, as well as felsic and mafic volcanic rocks of the Archean-Paleoproterozoic Sleaford complex (2560-2420 Ma; Fanning, 2002; Jagodzinski et al., 2012). Following deposition of the Hutchison Group metasediments (~2000-1850 Ma), Donington Suite intrusive rocks (varying in composition from gabbronorite to leucogranite) were emplaced around 1850 Ma (U-Pb zircon ages; Fanning, 1997). Following emplacement of the Donington Suite, transpressional convergence during the Kimban Orogeny (~1740-1700 Ma) resulted in regional metamorphism at amphibolite to granulite facies, and associated syn-

metamorphic deformation of the Archean-Proterozoic crust, as well as the formation of the Kalinjala Mylonite Zone (KMZ), which separates the Donington Suite from the Hutchison Group (Ferris et al., 2002). Local geology at Cape Donington, to the east of the KMZ, consists of outcropping coarse-grained, porphyritic, orthopyroxene-bearing granitoids (attributed to the Donington Suite), crosscutting metabasaltic and doleritic dykes, and biotite-hornblende-quartz-feldspathic gneisses (Mortimer, 1984).

5.3 Approach and Methodology

A geochemical study was undertaken on representative sample suites from the case studies (Figure 1). Each was selected due to association with the HS and a regional-scale spatial association with IOCG-type mineralization. The Cape Donington suite represents an exception to this, and as a pre-Hiltaba example, was selected for purposes of comparison. All samples from were obtained from drillcore which had been previously assayed. Initial mineral identification and sample characterization was made on polished thin sections and polished blocks by optical microscopy.

A FEI Quanta 450 scanning electron microscope (SEM) with energy-dispersive X-ray spectrometry and back-scatter electron (BSE) imaging capabilities (Adelaide Microscopy, University of Adelaide) was used at an accelerating voltage of 20 kV and beam current of 10 nA. Quantitative compositions of feldspars within representative samples were determined using a Cameca SX-Five Electron Probe Microanalyzer (EPMA).

Laser-Ablation Inductively-Coupled Mass Spectrometry (LA-ICP-MS) was used on selected samples to provide quantitative trace element data (as spot analyses) for plagioclase and alkali feldspars. This was performed on a Resonetics M-50-LR 193-nm Excimer laser microprobe coupled to an Agilent 7700cx Quadrupole ICP-MS at Adelaide Microscopy, University of Adelaide. A relatively large spot size of 50 µm was used for all analyses in order to generate increased counts during ablation. In addition, sweep times on heavier elements,

including REE, were increased to reduce signal disturbance. Details of the analytical methodology, calibration and accuracy/precision are given in Chapter 2. Minor and trace element LA-ICP-MS data are provided in Chapter 8 (Supplementary Material B).

5.4 Results

5.4.1 Sample suites

The sample suites are representative of various igneous intrusive rocks from each selected case study. Table 1 provides details, mineralogy and important features of case studies, while Table 2 highlights feldspar geochemistry, textures and relationships relevant for the present work.

The Olympic Dam sample suite comprises least-altered (Fig. 2a), sericite-hematite-altered (Fig. 2b) and mineralized ~1593 ± 1.2 Ma Roxby Downs Granite (RDG) (Jagodzinski, 2014) of the Hiltaba Suite (HS) from various drillholes proximal and distal to the Olympic Dam Breccia Complex (ODBC), including the strongly altered Horn Ridge Quartz Monzonite (HRQM – Fig. 2c). In addition, the Olympic Dam sample suite includes an albite-epidote altered quartz monzodiorite (Fig. 2d) representing a more primitive HS member from Phillip's Ridge, 17 km SE of Olympic Dam, and altered ~1850 Ma Donington Suite Granite (Fig. 2e) from the Wirrda Well prospect, 25 km SE of Olympic Dam. The Cape Donington sample suite consists of variably altered Donington Suite granite (Fig. 2f) and foliated leucogranite/aplite of the Donington Suite. Existing data from Moonta-Wallaroo was obtained from the Arthurton and Tickera Granites (HS members), as well as an undefined, albitized HS granite, while the Hillside data is from the Hillside granite, another HS member.

Summaries of granite petrography have been previously documented for Olympic Dam (Creaser, 1989; Ehrig et al., 2012; Kontonikas-Charos et al., 2015, 2017), Hillside (Conor et al., 2010; Ismail et al., 2014) and Moonta-Wallaroo (Conor et al., 2010; Kontonikas-Charos et al., 2014), respectively.

Table 1: Sample suite lithology and mineralogy

Locality	Lithology	Drillholes or ID	Rock type and texture	Main mineralogy
Olympic Dam (OD)	Least-altered Roxby Downs Granite	RD2492, RD2494, RD2495, RD2280, RD2274	Equigranular-porphyritic, medium- to coarse-grained granite	Alkali feldspar (40%), plagioclase (25%), quartz (20%), amphibole and biotite (10%), and accessories (5%) - zircon, apatite, magnetite, Fe-Ti-minerals (ilmenite, titanite), REE-U-minerals (synchysite, uraninite, uranothorite).
	Sericite-hematite-altered Roxby Downs Granite	RD2280, RD2531, RD2511, RD2316, RD3554	Equigranular-porphyritic, medium- to coarse-grained granite	K-feldspar (35%), sericite (25%), quartz (20%), chlorite (10%), variable amounts (up to 10%) of magnetite, hematite, rutile, carbonates (calcite, siderite, ankerite), disseminated sulphides (chalcopyrite, pyrite, sphalerite, galena, molybdenite), REE-U-minerals (synchysite, bastnäsite, uraninite, florencite). Trace amounts of albite.
	Mineralized Roxby Downs Granite	RD2316, RD3554	Coarse-grained, brecciated granite	K-feldspar (25%), sericite (25%), quartz (25%), variable amounts (up to 25%) of magnetite, hematite, chlorite, rutile, carbonates (calcite, siderite, ankerite), sulphides (chalcopyrite, bornite, chalcocite, pyrite, sphalerite, galena, molybdenite), REE-U minerals (bastnäsite, uranothorite, brannerite, coffinite, florencite). Albite preserved at depth.
	Horn Ridge Quartz Monzonite	RD2274	Medium- to coarse-grained, quartz monzonite	Alkali feldspar (45%), plagioclase (30%), quartz (10%), chlorite replacing mafic silicates (10%) and variable amounts (5%) of, magnetite, hematite, ilmenite, rutile, sericite, apatite, zircon.
Wirrda Well (WW)	Donington Suite granite	WRD46	Coarse-grained, porphyritic granite	Alkali feldspar (50%), plagioclase (30%), quartz (15%), biotite (7.5%), variable amounts (2.5%) of chlorite, hematite, sericite, apatite, zircon.
	Donington Suite granite	WRD33	Coarse-grained, porphyritic granite	Alkali feldspar (60%), quartz (20%), sericite (20%), variable amounts (10%) of rutile, hematite, apatite, sulphides (pyrite, chalcopyrite), siderite.
Phillip's Ridge (PD)	Quartz Monzodiorite	PD4	Quartz monzodiorite	Plagioclase (50%), alkali feldspar (20%), quartz (10%), biotite and amphibole (15%) and accessory minerals (5%) - magnetite, hematite, rutile, ilmenite, titanite, epidote, allanite, zircon, apatite, uranothorite, galena, pyrite.
Cape Donington (CD)	Donington Suite granite	PL11, PL13	Coarse-grained, porphyritic granite	Alkali feldspar (35%), plagioclase (35%), quartz (15%) biotite + amphibole (10%) and accessory minerals (5%): ilmenite, rutile, magnetite, zircon, apatite.
	Leucogranite/aplite	PL6, PL12	Foliated leucogranite/aplite	Alkali feldspar (40%), quartz (37.5%), plagioclase (20%) and accessory minerals (2.5%) - ilmenite, hematite, rutile, zircon.

Table 2: Feldspar textural relationships and chemistry

Mineral	Phase/texture	Description	Composition	Textural relationships	Lithology
Plagioclase	Andesine	Euhedral phenocrysts and occasionally as small subgrain aggregates rimming larger grains (only from Cape Donington).	~An_{31-38}	Phenocrysts are variably altered to albite and/or sericite. Rare, rapakivi rims recognised in Donington Suite granite (Cape Donington).	Donington Suite Granite (WRD46, PL11, PL13), Quartz Monzodiorite (PD4)
	Andesine-oligoclase	Euhedral phenocrysts typically displaying calcic-sodic core to rim compositional zoning.	~An_{25-40}	Phenocrysts are intensely altered and overprinted by porous albite and porous K-feldspar.	Least-altered Roxby Downs Granite (RD2492, 4, 5), Horn Ridge Quartz Monzonite (RD2274)
	Oligoclase	Occurs as free, euhedral to subhedral grains or rim overgrowths.	~An_{12-20}	Forms rims on pre-existing plagioclase and alkali feldspars (only Roxby Downs Granite).	Least-altered Roxby Downs Granite (RD2274, RD2280), leucogranite/aplite (PL6, PL12)
	Albite ± sericite ± epidote ± Ba-rich K-feldspar	Highly porous, fine-grained albite associated with various inclusions. May also occur as pure homogeneous albite devoid of inclusions.	~$Ab_{97}An_1Or_2$	Crosscuts and partially replaces all pre-existing alkali and plagioclase feldspars. Pure albite forms rims on plagioclase, and partially replaces mafic silicates.	All lithologies
Alkali feldspar	Cryptoperthite	Fully coherent intergrowth of sub-µm sized Ab-rich lamellae in Or-rich feldspar.	~$Or_{42-74}Ab_{25-55}An_{1-3}$	Preserved regions within alkali feldspar grains. Typically overprinted by patch perthite and porous K-feldspar.	Least-altered Roxby Downs Granite (RD2492, 4, 5, RD2274, RD2280), Horn Ridge Quartz Monzonite (RD2274)
	Microperthite	Regular semi-coherent Ab-rich lamellae in Or-rich feldspar. Optically visible lamellae.	~$Or_{76-93}Ab_{7-24}An_1$	Often found in association with cryptoperthite. May contain disseminated inclusions of sub-µm sized ilmenite or hematite.	Horn Ridge Quartz Monzonite (RD2274), Donington Suite granite (WRD-46, PL11, PL13)
	Patch perthite	Highly porous, incoherent clusters of Ab- and Or-rich subgrains.	~$Ab_{84}An_{14}Or_2$ ~$Or_{85}Ab_{14}An_1$	Forms mosaics or veins which crosscut crypto- and microperthite.	Least-altered Roxby Downs Granite (RD2492, 4, 5, RD2274, RD2280), Horn Ridge Quartz Monzonite (RD2274), Quartz Monzodiorite (PD4)
	Porous K-feldspar	Highly porous, variably red-stained K-feldspar.	~$Or_{98}Ab_2$	Crosscuts and partially replaces all pre-existing alkali and plagioclase feldspars.	All lithologies

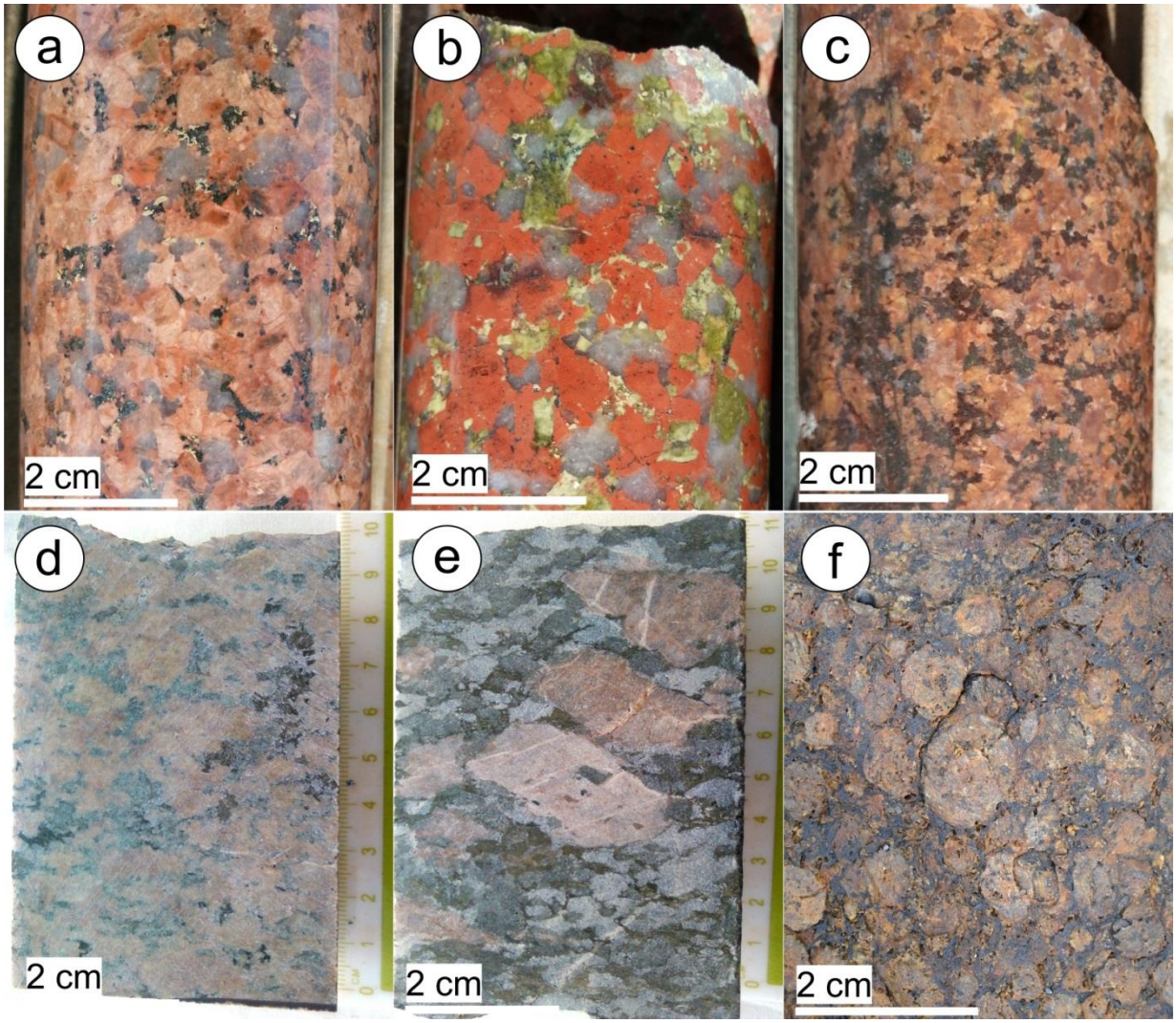

Figure 2: Hand specimen photographs displaying differences between sample colouration and textures at the macroscale. (a) Least-altered RDG. Note the pink colouration of feldspars and preservation of mafic minerals. (b) Sericite-hematite-altered RDG. Note the change from pink to red in feldspars and green/yellow of sericite. (c) HRQM. Note relatively greater abundance of mafic minerals as well as minor red staining of feldspars. (d) Phillip's Ridge quartz monzodiorite. The rock displays zones of pink reflecting sodic-calcic alteration, otherwise similar in appearance to the HRQM. (e) Donington Suite granite from Wirrda Well. This is very coarse-grained, contains large angular K-feldspar phenocrysts. (f) Donington Suite granite from Cape Donington. Coarse grained, rounded K-feldspar phenocrysts within a fine-grained silicate matrix.

5.4.2 Petrography

Important petrographic features of case studies, for which little or no previously published data is available, are briefly summarized and illustrated below. Mean electron probe microanalyses for plagioclase and alkali feldspars from the samples described below are given in Table 3.

Phillip's Ridge

The quartz monzodiorite intersected in drillhole PD-4 at Phillip's Ridge is medium- to coarse-grained, equigranular and variably altered. Plagioclase is the dominant mineral and forms coarse (>3 mm-sized) euhedral crystals, which have been partially recrystallized into a fine-grained intergrowth texture consisting of albite + sericite + epidote + Ba-rich K-feldspar (Fig. 3a). In addition, a homogeneous albite rim (~1-10 μm thick) is often visible in plagioclase which is adjacent to alkali feldspar grains. Alkali feldspar occurs as euhedral to subhedral grains displaying both cryptoperthitic textures (Fig. 3b), which have been overprinted by porous, near end-member albite and K-feldspar. Dusty sub-μm-sized hematite inclusions are disseminated throughout alkali feldspar grains. Quartz forms interstitially, often at the boundaries between plagioclase, alkali feldspar and mafic silicate minerals, but is also observed as a by-product of mafic silicate alteration. Hornblende and biotite occur as large (>2 mm-sized) euhedral to subhedral grains within mineral aggregates, often containing accessory phases. Hornblende displays irregular chemical zonation and is partially altered to actinolite + epidote + quartz, whereas biotite is partially replaced by chlorite + epidote (± allanite) + garnet + quartz ± K-feldspar ± albite (Fig. 3c, d - See Table 4 for epidote and garnet compositional data). Small (<10 μm) relicts of augite are occasionally preserved within hornblende.

Apatite occurs as large, equant to acicular grains (>1 mm-sized), which are often fractured and display oscillatory zoning and may contain monazite inclusions within the core. Moreover, apatite also forms small (<100 μm-sized), subhedral, variably porous crystals within mafic silicate phases, and is occasionally replaced by epidote. Magnetite contains trellis exsolutions

of ilmenite and shows evidence of replacement by hematite. Ilmenite also occurs as subhedral grains which, along with the trellis exsolutions, are observed to breakdown to intricate symplectites of rutile + hematite. Allanite is common throughout, forming as interstitial subhedral grains, with complex zonation patterns. It is also found within albitized plagioclase. Uranothorite often displays complex breakdown textures, and is associated with mafic silicates.

Wirrda Well

Donington Suite granite from the Wirrda Well prospect is coarse-grained, porphyritic and variably altered. Samples from drillhole WRD-46 are relatively fresh in comparison to those from WRD-33. Plagioclase and alkali feldspar are the dominant phases and both occur as >5 mm-sized phenocrysts with varying degrees of alteration. Plagioclase (~An_{25-40}) displays typical calcic core to sodic rim compositional zonation and is partially altered to K-feldspar + sericite ± albite ± chlorite in drillhole WRD-46 (Fig. 3e, f), and completely altered to K-feldspar + sericite ± dusty sub-µm-sized hematite inclusions in drillhole WRD-33. Myrmekite is observed in rims of plagioclase at some grain boundaries adjacent to alkali feldspar (e.g., Fig. 3e). The plagioclase component of this texture is altered to K-feldspar + sericite in samples from drillhole WRD33. Alkali feldspar displays microperthitic textures with irregular trails and zones of microporosity. Biotite is the dominant mafic silicate preserved in drillhole WRD-46, occurring as >1 mm-sized polycrystalline aggregates that have been variably altered to chlorite ± hematite ± rutile + quartz. In addition, oscillatory zoned apatite may occur as inclusions within biotite. In contrast, no plagioclase or mafic silicates are preserved within samples from drillhole WRD-33. The microperthitic texture of alkali feldspar has been obliterated by irregular, porous K-feldspar, which has been partially altered to sericite and chlorite. Hematite, rutile and apatite form clusters within zones of sericite and chlorite. In addition, fracturing and veining is common in altered Donington Suite granite, which may also contain variable amounts of Cu-Fe-sulphides such as chalcopyrite.

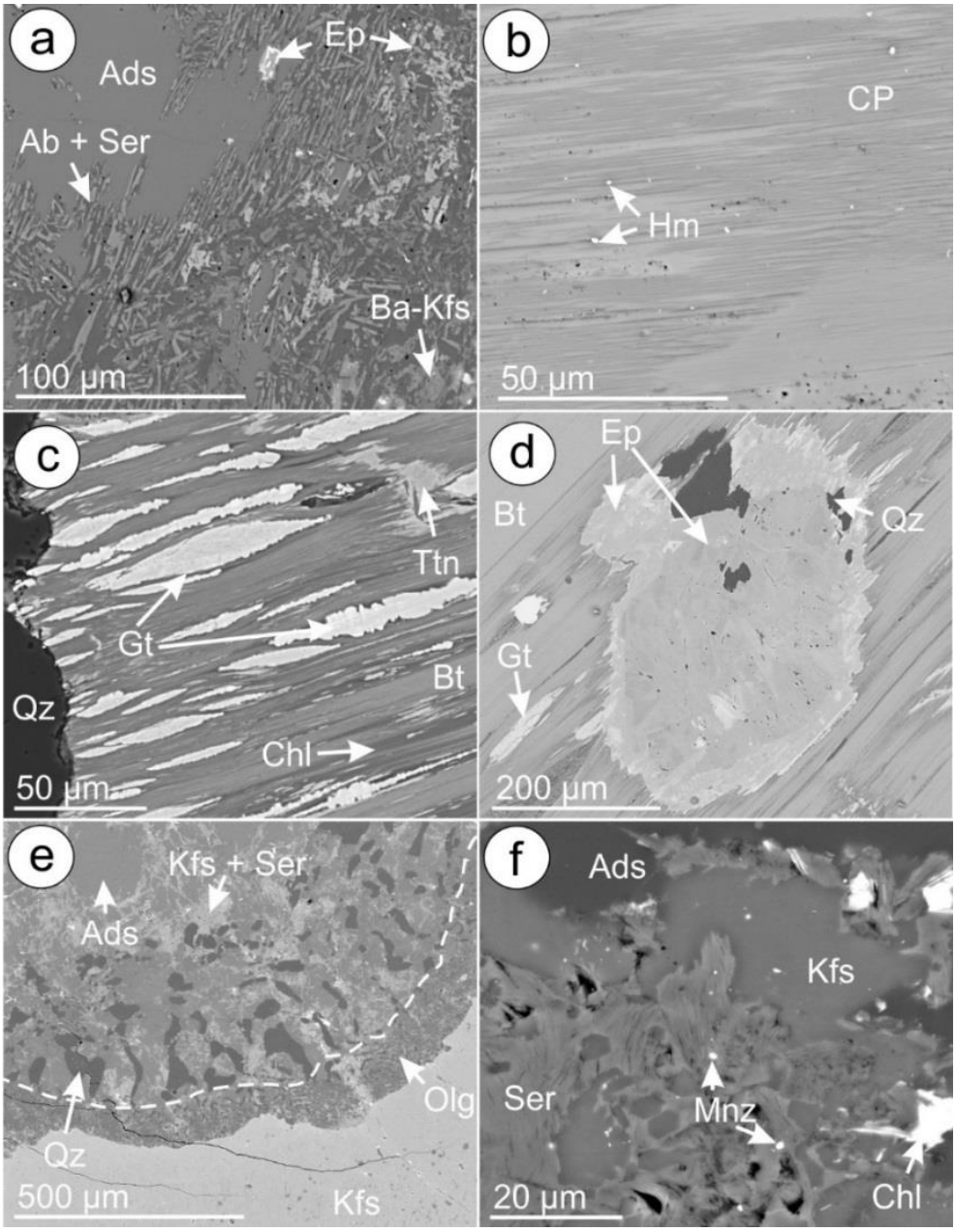

Figure 3: Backscatter scanning electron images outlining typical feldspar microtextures from the quartz monzodiorite at Phillip's Ridge (a-d) and the Donington Suite granite at Wirrda Well (e-f). (a) Andesine (Ads) replaced by fine intergrowth of albite (Ab), sericite (Ser), epidote (Ep) and Ba-rich K-feldspar (Ba-Kfs). (b) Cryptoperthite (CP) displaying heterogeneous replacement by porous K-feldspar along lamellae. Note the presence of disseminated sub-µm-sized hematite (Hm). (c) Biotite (Bt) partially replaced by chlorite, garnet (Gt) and titanite (Ttn) along cleavage plane. (d) Biotite replaced by epidote, garnet and quartz (Qz). Note the epidote appears to pseudomorph a prior mineral (possibly apatite)

(e) Myrmekite texture observed at the contact between plagioclase and alkali feldspar. Andesine is replaced by fine-grained K-feldspar + sericite. The white dashed line represents the calcic-sodic (Olg) boundary within plagioclase. (f) High-magnification image displaying andesine replacement by K-feldspar + sericite ± chlorite. Note disseminated monazite (Mnz) within the sericite.

Cape Donington

Samples from Cape Donington are representative of two lithologies: Donington Suite granite and a foliated leucogranite/aplite, interpreted to represent a marginal facies of the Donington Suite. In hand specimen, the Donington Suite granite appears coarse-grained, weakly-foliated and porphyritic with cm-scale, rounded megacrysts of feldspar surrounded by a finer matrix consisting of mafic minerals (e.g. Fig. 2f). Alkali feldspar is the dominant mineral which typically displays a microperthitic texture with disseminated sub-µm-sized bladed ilmenite inclusions as well as irregular trails of micropores (Fig. 4a). Alkali feldspar also occurs as smaller (~100 µm-sized) grains interstitial between large phenocrysts and other mineral phases such as plagioclase and quartz. Plagioclase forms as >3 mm-sized, euhedral to subhedral grains, often within or between the larger alkali feldspar megacrysts, and shows evidence of extremely sparse replacement by albite + sericite + epidote (Fig. 4b). Plagioclase also occasionally forms interstitial aggregates with quartz, often observed at the margin of larger plagioclase crystals (Fig. 4c). Hornblende (edenite) and biotite occur as large (>1 mm-sized), well preserved grains typically within alkali feldspar megacrysts, but also within a fine-grained fabric containing small polycrystalline aggregates of quartz, plagioclase, ilmenite and magnetite. Magnetite contains trellis exsolution of ilmenite, which also occurs separate of magnetite and is zoned with respect to Mn.

In hand specimen, the foliated leucogranite/aplite is fine-grained, dominantly quartz-feldspathic and contains 1-2 mm-sized, elongate grains of alkali feldspar, quartz and

plagioclase. Alkali feldspar is the most abundant mineral and is typically microperthitic and noticeably microporous (Fig. 4d). Plagioclase occurs as large euhedral to subhedral grains but may also form as polycrystalline aggregates with quartz along the margins of larger alkali feldspar and plagioclase grains. In addition, plagioclase adjacent to alkali feldspar often displays rims of homogeneous albite. Magnetite and ilmenite form small subhedral grains (<200 μm), often associated with one another. Occasionally ilmenite is observed to break down to fine-grained rutile + hematite symplectites.

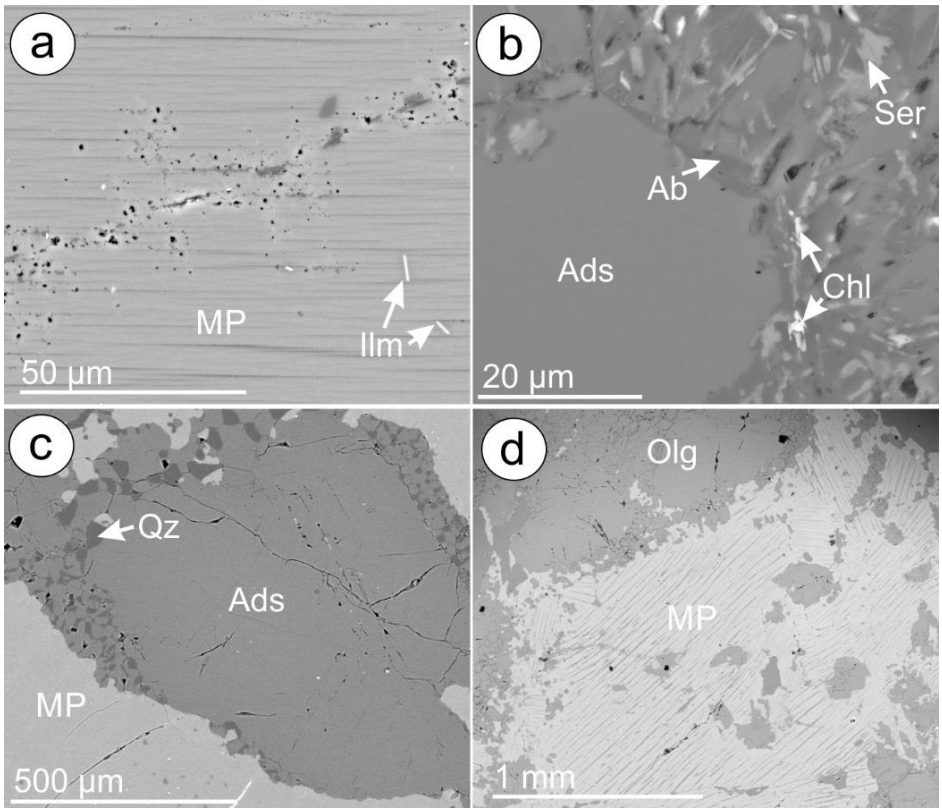

Figure 4: Backscatter electron images of feldspar microtextures from the Donington Suite granite (a-c) and foliated leucogranite/aplite (d) from Cape Donington. (a) Typical appearance of microperthite (MP), which has been irregularly replaced by porous K-feldspar and albite. Note the bladed ilmenite (Ilm) inclusions. (b) Sparse replacement of andesine (Ads) by albite (Ab) + sericite (Ser) + chlorite (Chl). (c) Large andesine grain rimmed by interstitial plagioclase + quartz (Qz). (d) Typical oligoclase (Olg) and microperthite morphologies in the foliated leucogranite/aplite.

Table 3: Mean electron probe microanalyses of feldspars from the Phillip's Ridge, Wirrda Well and Cape Donington sample suites

	Quartz Monzodiorite (Phillip's Ridge)		Donington Suite granite (Wirrda Well)		Donington Suite granite (Cape Donington)		Leucogranite/aplite (Cape Donington)	
	Andesine-Oligoclase (n = 10)	Oligoclase (n = 5)	Andesine (n = 15)	Oligoclase (n = 5)	Andesine (n = 30)	Microperthite (n = 45)	Oligoclase (n = 23)	Microperthite (n = 19)
Sample								
wt%								
SiO_2	58.61 (0.28)	62.84 (0.16)	58.11 (0.26)	60.71 (0.22)	58.25 (0.77)	64.05 (0.17)	63.04 (0.27)	64.24 (0.39)
Al_2O_3	24.61 (0.08)	22.32 (0.13)	25.57 (0.13)	24.04 (0.04)	25.82 (0.45)	18.59 (0.08)	22.65 (0.18)	18.55 (0.11)
FeO	0.27 (0.04)	0.07 (0.02)	0.08 (0.03)	0.08 (0.04)	0.08 (0.13)	0.02 (0.02)	0.02 (0.02)	0.03 (0.03)
CaO	6.27 (0.31)	3.15 (0.41)	7.14 (0.14)	5.06 (0.22)	7.67 (0.56)	0.07 (0.01)	3.86 (0.21)	0.06 (0.08)
SrO	0.11 (0.01)	0.10 (0.02)	0.12 (0.02)	0.09 (0.03)	0.21 (0.03)	0.05 (0.03)	0.19 (0.02)	0.03 (0.03)
BaO	0.03 (0.02)	0.04 (0.01)	0.01 (0.01)	0.01 (0.01)	0.01 (0.01)	0.35 (0.01)	0.01 (0.01)	0.01 (0.01)
Na_2O	7.70 (0.23)	9.79 (0.15)	7.52 (0.10)	8.55 (0.24)	7.43 (0.32)	1.77 (0.12)	9.69 (0.20)	1.61 (0.48)
K_2O	0.52 (0.07)	0.32 (0.10)	0.18 (0.03)	0.39 (0.26)	0.22 (0.03)	14.54 (0.13)	0.21 (0.05)	14.86 (0.67)
TOTAL	98.13 (0.32)	98.63 (0.17)	98.66 (0.24)	98.97 (0.25)	99.50 (0.27)	99.44 (0.21)	99.50 (0.19)	99.39 (0.30)
apfu								
Ca	0.31	0.15	0.35	0.24	0.37	0.00	0.18	0.00
Sr	0.00	0.00	0.00	0.00	0.01	0.00	0.01	0.00
Ba	0.00	0.00	0.00	0.00	0.00	0.01	0.00	0.00
Na	0.68	0.85	0.66	0.74	0.65	0.16	0.84	0.14
K	0.03	0.02	0.01	0.02	0.01	0.86	0.01	0.88
TOTAL	1.02	1.02	1.02	1.00	1.03	1.03	1.03	1.03
Al	1.32	1.18	1.37	1.27	1.37	1.02	1.19	1.01
Si	2.67	2.82	2.63	2.73	2.62	2.98	2.80	2.99
Fe	0.01	0.00	0.00	0.00	0.00	0.00	0.00	0.00
mol%								
Ab %	66.9 (1.53)	83.3 (1.37)	64.9 (0.68)	73.6 (0.94)	62.9 (2.65)	15.5 (0.96)	81.0 (1.26)	14.1 (4.18)
An %	30.1 (1.58)	14.8 (1.92)	34.0 (0.61)	24.1 (0.65)	35.9 (2.58)	0.4 (0.05)	17.8 (1.01)	0.3 (0.39)
Or %	3.0 (0.39)	1.9 (0.57)	1.1 (0.18)	2.3 (1.52)	1.2 (0.19)	84.1 (0.97)	1.2 (0.29)	85.56 (4.13)

Note: Figures in parentheses represent standard deviations.

Table 4: Mean electron probe microanalyses of epidote and garnet from the Phillip's Ridge

Quartz Monzodiorite (Phillip's Ridge)			
Epidote (n=6)		Garnet (n=16)	
wt%		wt%	
CaO	22.5 (0.24)	CaO	33.4 (0.31)
MgO	0.02 (0.01)	MgO	0.23 (0.14)
TiO_2	0.06 (0.03)	TiO_2	1.42 (1.05)
SiO_2	36.7 (0.16)	SiO_2	34.6 (0.42)
Al_2O_3	23.3 (0.41)	Al_2O_3	8.18 (0.86)
FeO	11.9 (0.35)	Fe_2O_3	16.6 (1.15)
MnO	0.38 (0.15)	MnO	0.19 (0.05)
F	<mdl	F	0.85 (0.20)
K_2O	0.01 (0.01)	K_2O	0.01 (0.01)
P_2O_5	0.14 (0.07)	P_2O_5	0.03 (0.02)
Na_2O	0.01 (0.01)	Na_2O	0.02 (0.02)
TOTAL	95.2 (0.21)	TOTAL	95.7 (0.63)
apfu	Epidote: $A_2B_3C_3O_{11}O(OH)$	apfu	Garnet: $A_6B_4C_6O_{24}$
Mg	0.00	Mg	0.06
Mn	0.03	Mn	0.03
Ca	1.90	Ca	6.10
Na	0.00	Na	0.01
K	0.00	K	0.00
Total A	**1.93**	Total A	**6.20**
Fe^{II}	0.79	Fe^{III}	2.13
Al	2.17	Al	1.64
Total B	**2.96**	Total B	**3.77**
Si	2.89	Si	5.89
Ti	0.01	Ti	0.18
P	0.01	P	0.00
Total C	**2.91**	Total C	**6.07**
		Adr	56.4 (2.57)
		Grs	43.5 (2.60)
		Sps	0.43 (0.12)

Note: Epidote based on 12.5 oxygens per formula unit. Garnet based on 24 oxygens per formula unit. Figures in parentheses represent standard deviations.

5.4.3 Chondrite-normalized REY fractionation patterns for feldspars

Feldspars of interest were analyzed by LA-ICP-MS to provide trace elements concentrations, including REY. Results are given in Tables 5-8. Data were chondrite-normalized (using values of McDonough and Sun, 1995), to allow comparative interpretation of fractionation patterns in each mineral. Figure 5 illustrates the mean REY chondrite-normalized fractionation patterns for all feldspars analyzed.

Crypto- and microperthitic alkali feldspar

Crypto- and microperthitic alkali feldspar were analyzed in five groups of samples: least-altered RDG, quartz monzodiorite (Phillip's Ridge), Donington Suite granite (Wirrda Well and Cape Donington) and foliated leucogranite/aplite (Cape Donington). The chondrite-normalized REY fractionation patterns (Figs. 5 and 6) for all five are characterized by varying degrees of La-Ce enrichment, strong positive Eu-anomalies and weak negative Y-anomalies (hereafter "Trend I"). Minor variation in the amplitude of the anomaly is attributed to differences in average ∑REY concentrations, ranging from 2.6 ppm (Donington Suite granite - Cape Donington) to 22 ppm (least altered RDG).

Igneous plagioclase

Igneous plagioclase was analyzed from least-altered RDG, quartz monzodiorite (Phillip's Ridge), Donington Suite granite (Wirrda Well and Cape Donington) and foliated leucogranite/aplite (Cape Donington). Figures 5 and 6 illustrate chondrite-normalized REY fractionation patterns for igneous plagioclase. These are characterized by LREE-enrichment, positive Eu-anomalies, minor negative Y-anomalies and HREE-depletion. Although resembling Trend I, these trends (hereafter "Trend II") are differentiated by a clear negative slope from La-Lu, and weaker positive Eu-anomalies. Average ∑REY concentrations range from 12 ppm (foliated leucogranite/aplite - Cape Donington) to 61 ppm (quartz monzodiorite

- Phillip's Ridge). Both andesine and oligoclase were analyzed from the same grains in least-altered RDG; average ∑REY concentrations are similar (43 ppm and 42 ppm, respectively).

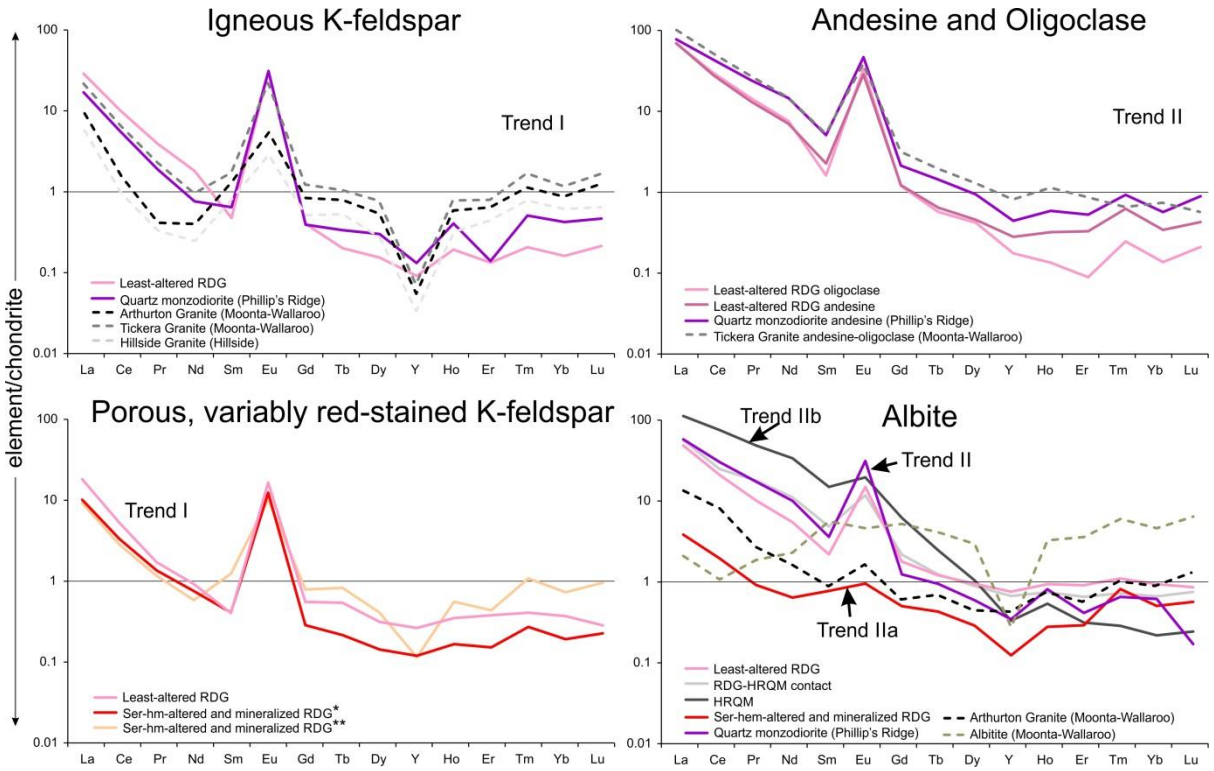

Figure 5: Mean chondrite-normalized REY fractionation patterns for alkali feldspars and plagioclase from the Hiltaba Suite samples. *samples of sericite-hematite altered and mineralized RDG from drillholes RD3554 and RD2511. **samples of sericite-hematite-altered and mineralized RDG from drillholes RD2316 and RD2531. Patterns represented by dashed lines are means obtained from previous studies (Kontonikas-Charos et al., 2014).

Porous, variably red-stained K-feldspar

All case studies contained porous, variably red-stained K-feldspar. The REY concentrations in some of these analyses were consistently below the detection limits and are not included on Figures 5 and 6. Only least-altered, sericite-hematite-altered and mineralized RDG, as well as Donington Suite granite (Wirrda Well) are discussed here. Except for K-feldspar from a vein crosscutting the Donington Suite granite, chondrite-normalized REY fractionation patterns for this category are analogous to Trend I. However, in sericite-hematite-altered and mineralized

RDG, where the only preserved feldspars are porous K-feldspar (variably red-stained) and albite, there appears to be differences in patterns between drillholes. Samples from drillholes RD3554 and RD2511 record a similar pattern to those observed for analogous K-feldspar in least-altered RDG outlined above (Trend I), but K-feldspar from drillholes RD2316 and RD2531 are characterized by a less intense, positive Eu-anomaly, a strong negative Y-anomaly, and steady HREE values. Average ∑REY concentrations range from 3.8 ppm from Donington Suite granite (Wirrda Well) to 10 ppm (least-altered RDG).

Porous K-feldspar found within veins crosscutting the Donington Suite granite from Wirrda Well displays a markedly different REY fractionation pattern, characterized by a strong negative Ce- and Y-anomalies, and a positive Eu-anomaly (Trend III; Fig. 6). The average ∑REY concentration is very low (~3 ppm).

Albite

Albite from least-altered RDG and quartz monzodiorite (Phillip's Ridge) displays chondrite-normalized REY fractionation patterns similar to those of Trend II for igneous plagioclase (Fig. 5). In addition, average ∑REY concentrations are broadly analogous, ranging from 36 ppm (least-altered RDG) to 55 ppm (quartz monzodiorite). Importantly, albite from sericite-hematite-altered and mineralized RDG (drillhole RD2316) records a weaker variant of Trend II (hereafter "Trend IIa"; Fig. 5) characterized by minor LREE-enrichment, slight negative Nd- and Y-anomalies and a very weak positive Eu-anomaly. The albite also contains very low average ∑REY (~3.5 ppm).

Albite from samples along the contact between the RDG and HRQM, display a REY fractionation pattern similar to Trend II, however with more pronounced LREE-enrichment and HREE-depletion, but a weaker Eu-anomaly (hereafter "Trend IIb"; Fig. 5). In the HRQM this apparent strengthening of Trend II continues, with extreme LREE-enrichment and HREE-depletion and a negligible Eu-anomaly. Average ∑REY concentrations complement the

observed pattern by increasing to ~39 ppm (RDG-HRQM contact) and ~96 ppm (HRQM). Unfortunately, igneous plagioclase is absent or extremely scarce in these two examples and was not analyzed.

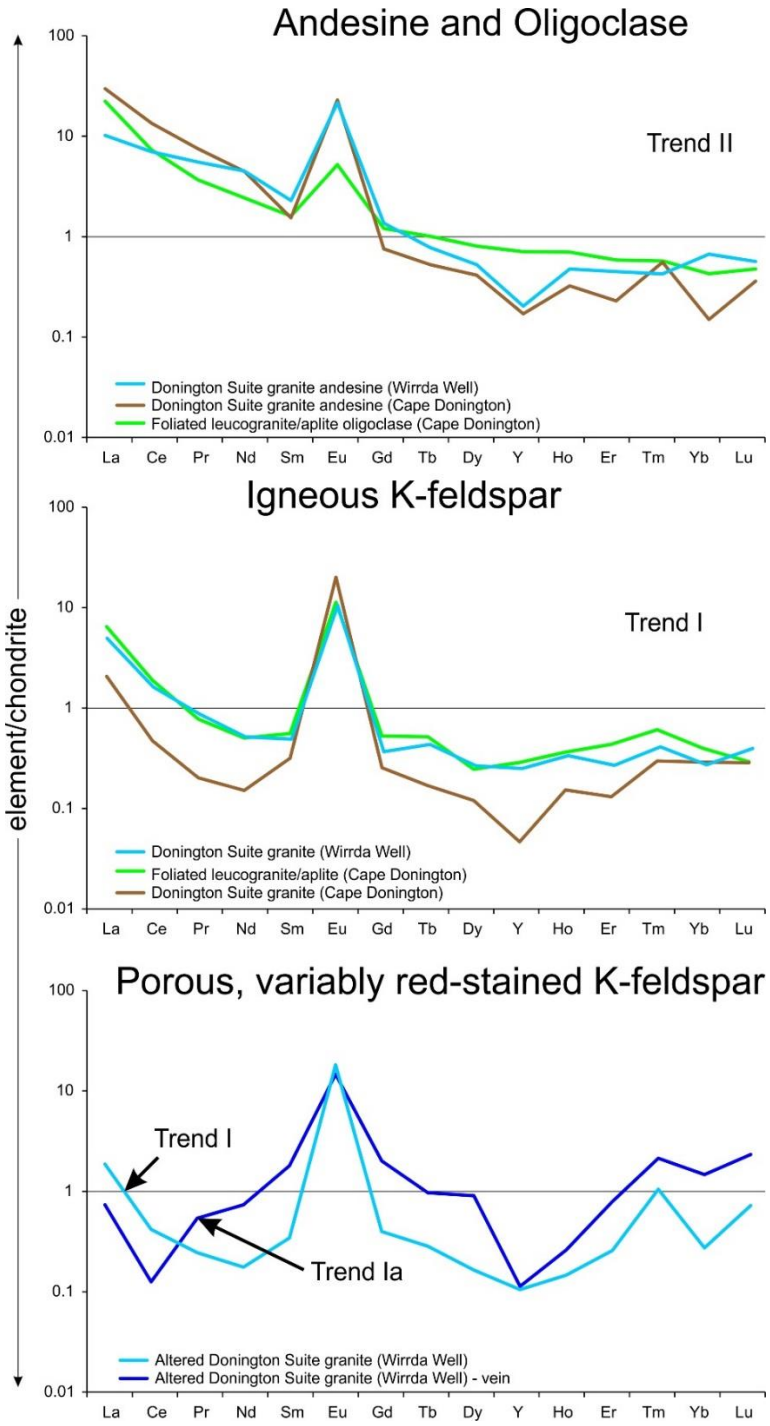

Figure 6: Mean chondrite-normalized REY fractionation patterns for alkali feldspars and plagioclase from pre-Hiltaba Suite samples.

Table 5: Summary of LA-ICP-MS data for crypto- and microperthite: REE, Y Pb, Th and U (ppm)

Element	Y	La	Ce	Pr	Nd	Sm	Eu	Gd	Tb	Dy	Ho	Er	Tm	Yb	Lu	Pb	Th	U	Σ REE+Y
OD – Least altered RDG																			
RD2494: CP (μ_{10})	<mdl	13	9.7	0.51	1.0	<mdl	2.9	<mdl	<mdl	<mdl	0.01	<mdl	<mdl	<mdl	<mdl	2.6	<mdl	<mdl	27
S.D.		1.3	0.95	0.05	0.19		0.22				0.01					0.26			2.4
Min	<mdl	9.8	7.8	0.40	0.66	<mdl	2.6	<mdl	<mdl	<mdl	<mdl	<mdl	<mdl	<mdl	<mdl	2.1	<mdl	<mdl	22
Max	<mdl	14	11	0.57	1.3	0.12	3.2	0.09	<mdl	<mdl	0.03	<mdl	<mdl	<mdl	<mdl	3.0	<mdl	0.01	29
RD2492: CP (μ_8)	0.17	7.7	5.9	0.30	0.59	0.06	2.2	<mdl	0.01	0.05	0.01	<mdl	0.02	<mdl	0.02	16	1.3	0.08	17
S.D.	0.33	1.4	1.4	0.09	0.36	0.06	0.39		0.01	0.08	0.02		0.01		0.00	34	3.2	0.15	4.0
Min	<mdl	6.0	3.8	0.17	0.19	<mdl	1.2	<mdl	<mdl	<mdl	<mdl	<mdl	<mdl	<mdl	<mdl	2.1	<mdl	<mdl	11
Max	1.0	11	9.1	0.47	1.5	0.21	2.5	0.20	0.03	0.25	0.05	0.12	0.02	0.12	0.02	107	9.6	0.46	26
CD – Foliated leucogranite																			
PL-12: MP (μ_{18})	0.36	1.9	1.2	0.06	0.20	0.07	0.81	0.09	0.01	0.05	0.01	0.06	0.02	0.05	0.02	69	0.07	0.03	4.8
S.D.	0.24	0.72	0.88	0.05	0.16	0.08	0.12	0.10	0.01	0.03	0.01	0.04	0.01	0.05	0.01	3.7	0.11	0.04	2.0
Min	<mdl	1.0	0.30	0.01	<mdl	<mdl	0.56	<mdl	<mdl	<mdl	<mdl	<mdl	<mdl	<mdl	<mdl	64	<mdl	<mdl	2.7
Max	0.77	3.3	3.0	0.17	0.60	0.20	0.99	0.33	0.04	0.12	0.04	0.14	0.04	0.17	0.03	78	0.49	0.16	8.7
CD - Donington Granite																			
PL-11: MP (μ_{14})	0.05	0.48	0.19	0.01	<mdl	<mdl	1.7	<mdl	<mdl	<mdl	<mdl	<mdl	0.02	0.05	<mdl	67	0.02	0.02	2.6
S.D.	0.04	0.25	0.13	0.01			0.11						0.01	0.03		5.5	0.01	0.01	0.46
Min	<mdl	0.32	0.08	<mdl	<mdl	<mdl	1.5	<mdl	<mdl	<mdl	<mdl	<mdl	<mdl	<mdl	<mdl	60	<mdl	0.01	2.3
Max	0.13	1.3	0.60	0.03	0.10	0.08	1.9	0.12	0.01	0.05	0.01	0.04	0.02	0.09	0.02	77	0.04	0.04	4.0
PL-13 - MP (μ_{13})	<mdl	0.53	0.27	0.02	<mdl	0.06	1.5	<mdl	<mdl	<mdl	0.01	<mdl	<mdl	0.05	0.02	65	0.02	0.01	2.5
S.D.		0.23	0.27	0.01		0.04	0.12				0.01			0.03	0.01	5.1	0.02	0.01	0.57
Min	<mdl	0.30	0.10	<mdl	<mdl	<mdl	1.4	<mdl	<mdl	<mdl	<mdl	<mdl	<mdl	<mdl	<mdl	56	<mdl	<mdl	2.1
Max	0.08	1.2	1.1	0.04	0.16	0.10	1.7	<mdl	0.02	0.08	0.02	0.06	<mdl	0.08	0.02	76	0.07	0.02	4.2

Table 6: Summary of LA-ICP-MS data for porous and red-stained K-feldspar: REE, Y Pb, Th and U (ppm)

Element	Y	La	Ce	Pr	Nd	Sm	Eu	Gd	Tb	Dy	Ho	Er	Tm	Yb	Lu	Pb	Th	U	Σ REE+Y
OD- Least-altered RDG																			
RD2492: Por Kfs (μ_6)	0.72	5.4	4.3	0.24	0.68	0.09	1.1	0.15	0.02	0.15	0.04	0.12	0.02	0.11	0.02	2.3	4.4	0.11	13
S.D.	1.3	3.5	2.7	0.15	0.67	0.08	0.98	0.25	0.03	0.28	0.07	0.22	0.03	0.21	0.02	0.82	9.6	0.19	7.5
Min	<mdl	1.00	0.71	0.04	0.07	<mdl	0.21	<mdl	<mdl	<mdl	<mdl	<mdl	<mdl	<mdl	<mdl	1.3	<mdl	<mdl	2.4
Max	3.6	11	8.4	0.46	2.1	0.23	2.6	0.70	0.10	0.77	0.18	0.62	0.09	0.59	0.05	3.7	26	0.53	23
RD2495: Por Kfs (μ_{15})	0.19	3.2	1.7	0.07	0.13	<mdl	0.74	0.09	0.03	<mdl	<mdl	<mdl	0.02	<mdl	<mdl	1.2	0.03	0.01	6.2
S.D.	0.34	1.6	0.83	0.05	0.11		0.14	0.13	0.07				0.01			0.81	0.03	0.01	2.9
Min	<mdl	1.0	0.71	0.02	<mdl	<mdl	0.50	<mdl	<mdl	<mdl	<mdl	<mdl	<mdl	<mdl	<mdl	0.43	<mdl	<mdl	2.4
Max	1.1	5.8	3.2	0.19	0.36	<mdl	0.93	0.43	0.23	<mdl	<mdl	<mdl	0.02	<mdl	<mdl	2.6	0.12	0.03	11
RD2280: Red Kfs (μ_{10})	0.13	1.8	1.4	0.09	0.25	0.12	0.43	0.09	0.01	0.06	0.01	0.04	0.02	0.05	0.02	1.7	0.10	0.02	4.5
S.D.	0.07	1.1	1.0	0.09	0.32	0.09	0.15	0.02	0.01	0.03	0.00	0.01	0.00	0.03	0.01	0.72	0.10	0.02	2.6
Min	0.06	0.50	0.65	0.03	<mdl	<mdl	0.21	<mdl	<mdl	<mdl	<mdl	<mdl	<mdl	<mdl	<mdl	0.92	<mdl	<mdl	1.9
Max	0.32	4.5	4.4	0.35	1.2	0.33	0.71	0.12	0.03	0.12	0.02	0.06	0.01	0.10	0.05	3.0	0.28	0.08	12
RD2280: Por Kfs (μ_{10})	0.10	8.3	6.7	0.31	0.66	0.08	2.1	0.09	0.01	<mdl	0.01	0.04	0.02	0.05	0.02	3.3	0.05	0.03	18
S.D.	0.05	1.8	1.9	0.16	0.26	0.06	0.55	0.06	0.02		0.01	0.01	0.01	0.03	0.02	0.78	0.05	0.03	4.3
Min	<mdl	6.1	4.3	0.12	0.23	<mdl	1.5	<mdl	<mdl	<mdl	<mdl	<mdl	<mdl	<mdl	<mdl	2.2	<mdl	0.01	14
Max	0.19	12	11	0.65	1.2	0.23	3.5	0.21	0.08	0.05	0.06	0.06	0.03	0.09	0.09	4.8	0.18	0.09	28
OD- HRQM																			
RD2274 - Por Kfs (μ_{14})	0.06	7.9	5.8	0.30	0.57	0.06	3.3	0.09	0.01	<mdl	0.01	<mdl	<mdl	<mdl	<mdl	5.6	0.17	0.06	18
S.D.	0.06	2.7	2.5	0.16	0.37	0.05	0.80	0.07	0.00		0.00					1.3	0.36	0.12	6.3
Min	<mdl	3.9	2.4	0.10	0.19	<mdl	1.7	<mdl	<mdl	<mdl	<mdl	<mdl	<mdl	<mdl	<mdl	3.4	<mdl	<mdl	9.9
Max	0.20	11	9.7	0.66	1.6	0.16	4.6	0.31	0.01	0.06	0.01	<mdl	<mdl	0.05	0.02	7.9	1.2	0.46	27
OD- Ser-Hm-altered RDG																			
RD2531: Red Kfs (μ_{11})	0.27	3.3	2.7	0.14	0.42	0.31	0.85	0.25	0.06	0.18	0.06	0.10	0.05	0.20	0.04	2.6	0.17	0.12	9.0
S.D.	0.18	2.3	2.1	0.12	0.14	0.14	0.27	0.17	0.01	0.13	0.02	0.06	0.02	0.13	0.01	0.44	0.11	0.11	4.8
Min	<mdl	0.57	0.55	0.04	0.23	0.10	0.54	<mdl	0.04	<mdl	0.04	<mdl	0.02	0.07	0.02	1.7	0.06	0.03	3.5
Max	0.67	8.7	7.0	0.43	0.72	0.54	1.4	0.50	0.07	0.41	0.11	0.18	0.11	0.55	0.06	3.2	0.36	0.39	19
RD2511: Red Kfs (μ_{11})	0.23	3.9	2.6	0.14	0.35	0.06	1.5	0.08	0.01	0.05	0.01	0.04	<mdl	0.05	<mdl	7.5	0.15	0.20	9.0
S.D.	0.09	0.68	0.66	0.05	0.14	0.03	0.20	0.04	0.00	0.02	0.00	0.02		0.01		1.6	0.07	0.25	1.6
Min	0.08	2.6	1.6	0.06	<mdl	<mdl	1.1	<mdl	<mdl	<mdl	<mdl	<mdl	<mdl	<mdl	<mdl	3.7	0.04	0.03	6.8
Max	0.41	5.2	3.7	0.23	0.65	0.10	1.9	0.14	0.01	0.08	0.01	0.06	<mdl	0.07	<mdl	9.6	0.30	0.96	12

Table 6: Summary of LA-ICP-MS data for porous and red-stained K-feldspar: REE, Y Pb, Th and U (ppm) continued

Element	Y	La	Ce	Pr	Nd	Sm	Eu	Gd	Tb	Dy	Ho	Er	Tm	Yb	Lu	Pb	Th	U	Σ REE+Y
OD – Mineralized RDG																			
RD2316: Red Kfs (μ_{21})	0.12	1.9	1.4	0.09	0.20	0.13	0.47	0.11	0.02	0.06	0.02	0.05	0.02	0.08	0.02	3.2	0.06	0.22	4.7
S.D.	0.11	1.2	0.84	0.07	0.13	0.07	0.32	0.05	0.01	0.03	0.01	0.03	0.01	0.05	0.01	3.1	0.15	0.35	2.4
Min	<mdl	0.48	0.28	0.02	<mdl	0.05	0.03	<mdl	0.01	<mdl	0.01	<mdl	<mdl	<mdl	<mdl	0.27	<mdl	0.02	1.6
Max	0.43	5.4	3.7	0.26	0.52	0.27	1.4	0.24	0.04	0.13	0.05	0.15	0.04	0.24	0.03	15	0.74	1.6	11
RD3554: Red Kfs (μ_{40})	0.15	1.9	1.7	0.11	0.30	0.06	0.47	<mdl	0.01	<mdl	0.01	<mdl	<mdl	0.05	<mdl	4.0	0.07	0.08	4.8
S.D.	0.15	1.5	2.0	0.15	0.47	0.06	0.19		0.01		0.01			0.02		2.4	0.09	0.08	4.2
Min	<mdl	0.15	0.10	0.01	<mdl	<mdl	0.14	<mdl	<mdl	<mdl	<mdl	<mdl	<mdl	<mdl	<mdl	0.94	<mdl	0.02	0.75
Max	0.78	7.8	12	0.81	2.9	0.24	0.92	0.21	0.04	0.10	0.03	0.06	0.02	0.11	0.03	13	0.52	0.42	24
WW – Donington Granite																			
WRD33: Kfs vein (μ_5)	0.16	0.17	0.07	0.05	0.32	0.26	0.85	0.39	0.03	0.21	0.01	0.12	0.05	0.23	0.06	0.42	0.06	0.04	3.0
S.D.	0.04	0.06	0.01	0.03	0.11	0.22	0.20	0.22	0.03	0.12	0.02	0.11	0.01	0.14	0.03	0.39	0.03	0.01	0.56
Min	0.12	0.07	0.06	<mdl	0.15	<mdl	0.49	<mdl	<mdl	<mdl	<mdl	<mdl	0.04	<mdl	<mdl	0.13	0.02	0.02	2.1
Max	0.23	0.24	0.09	0.08	0.48	0.65	1.1	0.58	0.07	0.37	0.04	0.29	0.06	0.38	0.10	1.2	0.08	0.05	3.7
WRD33: Por Kfs (μ_{16})	0.33	1.3	0.98	0.07	0.19	0.07	0.63	0.09	0.01	0.06	0.02	0.04	0.02	0.05	<mdl	16	0.04	0.04	3.8
S.D.	0.16	1.3	0.79	0.05	0.11	0.06	0.12	0.04	0.01	0.04	0.01	0.02	0.01	0.03		8.2	0.04	0.03	2.4
Min	0.07	0.05	0.04	<mdl	<mdl	<mdl	0.43	<mdl	0.01	<mdl	0.01	<mdl	<mdl	<mdl	<mdl	3.8	<mdl	0.01	0.92
Max	0.75	4.3	2.7	0.20	0.44	0.20	1.0	0.18	0.03	0.15	0.03	0.09	0.05	0.13	0.02	31	0.13	0.11	9.2
PR – Quartz Monzodiorite																			
PD4: Por Kfs (μ_{20})	<mdl	5.5	3.9	0.17	0.30	0.08	2.6	<mdl	0.01	0.06	0.02	<mdl	0.02	0.05	0.02	11	0.01	0.03	13
S.D.		2.4	1.9	0.09	0.19	0.14	1.1		0.02	0.09	0.03		0.02	0.09	0.02	7.9	0.02	0.07	5.5
Min	<mdl	0.64	0.32	0.01	<mdl	<mdl	0.83	<mdl	<mdl	<mdl	<mdl	<mdl	<mdl	<mdl	<mdl	4.1	<mdl	<mdl	1.9
Max	0.12	9.2	7.2	0.35	0.69	0.52	4.8	0.37	0.06	0.23	0.12	0.16	0.08	0.25	0.10	39	0.06	0.32	22
WW – Donington Granite																			
WRD46 - Por Kfs (μ_{23})	0.06	0.44	0.21	0.02	0.06	0.06	1.1	0.09	0.01	<mdl	<mdl	<mdl	0.02	0.05	<mdl	81	0.03	0.05	1.9
S.D.	0.06	0.33	0.25	0.02	0.06	0.08	0.49	0.09	0.01				0.04	0.03		20	0.08	0.11	1.0
Min	<mdl	0.07	0.02	<mdl	<mdl	<mdl	0.46	<mdl	<mdl	<mdl	<mdl	<mdl	<mdl	<mdl	<mdl	28	<mdl	<mdl	0.74
Max	0.26	1.2	0.98	0.08	0.17	0.24	2.0	0.24	0.03	0.13	0.02	0.08	0.17	0.18	0.04	114	0.40	0.57	4.1

Table 7: Summary of LA-ICP-MS data for igneous plagioclase: REE, Y Pb, Th and U (ppm)

Element	Y	La	Ce	Pr	Nd	Sm	Eu	Gd	Tb	Dy	Ho	Er	Tm	Yb	Lu	Pb	Th	U	Σ REE+Y
OD - Least-altered RDG																			
RD2495: Ads-Olg (μ_{11})	1.1	7.1	5.4	0.38	1.2	0.25	0.25	0.25	0.04	0.20	0.04	0.09	0.02	0.06	0.02	32	0.02	0.01	16
S.D.	0.22	1.1	1.1	0.08	0.40	0.10	0.04	0.11	0.01	0.06	0.01	0.03	0.01	0.03	0.01	0.90	0.03	0.02	2.9
Min	0.86	5.6	3.6	0.26	0.72	0.14	0.17	0.12	0.02	0.11	0.02	0.06	<mdl	<mdl	<mdl	30	<mdl	<mdl	13
Max	1.9	11	9.0	0.61	2.5	0.46	0.30	0.58	0.07	0.35	0.05	0.16	0.03	0.12	0.03	34	0.14	0.08	27
RD2495: Olg (μ_{10})	0.06	3.0	3.5	0.24	0.46	0.08	0.75	0.12	0.01	0.05	0.01	0.04	0.02	0.08	0.02	1.3	0.02	0.01	8.3
S.D.	0.03	0.88	0.75	0.06	0.17	0.05	0.10	0.03	0.01	0.03	0.01	0.02	0.00	0.04	0.01	0.20	0.01	0.00	1.9
Min	<mdl	2.0	2.5	0.17	0.21	<mdl	0.65	0.09	<mdl	<mdl	<mdl	<mdl	<mdl	<mdl	<mdl	0.93	<mdl	0.01	6.2
Max	0.11	4.5	4.6	0.35	0.71	0.15	0.92	0.16	0.02	0.08	0.02	0.06	0.02	0.16	0.03	1.5	0.04	0.02	12
RD2280: Olg (μ_{7})	0.44	3.4	2.5	0.18	0.57	0.11	0.24	0.10	0.02	0.08	0.02	0.04	0.02	<mdl	0.02	25	0.03	0.01	7.7
S.D.	0.17	0.43	0.55	0.04	0.12	0.04	0.03	0.05	0.00	0.03	0.01	0.02	0.01		0.01	0.53	0.04	0.01	1.1
Min	0.20	2.7	1.7	0.13	0.41	<mdl	0.21	<mdl	0.01	0.05	<mdl	<mdl	<mdl	<mdl	<mdl	24	<mdl	<mdl	5.9
Max	0.68	3.9	3.2	0.23	0.72	0.16	0.29	0.18	0.02	0.16	0.05	0.07	0.05	0.06	0.02	26	0.12	0.02	9.1
CD - Foliated Leucogranite																			
PL-12: Olg (μ_{20})	0.14	3.9	3.9	0.31	0.86	0.08	1.3	<mdl	0.01	0.05	0.01	<mdl	<mdl	<mdl	0.02	19	0.03	0.02	11
S.D.	0.05	1.2	1.8	0.15	0.45	0.04	0.10		0.00	0.02	0.01				0.01	0.92	0.05	0.02	3.5
Min	0.05	2.2	2.2	0.13	0.26	<mdl	1.2	<mdl	<mdl	<mdl	<mdl	<mdl	<mdl	<mdl	<mdl	17	<mdl	<mdl	6.7
Max	0.25	6.2	7.8	0.63	1.9	0.16	1.5	0.09	0.01	0.08	0.02	0.04	0.04	0.06	0.04	21	0.19	0.05	18
PL-6: Olg (μ_{11})	0.06	2.9	2.5	0.20	0.55	0.06	1.2	0.09	0.01	0.05	0.01	<mdl	0.02	<mdl	<mdl	18	<mdl	0.01	7.6
S.D.	0.04	0.65	0.53	0.06	0.14	0.03	0.10	0.02	0.01	0.02	0.01		0.01			0.98		0.01	1.4
Min	<mdl	2.1	1.8	0.11	0.39	<mdl	1.0	<mdl	<mdl	<mdl	<mdl	<mdl	<mdl	<mdl	<mdl	17	<mdl	<mdl	5.8
Max	0.16	4.0	3.3	0.31	0.80	0.12	1.4	0.10	0.02	0.09	0.02	0.06	0.03	0.07	0.02	20	0.03	0.02	9.7

Table 7: Summary of LA-ICP-MS data for igneous plagioclase: REE, Y Pb, Th and U (ppm) continued

Element	Y	La	Ce	Pr	Nd	Sm	Eu	Gd	Tb	Dy	Ho	Er	Tm	Yb	Lu	Pb	Th	U	Σ REE+Y
CD - Donington Granite																			
PL-13: Ads (μ_{15})	0.39	17	24	2.0	5.6	0.61	3.1	0.32	0.03	0.15	0.02	0.08	0.02	0.07	0.02	2.3	0.03	0.02	53
S.D.	0.20	7.1	8.8	0.71	1.9	0.21	0.20	0.15	0.02	0.07	0.01	0.05	0.02	0.09	0.02	0.60	0.03	0.02	19
Min	0.17	6.3	9.4	0.89	1.9	0.31	2.6	<mdl	0.01	<mdl	<mdl	<mdl	<mdl	<mdl	<mdl	1.5	<mdl	<mdl	23
Max	0.84	30	37	3.1	8.2	1.0	3.5	0.60	0.06	0.27	0.05	0.15	0.05	0.21	0.05	3.6	0.08	0.05	83
PL-11: Ads (μ_{10})	0.42	25	33	2.5	7.1	0.61	2.6	0.35	0.04	0.15	0.02	0.04	0.02	0.07	0.02	2.1	0.02	0.01	71
S.D.	0.13	3.0	3.0	0.19	0.70	0.26	0.20	0.12	0.02	0.07	0.02	0.04	0.02	0.08	0.01	0.26	0.03	0.02	6.5
Min	0.21	17	26	2.2	5.6	0.25	2.2	0.18	0.01	0.07	<mdl	<mdl	<mdl	<mdl	<mdl	1.7	<mdl	<mdl	56
Max	0.66	27	37	2.9	8.2	1.0	2.9	0.59	0.07	0.29	0.05	0.15	0.07	0.23	0.05	2.4	0.07	0.04	79
PR - Quartz Monzodiorite																			
PD4-2 - Olg (μ_{13})	0.57	20	27	2.2	6.2	0.69	2.7	0.31	0.04	0.20	0.02	0.05	0.02	0.05	0.02	1.6	0.05	0.05	60
S.D.	0.41	4.0	5.3	0.49	1.3	0.24	0.48	0.18	0.02	0.07	0.02	0.05	0.02	0.04	0.02	0.60	0.09	0.12	11
Min	0.20	12	16	1.3	3.1	0.29	1.1	<mdl	0.01	0.05	0.01	<mdl	<mdl	<mdl	<mdl	0.58	<mdl	<mdl	35
Max	2.0	29	40	3.0	8.2	1.3	3.3	0.71	0.08	0.33	0.06	0.17	0.06	0.16	0.08	2.8	0.38	0.54	83
PD4-4 - Olg (μ_{10})	0.22	1.7	3.1	0.37	1.2	0.24	0.91	0.14	0.02	0.08	0.01	0.06	0.02	0.05	0.02	17	0.02	0.02	7.9
S.D.	0.22	0.49	0.92	0.15	0.49	0.19	0.21	0.13	0.01	0.06	0.02	0.05	0.02	0.06	0.01	2.5	0.03	0.02	2.3
Min	<mdl	0.90	1.7	0.18	0.52	<mdl	0.44	<mdl	<mdl	<mdl	<mdl	<mdl	<mdl	<mdl	<mdl	13	<mdl	<mdl	4.4
Max	0.76	2.6	4.9	0.71	2.3	0.68	1.2	0.41	0.04	0.19	0.05	0.14	0.04	0.19	0.04	22	0.08	0.05	13
PD4-3 - Olg (μ_{18})	0.62	16	16	1.1	2.5	0.17	1.2	0.19	0.02	0.09	0.02	0.08	0.03	0.07	<mdl	0.95	0.03	0.03	38
S.D.	0.42	3.6	4.1	0.24	0.61	0.07	0.36	0.10	0.01	0.06	0.02	0.06	0.05	0.05		0.33	0.06	0.04	9.2
Min	0.10	12	12	0.87	1.7	<mdl	0.66	<mdl	0.01	<mdl	<mdl	<mdl	<mdl	<mdl	<mdl	0.35	<mdl	<mdl	29
Max	1.3	23	25	1.5	3.5	0.27	1.8	0.41	0.03	0.18	0.05	0.17	0.17	0.16	0.02	1.4	0.18	0.12	56
WW – Donington Granite																			
OD46-2 - Ads (μ_{14})	1.6	12	14	0.90	2.1	0.22	0.82	0.25	0.05	0.23	0.05	0.18	0.02	0.18	0.03	1.8	1.1	0.42	45
S.D.	1.3	5.8	6.8	0.72	2.0	0.13	0.26	0.18	0.03	0.19	0.04	0.07	0.02	0.14	0.02	0.68	1.3	0.37	29
Min	0.24	5.5	4.1	0.25	0.47	0.06	0.47	<mdl	0.01	<mdl	0.01	0.09	<mdl	0.05	<mdl	0.65	0.02	0.03	11
Max	3.3	21	21	2.1	5.4	0.36	1.2	0.46	0.09	0.45	0.09	0.27	0.04	0.38	0.05	2.3	3.3	0.90	87

Table 8: Summary of LA-ICP-MS data for albite: REE, Y Pb, Th and U (ppm)

Element	Y	La	Ce	Pr	Nd	Sm	Eu	Gd	Tb	Dy	Ho	Er	Tm	Yb	Lu	Pb	Th	U	ΣREE+Y
OD - Least-altered RDG																			
RD2494: Ab (μ_8)	0.62	16	16	1.1	2.5	0.17	1.2	0.19	0.02	0.09	0.02	0.08	0.03	0.07	0.02	0.95	0.03	0.03	38
S.D.	0.42	3.6	4.1	0.24	0.61	0.07	0.36	0.10	0.01	0.06	0.02	0.06	0.05	0.05	0.00	0.33	0.06	0.04	9.2
Min	0.10	12	12	0.87	1.7	<mdl	0.66	<mdl	<mdl	<mdl	<mdl	<mdl	<mdl	<mdl	<mdl	0.35	<mdl	<mdl	29
Max	1.3	23	25	1.5	3.5	0.27	1.8	0.41	0.03	0.18	0.05	0.17	0.17	0.16	0.04	1.4	0.18	0.12	56
RD2492: Ab (μ_5)	1.6	12	14	0.90	2.1	0.22	0.82	0.25	0.05	0.23	0.05	0.18	0.02	0.18	0.03	1.8	1.1	0.42	45
S.D.	1.3	5.8	6.8	0.72	2.0	0.13	0.26	0.18	0.03	0.19	0.04	0.07	0.02	0.14	0.02	0.68	1.3	0.37	29
Min	0.24	5.5	4.1	0.25	0.47	<mdl	0.47	<mdl	<mdl	<mdl	0.01	0.09	<mdl	0.05	<mdl	0.65	0.02	0.03	11
Max	3.3	21	21	2.1	5.4	0.36	1.2	0.46	0.09	0.45	0.09	0.27	0.04	0.38	0.05	2.3	3.3	0.90	87
RD2880: Ab (μ_{15})	0.16	2.7	3.0	0.19	0.54	0.07	0.25	0.10	0.01	0.06	0.01	0.05	0.02	0.05	0.02	1.9	0.10	0.04	7.2
S.D.	0.12	1.1	1.1	0.09	0.31	0.05	0.14	0.05	0.01	0.03	0.01	0.03	0.00	0.03	0.00	0.56	0.07	0.02	2.5
Min	<mdl	1.0	1.3	0.06	0.15	<mdl	0.04	<mdl	0.01	<mdl	<mdl	<mdl	<mdl	<mdl	<mdl	0.69	0.02	0.01	3.0
Max	0.41	4.7	4.2	0.38	1.1	0.14	0.43	0.20	0.03	0.12	0.03	0.13	0.02	0.10	0.03	2.9	0.23	0.07	11
OD – RDG-HRQMcontact																			
RD2274: Ab (μ_{19})	1.1	14	16	1.8	5.4	0.76	0.70	0.48	0.05	0.24	0.04	0.10	0.02	0.10	0.02	1.5	0.52	0.14	40
S.D.	0.77	9.4	8.2	1.4	5.1	0.77	0.40	0.49	0.04	0.21	0.03	0.06	0.01	0.08	0.01	1.6	1.4	0.15	23
Min	0.31	3.5	4.9	0.36	1.1	0.15	0.25	0.05	0.01	0.05	0.01	<mdl	<mdl	<mdl	<mdl	0.46	<mdl	0.01	12
Max	2.5	33	34	6.4	23	3.4	1.9	2.2	0.17	0.90	0.12	0.20	0.04	0.27	0.05	7.8	5.9	0.70	86
OD - HRQM																			
RD2274: Ab (μ_{10})	0.59	26	45	4.5	15	2.3	1.1	1.3	0.10	0.28	0.03	0.06	<mdl	0.05	<mdl	2.0	0.54	0.05	96
S.D.	0.14	11	22	2.2	8.3	1.1	0.39	0.73	0.05	0.10	0.03	0.04		0.02		1.7	0.46	0.03	46
Min	0.36	14	24	2.5	8.0	1.2	0.56	0.67	0.05	0.14	0.01	<mdl	<mdl	<mdl	<mdl	0.99	0.08	0.01	53
Max	0.78	45	81	8.7	30	4.2	1.8	2.7	0.19	0.42	0.11	0.17	<mdl	0.08	0.01	6.8	1.3	0.11	175
OD – Mineralized RDG																			
RD2316: Ab (μ_{10})	0.23	0.97	1.3	0.09	0.33	0.13	0.06	0.11	0.02	0.08	0.02	0.05	0.02	0.09	0.02	0.81	0.07	0.12	3.5
S.D.	0.28	0.81	1.4	0.09	0.35	0.06	0.03	0.03	0.01	0.05	0.00	0.01	0.02	0.03	0.01	0.27	0.11	0.15	2.5
Min	<mdl	0.18	0.23	0.02	<mdl	<mdl	<mdl	<mdl	0.01	<mdl	0.01	0.04	<mdl	0.05	<mdl	0.43	0.02	0.02	1.1
Max	1.0	3.0	4.9	0.31	1.1	0.21	0.10	0.15	0.02	0.15	0.02	0.07	0.07	0.16	0.05	1.2	0.40	0.55	10
PR – Quartz monzodiorite																			
PD4-1: Ab (μ_6)	0.80	24	30	2.5	6.6	0.77	3.1	0.33	0.03	0.23	0.06	0.06	0.03	0.12	0.02	1.8	0.02	0.01	68
S.D.	0.29	5.4	5.5	0.41	0.95	0.19	0.41	0.04	0.01	0.13	0.04	0.06	0.03	0.12	0.00	0.84	0.02	0.02	12
Min	0.47	15	21	1.8	5.1	0.54	2.4	0.28	0.02	0.07	0.02	<mdl	<mdl	<mdl	<mdl	0.39	<mdl	<mdl	48
Max	1.2	29	34	2.9	7.8	1.1	3.4	0.39	0.05	0.42	0.11	0.15	0.07	0.28	0.04	2.5	0.06	0.04	78
PD4-3: Ab (μ_5)	0.31	14	19	1.6	4.7	0.48	1.6	0.22	0.04	0.08	0.04	0.08	0.02	0.09	<mdl	0.93	<mdl	<mdl	41
S.D.	0.09	6.0	6.8	0.54	1.4	0.11	0.59	0.06	0.02	0.08	0.02	0.07	0.01	0.10		0.55			15
Min	0.19	5.9	9.4	0.91	2.7	0.34	0.70	0.17	0.02	<mdl	0.01	0.04	<mdl	<mdl	<mdl	0.42	<mdl	<mdl	21
Max	0.46	21	27	2.3	6.1	0.64	2.2	0.34	0.06	0.20	0.07	0.21	0.02	0.23	<mdl	1.8	<mdl	<mdl	59

5.5 Discussion

5.5.1 REY fractionation pattern comparison

Chondrite-normalized REY fractionation patterns obtained from selected feldspars show similarities and differences. The discriminating factors between trends are the slope (La/Lu) and degrees of enrichment in LREE relative to HREE, positive Eu-anomaly and negative Y-anomaly. A Eu/Eu* vs. Ce/Ce* binary plot distinguishes between the trends based on the strength of the anomalies (Figs. 7 and 8). Trend I (relative enrichment in La-Ce, strong positive Eu-anomaly and minor negative Y-anomaly) characterizes most alkali feldspars within the sample suite. This trend, as shown in Figure 5, has also been described for alkali feldspar from Hiltaba Suite granites from Moonta Wallaroo (Arthurton and Tickera granites; Fig. 5) and Hillside (Hillside granite; Ismail et al., 2014). In all cases, average ∑REY concentrations are very low (ranging from 3.8-10 ppm), and thus markedly different from those of Trend II, in which ∑REY is almost an order of magnitude higher (36-55 ppm). Trend II (relative LREE enrichment, positive Eu-anomaly, minor negative Y-anomaly and HREE-depletion) typifies igneous plagioclase and some albite analyzed from the sample suite. In addition, this trend is also characteristic of andesine-oligoclase and albite from the Arthurton and Tickera granites (Fig. 5). Trend IIa and IIb (bottom right corner of Fig. 5) show the extremes of ∑REY depletion (~3.5 ppm) and enrichment (~96 ppm) within Trend II, respectively. Notably, Trend IIa closely resembles the chondrite-normalized REY fractionation pattern obtained from albite found within an intensely albitized Hiltaba Suite granite from Moonta-Wallaroo (Fig. 5) and from prograde albite-pyroxene skarn from Hillside (Ismail et al., 2014). However, this trend differs slightly from Trend IIa, in that it features a negative Ce-anomaly and sharper Y-anomaly. Average ∑REY concentrations also differ (~15 ppm - Moonta Wallaroo). Trend IIb has only been found in albite from along the contact between the RDG-HRQM and within the HRQM itself. A negative Ce-anomaly is diagnostic of Trend Ia, which was obtained from hydrothermal

K-feldspar within crosscutting veins in the Donington Suite granite from Wirrda Well. This pattern is unique within the sample suite and also records the lowest average ∑REY concentration (3 ppm).

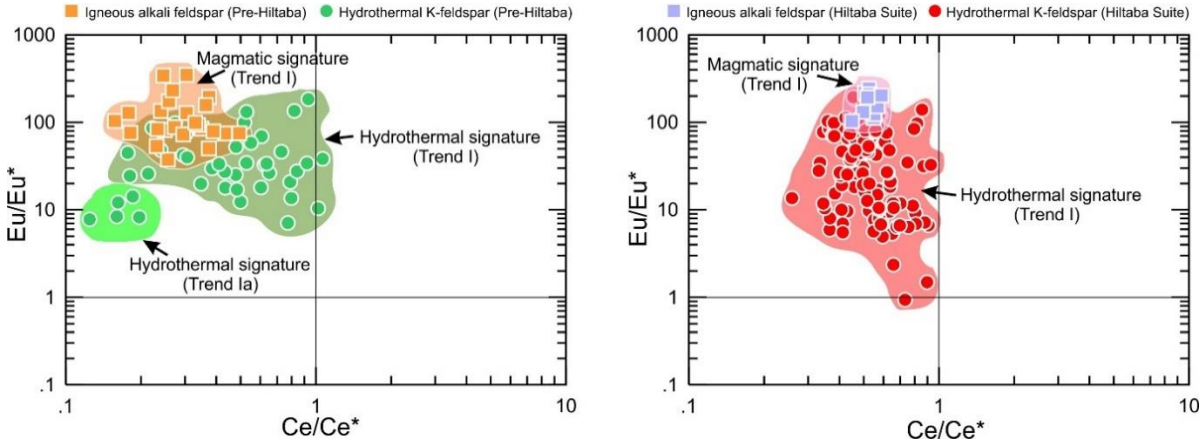

Figure 7: Eu/Eu* vs. Ce/Ce* binary plot of igneous and hydrothermal alkali feldspars from the sample suite. The plot allows for discrimination between distinct REY fractionation patterns. Eu/Eu* = $Eu_{CN}/[(Sm_{CN}+Gd_{CN})/2]$ and Ce/Ce* = $Ce_{CN}/[(La_{CN}+Pr_{CN})/2]$.

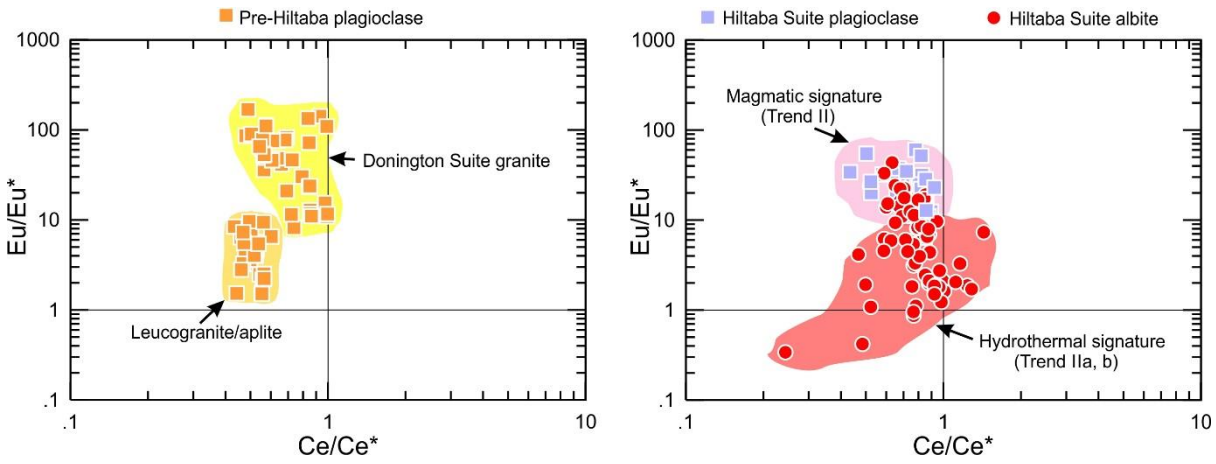

Figure 8: Eu/Eu* vs. Ce/Ce* binary plot of igneous and hydrothermal plagioclase from the sample suite discriminating between REY fractionation patterns. Eu/Eu* = $Eu_{CN}/[(Sm_{CN}+Gd_{CN})/2]$ and Ce/Ce* = $Ce_{CN}/[(La_{CN}+Pr_{CN})/2]$.

5.5.2 Geochemical and genetic implications

Igneous feldspars

The observed chondrite-normalized REY fractionation patterns for igneous feldspars are implicitly related to feldspar/melt partition coefficients. Factors such as the An content of plagioclase, temperature, pressure and fO_2 have been shown to affect partitioning of certain multivalent REE (e.g., Ce and Eu) between crystal and melt (e.g., Blundy and Wood, 1991; Bindeman et al., 1998; Bédard, 2006; Aigner-Torres et al., 2007). Nevertheless, all igneous feldspars analyzed from the sample suite record consistent enrichment in LREE relative to HREE and positive Eu-anomalies. Previous work on trace element partitioning between alkali feldspar/plagioclase and melt (e.g., Bindeman and Davis, 2000; Ren, 2004), has shown that the partition coefficients of REE for feldspar decrease from La-Lu (i.e., with increase in atomic radius). This is supported here by the negative slope (La/Lu) of Trends I and II, and explains the lower concentrations obtained for the HREE. Work by Bindeman and Davis (2000) and others provides strong evidence to suggest that there exists a coupled substitution between Ca and REE in the *M* site of feldspar. This is supported by the observed higher ∑REY concentrations in plagioclase than in alkali feldspar, as well as the positive correlation between Ca and REE in igneous plagioclase observed throughout the sample suite. The positive Eu-anomaly in both igneous alkali feldspar and plagioclase is explained by the behavior of Eu^{2+}, which substitutes for Sr^{2+}, Ca^{2+} and Na^{+} in the feldspar crystal lattice. Thus, during crystallization from a melt, feldspar becomes enriched in Eu, leaving the remaining melt depleted with respect to Eu.

Hydrothermal feldspars

Given the similarities in trends between crypto- and microperthitic alkali feldspar and porous, variably red-stained K-feldspar (Trend I), and between andesine-oligoclase with albite (Trend

II), the concentrations of REY and the respective chondrite-normalized fractionation patterns of hydrothermal feldspars appear to be largely inherited from the igneous feldspars they replace (e.g., Fig. 5). As reactions to form hydrothermal feldspar take place via coupled dissolution-reprecipitation in this case (e.g., Kontonikas-Charos et al., 2017), it appears that despite complete dissolution of the igneous phase, REY effectively remain at the site of the reaction front. This implies that the fluids responsible for replacement (e.g., albitization of plagioclase, recrystallization of alkali feldspar) are in equilibrium with the parent phase (igneous feldspar) in terms of REY concentrations, or that REY are simply immobile at this stage. In the case of igneous alkali feldspar recrystallization through circulation of post-magmatic fluids, it is widely accepted that this is largely isochemical, at least with respect to major elements (e.g., Parsons et al., 2009 and references therein). Nevertheless, working on the Klokken layered syenite intrusion in Greenland, Parsons et al. (2009) found that during recrystallization of braid cryptoperthite to patch perthite, trace elements, particularly Fe and Ti but also REE, were lost to the fluid. Unfortunately, in the present study, trace element analysis by laser ablation could not be performed due to the small scale of individual patch perthite grains within the least-altered RDG. The later, porous and variably red-stained K-feldspar overprint is, however, significantly depleted in ∑REY relative to the well-preserved cryptoperthitic alkali feldspar. Considering that this late K-feldspar overprints the initial recrystallization of cryptoperthitic alkali feldspar, it remains inconclusive whether REY were mobilized during or following deuteric coarsening. Irrespective of which alternative is correct, hydrothermal K-feldspar appears to be a very poor host of REY, and in terms of REY fractionation pattern, the hydrothermal replacement phase generally mimics that of its igneous predecessor.

Geochemical inheritance in feldspars is, however, not universal. Hydrothermal K-feldspar analyzed from crosscutting veins in the Donington Suite granite at Wirrda Well (Trend Ia), as well as albite from sericite-hematite-altered and mineralized RDG (Trend IIa), are markedly

different to Trends I and II, respectively. The strong negative Ce- and Y-anomalies, diagnostic of the K-feldspar, may be explained by preferential partitioning from the fluid, in which case the contemporaneous crystallization of hydrothermal REE-bearing mineral species would lay claim to certain elements during fluid/rock interaction. This is strongly supported by the presence and abundance of REE-fluorocarbonate phases, notably bastnäsite, as well as the observation of sub-µm-sized inclusions of monazite within the hydrothermal K-feldspar + sericite ± chlorite assemblage, which eventually replaces all plagioclase within the Donington Suite granite at Wirrda Well. The presence of xenotime may also explain the negative Y-anomaly. The albite trend (Trend IIa) is broadly similar to that of its counterparts in least-altered RDG (Trend II), however it is downscaled by an order of magnitude (e.g., Fig. 5) due to significant depletion in ∑REY, particularly LREE. The presence of bastnäsite and parisite within sericite-hematite-altered and mineralized RDG may explain the apparent relative depletion in LREE within feldspars. Given the deposit-scale REE-zonation at Olympic Dam (e.g., Ehrig et al., 2012), this may imply both structural and geochemical controls on REY distributions during mineralization and associated alteration, and may simply reflect the positive correlation between REY solubility and proximity to the ODBC.

In the absence of minerals that sequester REE or Y, albite may act as the primary repository for REY during alteration, with ∑REY concentrations exceeding 200 ppm in some cases (Kontonikas-Charos et al., 2014). Such albite is, however, granoblastic in texture, generally devoid of inclusions or micropores and is the result of high fluid/rock ratio metasomatism. Nonetheless, such a finding reinforces the ability of the albite crystal lattice to incorporate significant concentrations of REY. This is also supported by high ∑REY concentrations (~96 ppm) measured in albite from HRQM in drillhole RD2274. The texture of this albite is comparable to that observed throughout the sample suite and indicates that the coupled dissolution-precipitation mechanism may trap trace elements, including REY. This observation

in turn implies that either REY were mobile during the albitization stage, or that igneous plagioclase from the HRQM is enriched in REY relative to that in the RDG. Since the greater part of Eu within the plagioclase crystal lattice is divalent (e.g., Bindeman and Davis, 2000), the absence of a positive Eu-anomaly, in this case, may reflect relatively oxidized (higher fO_2) conditions (e.g., Figs. 7, 8), during which Eu^{2+} is liberated with the release of Ca^{2+} from the plagioclase.

5.5.3 Implications for IOCG systems and the Olympic Cu-Au Province

Given the ubiquity and high modal abundance of feldspars within granitic rocks, any changes to this mineral group will influence the bulk geochemistry, prevailing mineral assemblages and textures of the host rock. There is, however, still debate regarding the role of feldspar replacement reactions in alteration associated with IOCG deposit genesis. Experiments conducted by Oliver et al. (2004) showed that widespread alkali alteration (albitization) can be modelled in terms of simple fluid-rock mixing, via small shifts in the K-feldspar/albite equilibrium curve. In addition, with increasing amounts of fluid-rock interaction, fluids became increasingly enriched in K, Fe and Ca. Such studies may indicate that the early, pre-mineralization alteration, during which feldspars are replaced by albite, mafic silicates by chlorite, and Fe-Ti-oxides by rutile (e.g., Barton, 2014), may in fact represent the initial stages of major element exchange in the formation of IOCG systems. At Olympic Dam, trace elements concentrations in least-altered RDG surrounding the ODBC appear to be relatively stable across the 1 and 5 m intervals for which whole rock data are available, despite showing evidence of alkali alteration (Kontonikas-Charos et al., 2017). This argues for the ability of such feldspar replacement reactions to trap and lock in trace elements during this stage, in contrast to major elements (Na, K, Ca, Fe) which appear to be considerably more mobile. However, evidence from the present study shows that as fluid-rock interaction increases in the

RDG, significant remobilization of REY occurs during feldspar replacement reactions. This is highlighted by the differences in ∑REY from albite in least-altered RDG (36 ppm) and mineralized RDG (3.5 ppm). Prevailing mineral assemblages are supportive of this geochemical change with an abundance of discrete REE-bearing minerals observable within samples of mineralized RDG. Moreover, a similar finding has been documented for other regions within the Olympic Cu-Au Province, e.g., at Moonta-Wallaroo (Kontonikas-Charos et al., 2014) and Hillside (Ismail et al., 2014).

The evolution of feldspar chemistry and texture has been outlined in detail by Kontonikas-Charos et al (2017), who report that igneous plagioclase is no longer present within mineralized RDG within the ODBC. Given the abundance of plagioclase within least-altered RDG surrounding the Olympic Dam deposit, and the relatively high ∑REY concentration (>100 ppm) documented within igneous plagioclase in the present study, it is plausible to suggest that igneous plagioclase, and to a lesser extent alkali feldspar, represent a source of REY for subsequent precipitation of discrete REE-minerals (e.g., Van Dongen et al., 2010). REE and other trace elements are often considered to be concentrated within accessory phases of felsic rocks, with relatively little attention paid to REE concentrations within major rock-forming silicates, notably feldspars. Figure 9 illustrates the degree of which the feldspars contribute to the budget of whole-rock ∑REY in selected samples. It is clear that for some rocks, particularly least-altered RDG, HRQM and the quartz monzodiorite (Phillip's Ridge), a significant proportion of ∑REY are contained within the feldspars. This is not the case for altered Donington Suite granite from Wirrda Well and sericite-hematite-altered and mineralized RDG, in which igneous plagioclase is no longer present.

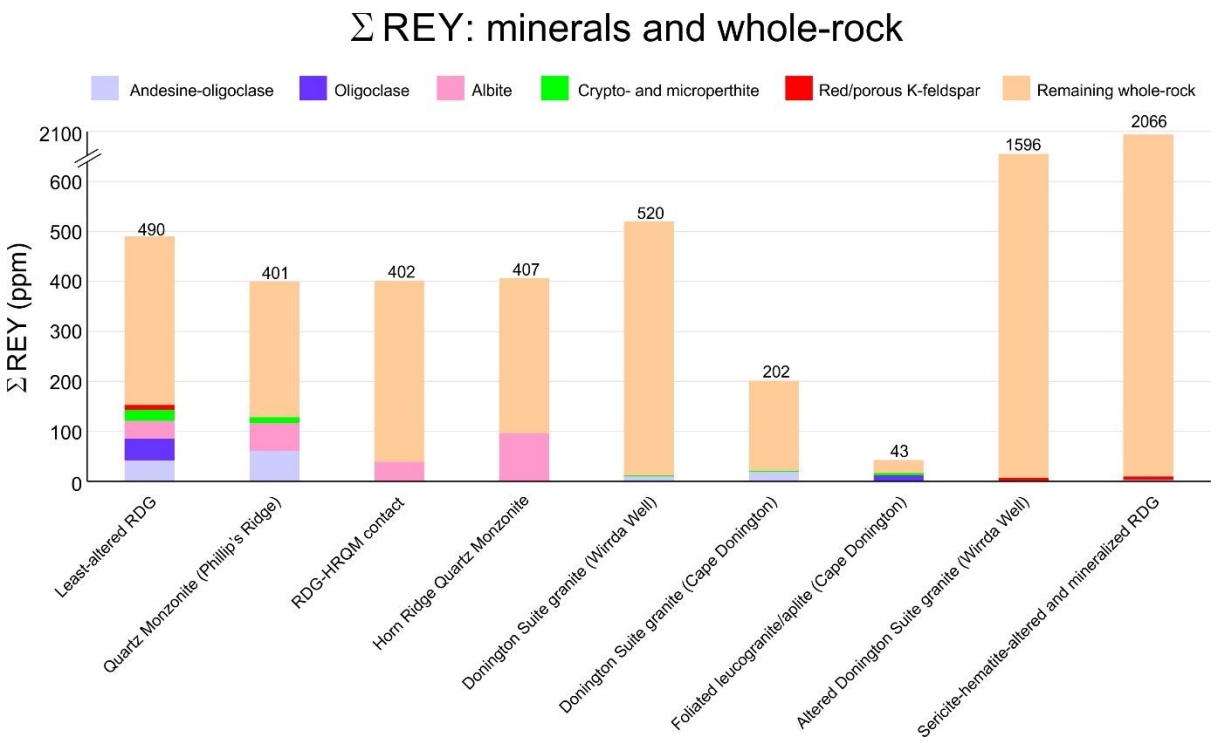

Figure 9: Stacked bar chart representing average ∑REY of minerals and whole rock from selected samples. Whole rock values obtained from sample intervals from 1-5 m. ∑REY for each sample are labelled on top of each column.

CDRR assists in the mobilization of elements from feldspars but also opens up nanoscale pore spaces for the mobilized elements to be subsequently crystallize as inclusions. Without a suitable trap, however, hydrothermal fluids may be easily lost from the system, reducing fluid flow and the potential for pervasive alteration. Considering the abundance of feldspars in granitoid-hosted IOCG systems, their role in re-concentrating REY, and potentially a range of other elements, including critical metals, should not be ignored. Identifying reaction pathways and product host phases for such metals is beyond the scope of the present work but future work should address the distributions of these elements in feldspars and in hydrothermal reaction products ranging from discrete REE-minerals to calc-silicates (e.g., Kontonikas-Charos et al., in press).

5.6 Conclusions

- Initial albitization traps REY from igneous plagioclase within the resultant albite + sericite + epidote assemblage. However, as fluid chemistry changes, or new external fluids are introduced, REY become soluble and are remobilized from albite to form discrete REE-bearing mineral assemblages (e.g., bastnäsite, parisite, monazite, xenotime etc.).
- This study further highlights the applicability of REY chondrite-normalized fractionation patterns for feldspars to identify evolutionary stages within magmatic-hydrothermal systems.
- The abundance of igneous plagioclase and its relatively high ∑REY concentrations measured within granite may, during post-magmatic alteration and mineralization, represent a source for REY in large granitoid-hosted IOCG systems. The inherent ability of CDRR to remobilize and trap trace elements likely contributed to deposit genesis in the case studies presented here.

5.7 Acknowledgements

BHP Billiton Olympic Dam kindly provided financial support and access to Olympic Dam samples and facilities. Staff at Adelaide Microscopy assisted with microanalysis. We also acknowledge the 'FOX' project (Trace elements in iron oxides), supported by BHP Billiton and the South Australian Government Mining and Petroleum Services Centre of Excellence.

5.8 References

Aigner-Torres, M., Blundy, J., Ulmer, P., Pettke, T., 2007. Laser ablation ICPMS study of trace element partitioning between plagioclase and basaltic melts: an experimental approach. Contributions to Mineralogy and Petrology 153, 647-667.

Barton, M., 2014. Iron oxide (–Cu–Au–REE–P–Ag–U–Co) systems. Treatise on Geochemistry (second edition, volume 13): Amsterdam, Elsevier 515-541.

Bau, M., 1991. Rare-earth element mobility during hydrothermal and metamorphic fluid-rock interaction and the significance of the oxidation state of europium. Chemical Geology 93, 219-230.

Bau, M., Dulski, P., 1995. Comparative study of yttrium and rare-earth element behaviours in fluorine-rich hydrothermal fluids. Contributions to Mineralogy and Petrology 119, 213-223.

Bédard, J.H., 2006. Trace element partitioning in plagioclase feldspar. Geochimica et Cosmochimica Acta 70, 3717-3742.

Belousova, E., Griffin, W., O'Reilly, S.Y., 2006. Zircon crystal morphology, trace element signatures and Hf isotope composition as a tool for petrogenetic modelling: examples from Eastern Australian granitoids. Journal of Petrology 47, 329-353.

BHP Billiton, 2016. http://www.bhpbilliton.com/home/investors/annualreporting2016.pdf

Bindeman, I.N., Davis, A.M., 2000. Trace element partitioning between plagioclase and melt: investigation of dopant influence on partition behavior. Geochimica et Cosmochimica Acta 64, 2863-2878.

Bindeman, I.N., Davis, A.M., Drake, M.J., 1998. Ion microprobe study of plagioclase-basalt partition experiments at natural concentration levels of trace elements. Geochimica et Cosmochimica Acta 62, 1175-1193.

Blundy, J.D., Wood, B.J., 1991. Crystal-chemical controls on the partitioning of Sr and Ba between plagioclase feldspar, silicate melts, and hydrothermal solutions. Geochimica et Cosmochimica Acta 55, 193-209.

Brugger, J., Etschmann, B., Pownceby, M., Liu, W., Grundler, P., Brewe, D., 2008. Oxidation state of europium in scheelite: tracking fluid–rock interaction in gold deposits. Chemical Geology 257, 26-33.

Bychkov, A., Kotelnikov, A., Romanenko, I., Senderov, E., 1989. Effect of isomorphic replacement of silicon by phosphorus on structural peculiarities of feldspars. Rossiiskaya Akademiya Nauk Savelevskii Per. 13 October, 119034 Moscow, Russia, 310-313.

Ciobanu, C.L., Wade, B.P., Cook, N.J., Mumm, A.S., Giles, D., 2013. Uranium-bearing hematite from the Olympic Dam Cu–U–Au deposit, South Australia: a geochemical tracer and reconnaissance Pb–Pb geochronometer. Precambrian Research 238, 129-147.

Conor, C.H., 1995. Moonta-Wallaroo region: an interpretation of the geology of the Maitland and Wallaroo 1: 100 000 sheet areas. Mines and Energy South Australia, Open File Envelope 8886

Conor, C., Raymond, O., Baker, T., Teale, G., Say, P., Lowe, G., 2010. Alteration and Mineralisation in the Moonta-Wallaroo Cu-Au Mining Field Region, Olympic Domain, South Australia. In: Porter T.M. (Ed.), Hydrothermal Iron Oxide Copper-Gold and Related Deposits: A Global Perspective 3, PGC Publishing, Adelaide, 1-24.

Courtney-Davies, L., Zhu, Z., Ciobanu, C.L., Wade, B.P., Cook, N.J., Ehrig, K., Cabral, A.R., Kennedy, A., 2016. Matrix-matched iron-oxide laser ablation ICP-MS U–Pb geochronology using mixed solution standards. Minerals 6, 85

Cowley, W., Conor, C., Zang, W., 2003. New and revised Proterozoic stratigraphic units on northern Yorke Peninsula. MESA Journal 29, 46-58.

Creaser, R.A., 1989. The geology and petrology of Middle Proterozoic felsic magmatism of the Stuart Shelf, South Australia. La Trobe University, Melbourne.

Creaser, R.A., 1996. Petrogenesis of a Mesoproterozoic quartz latite-granitoid suite from the Roxby Downs area, South Australia. Precambrian Research 79, 371-394.

D'Arco, P., Piriou, B., 1989. Fluorescence spectra of Eu^{3+} in synthetic polycrystalline anorthite: Distribution of Eu^{3+} in the structure. American Mineralogist 74, 191-199.

Ehrig, K., 2013. Geology of the Wirrda Well IOCG deposit. Powerpoint presentation, 10th

Annual SA Exploration and Mining Conference, Adelaide. http://www.saexplorers.com.au

Ehrig, K., McPhie, J., Kamenetsky, V., 2012. Geology and mineralogical zonation of the Olympic Dam Iron Oxide Cu-U-Au-Ag deposit, South Australia. In: Hedenquist J.W., Harris, M., Camus, F., (Eds.), Geology and Genesis of Major Copper Deposits and Districts of the World: A Tribute to Richard H. Sillitoe, 16. SEG Special Publication, 237–267.

Elderfield, H., Greaves, M.J., 1982. The rare earth elements in seawater. Nature 296, 214-219.

Fanning, C., Flint, R., Parker, A., Ludwig, K., Blissett, A., 1988. Refined Proterozoic evolution of the Gawler craton, South Australia, through U-Pb zircon geochronology. Precambrian Research 40, 363-386.

Fanning, C.M., 1997. Geochronological synthesis of southern Australia. Part II. The Gawler Craton. South Australian Department of Mines and Energy, Open file envelope 8918 (unpublished)

Fanning, C.M., 2002. Gawler Craton: synthesis of recent SHRIMP U–Pb geochronology. In: Gawler Craton 2002: State of Play. Department of Primary Industries and Resources Workshop Proceedings (CD). Office of Minerals and Energy Resources, South Australia.

Ferris, G.M., Schwarz, M.P., Heithersay, P., 2002. The geological framework, distribution, and controls of Fe-oxide Cu–Au mineralisation in the Gawler Craton, South Australia: Part 1—Geological and tectonic framework. In: Porter T.M. (Ed.), Hydrothermal iron oxide copper–gold and related deposits: A Global Perspective 2, PGC Publishing, Adelaide, 9-32.

Fleet, M.E., 1988. Tetrahedral-site occupancies in reedmergnerite and synthetic boron albite ($NaBSi_3O_8$). American Mineralogist 77, 76-84.

Garcia, D., Pascal, M-L., Roux, J., 1996. Hydrothermal replacement of feldspars in igneous enclaves of the Velay granite and the genesis of myrmekites. European Journal of Mineralogy 8, 703-718.

Gast, P.W., 1968. Trace element fractionation and the origin of tholeiitic and alkaline magma

types. Geochimica et Cosmochimica Acta 32, 1057-1086.

Goldschmidt, V.M., 1937. The principles of distribution of chemical elements in minerals and rocks. The seventh Hugo Müller Lecture, delivered before the Chemical Society on March 17th, 1937. Journal of the Chemical Society (Resumed), 655-673.

Haas, J.R., Shock, E.L., Sassani, D.C., 1995. Rare earth elements in hydrothermal systems: estimates of standard partial molal thermodynamic properties of aqueous complexes of the rare earth elements at high pressures and temperatures. Geochimica et Cosmochimica Acta 59, 4329-4350.

Haynes, D.W., Cross, K.C., Bills, R.T., Reed, M.H., 1995. Olympic Dam ore genesis; a fluid-mixing model. Economic Geology 90, 281-307.

Hayward, N., Skirrow, R., 2010. Geodynamic setting and controls on iron oxide Cu-Au (±U) ore in the Gawler craton, South Australia. In: Porter TM (Ed.), Hydrothermal Iron Oxide Copper-Gold & Related Deposits: A Global Perspective, 3-4, PGC Publishing, Adelaide, 105-131.

Henderson, P., 1984. General geochemical properties and abundances of the rare earth elements. In: Henderson P (Ed), Rare Earth Element Geochemistry, 1st ed, Elsevier

Hövelmann, J., Putnis, A., Geisler, T., Schmidt, B.C., Golla-Schindler, U., 2010. The replacement of plagioclase feldspars by albite: observations from hydrothermal experiments. Contributions to Mineralogy and Petrology 159, 43-59.

Huang, Q., Kamenetsky, V.S., McPhie, J., Ehrig, K., Meffre, S., Maas, R., Thompson, J., Kamenetsky, M., Chambefort, I., Apukhtina, O., 2015. Neoproterozoic (ca. 820–830 Ma) mafic dykes at Olympic Dam, South Australia: Links with the Gairdner Large Igneous Province. Precambrian Research 271, 160-172.

Ismail, R., Ciobanu, C.L., Cook, N.J., Teale, G.S., Giles, D., Mumm, A.S., Wade, B., 2014. Rare earths and other trace elements in minerals from skarn assemblages, Hillside iron

oxide–copper–gold deposit, Yorke Peninsula, South Australia. Lithos 184–187, 456-477.

Jagodzinski, E., 2005. Compilation of SHRIMP U-Pb geochronological data, Olympic Domain, Gawler Craton. South Australia, 2001-2003. Geoscience Australia Record 2005/020

Jagodzinski, E.A., Reid, A.J., Hand, M., 2012. SHRIMP U-Pb geochronology of Archaean to Palaeoproterozoic rocks from southern Eyre Peninsula. Report book 2012/00015, Department of Manufacturing, Trade, Innovation, Resources and Energy, South Australia, Adelaide.

Jagodzinski, E.A., 2014. The age of magmatic and hydrothermal zircon at Olympic Dam, Australian Earth Sciences Convention Proceedings, Geological Society of Australia Abstracts 110, 260.

Johnson, J.P., Cross, K.C., 1995. U-Pb geochronological constraints on the genesis of the Olympic Dam Cu-U-Au-Ag deposit, South Australia. Economic Geology 90, 1046-1063.

Kimata, M., 1988. The crystal structure of non-stoichiometric Eu-anorthite: an explanation of the Eu-positive anomaly. Mineralogical Magazine 52, 257-265.

Kneip, H-J., Liebau, F., 1994. Feldspars with trivalent non-tetrahedral cations: Experimental studies in the system $NaAlSi_3O_8$-$CaAl_2Si_2O_8$-$LaAl_3SiO_8$. European Journal of Mineralogy 6, 87-98.

Kontonikas-Charos, A., Ciobanu, C.L., Cook, N.J., 2014. Albitization and redistribution of REE and Y in IOCG systems: Insights from Moonta-Wallaroo, Yorke Peninsula, South Australia. Lithos 208–209, 178-201.

Kontonikas-Charos, A., Ciobanu, C.L., Cook, N.J., Ehrig, K., Kamenetsky, V.S., 2015. Deuteric coarsening and albitization in Hiltaba granites from the Olympic Dam IOCG deposit, South Australia. Proceedings, Mineral Resources in a Sustainable World, 13th Biennial SGA Meeting, 3:1099–1102.

Kontonikas-Charos, A., Ciobanu, C.L., Cook, N.J., Ehrig, K., Krneta, S., Kamenetsky, V.S., 2017. Feldspar evolution in the Roxby Downs Granite, host to Fe-oxide Cu-Au-(U) mineralisation at Olympic Dam, South Australia. Ore Geology Reviews 80, 838-859.

Kontonikas-Charos, A., Ciobanu, C.L., Cook, N.J., Ehrig, K., Ismail, R., Krneta, S., Basak, A., (in press). Feldspar mineralogy and rare earth element (re)mobilization in iron-oxide copper gold systems from South Australia: a nanoscale study. Mineralogical Magazine. https://doi.org/10.1180/minmag.2017.081.040

Krneta, S., Ciobanu, C.L., Cook, N.J., Ehrig, K., Kontonikas-Charos, A., 2016. Apatite at Olympic Dam, South Australia: A petrogenetic tool. Lithos 262, 470-485.

London, D., Černý, P., Loomis, J.L., Pan, J.J., 1990. Phosphorus in alkali feldspars of rare-element granitic pegmatites. Canadian Mineralogist, 28(4), 771-786.

Lottermoser, B., 1992. Rare earth elements and hydrothermal ore formation processes. Ore Geology Reviews 7, 25-41.

Mauger, A.J., Ehrig, K., Kontonikas-Charos, A., Ciobanu, C.L., Cook, N.J., Kamenetsky, V.S., 2016. Alteration at the Olympic Dam IOCG-U deposit: insights into distal to proximal feldspar and phyllosilicate chemistry from infrared reflectance spectroscopy. Australian Journal of Earth Sciences 63, 959-972.

McDonough, W.F., Sun, S-S., 1995. The composition of the Earth. Chemical Geology 120, 223-253.

McPhie, J., DellaPasqua, F., Allen, S., Lackie, M., 2008. Extreme effusive eruptions: palaeoflow data on an extensive felsic lava in the Mesoproterozoic Gawler Range Volcanics. Journal of Volcanology and Geothermal Research 172, 148-161.

Migdisov, A.A., Williams-Jones, A., Brugger, J., Caporuscio, F., 2016. Hydrothermal transport, deposition, and fractionation of the REE: Experimental data and thermodynamic calculations. Chemical Geology 439, 13-42.

Migdisov, A.A., Williams-Jones, A., 2014. Hydrothermal transport and deposition of the rare earth elements by fluorine-bearing aqueous liquids. Mineralium Deposita 49, 987-997.

Morad, S., El-Ghali, M., Caja, M., Sirat, M., Al-Ramadan, K., Mansurbeg, H., 2010. Hydrothermal alteration of plagioclase in granitic rocks from Proterozoic basement of SE Sweden. Geological Journal 45, 105-116.

Morales-Ruano, S., Both, R., Golding, S., 2002. A fluid inclusion and stable isotope study of the Moonta copper–gold deposits, South Australia: evidence for fluid immiscibility in a magmatic hydrothermal system. Chemical Geology 192, 211-226.

Mortimer, G.E., 1984. Early to middle Proterozoic granitoids, basaltic dykes and associated layered rocks of SE Eyre Peninsula, South Australia. Unpublished PhD thesis, University of Adelaide.

Oliver, N.H., Cleverley, J.S., Mark, G., Pollard, P.J., Fu, B., Marshall, L.J., Rubenach, M.J., Williams, P.J., Baker, T., 2004. Modeling the role of sodic alteration in the genesis of iron oxide-copper-gold deposits, Eastern Mount Isa block, Australia. Economic Geology 99, 1145-1176.

Papike, J.J., 1988. Chemistry of the rock-forming silicates: Multiple-chain, sheet, and framework structures. Reviews of Geophysics, 26, 407-444.

Parker, A.J., 1993. Gawler craton. Cleve and Moonta subdomains: South Australian Geological Survey Bulletin 54, 51-68.

Parsons, I., Thompson, P., Lee, M.R., Cayzer, N., 2005. Alkali feldspar microtextures as provenance indicators in siliciclastic rocks and their role in feldspar dissolution during transport and diagenesis. Journal of Sedimentary Research 75, 921-942.

Parsons, I., Magee, C.W., Allen, C.M., Shelley, J., Lee, M.R., 2009. Mutual replacement reactions in alkali feldspars II: trace element partitioning and geothermometry. Contributions to Mineralogy and Petrology 157, 663-687.

Pearce, N.J., Perkins, W.T., Westgate, J.A., Gorton, M.P., Jackson, S.E., Neal, C.R., Chenery, S.P., 1997. A compilation of new and published major and trace element data for NIST SRM 610 and NIST SRM 612 glass reference materials. Geostandards Geoanalytical Research 21, 115-144.

Perez, R.J., Boles, J.R., 2005. An empirically derived kinetic model for albitization of detrital plagioclase. American Journal of Science 305, 312-343.

Pun, A., Papike, J., Layne, G., 1997. Subsolidus REE partitioning between pyroxene and plagioclase in cumulate eucrites: An ion microprobe investigation. Geochimica et Cosmochimica Acta 61, 5089-5097.

Putnis, A., 2002. Mineral replacement reactions: from macroscopic observations to microscopic mechanisms. Mineralogical Magazine 66, 689-708.

Reeve, J.S., Cross, K.C., Smith, R.N., Oreskes, N., 1990. Olympic Dam copper-uranium-gold-silver deposit. Geology of the mineral deposits of Australia and Papua New Guinea 2:1009-1035.

Reid, A.J., Fabris, A., 2015. Influence of Preexisting Low Metamorphic Grade Sedimentary Successions on the Distribution of Iron Oxide Copper-Gold Mineralization in the Olympic Cu-Au Province, Gawler Craton. Economic Geology 110, 2147-2157.

Ren, M., 2004. Partitioning of Sr, Ba, Rb, Y, and LREE between alkali feldspar and peraluminous silicic magma. American Mineralogist 89, 1290-1303.

Schilling, J-G., Winchester, J., 1967 Rare-earth fractionation and magmatic processes. In: Runcorn SK (Ed), Mantles of the Earth and Terrestrial Planets. Interscience Publishers, New York, 267-283.

Skirrow, R.G., Bastrakov, E.N., Barovich, K., Fraser, G.L., Creaser, R.A., Fanning, C.M., Raymond, O.L., Davidson, G.J., 2007. Timing of iron oxide Cu-Au-(U) hydrothermal activity and Nd isotope constraints on metal sources in the Gawler craton, South Australia.

Economic Geology 102, 1441-1470.

Smith, J.V., 1974. Feldspar Minerals. Volume 2. Chemical and Textural Properties. Springer-Verlag.

Smith, M., Henderson, P., Jeffries, T., Long, J., Williams, C., 2004. The rare earth elements and uranium in garnets from the Beinn an Dubhaich Aureole, Skye, Scotland, UK: constraints on processes in a dynamic hydrothermal system. Journal of Petrology 45, 457-484.

Stix, J., Gorton, M.P., 1990. Variations in trace element partition coefficients in sanidine in the Cerro Toledo Rhyolite, Jemez Mountains, New Mexico: Effects of composition, temperature, and volatiles. Geochimica et Cosmochimica Acta 54, 2697-2708.

Towell, D.G., Winchester, J.W., Spirn, R.V., 1965. Rare-Earth distributions in some rocks and associated minerals of the batholith of southern California. Journal of Geophysical Research 70, 3485-3496.

Van Achterbergh, E., Ryan, C.G., Griffin, W.L., 2001. GLITTER user's manual: on-line interactive data reduction for the LA-ICP-MS microprobe. GEMOC Version 4:72

Van Dongen M., Weinberg, R.F., Tomkins, A.G., 2010. REE-Y, Ti, and P remobilization in magmatic rocks by hydrothermal alteration during Cu-Au deposit formation. Economic Geology 105, 763-776.

Wang, Y., Wang, Y., Merino, E., 1995. Dynamic weathering model: Constraints required by coupled dissolution and pseudomorphic replacement. Geochimica et Cosmochimica Acta 59, 1559-1570.

CHAPTER 6

FELDSPAR MINERALOGY AND RARE EARTH ELEMENT (RE)MOBILIZATION IN IRON-OXIDE COPPER GOLD SYSTEMS FROM SOUTH AUSTRALIA: A NANOSCALE STUDY

Alkis Kontonikas-Charos[1], Cristiana L. Ciobanu[2], Nigel J. Cook[2], Kathy Ehrig[3], Roniza Ismail[1], Sasha Krneta[1], Animesh Basak[4]

[1]*School of Physical Sciences, The University of Adelaide, Adelaide, SA, 5005, Australia*

[2]*School of Chemical Engineering, The University of Adelaide, Adelaide, SA, 5005, Australia*

[3]*BHP Billiton Olympic Dam, Adelaide, SA, 5000, Australia*

[4]*Adelaide Microscopy, The University of Adelaide, Adelaide, SA, 5005, Australia*

Article submitted for publication in Mineralogical Magazine, Special Issue 'EMC Meeting 2016', on 4 February 2017

Accepted 23 May 2017 (https://doi.org/10.1180/minmag.2017.081.040)

Statement of Authorship

Title of Paper	Feldspar mineralogy and rare earth element (re)mobilization in iron-oxide copper gold systems from South Australia: a nanoscale study
Publication Status	☐ Published ☑ Accepted for Publication ☐ Submitted for Publication ☐ Unpublished and Unsubmitted w ork w ritten in manuscript style
Publication Details	Kontonikas-Charos, A., Ciobanu, C.L., Cook, N.J., Ehrig, K., Ismail, R., Krneta, S., Basak, A. (in press). Feldspar mineralogy and rare earth element (re)mobilization in iron-oxide copper gold systems from South Australia: a nanoscale study. Mineral Magazine. https://doi.org/10.1180/minmag.2017.081.040

Principal Author

Name of Principal Author (Candidate)	Alkis Kontonikas-Charos		
Contribution to the Paper	Performed analytical work, carried out data processing and interpretation, oversaw development of work and wrote manuscript.		
Overall percentage (%)	60		
Certification:	This paper reports on original research I conducted during the period of my Higher Degree by Research candidature and is not subject to any obligations or contractual agreements with a third party that would constrain its inclusion in this thesis. I am the primary author of this paper.		
Signature		Date	11/07/17

Co-Author Contributions

By signing the Statement of Authorship, each author certifies that:

i. the candidate's stated contribution to the publication is accurate (as detailed above);

ii. permission is granted for the candidate in include the publication in the thesis; and

iii. the sum of all co-author contributions is equal to 100% less the candidate's stated contribution.

Name of Co-Author	Cristiana L. Ciobanu		
Contribution to the Paper	Helped define direction of research, supervised development of work, assisted with data interpretation and contributed to manuscript preparation.		
Overall percentage (%)	25		
Signature		Date	10 July 2017

Name of Co-Author	Nigel J. Cook		
Contribution to the Paper	Helped define direction of research, supervised development of work, assisted with data interpretation and contributed to manuscript preparation.		
Overall percentage (%)	10		
Signature		Date	10/7/17

Name of Co-Author	Kathy Ehrig		
Contribution to the Paper	Provided sample material and helped to evaluate and edit manuscript.		
Overall percentage (%)	2		
Signature		Date	10 July 2017

Name of Co-Author	Roniza Ismail		
Contribution to the Paper	Obtained preliminary LA-ICP-MS data collection for Hillside sample material.		
Overall percentage (%)	1		
Signature		Date	10/7/17

ON BEHALF OF DR. ISMAIL
(COULD NOT BE CONTACTED)

Name of Co-Author	Sasha Krneta		
Contribution to the Paper	Helped to evaluate and edit manuscript.		
Overall percentage (%)	1		
Signature		Date	11/7/2017

Name of Co-Author	Animesh Basak		
Contribution to the Paper	Assisted in operating analytical instrumentation (FIB-SEM).		
Overall percentage (%)	1		
Signature		Date	11/7/17

Abstract

Nanoscale characterization (TEM on FIB-SEM-prepared foils) was undertaken on feldspars undergoing transformation from early post-magmatic (deuteric) to hydrothermal stages in granite hosting the Olympic Dam Cu-U-Au-Ag deposit, and from the Cu-Au skarn at Hillside within the same iron-oxide copper-gold (IOCG) province, South Australia. These include complex perthitic textures, anomalously Ba-, Fe-, or REE-rich feldspars, and REE-fluorocarbonate + molybdenite assemblages, which pseudomorph pre-existing feldspars. Epitaxial orientations between cryptoperthite (magmatic), patch perthite (deuteric) and replacive albite (hydrothermal) within vein perthite, support interface-mediated reactions between pre-existing alkali feldspars and pervading fluid, irrespective of micron-scale crystal morphology. Such observations are consistent with a coupled dissolution-reprecipitation reaction mechanism, which assists in grain-scale element (re)mobilization via the generation of transient interconnected microporosity. Micron-scale aggregates of hydrothermal hyalophane (Ba-rich K-feldspar), crystallizing within previously albitized areas of andesine, reveal a complex assemblage of calc-silicate, As-bearing fluorapatite and Fe-oxides (along grain boundaries) within the enclosing albite + sericite assemblage at the nanoscale. Such inclusions are good REE repositories and their presence supports REE remobilization at the grain-scale during early hydrothermal alteration. Iron-metasomatism is recognized by nm-scale maghemite inclusions within 'red-stained' orthoclase, as well as by hematite in REE-fluorocarbonates, which reflect broader-scale zonation patterns typical for IOCG systems. Potassium-feldspar from the contact between alkali-granite and skarn at Hillside is characterized by 100-1,000 ppm REE+Y, attributable to pervasive nm-scale inclusions of calc-silicates, concentrated along microfractures or attached to pores. Feldspar replacement by REE-fluorocarbonates at Olympic Dam and nanoscale calc-silicate inclusions within feldspar at

Hillside, are both strong indicators of the role feldspars play in concentrating REE during metasomatism. Differences in mineralogical expression are due to availability of associated elements. Lattice-scale intergrowth assemblages, which are indicative of Fe-metasomatism, REE-enrichment and sulphide deposition at Olympic Dam, support a spatial and temporal relationship between these processes.

6.1 Introduction

Iron-oxide copper gold (IOCG) deposits of the Olympic Cu-Au Province, eastern Gawler Craton, South Australia (Fig. 1a) display significant enrichment in rare earth elements (REE) relative to average crustal values (Skirrow et al., 2007). Indeed, a marked enrichment in REE + Y (hereafter REY) and U is one defining characteristic of the IOCG deposit clan (Hitzman et al., 1992), and any genetic model for the deposits needs to account for this.

The >10 billion tonne Olympic Dam Cu-U-Au-Ag deposit is not only the largest IOCG system in the Gawler Craton, but is among the largest concentrations of REE on Earth (mean concentration ~0.17 wt. % La and 0.25 wt. % Ce; Ehrig et al., 2012). The deposit is also enriched in a diverse range of other elements considered as critical metals, such as Sc, Ga, In, Mo, Nb, Se, Sn, Sr, Te and W (Ehrig et al., 2012). REE are not recovered at present for several reasons, including: (i) a dominance of less-valuable light rare earths (LREE; La, Ce, Nd); (ii) occurrence within various fine-grained minerals (bastnäsite, florencite and subordinate synchysite, xenotime and monazite); (iii) their presence also within solid solution in common accessories (e.g. apatite; Krneta et al., 2016); and (iv) the intimate intergrowth of all REE-minerals with other phases, notably U-bearing minerals, down to the nanoscale.

Feldspars are, volumetrically, by far the dominant component of the Roxby Downs Granite (RDG), a Mesoproterozoic felsic granitoid that hosts, and is genetically associated with the IOCG system at Olympic Dam. These feldspars, and those from coeval Mesoproterozoic granitoids related to other IOCG systems within the Olympic Cu-Au Province, contain

measurable concentrations of REE and other trace elements (Y, Ga etc.), either within the feldspar lattice, or as sub-microscopic-scale inclusions of discrete REE-minerals (Kontonikas-Charos et al., 2014, 2015, 2017; Ismail et al., 2014). To understand the evolution of trace element concentrations in feldspars during fluid/rock interaction, and mechanisms of REE enrichment within broader models for IOCG genesis, these authors have investigated the microstructural, mineralogical and geochemical expression of such enrichment during feldspar evolution from magmatic to early hydrothermal stages.

Kontonikas-Charos et al. (2017) examined the sequence and mechanisms of feldspar replacement reactions that mark the onset of the IOCG-forming system at Olympic Dam. These start with late-magmatic development of rapakivi and anti-rapakivi textures between igneous plagioclase and alkali feldspar. The post-magmatic evolution comprises modification of alkali feldspar from cryptoperthite to patch perthite, overprinting of patch perthite by highly porous albite and K-feldspar, and replacement of plagioclase by albite + sericite ± Ba-rich K-feldspar. Importantly, the study showed that hydrothermal albite and K-feldspar formed within granitoids hosting the Olympic Dam deposit without supply of alkali metals from any external source. Kontonikas-Charos et al. (in review) provide trace element data for feldspars from different stages of the magmatic to hydrothermal transformation of plagioclase and alkali feldspar from Olympic Dam and prospects within the region. The evolution of feldspar microtextures and compositions are mirrored by changes in absolute REY concentrations and chondrite-normalized REY fractionation patterns. Initial albitization of igneous plagioclase traps REY within the resultant albite + sericite ± epidote assemblage.

The systematic changes in feldspars from least-altered to mineralized RDG at Olympic Dam (Kontonikas-Charos et al., in review) support the applicability of REY-fractionation trends in feldspars as geochemical tracers of hydrothermal alteration. Such an interpretation is concordant with studies of feldspars from rocks in areas further south in the Olympic Cu-Au

province: the Moonta-Wallaroo region (Kontonikas-Charos et al., 2014); and granites from the Hillside Cu-Au skarn deposit (Ismail et al., 2014). The marked decrease in ∑REY in feldspars with proximity to the Olympic Dam orebody hints at the release and remobilization of REY from feldspars into discrete REE minerals.

These studies have all emphasized the nature of the replacement reactions as dominantly pseudomorphic, thus presumably driven via a coupling of dissolution and reprecipitation rates at the interface between a pre-existing mineral and a pervading fluid (CDRR), as defined by Putnis (2002). Given that CDRR, the main type of feldspar transformation, begins at the nanoscale (Kontonikas-Charos et al., 2017), it is critical to understand prevailing mineral assemblages and phase relationships at the smallest scales (orientation boundaries, inclusions, etc.). In this contribution, we present examples from Olympic Dam and Hillside deposits, two types of IOCG systems with contrasting alteration styles (Fig. 1b; see below). These illustrate how the characterization of feldspars and associated REE-bearing minerals and/or discrete REE-minerals at the nanoscale allow us to constrain the sequence of reactions from primary magmatic assemblages to phases formed simultaneous with Fe-metasomatism and deposition of sulphide ore. Considering the abundance of feldspars in rocks hosting IOCG systems, any widespread feldspar replacement reactions will play a significant role in redistributing trace elements during the transition from magmatic to hydrothermal stages. Identifying host phases and reaction pathways for REE, and by implication, also other critical metals, is an important step towards establishing their long-term resource potential.

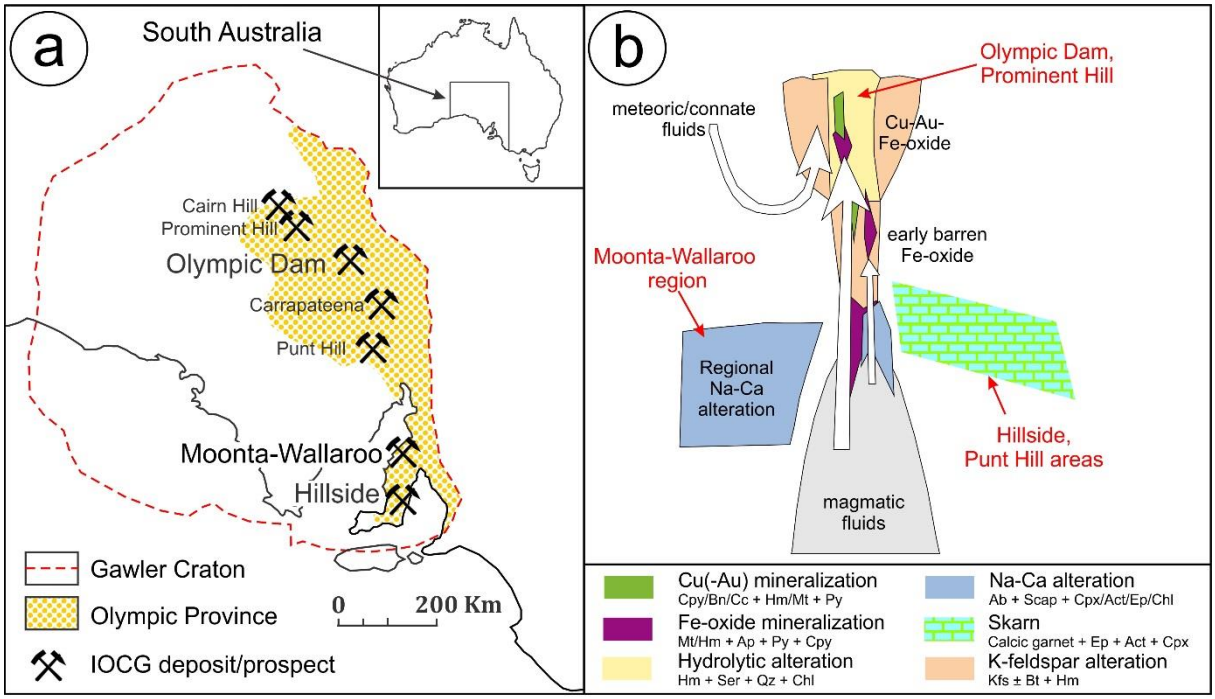

Figure 1: (a) Sketch map of the Gawler Craton, South Australia, showing the location of the Olympic Cu-Au province, the Olympic Dam deposit, the Hillside deposit, and other deposits/prospects mentioned in the text. (b) Sketch, after Barton and Johnson (1996), showing proposed crustal settings of selected South Australian IOCG deposits.

6.2 Background on IOCG deposits and feldspar alteration

Iron oxide copper-gold mineralization forms in a wide range of ore systems spanning from the Archean to the Phanerozoic (e.g. Groves et al., 2010). Genetic models for these deposits are still much debated, particularly regarding the role of igneous rocks, the sources of metals and fluids, and geodynamic settings (e.g. Hitzman et al., 1992; Barton and Johnson, 2004; Pollard, 2006; Groves et al., 2010). It is widely accepted, nonetheless, that IOCG systems are defined by broad alteration haloes comprising early sodic-calcic alteration and barren Fe-oxide alteration followed by deposition of Cu-Au-mineralization, often accompanied by hydrolytic alteration (Fig. 1b). The early albite ± calc-silicate (epidote ± actinolite ± diopside) ± magnetite alteration (Na-Ca-Fe alteration) as well as scapolite-bearing assemblages may be recognized

at the regional scale (Barton, 2014). In contrast, the ore-bearing alteration stage is typically found at the local scale and can be broadly subdivided into deeper potassic (K-feldspar ± biotite) and shallower hydrolytic (sericite ± chlorite ± carbonate) alteration, where magnetite and hematite are the dominant Fe-oxides, respectively (Barton, 2014). Terranes dominated by carbonate-rich protoliths are generally characterized by calc-silicate alteration (e.g. epidote/clinozoisite + actinolite + clinopyroxene + calcic garnet), with ore hosted within skarn. Based on gain or loss of different components, skarn formation is distinct from Na-Ca alteration of aluminous igneous or sedimentary protoliths which can also result in formation of calc-silicates (carbonate-hosted alteration; Barton, 2014).

The Olympic Cu-Au Province is one of the largest Mesoproterozoic IOCG provinces on Earth (Skirrow et al., 2007). Alteration ranges from the 'end-member' sericite-hematite-breccia hosted type (e.g. Olympic Dam and Prominent Hill deposits), to skarn-hosted polymetallic mineralization in the Punt Hill district (Groundhog prospect; e.g. Reid et al., 2011), strongly potassic-altered and minor skarn-hosted mineralization at Moonta-Wallaroo (small-scale Cu-Au veins; Conor et al., 2010) and Cu-Au skarn-IOCG deposit at Hillside, on the western margin of the Yorke Peninsula (e.g. Conor et al., 2010; Ismail et al., 2014) (Fig. 1a). Unlike other IOCG terranes in Australia (e.g. Cloncurry District), the Olympic Cu-Au Province also stands out in showing a characteristic enrichment in REE and U, irrespective of alteration style (e.g. Skirrow et al., 2007). An opportunity thus exists to understand the processes inherently responsible for such metal endowments within a range of host rocks and alteration styles, in which feldspars play key roles. Albitization, associated with the early sodic-calcic alteration stage, has been discussed down to the nanoscale in a broader petrological context, albeit not for IOCG systems, with significant implications for rock permeability and geochemistry (e.g. Plümper and Putnis, 2009). Moreover, hematite dusting of feldspars, often observed in rocks that have undergone subsolidus re-equilibration (e.g. Putnis et al., 2007), is recognized as Fe-

oxide staining of feldspar across the Olympic Cu-Au Province (e.g. Ismail et al., 2014; Kontonikas-Charos et al., 2015, 2017; Ismail, 2016). This phenomenon is also observed to increase in intensity with proximity to the ore-hosting Olympic Dam Breccia Complex (ODBC) (Kontonikas-Charos et al., 2017). Moreover, a recent study by Mauger et al. (2016) reported the regional presence of albite at Olympic Dam, as well as deposit-scale zonation of feldspar speciation, showing an increase in microcline/orthoclase ratio from surrounding least-altered-RDG to altered and mineralized RDG within the ODBC. This trend is complemented by an increase in the Fe/Mg ratio of chlorite in the same samples.

Many publications have dealt with mesoscopic/macroscopic-scale characterization of alteration haloes in IOCG systems (e.g. Barton 2014, and references therein). These authors have sought to show how alteration assemblages can provide a petrological context for ore deposition. Although various alteration signatures have been defined, and show some degree of continuity from deposit to deposit, the understanding of the mineral assemblages themselves, and their variation from the micron- to nanoscale, has lagged well behind. Issues such as the mobility and enrichment of trace elements, including U and REY, have also been dealt with using approaches based on basic petrographic and whole-rock analysis rather than any mineralogical studies at appropriate scales. Building upon an understanding of feldspar alteration from the macro- to micron scale (Kontonikas-Charos et al., 2017), the present study extends this knowledge down to the nanoscale. The main aim is to understand whether feldspars can track mobility of minor/trace elements during their alteration, and if so in what way.

6.3 Approach

Our main emphasis is on examples representing various stages of feldspar alteration in the RDG outside the orebody at Olympic Dam. An additional example from the early skarn at

Hillside has been investigated for comparison. The sample suite (Table 1) was selected based on several criteria including: (i) preservation of igneous and hydrothermal feldspars, (ii) anomalous trace and minor element concentrations as well as (iii) the presence of unusual REE- and sulphide-bearing mineral assemblage within the replacement areas. Examples from Olympic Dam include specimens that particularly show the sequence of feldspar alteration as introduced by Kontonikas-Charos et al. (2017), i.e. igneous alkali feldspars preserving post-magmatic recrystallization textures (deuteric coarsening), which are overprinted by albitization, K-feldspathization and hydrolytic (sericite + quartz) alteration (Fig. 2).

Table 1: Overview of samples investigated and correlation with previous work

Study case	Topic	Deposit	Sample ID /number of TEM foils	Drillhole/depth (mRL)	Relevant figures
A	Perthites	Olympic Dam (all samples from RDG outside the ODBC)	RX7865/2	RD2495/450m	Figs. 6 and 14 in Kontonikas-Charos et al. (2017)
B	Hydrothermal Ba-bearing K-feldspar (hyalophane)				Figs. 9d, 12 in Kontonikas-Charos et al. (2017)
C	Fe-metasomatism in red-stained K-feldspar		RX6698/1	RD2316/635m	Figs. 10a-b and 17 in Kontonikas-Charos et al. (2017)
D	Feldspar replacement by REE-fluorocarbonates + molybdenite		RX6687/1	RD2316/490 m	Fig. 11 in Kontonikas-Charos et al. (2017)
HS	K-feldspar with early endoskarn alteration	Hillside (alkali-granite)	GT30a/2	HDD407/582m	Figs. 7.1 & 7.2 in Ismail (2016)

Case study A (Fig. 2a) derives from a sample of RDG, ~4 km outside the ODBC, and is representative of the recrystallization of igneous alkali feldspar (cryptoperthite) to patch perthite following interaction with post-magmatic fluids. Mineralogy is typical of least-altered RDG. Plagioclase and alkali feldspar are partially overprinted by an assemblage of near end-member albite and rare hyalophane, together with preserved, but porous orthoclase. Igneous amphibole, biotite and Fe-(Ti)-oxides (magnetite, titanite and ilmenite) are preserved. The

sample provides insights into initial textural and geochemical changes occurring in the RDG prior to deposition of IOCG-type mineralization.

Case study B (Fig. 2b) is from the same sample, and addresses the hyalophane, which occurs exclusively as micron-scale aggregates within albitized cores of phenocrysts consisting of andesine. The sample was chosen to characterize the hyalophane morphology and relationships with enclosing albite, as well as to find evidence for the presence of other mineral inclusions. Such an approach is designed to understand, in further detail, the mineralogical changes within the feldspar assemblage from micro- to nanoscale following albitization.

Case study C (Fig. 2c) is from sericite-hematite-altered RDG located at depth (-635 mRL) within a drillhole targeting distal satellite mineralization approximately 4 km NE from the Olympic Dam deposit. Mineralogy and geochemistry are comparable to that seen at the margins of the ODBC. The sample contains variably red-stained K-feldspar, which occurs in association with sparse Cu-(Fe)-sulphide mineralization. There is no evident preservation of igneous plagioclase, amphibole or biotite within the sample. This case study was selected from one of the grains with highest Fe concentration (mean values of ~1.5 wt. % FeO; Kontonikas-Charos et al., 2017) to constrain whether Fe-metasomatized feldspar contains any Fe-oxides present as pore-hosted inclusions, disseminated inclusions, nanoparticles, or by inference, within the feldspar crystal lattice.

Case study D (Fig. 2d) is from mineralized RDG from the same distal satellite drillhole, but from a shallower depth (-490 mRL), at an interval containing Cu-U-Au-REE-Mo mineralization. Sulphides, particularly chalcopyrite and pyrite, are intimately associated with both magnetite and hematite; the latter extensively replacing the former (e.g., martitization). Of particular interest is a ~2 mm-sized lamellar intergrowth between REE-fluorocarbonates of the bastnäsite-synchysite group (Donnay and Donnay, 1953; Ni et al., 1993) and molybdenite, which has pervasively replaced an igneous feldspar grain. The significance of the sample is to

correlate Fe-metasomatism with deposition of the sulphide-oxide assemblage and associated REE-Mo mineralization.

A sample from Hillside is included for purposes of comparison with the material from Olympic Dam. The sample was collected at the immediate contact between alkali granite and garnet skarn, and is dominated by K-feldspar and quartz, with minor andradite, titanite, chlorite and calcite. K-feldspar characterized by high (100-1,000 ppm) concentrations of REY (Fig. 3; laser-ablation inductively coupled plasma mass spectrometry (LA-ICP-MS) spot analyses from Ismail, 2016). A key objective when investigating this case study was to establish whether such anomalous concentrations are due to inclusions of titanite and/or andradite, and if so, to observe any crystal modifications within the K-feldspar lattice which might accommodate such inclusions.

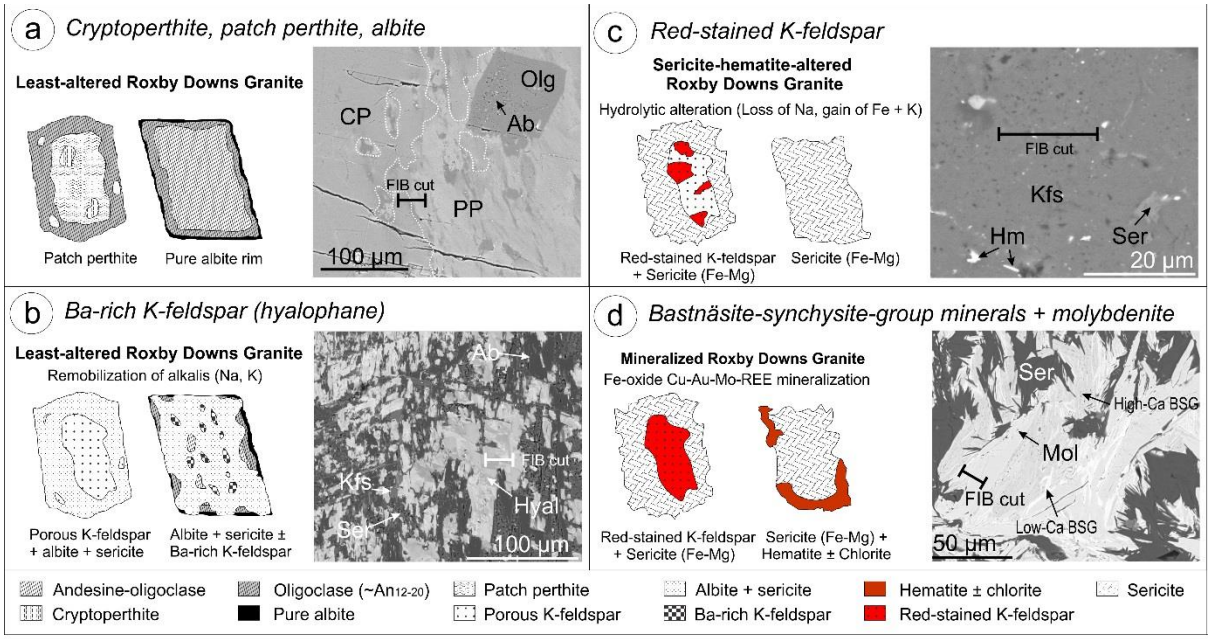

Figure 2: Schematic sketches and photomicrographs illustrating and providing a textural context for the four case studies from Olympic Dam considered in this contribution (A, B, C and D). Locations of FIB cuts are shown. Abbreviations: Ab - albite; BSG - bastnäsite-synchysite group minerals; CP - cryptoperthite; Hm - hematite; Hyal - hyalophane; Kfs - K-feldspar; Mol - molybdenite; Olg - oligoclase; PP - patch perthite; Ser - sericite.

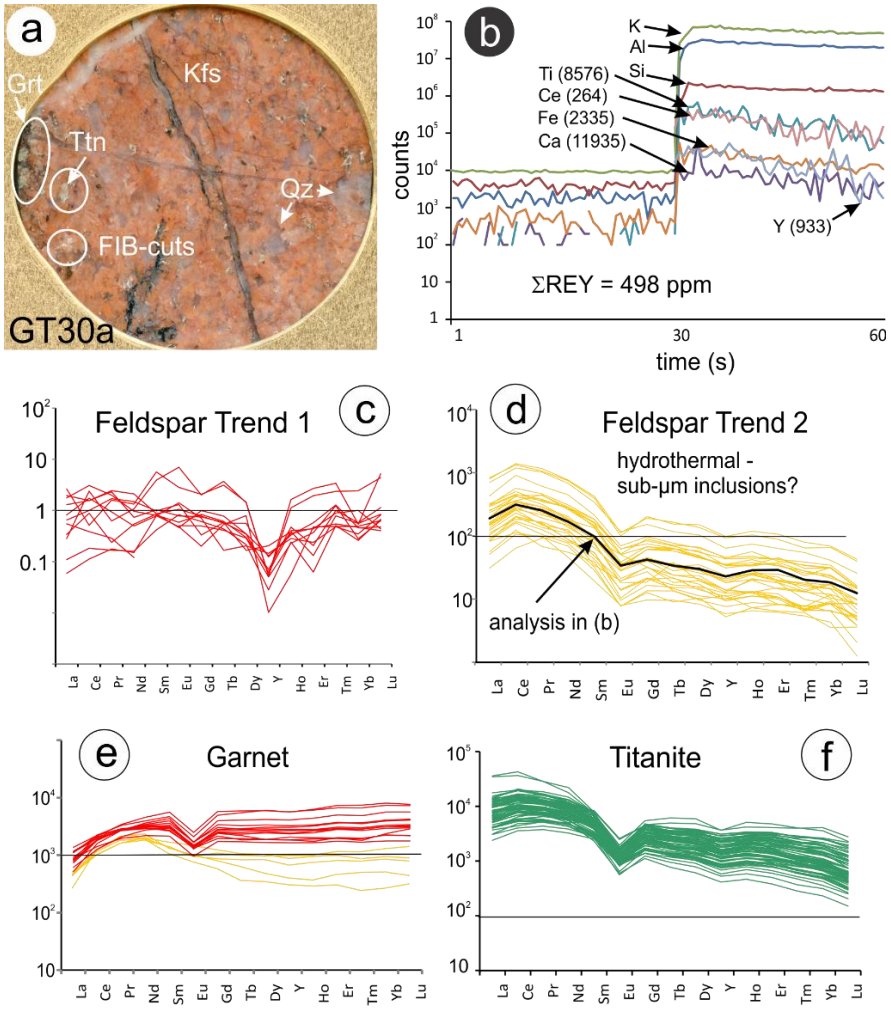

Figure 3: Overview of case study at Hillside (HS). (a) Polished block sample showing location of FIB cuts used in present study. (b) LA-ICP-MS downhole profile illustrating flat signals for REY in analyzed feldspars. (c-f) Chondrite-normalized REY fractionation patterns for feldspars, garnet and titanite. Note the very similar appearance of fractionation patterns for feldspar with inclusions and titanite and/or garnet.

6.4 Methods

Focused Ion Beam-Scanning Electron Microscopy (FIB-SEM) and Transmission Electron Microscopy (TEM) are the two microanalytical methods used in this study. All instrumentation is housed at Adelaide Microscopy (The University of Adelaide). FIB cross-section imaging and TEM sample preparation were performed on a FEI-Helios NanoLab Dual Focused Ion

Beam SEM. Procedures for extraction and thinning of TEM foils (<100 nm) followed Ciobanu et al. (2011). Thinned foils were attached to Cu grids for TEM investigation.

High-Resolution (HR)-TEM imaging in Bright Field mode (BF) and electron diffraction were performed using a Philips CM200 TEM. The instrument is equipped with a LaB6 source and operated at 160 and 200 kV, and utilizes a double-tilt holder and a Gatan Orius digital camera. Energy-dispersive X-Ray spectra (EDS) were acquired using an Oxford Instruments X-Max 65T SDD detector running Aztec software. Diffraction measurements were performed using DigitalMicrograph™ 3.11.1 and Winwulff© 1.4.0 software. Publicly available data from the American Mineralogist Crystal Structure Database were used for indexing of the electron diffractions.

High Angle Annular Dark Field - Scanning Transmission Electron Microscopy (HAADF STEM) imaging and EDS measurements were performed on an ultra-high resolution, probe-corrected, FEI Titan Themis S/TEM. This instrument is equipped with the X-FEG Schottky source and Super-X EDS geometry. The Super-X detector provides geometrically symmetric EDS detection with an effective solid angle of 0.8 Sr. Probe correction delivered sub-Angstrom spatial resolution and an inner collection angle greater than 50 mrad were used for HAADF experiments using the Fischione HAADF detector. EDS data was collected using both the Philips CM200 and Titan Themis instruments but the spectra shown in this contribution are from the Philips CM200 (spot size ~50 nm), except for the smallest inclusions, which were identified using the Titan Themis instrument (spot size 5-6 nm).

6.5 Results

6.5.1 Perthites

Case study A demonstrates the coexistence of various types of perthites, from cryptoperthites (CP) of igneous origin to patch- and vein perthites (PP and VP, respectively), of post-magmatic (deuteric) to early hydrothermal stages (Fig. 4a). Dense, parallel lamellae of albite form regular

intergrowths between orthoclase and albite, defining the fields of CP (Fig. 4b). Patch perthite occurs as coarser domains (hundreds of nm in size), which pseudomorphically replace areas of CP with both sharp and irregular boundaries (Fig. 4b, c). Relevant TEM-EDS spectra for each perthite type are shown in Supplementary Figure 1a-c (See Chapter 8, Supplementary Material C).

Despite the differences between the regular albite-orthoclase lamellar intergrowths in CP and the irregular albite in both PP and along the vein (Fig. 5a, b), electron diffractions obtained from the three types of perthites show the same orientation of the feldspars when the specimen is tilted down to [010] zone axis in the monoclinic cell of hyalophane/orthoclase and albite. Selected Areas of Electron Diffractions (SAEDS) are shown in Figure 5*c* and *d*. In detail, however, the SAEDs show satellite reflections along *h*00 (*h*=2*n*) and *h*0*l* (*h*=2*n*) directions (arrowed on Fig. 5c, d). These indicate the presence of (i) two-feldspar exsolutions (sets of satellites along *h*00) in CP, and (ii) reflections corresponding to a triclinic cell in albite in both cases (Fig. 5e, f), noting the presence of *h*00 (*h*≠2*n*) and *h*0*l* (*h*≠2*n*) reflections, which is forbidden for the *C*2/*m* monoclinic symmetry, and thus indicates transition to triclinic symmetry. The arrays of satellite spots with decreasing intensity from the main *h*00 (*h*=2n) reflections are typical of spinodal decomposition (Fig. 5f).

Sub-micron- to nanoscale pores, as well as mineral inclusions, are present throughout the PP, however the coarsest inclusions (several hundred nm in size) occur along the albite vein (Fig. 6a). Numerous sericite inclusions are observed, occasionally with variable orientations, and identified from SAEDs and TEM-EDS spectra (Fig. 6b, c, d).

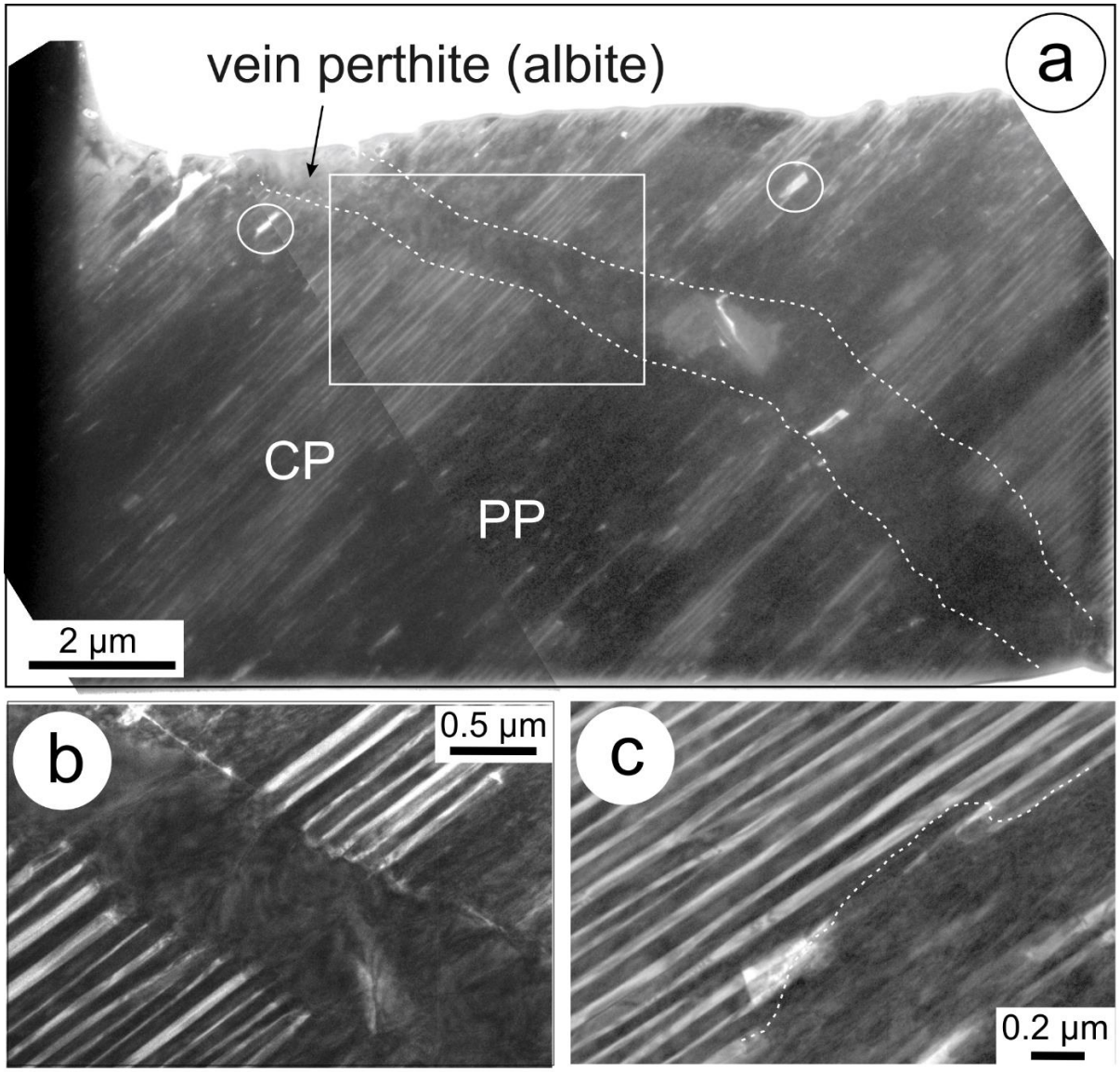

Figure 4: BF-TEM images (a-c) showing the main type of perthites (cryptoperthite: CP; patch perthite: PP, and vein perthite: VP) (case study A). Note the superimposition of lamellar PP onto CP in (b) in an area marked by the white rectangle in (a). In detail, such PP lamellae show replacement boundaries against the CP (dashed line) in (c). White circles in (a) represent micropores.

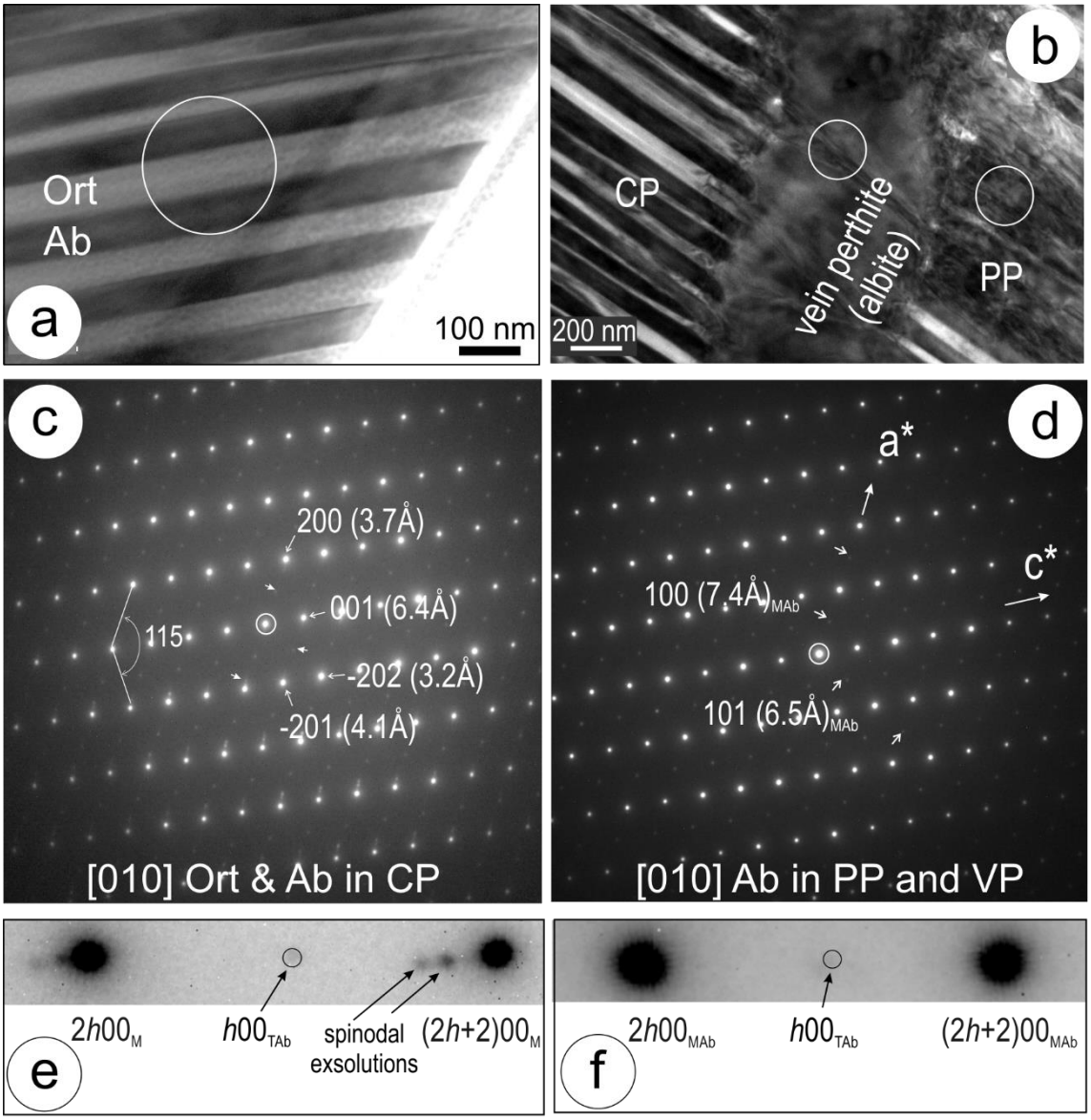

Figure 5: BF-TEM images (a-b) and corresponding SAED patterns down to [010] zone axis in feldspars as marked in (c-d) showing the epitaxial orientation between all three types of perthites from foil representing case study A (abbreviations as in Fig. 4). White circles mark the SAED areas, where (c) is for CP in (a), and (d) represents both PP and VP [circles in (b)]. Note the presence of satellite reflections (arrowed) in (c-d), indicating the orthoclase (Ort) and albite (Ab) intergrowths [spinodal decomposition in CP from (c)]. In (c-d), the presence of *h*00 (*h*≠2*n*) and *h*0*l* (*h*≠2*n*) reflections, forbidden for the *C*2/*m* monoclinic (M) symmetry, indicates transition to triclinic (T) symmetry. (e) and (f) Intervals between two main reflections along directions || to *c** axis from SAEDs in (c) and (d), respectively,

showing details of the two types of satellite reflections. Note the absence of satellites marking the feldspar intergrowths/decomposition present in CP (e) but not in PP, VP (f).

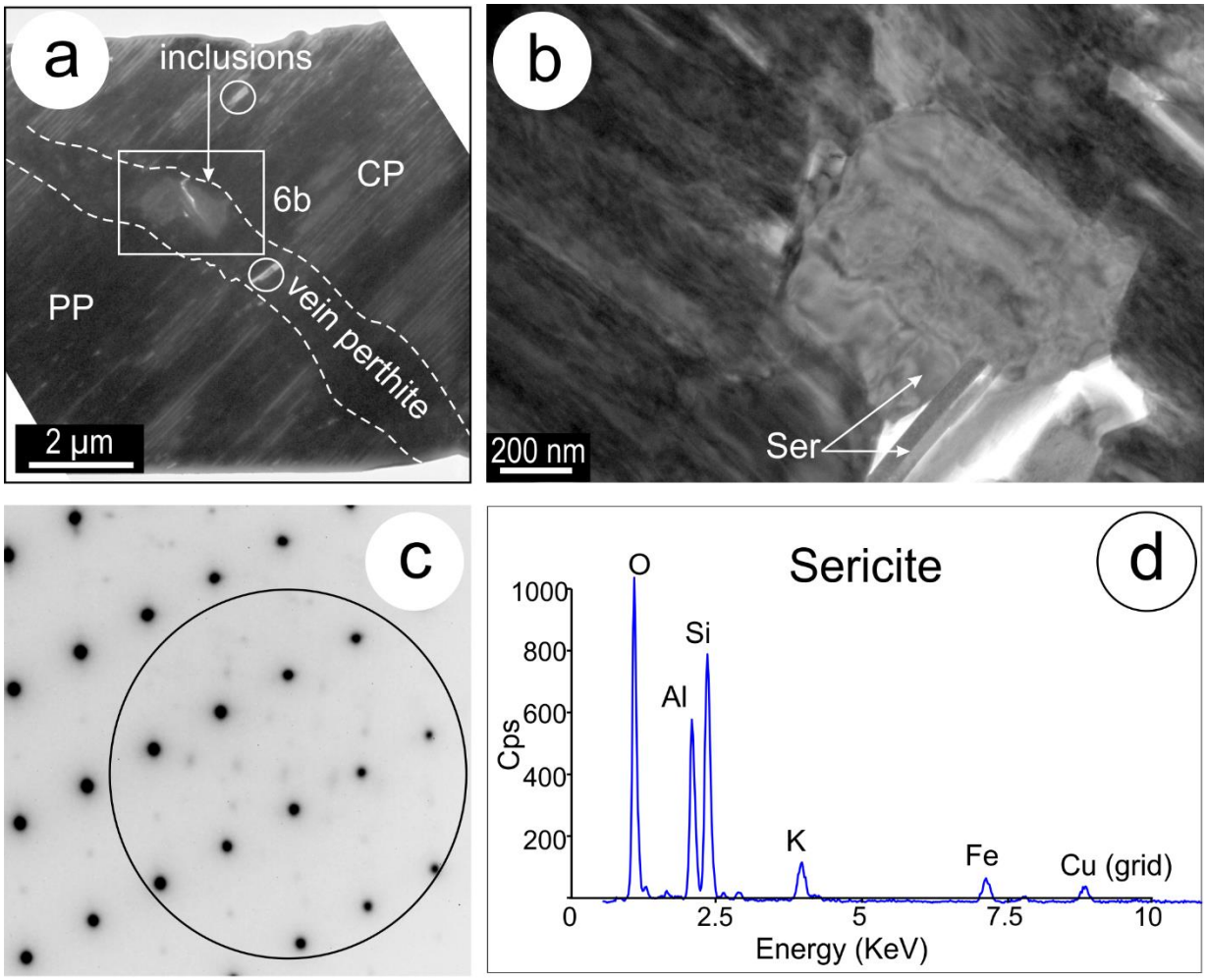

Figure 6: BF-TEM images (a-b), SAED pattern (c) and TEM-EDS spectrum (d) of sericite inclusions along the vein albite crosscutting the cryptoperthite (CP) and patch perthite (PP). (a) Inclusions location along the vein. Micropores are indicated by circles. (b) Detail showing the different morphologies and orientations of these inclusions, i.e. stubby and lamellar. (c) SAED pattern obtained from the larger, stubby inclusion where the weaker reflections (circled) are attributable to the coarser (sericite) inclusion within albite along the [010] zone axis, as shown in Fig. 5d. (d) Note the Fe peak on the spectrum obtained from the coarser inclusions (spot size ~50 nm). Cps - counts per second.

6.5.2 Hydrothermal potassium feldspar - hyalophane

Case study B is represented by the foil obtained from a previously albitized area of andesine, which shows characteristics typical of hydrothermal K-feldspar at Olympic Dam, such as Ba-enrichment ranging from 20-27% Celsian (Csn) (Kontonikas-Charos et al., 2017). The Ba-rich K-feldspar studied here is close to ideal hyalophane, $K_{0.75}Ba_{0.25}Al_{1.75}Si_{2.25}O_8$ (Hyal), i.e. $Hyal_{73}$-$Hyal_{100}$; mean $Hyal_{84}$, and is used as a descriptor for 'average' hyalophane henceforth. The complexity of the mineral assemblage down to the nm-scale, as indicated by TEM and HAADF-STEM imaging (Fig. 7), comprises a diversity of mineral inclusions, as well as variation in the size and morphology of the main components.

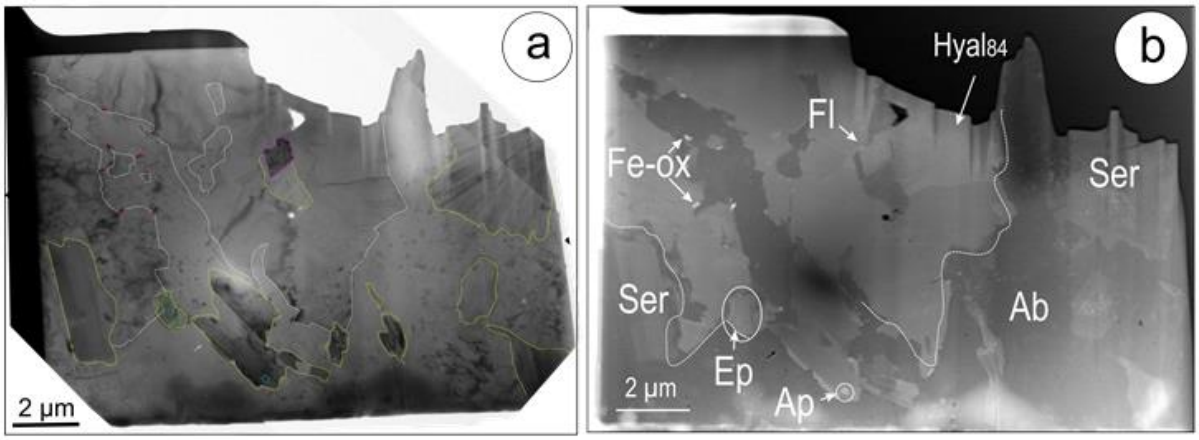

Figure 7: BF-TEM (a) and HAADF-STEM (b) images of foil containing hyalophane ($Hyal_{84}$; case study B). Line colours on (a) are drawn to show contacts between albite (Ab) and hyalophane (white), sericite inclusions (yellow), and inclusions of Fe-oxides (Fe-ox, red), fluorite (Fl, purple), epidote (Ep, green), and apatite (Ap, blue).

The middle part of the foil shows $Hyal_{84}$, occurring as an aggregate of platy grains (each several-µm in width) radially distributed around an inclusion core consisting of fluorite and sericite (Fig. 8a, b). Weak grain zonation with respect to Ba is also apparent on the HAADF STEM images (Fig. 8a). There is a ~7% compositional variation with respect to Csn. TEM-EDS spectra for hyalophane of variable composition, sericite and fluorite are shown in

Supplementary Figure 1d-g. Hyalophane is surrounded by albite, in which one side features sharp mutual boundaries, whereas the other displays irregular contacts comprising nm-size inclusions of Fe-oxides along the boundary (Fig. 7a, b). Such inclusions are more abundant in areas where islands of albite are also present within $Hyal_{84}$.

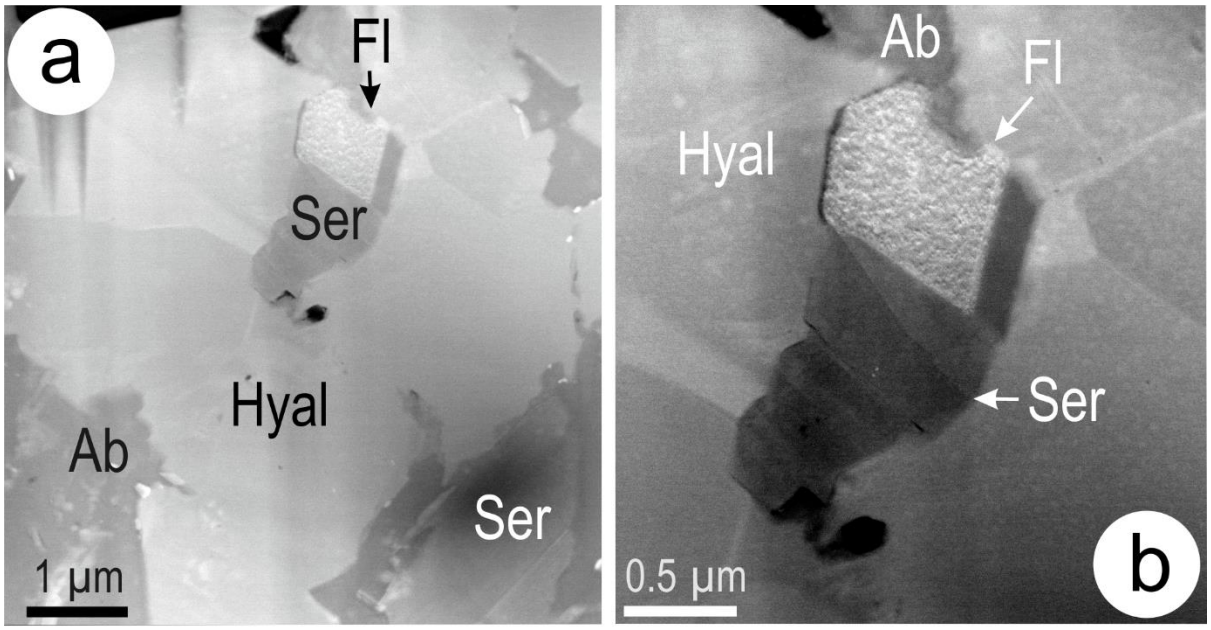

Figure 8: HAADF-STEM (a-b) showing details of the hyalophane (Hyal) aggregate in the middle part of the foil (case study B) surrounding an inclusion core comprising fluorite (Fl) and sericite (Ser).

The third most abundant mineral is sericite, which occurs as coarse (several µm-sized) radial or lamellar aggregates to nm-scale slivers mostly throughout the albite (Fig. 7). In detail, such slivers are characterized by stacking disorder along the *c** axis (Fig. 9a, c). The presence of chlorite is also suggested based on SAEDs obtained from some of the smaller inclusions (Fig. 9b, d). Inclusions of As-bearing fluorapatite (up to 200 nm in size) were also identified within sericite (Figs. 7 and 9e, f). Notably, an inclusion (~several hundred nm) of a calcic silicate is observed embedded within sericite along the contact between $Hyal_{84}$ and albite. This is identified as epidote based on TEM-EDS spectra and SAEDs down to [2-23] zone axis of epidote (Figs. 7, 9g-i).

A range of electron diffraction patterns were obtained from the two feldspars (Ab and $Hyal_{84}$) by tilting the specimen and also changing the foil orientation in the holder (Fig. 10). The two feldspars are observed to be oriented completely random to one another across their direct boundaries when the specimen is tilted on [1-10] zone axis in $Hyal_{84}$, and the adjacent albite is oriented down to [132] zone axis (Fig. 10a, d, respectively). The (*hh*0)* axis in $Hyal_{84}$ is parallel to (*hh*.2*l*)* in albite, and the (*hkl*)* directions in the two feldspars are also parallel to one another.

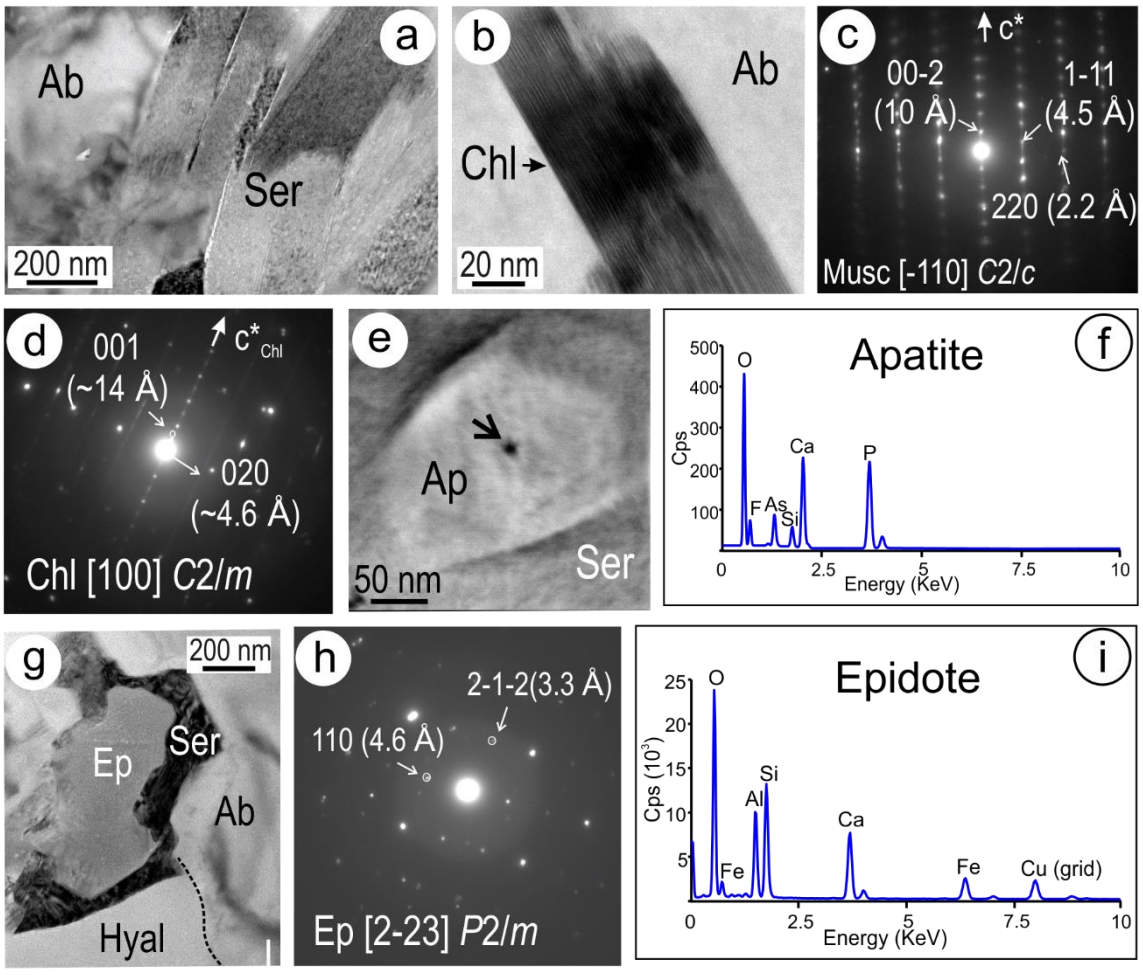

Figure 9: BF-TEM images of sericite (Ser; a) and chlorite (Chl; b) within albite with corresponding SAEDs on zone axes as marked in (c) and (d) respectively. (e-f) HAADF-STEM image and corresponding spectra for an inclusion of As-bearing fluorapatite (Ap) within sericite. The arrow in (e) indicates the location of the beam for EDS spectra (~5-6

nm). In (f), note F and As peaks in the apatite spectra. (g-i) BF-TEM image, SAED (down to zone axis as marked), and TEM-EDS spectra of an epidote (Ep) inclusion located at the boundary between hyalophane (Hyal) and albite (Ab). Note envelope of sericite around the epidote in (g).

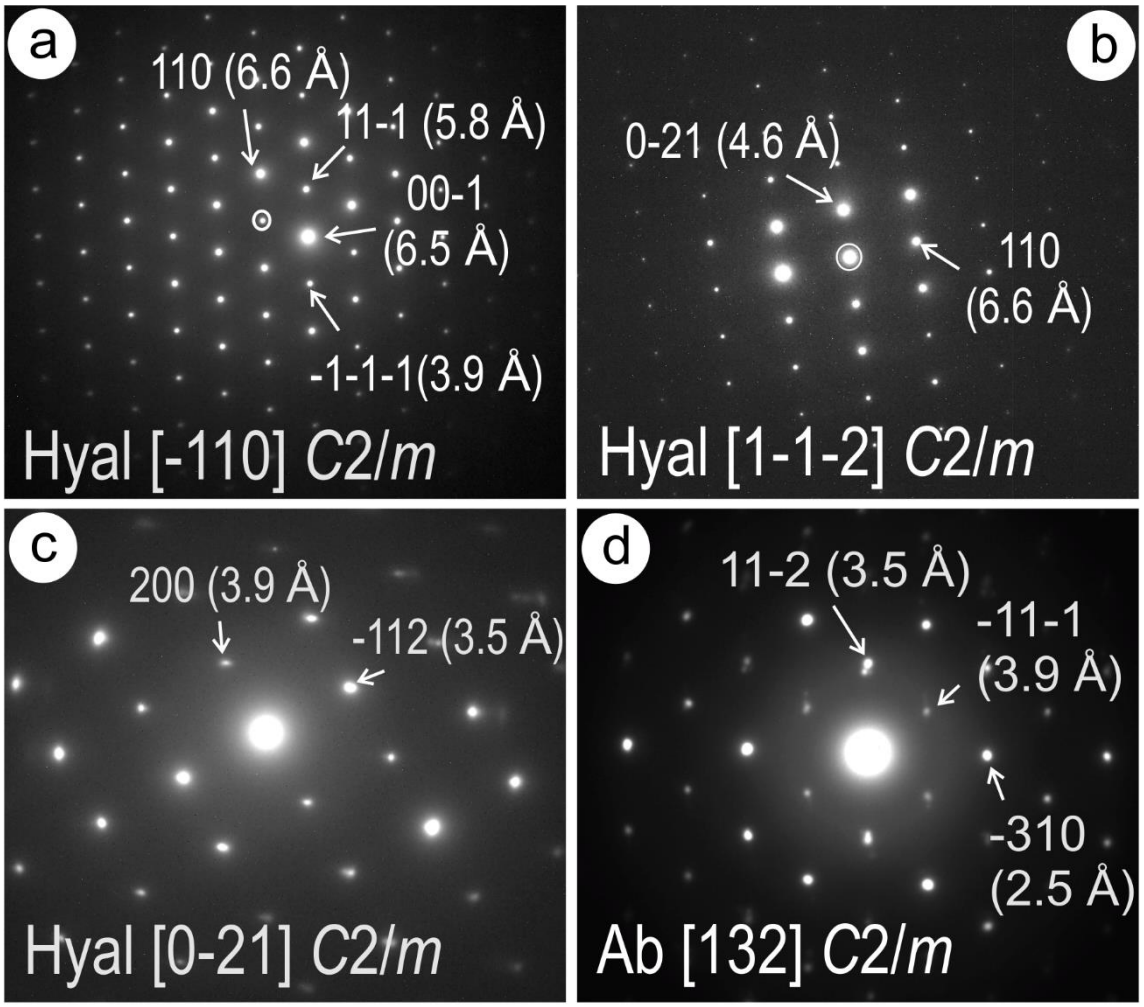

Figure 10: Selected SAED patterns showing zone axes as marked (square brackets) in feldspars from the foil representing case study B. (a-c) Highest-order zone axes obtained from hyalophane (Hyal) in different parts of the foil and at different specimen tilting. (d) SAED down to [132] zone axis in albite (Ab) is obtained at the same tilt with SAED down to [-110] zone axis in adjacent hyalophane shown in (a).

6.5.3 Red-stained potassium feldspar and advanced feldspar replacement: Fe and REE metasomatism

Reddening of igneous feldspar at Olympic Dam, termed here 'red-stained potassium feldspar' (K-Fs), is attributed to Fe-metasomatism. This is followed by complete pseudomorphic replacement of feldspar (plagioclase?) by sericite, accompanied by abundant REE-fluorocarbonates and sulphides (Kontonikas-Charos et al., 2017). Both are studied from two foils obtained from the same drillhole outside the Olympic Dam orebody. Iron metasomatism is expressed by the presence of Fe-oxide inclusions, which, although ubiquitous throughout all feldspars affected by alteration, or completely new (hydrothermal) feldspars (such as the hyalophane above), vary in both abundance (density) and size.

Case study C shows numerous inclusions of Fe-oxides, ranging in size from nm- to µm-scale, disseminated throughout the foil, which was cut across anomalously Fe-rich domains of preserved magmatic K-Fs. Abundant pores and thin slivers of chlorite are also present (Fig. 11). TEM-EDS spectra obtained from host K-Fs, Fe-oxides and chlorite are given in Supplementary Figure 1h-j.

In detail, Fe-oxides vary in size from tens to hundreds of nm over distances of <1 µm, suggesting that even smaller inclusions (nanoparticles) would also be present in such areas. Note that although pores are present, the Fe-oxide inclusions are not embedded within those pores (Fig. 12a). Electron diffractions obtained from the host K-Fs throughout the foil are consistent with a single feldspar grain. The highest order zone axes recorded, i.e. [-312] and [-11-1] in feldspar (SAEDs shown as Fig. 12b, c), could be indexed using the monoclinic cell of orthoclase.

Coherent lattice scale intergrowths between chlorite inclusions and orthoclase are inferred from electron diffractions obtained across such inclusions. The latter show epitaxial orientation with host feldspar, i.e. c* chlorite on [-210] zone axis is parallel with (110)* axis in on [-11-1]

zone axis in orthoclase (Fig. 12d, e). The speciation of the Fe-oxide inclusion hosted along the contact between the two silicates is traceable from satellite reflections on Figure 12e-f, which although relatively faint and irregular, could nevertheless be indexed as maghemite down to the [2-21] zone axis when using the space group *P*43.

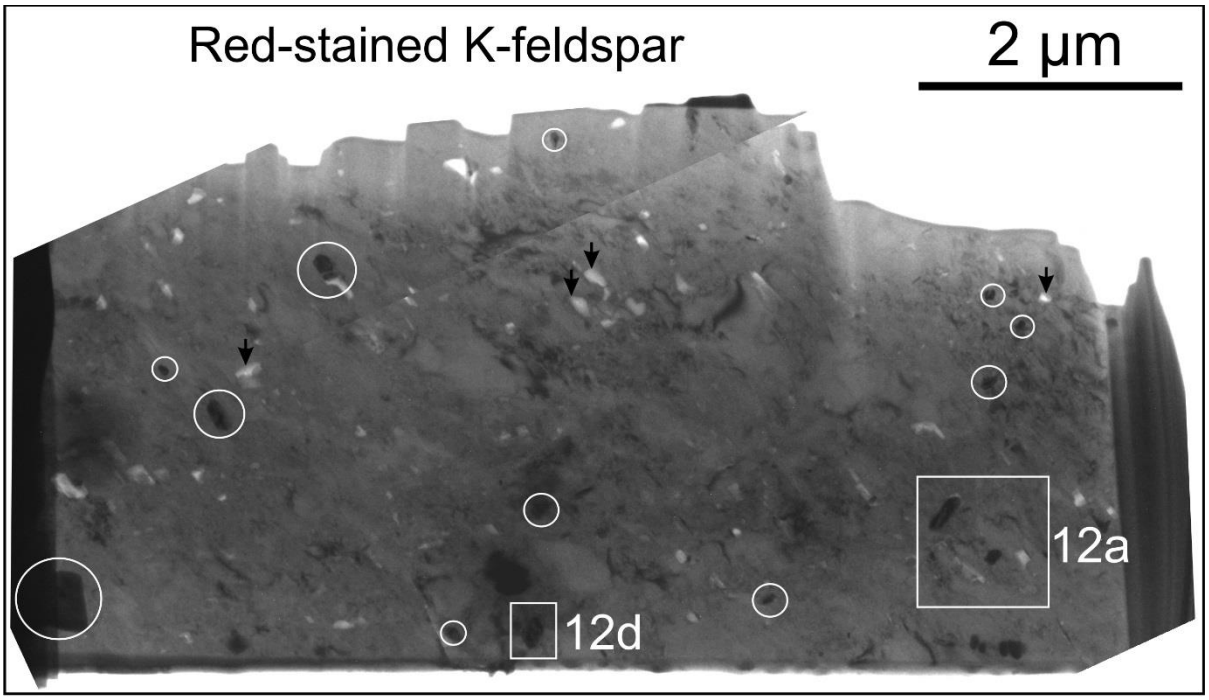

Figure 11: BF-TEM image showing red-stained K-feldspar foil and minerals identified in case study C (K-feldspar, Fe-oxide and chlorite). Inclusions of Fe-oxides are circled in (a). White squares are locations of areas shown in Figure 12. Black arrows indicate micropores.

Pseudomorphic replacement of feldspars (plagioclase, perthitic alkali-feldspar, red-stained K-feldspar) at Olympic Dam commonly results in micro-scale intergrowths of sericite + Fe-oxide assemblages, within which a variety of other mineral species can also be present (Kontonikas-Charos et al., 2017). Case study D is an exceptional example of this type of replacement, in which REE-fluorocarbonates + molybdenite are the major components. The sample is from a shallower interval (~150 m above case study C) and contains Cu-U-Au-REE-Mo mineralization, atypical for IOCG systems, as well as both magnetite and hematite, which are important components of the overall hydrothermal alteration assemblage. The foil

discussed here was cut across micron-scale patches in which REE-fluorocarbonates from the bastnäsite-synchysite group (BSG) form syntaxic intergrowths with one another (lamellae tens of microns in width, and comprising species with low-Ca and high-Ca compositions; Kontonikas-Charos et al., 2017), as well as also molybdenite (Fig. 13). Other components documented throughout this replacement assemblage are sericite, and minor quartz, Fe-oxides and K-feldspar, all filling the shape of a replaced feldspar phenocryst (Figure 11 in Kontonikas-Charos et al., 2017).

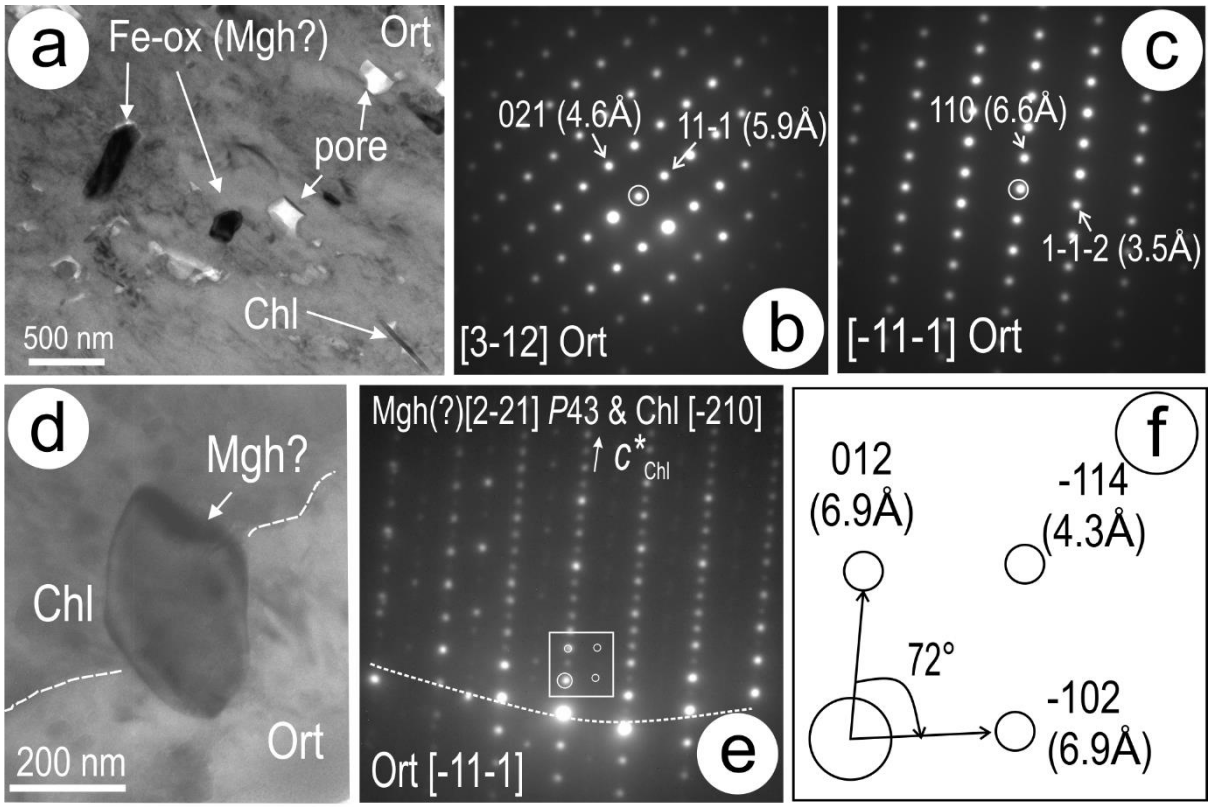

Figure 12: BF-TEM images and SAED patterns for host orthoclase (Ort) and inclusions in case study C. (a) Detail (large rectangle in Fig. 11a) showing size and morphology of Fe-oxide and chlorite (Chl) inclusions. Note also presence of pores. (b-c) Two SAED patterns (obtained at different tilts of the sample) showing the highest order zone axes (as marked) in orthoclase. (d) Detail (small circle in Fig. 11a) of an area where an inclusion of Fe-oxide (maghemite; Mgh?) is located at the boundary between orthoclase and a chlorite inclusion. (e) SAED pattern obtained from area in (d) showing coherent (epitaxial) intergrowths

between chlorite and orthoclase (zone axes as marked. Weaker reflections (such as those circled in the white rectangle) could be indexed as maghemite using *P*43 space group. (f) Schematic showing the reflections and used for maghemite indexing.

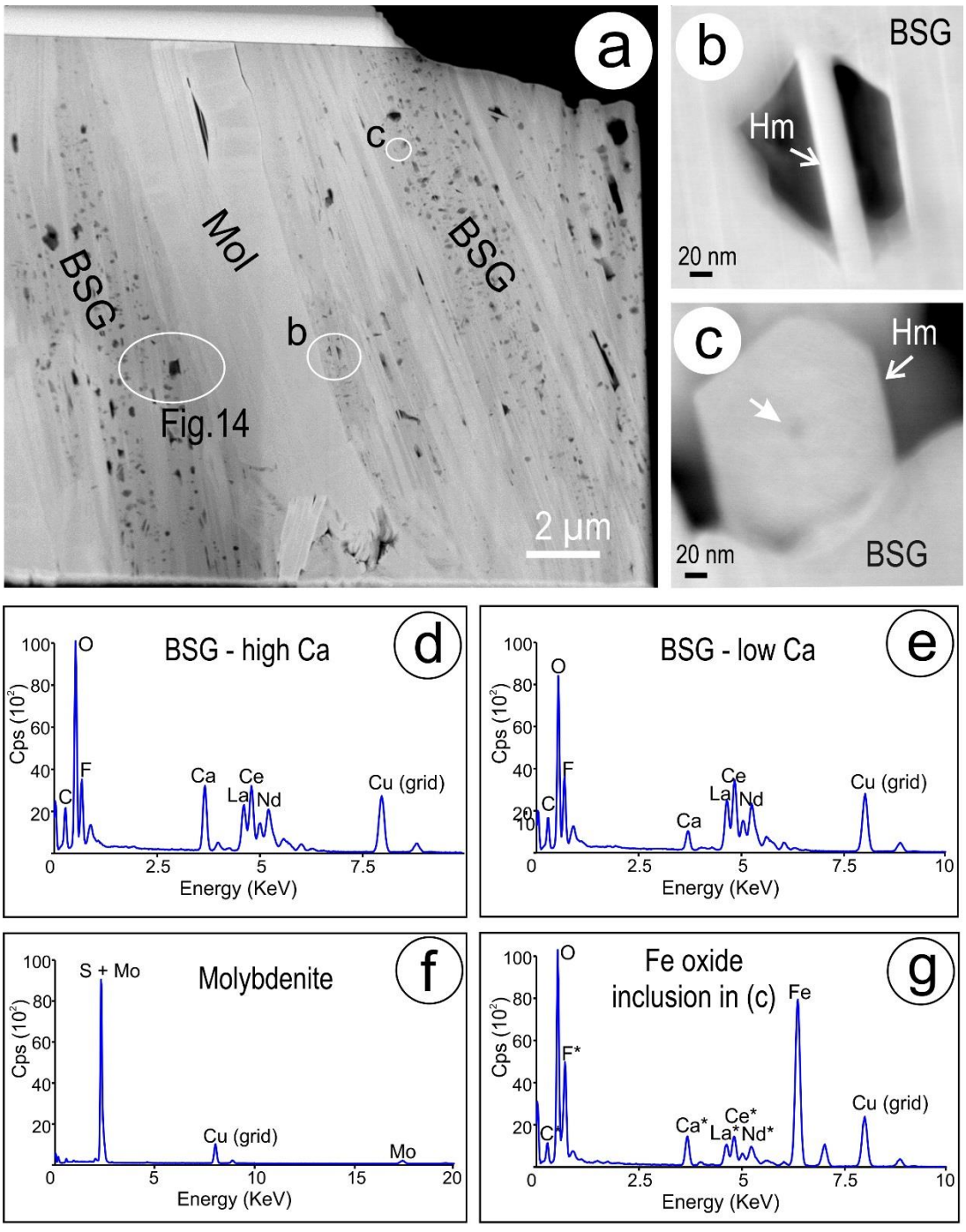

Figure 13: HAADF-STEM (a-c) images and TEM-EDS spectra (d-g) of mineral assemblage in case study D. (a) Low-resolution image of foil showing lamellar intergrowths between bastnäsite-synchysite group (BSG) species and molybdenite (Mol). Note the dark spots

within the BSG representing thinner areas around Fe-oxide inclusions produced by ion milling (see text for further explanation). (b, c) Higher-resolution images of areas circled in (a). Both are of Fe-oxide inclusions within the BSG. Note the lamellar (b) and hexagonal platelet morphology in (c) consistent with hematite (Hm). Appearance of (b) is due to milling from the TEM. Note the centred dark spot in (c), which correlates to the EDS spot. Arrow to the spot in the centre of the lamellae in (c) indicates location of EDS spectrum (spot size of ~5 nm). (d-g) TEM-EDS spectra of the BSG species (high- and low-Ca), molybdenite, and an Fe-oxide inclusion. Cps - counts per second.

On the HAADF-STEM image of this foil, the lamellar intergrowths between molybdenite and the BSG species are readily identifiable not only by the relative contrast in grey shades (molybdenite is brighter) but also by the pitted appearance of the BSG domains (Fig. 13a). Most of these pits are thinner areas of the foil (see below), however some contain single lamellae of Fe-oxide inclusions (Fig. 13b, c). The Fe-oxide is identified as hematite considering the lamellar morphology as seen from orientations either transversal (<20 nm width; Fig. 13b), or parallel (~150 nm wide; Fig. 13c) to the section of the pit. It is likely that the numerous pits are artefacts caused by such hematite inclusions removed during FIB milling. TEM-EDS spectra for BSG domains (high- and low-Ca), molybdenite and hematite are shown in Figure 13d-g.

High-resolution (HR)-TEM imaging of one of the thinner areas created by the milling as explained above (Fig. 14a) shows that the BSG minerals form sub-micron- (Fig. 14b) to lattice-scale intergrowths with one another (Fig. 14c). Lattice fringes along the *c** axis show relatively regular domains, some tens of nm in width, characterized by: (i) single layer type of ~4.5-5 Å width; and (ii) two layer types forming a sequence of ~28 Å width separated by a brighter and wider layer (Fig. 14c). These sequences are attributable to intervals of bastnäsite and parisite.

Although the ~35 nm interval of bastnäsite is relatively regular, stacking disorder is observed on one side (Fig. 14c).

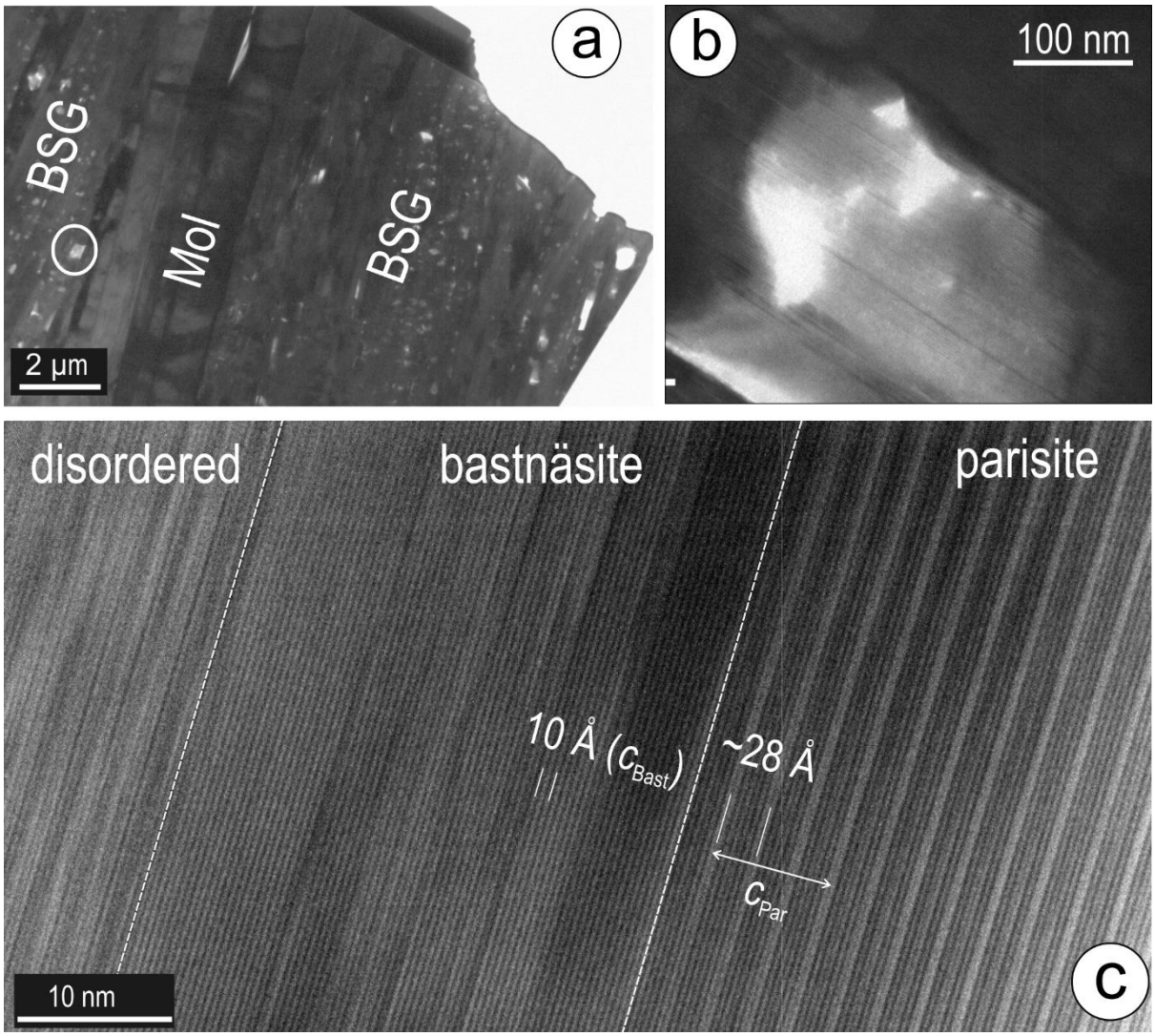

Figure 14: BF-TEM images showing details of the bastnäsite-synchysite group (BSG) intergrowths from the area marked on Figure 13a. (a, b) Location and low-magnification image of the BSG and molybdenite (Mol) intergrowths. Note the variation in thickness of the sample in (b). (c) High-resolution TEM image of BSG intergrowths in (b) outlining the more ordered stacking sequences over intervals of ~30-40 nm along the *c** axis. Bastnäsite and parisite, as well as a disordered stacking sequence are highlighted.

Electron diffraction patterns obtained with beam tilted perpendicular to the *c** axis of the BSG confirm that the main species throughout the foil are indeed bastnäsite and parisite, albeit

with disordering along the c* axis in both species (Fig. 15). The SAEDs show a distribution of reflections along *c** axis and parallel directions that are concurrent with previous TEM studies of BSG species showing crystal structural modularity typical of mixed-layer compounds, i.e. parisite is a 6-fold superstructure of bastnäsite when oriented on [21-30] or equivalent [-1100] zone axes (Fig. 15a, b). The four main BSG species: bastnäsite [$Ln(CO_3)F$]; parisite [$CaLn_2(CO_3)_3F_2$]; röntgenite [$Ca_2Ln_3(CO_3)_5F_3$]; and synchysite [$CaLn(CO_3)_2$], where Ln=REE, are formed by stacking sequences of several layer types and with correlation between the stacking period and chemical composition (Donnay and Donnay, 1953; Ni et al., 1993). HR-TEM studies have confirmed such correlation and numerous polytypes have subsequently been described following layer formalism (Van Landuyt and Amelinckx, 1975; Wu et al., 1998; Meng et al., 2001; 2002). One characteristic of these minerals is that they rarely form single crystals but rather occur as 'polycrystals' defined by syntaxic intergrowths of two or more species (Donnay and Donnay, 1953). Irregular sequences of layers are also common and they can explain the 'disordered species', commonly detected by X-ray diffraction (van Landuyt and Amelinckx, 1975).

Lattice-scale intergrowths such as those shown in Figure 14c are characterized by SAEDs with strong disorder along *c** (Fig. 15c). Intergrowths throughout this foil are, however, more complex and include other stacking sequences.

Molybdenite shows relatively coherent intergrowths with BSG minerals, albeit with minor rotation between the *c** axis in each respective mineral. The hexagonal polytype 2*H* is identified based on SAEDs down to [11-20] zone axis of molybdenite (Fig. 15d). Some crystal-structural disorder/twinning is indicated by satellite reflections (arrowed on Fig. 15d) and stacking along rows parallel to c^*_{2H}.

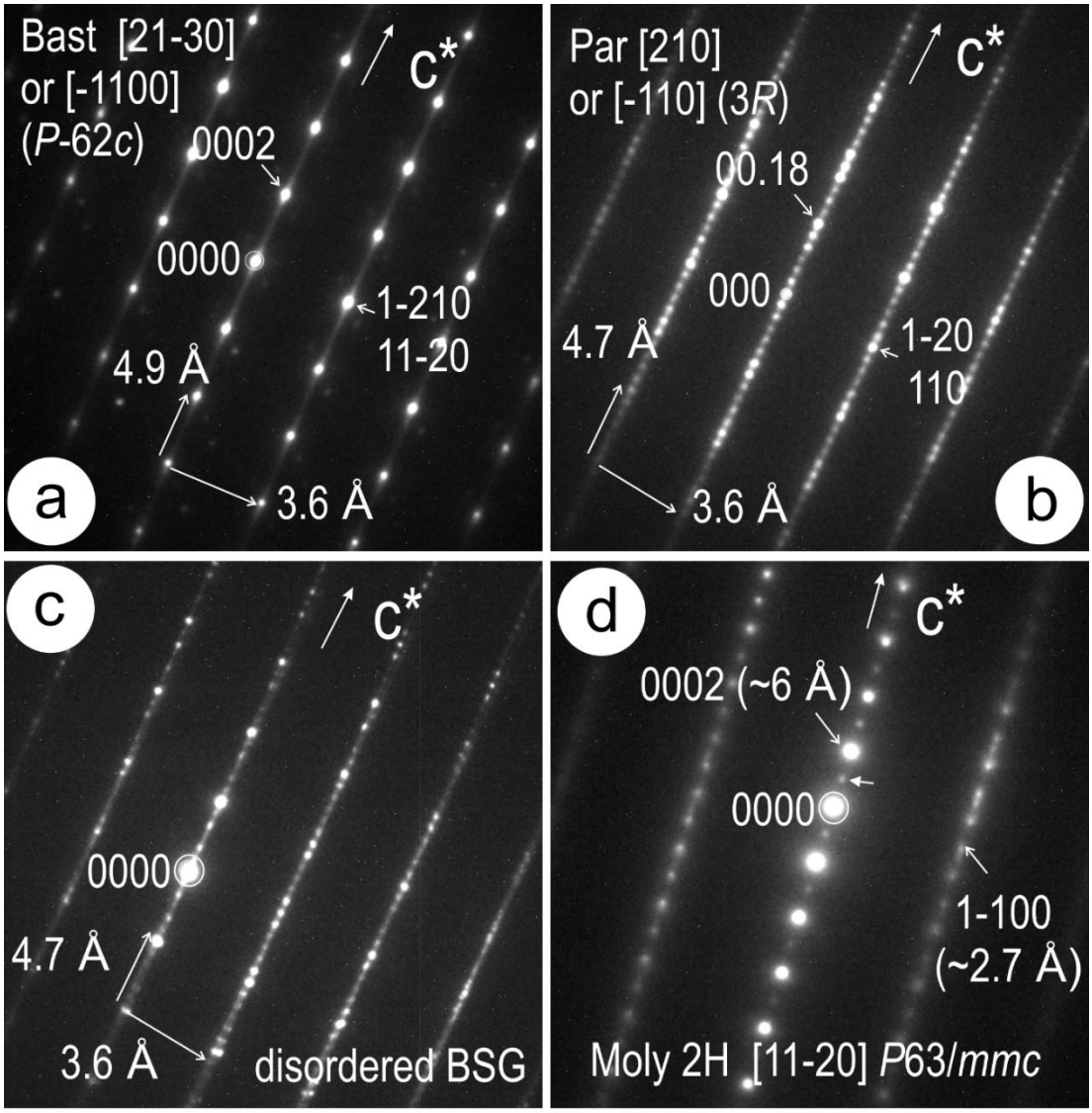

Figure 15: SAED patterns of bastnäsite, parisite and molybdenite on zone axes as marked by square brackets from case study D. All SAED patterns are obtained at the same sample tilt. (a) Note the streaking along *c** in bastnäsite indicative of stacking disorder. (b) Note the parent reflections of bastnäsite (brighter reflections) and the 6-fold superstructure satellites on c* corresponding to parisite. (c) SAED typical of lattice fringes as those in Figure 14c, showing disordered BSG phases intergrowths along the *c** axis and parallel directions (variation in satellite intensity, streaking). (d) SAED pattern of molybdenite indicative of polytype 2*H*. Crystal-structural disorder/twinning is indicated by satellite reflections (arrowed) and steaking along rows parallel to c^*_{2H}. Indexing of hexagonal cells as *hkil*, where $h+k+i=0$.

6.5.4 Hillside - endoskarn

Igneous feldspars containing anomalous concentration of REY (up to ~500 ppm ΣREY) were studied from two foils obtained from an area adjacent to domains with such measured values (Fig. 16a). FIB imaging shows that feldspar in both foils contains small pervasive inclusions of garnet and titanite (Fig. 16b, c). These are most abundant along fractures and/or trails, some of which form networks (Fig. 16d, e), as are well-defined pores (Fig. 16f). Aggregates of inclusions attached to pores and single larger (tens of nm) inclusions of calcic garnet (andradite) are also present (Fig. 16f-i).

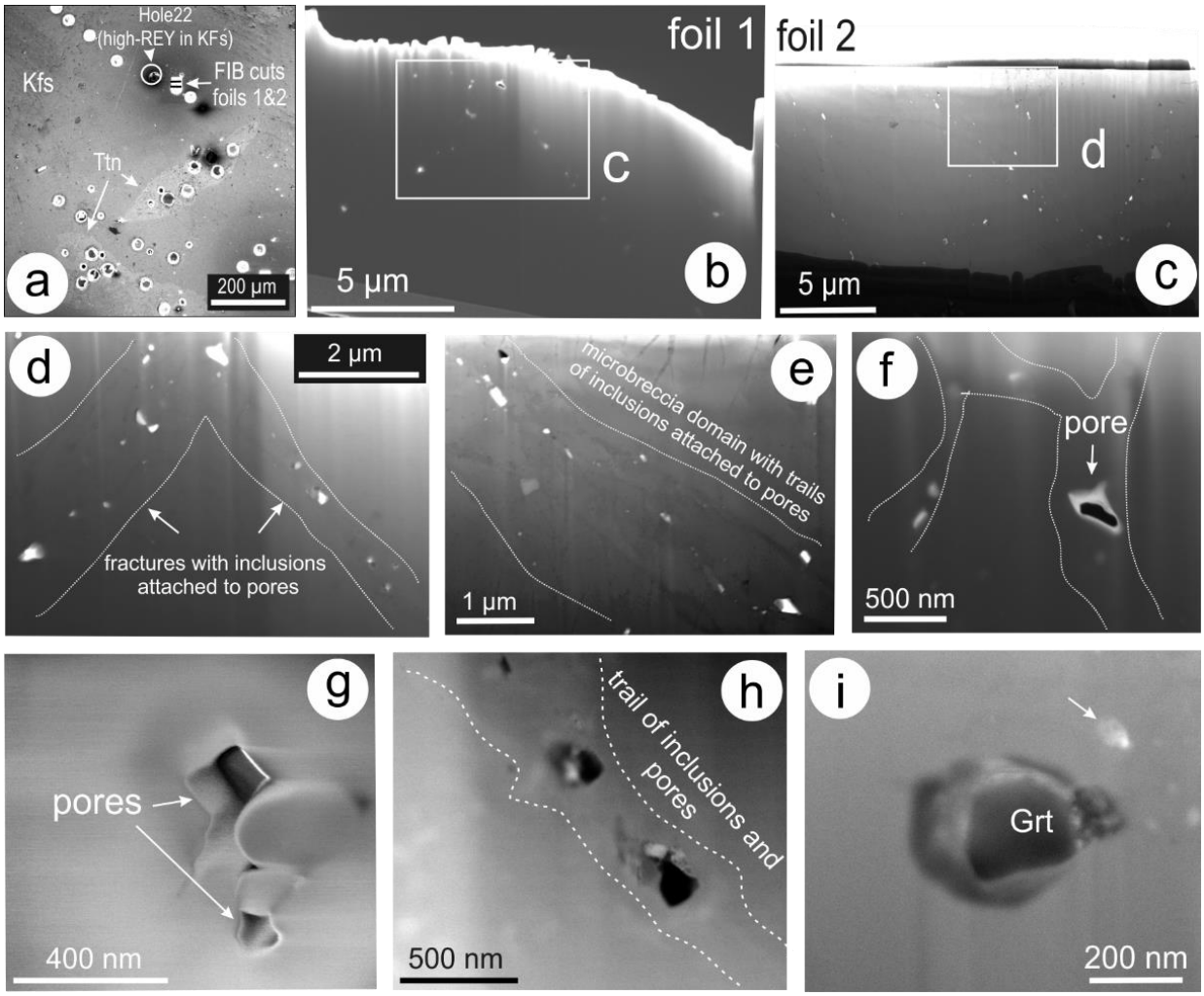

Figure 16: Secondary Electron (SE) images showing feldspar from the Hillside case study (HS) (a) Overview of foil locations from an area adjacent to domains from where LA-ICP-

MS data were obtained (Figure 3). (b-f) FIB cross-section imaging showing pervasive minute inclusions and pores in feldspar. Note concentration of inclusions and pores along fractures and/or trails (d-f). (g, h) Aggregated inclusions attached to pores and larger inclusions of garnet. (i) Nanometre-scale inclusions of garnet (Grt).

Electron diffraction patterns obtained from the host feldspar in both foils show single grains in each case, and the highest order zone axis recorded was indexed as [1-10] using the monoclinic cell (Fig. 17a). Electron diffractions obtained from a sub-micron inclusion of K-feldspar include (*h*0*l*) and (*hkl*) reflections, which do not meet the conditions $h = 2n$ and $h + k = 2n$ of the *C*2/*m* space group, and thus were indexed using the triclinic cell of microcline (Fig. 17b, c). Numerous inclusions of variable size (~5-50 nm) and habit (acicular to granular) were imaged from both foils (Fig. 17d-h). The acicular type is associated with lattice defects (Fig. 17d), whereas the granular inclusions are hosted within pores (Fig. 17f). Quartz and andradite are among the largest inclusions (>100 nm) identified using TEM-EDS. SAEDs of first order, i.e. [001] zone axis, are shown for garnet in Figure 17i. The TEM-EDS spectrum from the same inclusion show not only major Ca, Fe, Al and Si peaks but also minor peaks for Ti and REE (Fig. 17j). Many of the granular sub-µm to nm-scale inclusions in orthoclase can be attributed to such calcic (grandite series) garnets. These are main rock components in the skarn at Hillside and are also major REY carriers (Ismail et al., 2014; Ismail, 2016). Whereas the coarse orthoclase grains are magmatic, the microcline and quartz are most likely hydrothermal phases formed during the early metasomatism which produced endoskarn at the granite contact. The thin, acicular inclusions can be attributed to titanite, which is present as coarse (hundreds of µm) inclusions in adjacent areas.

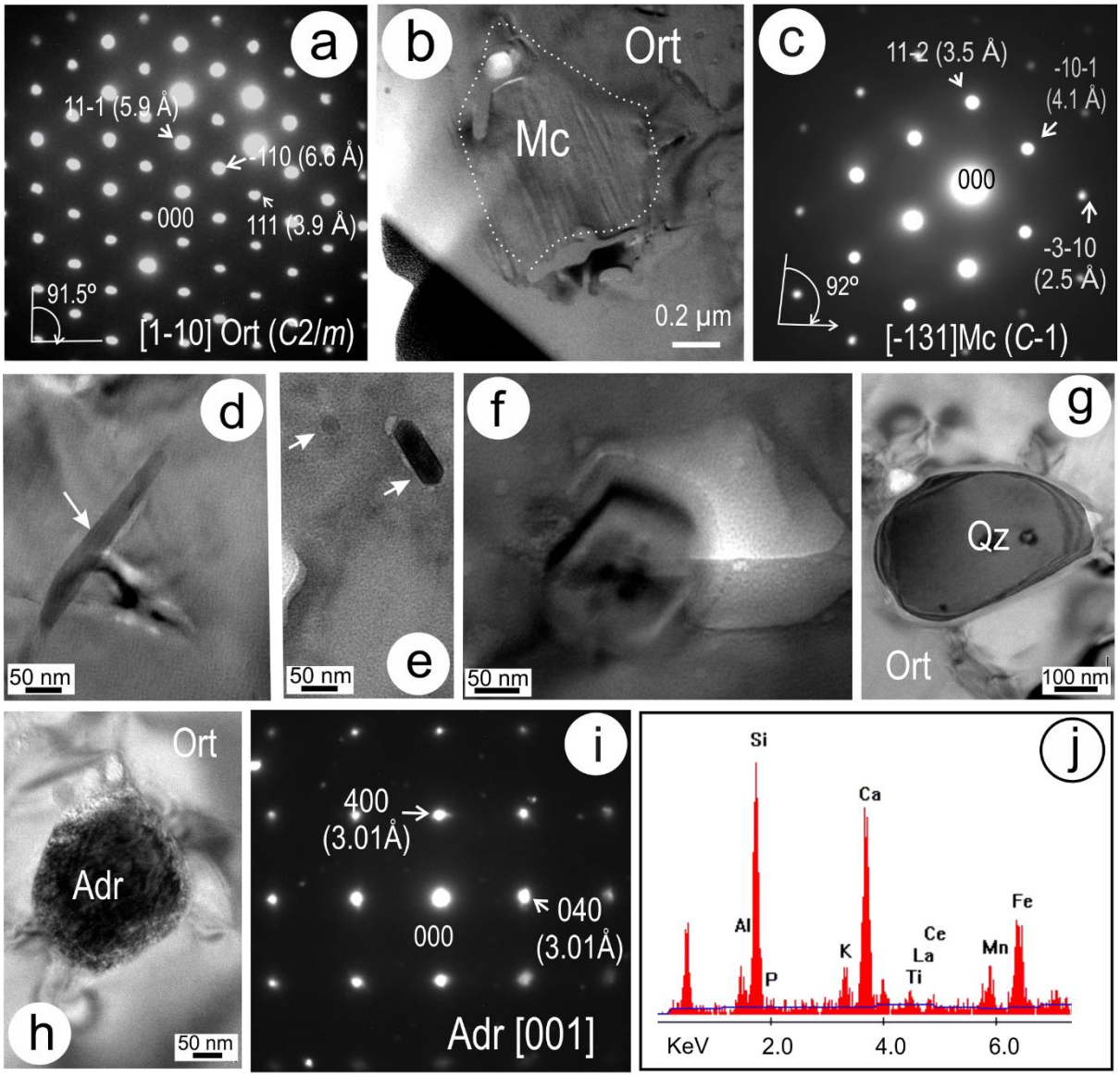

Figure 17: BF-TEM images, SAED patterns and TEM-EDS spectra from case study HS. (a) SAED pattern of orthoclase down to [1-10] zone axis. (b) High-resolution image of microcline (Mc) within orthoclase (Ort). (c) SAED pattern of microcline from (b). (d-h) Higher-resolution images of various inclusions within the orthoclase. Note the andradite within (h). (i) SAED pattern on [001] zone axis of andradite in (h). (j) TEM-EDS spectrum for andradite. Abbreviations: Adr – andradite; Mc – microcline; Ort – orthoclase; Qz -quartz.

6.6 Discussion

Nanoscale studies can constrain trace element redistribution in minerals and help track their mineralogy from initial host to new-formed products (Reich et al., 2011; Ciobanu et al., 2016, 2017). In addressing feldspars at the nanoscale, we firstly aimed to understand whether the assumptions of distinct magmatic and hydrothermal stages of feldspar evolution could be substantiated in greater detail. Secondly, we address whether feldspar transformation processes in different parts of a single large deposit such as Olympic Dam, or in a different but similarly anomalously REE-rich system (Hillside), have common features, or differ, and if so, in what ways. It is worth pointing out that thermodynamics and phase equilibria will need to be considered at the appropriate scale of reaction, i.e., considering the effects of particle size on reaction and stability in oxide-bearing systems (Navrotsky et al., 2008; Navrotsky, 2011). This issue, however, lies beyond the scope of the present study.

6.6.1 Magmatic to hydrothermal feldspars – grain scale (re)mobilization

Perthite transformation via coupled dissolution-reprecipitation reactions (CDRR), from magmatic stage to replacive albite at OD (Kontonikas-Charos et al., 2017) is further substantiated by the observations of case study A. The epitaxial orientations between CP (magmatic) and hydrothermal (PP and VP) feldspars (e.g., Fig. 4), are indicative of interface-mediated reactions between pre-existing alkali-feldspars and pervading fluid, irrespective of crystal morphology observed at the micron-scale, e.g. the cross-cutting relationships of vein perthite. The presence of Fe-bearing sericite, as inclusions, shows that some of the elements released during replacement, e.g. K and/or Fe, are trapped within the area of reaction (e.g., Fig. 5). Throughout the complex perthites, there is increased porosity at replacement contacts and even more so also along the albite vein (Fig. 4). Overall, this case study shows how grain-scale albitization enhances rock porosity, and likely also permeability, which facilitates element

remobilization (e.g. of K and Fe in this instance) and allows for discrete mineral precipitation within the reaction area, i.e. the parent alkali feldspar grain. Evidence supporting grain-scale element exchange during feldspar replacement is provided by hydrothermal experiments with plagioclase feldspars at 600 °C and 2 kbar (Hövelmann et al., 2010). These show that albitization leads to changes in oxygen isotope signatures, as well as mobilization of elements such as Al and Ti, that are otherwise considered largely immobile in hydrothermal environments.

The hypothesis that hydrothermal Ba-bearing K-feldspar (hyalophane), can form within areas of albitized plagioclase phenocrysts is further supported by the nanoscale complexity of the mineral assemblage in case study B. This is highlighted by the presence of nm-scale inclusions of calcic silicates (documented here for the first time at Olympic Dam), As-bearing apatite and Fe-oxides, which are located along reaction boundaries in albite (Figs. 6, 8). Formation of such minerals may be predictable since albitization of andesine in the phenocryst core releases Ca, whereas Ba, and K, necessary to form hyalophane, could be sourced from the perthite zones of the same phenocryst. Involvement of F-, Fe-, As-bearing fluids locally remobilizing, or introducing such elements at this stage is also feasible from the observed assemblage comprising fluorite (as a nucleation core for hyalophane), minute Fe-oxides, and As (within fluorapatite). The presence of chlorite, which has been documented here from the smaller sericite inclusions in albite, show that such fluids also carry Mg, even though this could be remobilized from igneous amphiboles observed within the same phenocryst (Kontonikas-Charos et al., 2017). Such reactions and the occurrence of hyalophane, often with grain zonation with respect to Ba, are observed in samples from other parts of the RDG at Olympic Dam (e.g. adjacent to the ODBC; Kontonikas-Charos et al., 2017), or in the early and distal skarn at Hillside (Ismail, 2016).

Both foils discussed above, obtained from the same polished block sample, are illustrative of the preservation of initial rock compositions following mineral reactions driven via CDRR, and in this case, supported by whole-rock geochemistry (Kontonikas-Charos et al., 2017). The large size of magmatic feldspars, the presence of perthites, and the zonation between both alkali feldspar and plagioclase (rapakivi textures), all assist grain-scale element recycling, a type of remobilization that may also lead to telescoping of alteration styles.

6.6.2 Broader scale zonation patterns: metasomatism and advanced feldspar replacement

At Olympic Dam, fluids become richer in Fe, REE as reactions between feldspars and fluids progress. Red-staining of K-feldspar, observed pervasively within and outside the ODBC is likely the initial stage of Fe-metasomatism and suggests the presence of nanoscale hematite (or other Fe-oxides) (Kontonikas-Charos et al., 2017). Comparably, dusty inclusions of Fe-oxides are reported from early skarn (in which feldspars are preserved) at Hillside (Ismail et al., 2014; Ismail, 2016). Studies of granitic terranes elsewhere contend that the presence of hematite in porous, red-clouded feldspars is strong evidence for large-scale crustal fluid–rock interaction (Putnis et al., 2007).

The results here show abundant, nm-scale inclusions of Fe-oxides throughout red-stained orthoclase (case study C) and also in a REE-fluorocarbonate + molybdenite assemblage that has completely pseudomorphed a pre-existing feldspar (case study D). Speciation of the Fe-oxide itself appear to be maghemite and hematite in the two case studies, respectively. Although more data is necessary to confirm the identification of maghemite, this is likely to form of behalf of a precursor magnetite and such results are, moreover, concurrent with the presence of co-existing chlorite. Both chlorite and magnetite/maghemite are indicative of a more reduced environment (presence of Fe^{2+} in the system) prior to the sericite (hydrolytic)

stage, which is expressed in the BSG-molybdenite assemblage hosting hematite. Differences between precipitation rates can be invoked to explain the relative lack of open pores around the Fe-oxides in the advanced replacement of feldspars compared to the perthites. The replacement reactions are, nevertheless, of comparable CDRR type, as evidenced by epitaxial intergrowths observed at the nanoscale, i.e. between orthoclase and chlorite, among REE-fluorocarbonate species, and between REE-fluorocarbonates and molybdenite.

Notably Fe-metasomatism, as it becomes prominent, is associated with more complex alteration assemblages, which may be associated with ore deposition, i.e. REE, Ca, F, as well as Mo and S (case study D). This is initiated by the replacement of feldspars that can lead to diverse mineral assemblages, if sufficiently advanced, and ultimately with the potential to obliterate recognizable granite within the ODBC. The strong correlation between precipitation of hematite, REE, and ore sulphides is unequivocal evidence that Fe-metasomatism and sulphide deposition are associated with one another in time and space within the host granite.

The two examples here, the simpler assemblage in the red-stained feldspar, and the mineralogically-diverse assemblages attributable to advanced replacement in the REE-fluorocarbonate-molybdenite, are from the same drillhole, and overlie an interval displaying pronounced albitization (Krneta et al., 2016; Kontonikas-Charos et al., 2017). The red-stained K-feldspar and mineralized sample occurs 150 m above the other. Such mineralogical differences can be explained by progressive metasomatism being enhanced by an increase in fluid/rock ratios. Early feldspar alteration of the perthite type observed at depth would have increased pore-controlled permeability (as shown in case study A), assisting an upwards-directed focusing of fluids at higher rates than otherwise expected in granitic rocks, leading to advanced metasomatism and ore deposition above the albitized interval.

The nm-scale of the calc-silicate inclusions within orthoclase documented here from the skarn-granite contact at Hillside (Figs. 16, 17), is a further example of metasomatism traceable

down to the nanoscale. The evidence shows that, in the absence of plagioclase, Ca and Fe can be sourced from a carbonate protolith leading to formation of abundant calc-silicates. Hillside, like most skarn systems (Meinert, 1992), displays a deposit-scale zonation of calc-silicate assemblages (of which andradite is a main component) relative to magmatic contacts (Ismail et al., 2014; Ismail, 2016). Although the skarn zoning is preferentially a function of protolith replacement, feldspars can also host REY and other trace elements in substantial amounts when affected by endoskarn formation, as outlined below.

6.6.3 Rare earth element remobilization: the role of feldspars in defining IOCG mineral signatures

In both deposits discussed here, igneous feldspars are modest hosts for REY, with ΣREY ranging between a few ppm (K-feldspars) to tens of ppm (plagioclase), although they have distinct chondrite-normalized patterns that can be correlated with alteration stages (e.g., Ismail et al., 2014; Kontonikas-Charos et al., 2014; in review). An increase in ΣREY is observed with progressive albitization, e.g., replacive albite (VP) hosts slightly more REY than PP at OD (means 36 ppm and 24 ppm, respectively; Kontonikas-Charos et al., in review), and red-stained, porous K-feldspar has the lowest ΣREY of all (mean 5-6 ppm; Kontonikas-Charos et al., in review). Although the red-stained feldspar is a product of Fe-metasomatism, the latter is inefficient with respect to CDRR-driven remobilization/concentration of REY from the local reaction environment since it lacks the more complex trace element signature of either the fluids or the parent feldspar. If this can be substantiated by other studies, zonation halos enclosing these deposits are most likely due to such reaction rather than to an influx of hydrothermal fluids external to the pluton. In cases where CDRR is not operative, feldspars (particularly albite), can retain as much as 200 ppm ΣREY (e.g. feldspathic schist at Moonta-

Wallaroo; Kontonikas-Charos et al., 2014), and with chondrite-normalized fractionation patterns that mimic those of the whole rock.

Feldspars become strongly depleted in REY if Ca or other elements are available to form discrete REE-minerals (BSG, monazite, allanite, etc.), accessories (titanite, apatite), or calc-silicates (epidote, garnet). Moreover, such minerals are good REY-repositories which can readily occur as nanoscale inclusions within feldspars (e.g., epidote and apatite in case study D), and may increase in abundance to account for as much 500 ppm ΣREY (e.g., andradite and titanite in orthoclase at Hillside; Ismail et al., 2014). The distinct chondrite-normalized REY fractionation patterns (Fig. 3), and ΣREY concentrations in the tens to hundreds of ppm range, are atypical for igneous feldspar. These patterns can nevertheless be explained by the nanoscale observations, which show an abundance of small, regularly distributed mineral inclusions. Their small size and homogeneous distribution is supported by the flatness of signals for REY on time-resolved downhole LA-ICP-MS profiles (Fig. 3b). Potentially, <5 nm-sized nanoparticles, which cannot be readily visualized using instrumentation employed here, may also be present.

The observed marked decrease in ∑REY in feldspars with proximity to the Olympic Dam orebody (Kontonikas-Charos et al., in review) hints at the release and local remobilization of REY from feldspars to form discrete REE-minerals. This scenario is illustrated by the example of the REE-fluorocarbonates-molybdenite assemblage (Fig. 12) in the drillhole intersecting the distal satellite mineralization. Evidence for pre-existing feldspars would be obliterated with increasing fluid/ratio metasomatism, but as shown here, Fe-metasomatism is contemporaneous with REE-enrichment when mineralizing fluids (Mo, Cu, Au) are released. Rapid uplift of already albitized granite could focus such fluids in the cupola areas of the RDG and explain the REE enrichment in the mineralized hematite breccias at OD. In contrast, the REE

enrichment in skarns will concentrate these elements into calc-silicates rather than as REE-discrete minerals, as known from Hillside (Ismail et al., 2014).

6.7 Implications and outlook

The complexity of the mineral reactions documented here suggests that placing formal labels on alteration stages such as 'sodic', 'calcic' and 'potassic', and arranging these in a systematic sequence, may not adequately reflect what really took place prior to, and at the time of IOCG ore formation. Alteration stages may have overlapped with one another and reaction products may have been metastable, e.g., preservation of monoclinic-triclinic transitions in feldspar. Moreover, this highlights the importance of detailed petrography and mineralogy, together with geochemistry, in order to support interpretations made on alteration stages within magmatic-hydrothermal systems.

CDRR, as documented here for reactions during post-magmatic perthite formation, therefore not only assists in the mobilization of elements from feldspar but also opens up nanoscale pore spaces for the mobilized elements to be trapped as inclusions. This supports the overall hypothesis that albitization and other expressions of feldspar alteration enhance rock porosity and drive element remobilization. Without a suitable trap mechanism at the deposit scale (e.g., cap rock, fault structures etc.), however, hydrothermal fluids may be easily lost from the system. The enhanced porosity, and likely permeability, resulting from CDRR is not only critical for the REE distribution but is observed in a broad variety of ore and alteration assemblages across the Olympic Dam deposit. The importance of CDRR at OD is documented, for example, in assemblages involving uraninite (Macmillan et al., 2016a, b; in press).

Although this contribution has focussed exclusively on the nanoscale evidence for REY release from feldspars, similar mechanisms may also apply to other critical metals which may be initially concentrated within the feldspar lattice, and which seldom form independent

minerals in igneous rocks. These include Ga, Sc and Nb, all of which are enriched at Olympic Dam relative to crustal values. Considering the abundance of feldspars in granitoid-hosted IOCG systems, their role in re-concentrating a whole range of critical metals should not be ignored. Identifying reaction pathways and product host phases for these critical metals is beyond the scope of the present work but future work should address the distributions of these elements in feldspars and in hydrothermal reaction products ranging from discrete REE-minerals to calc-silicates. This represents an essential step towards establishing and unlocking their long-term resource potential.

6.8 Acknowledgements

This is a contribution to the 'FOX' project (characterization of Fe-oxides), supported by BHP Billiton Olympic Dam and the South Australian Government Mining and Petroleum Services Centre of Excellence. AKC acknowledges the Deep Exploration Technologies Co-operative Research Centre for scholarship support. NJC acknowledges support from the ARC Research Hub for Australian Copper-Uranium. Constructive comments from reviewers Oliver Plümper, Tina Hill and Artur Deditius, and from Special Issue editors Erik Jonsson and John Bowles, helped us improve the manuscript.

6.9 References

Barton, M., 2014. Iron oxide (–Cu–Au–REE–P–Ag–U–Co) systems. Treatise on Geochemistry, 2nd edition, vol. 13. Elsevier, Amsterdam, pp. 515–541.

Barton, M.D., Johnson, D.A., 1996. Evaporitic-source model for igneous-related Fe oxide–(REE-Cu-Au-U) mineralisation. Geology 24, 259–262.

Ciobanu, C.L., Cook, N.J., Utsunomiya, S., Pring, A., Green, L., 2011. Focussed ion beam transmission electron microscopy applications in ore mineralogy: bridging micro and nanoscale observations. Ore Geology Reviews 42, 6–31.

Ciobanu, C.L., Cook, N.J., Maunders, C., Wade, B.P., Ehrig, K., 2016. Focused Ion Beam and Advanced Electron Microscopy for Minerals: Insights and Outlook from Bismuth Sulphosalts Minerals 6, 112, doi:10.3390/min6040112.

Ciobanu, C.L., Cook, N.J., Ehrig, K., 2017. Ore minerals down to the nanoscale: Cu-(Fe)-sulphides from the Iron Oxide Copper Gold deposit at Olympic Dam, South Australia. Ore Geology Reviews 81, 1218-1235.

Conor, C., Raymond, O., Baker, T., Teale, G., Say, P., Lowe, G., 2010. Alteration and mineralisation in the Moonta-Wallaroo Cu–Au mining field region, Olympic domain, South Australia. In: Porter, M. (Ed.), Hydrothermal Iron Oxide Copper–Gold and Related Deposits: A Global Perspective 3, 1–24.

Donnay, G., Donnay, J.D.H., 1953. The crystallography of bastnaesite-(Ce), parisite, roentgenite-(Ce) and synchysite-(Ce). American Mineralogist 38, 932-963.

Ehrig, K., McPhie, J., Kamenetsky, V., 2012. Geology and mineralogical zonation of the Olympic Dam iron oxide Cu-U-Au-Ag deposit, South Australia. In: Hedenquist, J.W., Harris, M., Camus, F., (Eds.), Geology and Genesis of Major Copper Deposits and Districts of the World: A Tribute to Richard H. Sillitoe. Society of Economic Geologists Special Publication 16, 237–267.

Groves, D.I., Bierlein, F.P., Meinert, L.D., Hitzman, M.W., 2010. Iron oxide copper-gold (IOCG) deposits through earth history: implications for origin, lithospheric setting, and distinction from other epigenetic iron oxide deposits. Economic Geology 105, 641–654.

Hitzman, M.W., Oreskes, N., Einaudi, M.T., 1992. Geological characteristics and tectonic setting of Proterozoic Iron Oxide (Cu-U-Au-REE) deposits. Precambrian Research 58, 241–287.

Hövelmann, J., Putnis, A., Geisler, T., Schmidt, B.C., Golla-Schindler, U., 2010. The replacement of plagioclase feldspars by albite: observations from hydrothermal experiments. Contributions to Mineralogy and Petrology 159, 43–59.

Ismail, R., 2016. Spatial-Temporal Evolution of Skarn Alteration in IOCG Systems: Evidence from Petrography, Mineral Trace Element Signatures and Fluid Inclusion Studies at Hillside, Yorke Peninsula, South Australia. Unpublished Ph.D. thesis, The University of Adelaide.

Ismail, R., Ciobanu, C.L., Cook, N.J., Teale, G.S., Giles, D., Schmidt Mumm, A., Wade, B., 2014. Rare earths and other trace elements in minerals from skarn assemblages, Hillside iron oxide–copper–gold deposit, Yorke Peninsula, South Australia. Lithos 184–187, 456–477.

Kontonikas-Charos, A., Ciobanu, C.L., Cook, N.J., 2014. Albitization and redistribution of REE and Y in IOCG systems: Insights from Moonta-Wallaroo, Yorke Peninsula, South Australia. Lithos 208–209, 178-201.

Kontonikas-Charos, A., Ciobanu, C.L., Cook, N.J., Ehrig, K., Kamenetsky, V.S., 2015. Deuteric coarsening and albitization in Hiltaba granites from the Olympic Dam IOCG deposit, South Australia. Proceedings, Mineral Resources in a Sustainable World, 13th Biennial SGA Meeting, Nancy, France, August 2015, vol. 3, pp. 1099–1102.

Kontonikas-Charos, A., Ciobanu, C.L., Cook, N.J., Ehrig, K., Krneta, S., Kamenetsky, V.S., 2017. Feldspar evolution in the Roxby Downs Granite, host to Fe-oxide Cu-Au-(U) mineralisation at Olympic Dam, South Australia. Ore Geology Reviews 80, 838-859.

Kontonikas-Charos, A., Ciobanu, C.L., Cook, N.J., Ehrig, K., Krneta, S., Kamenetsky, V.S., (in review). Rare earth element geochemistry of feldspars: Examples from Fe-oxide Cu-Au systems in the Olympic Cu-Au Province, South Australia. Mineralogy and Petrology.

Krneta, S., Ciobanu, C.L., Cook, N.J., Ehrig, K., Kontonikas-Charos, A., 2016. Apatite at Olympic Dam, South Australia: a petrogenetic tool. Lithos 262, 470–485.

Macmillan, E., Cook, N.J., Ehrig, K., Ciobanu, C.L., Pring, A., 2016a. Uraninite from the Olympic Dam IOCG-U-Ag deposit: Linking textural and compositional variation to temporal evolution. American Mineralogist 101, 1295–1320.

Macmillan, E., Ciobanu, C.L., Ehrig, K., Cook, N.J., Pring, A., 2016b Chemical zoning and lattice distortion in uraninite from Olympic Dam, South Australia. American Mineralogist 101, 2351-2354.

Macmillan, E., Ciobanu, C.L., Ehrig, K., Cook, N.J., Pring, A., (in press). Replacement of uraninite by bornite via coupled dissolution-reprecipitation: Evidence from texture and microstructure. The Canadian Mineralogist, doi 10.3749/canmin.1600031.

Mauger, A.J., Ehrig, K., Kontonikas-Charos, A., Ciobanu, C.L., Cook, N.J., Kamenetsky, V.S., 2016. Alteration at the Olympic Dam IOCG–U deposit: insights into distal to proximal feldspar and phyllosilicate chemistry from infrared reflectance spectroscopy. Australian Journal of Earth Sciences 63, 959-972.

Meinert, L.D., 1992. Skarns and skarn deposits. Geoscience Canada Reprint Series 6, 117–134.

Meng, D.W., Wu, X.L., Mou, T., Li, D.X., 2001. Determination of six new polytypes in parisite-(Ce) by means of high resolution electron microscopy. Mineralogical Magazine 65, 797-806.

Meng, D.W., Wu, X.L., Han, Y.J., Meng, X., 2002. Polytypism and microstructures of the mixed-layer member B_2S, $CaCe_3(CO_3)_4F_3$ in the bastnaesite-(Ce)-synchysite-(Ce) series. Earth and Planetary Science Letters 203, 817-828.

Navrotsky, A., 2011. Nanoscale Effects on Thermodynamics and Phase Equilibria in Oxide Systems. ChemPhysChem 12, 2207–2215.

Navrotsky, A., Mazeina, L., Majzlan, J., 2008. Size-Driven Structural and Thermodynamic Complexity in Iron Oxides. Science 319, 1635-1638.

Ni, Y.X., Hughes, J.M., Mariano, A.N., 1993. The atomic arrangement of bastnaesite-(Ce), $Ce(CO_3)F$, and structural elements of synchysite-(Ce), roentgenite-(Ce), and parisite-(Ce). American Mineralogist 78, 415-418.

Plümper, O., Putnis, A., 2009. The complex hydrothermal history of granitic rocks: multiple feldspar replacement reactions under subsolidus conditions. Journal of Petrology 50, 967–987.

Pollard, P.J., 2006. An intrusion-related origin for Cu–Au mineralization in iron oxide–copper–gold (IOCG) provinces. Mineralium Deposita 41, 179–187.

Putnis, A., 2002. Mineral replacement reactions: from macroscopic observations to microscopic mechanisms. Mineralogical Magazine 66, 689–708.

Putnis, A., Hinrichs, R., Putnis, C.V., Golla-Schindler, U., Collins, L.G., 2007. Hematite in porous red-clouded feldspars: evidence of large-scale crustal fluid–rock interaction. Lithos 95, 10–18.

Reich, M., Hough, R.M., Deditius, A., Utsunomiya, S., Ciobanu, C.L., Cook, N.J., 2011. Nanogeoscience in ore systems research: Principles, methods, and applications: Introduction and preface to the special issue. Ore Geology Reviews 42, 1-5.

Reid, A.J., Swain, G.S. Mason, D., Maas, R., 2011. Nature and timing of Cu-Au-Zn-Pb mineralisation at Punt Hill, eastern Gawler Craton. MESA Journal 60, 7–17.

Skirrow, R.G., Bastrakov, E.N., Barovich, K., Fraser, G.L., Creaser, R.A., Fanning, C.M., Raymond, O.L., Davidson, G.J., 2007. Timing of iron oxide Cu-Au-(U) hydrothermal

activity and Nd isotope constraints on metal sources in the Gawler craton, South Australia. Economic Geology 102, 1441–1470.

Van Landuyt, J., Amelinckx, S., 1975. Multiple beam direct lattice imaging of new mixed-layer compound of the bastnaesite– synchysite series. American Mineralogist 60, 351-358.

Wu, X.L., Meng, D.W., Pan, Z.L., Yang, G.M., 1998. Transmission electron microscopic study of new, regular, mixed-layer structures in calcium – rare earth fluorocarbonate minerals. Mineralogical Magazine 62, 55-64.

CHAPTER 7

SUMMARY, RECOMMENDATIONS AND IMPLICATIONS

CHAPTER 7: SUMMARY, RECOMMENDATIONS AND IMPLICATIONS

7.1 Summary

7.1.1 Feldspar replacement reactions in magmatic-hydrothermal systems

Feldspar replacement reactions are a ubiquitous feature of the rocks investigated here. Such reactions occur across the time-space spectrum of magmatic-hydrothermal systems, from post-magmatic (deuteric) to early and late hydrothermal stages, and at scales ranging from regional- (tens to hundreds of km) and deposit- to micro- and nanoscale. Due to the metastability of the feldspar crystal lattice, any contact or exposure to fluid(s) which is/are in disequilibrium, will produce a chemical reaction. The resultant textures and assemblages are largely dependent on the host rock lithology, style of fluid/rock interaction, as well as temperature, pH and redox conditions.

Of the metasedimentary rocks studied here, the majority of them show evidence of high fluid/rock ratio metasomatism. Although formed at different metamorphic grades (e.g., greenschist to lower amphibolite facies), alteration textures (consisting of chlorite and albite-biotite assemblages) are generally granoblastic and show minimal signs of increased porosity or cogenetic inclusions (in stark contrast to altered igneous rocks). Moreover, significant shifts in geochemistry are apparent, and dominant mineral assemblages may contain uncharacteristically high concentrations of trace elements. For example, albite from the Doora Member (albite-biotite schist) at Moonta-Wallaroo contains ~200 ppm ∑REY in solid solution, an anomaly supported by time-resolved LA-ICP-MS downhole profiles, and subsequent nanoscale investigation by TEM (e.g., Fig. 10 in Kontonikas-Charos et al., 2014; Chapter 3).

In general, igneous rocks which come into contact with fluids (either deuteric or hydrothermal) will show evidence of coupled dissolution-reprecripitation reactions (CDRR; e.g., Putnis, 2002), typically preserved in feldspars (although not restricted to them). Characteristic features of such reactions are: (i) a sharp reaction front between the parent and product phases, (ii) marked porosity in the product phase, as well as the presence of cogenetic precipitates and (iii) a pseudomorphic replacement of the parent phase. Through a combination of FIB-SEM and TEM techniques, an epitaxial relationship between cryptoperthite and patch perthite has been determined, indicative of interface-mediated reactions between pre-existing alkali feldspars and pervading fluid. Such a relationship is typical for CDRR and has also been documented for the albitization of plagioclase here and in other studies (e.g., Hövelmann et al., 2010). In addition, there is a marked increase in porosity at replacement contacts, reaffirming the generation of porosity via the coupled dissolution-reprecipitation mechanism.

The CDRR mechanism facilitates fluid propagation through rocks which have very low intrinsic permeability (e.g., granitic lithologies), via the generation of transient pathways of interconnected nano- and micropores (e.g., Putnis, 2002; 2009; 2015; Plümper et al., 2017). In principle, CDRR involve the dissolution of a parent phase during mineral/fluid interaction, which produces an interfacial fluid-film that may be supersaturated with respect to certain phases, and subsequently leads to the nucleation of a product phase (e.g., Putnis, 2009; Ruiz-Agudo et al., 2014). Critically, the autocatalytic nature of this process and the generation of porosity allows for continuity between the fluid reservoir and reaction boundary, whilst maintaining the overall integrity of the host rock. Porosity will form either as a result of molar volume and/or solubility differences between the parent and product phases (e.g., Putnis, 2002). In regards to feldspar replacement reactions documented here, it appears that porosity associated with the isochemical recrystallization of cryptoperthite to patch perthite is a result of differences in solubility rather than molar volume. This is due to the coherency and strained

nature of cryptoperthite rendering it more soluble relative to the incoherent, strain-free patch perthite. Conversely, the albitization of plagioclase may generate porosity due to differences in molar volume between plagioclase and albite. However, this is dependent on numerous assumptions which are integral when expressing the reaction as a balanced equation. Applying equations proposed by Merino (1975), Boles (1982) and Engvik et al. (2008), replacement of plagioclase (oligoclase) by albite in the Roxby Downs Granite (RDG) may be given by:

$$(1)\quad Na_{0.8}Ca_{0.2}Al_{1.2}Si_{2.8}O_8 \text{ (oligoclase)} + 0.2\ Na^{+} \text{ (aq.)} + 0.2\ H_4SiO_4 \text{ (aq.)} \downarrow NaAlSi_3O_8 \text{ (albite)} + 0.2\ Ca^{2+} \text{ (aq.)} + 0.2\ Al^{3+} \text{ (aq.)} + 0.8\ OH^{-} \text{ (aq.)}$$

$$(2)\quad Na_{0.8}Ca_{0.2}Al_{1.2}Si_{2.8}O8 \text{ (oligoclase)} + 0.4\ Na^{+} \text{ (aq.)} + 0.8\ H_4SiO_4 \text{ (aq.)} \downarrow 1.2\ NaAlSi_3O_8 \text{ (albite)} + 0.2\ Ca^{2+} \text{ (aq.)} + 1.6\ H_2O \text{ (aq.)}$$

Equation (1) implies mobility of Al^{3+}, which, given the close association of sericite with replacive albite, may be released from plagioclase and incorporated in sericite. This hypothesis is preferred in the case of the RDG due to the co-precipitation of sericite with albite, and therefore, associated porosity would be due to a molar volume-deficit reaction from oligoclase (~265.32 g) to albite (~262.12 g). Equation (2), however, conserves Al within the product albite, and therefore would require excess albite (1.2 moles) to account for this. In this case, the increase in molar volume in the product phase would limit the amount of porosity generated, and thus the progression of the reaction. Such an equation may indeed be more suitable for the formation of thin pure albite rims (devoid of porosity and co-precipitates) around igneous plagioclase, discussed in Kontonikas-Charos et al., 2017 (Chapter 4).

Regardless of which equation is most suitable, the albitization of plagioclase principally involves consumption of Na^{+}, Si^{-4} and H^{+}, and the release of Ca^{2+} and Al^{3+}. Deposit-scale albitization would thus significantly affect the geochemistry of host rocks, but would also

require a source of Na. The metasomatism of local and regional evaporites has been inferred as a source of Na in numerous IOCG terranes (e.g., Conor et al., 2010; Bernal et al., 2017). Aside from the introduction of Na-rich fluids, a feasible source may be the alteration of Na-amphiboles (e.g., edenite) to chlorite. Moreover, the recrystallization of cryptoperthite to patch perthite may provide Na, as the generation of porosity through this reaction is not fully accounted for by molar volume reduction. Some feldspar components are thus expected to be lost to the fluid (e.g., Walker et al., 1995). Beyond these potential sources, a seminal study by Orville (1963) showed that Na-rich fluids are not necessarily required for albitization, and that a fluid simply has to be of suitable temperature to facilitate exchange between Na^+ and K^+.

7.2 Research gaps and recommendations

7.2.1 The role of alkali alteration in IOCG systems

The major element exchange (Na-Ca-K-Fe) typical for IOCG systems is a result of multiple alteration stages, which may overlap one another. Often preserved at depth or at the peripheries of IOCG systems (Barton, 2014), the early alkali (Na-Ca) alteration stage appears to be the beginning of this process.

The ambiguity surrounding the role of alkali alteration has persisted since the conception of IOCG systems (e.g., Hitzman et al., 1992). Generally, alkali alteration is considered barren with respect to base metals (e.g., Barton, 2014; references therein). However, attempts at constraining the direct influence of alkali alteration on metal endowment in IOCG systems have been made (e.g., Cloncurry District; Oliver et al., 2004). In this case, early Na-Ca assemblages recorded significant Zn and Pb loss; however results were inconclusive with regards to Cu. Such studies are often inhibited by the open-system style of IOCG mineralization which potentially renders mass-balance calculations misleading. However, an explanation for

this widespread metal-loss is presented here. A likely scenario is that metals are stripped from the host rocks during initial alkali alteration and are subsequently transported and concentrated during later stages of IOCG genesis, possibly associated with the more acidic, lower temperature (~300 °C) Fe-K-assemblages (e.g., Bastrakov et al., 2007) This is supported by observed mineralogical relationships in IOCG systems. Reported Na-Ca assemblages generally comprise albite + sericite + epidote (replacing feldspars), chlorite + actinolite (replacing mafic minerals) and rutile + titanite (replacing Fe-Ti-oxides), which are often seen to transition into more Fe-K-rich assemblages (e.g., hematite + sericite + K-feldspar) associated with Cu-Au mineralization (e.g., Barton, 2014). Moreover, experiments conducted by Oliver et al. (2004) showed that small increases in fluid/rock interaction produced widespread albitization and K-Fe-Ca-enrichment within fluids.

Applying this to a natural system, these enriched fluids can potentially precipitate subsequent K-Fe-Ca-rich assemblages, i.e. reflecting the transition from Na-Ca alteration in IOCG systems. Oliver et al. (2004) also concluded that precipitation of Cu-Au mineralization was the result of mixing Cu-bearing brines of magmatic origin, modified by albitization, with S-bearing fluids or due to reaction between the brine and S-bearing rocks. Therefore, although the influence of base metals is difficult to constrain, it appears that initial alkali alteration does indeed play a role in the major element exchange characteristic of IOCG systems. This is reaffirmed by supporting textures and geochemistry observed across the least-altered RDG to mineralized RDG continuum at Olympic Dam (Kontonikas-Charos et al., 2017). The deposit-scale alteration transition at Olympic Dam, e.g., Na-(Ca)-assemblages overprinted by Fe-K-rich assemblages (e.g., hematite + sericite + K-feldspar) associated with Cu-Au mineralization, is also mimicked at the nanoscale by the superimposition of hydrothermal K-feldspar (variably red-stained) in albitized zones. Furthermore, nanoscale (~10 nm-sized) Fe-oxide inclusions

within bastnäsite further underpins the significance of the relationship between Fe-metasomatism and REE remobilization at Olympic Dam.

Results presented here suggest that alkali alteration associated with granitoid-hosted IOCG systems typically progresses via CDRR, however such a process is similarly recognized for other minerals within the same systems (e.g., apatite; Krneta et al., 2016, and uranium minerals – uraninite, coffinite, brannerite; Macmillan et al., 2016a; b; c; in press). This mechanism not only facilitates the mobilization of elements from minerals within host rocks (including mafic silicates and Fe-Ti-oxides), but also opens up nanoscale pore spaces for the mobilized elements to be subsequently transported and trapped as inclusions. Considering the abundance of feldspars in granitoid-hosted IOCG systems, their role in re-concentrating REY, and potentially a range of other elements, may be significant. Although requiring a number of assumptions, using thermodynamic and geochemical calculations can provide reaction pathways for alkali alteration and identify product host phases for remobilized elements, leading to a greater understanding of the role of alkali alteration in IOCG systems and potentially other magmatic-hydrothermal terranes.

7.2.2 Geochemical modelling: albitization of plagioclase

The majority of feldspar trace element studies often focus on crystal/melt interaction (e.g., igneous feldspars; Papike, 1988; Pun et al., 1997), or doped synthesis experiments (see section 1.1.4). However, perhaps due to their low concentrations (particularly of REE), trace elements in hydrothermal feldspars are comparatively less studied. Numerous authors have reported that certain aqueous REE-complexes are sensitive to pH, temperature, salinity, redox conditions and fluid composition (e.g., Haas et al., 1995; Migdisov and Williams-Jones, 2014; Migdisov et al., 2016), stimulating attempts to unlock their potential as geochemical tracers in minerals preserved within magmatic-hydrothermal systems. Results from Chapters 3 and 5 (Kontonikas-

Charos et al., 2017; in review) highlight how the geochemical signatures of feldspars are able to distinguish between magmatic and hydrothermal stages within IOCG systems, based on variations in Eu-, Ce- and Y-anomalies, and changes in REY-slopes (LREE/HREE ratio) of reproducible chondrite-normalized fractionation patterns. Although robust measurements of physico-chemical conditions are not calculated here, the applicability and interpretations of feldspar REY fractionation patterns are supported by detailed petrography and whole-rock geochemistry.

This supports the applicability of REE geochemical studies in constraining petrogenesis. Based on measureable ∑REY concentrations and reproducible fractionation patterns, geochemical models tracking changes in REE partitioning during albitization of plagioclase is a suitable future avenue of research. To achieve this, certain parameters must be outlined for both the fluids and minerals involved. The ability of aqueous solutions to mobilize REE from minerals is reliant on the stability of REE-complexes formed with ligands in the solutions (Migdisov et al., 2016). Therefore, constraining the thermodynamic properties and stabilities of common ligands which complex with REE (e.g., chloride, fluoride, carbonate etc.) is paramount. Consequently, numerous geochemical modelling studies have aimed to achieve this (e.g., Smith et al., 2004; Brugger et al., 2008; Migdisov et al., 2016). They have shown that the most soluble and stable ligands, and thus most effective for REE transport, are chloride (Cl^-) and sulphate (SO_4^{2-}), whereas fluoride (F^-), carbonate (CO_3^{2-}) and phosphate (PO_4^{3-}) ligands are less soluble and more suitable for complexing during the deposition of REE-minerals (e.g., REE-fluorocarbonates and REE-phosphates). Therefore, in order to gain insights into REE remobilization from plagioclase during albitization, the activity levels of the various REE-complexes, particularly REE-Cl^- and REE-SO_4^{2-}, within the fluids must be determined.

An effective means of obtaining an estimate of hydrothermal fluid properties is through fluid inclusions. A study by Oreskes and Einaudi (1992) reported a range of salinities and solute chemistry within quartz and fluorite fluid inclusions from hematite breccias at Olympic Dam, and also from K-feldspar-apatite veins at Acropolis. Two-phase inclusions contained salinities ranging from 7.3 - 23.7 wt. % NaCl equivalent, while three-phase fluid inclusions had as much as 42 wt. % NaCl equivalent. A range of other solutes were also identified including KCl, $CaCl_2$, $FeCl_2$, CaF_2 and CO_2. The homogenization temperatures indicated a range from 110 – 420 °C, with the upper limit associated with early, high temperature alteration, whereas hematite-breccia formation is inferred to have occurred at temperatures between 200 - 400 °C. In order to apply these fluid parameters to a geochemical model for albitization, the geochemistry and partition coefficients of plagioclase and albite must be determined. This is reliant on the coupled substitution of $2Ca^{2+}$ for $REE^{3+} + Na^{+}$ mechanism in plagioclase and albite (outlined in Chapters 1 and 5), which is ideal for this reaction. The initial REE concentration of the fluid is assumed from whole-rock assays of the least-altered RDG (i.e., Smith et al., 2004). The Geochemist's Workbench® software provides activity levels for REE-complexes, and allows for the input of necessary geochemical data and various fluid parameters to create hypothetical geochemical models that are able to predict changes in REE concentration and fractionation patterns during albitization of plagioclase based on an idealized fluid. Although this method requires numerous assumptions (e.g., relative mineral solubilities, redox conditions, pH), it can utilize certain minerals and their reactions as petrogenetic tools for exploration.

The potential to use feldspar REY fractionation patterns as vectors to ore is inhibited by the fact that it requires sampling, detailed petrography and analysis by LA-ICP-MS. However, given the scope of work already completed here, a further step would be to undertake a detailed fluid inclusion study of feldspars across the continuum from least-altered to mineralized RDG.

Given that the fluid inclusion study by Oreskes and Einaudi (1992) was performed on a limited number of samples and across a limited range of litholgies, a more holistic and modern study might provide additional insights into fluid parameters and their systematic variation, and thus would be an essential pre-requisite for application of geochemical modelling outlined above.

7.3 Implications

7.3.1 Evolution of the Olympic Dam deposit

Numerous attempts have been made to constrain the genesis of Olympic Dam since its discovery in 1975 (Roberts and Hudson, 1983; Reeve et al., 1990; Oreskes and Einaudi, 1990; 1992; Haynes et al., 1995; Johnson and Cross, 1995; McPhie et al., 2011; 2016). Initially proposed to be a stratabound sediment-hosted Cu-Au deposit (albeit, a speculative model based on limited data), the general consensus at Olympic Dam is that it formed as a result of progressive hydrothermal brecciation and Fe-metasomatism of the RDG, likely driven and sourced by the emplacement of the Hiltaba Suite and Gawler Range Volcanics (e.g., Reynolds, 2000). However, the presence of a stratigraphically continuous bedded clastic facies unit within the Olympic Dam Breccia Complex (ODBC) has historically been controversial. Early studies interpreted this as a volcaniclastic unit, broadly contemporaneous with brecciation and mineralization, and deposited within maar-diatremes (i.e., the maar-diatreme model favoured by Reeve et al., 1990; Oreskes and Einaudi, 1990; Johnson and Cross, 1995, and Haynes et al., 1995). However, McPhie et al. (2011; 2016) showed that the provenance of the bedded clastic facies unit extends beyond the Olympic Dam area and formed part of a sedimentary basin that existed prior to the ODBC formation. Consequently, the sources of metals and fluids remains a topic of contemporary debate (e.g., contributions from mafic dykes vs. granite-derived fluids vs. meteoric fluids). Dating of hydrothermal minerals within the ODBC indicates that it formed

shortly after emplacement of the RDG (e.g., Johnson and Cross, 1995; Jagodzinski, 2005; 2014; Ciobanu et al., 2013; Courtney-Davies et al., 2016). However, evidence has recently accumulated to suggest that regional-scale tectonic events, post-dating the established ~1590 Ma age for the ODBC, have impacted on mineralization at Olympic Dam and across the Gawler Craton. The ages of these events are broadly contemporaneous with supercontinent cycles, including the break-up of Columbia (1600-1300 Ma), amalgamation and break up of Rodinia (1300-1100 Ma and 850-600 Ma), and amalgamation of Gondwana (600-300 Ma) (Kamenetsky et al., 2015).

The findings within this dissertation present several new lines of evidence with regard to the genesis of the RDG and consequently, Olympic Dam.

Firstly, feldspar textures and geochemistry, along with the presence of microgranular mafic enclaves, multiple generations of magmatic magnetite (Ti-rich and Ti-poor) and apatite textures, point towards late-stage magma mixing/contamination with a more mafic unit in the RDG. This is supported by geobarometric estimates, based on Al-in-hornblende (Schmidt, 1992; Anderson and Smith, 1995), and corrected for temperature by the amphibole-plagioclase geothermometer (Blundy and Holland, 1990), which indicate pressures of ~2.2 kbar, corresponding to a final crystallization depth of 6-8 km for the RDG. Similar estimates were obtained by Creaser (1996) from quartz monzodiorite within the same pluton. The mixing of felsic and mafic magmas, as well as the introduction of pre- and syn-brecciation mafic dykes within the RDG, represents coeval felsic and mafic magmatism consistent with crustal continuum models for fertile IOCG systems (Groves et al., 2010). The rate of ascent and speed at which the RDG cooled prior to brecciation and 'unroofing' is unclear, however the significant geochemical and mineralogical zonation observed in the ODBC (e.g., Ehrig et al.,

2012) may be due to response to both the evolution of hydrothermal fluids and heterogeneous phase crystallization of RDG.

Secondly, the presence of Na-bearing assemblages at depth (~700 m) within the ODBC is concordant with proposed models for IOCG systems (however, notably absent from the IOCG *sensu stricto* class) in which deep sodic alteration transitions to shallower potassic and/or hydrolytic alteration (e.g., Hitzman et al., 1992; Barton, 2014). This 'telescoping' of alteration assemblages is supported by higher $a\mathrm{Na}^+$ than $a\mathrm{K}^+$ at higher temperatures (e.g., Orville, 1963). However, it is important to highlight that in the case of the RDG, albitization, thus far, has not been observed to produce barren, monomineralic albitites as reported from other IOCG terranes, e.g., from Cloncurry, Queensland (Mark, 1998; Oliver et al., 2004; Bertelli and Baker, 2010) and the Great Bear Magmatic Zone, Canada (Montreuil et al., 2016). A possible explanation is that the protoliths of albitites formed in association with IOCG deposits tend to be precursor sedimentary units, of which none are preserved *in situ* at Olympic Dam. Alternatively, metal exchange and recycling at Olympic Dam, might have resulted in widespread destruction of initial intense sodic alteration, which when preserved, is present at much greater depths, due to the giant scale of the deposit. Nevertheless, there is a clear remobilization of Na from the host RDG, which indeed leads to local albitization; and may also produce Na-(Ca)-assemblages elsewhere in the Olympic Dam area (e.g., albite + epidote + andradite-rich garnet at Phillip's Ridge; Kontonikas-Charos et al., in review; Chapter 5). This is further supported by Ehrig et al. (in press; Chapter 8 – Additional Material K). Moreover, the preservation of albitization at depth and to the peripheries of the ODBC is further established by deposit-scale hyperspectral investigations into feldspar alteration (Mauger et al., 2016; Chapter 8 – Additional Material D), and highlights the critical role that successive alteration events play in the formation of giant orebodies such as Olympic Dam.

Thirdly¸ given the high modal abundance of feldspars (65%) within least-altered RDG surrounding the Olympic Dam deposit, and the relatively high combined ∑REY concentration (~70 ppm) documented in Chapter 5 (Kontonikas-Charos et al., in review), it is plausible to suggest that igneous feldspars represent a source of REY for subsequent precipitation of REE-minerals (e.g., Van Dongen et al., 2010). Often considered to be concentrated in accessory phases of felsic rocks, relatively little attention has been paid to REE concentrations within major rock-forming silicates. However, it is evident from comparison of ∑REY of feldspars and whole-rock ∑REY from least-altered RDG, that a reasonable proportion of REY are contained within the feldspars.

Finally, the remobilization of REE at Olympic Dam is also documented in recent studies of other minerals within the RDG. In particular, the evolution of apatite from early-late magmatic and hydrothermal stages shows a progressive depletion of REE (predominantly LREE) with increasing proximity to the ODBC and Cu-Au mineralization (Krneta et al., 2016; Chapter 8 – Additional Material E). Moreover, multiple stages of U dissolution and reprecipitation are recorded in U-bearing minerals within the RDG and ODBC (Macmillan et al., 2016a, b, c; in press), further emphasizing the widespread element recycling and remobilization occurring within the Olympic Dam deposit.

7.3.2 The link between albitization and REE remobilization in IOCG systems

The generation of interconnected porosity during albitization allows fluids to percolate through significant volumes of largely impermeable rock (e.g., Plümper et al., 2017). This process allows for trace element remobilization from feldspars, as well as recrystallization of other phases within the host rocks (Figure 1). In the majority of granitic litholgies reported here, igneous feldspars are modest hosts for REY, with ΣREY ranging between a few ppm (K-feldspars) to tens of ppm (plagioclase). Nevertheless, reproducible chondrite-normalized REY-

fractionation patterns can be correlated with alteration stages (e.g., Ismail et al., 2014; Kontonikas-Charos et al., 2014; Chapter 3; in review; Chapter 5). An increase in ΣREY is observed with progressive albitization at early stages, however this trend reverses with the transition to Fe-K-alteration, in which albite becomes REY-depleted (ΣREY from ~ 35 to 3.5 ppm) and red-stained K-feldspar predominates (Kontonikas-Charos et al., in review; Chapter 5). Although the red-stained K-feldspar is a product of Fe-metasomatism, it is a particularly poor host of REY.

Moreover, feldspars become strongly depleted in REY if Ca becomes available to form discrete REE-minerals (REE-fluorocarbonates of the bastnäsite-synchysite group, allanite, etc.), accessories (titanite, apatite), or calc-silicates (epidote, garnet). Such minerals can form nanoscale inclusions within hydrothermal feldspars (e.g., epidote and apatite), and may increase in abundance to account for as much 500 ppm ΣREY (e.g., andradite and titanite in orthoclase at Hillside; Ismail et al., 2014; Kontonikas-Charos et al., in press; Chapter 6). The presence of these inclusions is a testament to the intimate relationship between REY remobilization and hydrothermal feldspar alteration.

The observed marked decrease in ∑REY in feldspars with proximity to the Olympic Dam orebody (Kontonikas-Charos et al., in review; Chapter 5), as well as with increasing alteration at Moonta-Wallaroo and Hillside (Ismail et al., 2014; Kontonikas-Charos et al., 2014; Chapter 3) hints at the release and local remobilization of REY from feldspars to form discrete REE-minerals. This scenario is supported by documentation of assemblages containing REE-fluorocarbonates and molybdenite which replace pre-existing feldspar in mineralized RDG (Fig. 12 in Kontonikas-Charos et al., in press; Chapter 6). Pre-existing feldspars would be obliterated with increasing fluid/rock ratios, but as evidenced here, Fe-metasomatism is contemporaneous with REE-enrichment when mineralizing fluids (Mo, Cu, Au) are released. Rapid uplift of albitized granite could focus such fluids in the cupola areas of the RDG and

explain the REE enrichment in the mineralized hematite breccias at Olympic Dam. In contrast, REE enrichment in skarns will preferentially be hosted within calc-silicate minerals, rather than crystallizing as REE-minerals, as seen at Hillside (Ismail et al., 2014). Furthermore, in the absence of dominant REE repository minerals, the albite itself may contain the bulk REE of the host rock (ΣREY ~200 ppm), as reported within metasedimentary lithologies at Moonta-Wallaroo (e.g., the Doora Member albite-biotite-schist Kontonikas-Charos et al., 2014; Chapter 3).

Although the primary focus of this study has been feldspars, significant element contributions from other major phases have also been documented (summarized in Figure 1). Within the granitic lithologies studied here, mafic silicate minerals, particularly amphibole and biotite, are a useful example. In the early stages of Na-(Ca) alteration, amphibole is altered to actinolite ± epidote and biotite replaced by chlorite ± titanite. Transitioning to more acidic conditions, where hematite predominates over magnetite, amphibole is replaced solely by chlorite, whereas biotite is replaced by chlorite + hematite. In addition, more resistate phases such as apatite (and zircon), show signs of REY-depletion rims resulting from influx of fluids associated with early alkali alteration (e.g., Kontonikas-Charos et al., 2014; Chapter 4; Krneta et al., 2016; Chapter 8 - Additional Material E). Other accessory minerals, such as Fe-Ti-oxides (ilmenite) and titanite, are replaced by rutile ± hematite ± REE-minerals. Such reactions, accompanying albitization, also release both major and minor (REE) elements within the fluids and facilitate the concentration and subsequent deposition of REE-minerals during formation of IOCG systems.

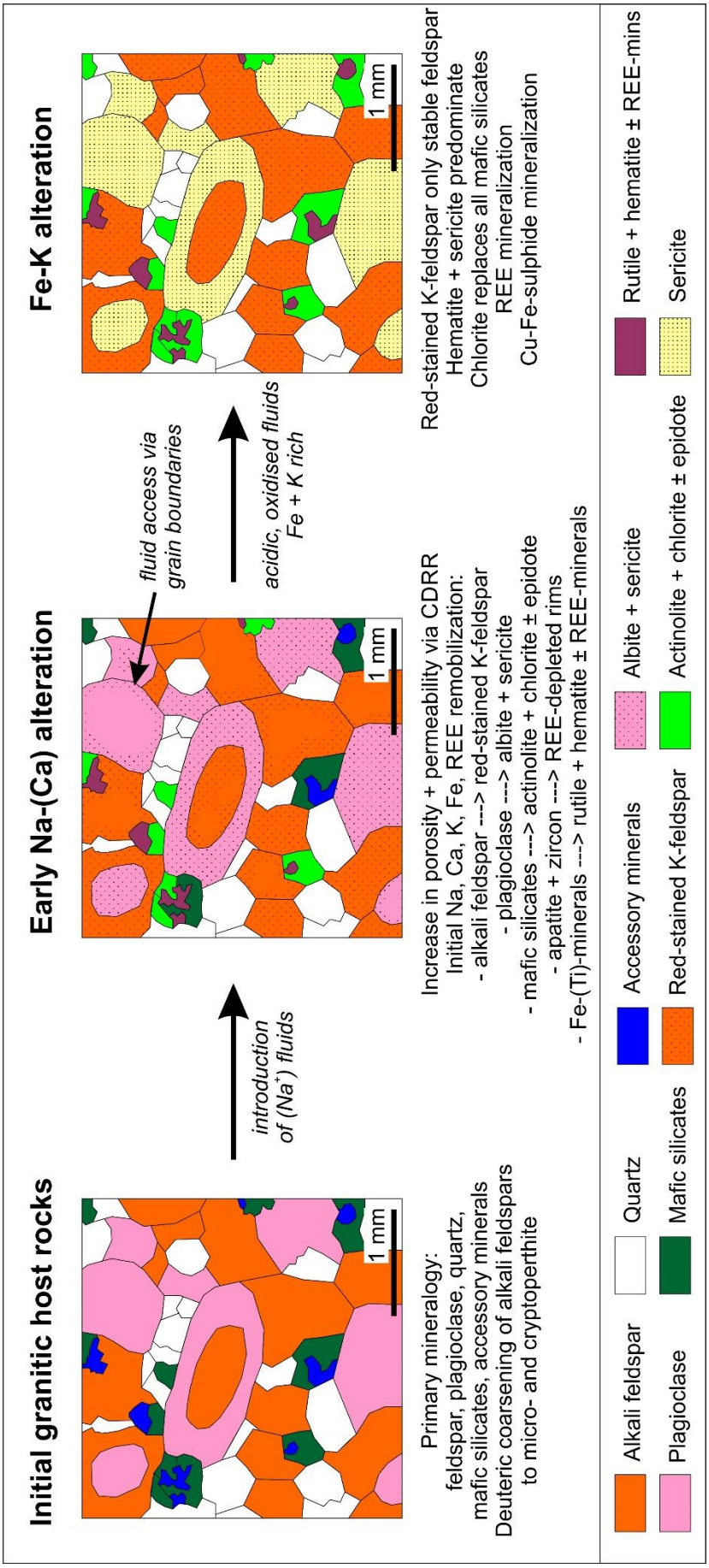

Figure 1: Schematic outlining mineralogical and textural changes in granitic host rocks during Na-(Ca)-alteration and Fe-K alteration of granitic host rocks in IOCG systems. Fluids initially gain access via CDRR and the generation of porosity in feldspars, facilitating element remobilization from all minerals.

Anderson, J.L., Smith, D.R., 1995. The effects of temperature and fO_2 on the Al-in-hornblende barometer. American Mineralogist 80, 549-559.

Barton, M., 2014. Iron oxide (–Cu–Au–REE–P–Ag–U–Co) systems. Treatise on Geochemistry (second edition, volume 13): Amsterdam, Elsevier, 515-541.

Bastrakov, E.N., Skirrow, R.G., Davidson, G.J., 2007. Fluid evolution and origins of iron oxide Cu-Au prospects in the Olympic Dam district, Gawler Craton, South Australia. Economic Geology 102, 1415-1440.

Bertelli, M., Baker, T., 2010. A fluid inclusion study of the Suicide Ridge Breccia Pipe, Cloncurry district, Australia: Implication for Breccia Genesis and IOCG mineralization. Precambrian Research 179, 69-87.

Bernal, N.F., Gleeson, S.A., Smith, M.P., Barnes, J.D., Pan, Y., 2017. Evidence of multiple halogen sources in scapolites from iron oxide-copper-gold (IOCG) deposits and regional Na Cl metasomatic alteration, Norrbotten County, Sweden. Chemical Geology 451, 90-103.

Blundy, J.D., Holland, T.J., 1990. Calcic amphibole equilibria and a new amphibole-plagioclase geothermometer. Contributions to Mineralogy and Petrology 104, 208-224.

Boles, J.R., 1982. Active albitization of plagioclase, gulf coast Tertiary. American Journal of Science 282, 165-180.

Brugger, J., Etschmann, B., Pownceby, M., Liu, W., Grundler, P., Brewe, D., 2008. Oxidation state of europium in scheelite: tracking fluid–rock interaction in gold deposits. Chemical Geology 257, 26-33.

Ciobanu, C.L., Wade, B.P., Cook, N.J., Mumm, A.S., Giles, D., 2013. Uranium-bearing hematite from the Olympic Dam Cu–U–Au deposit, South Australia: a geochemical tracer and reconnaissance Pb–Pb geochronometer. Precambrian Research 238, 129-147.

Conor, C., Raymond, O., Baker, T., Teale, G., Say, P., Lowe, G., 2010. Alteration and Mineralisation in the Moonta-Wallaroo Cu-Au Mining Field Region, Olympic Domain,

South Australia. In: Porter TM (Ed.), Hydrothermal Iron Oxide Copper-Gold & Related Deposits: A Global Perspective 3, PGC Publishing, Adelaide, 1-24.

Courtney-Davies, L., Zhu, Z., Ciobanu, C.L., Wade, B.P., Cook, N.J., Ehrig, K., Cabral, A.R., Kennedy, A., 2016. Matrix-matched iron-oxide laser ablation ICP-MS U–Pb geochronology using mixed solution standards. Minerals 6, 85.

Creaser, R.A., 1996. Petrogenesis of a Mesoproterozoic quartz latite-granitoid suite from the Roxby Downs area, South Australia. Precambrian Research 79, 371-394.

Ehrig, K., McPhie, J., Kamenetsky, V., 2012. Geology and mineralogical zonation of the Olympic Dam Iron Oxide Cu-U-Au-Ag deposit, South Australia. In: Hedenquist J.W., Harris, M., Camus, F., (Eds.), Geology and Genesis of Major Copper Deposits and Districts of the World: A Tribute to Richard H. Sillitoe, 16. SEG Special Publication, 237–267.

Ehrig, K., Kamenetsky, V.S., McPhie, J., Apukhtina, O., Ciobanu, C.L., Cook, N.J., Kontonikas-Charos, A., Krneta, S., (in press). The IOCG-IOA ore system at Olympic Dam and nearby prospects, South Australia. Proceedings from the 14th Biennial SGA Meeting, Quebec City, Canada, 2017.

Engvik, A.K., Putnis, A., Gerald, J.D.F., Austrheim, H., 2008. Albitization of granitic rocks: the mechanism of replacement of oligoclase by albite. The Canadian Mineralogist 46, 1401-1415.

Groves, D.I., Bierlein, F.P., Meinert, L.D., Hitzman, M.W., 2010. Iron Oxide Copper-Gold (IOCG) Deposits through Earth History: Implications for Origin, Lithospheric Setting, and Distinction from Other Epigenetic Iron Oxide Deposits. Economic Geology 105, 641-654.

Haas, J.R., Shock, E.L., Sassani, D.C., 1995. Rare earth elements in hydrothermal systems: estimates of standard partial molal thermodynamic properties of aqueous complexes of the rare earth elements at high pressures and temperatures. Geochimica et Cosmochimica Acta 59, 4329-4350.

Haynes, D.W., Cross, K.C., Bills, R.T., Reed, M.H., 1995. Olympic Dam ore genesis; a fluid-mixing model. Economic Geology 90, 281-307.

Hitzman, M.W., Oreskes, N., Einaudi, M.T., 1992. Geological characteristics and tectonic setting of proterozoic iron oxide (Cu-U-Au-REE) deposits. Precambrian Research 58, 241-287.

Hövelmann, J., Putnis, A., Geisler, T., Schmidt, B.C., Golla-Schindler, U., 2010. The replacement of plagioclase feldspars by albite: observations from hydrothermal experiments. Contributions to Mineralogy and Petrology 159, 43-59.

Ismail, R., Ciobanu, C.L., Cook, N.J., Teale, G.S., Giles, D., Mumm, A.S., Wade, B., 2014. Rare earths and other trace elements in minerals from skarn assemblages, Hillside iron oxide–copper–gold deposit, Yorke Peninsula, South Australia. Lithos 184–187, 456-477.

Jagodzinski, E., 2005. Compilation of SHRIMP U-Pb geochronological data, Olympic Domain, Gawler Craton. South Australia, 2001-2003. Geoscience Australia Record 2005/020

Jagodzinski, E.A., 2014. The age of magmatic and hydrothermal zircon at Olympic Dam, Australian Earth Sciences Convention Proceedings, Geological Society of Australia Abstracts 110, 260.

Johnson, J.P., Cross, K.C., 1995. U-Pb geochronological constraints on the genesis of the Olympic Dam Cu-U-Au-Ag deposit, South Australia. Economic Geology 90, 1046-1063.

Kamenetsky, V.S., Ehrig, K., Maas, R., Meffre, S., Kamenetsky, M., McPhie, J., Apukhtina, O., Huang, Q., Thompson, J., Ciobanu, C.L., Cook, N.J., 2015. The supergiant Olympic Dam Cu-U-Au-Ag Ore Deposit: Toward a new genetic model. Society of Economic Geologists, SEG 2015: World Class Ore Deposits: Discovery to Recovery, Hobart, TAS, Australia; 09/2015.

Kontonikas-Charos, A., Ciobanu, C.L., Cook, N.J., 2014. Albitization and redistribution of REE and Y in IOCG systems: Insights from Moonta-Wallaroo, Yorke Peninsula, South Australia. Lithos 208–209, 178-201.

Kontonikas-Charos, A., Ciobanu, C.L., Cook, N.J., Ehrig, K., Krneta, S., Kamenetsky, V.S., 2017. Feldspar evolution in the Roxby Downs Granite, host to Fe-oxide Cu-Au-(U) mineralisation at Olympic Dam, South Australia. Ore geology reviews 80, 838-859.

Kontonikas-Charos, A., Ciobanu, C.L., Cook, N.J., Ehrig, K., Ismail, R., Krneta, S., Basak, A. (in press) Feldspar mineralogy and rare earth element (re)mobilization in iron-oxide copper gold systems from South Australia: a nanoscale study. Mineral Magazine. https://doi.org/10.1180/minmag.2017.081.040

Kontonikas-Charos, A., Ciobanu, C.L., Cook, N.J., Ehrig, K., Krneta, S., Kamenetsky, V.S., (in review). Rare earth element geochemistry of feldspars: Examples from Fe-oxide Cu-Au systems in the Olympic Cu-Au Province, South Australia. Mineralogy and Petrology.

Krneta, S., Ciobanu, C.L., Cook, N.J., Ehrig, K., Kontonikas-Charos, A., 2016. Apatite at Olympic Dam, South Australia: A petrogenetic tool. Lithos 262, 470-485.

Macmillan, E., Cook, N.J., Ehrig, K., Ciobanu, C.L., Pring, A., 2016a. Uraninite from the Olympic Dam IOCG-U-Ag deposit: Linking textural and compositional variation to temporal evolution. American Mineralogist 101, 1295–1320.

Macmillan, E., Ciobanu, C.L., Ehrig, K., Cook, N.J., Pring, A., 2016b. Chemical zoning and lattice distortion in uraninite from Olympic Dam, South Australia. American Mineralogist 101, 2351-2354.

Macmillan, E., Ciobanu, C.L., Ehrig, K., Cook, N.J., Pring, A., 2016c. Replacement of uraninite by bornite via coupled dissolution-reprecipitation: Evidence from texture and microstructure. The Canadian Mineralogist 54, 1369-1383.

Macmillan, E., Cook, N.J., Ehrig, K., Pring, A., 2017 Chemical and textural interpretation of late-stage coffinite and brannerite from the Olympic Dam IOCG-Ag-U deposit. Mineralogical Magazine (in press).

Mark, G., 1998. Albitite formation by selective pervasive sodic alteration of tonalite plutons in the Cloncurry district, Queensland. Australian Journal of Earth Sciences 45, 765-774.

Mauger, A., Ehrig, K., Kontonikas-Charos, A., Ciobanu, C., Cook, N., Kamenetsky, V., 2016. Alteration at the Olympic Dam IOCG–U deposit: insights into distal to proximal feldspar and phyllosilicate chemistry from infrared reflectance spectroscopy. Australian Journal of Earth Sciences 63, 959-972.

McPhie, J., Kamenetsky, V.S., Chambefort, I., Ehrig, K., Green, N., 2011. Origin of the supergiant Olympic Dam Cu-U-Au-Ag deposit, South Australia: Was a sedimentary basin involved? Geology 39, 795-798.

McPhie, J., Orth, K., Kamenetsky, V., Kamenetsky, M., Ehrig, K., 2016. Characteristics, origin and significance of Mesoproterozoic bedded clastic facies at the Olympic Dam Cu–U–Au–Ag deposit, South Australia. Precambrian Research 276, 85-100.

Merino, E., 1975. Diagenesis in Tertiary sandstones from Kettleman North Dome, California. I. Diagenetic mineralogy. Journal of Sedimentary Research 45, 320-336.

Migdisov, A., Williams-Jones, A., Brugger, J., Caporuscio, F., 2016. Hydrothermal transport, deposition, and fractionation of the REE: Experimental data and thermodynamic calculations. Chemical Geology 439, 13-42.

Migdisov, A.A., Williams-Jones, A., 2014. Hydrothermal transport and deposition of the rare earth elements by fluorine-bearing aqueous liquids. Mineralium Deposita 49, 987-997.

Montreuil, J.-F., Corriveau, L., Potter, E.G., 2015. Formation of albitite-hosted uranium within IOCG systems: the Southern Breccia, Great Bear magmatic zone, Northwest Territories, Canada. Mineralium Deposita 50 (3), 293-325.

Oliver, N.H., Cleverley, J.S., Mark, G., Pollard, P.J., Fu, B., Marshall, L.J., Rubenach, M.J., Williams, P.J., Baker, T., 2004. Modeling the role of sodic alteration in the genesis of iron oxide-copper-gold deposits, Eastern Mount Isa block, Australia. Economic Geology 99, 1145-1176.

Oreskes, N., Einaudi, M.T., 1990. Origin of rare earth element-enriched hematite breccias at the Olympic Dam Cu-U-Au-Ag deposit, Roxby Downs, South Australia. Economic Geology 85, 1-28.

Oreskes, N., Einaudi, M.T., 1992. Origin of hydrothermal fluids at Olympic Dam; preliminary results from fluid inclusions and stable isotopes. Economic Geology 87, 64-90.

Orville, P.M., 1963. Alkali ion exchange between vapor and feldspar phases. American Journal of Science 261, 201-237.

Papike, J.J., 1988. Chemistry of the rock-forming silicates: Multiple-chain, sheet, and framework structures. Reviews of Geophysics 26, 407-444.

Plümper, O., Botan, A., Los, C., Liu, Y., Malthe-Sørenssen, A., Jamtveit, B., 2017. Self-induced nanofluidic transport enables crustal-scale metamorphism. In EGU: General Assembly Conference Abstracts (Vol. 19, p. 5479).

Pun, A., Papike, J., Layne, G., 1997. Subsolidus REE partitioning between pyroxene and plagioclase in cumulate eucrites: An ion microprobe investigation. Geochimica et Cosmochimica Acta 61, 5089-5097.

Putnis, A., 2002. Mineral replacement reactions: from macroscopic observations to microscopic mechanisms. Mineralogical Magazine 66, 689-708.

Putnis, A., 2009. Mineral replacement reactions. Reviews in Mineralogy and Geochemistry 70, 87-124.

Putnis, A., 2015. Transient porosity resulting from fluid–mineral interaction and its consequences. Reviews in Mineralogy and Geochemistry 80, 1-23.

Reeve, J., Cross, K., Smith, R., Oreskes, N., 1990. Olympic Dam copper-uranium-gold-silver deposit. In: Hughes, F.E. (Ed.), Geology of the mineral deposits of Australia and Papua New Guinea 2, The Australasian Institute of Mining and Metallurgy, Melbourne, 1009-1035.

Reynolds, L. J., 2000. Geology of the Olympic Dam Cu-U-Au-Ag-REE deposit. In: Porter, T.M. (ed.), Hydrothermal Iron Oxide Copper-Gold and Related Deposits: A Global Perspective 1, PGC Publishing, Adelaide, 93-104.

Roberts, D., Hudson, G., 1983. The Olympic Dam copper-uranium-gold deposit, Roxby Downs, South Australia. Economic Geology 78, 799-822.

Ruiz-Agudo, E., Putnis, C., Putnis, A., 2014. Coupled dissolution and precipitation at mineral–fluid interfaces. Chemical Geology 383, 132-146.

Smith, M., Henderson, P., Jeffries, T., Long, J., Williams, C., 2004. The rare earth elements and uranium in garnets from the Beinn an Dubhaich Aureole, Skye, Scotland, UK: constraints on processes in a dynamic hydrothermal system. Journal of Petrology 45, 457-484.

Schmidt, M.W., 1992. Amphibole composition in tonalite as a function of pressure: an experimental calibration of the Al-in-hornblende barometer. Contributions to Mineralogy and Petrology 110, 304-310.

Van Dongen M., Weinberg, R.F., Tomkins, A.G., 2010. REE-Y, Ti, and P remobilization in magmatic rocks by hydrothermal alteration during Cu-Au deposit formation. Economic Geology 105, 763-776.

Walker, F.D.L., Lee, M.R., Parsons, I., 1995. Micropores and micropermeable texture in alkali feldspars: geochemical and geophysical implications. Mineralogical Magazine 59, 505-534.

CHAPTER 8

ADDITIONAL AND SUPPLEMENTARY MATERIAL

SUPPLEMENTARY MATERIAL A

FOR CHAPTER 3 - ALBITIZATION AND REDISTRIBUTION OF REE AND Y IN IOCG SYSTEMS: INSIGHTS FROM MOONTA-WALLAROO, YORKE PENINSULA, SOUTH AUSTRALIA

ELECTRONIC APPENDIX A FOR CHAPTER 3

Electronic Appendix A Table 1. Electron probe micranalyses of epidote and actinolite

	EPIDOTE			ACTINOLITE						
	38PBD1			38PBD2						
	8	**9**	**10**	**6**	**7**	**8**	**1**	**2**	**3**	**4**
F				0.09	0.23	0.80	0.82	0.39	0.24	0.77
Na_2O	0.05	0.25	0.05	0.15	0.36	0.35	0.84	0.56	0.68	0.62
SiO_2	37.86	34.70	35.66	54.28	55.48	54.02	52.70	54.57	53.77	54.49
MgO	0.01	0.15		12.95	13.09	14.34	13.89	15.77	14.29	15.76
Al_2O_3	22.85	20.46	22.02	0.23	0.72	1.06	2.40	0.99	1.68	0.95
Cl	0.02	0.08	0.16	0.03		0.07	0.10	0.03	0.07	0.03
K_2O				0.04	0.11	0.13	0.25	0.22	0.24	0.23
CaO	23.52	23.10	22.92	12.41	11.58	12.44	11.95	12.12	11.77	11.91
TiO_2						0.05	0.04	0.05	0.10	0.05
FeO				17.91	17.68	15.44	15.51	13.39	15.87	13.47
Fe_2O_3	12.40	12.60	11.61							
MnO	0.09	0.04	0.09	0.21	0.17	0.15	0.16	0.18	0.19	0.20
Total	**96.42**	**91.21**	**92.21**	**98.32**	**99.53**	**98.80**	**98.64**	**98.31**	**98.90**	**98.51**
Calculated formulae										
Ca	1.992	2.101	2.037	1.949	1.789	1.938	1.872	1.872	1.826	1.843
Na	0.004	0.021	0.004	0.022	0.050	0.050	0.119	0.079	0.095	0.087
K	0.000	0.000	0.000	0.000	0.000	0.000	0.000	0.000	0.000	0.000
Total	**1.996**	**2.121**	**2.041**	**1.971**	**1.838**	**1.987**	**1.991**	**1.951**	**1.921**	**1.930**
Mg	0.001	0.019	0.000	2.829	2.812	3.107	3.025	3.389	3.083	3.393
Fe	0.819	0.894	0.805	2.195	2.132	1.878	1.897	1.615	1.922	1.628
Mn	0.006	0.003	0.006	0.026	0.021	0.018	0.020	0.022	0.023	0.024
Al	2.129	2.047	2.153	0.040	0.122		0.049			
Ti	0.000	0.000	0.000	0.000	0.000	0.011	0.009	0.010	0.022	0.010
Total	**2.955**	**2.963**	**2.964**	**5.091**	**5.087**	**5.014**	**5.000**	**5.037**	**5.051**	**5.056**
Si	2.992	2.946	2.959	7.957	8.002	7.857	7.707	7.869	7.787	7.875
Aliv						0.182	0.365	0.169	0.287	0.163
Total	**2.992**	**2.946**	**2.959**	**7.957**	**8.002**	**8.039**	**8.072**	**8.038**	**8.075**	**8.037**
Fe/(Fe+Mg)				**0.44**	**0.43**	**0.38**	**0.39**	**0.33**	**0.39**	**0.33**
Fe/(Fe+Al)	**0.28**	**0.31**	**0.27**							
F	0.000	0.000	0.000	0.042	0.105	0.369	0.377	0.176	0.111	0.351
Cl	0.003	0.012	0.023	0.007	0.000	0.017	0.024	0.006	0.016	0.007
(OH)	0.997	0.988	0.977	1.951	1.895	1.614	1.598	1.818	1.873	1.643
Total	**1.000**	**1.000**	**1.000**	**2.000**	**2.000**	**2.000**	**2.000**	**2.000**	**2.000**	**2.000**

Electronic Appendix Table 2. Electron probe microanalyses of apatite

	Arthurton granite	Felsic volcanic (Weetula Fm)		Albitite		Calc-silicate schist		Limestone
	227DDH2	212DDH2		33DDH1		38PBD1	38PBD2	190DDH2a
		area 1	area 2	area 1	area 2			
	Mean	Mean	Mean	Mean	Mean	Mean	Mean	Mean
	(n=3)	(n=4)	(n=4)	(n=4)	(n=3)	(n=3)	(n=4)	(n=2)
F	4.55	4.21	5.33	4.48	4.52	3.55	3.62	3.38
Na_2O		0.05	0.05					0.43
MgO								0.04
Al_2O_3	0.03	0.34	0.06				0.04	0.44
SiO_2	0.41	1.14	0.45	0.25	0.18	0.15	0.14	0.81
P_2O_5	42.98	43.24	43.76	43.41	43.45	43.71	43.37	43.83
SO_2	0.07	0.03	0.02	0.05	0.10	0.03	0.06	0.02
Cl	0.05	0.22	0.27	0.05	0.03	0.04	0.01	0.31
K_2O	0.01	0.11	0.03					0.03
CaO	47.41	51.43	52.77	52.65	50.15	47.56	51.43	55.48
TiO_2	0.02	0.03						
MnO		0.04	0.03	0.03		0.03		0.07
FeO	0.76	0.31	0.06	0.09	0.03	0.22	0.07	0.04
SrO	0.04	0.07	0.05	<0.03	0.05	0.05	0.04	<0.03
Y_2O_3	0.15	0.07	0.12	<0.04	0.08	0.06	0.11	
La_2O_3	0.55							
Ce_2O_3	0.47	<0.05	0.20		<0.05	<0.05	<0.05	
Pr_2O_3	0.15	0.11	0.15	0.10	0.14	0.12	0.06	0.09
Nd_2O_3	0.29	0.16	0.27	0.18	0.20	0.19	0.17	0.11
Sm_2O_3								
Eu_2O_3	0.14	0.10	0.10	0.15	0.13	0.13	0.12	0.10
Tb_2O_3			<0.05	<0.04	<0.04	<0.04		
Gd_2O_3				<0.04		<0.04		
Dy_2O_3	0.32	0.25	0.33	0.28	0.28	0.26	0.28	0.30
Total	**98.40**	**101.90**	**104.04**	**101.73**	**99.33**	**96.10**	**99.53**	**105.48**
Calculated formulae								
Ca	4.465	4.698	4.702	4.826	4.670	4.578	4.842	4.991
Sr	0.002	0.003	0.003	0.000	0.002	0.003	0.002	0.000
Mg	0.000	0.000	0.000	0.000	0.000	0.000	0.000	0.004
Mn	0.000	0.003	0.002	0.002	0.000	0.002	0.000	0.005
Y	0.007	0.003	0.005	0.000	0.004	0.003	0.005	0.000
La	0.018	0.000	0.000	0.000	0.000	0.000	0.000	0.000
Ce	0.015	0.000	0.006	0.000	0.000	0.000	0.000	0.000
Pr	0.005	0.004	0.005	0.003	0.004	0.004	0.002	0.003
Nd	0.009	0.005	0.008	0.005	0.006	0.006	0.005	0.003
Sm	0.000	0.000	0.000	0.000	0.000	0.000	0.000	0.000
Eu	0.004	0.003	0.003	0.004	0.004	0.004	0.004	0.003
Gd	0.000	0.000	0.000	0.000	0.000	0.000	0.000	0.000
Tb	0.000	0.000	0.000	0.000	0.000	0.000	0.000	0.000
Dy	0.009	0.007	0.009	0.008	0.008	0.008	0.008	0.008
Na	0.000	0.008	0.008	0.000	0.000	0.000	0.000	0.070
K	0.001	0.011	0.003	0.000	0.000	0.000	0.000	0.003
Fe	0.050	0.020	0.004	0.006	0.002	0.015	0.005	0.003
Ti	0.001	0.002	0.000	0.000	0.000	0.000	0.000	0.000
Al	0.003	0.034	0.006	0.000	0.000	0.000	0.004	0.043
Total	**4.589**	**4.802**	**4.764**	**4.855**	**4.700**	**4.622**	**4.876**	**5.136**
ΣREY	0.067	0.021	0.036	0.021	0.026	0.024	0.024	0.017
P	3.198	3.121	3.081	3.144	3.197	3.325	3.226	3.115
S	0.006	0.002	0.001	0.004	0.008	0.003	0.005	0.002
Si	0.036	0.097	0.037	0.022	0.016	0.014	0.013	0.068
Total	**3.240**	**3.220**	**3.119**	**3.170**	**3.221**	**3.341**	**3.244**	**3.185**
F	1.264	1.136	1.402	1.212	1.242	1.008	1.005	0.897
Cl	0.008	0.032	0.038	0.007	0.004	0.006	0.002	0.044

* As was consistently below minimum detection limit

Electronic Appendix Table 3. Electron probe microanalyses of zircon

	Arthurton Granite	Tickera granite				Albitite	
	227DDH2	33PBD1	33PBD1	33PBD1	33PBD1	33DDH1	
	4	1	2	3	4	5	
F						0.99	
Al_2O_3						1.28	
SiO_2	31.99	29.74	28.88	29.17	31.16	33.21	
SiO_2	0.02				0.02	0.23	
Cl						0.08	
K_2O						1.08	
CaO					0.03	0.06	
TiO_2	0.13				0.03		
FeO	0.22	0.17	0.26	0.21	0.47	1.50	
SrO	0.52	0.48	0.54	0.50	0.52	0.49	
Y_2O_3	0.17	0.12	0.08	0.06	0.40	0.22	
ZrO_2	66.37	63.14	63.49	62.69	67.18	56.69	
Pr_2O_3	0.15	0.18	0.17	0.16	0.20	0.12	
Nd_2O_3	0.16	0.21	0.12	0.12	0.15	0.16	
Eu_2O_3	0.14	0.19	0.18	0.12	0.17	0.16	
Gd_2O_3	0.11						
Tb_2O_3	0.03						
Dy_2O_3	0.46	0.39	0.39	0.35	0.42	0.46	
Er_2O_3	0.08				0.14		
HfO_2	1.61	1.46	1.28	1.25	1.34	1.29	
UO_2	0.04	0.08			0.11	0.29	
Total	**102.20**	**96.16**	**95.40**	**94.64**	**102.35**	**97.32**	
Calculated formulae							
Ca	0.000	0.000	0.000	0.000	0.001	0.002	
Sr	0.009	0.009	0.010	0.010	0.009	0.009	
Y	0.003	0.002	0.001	0.001	0.006	0.003	
Pr	0.002	0.002	0.002	0.002	0.002	0.001	
Nd	0.002	0.002	0.001	0.001	0.002	0.002	
Eu	0.001	0.002	0.002	0.001	0.002	0.002	
Gd	0.001	0.000	0.000	0.000	0.000	0.000	
Tb	0.000	0.000	0.000	0.000	0.000	0.000	
Dy	0.005	0.004	0.004	0.004	0.004	0.005	
Er	0.001	0.000	0.000	0.000	0.001	0.000	
U	0.000	0.001	0.000	0.000	0.001	0.002	
K	0.000	0.000	0.000	0.000	0.000	0.042	
Fe	0.005	0.004	0.006	0.005	0.011	0.034	
Ti	0.000	0.000	0.000	0.000	0.000	0.000	
Al	0.000	0.000	0.000	0.000	0.000	0.046	
Zr	0.989	1.002	1.019	1.009	1.005	0.839	
Hf	0.013	0.013	0.012	0.011	0.011	0.011	
Total	**1.031**	**1.041**	**1.059**	**1.045**	**1.056**	**0.996**	
S	0.001	0.000	0.000	0.000	0.001	0.007	
Si	0.978	0.968	0.951	0.963	0.956	1.007	
Total	**0.978**	**0.968**	**0.951**	**0.963**	**0.956**	**1.014**	
F	0.000	0.000	0.000	0.000	0.000	0.095	
Cl	0.000	0.000	0.000	0.000	0.000	0.004	

Electronic Appendix Table 4. Electron probe microanalyses of rutile and titanite

	RUTILE							TITANITE	
	Arthurton granite		Albitite					Calc-silicate schist	
	227DDH2		33DDH1					38PBD2	
	1	2	7	8	9	10	11	5	6
F			0.39	0.45	0.38	0.44	0.42	1.01	1.08
Na_2O	0.02	0.02	0.01	0.01	0.09	0.03	0.02	0.02	0.02
MgO	0.34		0.01	0.01	0.03	0.13	0.01	0.03	0.04
Al_2O_3	0.13	0.02	0.05	0.06	0.18	0.18	0.10	1.32	1.49
SiO_2	0.28	0.07	0.20	0.27	0.83	0.37	0.26	29.99	30.50
CaO	0.04		0.17	0.19	0.17	0.17	0.15	27.52	28.10
TiO_2	97.09	97.44	96.41	96.86	91.24	95.51	92.13	34.09	34.77
V_2O_3	0.39	0.34	0.33	0.37	0.34	0.44	0.37	0.27	0.27
FeO	1.07	0.74	1.12	0.71	4.08	1.77	3.67	3.02	2.50
SrO								0.12	0.16
Y_2O_3								0.67	0.29
ZrO_2	0.09	0.15			0.07		0.04		
Nb_2O_5	0.56	0.66	0.59	0.38	0.75	0.32	0.29	0.37	0.18
Pr_2O_3	0.09	0.10	0.09	0.10	0.22	0.11	0.11	0.15	0.19
Nd_2O_3	0.18	0.09	0.12	0.19	0.14	0.16	0.18	0.63	0.39
Sm_2O_3	0.06	0.02	0.11		0.01	0.01	0.00	0.14	0.13
Eu_2O_3	0.12	0.17	0.13	0.10	0.18	0.13	0.22	0.19	0.11
Gd_2O_3								0.21	0.08
Tb_2O_3	0.00	0.02		0.04		0.04		0.04	0.04
Dy_2O_3	0.32	0.31	0.34	0.30	0.30	0.34	0.32	0.48	0.36
Ta_2O_5	0.04	0.12							
PbO			0.08		0.11	0.10	0.06		
UO_2					0.32	0.09			
Total	**100.81**	**100.27**	**99.76**	**99.57**	**99.07**	**99.88**	**97.96**	**99.27**	**99.64**
Calculated formulae									
Ca	0.001	0.000	0.002	0.003	0.003	0.002	0.002	**0.982**	**0.993**
Sr	0.000	0.000	0.000	0.000	0.000	0.000	0.000	0.002	0.003
Mg	0.007	0.000	0.000	0.000	0.001	0.003	0.000	0.001	0.002
Y	0.000	0.000	0.000	0.000	0.000	0.000	0.000	0.012	0.005
Pr	0.000	0.000	0.000	0.000	0.001	0.001	0.001	0.002	0.002
Nd	0.001	0.000	0.001	0.001	0.001	0.001	0.001	0.008	0.005
Sm	0.000	0.000	0.001	0.000	0.000	0.000	0.000	0.002	0.001
Eu	0.001	0.001	0.001	0.000	0.001	0.001	0.001	0.002	0.001
Gd	0.000	0.000	0.000	0.000	0.000	0.000	0.000	0.002	0.001
Tb	0.000	0.000	0.000	0.000	0.000	0.000	0.000	0.000	0.000
Dy	0.001	0.001	0.001	0.001	0.001	0.001	0.001	0.005	0.004
Pb	0.000	0.000	0.000	0.000	0.000	0.000	0.000	0.000	0.000
U	0.000	0.000	0.000	0.000	0.001	0.000	0.000	0.000	0.000
Na	0.001	0.000	0.000	0.000	0.002	0.001	0.000	0.001	0.001
Fe	0.011	0.007	0.011	0.007	0.042	0.018	0.038	0.076	0.062
Ti	0.970	0.979	0.966	0.969	0.931	0.957	0.946	**0.855**	**0.863**
Nb	0.004	0.005	0.004	0.003	0.005	0.002	0.002	0.006	0.003
Ta	0.000	0.000	0.000	0.000	0.000	0.000	0.000	0.000	0.000
Al	0.000	0.000	0.000	0.000	0.000	0.000	0.000	0.000	0.000
Zr	0.001	0.001	0.000	0.000	0.000	0.000	0.000	0.000	0.000
V	0.005	0.004	0.004	0.005	0.004	0.005	0.005	0.008	0.008
Si	0.004	0.001	0.003	0.004	0.011	0.005	0.003	**0.999**	**1.006**
Total	**1.005**	**1.001**	**0.995**	**0.993**	**1.004**	**0.998**	**1.001**	**2.964**	**2.962**
ΣREY	**0.003**	**0.003**	**0.004**	**0.003**	**0.004**	**0.004**	**0.004**	**0.033**	**0.020**
F	0.000	0.000	0.016	0.019	0.016	0.018	0.018	**0.107**	**0.112**

Electronic Appendix Table 5. Electron probe microanalyses of synchysite-(Ce) and basnasite-(Ce)

	SYNCHYSITE-(CE) Albitite 33 DDH1					BASTNASITE-(CE) Calc-silicate schist 33 PBD1			
	1	**2**	**3**	**5**	**6**	**1**	**2**	**3**	**4**
F	3.37	3.33	3.60	3.19	3.34	6.71	7.51	7.37	8.25
MgO						0.39		0.90	0.35
Al_2O_3						0.29		0.65	0.51
SiO_2	0.04	0.03	0.08	0.07	0.04	0.64	0.42	1.75	4.69
P_2O_5									0.19
SO_2							0.24	0.42	1.92
Cl	0.04	0.04	0.03	0.04	0.04	0.15	0.31	0.12	0.29
CaO	17.99	17.97	17.01	17.87	17.73	4.13	5.03	3.93	4.87
TiO_2	0.23	0.24	1.21	0.20	0.40			0.23	
FeO	0.13		0.45			0.83	0.39	1.90	3.79
As_2O_3						0.04			0.02
Y_2O_3	1.43	1.54	1.59	1.62	1.51	5.17	5.65	5.45	4.36
La_2O_3	10.78	11.54	11.91	10.93	12.30	15.84	14.66	13.12	13.07
Ce_2O_3	24.16	24.48	25.41	24.36	25.35	32.73	31.22	29.42	26.21
Pr_2O_3	2.92	2.73	3.01	2.92	2.75	3.53	3.47	3.45	2.91
Nd_2O_3	10.11	9.72	9.94	10.44	9.29	11.58	12.27	12.38	9.63
Sm_2O_3	1.92	1.83	1.63	1.95	1.53	1.84	2.12	1.93	1.52
Eu_2O_3	0.52	0.43	0.46	0.46	0.40	0.59	0.67	0.65	0.55
Gd_2O_3	1.52	1.43	1.32	1.45	1.14	1.72	2.04	1.95	1.48
Tb_2O_3	0.18	0.17	0.14	0.16	0.14	0.26	0.28	0.25	0.20
Dy_2O_3	0.91	0.92	0.99	0.94	0.96	1.56	1.62	1.58	1.32
Ho_2O_3	0.44	0.49	0.42	0.52	0.41	0.61	0.76	0.71	0.45
Er_2O_3						0.31	0.38	0.34	0.21
Yb_2O_3						0.14	0.14	0.18	0.10
WO_3	0.11	0.01	0.12	0.05	0.09	0.16	0.26	0.17	0.14
PbO						0.06			0.05
ThO_2						1.16	1.86	1.12	0.55
UO_2					0.01	0.10	0.12	0.09	0.06
Total	**76.80**	**76.91**	**79.34**	**77.17**	**77.43**	**90.54**	**91.43**	**90.05**	**87.67**
Calculated formulae									
Ca	**0.951**	**0.952**	**0.861**	**0.951**	**0.933**	0.183	0.216	0.162	0.182
Mg	0.000	0.000	0.000	0.000	0.000	0.024	0.000	0.052	0.018
Y	0.038	0.041	0.040	0.043	0.040	0.114	0.121	0.112	0.081
La	0.196	0.210	0.208	0.200	0.223	0.242	0.217	0.187	0.168
Ce	**0.436**	**0.443**	**0.439**	**0.443**	**0.456**	**0.496**	**0.459**	**0.416**	**0.335**
Pr	0.052	0.049	0.052	0.053	0.049	0.053	0.051	0.048	0.037
Nd	0.178	0.172	0.168	0.185	0.163	0.171	0.176	0.171	0.120
Sm	0.033	0.031	0.026	0.033	0.026	0.026	0.029	0.026	0.018
Eu	0.009	0.007	0.007	0.008	0.007	0.008	0.009	0.009	0.007
Gd	0.025	0.023	0.021	0.024	0.019	0.024	0.027	0.025	0.017
Tb	0.003	0.003	0.002	0.003	0.002	0.004	0.004	0.003	0.002
Dy	0.014	0.015	0.015	0.015	0.015	0.021	0.021	0.020	0.015
Ho	0.007	0.008	0.006	0.008	0.006	0.008	0.010	0.009	0.005
Er	0.000	0.000	0.000	0.000	0.000	0.004	0.005	0.004	0.002
Yb	0.000	0.000	0.000	0.000	0.000	0.002	0.002	0.002	0.001
Pb	0.000	0.000	0.000	0.000	0.000	0.001	0.000	0.000	0.000
Th	0.000	0.000	0.000	0.000	0.000	0.011	0.017	0.010	0.004
U	0.000	0.000	0.000	0.000	0.000	0.001	0.001	0.001	0.000
Fe	0.005	0.000	0.016	0.000	0.000	0.026	0.012	0.055	0.099
Ti	0.008	0.009	0.043	0.008	0.015	0.000	0.000	0.007	0.000
Al	0.000	0.000	0.000	0.000	0.000	0.014	0.000	0.030	0.021
Total	**1.956**	**1.962**	**1.905**	**1.973**	**1.953**	**1.433**	**1.376**	**1.347**	**1.133**
SREY	**0.992**	**1.002**	**0.985**	**1.015**	**1.006**	**1.173**	**1.130**	**1.031**	**0.808**
P	0.000	0.000	0.000	0.000	0.000	0.000	0.000	0.000	0.006
S	0.000	0.000	0.000	0.000	0.000	0.000	0.009	0.015	0.063
As	0.000	0.000	0.000	0.000	0.000	0.001	0.000	0.000	0.000
Si	0.002	0.002	0.004	0.003	0.002	0.026	0.017	0.067	0.164
W	0.001	0.000	0.002	0.001	0.001	0.002	0.003	0.002	0.001
CO_3	1.996	1.998	1.995	1.996	1.997	0.971	0.971	0.916	0.767
Total	**2.000**	**2.000**	**2.000**	**2.000**	**2.000**	**1.000**	**1.000**	**1.000**	**1.000**
F	1.051	1.041	1.075	1.000	1.036	0.879	0.954	0.899	0.910
Cl	0.004	0.004	0.003	0.003	0.003	0.011	0.021	0.008	0.017
OH						0.111	0.025	0.093	0.073
Total	**1.054**	**1.045**	**1.078**	**1.004**	**1.039**	**1.000**	**1.000**	**1.000**	**1.000**

Electronic Appendix Table 6a. Summary of LA-CP-MS data for apatite: REE, Pb, Th and U (ppm)

	Y	La	Ce	Pr	Nd	Sm	Eu	Gd	Tb	Dy	Ho	Er	Tm	Yb	Lu	ΣREY	^{206}Pb	^{207}Pb	^{208}Pb	Th	U
ALTERED MAGMATIC ROCKS																					
Tickera 33PBD1																					
mean (n=16)	2796	3831	8705	1023	3892	689	41	642	84	496	100	276	35	211	32	22854	39	4.4	28	214	38
S.D.	336	469	995	122	497	94	3.6	89	12	71	13	36	4.3	24	3.6	2697	11	1.2	6.5	40	10
Maximum	3561	4731	10816	1292	5057	933	48	868	115	671	134	361	43	257	39	28917	61	6.6	49	322	57
Minimum	2339	3147	7224	857	3200	566	35	517	66	395	80	224	28	171	25	18936	22	2.9	20	154	22
Arthurton 227DDH2																					
mean (n=17)	1139	476	1707	257	1096	203	29	197	26	157	34	105	14	96	18	5553	45	4.9	21	176	50
S.D.	784	525	1894	284	1181	209	30	185	22	129	26	71	9.3	62	11	5407	72	7.1	28	240	82
Maximum	2802	1624	5850	875	3635	638	93	587	72	433	88	259	33	227	41	17259	233	23	86	754	269
Minimum	374	6.4	30	6.0	37	13	2.1	27	4.6	37	10.0	35	4.9	31	6.8	628	0.89	0.10	0.81	3.3	0.41
Felsic Volcanic 212DDH1																					
mean (n=29)	464	734	1087	106	394	71	12	81	10	62	14	45	6.4	45	9.0	3089	22	2.6	6.2	57	25
S.D.	167	482	706	68	255	41	3.9	41	4.5	25	5.5	17	2.3	16	2.9	1764	13	1.2	3.3	44	14
Maximum	912	1916	2900	281	1147	210	21	227	25	137	29	88	12	80	15	7434	46	4.7	14	226	60
Minimum	237	125	235	29	130	28	6.7	34	4.6	28	6.9	24	3.5	25	5.2	1179	2.5	0.72	0.54	1.3	1.6
Albitite 33DDH1																					
mean (n=12)	764	554	1726	242	1065	192	27	170	20	110	22	64	8.8	62	12	5038	9.4	2.1	3.9	16	6.3
S.D.	97	161	403	46	187	29	4.2	31	3.0	16	3.5	9.5	1.2	9.8	2.2	936	7.6	0.50	4.8	4.9	1.9
Maximum	879	899	2502	324	1326	240	35	215	25	140	28	81	11	78	15	6787	32	2.9	19	27	9.8
Minimum	595	303	1035	159	740	151	19	119	16	81	17	52	6.7	49	7.1	3361	2.1	1.3	0.93	7.1	4.0
INTENSELY ALTERED MAGMATIC ROCKS																					
Moonta Porphyry 197DDH1																					
mean (n=5)	3669	190	615	102	553	204	32	392	74	513	109	301	37	215	31	7037	3.6	0.77	2.8	18	2.3
S.D.	1501	94	318	53	277	103	15	184	35	241	49	131	16	96	12	3110	2.4	0.45	3.4	26	1.2
Maximum	5633	301	992	165	896	325	50	638	119	824	174	479	58	341	47	11016	7.2	1.3	9.4	68	3.9
Minimum	2026	60	184	31	174	65	13	162	29	224	54	161	19	117	20	3339	0.65	0.33	0.45	0.97	0.54
METAMORPHIC ROCKS																					
Chlorite schist 158DDH1																					
(n=1)	866	629	1772	249	1119	234	8.3	233	31	182	35	87	10	53	7.2	5515	22	3.1	11	86	24
Calc-silicate schist 38PBD2																					
mean (n=7)	894	443	1534	229	1126	234	22	233	26	150	29	78	9.5	52	6.5	5066	13	7.0	7.3	12	5.8
S.D.	147	220	613	53	150	28	2.3	46	4.5	27	5.2	15	2.2	8.8	0.94	874	10	6.5	6.7	2.2	1.7
Maximum	1093	898	2800	339	1382	275	27	300	32	195	37	97	13	62	7.7	6826	37	22	24	18	9.2
Minimum	684	268	989	174	914	188	19	168	19	117	21	52	5.9	35	5.1	3945	3.9	2.4	3.1	10	3.9
Limestone 190DDH2b																					
mean (n=4)	89	50	150	23	107	27	3.3	28	3.8	21	3.5	8.4	0.88	4.7	0.64	520	2.8	0.77	0.97	3.3	2.5
S.D.	49	16	47	6.9	32	6.6	0.61	9.7	1.5	10	1.8	5.4	0.67	3.5	0.53	162	0.68	0.04	0.16	1.3	0.63
Maximum	173	72	213	31	145	36	4.0	43	6.1	38	6.5	18	2.0	11	1.5	728	3.4	0.81	1.1	4.4	3.2
Minimum	46	30	92	14	68	19	2.4	17	2.0	11	1.8	3.9	0.39	2.1	0.28	354	1.7	0.72	0.72	1.3	1.5

Electronic Appendix Table 6b. Summary of LA-CP-MS data for apatite: other elements (ppm)

	Na	Mg	Al	Si	K	Sc	Ti	V	Mn	Fe	Cu	Ga	As	Rb	Sr	Zr	Ba
ALTERED MAGMATIC ROCKS																	
Tickera 33PBD1																	
mean (n=16)	238	675	735	6140	24	1.2	274	8.4	288	2365	-	2.2	24	0.66	69	9.4	0.56
S.D.	61	951	960	1477	25	0.75	586	3.3	55	2045	-	0.93	4.0	0.29	2.5	9.7	0.28
Maximum	449	3271	3419	9593	98	3.0	2079	16	348	7745	-	4.6	32	1.6	76	36	1.1
Minimum	171	34	0.82	4218	7.6	0.51	1.8	2.2	154	580	-	1.2	19	0.34	66	2.1	0.21
Arthurton 227DDH2																	
mean (n=17)	161	412	269	2052	17	2.0	168	7.5	281	1092	-	0.44	176	0.30	136	1.4	1.1
S.D.	58	1039	658	2222	20	1.9	272	3.4	49	2018	-	0.74	67	0.18	18	1.3	0.71
Maximum	304	4501	2834	9493	86	6.3	862	18	472	8948	-	3.3	244	0.66	165	3.4	3.1
Minimum	83	9.0	0.76	227	2.5	0.11	1.3	4.6	252	206	-	0.04	42	0.13	104	0.02	0.12
Felsic Volcanic 212DDH1																	
mean (n=29)	266	47	120	1065	135	0.83	6.1	1.8	230	791	-	0.42	44	0.56	204	12	4.6
S.D.	217	31	209	931	269	0.37	7.5	4.0	102	464	-	0.30	15	0.97	72	53	7.8
Maximum	1133	172	982	3879	1340	1.7	33	23	378	2376	-	1.4	90	4.6	482	291	32
Minimum	64	15	0.26	384	2.0	0.22	1.6	0.25	66	333	-	0.12	27	0.03	129	0.05	0.65
Albitite 33DDH1																	
mean (n=12)	358	38	25	1425	32	1.6	108	2.1	111	683	-	0.65	51	0.31	102	0.43	1.5
S.D.	45	31	52	383	62	0.62	331	0.59	5.0	240	-	0.32	8.2	0.15	3.7	0.35	0.30
Maximum	427	137	173	2254	236	3.0	1207	2.9	118	1436	-	1.6	67	0.76	108	1.5	1.8
Minimum	262	24	1.4	872	12	0.88	5.5	1.1	100	472	-	0.20	35	0.13	94	0.22	0.93
INTENSELY ALTERED MAGMATIC ROCKS																	
Moonta Porphyry 197DDH1																	
mean (n=5)	821	391	338	1673	225	0.36	28	0.93	126	1440	-	0.41	13	2.6	118	2.6	1.3
S.D.	206	407	310	903	119	0.22	23	0.83	14	1090	-	0.24	2.7	2.2	1.6	2.8	1.5
Maximum	1009	1171	909	3046	355	0.70	56	2.4	141	2776	-	0.79	17	5.2	120	6.3	3.9
Minimum	420	31	39	673	69	0.09	1.6	0.09	101	352	-	0.07	9.2	0.29	117	0.11	0.11
METASEDIMENTS																	
Chl schist 158DDH1																	
(n=1)	104	142	88	1451	11	-	11	1.6	327	493	6.0	0.49	9.1	0.16	168	<mdl	0.46
Calc-silicate schist 38PBD2																	
mean (n=7)	400	164	303	2475	22	5.8	4.9	46	1067	3.6	4.2	0.76	182	0.73	88	<mdl	1.4
S.D.	388	121	629	2100	13	2.3	1.1	4.7	415	2.9	1.6	0.30	13	0.51	8.9	<mdl	0.74
Maximum	1347	364	1841	7587	47	9.9	5.9	53	1657	9.0	7.6	1.2	203	1.6	104	<mdl	2.4
Minimum	188	22	1.5	1357	9.4	3.8	2.9	40	590	0.56	2.5	0.32	163	0.17	75	<mdl	0.00
Limestone 190DDH2b																	
mean (n=4)	616	1663	1574	4120	271	56	2.9	1066	3697	154	150	0.86	72	1.7	99	46	9.3
S.D.	816	1370	1292	3720	228	45	2.7	391	3464	182	244	0.79	53	1.6	24	24	6.5
Maximum	2027	3854	3130	9949	651	128	7.3	1374	9368	453	573	2.2	157	4.3	133	71	18
Minimum	105	277	99	525	45	17	0.36	399	585	3.9	0.56	0.09	26	0.08	67	19	2.5

Electronic Appendix Table 7. Summary of LA-CP-MS data for zircon (ppm)

	Na	Mg	Al	P	K	Ca	Sc	Ti	V	Mn	Fe	Cu	Zn	Ga	As	Rb	Sr	Nb	Mo	Sn	Ba	Hf	Ta	W
ALTERED MAGMATIC ROCKS																								
Tickera granite 33PBD1-Zr-6																								
Mean (n=6)	435	5367	6039	986	72	1344	651	4339	29	312	11422	5.1	18	6.6	12	1.7	15	55	1.8	14	7.9	10965	5.9	4.2
S.D	93	6100	5681	570	37	746	147	6941	26	138	8617	2.6	15	5.3	6.6	0.20	6.0	86	0.35	23	5.2	801	5.4	3.8
Maximum	601	18409	17661	1738	152	2830	953	19464	86	493	26464	9.6	49	17	24	2.1	26	247	2.3	66	16	11836	18	12
Minimum	295	98	440	360	46	522	522	60	11	91	2032	1.8	3.9	0.65	3.8	1.5	7.0	7.5	1.3	1.9	3.7	9324	3.0	0.50
Arthurton granite 193DDH1																								
Mean (n=10)	72	196	5613	1590	4191	919	419	33	12	11	3545	31	50	2.7	3.8	10	475	4.1	1.7	0.76	21	10030	1.7	1.7
S.D	70	222	6919	665	6760	697	25	16	7.6	7.8	3545	24	51	2.5	1.9	13	537	0.86	0.92	0.37	31	419	0.43	0.85
Maximum	233	617	18330	2885	20936	2408	453	68	25	25	10097	71	164	6.9	7.4	40	1675	5.4	4.1	1.4	110	10650	2.7	3.3
Minimum	14	9.7	145	630	24	192	377	14	2.8	3.7	94	2.2	3.2	0.31	0.46	0.45	14	2.9	0.86	0.26	0.93	9337	1.2	0.68
INTENSELY ALTERED MAGMATIC ROCKS																								
Albitite 33DDH1																								
Mean (n=2)	267	27	950	185	673	424	269	20	4.3	31	5023	1.3	0.96	1.3	9.8	3.1	6.8	3.5	4.3	1.4	32	4205	0.87	0.58
S.D	244	21	365	5.1	159	231	25	11	4.0	27	3467	0.43	0.04	0.59	6.5	0.44	5.1	0.80	0.44	0.83	16	259	0.08	0.08
Maximum	511	48	1315	190	832	655	293	31	8.3	58	8490	1.7	0.99	1.9	16	3.5	12	4.3	4.8	2.3	48	4464	0.95	0.65
Minimum	24	5.2	585	180	514	193	244	8.4	0.32	3.3	1556	0.84	0.92	0.71	3.2	2.6	1.6	2.7	3.9	0.60	16	3946	0.79	0.50

	Y	La	Ce	Pr	Nd	Sm	Eu	Gd	Tb	Dy	Ho	Er	Tm	Yb	Lu	ΣREY	^{206}Pb	^{207}Pb	^{208}Pb	Th	U
ALTERED MAGMATIC ROCKS																					
Tickera granite 33PBD1-Zr-6																					
Mean (n=6)	4206	11	97	10	56	56	14	145	52	556	161	670	132	1154	183	7170	443	46	42	893	661
S.D	1005	8.6	28	3.4	16	19	5.3	45	15	149	39	173	36	308	46	1330	66	8.2	11	443	104
Maximum	6018	29	136	16	84	83	24	204	72	741	225	979	197	1722	269	9072	521	57	54	1620	813
Minimum	2937	4.4	66	7.1	42	28	7.4	79	29	340	113	468	93	820	135	5267	369	36	24	337	516
Arthurton granite 193DDH1																					
Mean (n=10)	1937	25	116	12	64	29	8.1	79	23	226	64	252	48	424	73	3379	251	29	30	370	243
S.D	293	29	67	9.3	45	10	2.3	17	4.3	40	10	37	6.4	61	9.7	471	33	4.4	7.5	69	37
Maximum	2318	98	268	33	167	46	12	106	28	276	78	289	56	522	94	4035	308	38	43	490	320
Minimum	1397	1.7	54	2.3	19	15	4.2	54	15	155	44	178	36	306	55	2349	183	21	20	270	182
INTENSELY ALTERED MAGMATIC ROCKS																					
Albitite 33DDH1																					
Mean (n=2)	1632	2.8	59	5.5	25	30	7.9	66	24	234	59	231	45	391	67	2878	199	22	35	204	200
S.D	1049	2.3	39	4.9	21	26	7.0	56	19	174	39	139	26	216	35	1853	52	5.1	17	105	86
Maximum	2681	5.1	99	10	46	56	15	122	43	408	98	370	71	607	101	4731	251	27	53	309	286
Minimum	583	0.53	20	0.57	4.4	4.6	0.96	10	4.6	59	19	92	19	175	32	1025	147	17	18	100	114

Electronic Appendix Table 8. Summary of LA-CP-MS data for rutile, titanite and calcite (ppm)

	Na	Mg	Al	Si	P	K	Ca	Sc	V	Cr	Mn	Fe	Cu	Zn	Ga	Rb	Sr	Zr	Nb	Mo	Sn	Sb	Ba	Hf	Ta	W
RUTILE -ALTERED MAGMATIC ROCKS																										
Felsic Volcanic 212DDH1																										
Mean (n=2)	245	196	194	3249	12	37	1087	243	216	5.7	142	2548	12	10	0.85	0.30	8.1	797	7092	1.8	108	0.53	18	47	773	13
S.D.	125	24	95	2.7	2.9	21	833	43	27	1.7	90	204	0.55	3.2	0.43	0.09	4.3	155	1780	0.02	10	0.22	10	7.8	393	0.36
Maximum	370	220	289	3252	15	59	1920	286	243	7.4	232	2752	12	13	1.3	0.40	12	952	8871	1.8	118	0.75	28	55	1166	13
Minimum	120	172	99	3247	9.4	16	254	199	188	4.0	52	2344	11	7.1	0.43	0.21	3.9	641	5312	1.7	97	0.31	8.0	39	380	13
RUTILE - INTENSELY ALTERED MAGMATIC ROCKS																										
Moonta Porphyry 197DDH1																										
Mean (n=2)	160	6842	9649	15047	11	2520	829	398	135	8.9	37	13374	417	24	7.1	15	6.1	102	7738	0.39	514	0.18	7.2	9.3	1049	51
S.D.	13	4859	6137	9154	1.9	1165	221	69	5.0	1.0	9.4	5029	236	9.0	4.0	8.4	1.5	32	380	0.09	14	0.11	0.31	1.1	156	5.7
Maximum	174	11701	15786	24201	13	3685	1050	467	140	10.0	46	18403	654	33	11	23	7.6	133	8117	0.48	528	0.29	7.5	10	1204	57
Minimum	147	1983	3513	5893	9.4	1355	608	329	130	7.9	28	8346	181	15	3.1	6.5	4.7	70	7358	0.30	501	0.08	6.9	8.2	893	46
TITANITE - METASEDIMENTS																										
Calc-sillicate schist 38PBD2																										
Mean (n=3)	622	922	7238	6202	39	3.9	912	60	130	17653	6.8	10	15	17	6.4	58	3.7	2555	193	1707	14	545	2.2	12	67	8.2
S.D.	381	401	1270	8557	20	0.37	173	16	32	2693	6.9	6.3	4.4	2.1	1.9	8.1	2.5	190	67	94	3.8	63	0.66	2.8	5.2	3.3
Maximum	1156	1480	8779	18302	67	4.2	1106	78	171	20417	17	19	21	20	9.0	70	7.2	2822	277	1834	18	631	3.1	14	75	12
Minimum	288	557	5669	38	20	3.4	685	39	92	14003	0.95	4.3	11	15	4.4	52	1.5	2399	114	1610	9.0	482	1.5	7.7	63	4.1
CALCITE - ALTERED MAGMATIC ROCKS																										
Tickera granite 33PBD2																										
Mean (n=6)	48	833	70	285	9.6	21	-	8.0	0.20	-	7743	808	-	-	0.06	0.10	105	-	-	-	-	-	2.4	-	-	0.04
S.D.	13	385	59	143	2.2	20	-	2.5	0.08	-	1295	117	-	-	0.04	0.07	21	-	-	-	-	-	1.4	-	-	0.02
Maximum	62	1397	179	429	13	63	-	11	0.34	-	10454	981	-	-	0.12	0.23	131	-	-	-	-	-	4.5	-	-	0.09
Minimum	21	433	2.8	11	7.2	4.3	-	3.5	0.11	-	6662	593	-	-	0.00	0.02	63	-	-	-	-	-	0.27	-	-	0.01
CALCITE - METASEDIMENTS																										
CALCITE - Calc-sllicate schist 38PBD1																										
Mean (n=6)	260	3636	15	334	62	11	-	32	0.87	-	4572	18354	6.5	1.9	0.24	0.16	171	-	-	-	-	-	0.68	-	-	-
S.D.	18	1132	18	141	9.8	6.2	-	5.9	0.18	-	2673	3326	9.1	3.1	0.08	0.14	20	-	-	-	-	-	0.36	-	-	-
Maximum	286	5238	43	541	84	24	-	43	1.1	-	10073	23622	23	8.8	0.33	0.43	201	-	-	-	-	-	1.1	-	-	-
Minimum	237	1600	0.07	180	56	5.6	-	23	0.56	-	2281	12754	0.03	###	0.11	0.01	135	-	-	-	-	-	0.06	-	-	-

	Y	La	Ce	Pr	Nd	Sm	Eu	Gd	Tb	Dy	Ho	Er	Tm	Yb	Lu	ΣREY	^{206}Pb	^{207}Pb	^{208}Pb	Th	U
RUTILE -ALTERED MAGMATIC ROCKS																					
Felsic Volcanic 212DDH1																					
Mean (n=2)	90	10	36	4.9	18	5.4	1.4	8.2	2.5	22	5.7	21	4.4	44	7.0	281	99	61	82	163	28
S.D.	43	6.9	21	2.9	9.8	2.7	0.76	4.5	1.1	11	2.8	9.2	1.7	20	3.1	140	35	25	33	79	9.4
Maximum	132	17	58	7.8	28	8.1	2.2	13	3.6	33	8.4	30	6.0	64	10	421	134	87	114	243	38
Minimum	47	3.4	15	2.0	8.1	2.7	0.65	3.7	1.4	11	2.9	12	2.7	24	3.9	140	65	36	49	84	19
RUTILE - INTENSELY ALTERED MAGMATIC ROCKS																					
Moonta Porphyry 197DDH1																					
Mean (n=2)	72	0.41	0.99	0.19	0.66	0.65	0.34	1.1	0.69	9.9	4.1	23	7.2	76	12	209	46	19	27	3.8	18
S.D.	14	0.13	0.51	0.08	0.40	0.43	0.00	0.01	0.22	1.7	1.4	9.6	3.5	34	6.3	70	9.5	4.8	7.4	1.8	1.9
Maximum	87	0.53	1.5	0.27	1.1	1.1	0.34	1.2	0.91	12	5.5	33	11	110	18	279	56	24	34	5.6	20
Minimum	58	0.28	0.48	0.11	0.26	0.22	0.34	1.1	0.47	8.1	2.8	13	3.7	42	5.9	140	37	14	20	2.0	16
TITANITE - METAMORPHIC ROCKS																					
Calc-sillicate schist 38PBD2																					
Mean (n=3)	9.5	773	4400	791	3635	812	96	631	91	551	96	271	35	205	18	14959	180	53	74	78	92
S.D.	2.2	204	1060	158	597	73	2.2	59	7.1	31	7.2	20	2.8	18	1.0	2277	96	33	53	34	32
Maximum	13	961	5585	987	4459	911	97	690	97	584	106	294	38	228	19	17877	311	100	148	124	134
Minimum	7.3	488	3012	600	3060	737	93	550	81	510	89	246	31	185	17	12320	84	25	32	43	57
CALCITE - ALTERED MAGMATIC ROCKS																					
Tickera granite 33PBD2																					
Mean (n=6)	86	29	67	8.0	29	8.6	1.5	10.0	2.1	14	3.1	9.8	1.6	12	1.9	284	0.57	0.24	0.42	0.25	0.05
S.D.	15	7.0	15	1.6	5.6	1.6	0.19	1.3	0.18	2.2	0.65	1.8	0.28	2.1	0.47	35	0.17	0.12	0.15	0.07	0.08
Maximum	111	42	95	11	40	11	1.8	11	2.3	18	4.3	12	2.1	15	2.5	342	0.89	0.47	0.65	0.36	0.24
Minimum	69	19	49	6.3	23	6.6	1.3	8.0	1.8	11	2.3	7.4	1.3	9.3	1.3	233	0.39	0.12	0.25	0.12	0.00
CALCITE - METASEDIMENTS																					
CALCITE - Calc-sllicate schist 38PBD1																					
Mean (n=6)	166	946	1458	151	497	63	6.7	43	5.7	34	6.6	19	2.5	14	1.8	3415	3.5	1.6	2.7	4.3	0.13
S.D.	34	247	341	32	86	6.1	0.21	2.3	0.83	7.3	1.5	4.8	0.63	3.3	0.42	658	0.68	0.34	0.57	2.7	0.08
Maximum	222	1227	1971	194	608	73	7.0	47	7.2	47	9.4	28	3.7	20	2.6	4323	4.4	2.1	3.5	9.6	0.28
Minimum	132	560	972	104	368	54	6.5	39	4.9	28	5.2	15	1.9	11	1.4	2410	2.5	1.1	2.0	2.1	0.00

ELECTRONIC APPENDIX B FOR CHAPTER 3

Electronic Appendix B. Analytical methodology

Electron Probe Microanalysis (EPMA)

Standards, X-ray lines, count times and typical minimum detection limits (mdl) are given in the table below.

Element	**Standard**	**X-ray line**	**Count time (s)** unknown/background	**Average mdl** (ppm)
Na	Albite	Na Kα	20/10	120
K	Sanadine	K Kα	20/10	130
Ca	Wollastonite	Ca Kα	20/10	120
Mn	Rhodonite	Mn Kα	20/10	300
Mg	Almandine	Mg Kα	20/10	220
Fe	Almandine	Fe Kα	20/10	350
Al	Almandine	Al Kα	20/10	250
Si	Almandine	Si Kα	20/10	300
Ti	Rutile	Ti Kα	20/10	150
F	Synthetic CaF_2	F Kα	30/15	300
Cl	Tugtupite	Cl Kα	30/15	200
P	Apatite	P Kα	20/10	200
Sr	Celestite	Sr Lα	20/10	600
Y	Synthetic REE-aluminosilicate	Y Lα	20/10	380
Zr	Synthetic zircon	Zr Lα	20/10	325
La	La-Ca-Al-silicate	La Lα	20/10	395
Ce	Ce-Ca-Al-silicate	Ce Lα	20/10	540
Pr	Pr-Ca-Al-silicate	Pr Lß	20/10	900
Nd	Nd-Ca-Al-silicate	Nd Lß	20/10	750
Sm	Sm-Ca-Al-silicate	Sm Lß	20/10	860
Eu	EuF_3	Eu Lß	20/10	1500
Gd	Gd-Ca-Al-silicate	Gd Lß	20/10	1000
Tb	Tb metal	Tb Lα	20/10	580
Dy	Dy-Ca-Al-silicate	Dy Lß	20/10	600
Ho	Ho metal	Ho Lα	20/10	1100
Er	Er-Ca-Al-silicate	Er Lß	20/10	640
Yb	Yb metal	Yb Lα	20/10	1000
Hf	Zircon	Hf Lα	20/10	740
Ta	Ta metal	Ta Lα	20/10	1025
W	W metal	W Lα	20/10	750
Pb	Synthetic Pb-silicate	Pb Mß	20/10	375
Th	Huttonite	Th Mα	20/10	1500
U	UO_2	U Mß	20/10	360

Laser-Ablation Inductively-Coupled Mass Spectrometry (LA-ICP-MS)

All multi-element LA-ICP-MS data was collected on a Resonetics M-50-LR 193-nm Excimer laser microprobe coupled to an Agilent 7700cx Quadrupole ICP-MS (Adelaide Microscopy). This new-generation laser system offers excellent spatial resolution coupled with sub-ppm level sensitivity for most trace elements.

Trace element spot analysis was made with a uniform spot size diameter of 30 μm for silicates and 22 μm for oxides and phosphates. The laser system was operated at pulse rates of 10 Hz and power levels of 50%

power level; laser energy was typically 6-9 J/cm^{-2}, giving an ablation rate of approx. 1.5μm/s^{-1}. The following basic set of isotopes were monitored: ^{23}Na, ^{24}Mg, ^{27}Al, ^{29}Si, ^{31}P, ^{39}K, ^{43}Ca, ^{45}Sc, ^{47}Ti, ^{48}Ti, ^{49}Ti, ^{51}V, ^{53}Cr, ^{55}Mn, ^{57}Fe, ^{58}Fe, ^{59}Co, ^{60}Ni, ^{65}Cu, ^{66}Zn, ^{69}Ga, ^{75}As, ^{85}Rb, ^{88}Sr ^{89}Y, ^{90}Zr, ^{93}Nb, ^{95}Mo, ^{118}Sn, ^{133}Cs, ^{137}Ba, ^{139}La, ^{140}Ce, ^{141}Pr, ^{146}Nd, ^{147}Sm, ^{153}Eu, ^{157}Gd, ^{159}Tb, ^{163}Dy, ^{165}Ho, ^{166}Er, ^{169}Tm, ^{172}Yb, ^{175}Lu, ^{178}Hf, ^{181}Ta, ^{182}W, ^{206}Pb, ^{207}Pb, ^{208}Pb, ^{232}Th and ^{238}U. Multiple isotopes of Fe and Ti were measured to test for data consistency. Analysis time for each spot analysis was a uniform 90 seconds, comprising a 30-second measurement of background (laser-off), and 60-second analysis of the unknown (laser-on).

Standard reference materials for all mineral matrices were NIST-610 using coefficients given by Pearce et al. (1997). Standards were run after each 20-24 unknowns; detection limits were calculated for each element in each spot analysis. Internal calibration was achieved using concentration values of Al (feldspars), Ca (apatite, calcite, and titanite), Ti (rutile) and Zr (zircon), using values obtained via EPMA. Data reduction was performed using Glitter software (Van Achterbergh et al., 2001).

LA-ICP-MS element maps of different-sized areas of large K-feldspar and albite grains were generated to obtain visual images of trace element distributions. Mapping was conducted using the same Resonetics M-50-LR instrument as above. The M-50 instrument utilizes a two-volume small volume ablation cell (Laurin Technic Pty designed for excellent trace element sensitivity (e.g., Müller et al. 2009). Ablation was performed in an atmosphere of UHP He (0.7 l/min), and upon exiting the cell the aerosol cell is mixed with Ar (0.93 l/min) immediately after the ablation cell, after which the mix is passed through a pulse-homogenizing device or "squid" prior to direct introduction into the torch. The ICPMS was optimized daily to maximize sensitivity on isotopes of the mass range of interest, while keeping production of molecular oxide species (i.e., ^{232}Th^{16}O/^{232}Th) and doubly charged ion species (i.e. ^{140}Ce^{2+}/^{140}Ce^{+}) as low as possible, and usually <0.2%.

Imaging of grains was performed by ablating sets of parallel line rasters in a grid across the sample. A beam size of 6–22 μm (depending on desired resolution and counts) and a scan speed of 1.5 x beam size (μm/s) were chosen which resulted in the desired sensitivity of elements of interest, and adequate spatial resolution for the study. To ensure the lines covered the entire selected area, spacing between lines was always equal to the beam size. The effect of redeposition during mapping was minimized by pre-ablating each line prior to its main data collection run. A laser repetition of 10 Hz was selected at a constant energy output of 100 mJ, resulting in an energy density of ≈6 J/cm^2 at the target. Using these beam conditions depth of ablation during mapping was around 5-10 μm. A set of 21 elements were analyzed with dwell time for all masses set to 0.003 seconds, resulting in a total sweep time was ~0.07 seconds. A 30 second background acquisition was acquired at the start of every raster, and to allow for cell wash-out, gas stabilization, and computing processing, a delay of 20 seconds was used after each line. Identical rasters were done on USGS reference glasses NIST SRM 610 at the start and end of a mapping run. Further details of practices used in the University of Adelaide LA-ICP-MS laboratory, particularly with respect to generation of trace element maps, are given by Cook et al. (2013).

Element maps were compiled and processed using the program Iolite developed by the Melbourne Isotope Group at Melbourne University (e.g., Woodhead et al., 2007). Iolite is an open source software

package for processing ICP-MS data, and is an add-in for the data analysis program Igor developed by WaveMetrics. A typical mapping run was analyzed over a 6-7 hour session, in which significant instrument drift could occur. To correct for this, standards were analyzed immediately before and after the run to assess drift and if present, was corrected for by applying a linear fit between the two sets of standards. Following this, for each raster and every element, the average background was subtracted from its corresponding raster, and the rasters were compiled into a two-dimensional image displaying combined background/drift corrected intensity for each element.

References

Cook, N.J., Ciobanu, C.L., Meria, D., Silcock, D., Wade, B., 2013. Arsenopyrite-pyrite association in an orogenic gold ore: tracing mineralization history from textures and trace elements. Economic Geology, 108, 1273-1283.

Muller, W., Shelley, M., Miller, P., Broude, S., 2009 Initial performance metrics of a new custom-designed ArF excimer LA-ICPMS system coupled to a two-volume laser-ablation cell. Journal of Analytical Atomic Spectrometry 24, 209–214.

Pearce, N.J.G., Perkins, W.T., Westgate, J.A., Gorton, M.P., Jackson, S.E., Neal, C.R., Chenery, S.P., 1997. A compilation of new and published major and trace element data for NIST SRM 610 and NIST SRM 612 glass reference material. Geostandards Newsletter 21, 115–144.

Van Achterbergh, E., Ryan, C.G., Jackson, S.E., Griffin, W.L., 2001 LA-ICP-MS in the Earth Sciences - Appendix 3, data reduction software for LA-ICP-MS. In: Sylvester, P.J. (Ed.), Mineralogical Association of Canada Short Course vol. 29, p. 239-243.

Woodhead, J.D., Hellstrom, J., Hergt, J.M., Greig, A., Maas, R., 2007 Isotopic and elemental imaging of geological materials by laser ablation inductively coupled plasma-mass spectrometry. Geostandards and Geoanalytical Research 31, 331–343.

SUPPLEMENTARY MATERIAL B

FOR CHAPTER 5 - RARE EARTH ELEMENT GEOCHEMISTRY OF FELDSPARS: EXAMPLES FROM FE-OXIDE CU-AU SYSTEMS IN THE OLYMPIC CU-AU PROVINCE, SOUTH AUSTRALIA

ELECTRONIC APPENDIX A FOR CHAPTER 5

Electronic Appendix

Table 1: Summary of LA-ICP-MS data for crypto- and microperthite: Minor and trace elements (ppm)

Element	Mg	P	Sc	Ti	V	Cr	Mn	Fe	Co	Ni	Cu	Zn	Ga	As	Rb	Sr	Zr	Nb	Mo	Sn	Cs	Ba
OD – Least-altered RDG																						
RD2494: CP (μ_{10})	4.16	17	15	172	0.09	<mdl	9.33	530	<mdl	<mdl	<mdl	1.39	40	<mdl	240	183	<mdl	<mdl	<mdl	<mdl	0.44	2547
S.D.	2.59	3.27	0.26	23	0.02		9.44	86				1.02	2.42		38	12					0.15	339
Min	1.68	13	15	138	0.07	<mdl	0.47	479	<mdl	<mdl	<mdl	<mdl	35	<mdl	193	170	<mdl	<mdl	<mdl	<mdl	0.24	2015
Max	8.31	23	16	225	0.13	<mdl	34	782	<mdl	<mdl	<mdl	3.19	44	<mdl	307	209	0.13	<mdl	<mdl	<mdl	0.72	3101
RD2492: CP (μ_8)	2.66	12	16	133	0.11	<mdl	21	619	<mdl	<mdl	0.51	2.77	39	1.21	321	181	0.15	<mdl	<mdl	<mdl	0.97	2068
S.D.	1.08	4.25	0.51	25	0.03		20	206			0.25	2.75	8.07	0.69	78	31	0.20				0.56	887
Min	1.45	<mdl	16	109	0.08	<mdl	0.69	473	<mdl	<mdl	<mdl	<mdl	26	<mdl	235	111	<mdl	<mdl	<mdl	<mdl	0.24	692
Max	4.89	19	17	195	0.16	0.98	64	1075	<mdl	<mdl	0.97	8.90	57	2.72	494	208	0.53	0.08	<mdl	0.64	1.92	4120
CD – Foliated leucogranite																						
PL-12: MP (μ_{18})	3.89	53	1.36	9.61	0.07	1.38	1.49	214	<mdl	0.38	1.55	1.35	31	1.77	733	58	0.25	<mdl	<mdl	0.90	9.58	212
S.D.	3.35	17	0.27	3.67	0.07	0.56	0.55	61		0.48	0.35	0.51	4.39	0.38	61	3.34	0.45			0.33	1.11	40
Min	0.62	24	0.96	4.52	<mdl	<mdl	1.02	112	<mdl	<mdl	1.02	<mdl	24	1.17	678	52	<mdl	<mdl	<mdl	0.54	7.51	164
Max	12	86	1.98	19	0.22	2.09	2.85	334	0.26	1.56	2.50	2.42	37	2.37	884	64	1.45	0.20	0.28	1.61	12	319
CD - Donington Granite																						
PL-11: MP (μ_{14})	3.02	47	1.19	82	<mdl	<mdl	3.99	241	<mdl	<mdl	0.45	0.92	68	1.25	478	215	<mdl	0.22	<mdl	0.32	6.88	2860
S.D.	2.14	8.26	0.32	26			2.51	55			0.22	0.47	3.48	0.48	42	10		0.11		0.13	0.34	127
Min	0.91	34	0.77	29	<mdl	<mdl	0.54	157	<mdl	<mdl	<mdl	<mdl	58	<mdl	412	194	<mdl	<mdl	<mdl	<mdl	6.34	2568
Max	9.05	61	1.89	122	0.08	0.83	9.56	370	0.08	<mdl	1.10	2.22	73	2.17	567	233	0.14	0.38	0.23	0.68	7.37	3029
PL-13 - MP (μ_{13})	2.30	40	1.02	111	0.06	0.85	6.18	282	<mdl	<mdl	0.49	0.97	59	1.43	435	215	<mdl	0.18	<mdl	0.28	6.13	2478
S.D.	0.83	7.10	0.21	77	0.05	0.15	7.31	104			0.22	0.42	1.81	0.62	34	13		0.10		0.05	0.61	105
Min	1.03	28	0.68	23	<mdl	<mdl	1.14	171	<mdl	<mdl	<mdl	<mdl	55	0.74	400	185	<mdl	<mdl	<mdl	<mdl	5.20	2315
Max	4.10	53	1.45	272	0.19	0.96	29	538	0.08	0.37	0.90	2.18	63	2.80	503	230	0.14	0.38	0.24	0.36	7.62	2740

Table 2: Summary of LA-ICP-MS data for porous and red-stained K-feldspar: Minor and trace elements (ppm)

Element	Mg	P	Sc	Ti	V	Cr	Mn	Fe	Co	Ni	Cu	Zn	Ga	As	Rb	Sr	Zr	Nb	Mo	Sn	Cs	Ba
OD- Least-altered RDG																						
RD2492: Por Kfs (μ_6)	18	<mdl	20	97	0.28	<mdl	29	686	0.08	<mdl	0.50	2.81	37	1.29	657	89	0.50	0.08	<mdl	<mdl	2.15	1979
S.D.	13		10	52	0.35		8.12	381	0.11		0.18	0.74	9.07	0.81	77	67	0.81	0.11			0.29	1112
Min	2.57	<mdl	15	36	0.07	<mdl	20	276	<mdl	<mdl	<mdl	1.80	30	<mdl	541	35	<mdl	<mdl	<mdl	<mdl	1.61	978
Max	36	15	43	181	1.04	1.50	43	1218	0.33	<mdl	0.81	3.75	56	2.87	733	221	2.28	0.31	<mdl	0.54	2.45	4160
RD2495: Por Kfs (μ_{15})	43	<mdl	16	57	0.15	<mdl	78	530	0.12	<mdl	1.27	7.05	34	0.89	733	81	0.13	<mdl	<mdl	<mdl	2.36	1470
S.D.	19		0.56	11	0.06		43	145	0.09		2.07	4.71	2.43	0.56	49	43	0.18				0.51	426
Min	20	<mdl	16	43	0.07	<mdl	41	344	<mdl	<mdl	<mdl	2.35	30	<mdl	660	43	<mdl	<mdl	<mdl	<mdl	1.59	868
Max	68	11	17	77	0.27	<mdl	168	718	0.34	<mdl	6.68	15	37	2.10	836	182	0.56	<mdl	0.28	0.28	3.27	2083
RD2280: Red Kfs (μ_{10})	442	15	1.20	32	0.16	1.01	81	1794	0.18	<mdl	1.69	7.50	33	1.11	630	60	1.86	<mdl	<mdl	0.64	1.14	1388
S.D.	323	2.48	0.24	17	0.11	0.32	67	807	0.10		0.66	4.92	2.62	0.40	50	10	1.93			0.45	0.26	311
Min	31	12	0.77	16	0.07	<mdl	14	1111	0.08	<mdl	0.78	1.75	30	0.72	568	45	<mdl	<mdl	<mdl	<mdl	0.82	929
Max	1229	22	1.53	75	0.41	1.81	210	3539	0.41	0.49	2.76	15	38	2.20	704	75	7.10	<mdl	0.95	1.78	1.83	1793
RD2280: Por Kfs (μ_{10})	385	17	1.05	188	0.12	0.90	19	1521	0.10	<mdl	1.07	5.08	56	1.06	478	65	0.58	0.16	<mdl	0.43	1.08	5200
S.D.	250	5.24	0.25	40	0.09	0.24	7.05	384	0.08		0.60	3.56	7.08	0.45	23	16	0.45	0.22		0.34	0.16	828
Min	35	12	0.67	141	<mdl	<mdl	14	1129	<mdl	<mdl	<mdl	1.63	44	<mdl	425	47	<mdl	<mdl	<mdl	<mdl	0.79	4021
Max	728	27	1.68	273	0.37	1.43	41	2680	0.35	0.51	2.31	15	67	2.03	525	94	1.45	0.75	<mdl	1.19	1.34	6547
OD- HRQM																						
RD2274 - Por Kfs (μ_{14})	127	17	0.78	145	0.09	<mdl	38	1286	0.22	<mdl	1.49	11	44	0.79	413	322	0.35	<mdl	<mdl	<mdl	1.07	3558
S.D.	103	7.50	0.12	47	0.07		31	653	0.50		1.67	7.32	6.56	0.28	58	60	0.29				0.24	788
Min	14	8.24	0.64	77	<mdl	<mdl	7.66	837	<mdl	<mdl	<mdl	2.19	32	<mdl	326	228	<mdl	<mdl	<mdl	<mdl	0.62	2232
Max	343	34	0.96	243	0.30	<mdl	112	3223	1.88	<mdl	5.50	27	59	1.45	512	399	1.06	0.06	<mdl	0.44	1.53	5174
OD- Ser-Hm-altered RDG																						
RD2531: Red Kfs (μ_{11})	1282	256	12	86	0.83	3.04	85	4248	7.83	1.13	3.35	25	35	2.86	573	89	4.96	0.13	0.79	1.08	2.31	1628
S.D.	925	36	1.61	44	0.35	0.70	44	1956	4.24	0.49	0.64	16	4.20	1.06	27	18	4.07	0.03	0.36	0.60	0.76	473
Min	39	199	9.50	38	0.48	2.11	38	1387	0.76	0.65	2.65	8.74	30	1.87	535	63	0.18	0.10	0.41	0.34	1.52	645
Max	2428	324	15	178	1.40	4.38	180	7522	14	2.38	4.67	51	45	5.90	616	119	11	0.18	1.65	2.10	4.14	2505
RD2511: Red Kfs (μ_{11})	653	12	18	105	0.26	<mdl	11	1970	0.58	0.63	1.45	8.61	62	2.99	442	92	2.80	0.07	1.80	0.85	1.29	1952
S.D.	476	5.43	3.77	12	0.11		4.64	434	0.33	0.24	0.93	2.46	9.93	1.20	30	13	2.48	0.04	5.14	0.32	0.34	210
Min	92	<mdl	13	88	0.13	<mdl	5.97	1263	0.23	<mdl	0.44	5.25	45	1.08	398	65	0.24	<mdl	<mdl	0.36	0.95	1729
Max	1515	22	24	125	0.46	1.11	22	2577	1.27	1.03	3.43	13	78	5.15	490	117	7.68	0.15	18	1.33	1.98	2461

Table 2: Summary of LA-ICP-MS data for porous and red-stained K-feldspar: Minor and trace elements (ppm) continued

Element	Mg	P	Sc	Ti	V	Cr	Mn	Fe	Co	Ni	Cu	Zn	Ga	As	Rb	Sr	Zr	Nb	Mo	Sn	Cs	Ba
OD – Mineralized RDG																						
RD2316: Red Kfs (μ_{21})	147	12	1.20	31	0.20	1.51	87	2507	1.02	0.58	6.08	7.28	34	5.76	583	50	0.59	<mdl	0.32	<mdl	1.35	1454
S.D.	130	5.02	0.49	13	0.20	0.75	56	1386	3.02	0.57	9.66	2.64	4.34	5.69	75	21	0.66		0.56		0.38	637
Min	9.87	<mdl	0.61	10	0.06	<mdl	27	1426	<mdl	<mdl	<mdl	4.22	29	0.89	465	22	<mdl	<mdl	<mdl	<mdl	0.75	524
Max	525	25	2.27	53	0.82	4.04	238	6655	14	2.49	31	15	46	19	770	92	2.67	0.10	2.69	0.48	2.60	3724
RD3554: Red Kfs (μ_{40})	212	<mdl	7.30	45	0.47	<mdl	31	2261	1.84	0.52	4.22	21	36	11	419	162	0.65	0.15	0.66	0.29	0.81	2585
S.D.	143		4.49	20	0.40		25	1198	1.67	0.46	3.62	15	8.13	15	54	92	0.83	0.17	1.24	0.16	0.18	985
Min	9.74	<mdl	2.37	5.95	<mdl	<mdl	4.30	527	0.25	<mdl	0.45	3.99	24	2.18	342	46	<mdl	<mdl	<mdl	<mdl	0.49	965
Max	597	16	18	106	1.81	1.14	103	5153	7.57	2.50	18	64	56	67	589	360	3.86	0.97	6.64	0.72	1.26	4492
WW – Donington Granite																						
WRD33: Kfs vein (μ_{5})	361	263	43	40	0.87	4.29	26	303	0.65	1.88	4.48	8.78	31	1.92	435	249	0.30	0.12	0.33	0.48	0.86	2455
S.D.	320	17	4.35	15	0.36	0.77	11	249	0.42	1.30	1.07	6.45	5.15	1.17	56	118	0.09	0.02	0.28	0.13	0.28	413
Min	6.08	241	39	19	0.59	2.87	7.78	43	0.29	0.69	3.59	4.16	23	<mdl	365	119	0.22	0.08	<mdl	<mdl	0.48	1877
Max	794	292	49	57	1.53	5.03	42	646	1.44	4.28	6.52	21	38	3.51	501	397	0.47	0.14	0.68	0.64	1.33	3075
WRD33: Por Kfs (μ_{16})	634	15	1.46	62	0.20	<mdl	91	888	0.16	<mdl	7.01	22	47	0.94	407	251	2.59	0.07	0.40	0.74	1.55	3363
S.D.	574	9.13	0.90	41	0.21		62	454	0.07		7.16	13	8.53	0.36	26	53	2.51	0.09	0.67	0.51	0.32	444
Min	29	<mdl	0.76	10	<mdl	<mdl	31	247	<mdl	<mdl	0.72	6.10	37	<mdl	339	173	<mdl	<mdl	<mdl	<mdl	1.07	2791
Max	1654	44	3.41	146	0.84	0.92	283	2314	0.27	0.39	27	56	68	1.64	439	351	7.30	0.36	2.14	1.78	2.27	4511
PR – Quartz Monzodiorite																						
PD4: Por Kfs (μ_{20})	7.20	43	2.84	151	0.13	1.62	296	1552	0.15	0.72	4.59	55	82	2.03	431	363	<mdl	<mdl	<mdl	0.66	2.67	3954
S.D.	7.91	11	0.67	58	0.08	0.98	184	615	0.12	0.63	2.26	35	19	0.87	54	68				0.29	0.82	1112
Min	1.22	28	1.54	56	<mdl	<mdl	26	715	<mdl	<mdl	2.04	2.03	46	0.77	326	241	<mdl	<mdl	<mdl	<mdl	0.88	1777
Max	37	69	3.80	273	0.30	3.41	606	2743	0.43	2.39	11	116	121	4.26	529	580	0.19	0.12	1.11	1.09	3.99	6553
WW – Donington Granite																						
WRD46 - Por Kfs (μ_{23})	9.2	31	2.41	53	0.18	0.79	18	807	0.24	0.52	1.85	4.39	62	0.91	465	188	0.20	<mdl	<mdl	0.39	2.20	2635
S.D.	8.8	11	0.74	18	0.31	0.40	30	626	0.43	0.34	1.00	2.60	5.47	0.30	99	30	0.45			0.10	0.94	291
Min	1.5	13	1.19	31	<mdl	<mdl	1.54	132	<mdl	<mdl	1.18	<mdl	52	<mdl	346	98	<mdl	<mdl	<mdl	<mdl	1.03	2248
Max	32	54	4.36	90	1.27	1.47	144	2115	1.84	1.61	6.44	9.72	74	2.09	639	224	1.91	0.15	0.33	0.55	3.86	3491

Table 3: Summary of LA-ICP-MS data for igneous plagioclase: Minor and trace elements (ppm)

Element	Mg	P	Sc	Ti	V	Cr	Mn	Fe	Co	Ni	Cu	Zn	Ga	As	Rb	Sr	Zr	Nb	Mo	Sn	Cs	Ba
OD - Least-altered RDG																						
RD2495: Ads-Olg (μ_{11})	771	46	1.29	68	0.85	0.87	22	2422	0.27	<mdl	0.55	5.13	36	0.91	7.95	185	0.21	<mdl	<mdl	0.33	0.26	142
S.D.	1748	5.29	0.21	27	1.93	0.28	19	1486	0.59		0.17	7.59	3.35	0.17	3.59	56	0.34			0.12	0.23	95
Min	18	36	1.03	23	<mdl	<mdl	4.29	1358	<mdl	<mdl	<mdl	<mdl	32	<mdl	2.75	124	<mdl	<mdl	<mdl	<mdl	<mdl	40
Max	6214	53	1.79	107	6.87	1.58	75	6931	2.13	0.84	0.76	29	44	1.16	17	303	1.15	<mdl	<mdl	0.60	0.70	292
RD2495: Olg (μ_{10})	22	12	13	96	0.12	<mdl	8.47	771	0.09	<mdl	<mdl	1.42	29	<mdl	4.76	203	<mdl	<mdl	<mdl	<mdl	0.19	236
S.D.	8.72	2.95	0.32	5.83	0.04		5.22	59	0.01			0.46	1.39		2.16	26					0.13	110
Min	12	<mdl	13	86	0.08	<mdl	3.09	690	<mdl	<mdl	<mdl	0.66	26	<mdl	1.76	176	<mdl	<mdl	<mdl	<mdl	<mdl	118
Max	38	15	13	103	0.20	<mdl	19	884	0.11	<mdl	0.49	2.17	31	<mdl	7.97	243	<mdl	<mdl	<mdl	<mdl	0.42	424
RD2280: Olg (μ_{7})	100	19	1.66	19	0.13	1.12	8.00	1188	0.12	0.39	0.86	1.47	42	1.60	7.82	89	0.21	<mdl	<mdl	0.43	0.09	44
S.D.	106	1.63	0.17	2.40	0.11	0.15	4.75	73	0.04	0.19	0.29	0.43	1.85	0.19	3.49	13	0.22			0.29	0.08	14
Min	18	17	1.36	16	0.06	0.87	4.33	1098	<mdl	<mdl	0.58	1.00	38	1.40	4.51	70	<mdl	<mdl	<mdl	<mdl	<mdl	26
Max	319	22	1.89	24	0.37	1.35	17	1318	0.17	0.69	1.46	2.11	45	1.93	14	109	0.67	<mdl	0.27	1.06	0.26	67
CD - Foliated Leucogranite																						
PL-12: Olg (μ_{20})	2.69	53	2.66	15	0.06	0.78	16	258	<mdl	<mdl	0.92	2.36	35	0.83	1.57	14	0.09	<mdl	<mdl	0.32	0.04	0.44
S.D.	3.06	9.97	0.65	3.14	0.02	0.23	2.37	49			0.18	1.02	1.04	0.18	1.39	0.96	0.14			0.10	0.02	0.23
Min	0.74	37	1.60	9.06	<mdl	<mdl	13	207	<mdl	<mdl	0.68	0.98	33	<mdl	0.43	12	<mdl	<mdl	<mdl	<mdl	<mdl	<mdl
Max	14	71	3.63	24	0.11	1.19	21	424	0.12	<mdl	1.44	5.71	37	1.27	7.33	16	0.60	0.16	0.25	0.66	0.07	1.01
PL-6: Olg (μ_{11})	12	46	1.21	18	0.06	0.89	6.49	371	<mdl	<mdl	0.47	3.33	33	0.74	0.93	11	<mdl	<mdl	<mdl	0.34	<mdl	<mdl
S.D.	18	4.66	0.19	9.96	0.01	0.23	0.89	46			0.14	0.58	1.54	0.20	0.51	0.56				0.06		
Min	2.10	39	0.89	7.56	<mdl	<mdl	5.39	321	<mdl	<mdl	<mdl	2.39	31	<mdl	0.44	9.92	<mdl	<mdl	<mdl	<mdl	<mdl	<mdl
Max	56	54	1.44	43	0.08	1.19	8.45	467	<mdl	<mdl	0.68	4.05	35	1.14	1.83	12	0.10	0.30	0.32	0.42	0.08	0.45
CD - Donington Granite																						
PL-13: Ads (μ_{15})	9.15	49	0.98	29	0.06	0.82	13	469	<mdl	<mdl	<mdl	4.96	31	1.24	0.45	215	<mdl	0.07	<mdl	0.31	<mdl	28
S.D.	0.91	5.68	0.13	15	0.02	0.23	0.67	30				0.80	1.68	0.29	0.14	7.11		0.05		0.09		3.44
Min	7.48	43	0.69	9.04	<mdl	<mdl	12	435	<mdl	<mdl	<mdl	3.83	27	0.86	0.22	208	<mdl	<mdl	<mdl	<mdl	<mdl	23
Max	11	58	1.14	58	0.12	1.31	14	546	0.12	<mdl	0.54	6.05	33	1.85	0.69	233	0.10	0.15	<mdl	0.55	0.06	34

Table 3: Summary of LA-ICP-MS data for igneous plagioclase: Minor and trace elements (ppm) continued

Element	Mg	P	Sc	Ti	V	Cr	Mn	Fe	Co	Ni	Cu	Zn	Ga	As	Rb	Sr	Zr	Nb	Mo	Sn	Cs	Ba
PL-11: Ads (μ_{10})	8.11	40	0.77	11	0.07	<mdl	9.75	427	<mdl	<mdl	<mdl	4.96	30	1.10	0.67	215	<mdl	<mdl	<mdl	0.33	0.04	23
S.D.	1.50	4.22	0.10	7.22	0.01		1.23	43				0.79	1.10	0.32	0.42	5.27				0.10	0.03	2.28
Min	5.31	34	0.59	5.00	<mdl	<mdl	7.75	353	<mdl	<mdl	<mdl	3.72	28	<mdl	0.27	206	<mdl	<mdl	<mdl	<mdl	<mdl	20
Max	11	47	0.92	32	0.10	0.97	12	500	0.09	<mdl	0.60	6.58	31	1.92	1.58	221	0.40	0.07	<mdl	0.49	0.13	27
PR - Quartz Monzodiorite																						
PD4-2 - Olg (μ_{13})	128	48	1.41	206	0.29	1.57	23	2049	0.11	<mdl	4.62	6.27	32	1.85	9.65	430	<mdl	<mdl	<mdl	0.64	0.35	510
S.D.	115	12	0.34	59	0.18	1.14	17	287	0.08		0.42	3.86	5.28	0.25	9.55	25				0.15	0.12	276
Min	11	23	0.88	99	<mdl	<mdl	8.20	1720	<mdl	<mdl	3.97	1.87	25	1.34	1.64	381	<mdl	<mdl	<mdl	0.42	0.23	220
Max	451	69	2.25	297	0.70	4.67	58	2656	0.28	0.93	5.77	16	42	2.19	30	470	0.45	<mdl	0.70	0.99	0.71	969
PD4-4 - Olg (μ_{10})	49	33	1.60	129	0.17	2.41	29	2162	0.16	<mdl	3.59	6.32	31	1.82	2.83	386	<mdl	<mdl	<mdl	0.78	0.22	280
S.D.	16	9.04	0.65	27	0.11	0.58	26	554	0.10		0.29	2.90	2.35	0.35	2.16	22				0.24	0.08	100
Min	15	25	0.65	90	<mdl	1.55	7.76	1561	<mdl	<mdl	3.07	2.86	25	1.19	0.61	346	<mdl	<mdl	<mdl	0.37	0.06	127
Max	81	54	2.61	188	0.38	3.39	83	3338	0.28	0.84	4.08	12	34	2.41	6.66	423	0.13	0.16	<mdl	1.21	0.35	494
PD4-3 - Olg (μ_{18})	190	47	1.55	188	0.16	1.90	47	2332	0.27	<mdl	4.40	6.75	31	1.79	7.43	399	<mdl	<mdl	<mdl	0.76	0.33	375
S.D.	197	13	0.50	52	0.09	0.74	43	566	0.17		0.57	4.37	3.44	0.52	7.31	34				0.21	0.11	163
Min	40	27	0.51	63	<mdl	<mdl	7.45	1547	<mdl	<mdl	3.10	1.92	26	0.82	0.89	336	<mdl	<mdl	<mdl	0.50	0.16	132
Max	656	68	2.85	279	0.40	2.94	160	3772	0.80	1.20	5.23	17	38	2.85	25	453	0.50	0.17	0.83	1.29	0.67	645
WW – Donington Granite																						
OD46-2 - Ads (μ_{14})	40	32	1.47	12	0.15	1.74	9.63	881	0.26	<mdl	2.39	8.63	28	1.58	2.83	226	<mdl	<mdl	<mdl	0.66	0.36	39
S.D.	31	11	0.39	4.24	0.08	0.50	2.99	512	0.42		0.31	2.94	1.96	0.35	2.16	7.97				0.20	0.28	22
Min	2.1	22	1.07	6.20	<mdl	1.33	6.15	310	<mdl	<mdl	1.91	4.11	24	0.98	0.61	213	<mdl	<mdl	<mdl	0.34	0.11	21
Max	98	53	2.36	20	0.25	2.72	15	2166	1.48	1.82	3.06	14	30	2.09	6.66	241	0.50	<mdl	0.70	1.03	0.89	97

Table 4: Summary of LA-ICP-MS data for albite: Minor and trace elements (ppm)

Element	Mg	P	Sc	Ti	V	Cr	Mn	Fe	Co	Ni	Cu	Zn	Ga	As	Rb	Sr	Zr	Nb	Mo	Sn	Cs	Ba
OD - Least-altered RDG																						
RD2494: Ab (μ_8)	2328	13	15	106	0.51	<mdl	175	2616	0.64	<mdl	2.02	14	30	0.72	121	243	0.17	0.06	<mdl	<mdl	2.55	297
S.D.	1708	4.16	0.45	21	0.73		67	906	0.49		4.28	6.20	3.00	0.26	34	89	0.32	0.11			2.14	55
Min	639	<mdl	14	69	0.07	<mdl	74	1384	0.24	<mdl	<mdl	4.85	23	<mdl	55	147	<mdl	<mdl	<mdl	<mdl	0.77	229
Max	6489	18	16	137	2.39	<mdl	285	4396	1.76	0.80	13	28	33	1.15	171	382	1.00	0.36	<mdl	<mdl	7.63	372
RD2492: Ab (μ_5)	136	16	17	77	0.85	<mdl	70	1565	0.09	<mdl	0.62	4.46	24	3.39	51	152	0.70	0.08	<mdl	<mdl	1.44	201
S.D.	34	6.78	1.23	8.49	0.36		9.44	772	0.04		0.22	0.78	1.67	1.42	18	17	0.33	0.09			0.97	86
Min	82	<mdl	15	68	0.61	<mdl	56	967	<mdl	<mdl	<mdl	3.19	22	1.08	20	129	0.18	<mdl	<mdl	<mdl	0.41	122
Max	170	26	18	91	1.46	<mdl	80	2888	0.15	<mdl	0.88	5.28	27	4.69	64	172	1.03	0.24	<mdl	0.44	2.53	338
RD2880: Ab (μ_{15})	778	16	1.17	66	2.25	1.04	69	2807	0.19	<mdl	6.52	10	30	1.07	112	147	0.89	0.37	<mdl	0.59	1.67	65
S.D.	340	1.59	0.31	64	1.78	0.32	42	1068	0.13		2.90	4.16	5.59	0.37	72	70	0.70	0.65		0.29	2.19	22
Min	322	15	0.77	17	0.06	<mdl	27	1174	0.08	<mdl	1.54	5.23	18	<mdl	27	79	<mdl	<mdl	<mdl	<mdl	0.13	38
Max	1577	21	1.81	235	5.89	1.78	158	3945	0.56	0.41	10	18	36	1.83	252	332	2.32	2.11	0.23	1.15	8.80	104
OD – RDG-HRQM contact																						
RD2274: Ab (μ_{19})	798	13	1.04	59	0.70	<mdl	64	2690	0.34	<mdl	5.27	8.56	32	9.29	84	211	0.60	0.16	<mdl	0.30	1.83	190
S.D.	323	3.95	0.26	18	0.28		51	497	0.20		4.65	5.61	5.43	3.16	29	93	0.47	0.13		0.15	1.03	73
Min	156	<mdl	0.62	5.21	0.29	<mdl	32	2006	0.09	<mdl	1.20	0.86	13	4.27	5.39	39	<mdl	<mdl	<mdl	<mdl	0.09	14
Max	1260	22	1.65	95	1.58	0.82	253	3650	0.75	0.47	19	24	36	18	121	491	1.59	0.57	<mdl	0.62	4.02	331
OD - HRQM																						
RD2274: Ab (μ_{10})	895	25	3.43	112	3.16	<mdl	73	4054	0.62	<mdl	2.48	10	28	2.26	165	415	0.50	<mdl	<mdl	0.33	2.46	1075
S.D.	205	12	0.83	38	0.81		24	609	0.24		0.93	2.05	7.33	0.89	54	156	0.43			0.16	1.50	608
Min	530	<mdl	2.29	65	1.49	<mdl	28	3083	0.25	<mdl	1.06	7.38	13	1.20	67	112	<mdl	<mdl	<mdl	<mdl	0.95	250
Max	1181	51	5.15	183	4.21	<mdl	108	4822	0.98	0.40	4.65	13	38	4.06	235	538	1.53	0.06	<mdl	0.55	4.87	2211
OD – Mineralized RDG																						
RD2316: Ab (μ_{10})	495	<mdl	1.30	11	1.05	1.17	49	3343	0.53	0.60	3.05	8.71	23	5.60	40	60	0.58	<mdl	0.24	0.41	0.38	71
S.D.	333		0.49	5.95	0.88	0.26	35	2335	0.84	0.53	3.61	5.73	6.63	4.41	24	9.06	0.82		0.06	0.37	0.23	52
Min	138	<mdl	0.37	3.12	0.09	<mdl	12	742	0.08	<mdl	0.44	2.10	14	1.76	11	50	<mdl	<mdl	<mdl	<mdl	0.12	25
Max	1149	<mdl	2.01	22	2.62	1.63	115	7605	2.84	1.92	12	21	34	13	73	79	2.61	0.07	0.32	1.36	0.82	172
PR – Quartz monzodiorite																						
PD4-1: Ab (μ_6)	72	39	1.37	112	0.19	1.58	7.70	1856	0.08	<mdl	3.98	13	26	1.94	1.95	438	<mdl	<mdl	<mdl	0.53	0.45	255
S.D.	33	12	0.46	30	0.24	0.59	1.01	617	0.10		0.38	16	4.18	0.10	0.75	22				0.17	0.29	48
Min	42	24	0.72	65	<mdl	<mdl	6.51	1369	<mdl	<mdl	3.48	2.21	20	1.85	0.90	405	<mdl	<mdl	<mdl	0.32	0.25	183
Max	126	55	1.82	149	0.60	1.96	8.73	2901	0.24	0.84	4.54	41	32	2.11	2.67	464	<mdl	<mdl	<mdl	0.75	0.95	316
PD4-3: Ab (μ_5)	874	35	1.36	180	0.56	2.32	117	3772	0.57	0.60	4.07	19	24	1.75	152	329	0.09	<mdl	<mdl	0.64	1.64	225
S.D.	460	8.02	0.44	29	0.78	0.44	40	1050	0.40	0.51	0.43	17	1.89	0.23	80	48	0.12			0.27	1.96	71
Min	474	25	0.79	141	0.10	1.58	74	2259	0.22	<mdl	3.27	7.31	22	1.37	51	243	<mdl	<mdl	<mdl	0.34	0.28	93
Max	1625	46	1.89	213	2.12	2.79	180	5204	1.31	1.52	4.45	52	28	2.05	259	385	0.32	<mdl	0.28	1.12	5.50	297

ELECTRONIC APPENDIX B FOR CHAPTER 5

Table 1: Summary of 1 σ errors and minimum detection limits (MDL) for crypto- and microperthite LA-ICP-MS data: REE, Y Pb, Th and U (ppm)

Element	Y	La	Ce	Pr	Nd	Sm	Eu	Gd	Tb	Dy	Ho	Er	Tm	Yb	Lu	Pb	Th	U
OD – Least altered RDG																		
RD2494: CP (μ_{10})																		
1 σ error	0.007	0.410	0.333	0.032	0.097	0.022	0.125	0.024	0.002	0.005	0.002	0.005	0.001	0.005	0.001	0.189	0.001	0.001
MDL	0.004	0.002	0.004	0.001	0.006	0.008	0.002	0.009	0.002	0.003	0.001	0.005	0.002	0.005	0.069	0.008	0.002	0.001
RD2492: CP (μ_8)																		
1 σ error	0.017	0.264	0.210	0.023	0.071	0.023	0.097	0.024	0.003	0.012	0.003	0.005	0.002	0.010	0.003	0.550	0.046	0.007
MDL	0.003	0.003	0.001	0.001	0.008	0.013	0.003	0.011	0.003	0.080	0.004	0.090	0.001	0.013	0.004	0.012	0.002	0.002
CD – Foliated leucogranite																		
PL-12: MP (μ_{18})																		
1 σ error	0.106	0.271	0.198	0.039	0.156	0.073	0.212	0.078	0.013	0.063	0.016	0.053	0.011	0.055	0.009	4.629	0.034	0.018
MDL	0.041	0.013	0.006	0.010	0.045	0.032	0.006	0.062	0.010	0.020	0.005	0.022	0.009	0.014	0.001	0.288	0.015	0.011
CD - Donington granite																		
PL-11: MP (μ_{14})																		
1 σ error	0.016	0.090	0.058	0.013	0.043	0.032	0.192	0.020	0.003	0.013	0.005	0.011	0.004	0.016	0.004	3.866	0.011	0.011
MDL	0.070	0.005	0.004	0.004	0.029	0.033	0.005	0.037	0.003	0.023	0.005	0.021	0.003	0.033	0.005	0.140	0.010	0.008
PL-13 - MP (μ_{13})																		
1 σ error	0.037	0.085	0.054	0.012	0.048	0.027	0.195	0.040	0.005	0.018	0.006	0.008	0.005	0.023	0.005	3.078	0.012	0.018
MDL	0.003	0.008	0.003	0.005	0.014	0.012	0.012	0.054	0.003	0.008	0.003	0.003	0.005	0.036	0.003	0.134	0.007	0.011

Table 2: Summary of 1 σ errors and minimum detection limits (MDL) for porous and red-stained K-feldspar LA-ICP-MS data: REE, Y Pb, Th and U (ppm)

Element	Y	La	Ce	Pr	Nd	Sm	Eu	Gd	Tb	Dy	Ho	Er	Tm	Yb	Lu	Pb	Th	U
OD- Least-altered RDG																		
RD2492: Por Kfs (μ_6)																		
1 σ error	0.055	0.219	0.184	0.026	0.101	0.036	0.072	0.048	0.006	0.033	0.008	0.024	0.005	0.028	0.005	0.131	0.136	0.013
MDL	0.001	0.003	0.004	0.002	0.014	0.014	0.004	0.008	0.002	0.007	0.002	0.003	0.002	0.004	0.032	0.011	0.002	0.007
RD2495: Por Kfs (μ_{15})																		
1 σ error	0.041	0.198	0.239	0.032	0.118	0.043	0.057	0.045	0.005	0.016	0.005	0.012	0.003	0.011	0.002	0.083	0.091	0.007
MDL	0.002	0.002	0.001	0.003	0.012	0.016	0.003	0.008	0.002	0.004	0.002	0.005	0.001	0.004	0.001	0.008	0.001	0.001
RD2280: Red Kfs (μ_{10}) – AKC16																		
1 σ error	0.038	0.126	0.107	0.023	0.085	0.058	0.067	0.043	0.006	0.027	0.007	0.016	0.005	0.026	0.007	0.144	0.020	0.010
MDL	0.018	0.010	0.010	0.010	0.053	0.076	0.015	0.071	0.006	0.032	0.006	0.025	0.008	0.033	0.004	0.025	0.007	0.009
RD2280: Por Kfs (μ_{10}) – AKC21																		
1 σ error	0.074	0.459	0.433	0.067	0.243	0.087	0.197	0.064	0.010	0.040	0.011	0.032	0.008	0.033	0.009	0.265	0.038	0.021
MDL	0.017	0.012	0.012	0.010	0.039	0.029	0.015	0.051	0.005	0.024	0.004	0.028	0.007	0.019	0.004	0.019	0.007	0.006
OD- HRQM																		
RD2274 - Por Kfs (μ_{14})																		
1 σ error	0.024	0.296	0.236	0.033	0.108	0.033	0.171	0.034	0.004	0.015	0.004	0.010	0.004	0.011	0.004	0.265	0.016	0.010
MDL	0.007	0.006	0.008	0.004	0.023	0.032	0.007	0.020	0.004	0.019	0.005	0.015	0.005	0.016	0.004	0.014	0.005	0.003
OD- Ser-Hm-altered RDG																		
RD2531: Red Kfs (μ_{11}) – AKC1																		
1 σ error	0.088	0.335	0.257	0.053	0.204	0.127	0.174	0.135	0.022	0.088	0.026	0.057	0.019	0.102	0.019	0.302	0.048	0.037
MDL	0.082	0.177	0.089	0.058	0.294	0.293	0.081	0.264	0.048	0.147	0.055	0.076	0.040	0.089	0.033	0.084	0.039	0.031
RD2511: Red Kfs (μ_{11}) – AKC9																		
1 σ error	0.041	0.184	0.137	0.023	0.085	0.032	0.107	0.045	0.004	0.025	0.006	0.018	0.005	0.022	0.004	0.355	0.024	0.023
MDL	0.006	0.003	0.002	0.001	0.014	0.010	0.007	0.041	0.004	0.013	0.004	0.014	0.004	0.013	0.003	0.013	0.009	0.003

Table 2: Summary of 1 σ errors and minimum detection limits (MDL) for porous and red-stained K-feldspar LA-ICP-MS data: REE, Y Pb, Th and U (ppm) continued

Element	Y	La	Ce	Pr	Nd	Sm	Eu	Gd	Tb	Dy	Ho	Er	Tm	Yb	Lu	Pb	Th	U
OD – Mineralized RDG																		
RD2316: Red Kfs (μ_{21}) – RX6698, RX6700																		
1 σ error	0.078	0.180	0.173	0.039	0.159	0.098	0.085	0.083	0.014	0.065	0.017	0.045	0.012	0.066	0.013	0.309	0.036	0.080
MDL	0.035	0.019	0.023	0.015	0.113	0.151	0.034	0.141	0.020	0.069	0.017	0.047	0.017	0.095	0.019	0.072	0.020	0.022
RD3554: Red Kfs (μ_{40}) – RX7326, RX7331, RX7332																		
1 σ error	0.032	0.129	0.134	0.021	0.077	0.030	0.045	0.028	0.004	0.017	0.004	0.012	0.003	0.018	0.004	0.175	0.015	0.012
MDL	0.002	0.001	0.002	0.002	0.009	0.007	0.002	0.008	0.001	0.004	0.001	0.003	0.001	0.004	0.001	0.006	0.001	0.001
WW – Donington granite																		
WRD33: Kfs vein (μ_5) – AKC33																		
1 σ error	0.094	0.079	0.030	0.027	0.162	0.136	0.212	0.134	0.014	0.073	0.011	0.045	0.020	0.116	0.025	0.143	0.025	0.025
MDL	0.115	0.054	0.069	0.038	0.291	0.195	0.099	0.392	0.025	0.212	0.009	0.121	0.040	0.228	0.057	0.108	0.038	0.031
WRD33: Por Kfs (μ_{16}) – AKC33, AKC34																		
1 σ error	0.046	0.081	0.069	0.015	0.059	0.038	0.065	0.034	0.007	0.027	0.007	0.018	0.005	0.019	0.004	0.602	0.011	0.010
MDL	0.006	0.007	0.004	0.006	0.012	0.030	0.005	0.028	0.006	0.014	0.004	0.010	0.004	0.011	0.004	0.013	0.005	0.004
PR – Quartz monzodiorite																		
PD4: Por Kfs (μ_{20}) – PD4.1B, 3B, 4B																		
1 σ error	0.033	1.817	2.051	0.193	0.630	0.090	0.471	0.090	0.010	0.041	0.011	0.021	0.007	0.037	0.008	1.161	0.068	0.026
MDL	0.003	0.008	0.009	0.008	0.055	0.069	0.006	0.045	0.012	0.062	0.018	0.011	0.009	0.054	0.007	0.354	0.004	0.003
WW – Donington granite																		
WRD46 - Por Kfs (μ_{23}) – WW-46.1, 2																		
1 σ error	0.042	0.286	0.137	0.018	0.067	0.029	0.636	0.046	0.008	0.031	0.010	0.026	0.018	0.029	0.012	34.23	0.016	0.041
MDL	0.009	0.008	0.005	0.003	0.052	0.042	0.010	0.069	0.003	0.015	0.001	0.011	0.007	0.014	0.009	0.260	0.008	0.008

Table 3: Summary of 1 σ errors and minimum detection limits (MDL) for igneous plagioclase LA-ICP-MS data: REE, Y Pb, Th and U (ppm).

Element	Y	La	Ce	Pr	Nd	Sm	Eu	Gd	Tb	Dy	Ho	Er	Tm	Yb	Lu	Pb	Th	U
OD - Least-altered RDG																		
RD2495: Ads-Olg (μ_{11}) – RX7865																		
1 σ error	0.079	0.907	0.849	0.144	0.527	0.161	0.233	0.137	0.014	0.058	0.012	0.038	0.011	0.034	0.007	0.276	0.037	0.014
MDL	0.020	0.007	0.012	0.008	0.066	0.036	0.010	0.077	0.005	0.035	0.001	0.043	0.007	0.016	0.005	0.067	0.013	0.005
RD2495: Olg (μ_{10}) – RX7865																		
1 σ error	0.058	0.641	0.722	0.088	0.267	0.070	0.094	0.059	0.006	0.027	0.004	0.010	0.002	0.008	0.002	0.070	0.004	0.002
MDL	0.003	0.002	0.003	0.001	0.018	0.009	0.004	0.011	0.052	0.004	0.002	0.003	0.002	0.007	0.002	0.010	0.001	0.001
RD2280: Olg (μ_{7}) – AKC16																		
1 σ error	0.026	0.177	0.198	0.041	0.138	0.048	0.095	0.051	0.005	0.029	0.005	0.021	0.006	0.040	0.008	0.133	0.010	0.008
MDL	0.026	0.009	0.016	0.017	0.071	0.061	0.012	0.117	0.006	0.040	0.006	0.038	0.005	0.022	0.011	0.043	0.008	0.010
CD - Foliated leucogranite																		
PL-12: Olg (μ_{20})																		
1 σ error	0.145	0.479	0.371	0.067	0.280	0.141	0.073	0.141	0.020	0.096	0.021	0.057	0.010	0.051	0.008	2.395	0.013	0.008
MDL	0.003	0.005	0.005	0.005	0.022	0.041	0.008	0.041	0.006	0.019	0.007	0.013	0.004	0.034	0.007	0.172	0.013	0.011
PL-6: Olg (μ_{11})																		
1 σ error	0.112	0.321	0.278	0.060	0.255	0.106	0.084	0.106	0.016	0.080	0.017	0.051	0.010	0.051	0.010	1.278	0.025	0.014
MDL	0.004	0.007	0.002	0.005	0.054	0.020	0.007	0.038	0.005	0.026	0.005	0.015	0.007	0.018	0.005	0.093	0.010	0.007

Table 3: Summary of 1 σ errors and minimum detection limits (MDL) for igneous plagioclase LA-ICP-MS data: REE, Y Pb, Th and U (ppm) continued

Element	Y	La	Ce	Pr	Nd	Sm	Eu	Gd	Tb	Dy	Ho	Er	Tm	Yb	Lu	Pb	Th	U
CD - Donington granite																		
PL-13: Ads (μ_{15})																		
1 σ error	0.071	0.646	0.674	0.111	0.431	0.140	0.199	0.100	0.014	0.061	0.007	0.029	0.005	0.019	0.006	1.100	0.034	0.020
MDL	0.003	0.006	0.008	0.005	0.015	0.028	0.008	0.015	0.007	0.018	0.007	0.016	0.004	0.004	0.005	0.047	0.019	0.009
PL-11: Ads (μ_{10})																		
1 σ error	0.029	0.232	0.202	0.048	0.195	0.063	0.167	0.059	0.006	0.036	0.008	0.017	0.006	0.011	0.003	1.114	0.006	0.005
MDL	0.010	0.005	0.002	0.009	0.045	0.022	0.009	0.038	0.005	0.032	0.010	0.006	0.012	0.007	0.004	0.054	0.007	0.008
PR - Quartz monzodiorite																		
PD4-2 - Olg (μ_{13})																		
1 σ error	0.153	1.238	1.338	0.289	1.161	0.414	0.493	0.293	0.032	0.153	0.024	0.073	0.012	0.043	0.011	0.485	0.017	0.013
MDL	0.030	0.012	0.020	0.007	0.085	0.132	0.021	0.051	0.011	0.036	0.004	0.045	0.018	0.064	0.015	0.419	0.020	0.019
PD4-4 - Olg (μ_{10})																		
1 σ error	0.172	1.606	1.954	0.347	1.417	0.440	0.470	0.315	0.036	0.149	0.024	0.060	0.010	0.083	0.003	0.495	0.015	0.007
MDL	0.071	0.007	0.011	0.005	0.059	0.070	0.024	0.105	0.015	0.071	0.005	0.015	0.012	0.047	0.010	0.423	0.019	0.012
PD4-3 - Olg (μ_{18})																		
1 σ error	0.197	1.436	1.750	0.326	1.331	0.478	0.489	0.302	0.039	0.171	0.032	0.066	0.011	0.075	0.012	0.435	0.026	0.018
MDL	0.043	0.008	0.010	0.006	0.069	0.102	0.011	0.042	0.012	0.074	0.003	0.009	0.012	0.020	0.013	0.429	0.029	0.019
WW – Donington granite																		
OD46-2 - Ads (μ_{14})																		
1 σ error	0.111	1.538	2.529	0.320	1.406	0.297	0.866	0.171	0.025	0.121	0.021	0.052	0.005	0.082	0.009	15.22	0.010	0.014
MDL	0.037	0.014	0.003	0.021	0.059	0.051	0.008	0.131	0.006	0.012	0.006	0.020	0.006	0.033	0.006	0.584	0.022	0.013

Table 4: Summary of 1 σ errors and minimum detection limits (MDL) for albite LA-ICP-MS data: REE, Y Pb, Th and U (ppm)

Element	Y	La	Ce	Pr	Nd	Sm	Eu	Gd	Tb	Dy	Ho	Er	Tm	Yb	Lu	Pb	Th	U
OD - Least-altered RDG																		
RD2494: Ab (μ_8) – RX7860																		
1 σ error	0.043	0.514	0.555	0.055	0.161	0.040	0.065	0.041	0.005	0.021	0.005	0.015	0.005	0.015	0.003	0.080	0.005	0.005
MDL	0.004	0.003	0.001	0.005	0.004	0.015	0.004	0.015	0.003	0.010	0.002	0.006	0.003	0.005	0.001	0.008	0.003	0.002
RD2492: Ab (μ_5) – RX7864																		
1 σ error	0.086	0.403	0.470	0.049	0.162	0.052	0.058	0.052	0.009	0.037	0.008	0.030	0.005	0.033	0.005	0.096	0.051	0.025
MDL	0.266	0.649	0.170	0.137	0.466	5.312	0.141	5.956	0.069	0.012	0.030	2.267	0.493	0.008	0.001	1.364	0.030	0.667
RD2880: Ab (μ_{15}) – AKC17																		
1 σ error	0.241	0.314	0.418	0.080	0.336	0.136	0.087	0.167	0.022	0.121	0.029	0.089	0.019	0.106	0.019	0.262	0.254	0.047
MDL	0.015	0.010	0.008	0.010	0.062	0.034	0.015	0.062	0.009	0.031	0.011	0.024	0.007	0.042	0.010	0.023	0.007	0.006
OD – RDG-HRQM contact																		
RD2274: Ab (μ_{19})																		
1 σ error	0.113	0.514	0.649	0.101	0.390	0.144	0.074	0.113	0.014	0.062	0.014	0.039	0.008	0.047	0.008	0.119	0.036	0.022
MDL	0.009	0.006	0.006	0.005	0.026	0.035	0.008	0.034	0.003	0.018	0.003	0.009	0.005	0.019	0.005	0.017	0.005	0.003
OD - HRQM																		
RD2274: Ab (μ_{10})																		
1 σ error	0.062	0.838	1.492	0.184	0.711	0.228	0.085	0.166	0.017	0.058	0.010	0.023	0.005	0.024	0.004	0.124	0.039	0.010
MDL	0.010	0.008	0.007	0.005	0.017	0.024	0.007	0.023	0.006	0.018	0.002	0.018	0.002	0.023	0.003	0.014	0.004	0.004
OD – Mineralized RDG																		
RD2316: Ab (μ_{10})																		
1 σ error	0.048	0.083	0.093	0.021	0.095	0.066	0.028	0.065	0.011	0.047	0.006	0.028	0.012	0.042	0.010	0.103	0.019	0.023
MDL	0.021	0.017	0.013	0.013	0.072	0.104	0.027	0.081	0.014	0.047	0.017	0.052	0.013	0.065	0.011	0.038	0.021	0.015
PR – Quartz monzodiorite																		
PD4-3: Ab (μ_5)																		
1 σ error	0.140	1.022	1.200	0.254	1.084	0.370	0.338	0.252	0.038	0.081	0.033	0.079	0.012	0.080	0.010	0.318	0.009	0.009
MDL	0.020	0.021	0.040	0.023	0.062	0.050	0.054	0.067	0.020	0.040	0.015	0.042	0.030	0.046	0.045	0.385	0.020	0.010

Table 5: Summary of 1 σ errors and minimum detection limits (MDL) for crypto- and microperthite LA-ICP-MS data: Minor and trace elements (ppm)

Element	Mg	P	Sc	Ti	V	Cr	Mn	Fe	Co	Ni	Cu	Zn	Ga	As	Rb	Sr	Zr	Nb	Mo	Sn	Cs	Ba
OD – Least-altered RDG																						
RD2494: CP (μ_{10}) – RX7860																						
1 σ error	0.396	4.248	0.545	8.089	0.037	0.173	0.385	19.77	0.013	0.049	0.163	0.262	2.715	0.208	9.321	5.650	0.015	0.006	0.019	0.037	0.035	79.85
MDL	0.027	6.222	0.145	4.702	0.071	0.335	0.243	3.146	0.023	0.093	0.331	0.281	0.006	0.403	0.013	0.006	0.008	0.007	0.041	0.067	0.006	0.046
RD2492: CP (μ_8) – RX7864																						
1 σ error	0.645	3.731	0.573	6.903	0.039	0.223	0.760	20.26	0.013	0.041	0.185	0.331	1.305	0.315	10.68	5.593	0.025	0.007	0.024	0.053	0.053	64.17
MDL	0.024	6.515	0.127	4.826	0.071	0.453	0.255	3.231	0.019	0.080	0.364	0.294	0.006	0.538	0.024	0.005	0.010	0.004	0.059	0.074	0.007	0.026
CD – Foliated leucogranite																						
PL-12: MP (μ_{18})																						
1 σ error	2.002	16.18	0.276	3.000	0.054	0.636	0.577	29.02	0.006	0.160	0.736	0.791	2.097	0.924	34.48	3.522	0.083	0.020	0.027	0.433	0.866	16.24
MDL	0.175	24.87	0.220	1.700	0.038	1.388	1.076	17.97	0.034	0.105	1.531	0.790	0.019	1.695	0.086	0.006	0.013	0.011	0.021	0.489	0.020	0.033
CD - Donington granite																						
PL-11: MP (μ_{14})																						
1 σ error	0.262	7.752	0.151	7.196	0.026	0.336	0.446	23.65	0.018	0.068	0.232	0.491	2.926	0.552	18.86	7.051	0.031	0.050	0.011	0.130	0.471	116.0
MDL	0.046	9.839	0.087	0.220	0.024	0.712	0.433	7.361	0.005	0.074	0.259	0.635	0.017	0.574	0.034	0.006	0.017	0.004	0.035	0.258	0.016	0.023
PL-13 - MP (μ_{13})																						
1 σ error	0.261	8.393	0.157	6.175	0.019	0.235	0.364	22.83	0.015	0.080	0.208	0.459	3.086	0.509	18.13	7.634	0.037	0.058	0.024	0.156	0.397	113.8
MDL	0.034	9.038	0.088	0.224	0.031	0.525	0.412	6.985	0.015	0.036	0.372	0.547	0.009	0.603	0.045	0.003	0.009	0.004	0.033	0.242	0.010	0.046

Table 6: Summary of 1 σ errors and minimum detection limits (MDL) for porous and red-stained K-feldspar LA-ICP-MS data: Minor and trace elements (ppm)

Element	Mg	P	Sc	Ti	V	Cr	Mn	Fe	Co	Ni	Cu	Zn	Ga	As	Rb	Sr	Zr	Nb	Mo	Sn	Cs	Ba
OD- Least-altered RDG																						
RD2492: Por Kfs (μ_6) – RX7864																						
1 σ error	0.700	4.101	0.736	6.767	0.061	0.291	0.990	23.69	0.022	0.046	0.219	0.416	1.343	0.396	21.45	3.333	0.061	0.022	0.012	0.066	0.105	63.18
MDL	0.022	6.396	0.118	4.669	0.069	0.445	0.241	3.236	0.019	0.048	0.324	0.239	0.015	0.494	0.023	0.005	0.002	0.005	0.017	0.067	0.006	0.120
RD2495: Por Kfs (μ_{15}) – RX7865																						
1 σ error	2.038	3.908	0.646	4.399	0.051	0.216	2.516	22.06	0.027	0.059	0.229	0.645	1.266	0.328	22.52	2.754	0.032	0.010	0.038	0.049	0.112	42.54
MDL	0.030	6.427	0.155	4.642	0.071	0.384	0.249	3.254	0.018	0.097	0.324	0.249	0.015	0.479	0.011	0.002	0.008	0.003	0.029	0.066	0.004	0.014
RD2280: Red Kfs (μ_{10}) – AKC16																						
1 σ error	16.05	7.636	0.172	3.521	0.058	0.479	2.845	132.4	0.070	0.152	0.493	1.247	1.442	0.552	20.09	2.153	0.179	0.017	0.076	0.170	0.102	48.79
MDL	0.105	14.40	0.172	2.394	0.063	0.741	0.438	12.53	0.081	0.212	0.578	0.848	0.036	0.928	0.051	0.019	0.039	0.011	0.091	0.202	0.024	0.111
RD2280: Por Kfs (μ_{10})																						
1 σ error	12.58	9.249	0.199	19.81	0.070	0.538	1.054	112.8	0.076	0.150	0.557	1.343	2.353	0.657	18.18	2.603	0.177	0.070	0.037	0.166	0.124	171.4
MDL	0.115	13.23	0.144	2.019	0.046	0.730	0.385	10.97	0.078	0.161	0.489	0.601	0.017	0.723	0.035	0.020	0.026	0.014	0.061	0.172	0.018	0.090
OD- HRQM																						
RD2274 - Por Kfs (μ_{14}) – AKC21																						
1 σ error	5.358	5.698	0.108	7.073	0.033	0.242	1.660	64.69	0.046	0.098	0.318	1.208	1.729	0.408	14.45	9.902	0.064	0.010	0.054	0.075	0.083	117.4
MDL	0.075	8.389	0.089	1.110	0.032	0.420	0.265	6.751	0.046	0.139	0.296	0.306	0.026	0.660	0.028	0.007	0.008	0.004	0.069	0.095	0.013	0.076
OD- Ser-Hm-altered RDG																						
RD2531: Red Kfs (μ_{11})																						
1 σ error	53.07	127.9	1.020	14.57	0.288	1.346	4.767	1044	0.694	0.588	1.374	5.592	2.273	1.460	23.46	3.381	0.463	0.059	0.320	0.339	0.252	69.64
MDL	0.318	259.7	0.915	10.37	0.482	2.785	6.729	77.79	0.245	0.653	2.639	3.282	0.230	2.481	0.143	0.091	0.132	0.071	0.433	0.184	0.062	1.042
RD2511: Red Kfs (μ_{11})																						
1 σ error	20.86	5.961	0.735	6.429	0.064	0.257	0.527	98.83	0.087	0.202	0.310	0.884	2.249	0.543	14.63	3.141	0.234	0.022	0.170	0.134	0.095	64.89
MDL	0.070	7.188	0.150	4.792	0.061	0.413	0.222	3.544	0.022	0.052	0.247	0.134	0.019	0.499	0.073	0.055	0.109	0.004	0.033	0.073	0.010	0.056

Table 6: Summary of 1 σ errors and minimum detection limits (MDL) for porous and red-stained K-feldspar LA-ICP-MS data: Minor and trace elements (ppm) continued

Element	Mg	P	Sc	Ti	V	Cr	Mn	Fe	Co	Ni	Cu	Zn	Ga	As	Rb	Sr	Zr	Nb	Mo	Sn	Cs	Ba
OD – Mineralized RDG																						
RD2316: Red Kfs (μ_{21}) – RX6698, RX6700																						
1 σ error	138.1	7.665	0.252	6.426	0.208	1.006	4.436	237.4	0.147	0.389	2.264	1.657	1.577	14.35	17.54	1.952	0.817	0.039	0.160	0.169	0.111	48.29
MDL	0.175	13.36	0.256	3.747	0.117	1.653	0.682	22.21	0.095	0.428	0.659	0.688	0.094	1.473	0.050	0.033	0.047	0.029	0.194	0.208	0.027	0.185
RD3554: Red Kfs (μ_{40}) – RX7326, RX7331, RX7332																						
1 σ error	23.16	3.472	0.336	3.268	0.071	0.173	17.36	404.8	0.287	0.183	29.46	1.765	1.343	1.444	13.17	6.155	0.104	0.027	0.264	0.076	0.060	78.63
MDL	0.044	4.703	0.063	1.875	0.031	0.225	0.173	2.989	0.015	0.043	0.482	0.211	0.009	1.117	0.014	0.003	0.005	0.003	0.016	0.056	0.004	0.017
WW – Donington granite																						
WRD33: Kfs vein (μ_5)																						
1 σ error	13.16	139.6	2.324	13.15	0.362	2.202	4.138	44.11	0.262	0.774	1.864	4.220	2.200	0.958	16.31	9.460	0.125	0.042	0.172	0.244	0.182	99.96
MDL	0.539	263.0	1.280	21.69	0.558	4.092	7.466	45.75	0.325	1.229	3.794	5.340	0.131	1.916	0.130	0.123	0.192	0.115	0.327	0.365	0.096	0.475
WRD33: Por Kfs (μ_{16})																						
1 σ error	23.95	5.208	0.137	3.968	0.044	0.296	3.258	2184	0.049	0.124	0.764	1.644	1.764	0.396	13.35	9.029	0.174	0.021	0.097	0.120	0.099	105.9
MDL	0.135	7.796	0.083	1.402	0.035	0.441	0.253	5.357	0.037	0.117	0.330	0.333	0.030	0.572	0.028	0.011	0.021	0.008	0.043	0.083	0.014	0.053
PR – Quartz monzodiorite																						
PD4: Por Kfs (μ_{20}) – 1B, 3B, 4B																						
1 σ error	0.739	12.47	0.475	19.42	0.079	0.970	15.49	181.1	0.081	0.385	2.083	5.007	4.688	0.980	23.30	15.72	0.029	0.013	0.091	0.367	0.425	238.1
MDL	0.450	21.99	0.295	1.665	0.099	1.614	1.127	23.24	0.046	0.030	4.064	0.521	0.023	1.781	0.362	0.016	0.078	0.003	0.062	0.674	0.237	0.090
WW – Donington granite																						
WRD46 - Por Kfs (μ_{23})																						
1 σ error	20.24	7.450	0.365	6.712	0.088	0.421	21.47	1168	0.229	0.366	0.856	1.281	3.252	0.422	21.09	11.56	0.061	0.020	0.036	0.209	0.293	199.8
MDL	0.214	11.55	0.154	1.172	0.040	0.553	0.604	12.17	0.013	0.059	1.496	0.279	0.024	0.811	0.205	0.007	0.021	0.004	0.011	0.261	0.106	0.050

Table 7: Summary of 1 σ errors and minimum detection limits (MDL) for igneous plagioclase LA-ICP-MS data: Minor and trace elements (ppm)

Element	Mg	P	Sc	Ti	V	Cr	Mn	Fe	Co	Ni	Cu	Zn	Ga	As	Rb	Sr	Zr	Nb	Mo	Sn	Cs	Ba
OD - Least-altered RDG																						
RD2495: Ads-Olg (μ_{11})																						
1 σ error	27.21	9.535	0.215	6.027	0.110	0.414	1.135	108.1	0.085	0.120	0.327	1.194	1.855	0.474	0.623	6.331	0.074	0.011	0.042	0.175	0.072	9.515
MDL	0.093	13.66	0.134	0.658	0.015	0.722	0.550	9.671	0.020	0.060	0.550	0.731	0.007	0.914	0.022	0.007	0.020	0.011	0.012	0.303	0.020	0.028
RD2495: Olg (μ_{10})																						
1 σ error	0.832	3.652	0.509	5.475	0.039	0.183	0.369	24.78	0.023	0.050	0.159	0.266	1.121	0.227	1.169	5.988	0.019	0.006	0.013	0.042	0.034	10.17
MDL	0.064	6.101	0.138	4.335	0.064	0.344	0.232	2.962	0.013	0.051	0.320	0.229	0.022	0.399	0.016	0.005	0.003	0.005	0.030	0.067	0.004	0.013
RD2280: Olg (μ_7) – AKC16																						
1 σ error	3.722	9.448	0.213	2.935	0.057	0.480	0.517	72.60	0.056	0.168	0.325	0.653	1.703	0.793	0.443	3.012	0.065	0.014	0.053	0.167	0.028	2.297
MDL	0.104	18.80	0.207	2.898	0.078	1.121	0.554	18.15	0.099	0.353	0.710	0.926	0.077	1.583	0.076	0.022	0.041	0.021	0.084	0.287	0.034	0.145
CD - Foliated leucogranite																						
PL-12: Olg (μ_{20})																						
1 σ error	0.237	9.615	0.260	2.202	0.023	0.371	0.991	21.19	0.019	0.052	0.411	0.692	2.066	0.408	0.194	0.863	0.031	0.008	0.020	0.161	0.013	0.219
MDL	0.059	12.32	0.137	0.852	0.035	0.737	0.527	9.999	0.023	0.050	0.919	0.586	0.023	0.781	0.056	0.002	0.010	0.002	0.024	0.262	0.023	0.015
PL-6: Olg (μ_{11})																						
1 σ error	0.808	9.048	0.178	3.011	0.019	0.431	0.535	25.44	0.023	0.009	0.265	0.878	1.665	0.333	0.174	0.623	0.030	0.022	0.012	0.178	0.014	0.153
MDL	0.045	12.14	0.101	0.938	0.023	0.955	0.523	8.476	0.005	0.029	0.485	0.460	0.007	0.791	0.039	0.053	0.021	0.013	0.038	0.342	0.007	0.038
CD - Donington granite																						
PL-13: Ads (μ_{15})																						
1 σ error	0.665	8.966	0.169	3.874	0.032	0.452	0.841	43.02	0.028	0.021	0.144	1.144	1.772	0.594	0.125	9.800	0.022	0.041	0.054	0.188	0.007	2.441
MDL	0.058	11.46	0.096	0.454	0.045	0.775	0.506	9.468	0.011	0.020	0.197	0.548	0.007	0.723	0.018	0.004	0.033	0.003	0.033	0.312	0.013	0.021

Table 7: Summary of 1 σ errors and minimum detection limits (MDL) for igneous plagioclase LA-ICP-MS data: Minor and trace elements (ppm) continued

Element	Mg	P	Sc	Ti	V	Cr	Mn	Fe	Co	Ni	Cu	Zn	Ga	As	Rb	Sr	Zr	Nb	Mo	Sn	Cs	Ba
PL-11: Ads (μ_{10})																						
1 σ error	0.501	7.562	0.133	1.821	0.022	0.290	0.606	36.91	0.019	0.057	0.182	1.026	1.572	0.498	0.124	7.363	0.022	0.007	0.031	0.158	0.015	1.935
MDL	0.040	10.65	0.113	0.501	0.033	0.588	0.489	8.789	0.009	0.043	0.266	0.622	0.008	0.631	0.022	0.043	0.032	0.007	0.021	0.291	0.008	0.213
PR - Quartz monzodiorite																						
PD4-2 - Olg (μ_{13})																						
1 σ error	11.45	12.57	0.347	23.35	0.121	0.828	1.539	240.9	0.073	0.166	2.150	1.591	2.075	0.802	0.894	17.71	0.045	0.021	0.062	0.311	0.158	30.86
MDL	0.424	22.22	0.330	2.062	0.095	1.060	1.236	22.66	0.057	0.072	4.622	0.847	0.018	1.702	0.439	0.044	0.034	0.056	0.104	0.595	0.305	0.089
PD4-4 - Olg (μ_{10})																						
1 σ error	8.290	13.23	0.380	16.93	0.080	0.992	1.920	151.2	0.094	0.174	1.678	1.640	2.300	0.859	1.192	15.71	0.025	0.005	0.031	0.383	0.124	21.62
MDL	0.494	25.84	0.212	2.801	0.064	2.406	1.219	29.11	0.065	0.032	3.526	0.811	0.035	1.804	0.473	0.018	0.011	0.016	0.087	0.576	0.153	0.126
PD4-3 - Olg (μ_{18})																						
1 σ error	17.68	14.33	0.388	24.38	0.094	0.900	2.979	229.3	0.127	0.157	2.001	1.736	2.346	0.885	1.716	17.37	0.042	0.011	0.046	0.369	0.162	24.64
MDL	0.509	26.54	0.357	2.425	0.088	1.495	1.321	24.30	0.118	0.067	4.398	0.974	0.040	1.723	0.439	0.022	0.010	0.009	0.092	0.695	0.296	0.371
WW – Donington granite																						
OD46-2 - Ads (μ_{14})																						
1 σ error	10.74	13.35	0.385	6.569	0.174	0.961	1.157	173.5	0.112	0.176	1.186	2.096	2.049	0.853	1.469	13.36	0.011	0.006	0.030	0.348	0.176	6.125
MDL	0.466	26.12	0.235	2.481	0.112	2.169	1.289	28.74	0.025	0.062	2.379	0.441	0.053	1.827	0.347	0.027	0.035	0.070	0.096	0.641	0.170	0.112

Table 8: Summary of 1 σ errors and minimum detection limits (MDL) for albite LA-ICP-MS data: Minor and trace elements (ppm)

Element	Mg	P	Sc	Ti	V	Cr	Mn	Fe	Co	Ni	Cu	Zn	Ga	As	Rb	Sr	Zr	Nb	Mo	Sn	Cs	Ba
OD - Least-altered RDG																						
RD2494: Ab (μ_8)																						
1 σ error	78.62	3.734	0.526	5.286	0.057	0.163	6.235	96.52	0.061	0.086	0.266	1.171	2.261	0.248	4.614	7.491	0.023	0.011	0.024	0.036	0.126	10.27
MDL	0.029	6.134	0.129	4.505	0.067	0.355	0.228	3.165	0.024	0.084	0.315	0.261	0.022	0.402	0.019	0.005	0.008	0.004	0.030	0.052	0.008	0.019
RD2492: Ab (μ_5)																						
1 σ error	5.174	1145	21.53	855.1	10.99	62.62	43.64	585.1	1.289	2.939	58.91	28.02	2.623	76.95	4.453	0.473	2.501	1.023	3.474	10.64	0.689	5.516
MDL	4.465	15.68	0.605	4.975	0.083	0.260	2.290	53.46	0.026	0.059	0.228	0.500	0.885	0.508	1.750	4.705	0.073	0.017	0.021	0.064	0.073	6.458
RD2880: Ab (μ_{15}) – AKC17																						
1 σ error	26.91	10.20	0.241	45.34	0.379	0.760	2.675	330.6	0.115	0.209	1.138	1.965	1.538	0.612	4.545	4.914	0.709	0.446	0.090	0.225	0.142	13.
MDL	0.145	16.03	0.170	2.471	0.062	0.801	0.467	13.06	0.083	0.209	0.569	0.666	0.038	0.848	0.040	0.018	0.041	0.017	0.140	0.176	0.016	0.128
OD – RDG-HRQM contact																						
RD2274: Ab (μ_{19})																						
1 σ error	26.54	5.873	0.137	4.181	0.104	0.257	2.475	4623	0.087	0.145	0.722	1.239	1.306	1.335	2.951	6.337	0.108	0.040	0.030	0.097	0.113	8.912
MDL	0.083	9.341	0.097	1.332	0.037	0.431	0.279	6.043	0.043	0.124	0.343	0.389	0.032	1.004	0.033	0.017	0.025	0.009	0.034	0.092	0.014	0.055
OD - HRQM																						
RD2274: Ab (μ_{10})																						
1 σ error	30.28	6.580	0.217	5.771	0.202	0.271	2.366	192.7	0.087	0.111	0.401	1.094	1.162	0.520	5.894	12.89	0.068	0.015	0.048	0.086	0.129	35.86
MDL	0.082	8.156	0.087	1.088	0.030	0.451	0.254	6.173	0.035	0.133	0.277	0.351	0.017	0.526	0.032	0.011	0.015	0.011	0.026	0.091	0.009	0.082
OD – Mineralized RDG																						
RD2316: Ab (μ_{10}) – RX6700																						
1 σ error	17.76	5.457	0.198	2.390	0.152	0.608	2.131	269.3	0.075	0.260	0.485	1.481	1.260	1.343	1.986	2.008	0.093	0.023	0.112	0.137	0.056	4.432
MDL	0.151	8.880	0.165	2.239	0.081	1.103	0.437	13.65	0.079	0.275	0.407	0.415	0.047	1.845	0.039	0.020	0.039	0.023	0.171	0.123	0.018	0.163
PR – Quartz monzodiorite																						
PD4-3: Ab (μ_5)																						
1 σ error	34.36	12.57	0.336	21.27	0.145	1.018	6.282	376.3	0.198	0.414	1.836	2.670	1.784	0.868	9.248	13.70	0.044	0.029	0.056	0.346	0.298	14.32
MDL	0.466	25.08	0.249	3.038	0.117	1.856	1.276	25.58	0.039	0.022	4.040	0.806	0.050	1.622	0.410	0.039	0.064	0.012	0.022	0.545	0.224	0.198

SUPPLEMENTARY MATERIAL C

FOR CHAPTER 6 - FELDSPAR MINERALOGY AND RARE EARTH ELEMENT (RE)MOBILIZATION IN IRON-OXIDE COPPER GOLD SYSTEMS FROM SOUTH AUSTRALIA: A NANOSCALE STUDY

ELECTRONIC APPENDIX A FOR CHAPTER 6

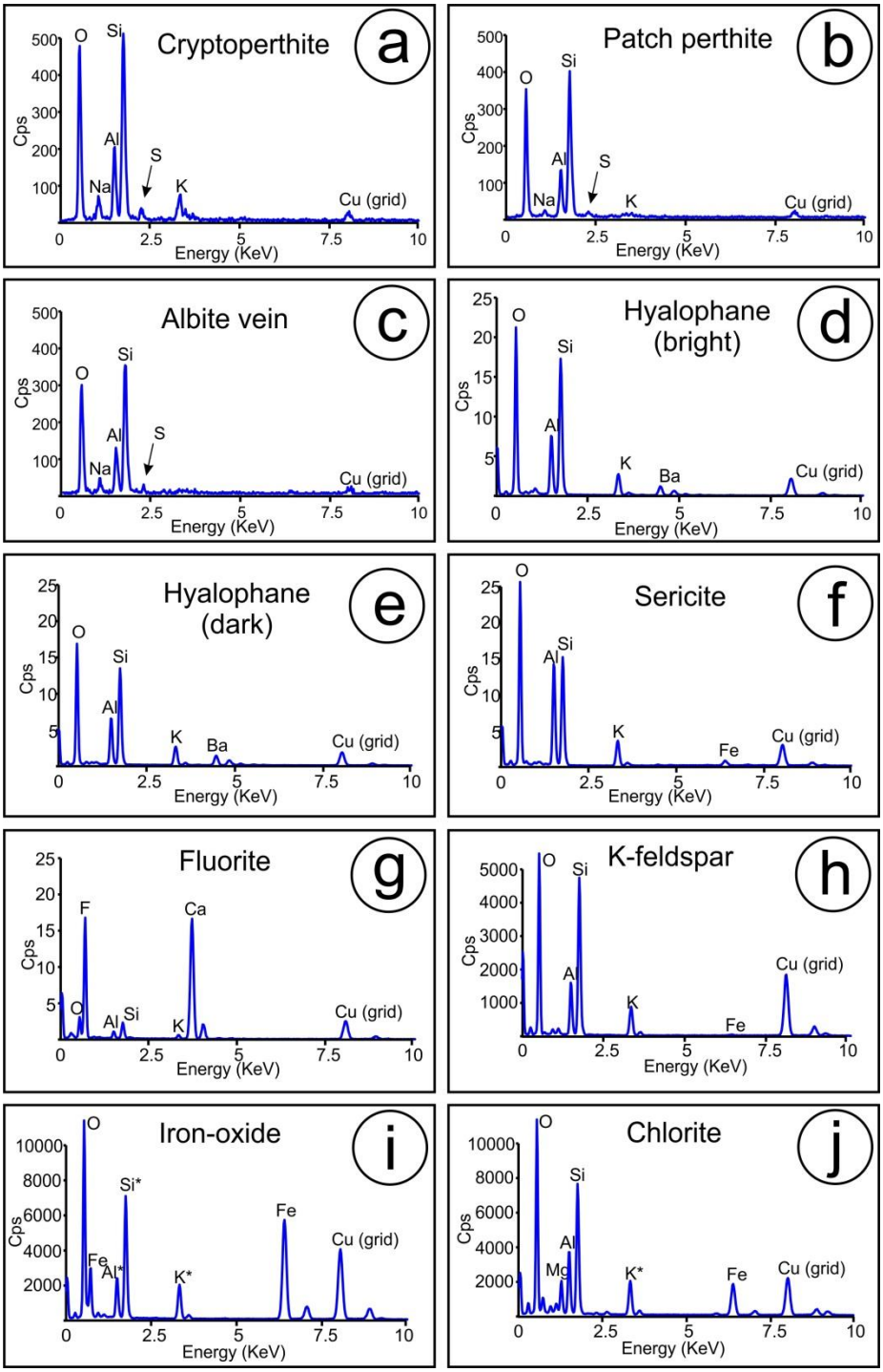

FIG 1 TEM-EDS spectra for various minerals identified. (a-c) Spectra corresponding to the perthite varieties for case study A shown in Fig. 4. (d-g) Spectra corresponding to various inclusions within the albite + sericite + hyalophane + fluorite assemblage for case study B shown in Fig. 8. Note: composition of hyalophane differs in association with brighter and darker zones visible on the HAADF-STEM images. (h-j) Spectra corresponding to K-feldspar, iron-oxide inclusions and chlorite found in case study C shown in Fig. 11. Note: for (i) element peaks marked as * represent interference with host K-feldspar due to small size of Fe-oxide inclusion. Beam size ~50 nm. Abbreviations: Cps - counts per second.

ADDITIONAL MATERIAL D

ALTERATION AT THE OLYMPIC DAM IOCG-U DEPOSIT: INSIGHTS INTO DISTAL TO PROXIMAL FELDSPAR AND PHYLLOSILICATE CHEMISTRY FROM INFRARED REFLECTANCE SPECTROSCOPY

Alan J. Mauger[1], Kathy Ehrig[2], **Alkis Kontonikas-Charos**[3], Cristiana L. Ciobanu[4], Nigel J. Cook[4], Vadim S. Kamenetsky[5]

[1]*Geological Survey of South Australia, Adelaide, SA, 5000, Australia*

[2]*BHP Billiton Olympic Dam, Adelaide, SA, 5000, Australia*

[3]*School of Physical Sciences, The University of Adelaide, Adelaide, SA, 5005, Australia*

[4]*School of Chemical Engineering, The University of Adelaide, Adelaide, SA, 5005, Australia*

[5]*School of Physical Sciences, University of Tasmania, Hobart, TAS, 7001, Australia*

Article published in Australian Journal of Earth Sciences 63 (8), 959-972

AUSTRALIAN JOURNAL OF EARTH SCIENCES, 2016
VOL. 63, NO. 8, 959–972
http://dx.doi.org/10.1080/08120099.2016.1264474

Alteration at the Olympic Dam IOCG–U deposit: insights into distal to proximal feldspar and phyllosilicate chemistry from infrared reflectance spectroscopy

A. J. Mauger[a], K. Ehrig[b], A. Kontonikas-Charos[c], C. L. Ciobanu[d], N. J. Cook[d] and V. S. Kamenetsky[e]

[a]Geological Survey of South Australia, Adelaide, SA 5000, Australia; [b]BHP Billiton Olympic Dam, Adelaide, SA 5000, Australia; [c]School of Physical Sciences, University of Adelaide, Adelaide, SA 5005, Australia; [d]School of Chemical Engineering, University of Adelaide, Adelaide, SA 5005, Australia; [e]School of Physical Sciences, University of Tasmania, Hobart, Tas 7001, Australia

ABSTRACT

Twenty thousand metres of diamond drill core representing a 14 km cross-section from weakly to intensely altered Roxby Downs Granite through the Olympic Dam Breccia Complex, host to the Olympic Dam iron-oxide–copper–gold–uranium deposit in South Australia, was analysed using the HyLogger-3 spectral scanner. Thermal and shortwave infrared spectroscopy results from 30 drill holes provide insight into the spatial relationships between quartz, orthoclase–microcline, albite–oligoclase and progressively changing sericite and chlorite compositions. The relative proportions of quartz, feldspars and phyllosilicates were mapped with thermal infrared spectroscopy. Variations in the chemistry of sericite and chlorite were extracted by proxy from their shortwave infrared spectral response, together with their relative spatial distribution. HyLogger scanning has revealed four deposit-scale mineralogical trends, progressing from least-altered Roxby Downs Granite into mineralisation where most of the feldspar has been replaced by sericite + hematite + quartz: (1) a progressive Al–OH wavelength shift of 2205 nm to 2210 nm for sericite, followed by a spatially rapid reversal corresponding to lower phengite/muscovite abundance ratios; (2) progressive Mg/Fe–OH wavelength shift of 2248 nm to 2252 nm reflecting an increase in the Fe:Mg ratio of chlorite; (3) increasing ratio of microcline to orthoclase followed by a rapid decrease; and (4) slightly decreasing ratio of albite to oligoclase followed by plagioclase destruction prior to albite replacement by sericite. The HyLogger feldspar results support recent petrographic evidence for hydrothermal albite and K-feldspar at the Olympic Dam deposit, not previously reported. The spectral results from continuous HyLogger scans also show that the microscopic observations and proposed feldspar replacement reactions are not locally isolated phenomena, but are applicable at the deposit and regional-scale. A modified quartz–K-feldspar–plagioclase ternary diagram utilising mineralogy interpreted from HyLogger thermal infrared spectra (QAP_{TIR}) diagram along with supporting data on the abundance ratios of orthoclase/microcline and albite/plagioclase, and the wavelength shifts in characteristic absorption features for sericite and chlorite, can be used as empirical vectors towards mineralisation within the Olympic Dam mineral system, with potential application to other IOCG ore-forming systems. Intrusion of Gairdner Dyke Swarm dolerite dykes into sericite ± hematite altered Roxby Downs Granite results in retrograde albite–chlorite–magnetite alteration envelopes (up to tens of metres thick) overprinting the original sericite ± hematite alteration zone and needs to be carefully evaluated to ensure that such areas are not falsely downgraded during exploration.

ARTICLE HISTORY
Received 24 February 2016
Accepted 20 November 2016

KEYWORDS
Olympic Dam IOCG–U deposit; reflectance spectroscopy; HyLogger-3; microcline; orthoclase; albite; plagioclase; muscovite; phengite

Introduction

The Olympic Dam iron-oxide–Cu–U–Au–Ag deposit is the world's largest reported uranium, fifth largest copper and third largest gold resource (BHP Billiton, 2016). It is widely accepted as the type example of the iron oxide–Cu–Au (IOCG) class of ore deposits (e.g. Groves, Bierlein, Meinert, & Hitzman, 2010; Williams et al., 2005). The deposit is located approximately 520 km NNW of Adelaide, South Australia on the eastern margin of the Gawler Craton (Figure 1). Cu–U–Au–Ag mineralisation occurs within iron oxide breccias, which are derived predominately by intense hematitic and sericitic alteration and brecciation of the *ca* 1.6 Ga Roxby Downs Granite (RDG) (e.g. Reeve, Cross, Smith, & Oreskes, 1990). Multiple mineralogical zonation patterns across the deposit and areas immediately adjacent to the deposit are well documented, yet mineralogical changes occurring distal to mineralisation within the RDG have been previously described as simply progressive alteration of plagioclase and K-feldspar to sericite (Ehrig, McPhie, & Kamenetsky, 2012). A recent microscopic study of feldspars (Kontonikas-Charos et al., 2017) in apparently unaltered RDG revealed a previously unrecognised systematic alteration pattern of magmatic and post-magmatic/

CONTACT A. J. Mauger alan.mauger@sa.gov.au
Editorial handling: Jon Huntington
© 2016 Geological Society of Australia

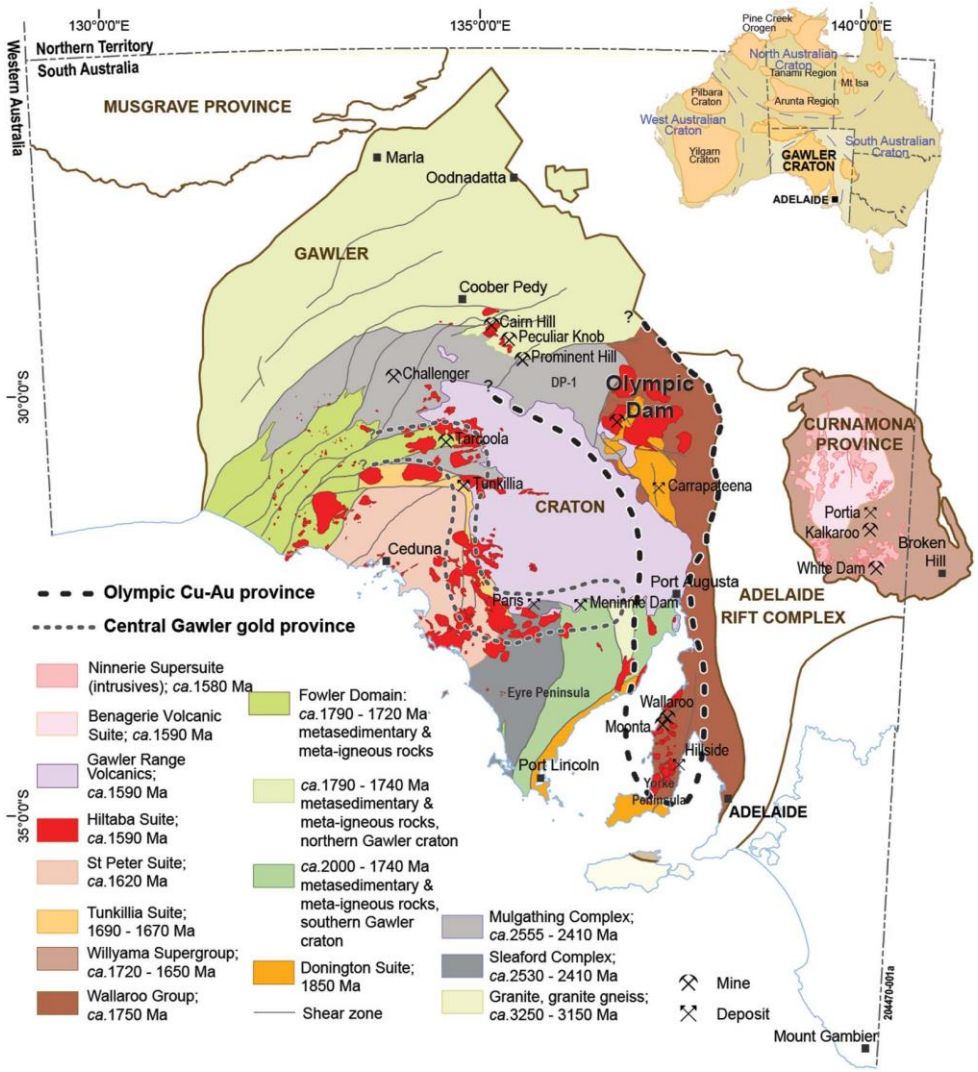

Figure 1. Regional geological setting (modified from Reid & Fabris, 2015) of OD in the Gawler Craton, South Australia showing the main lithotectonic elements. The inset provides context with respect to selected pre-Cambrian terranes of Australia.

hydrothermal feldspars occurring up to several kilometres away from mineralisation.

Infrared reflectance spectroscopy on drill core has been used to define compositional changes in feldspars, muscovite and chlorite in the distal and proximal areas of a range of mineralised systems (e.g. Cudahy et al., 2009; Huntington et al., 2004; Mauger, Gordon, Reid, & Kitto, 2012; Scott & Yang, 1997; Tilley et al., 2014; Travers & Wilson, 2015). Compositional changes of white micas proximal to mineralisation at the Olympic Dam (OD) deposit were published by Tappert, Rivard, Giles, Tappert, & Mauger (2011, 2013). The study reported here utilised HyLogger-3^{TM} to assess potential aluminosilicate compositional changes across the entire exposed ore-forming system at OD. As such, the HyLogger method is the primary focus of this paper including the broader geological and exploration implications.

Olympic Dam geology and mineralogical zonation

The Olympic Dam Cu–U–Au–Ag deposit is hosted within the Olympic Dam Breccia Complex (ODBC), which occurs entirely within the Mesoproterozoic RDG (Reeve et al., 1990). The RDG is part of the regional Hiltaba Suite granites, which intruded the Paleoproterozoic Hutchinson Group metasediments and iron formations, Donington Suite granitoids, Wallaroo Group metasediments and volcanics, and the Gawler Range Volcanics (Hand, Reid, & Jagodzinski, 2007). The deposit is overlain by approximately 350 m of Neoproterozoic to Cambrian sedimentary rocks of the Stuart Shelf (Preiss, 1993).

The ODBC consists of weakly to intensely altered and brecciated clasts of the major and minor constituent rock types. The primary host rock within the ODBC is the RDG [≈50 vol% alkali feldspars, subequal amounts (20–25 vol%) of plagioclase and quartz, with minor concentrations of biotite, amphibole, magnetite, titanite, apatite, fluorite, ankerite, synchysite, allanite and uranothorite] (Reeve et al., 1990). However, subordinate bedded clastic facies and mafic–ultramafic lavas/dykes are also present within the ODBC (Figure 2). Variably altered clasts of *ca* 1590 Ma Gawler Range Volcanic felsic feldspar-phyric lavas are also present (Ehrig et al., 2012, McPhie, Orth, Kamenetsky, Kamenetsky, & Ehrig, 2016). The Gairdner Dyke Swarm (GDS) dolerite dykes (*ca* 830–820 Ma, Huang et al., 2015) intrude the ODBC and RDG. The ODBC has an areal extent of approximately 50 km^2 at the contact with the overlying Stuart Shelf sedimentary rocks (cover sequence). The ODBC contact with the least-altered to weakly altered RDG is gradational and is defined by the last occurrence of biotite ('biotite-out' in Figure 2) when moving from RDG towards the outer edge of the ODBC (Ehrig et al., 2012). Alteration intensity and brecciation increase gradually from the outer edges of the ODBC towards the geographic centre of the deposit.

Feldspar alteration commences in the least-altered RDG (distal to the ODBC), continues into sericite + hematite altered RDG and mineralised RDG (on the outer edges of the ODBC) and finally ends in the barren hematite + quartz + barite breccias (central parts of the deposit). Early igneous feldspars (outside the ODBC/biotite–out contour, Figure 2) consist of $\sim An_{27–34}$ and $\sim An_{12–20}$ (more abundant) plagioclases and $\sim Or_{55}Ab_{43}An_2$ alkali feldspars. Rapakivi and anti-rapakivi textures are present. The transition from cryptoperthite to patch perthite textures records the post-magmatic evolution of the alkali feldspars. Highly porous, near end-member albite and K-feldspar overprint patch perthite and albite + sericite ± Ba-rich K-feldspar replace igneous plagioclase. Within the ODBC, all igneous plagioclase is replaced by sericite, primary mafic minerals are not preserved, and the abundance of hematite and sulfides increases relative to the least-altered RDG. Most K-feldspar is replaced by sericite, and albite is partially preserved at depth (Kontonikas-Charos et al., 2017).

The mineralised rock volume is approximately 6 km long and 4 km wide, and extends typically to depths of 800 m beneath the cover sequence, with mineralisation occurring locally to depths as much as 2.3 km beneath the surface. Disseminated pyrite, copper sulfide (chalcopyrite, bornite, chalcocite), uraninite, coffinite, brannerite and Au–Ag mineralisation is associated with intense, texturally destructive, hematite and sericite alteration and brecciation. There is a positive spatial correlation of Cu, U, Au, Ag and hematite (Reeve et al., 1990). The dominant gangue minerals in the deposit are hematite (±magnetite), quartz, sericite, chlorite, fluorite, siderite, barite and K-feldspar (Oreskes & Einaudi, 1990).

According to Ehrig et al. (2012), three hydrothermal alteration assemblages (magnetite + apatite + siderite + chlorite + quartz, hematite + sericite + fluorite and hematite + quartz + barite) within the ODBC reflect the transition from early, deep Fe^{2+} to late, shallow Fe^{3+} and sulfide to sulfate-dominated conditions. Sulfide mineral zonation (i.e. distal and deep to proximal and shallow) includes sphalerite → galena → pyrite → chalcopyrite → bornite → chalcocite → native copper, with further evidence for an early base-metal-poor association of Mo–W–Sn–As–Sb mineralisation having been overprinted by base metal-rich (Cu–Pb–Zn) mineralisation.

Sample selection

The primary purpose of this study was to determine whether reflectance spectroscopy could identify systematic mineralogical changes within the relatively unaltered RDG distal to the ODBC and mineralisation. A secondary purpose was to use reflectance spectroscopy to verify alteration types in all major and minor rock types and mineralisation styles. Diamond drill holes were selected along a 14 km-long SW–NE cross-section of the system (Figure 2), which traversed from least-altered RDG into the ODBC, through mineralisation and barren core, and finally returning to unaltered RDG. The section contains 26 drill holes. Four additional off-section drill holes were also selected to ensure that all major and minor lithological types were scanned. Locations of each scanned drill hole are shown in Figure 2. These 30 drill holes totalled 20 000 m of diamond core. The average length for the vertical to near-vertical drill holes is 950 m, but the actual lengths vary from 465 m to 2329 m. Drill holes were also selected on the basis of their physical condition; the most intact with high core recovery were preferred. HyLogger-3 technology is compromised when the core is presented as quarter section remnants in the bottom of metal trays. Interference from the surrounding metal tray may also degrade the spectral response and thus affects the interpretation of mineralogy from the spectra (Schodlok et al., 2016a).

Methodology

Data collection

Diamond drill core was shipped from the OD mine core storage facility to Adelaide (Glenside Drill Core Storage Facility) for scanning and returned to the mine site after analysis; 2000 m per shipment in 3-week rotations. Dry, clean core was scanned using the HyLogger-3 (Schodlok et al., 2016a), which delivered four data streams that comprised an integrated

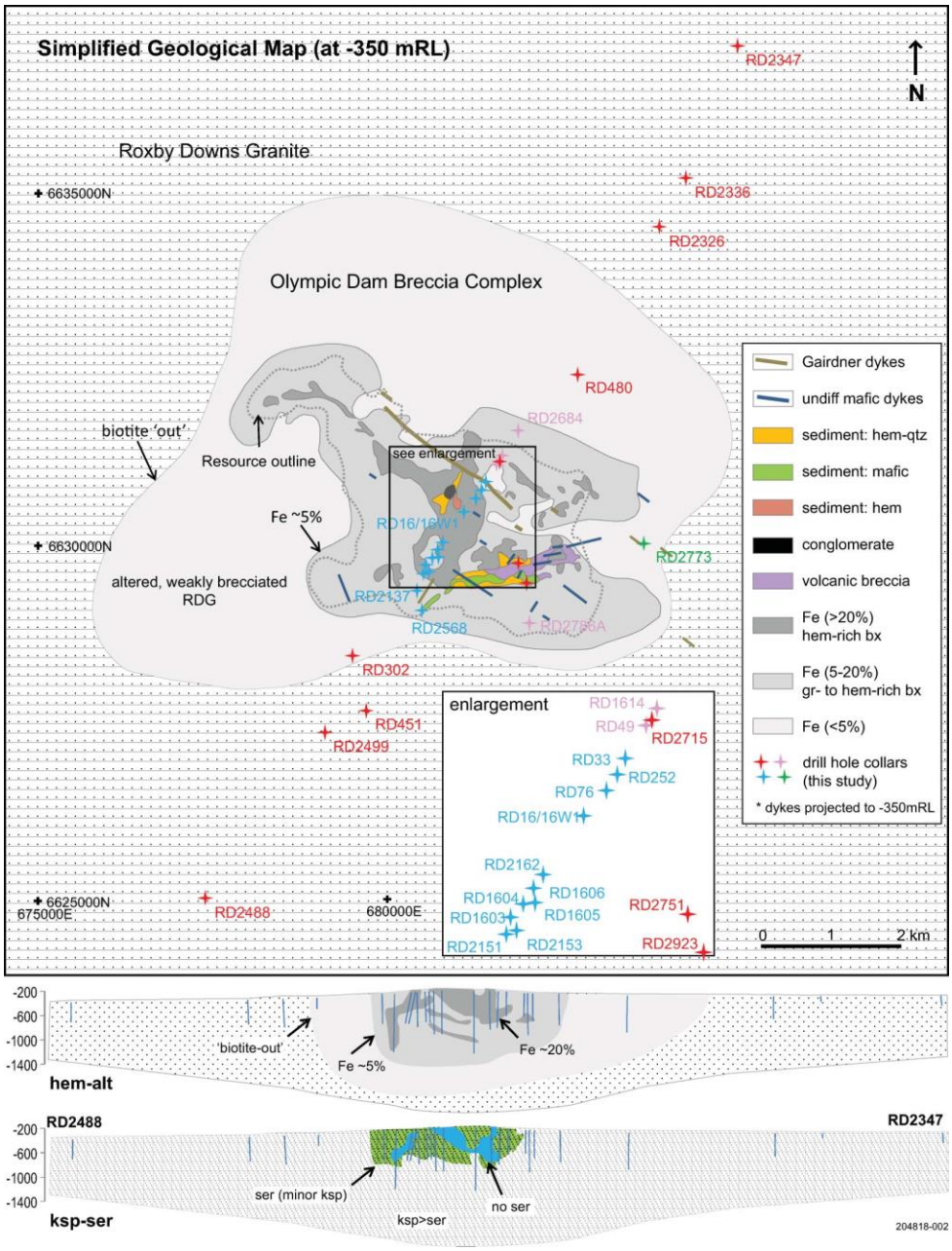
Simplified Geological Map (at -350 mRL)
N
Roxby Downs Granite
6635000N
6630000N
6625000N
675000E
680000E
Olympic Dam Breccia Complex
biotite 'out'
Resource outline
Fe ~5%
see enlargement
altered, weakly brecciated RDG
RD2347
RD2336
RD2326
RD480
RD2684
RD16/16W1
RD2773
RD2137
RD2568
RD2736A
RD302
RD451
RD2499
RD2488
enlargement
RD1614
RD49
RD2715
RD33
RD252
RD76
RD16/16W1
RD2162
RD1604
RD1606
RD1603
RD1605
RD2751
RD2151
RD2153
RD2923
Gairdner dykes
undiff mafic dykes
sediment: hem-qtz
sediment: mafic
sediment: hem
conglomerate
volcanic breccia
Fe (>20%) hem-rich bx
Fe (5-20%) gr- to hem-rich bx
Fe (<5%)
drill hole collars (this study)
* dykes projected to -350mRL
0 1 2 km
-200
-600
-1000
-1400
'biotite-out'
Fe ~5%
Fe ~20%
hem-alt
RD2488
RD2347
ser (minor ksp)
ksp>ser
no ser
ksp-ser
204818-002

package of high-resolution colour imagery, visible to shortwave infrared reflected light spectra (VIS-SWIR), reflected thermal infrared spectra (TIR) and a laser profile measured lengthways along the centre of the core. These four data streams were collected by four instruments physically located 100 mm from each neighbour. Each instrument provided data at different spatial resolutions (Schodlok et al., 2016a), which were resampled to the following specifications: 8 mm VIS-SWIR and TIR spectra; 0.125 mm three-band colour image; 0.0625 mm laser profile. When viewed interactively using 'The Spectral Geologist—Core' (TSG) software (Merry & Pontual, 2016), all four data streams were co-located, having undergone co-registration during the importation of the raw data.

During scanning, the depths from the start and end of each tray were entered by the operator. These numbers are commonly insufficient to accurately record a depth hiatus such as that caused by core loss during drilling. This depth information was refined during post-processing using a technique called 'interactive depth logging.' The output was a non-linear scalar (numerical list) registering depths drilled against the index number for each spectrum in the core. This depth scalar performs a critical role in data presentation and reporting. It also provides the link between external data sets such as assays and the HyLogger data. Any comma-delimited text (csv) file with 'from' and 'to' depth fields can be imported into the TSG file for analytical and comparative purposes.

Data processing

The laser profilometer was used during processing to assess the quality of the core and to identify gaps in the core strings within the trays. A mask was produced using, in part, the laser data to eliminate those components of the data that did not represent mineralogy related to the lithologies that were drilled, e.g. bottom of core tray, writing on the core or core depth markers.

Data from each of the three wavelength ranges were analysed separately: visible-near infrared (VNIR), shortwave infrared (SWIR) and thermal infrared (TIR). The logic behind this separation is based on the understanding that the physical processes being measured in the sample are different for each of the three wavelength ranges. Each wavelength range has its own spectral library. Mineral species spectra in one range are not necessarily available in the other two.

The presence and quantity of minerals present at a particular point on the core were determined using 'The Spectral Assistant' (TSA) algorithm, a component of TSG. The algorithm embedded in TSA (Berman & Bischof, 1997) is a form of end-member unmixing, a technique widely used in hyperspectral image processing. The potential end-members present in the data are provided in a spectral library (Schodlok, Green & Huntington, 2016b), which has been prepared using well-characterised samples, some of which are preserved in museums and other collections. This library consists of groups of 12 VNIR, 47 SWIR and 110 TIR replicate mineral spectra incorporating minerals regardless of geological affinity. By mathematically constraining the library to only those minerals that may be present based on the geology of the environment being studied, the quality of the result improves markedly, and the speed of processing increases. The risk of excluding a potential candidate is elevated but can be compensated by examining residuals from modelling and reinstating excluded components as necessary.

The easiest method of interaction with TSA is through the 'Summary' screen in TSG. On the 'Summary' screen, the operator can 'Change TSA's allowed minerals.' For this plot, both the 'bin' size and the noise reduction option, called the 'subset percentage,' need to be used in a consistent manner within a single project where multiple holes are compared. In this case, a bin size of 5 m and no noise reduction were chosen. The subsets of minerals in the libraries used for the OD study are listed in Table 1. The advantage of the 'Summary' screen presentation is that all minerals are reported together irrespective of whether they are major or minor components of the core sample. By binning into a histogram, a larger statistical sample (maximum of 625 spectra) is collected rather than results from a single spectrum.

TSA reports, by default, minerals contributing greater than 15% towards the combined spectra measured from the 64 sq. mm area of sample. The 15% is user-changeable. Again, by default, for the VNIR and SWIR only two minerals are reported and in TIR, three. Every spectral pixel can, potentially, yield up to seven component minerals. Based on the senior author's thin-section observations from a variety of deposits, it is clear that heterogeneity and grainsize will influence how well seven minerals can represent the complexity of a natural mixture of those dimensions.

Analysis of TIR spectra using TSA revealed a limitation to the implementation of the algorithm. This arose from the observation that minerals do not have unique TIR spectra, but rather, that a mineral may have several signature TIR spectra. The reasons for this are numerous, and include, but are not restricted to, crystallographic orientation of observation, grainsize, surface roughness and fine surface dusting. In order to accommodate such variability into the TSA algorithm, all variants of each mineral were provided to the library.

Figure 2. Geological map and cross-sections of OD depicting the major basement rock/alteration types. The 'biotite-out' contour (Ehrig et al., 2012) represents the last occurrence of biotite [moving from the Roxby Downs Granite (RDG) towards the deposit centre] and defines the outer extent of the Olympic Dam Breccia Complex (ODBC). Drill holes reported in this study are located along a SW–NE drill traverse. Drill holes depicted in red, green, blue are described in Figure 7. Areas shaded with different grey levels show the progressive increase in iron concentration (i.e. <5%, 5–20%, >20%) moving towards the deposit centre. Other features are Gairdner dolerite dykes (Huang et al., 2015), *ca* 1590 Ma mafic and ultramafic dykes (abbrev. undiff mafic dykes), interbedded sandstones and red mudstones (sediment: hm–qtz), green sandstones and mudstones (sediment: mafic) sourced from mafic–ultramafic lithologies, thinly bedded mudstones (sediment: hm), polymictic volcanic clast-conglomerate (conglomerate) and breccias with feldspar-phyric felsic volcanic clasts (volcanic breccia). The Fe 5% contour below the level of drilling is for schematic purposes. The upper cross-section shows the progressive increase in Fe concentration (hem–alt). The lower cross-section shows the logged relative abundance of K-feldspar and sericite [i.e. ksp > ser, ser (minor ksp), no ser].

Table 1. Constrained VNIR-SWIR-TIR spectral library used for OD (TSG Version 7 Minerals).

VNIR mineral	TIR mineral	TIR mineral
Goethite	Quartz	Amphibole ML48
Hematite	Anorthoclase	Edenite
	Microcline	Ferro-hornbl.
SWIR mineral	Orthoclase	Hornblende
Dickite	Albite	Kaersutite
KaolinitePX	Anorthite	Tschermakite
KaoliniteWX	Bytownite	Anthophyllite
Nacrite	Labradorite	Gedrite
Muscovite	Andesine	Grunerite
Paragonite	Oligoclase	Holmquistite
Phengite	Augite	Mn-cummingt.
Diaspore	Diopside	Arfvedsonite
Pyrophyllite	Hedenbergite	Glaucophane
Topaz	Enstatite	Tourmaline
ChloriteFe	Fayalite	Ankerite
ChloriteFeMg	Forsterite	Siderite
ChloriteMg	Olivine	Calcite
Biotite	Zircon	Dolomite
Phlogopite	Kaolinite	Dolomite Fe
Actinolite	Kaolinite PX	Barite
Hornblende	Illite	Gypsum
Tourmaline	Muscovite	Apatite
TourmalineFe	Paragonite	Cassiterite
Ankerite	Pyrophyllite	Hematite
Siderite	Topaz	Ilmenite
Calcite	Chlorite	Magnetite
Dolomite	Biotite	Chromite
Gypsum	Phlogopite	Rutile
MuscoviticIllite	Actinolite	
ParagoniticIllite		
PhengiticIllite		

The issue then arose that all three possible mineral selections assigned by TSA to a single TIR spectrum could potentially be allocated to the same mineral. TSA then fails to report the actual heterogeneity of the sample.

Two recent refinements provide tools within TSG to address these shortcomings. The first introduces the concept of domains. By subdividing the drill hole into zones of geologically logical mineral associations ('domains'), the mineral spectral libraries can be further limited within each zone. For example, where a mafic igneous body, such as a dyke, has intruded metasediments those minerals that are unique to the dyke can be isolated to the dyke separate from the host rocks. TSA has the option of recognising the domains and their particular library subsets. The second development is to substitute an alternative classification technique to TSA. Constrained least-squares fitting (CLS) (Schodlok et al., 2016a) utilises domaining to operate on a reduced mineral library, but the algorithm is faster and enables a greater number of components to be reported in the results. The risk is that CLS may over-fit the spectral curve with too many components in the solution. This can also be controlled via the use of residuals, geological insight and seeking a minimum solution using a restricted mineral set or RMS (Schodlok et al., 2016a) rather than a total solution.

Once the operator is satisfied with the results presented in the 'Summary' screen, the mineral abundances or scalars can be extracted as comma-delimited text files. Even though extensive spectral detail is available for the 30 scanned drill holes (e.g. a total of 2 944 736 mineral spectra), it was necessary to sub-sample each drill-hole dataset so that the subsequent analysis external to TSG was manageable and to identify systematic mineral changes across the whole ore-forming system.

Plagioclase, K-feldspar, white mica and chlorite spectral characteristics

Cudahy *et al.* (2009) successfully demonstrated the use of thermal infrared (TIR) to determine plagioclase composition in Archean gold mineral systems. TIR library spectra for pure species in the plagioclase solid solution from albite (Na end-member) to anorthite (Ca end-member) exhibit systematic variation along the series reflecting the chemical transition. It is possible to monitor not only absorption features but also peaks. First-pass analysis reveals four spectral features of plagioclase whose changing wavelength appears to correlate with changing chemistry: 7945–8241 nm [spectral absorption feature (minima)], 8537–8875 nm [spectral reflection peak feature (maxima)], 9002–9256 nm (minima) and 9289–9933 nm (minima). The two best discriminators are the 7945–8241 nm (minima) and 8537–8875 nm (maxima) features, where each feature moves to longer wavelengths with increasing Ca, such that an approximately 50 nm shift occurs with every 20% increase in anorthite (An) content.

Microcline and orthoclase have distinct TIR spectral characteristics. At wavelengths 12981 nm and 13704 nm, the microcline spectra display distinctive reflection peaks, which are subdued to absent in orthoclase (Figure 3). The region between 8160 nm and 10233 nm exhibits complex reflection and absorption features for all K-feldspar; however, orthoclase presents with a simple two-peaks-and-a-trough signature. Microcline has four peaks with the 9558 nm peak of orthoclase splitting into three peaks that vary in location. The lower wavelength peak ranges from 8561 nm to 8739 nm and appears to be a common feature of the K-feldspar series. There are sufficient observable differences between microcline and orthoclase to be confident that TSA or CLS can separate the mineral species.

White micas and chlorites in the shortwave infrared wavelengths have received comprehensive attention (Huntington *et al.*, 1999). Their characteristics can be summarised as follows. White mica or sericite includes members of the muscovite solid solution series from muscovite through phengite to celadonite (Monier & Robert, 1986). The significant chemical change is the loss of Al, as it is replaced by Fe and/or Mg. This change was identified in the spectral response by the changing wavelength of the key 2200 nm absorption feature, which tends to move towards longer wavelengths in proportion to the loss of Al.

Chlorites also display changing spectral characteristics depending upon the relative proportions of Fe and Mg in the crystal lattice. The 'Mg number', calculated as Mg# = 100 × [MgO / (FeO + MgO)] (mol. %), measures the chemical gradient between the Fe and Mg end-members of the chlorite solid solution series (Tilley et al., 2014). Both the 2250 nm and 2350 nm absorption features in chlorite change systematically with variations in the Mg number. In both instances, the

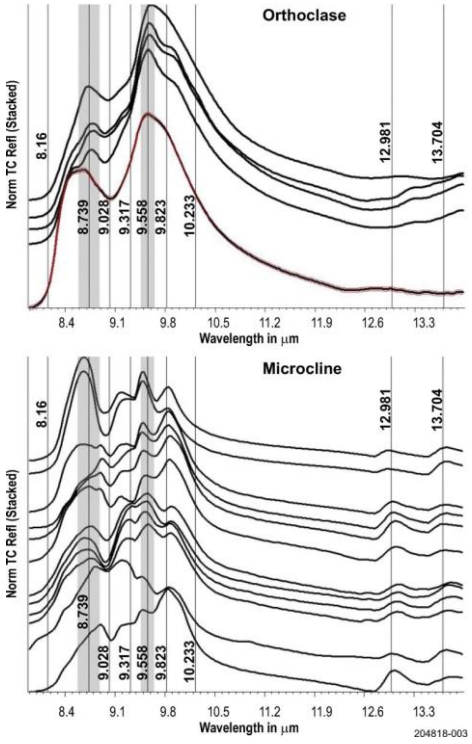

Figure 3. Comparison of orthoclase (top) with microcline (bottom) thermal infrared reflectance spectra courtesy of CSIRO (TSA-TSG TIR reference set MS3, 2011, pers. comm.). The x axis shows the wavelength (μm). The y axis is normalised temperature-corrected reflectance (stacked). In the text, key features are identified by their wavelengths in nanometres, e.g. the 8739 nm feature in the text is the 8.739 μm feature in this figure. Points of difference of note between orthoclase and microcline are (a) the different number of maxima around 9.558 μm and (b) the two features of microcline at 12.981 μm and 13.704 μm.

wavelength positions move to longer wavelengths with increasing Fe content.

Results

Graphs of the TIR and SWIR mineralogy results for each drill hole were produced to quickly assess if any systematic changes in mineralogy occurred when progressing (1) down each drill hole and (2) from distal to proximal, and then back to distal across the entire deposit. The TIR and SWIR mineralogy (as relative weight percentage) graphs for each drill hole at the resolution of 5 m intervals are shown in the Supplementary Papers.

RD2773: the deepest drill hole at Olympic Dam

As an example of results delivered for each drill hole, we describe RD2773, which is the deepest near-vertical oriented drill hole at OD and is located on the southeast margin of the deposit (Figure 2). Results for this hole are presented using graphic tools from TSG in Figure 4. Typical examples of drill core intervals discussed below are shown in Figure 5. The cover sequence rocks cored from 245 m (down hole depth) consist of shales [Figure 5 (1); Tregolana Shale] characterised by white mica, albite and quartz. A basal conglomerate, approximately 29 m thick, occurs below the shales. The basement rocks (extending from 370 to 2328.9 m) are dominated by RDG, GDS dolerite to basaltic dykes and so-called 'deep mineralisation' adjacent to an intensely altered sub-volcanic (?) felsic unit that texturally appears to predate RDG (Apukhtina, 2016). The upper parts of the basement (~370–1000 m depth) consist of sericite-altered and very weakly brecciated RDG with phengite > muscovite, subequal amounts of orthoclase and microcline, and minor amounts of albite [Figure 5 (2)]. The middle section (~1000–1750 m) contains chlorite-altered RDG [Figure 5 (3, 5)] with Fe-rich chlorite, subequal muscovite and phengite, orthoclase, microcline, oligoclase and minor amounts of albite. This domain is intruded by subvertically oriented GDS dolerites/basalts (~1250–1375 m) [Figure 5 (4)], which is distinct from altered RDG by the presence of pyroxene and Mg-rich chlorite. The deepest part of the drill hole (~1750–2200 m) intersects an intensely sericite-altered sub-volcanic (?) felsic unit [Figure 5 (6)] with muscovite but lacking orthoclase and microcline. Paragenetically early magnetite–apatite–pyrite–chalcopyrite-uraninite mineralisation [Figure 5 (7)] is associated with the contact between the felsic unit and phengite-altered RDG from ~2200–2329 m (end of hole), which also lacks orthoclase and microcline.

Aluminosilicate mineralogical trends

In this section, we focus on aluminosilicate mineralogical changes outside the areas of mineralisation with the goal of identifying systematic changes in the major rock-forming minerals in the RDG distal to significant iron-oxide alteration. Scalars selected for interpretation were: quartz, K-feldspar (microcline and orthoclase), Na-feldspar (albite and plagioclase >An10), white mica (muscovite and phengite), chlorite (Fe-chlorite and Fe–Mg-chlorite) and Cu assay values (ppm).

One method of presenting the data, which allows for deposit-scale mineralogical/chemical trends to be identified with respect to any scalar involves reporting single values per hole (e.g. 'metres of mineral per drill hole') and plotting these values in the relative spatial positions along the cross-section. 'Metres of mineral per drill hole' is derived from recording every pixel that registers that mineral in its spectra and assigning a value of 0.8 cm (the size of the pixel) times its weight proportion in the mixture of that pixel, and then totalling those numbers over the section scanned.

The maximum Cu concentration in the basement samples from each drill hole, white mica and chlorite wavelength variation, 'metres of mineral per drill hole' for microcline–orthoclase and albite–oligoclase, and the ratios of microcline

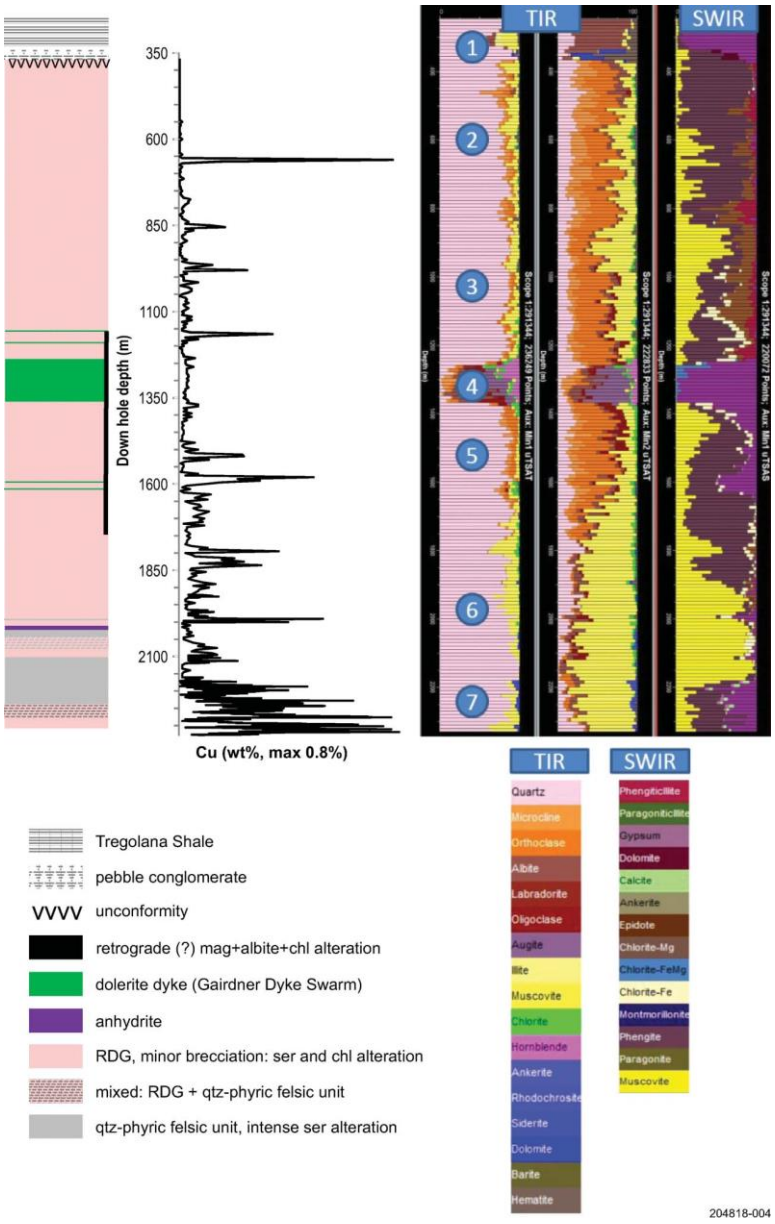

Figure 4. Drill hole RD2773 down hole plots of logged geology/alteration, Cu (wt%), spectra and mineral interpretations using 'The Spectral Geologist—Hot Core' software. The three spectral columns on the right are histograms showing the relative abundance of mineral species distributed down the hole. The two TIR columns relate to mineralogy determined from the thermal infrared spectra. The left column presents the dominant mineral in the core, and the right-hand column displays the second most dominant mineral. The SWIR column relates to the dominant minerals identified in the shortwave infrared spectra. The two far-right columns are colour legends for the TIR and SWIR mineralogy columns. Refer to Figure 5 for a discussion of the circled numbers.

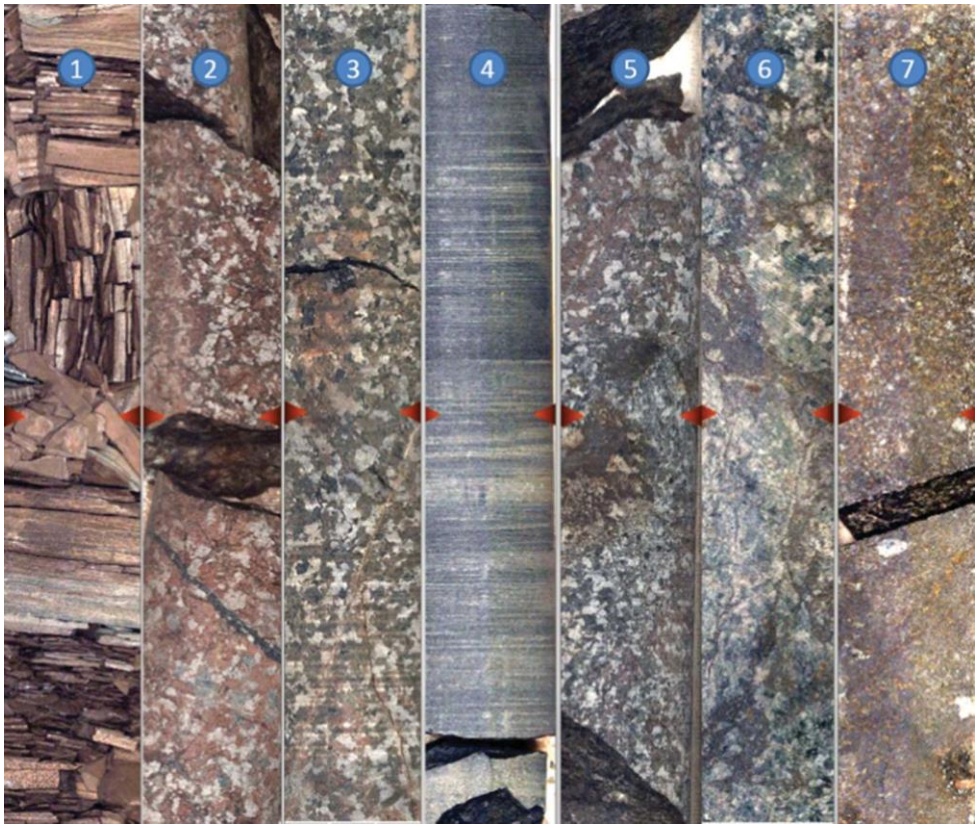

Figure 5. Diamond drill core images from key domains down RD2773. The numbers refer to locations in Figure 4. Images are: (1) 280.29–280.56 m, Tregolana Shale; (2) 560.27–560.57 m, phengite-altered RDG; (3) 1121.36–1121.66 m, weak albite altered RDG; (4) 1340.44–1340.74 m, Gairdner dolerite dyke; (5) 1549.53–1549.83 m, magnetite + albite + chlorite + phengite + muscovite altered Roxby Downs Granite; (6) 1982.65–1982.94 m, muscovite altered, brecciated RDG; and (7) 2208.08–2208.38 m, sulfide-bearing, brecciated and comminuted contact between RDG and quartz-phyric felsic unit.

to orthoclase and albite to plagioclase are plotted for drill holes located along the cross-section (excluding off-section drill holes RD2773, RD2923, RD2786A, RD2751) in Figure 6. The 'biotite-out' contour (Figure 2) is displayed on the Cu profile for reference. Progressing from left to centre in each graph (relatively unaltered RDG → ODBC → mineralisation → barren core), four deposit-scale trends are noteworthy: (1) progressive wavelength shift of 2205 nm to 2210 nm for sericite, followed by a spatially rapid reversal; (2) progressive wavelength shift of 2248 nm to 2252 nm for chlorite; (3) slightly increasing microcline to orthoclase ratio, followed by a rapid decrease; and (4) relatively flat albite to plagioclase ratio, followed by a rapid increase, then decrease. These four trends reflect: (1) a change in the white mica composition; (2) an increase in the Fe:Mg ratio of chlorite; (3) progressive microcline replacement, the possible formation of new orthoclase, followed by replacement of orthoclase; and (4) the presence of significant albite, progressive albite and oligoclase replacement, followed by sudden breakdown of oligoclase causing the peak in the albite to oligoclase ratio at the outer edge of the ODBC. Even though the trends reflect the relative changes in mineral pair abundances (i.e. microcline–orthoclase and albite–oligoclase), the absolute concentrations of the feldspars are decreasing from distal to proximal because of the progressive and extensive replacement of feldspars first by hydrothermal feldspars and sericite, then by sericite + hematite, followed by hematite replacement of sericite.

GOCAD software was used to display both down hole and along section mineralogical/chemical variability. A 3D model volume was prepared encapsulating all drill holes in the project. Using drill-hole down hole survey data and surveyed drill collar locations the drill strings were introduced to the model as drill holes. All the numerical data that TSG produced or stored were exported as .csv files to enable properties to be attached to the

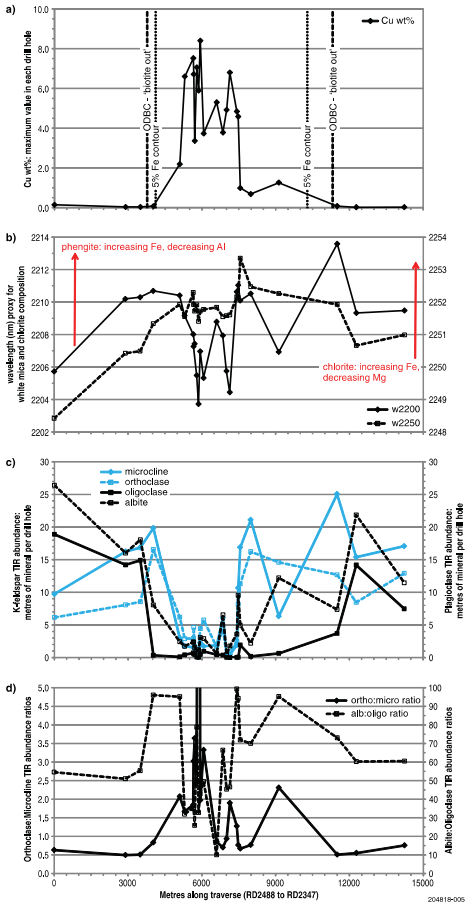

Figure 6. Sections for: (a) maximum Cu values pre-hole, (b) average white mica and chlorite absorption feature wavelengths per hole, (c) metres of mineral per hole: microcline–orthoclase and albite–oligoclase abundances, and (d) ratios of microcline to orthoclase and albite to oligoclase calculated from metres of mineral per hole.

drill holes in GOCAD. A series of cross-sections were prepared as a surface connecting those holes that lie close to the NE–SW section and excluded the off-section holes. The surface was then coloured by interpolating values from the numerical values attached to the drill strings. Warmer colours in the sections represent higher abundances. GOCAD cross-sections aligned with the two geological cross-sections, hematite alteration (hem-alt) and K-feldspar–sericite (ksp-ser) distributions (Figure 7) from top to bottom display Cu concentration, W2200 (i.e. 2200 nm), muscovite, phengite, W2250 (i.e. 2250 nm), Fe-chlorite and Mg-chlorite, orthoclase, microcline, albite and oligoclase (>An10), which provide further support for the four deposit-scale mineralogical/chemical trends mentioned above. Results from the last four drill holes (RD480, RD2326, RD2336 and RD2347) on the northeastern part of the cross-section are not displayed. The southwestern and central parts clearly display systematic variation in aluminosilicate mineral alteration patterns.

Discussion

Based on whole-rock chemistry and bulk mineralogy, Ehrig *et al.* (2012) described deposit-scale hydrothermal alteration of magmatic aluminosilicate minerals when progressing from the least-altered RDG, through weakly altered and brecciated RDG, and into hematite alteration and mineralisation at the OD deposit (Figure 2). Detailed microscopic characterisation of the feldspars by Kontonikas-Charos *et al.* (2017) showed, for the first time, post-magmatic alteration of plagioclase and K-feldspar, in the least-altered RDG, via the formation of replacive albite and porous hydrothermal K-feldspar. The study documented distal, isochemical magmatic feldspar replacement and the subsequent systematic alteration of replacive albite and hydrothermal K-feldspar by sericite and hematite towards mineralisation. HyLogger with TIR results presented in the current study (Figures 6 and 7) also reveal the presence of albite distal to the ODBC and the preservation of albite relics within areas of sulfide mineralisation, and systematic changes to plagioclase and K-feldspars at the deposit scale, which correspond to the major distal to proximal alteration zones described by Ehrig *et al.* (2012) and Kontonikas-Charos *et al.* (2017). However, HyLogger with TIR apparently does not have the ability to resolve magmatic from hydrothermal albite and K-feldspar. It did identify orthoclase and microcline, the latter of which Kontonikas-Charos *et al.* (2017) did not describe. Further mineralogical characterisation (such as XRD or automated modal mineralogy methods) is required to determine if the chemical differences between magmatic and hydrothermal K-feldspar are of sufficient magnitude to cause spectral shifts that HyLogger TIR can detect.

Paragentically early albitisation (i.e. albite replacement of feldspars, Mg-chlorite replacement of mafic minerals, and alteration of Fe–Ti oxides by rutile) preserved as relicts within the alteration system is not unique to OD. Early rare albite was previously recognised in the OD region at the Murdie Murdie prospect as 'microcline that replaced albite' and at the Emmie Bluff prospect as 'albite veins … found within the rhyodacite' (Bastrakov, Skirrow, & Davidson, 2007). Skirrow *et al.* (2007) noted that 'K-feldspar-bearing magnetite–calcsilicate alteration is known mainly from the OD district, where early albite alteration has been almost entirely replaced by K-feldspar.' According to Hayward and Skirrow (2010) 'albitic alteration is rare in the OD district, but it may be present at deeper levels where large-scale magnetite alteration is interpreted from geophysical modelling.'

White mica results (Figures 4, 6 and 7) are consistent with trends observed within the OD deposit (Tappert *et al.*, 2011, 2103) and other IOCG occurrences in the Olympic Domain of the eastern Gawler Craton (e.g. Emmie Bluff; Huntington *et al.*, 2004). Distal muscovite is depleted in Al, which is replaced by Fe producing a more phengitic white mica proximal to

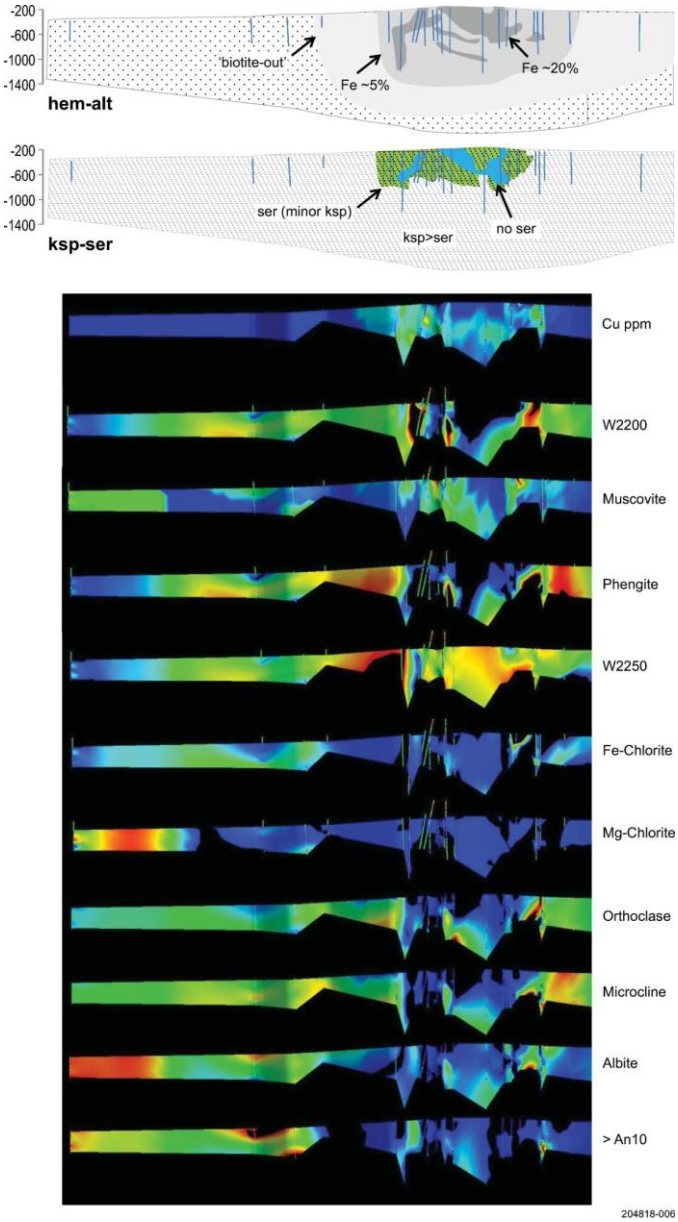

Figure 7. GOCAD sections aligned with two geological cross-sections, hematite alteration (hem-alt) and K-felspar–sericite (ksp–ser) distribution, showing Cu values, W2200, muscovite and phengite W2250, Fe-chlorite and Mg-chlorite orthoclase, microcline, albite and An > 10 variations with depth along the SW–NE cross-section. Warmer colours indicate higher values or higher abundances. The Fe 5% contour below the level of drilling is for schematic purposes in the upper cross-section. Also note that Mg-chlorite in the least-altered RDG replaces the primary ferromagnesian minerals. This Mg-chlorite is replaced by sericite. Mg-chlorite is present in RD2488, least-altered RDG, at the southern end of the cross-section line. The apparent sharp increase in Mg-chlorite between RD2488 and RD2499 is a contouring artefact.

Table 2. Normative quartz (Q), alkali feldspars (A) and plagioclase (P) plotted in Figure 8.

Sample	Q	A	P
RD2488	35.41708	24.68256	45.77725
RD2499	37.36938	29.65444	33.95272
RD451	36.82916	31.43031	35.85346
RD302	41.94995	39.07887	22.30678
RD2568	65.37560	9.973981	7.914882
RD2137	60.67238	5.208460	4.736824
RD2151	45.96081	5.271764	5.626454
RD2153	46.33146	6.952329	6.837350
RD1603	58.01827	2.650368	3.211023
RD1604	48.65525	1.529576	1.624835
RD1605	48.07605	1.649129	2.013759
RD1606	45.29440	7.719529	7.212759
RD2162	46.44297	8.465026	8.785899
RD2751	60.38918	3.693864	2.451768
RD16	54.73798	12.53728	9.023382
RD76	35.19323	0.917438	0.763127
RD252	60.86621	1.906406	2.081476
RD33	65.05526	5.586978	4.876905
RD49	60.79508	22.97025	14.55147
RD1614	58.65818	29.85391	16.59540
RD2684	42.34453	38.03924	17.86410
RD480	48.35983	24.99608	23.37651
RD2326	39.93469	40.20004	21.30522
RD2336	36.18646	31.13355	37.90172
RD2347	39.58402	33.80330	28.02169
RD2786a	43.20512	33.27290	14.45916
RD2773	60.84220	14.90015	12.51506
RD2715	45.69262	30.57043	22.58829
RD2923	43.27101	0.509853	1.019706

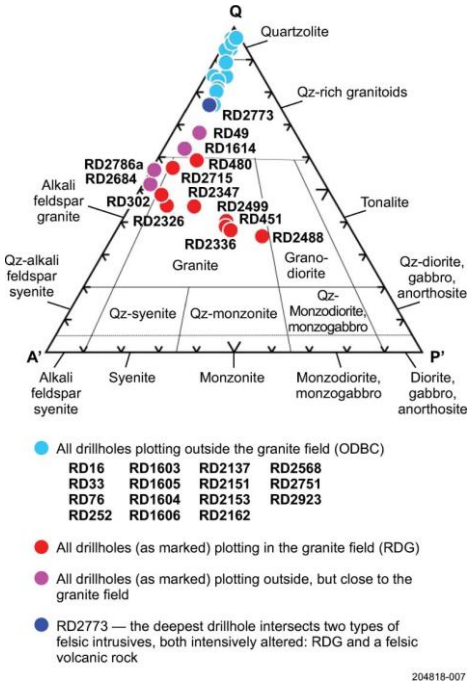

Figure 8. Modified QAPTIR diagram based on CIPW normative compositions calculated from TIR reflectance spectroscopy data and IUGS classification for granitoids rocks intersected in drill holes shown in Figure 2. Q, quartz; A', K-feldspars + 0.33 albite; P', 2/3 albite + all the other plagioclase feldspars identified by TIR. The split between albite compositions is in agreement with the presence of perthitic K-feldspars within the RDG.

mineralisation. The absorption feature at 2200 nm supports this interpretation. The pattern of Mg-chlorite distally and Fe-chlorite proximally to mineralisation at OD was also observed at the Emmie Bluff IOCG prospect (Huntington *et al.*, 2004). The absorption feature at 2250 nm largely measures the continuum between the two-chlorite end-members.

Quartz, K-feldspar and plagioclase abundance data were used to populate a ternary diagram (Figure 8) similar to the standard QAP diagram used by igneous petrologists. For the purposes of this paper, this plot, called the QAP_{TIR} diagram, represents a modified QAP diagram, which is otherwise based on CIPW normative compositions calculated from whole-rock analyses, as given by Kontonikas-Charos *et al.* (2017). Q_{TIR} was scaled by 0.85 because Hill and Mauger (2016) determined an $R^2 = 0.84$ correlation for quartz between XRD analyses and TSG TIR reported weights using a 0.85 regression factor. Additional scaling factors for the P_{TIR} axis of 0.35 and the A_{TIR} axis of 1.25 were used so that holes from the distal RDG plotted close to the 'Fresh RDG' in the 'Granite' field as presented by Kontonikas-Charos *et al.* (2017).

Moving in from 'unaltered' RDG towards mineralisation a trajectory follows increasing alteration of the granite shown by the degree of iron metasomatism from RD2488 towards RD302, then towards RD2568 and RD2923 at the quartz-rich apex in the barren core of the deposit, reverse back towards RD1614, RD2684 and RD2336 out the other side into weakly altered RDG. In summary, the trend starts distally with constant low quartz only changing with respect to the proportion of feldspar species from plagioclase-dominant to K-feldspar-dominant. Closer to the ODBC, the plagioclase is consumed, and the trend moves along the low plagioclase axis until K-feldspar is destroyed, and the only silicate remaining is quartz (Figure 8). This trend reverses between the centre of the ore body and the distal granite.

For the QAP_{TIR} plot, the absolute values for quartz, K-feldspar and plagioclase derived from TSG may be subjected to further refinement as more XRD:TIR correlated datasets become available, but removal of the various scaling factors only reduces the linearity of the plot. The trends from distal to proximal to distal remain. The implication is that using HyLogger data, which provides dense observations, in conjunction with the QAP_{TIR} plot, makes it possible to identify a location within the OD IOCG mineral system along the continuum from distal to proximal. This can potentially serve as a significant vector towards mineralisation.

Retrograde chlorite–albite–magnetite alteration caused by younger mafic dykes

Geological logging of RD2773 revealed that chlorite–albite–magnetite alteration of the sericite ± hematite altered

RDG adjacent to GDS dolerite/basalts is clearly related to the intrusion of the GDS dykes. Fe-rich chlorite replaces earlier formed white mica. Reflectance spectroscopy also revealed the presence of increased concentrations of orthoclase and albite–oligoclase in the chlorite alteration halo around the dolerite dykes. This previously unrecognised alteration is interpreted as retrograde albitisation caused by the dyke intrusion. We postulate that fluid circulation induced by the cooling dyke resulted in albite formation, similar to the growth of replacive albite in the RDG described by Kontonikas-Charos *et al.* (2017). The presence of chlorite–albite–magnetite alteration is typically considered to be distal to ore zones within the ODBC. However, given these new findings, exploration downgrading of an area based on the presence of chlorite–albite–magnetite alteration needs to be reconsidered and evaluated on a case-by-case basis, particularly when GDS intrude ore zones.

HyLogger methodological limitations and improvement opportunities

As discussed in the Data Processing section, HyLogging with VIR-SWIR-TIR sensors is a bulk mineralogical characterisation method, which relies on well-characterised spectral mineral libraries to identify the presence of minerals. As such, it cannot always resolve superimposed metamorphic or alteration events in a sample. Microscopic methods are required to supplement HyLogger results.

The spectral fit and subsequent mineral identification and quantification may not be unique for minerals with complex reflectance spectra. With the interpretation of TIR spectra still a relatively new method, future studies need to focus on a comparison of TIR minerals in mixed mineral systems with other bulk mineralogical methods such as quantitative X-ray diffraction analysis or modal mineralogy determined via automated mineralogical measurements systems with energy-dispersive analysis.

Conclusions and implications

The application of the HyLogger-3 technology with its TIR sensors at the OD deposit has demonstrated its utility in identifying deposit-scale aluminosilicate alteration trends across the entire mineralising system, from distal weakly altered RDG, to areas proximal to mineralisation. An advantage of this technology is in providing a high-density data cloud that enables a higher level of confidence to be given to the interpreted geological trends. The use of the modified quartz–K-feldspar–plagioclase ternary diagram (QAP_{TIR}) offers a new method of identifying vectors towards mineralisation. While the previously understood chemical behaviour of sericite and chlorite in IOCG environments has been confirmed in the present study, the patterns of plagioclase, orthoclase and albite distribution in the OD mineral system have only recently been recognised (Kontonikas-Charos *et al.*, 2017). In the present study, comprehensive hyperspectral logging has extended this documentation to provide a new understanding of the processes of alteration and mineralisation in an IOCG system.

Acknowledgements

BHP Billiton Ltd supported the scanning of 20 000 m of core by providing logistical support in shipping the core to and from Adelaide. The HyLogger 3 technology has been developed by CSIRO and funded by the Australian Government's National Collaborative Research Infrastructure Strategy through the agency of AuScope Pty Ltd. The original prototype was developed in the AMIRA Project P685 completed in 2002. Simon van der Wielen, who assisted with GOCAD modelling, Georgina Gordon, Les Tucker and Sam Williams along with Core Library staff made significant contributions in data collection and processing at various stages of the project. The contributions of the editors, Garry Davidson and an anonymous reviewer are also gratefully acknowledged.

HyLogging, HyLogger, HyLogger-3, TSG and TSA are trademarks of CSIRO. GOCAD is a trademark of Paradigm.

Disclosure statement

No potential conflict of interest was reported by the authors.

Supplementary Papers

HyLogger summary results from 30 drill holes along a 14 km transect through the OD mine. Each graph with its drill-hole name displays, on the upper graph, the TIR mineralogy and, on the lower graph, the SWIR mineralogy plotted as a histogram on 5 m intervals. The minerals are reported as relative weight percent, and the plots have been filtered to remove component minerals representing less than 5% of the graph.

References

Apukhtina, O. (2016). *Distribution, petrology, geochemistry and geochronology of carbonate assemblages at the Olympic Dam deposit* (unpublished PhD thesis). Hobart Tasmania: University of Tasmania, 240 p.

Bastrakov, E., Skirrow, R., & Davidson, G. (2007). Fluid evolution and origins of iron oxide Cu-Au prospects in the Olympic Dam district, Gawler Craton, South Australia. *Economic Geology, 102*, 1415–1440.

Berman, M. & Bischof, L. (1997). The algorithms underlying the Spectral Assistant software. Mathematical and Information Sciences Report 97/87, Exploration and Mining Report 427R. *CSIRO/AMIRA Project P435*. Retrieved from ftp://ftp.csiro.au/arrc/AMIRA P435 Project Reports.

BHP Billiton (2016). Retrieved from http://www.bhpbilliton.com/investors/annualreporting2016)

Cudahy, T., Hewson, R., Cacceta, M., Roache, A., Whitbourn, L., Connor, P., ... Quigley, M. (2009). Drill core logging of plagioclase feldspar composition and other minerals associated with Archean gold mineralization at Kambalda, Western Australia, using bidirectional thermal infrared reflectance system. In R. Bedell (Ed.), *Remote sensing and spectral geology* (pp. 223–235). Littleton, Colorado: Society of Economic Geologists. Reviews in Economic Geology 16.

Ehrig, K., McPhie, J., & Kamenetsky, V. (2012). Geology and mineralogical zonation of the Olympic Dam iron oxide Cu–U–Au–Ag deposit, South Australia. In J. W. Hedenquist, M. Harris & F. Camus (Eds.), *Geology and genesis of major copper deposits of the world* (pp. 237–267). Littleton: Colorado Society of Economic Geologists, Special Publication 16.

Groves, D. I., Bierlein, F. P., Meinert, L. D., & Hitzman, M. W. (2010). Iron Oxide Copper–Gold (IOCG) Deposits through Earth history: Implications for origin, lithospheric setting, and distinction from other epigenetic iron oxide deposits. *Economic Geology, 105*, 641–654.

Hand, M., Reid, A., & Jagodzinski, E. (2007). Tectonic framework and evolution of the Gawler Craton, southern Australia. *Economic Geology, 102*, 1377–1395.

Hayward, N. & Skirrow, R.G. (2010). Geodynamic Setting and controls on iron Oxide Cu-Au (±U) ore in the Gawler Craton, South Australia. In T. M. Porter (Ed.), *Hydrothermal iron oxide copper-gold and related deposits: A global perspective, v. 3-advances in the understanding of IOCG deposits* (pp. 119–146). Adelaide, SA: PGC Publishing.

Hill, A. J., & Mauger, A. J. (2016). HyLogging unconventional petroleum core from the Cooper Basin, South Australia. *Australian Journal of Earth Sciences, 63*, 1087–1097. http://dx.doi.org/10.1080/08120099.2016.1261369

Huang, Q., Kamenetsky, V. S., McPhie, J., Ehrig, K., Meffre, S., Maas, R., … Hi, Y. (2015). Neoproterozoic (ca. 820–830 Ma) mafic dykes at Olympic Dam: Links with the Gairdner Large Igneous Province. *Precambrian Research, 271*, 160–172.

Huntington, J. F., Cudahy, T. J., Yang, K., Scott, K. M., Mason, P., Gary, D. J., Berman, M., Bischof, L., Reston, M., Mauger, A.J., Keeling, J. L., & Phillips, R. N. (1999). Mineral mapping with field spectroscopy for exploration – Final Report. Exploration and Mining report 419R. *CSIRO/AMIRA Project P435*. Retrieved from ftp://ftp.csiro.au/arrc/AMIRA P435 Project Reports.

Huntington, J., Mauger, A., Skirrow, R., Bastrakov, E., Connor, P., Mason, P., Keeling, J., Coward, D., Berman, M., Phillips, R., Whitbourn, L., & Heithersay, P. (2004). Automated mineralogical logging of core from the Emmie Bluff, iron oxide copper–gold prospect, South Australia. *AusIMM Publication Series* No.**5/2004**, PACRIM 2004, Adelaide SA, 19–22 September 2004, 223–230.

Kontonikas-Charos, A., Ciobanu, C. L., Cook, N. J., Ehrig, K., Krneta, S., & Kamenetsky, V. S. (2017). Feldspar evolution in the Roxby Downs Granite, host to Fe-oxide Cu–Au–(U) mineralization at Olympic Dam, South Australia. *Ore Geology Reviews, 80*, 838–859, doi: 10.1016/j.oregeorev.2016.08.019.

Mauger, A., Gordon, G., Reid, A., & Kitto, J. (2012). *Quantifying downhole silicate mineralogy – HyLogger with thermal infrared*. Australian Society of Exploration Geophysicists, 22nd International Geophysical Conference and Exhibition, 26–29 February 2012, Brisbane, Australia.

McPhie, J., Orth, K., Kamenetsky, V., Kamenetsky, M., & Ehrig, K. (2016). Characteristics, origin and significance of Mesoproterozic bedded clastic facies at the Olympic Dam Cu–U–Au–Ag deposit, South Australia. *Precambrian Research*, *276*, 85–100.

Merry, N., & Pontual, S. (2016). TSG documentation, manual and interface. AusSpec International Pty Ltd, In P. Mason, M. Berman, P. Warren, Y. Guo, A. Green, R. Lagerstrom, L. Bischolf, & J. Huntington (1998–2016). The Spectral Geologist. CSIRO Divisions of Earth Science & Resource Engineering, and Mathematics, Informatics & Statistics.

Monier, G, & Robert, J.-L. (1986). Muscovite solid solutions in the system K_2O–MgO–FeO–Al_2O_3–SiO_2–H_2O: an experimental study at 2 kbar P_{H2O} and comparison with natural Li-free white micas. *Mineralogical Magazine, 50*, 257–266

Oreskes, N. & Einaudi, M. T. (1990). Origin of rare earth element-enriched hematite breccias at the Olympic Dam Cu–U–Au–Ag deposit, Roxby Downs, South Australia. *Economic Geology, 85*, 1–28.

Preiss, W. V. (1993). Neoproterozoic. In J. F. Drexel, W. V. Preiss & A. J. Parker, (Eds.). *The geology of South Australia, the Precambrian* (Vol. 1, pp. 171–203). Adelaide, SA: Geological Survey of South Australia Bulletin 54.

Reeve, J., Cross, K., Smith, R., & Oreskes, N. (1990). Olympic Dam copper–uranium–gold–silver deposit. In F. E. Hughes (Ed.), *Geology of the mineral deposits of Australia and Papua New Guinea* (pp. 1009–1035). Melbourne Vic: Australasian Institute of Mining and Metallurgy, Monograph 14.

Reid, A., & Fabris, A. (2015) Influence of pre-existing low metamorphic grade sedimentary successions on the distribution of iron oxide copper–gold mineralization in the Olympic Cu–Au Province, Gawler Craton. *Economic Geology, 110*, 2147–2157.

Schodlok, M. C., Whitbourn, L. B., Huntington, J. F., Mason, P., Green, A. A., Berman, M., ... Martinez, R. (2016a). HyLogger-3, A visible to shortwave and thermal infrared reflectance spectrometer system for drill core logging: Functional description. *Australian Journal of Earth Sciences, 63*, 929–940. doi 10.1080/08120099.2016.1231133.

Schodlok, M. C., Green, A. A., & Huntington, J. F. (2016b). A reference library of thermal infrared mineral reflectance spectra for the HyLogger-3 drill core logging system. *Australian Journal of Earth Sciences, 63*, 941–949. doi: 10.1080/0812009.2016.1234508.

Scott, K. M., & Yang, K. (1997). Spectral reflectance studies on white mica. AMIRA Exploration and Mining Report 439R. *CSIRO/AMIRA Project P435*. Retrieved from ftp://ftp.csiro.au/arrc/AMIRA P435 Project Reports.

Skirrow, R., Bastrakov, E., Barovich, K., Fraser, G., Creaser, R., Fanning, C., ... Davidson, G. (2007). Timing of iron oxide Cu–Au– (U) hydrothermal activity and Nd isotope constraints on metal sources in the Gawler Craton, South Australia. *Economic Geology, 102*, 1441–1470.

Tappert, M. C., Rivard, B., Giles, D., Tappert, R., & Mauger, A. (2011). Automated drill core logging using visible and near-infrared reflectance spectroscopy: A case study using the Olympic Dam IOCG Deposit, South Australia. *Economic Geology*, *106*, 289–296.

Tappert, M. C., Rivard, B., Giles, D., Tappert, R., & Mauger, A. (2013). The mineral chemistry, near-infrared, and mid-infrared reflectance spectroscopy of phengite from the Olympic Dam IOCG deposit, South Australia. *Ore Geology Reviews*, *53*, 26–38.

Tilley, D., Clissold, M., Huntington, J., LeGras, M., David, I., Taylor, B., & Cooper, I. (2014). *Chlorite compositional changes in response to mineralization*. Examples from the Nymagee Mine and Great Cobar deposit NSW. The 3rd National Virtual Core Library Symposium, *AESC 2014*, Newcastle, NSW, Australia, 8 July 2014. Retrieved from http://www.auscope.org.au/wp-content/uploads/2015/12/AESC_Tilley_final_widescreen.pdf

Travers, S. J. & Wilson, C. J. L. (2015). Reflectance spectroscopy and alteration assemblages at the Leven Star gold deposit, Victoria, Australia. *Australian Journal of Earth Sciences*, *62*, 873–882.

Williams, P. J., Barton, M. D., Johnson, D. A., Fontbot, L., De Haller, A., Mark, G., … Marschik, R. (2005). Iron Oxide Copper–Gold Deposits: Geology, Space–Time Distribution, and Possible Modes of Origin. *Economic Geology 100th Anniversary Volume, 37*, 1–405.

ADDITIONAL MATERIAL E

APATITE AT OLYMPIC DAM, SOUTH AUSTRALIA: A PETROGENETIC TOOL

Sasha Krneta[1], Cristiana L. Ciobanu[2], Nigel J. Cook[2], Kathy Ehrig[3], **Alkis Kontonikas-Charos**[1]

[1]School of Physical Sciences, The University of Adelaide, Adelaide, SA, 5005, Australia

[2]School of Chemical Engineering, The University of Adelaide, Adelaide, SA, 5005, Australia

[3]BHP Billiton Olympic Dam, Adelaide, SA, 5000, Australia

Article published in Lithos 262, 470-485.

Lithos 262 (2016) 470–485

Contents lists available at ScienceDirect

Lithos

journal homepage: www.elsevier.com/locate/lithos

Apatite at Olympic Dam, South Australia: A petrogenetic tool

Sasha Krneta [a,*], Cristiana L. Ciobanu [b], Nigel J. Cook [b], Kathy Ehrig [c], Alkis Kontonikas-Charos [a]

[a] School of Physical Sciences, University of Adelaide, Adelaide, SA 5000, Australia
[b] School of Chemical Engineering, University of Adelaide, Adelaide, SA 5000, Australia
[c] BHP Billiton, Olympic Dam, Adelaide, SA 5000, Australia

ARTICLE INFO

Article history:
Received 26 April 2016
Accepted 24 July 2016
Available online 6 August 2016

Keywords:
Fluorapatite
Olympic Dam
Chemical composition
Hydrothermal fluids
Grain-scale zoning

ABSTRACT

The >10,000 million tonne Olympic Dam Cu–Au–U–Ag deposit, (eastern Gawler Craton, South Australia) is one of the largest orebodies in the World. The deposit is hosted within the Olympic Dam Breccia Complex, placed at the centre of, and resulting from multiple brecciation and Fe-metasomatism of the Roxby Downs Granite (RDG). The latter is part of a larger batholith emplaced at ~1.6 Ga. Apatite petrography and chemistry were studied in non-mineralised RDG and coeval granitoids and dolerites, as well as in mineralised RDG from deep (>2 km) and distal (2.7 km to NE) locations. In both latter cases, although the mineralisation corresponds to the same, early chalcopyrite–pyrite–magnetite ± hematite stage identified in the outer and deeper zones of the deposit itself, the character of granite alteration differs: sericite–chlorite alteration with all feldspar replaced in the deep location; and red-stained K-feldspar on top of prevailing albitization in the distal location. Close-to end-member fluorapatite is a key accessory mineral in all igneous rocks and a common product of early hydrothermal alteration within mineralised granite. Variations in habit, morphology and textures correlate with chemical trends expressed as evolving Cl/F ratios, and concentrations of REE + Y (hereafter REY), Sr, Mn, S, Si and Na. Magmatic apatite is unzoned in the dolerite but features core to REY-enriched rim zonation in the granitoids. Increases in Cl- and Sr-contents correlate with rock basicity. Calculation of Cl in the vapour phase relative to melt at the apatite saturation temperature for zoned apatite in the RDG shows higher values for grains with inclusion-rich cores associated with mafic enclaves, concordant with assimilation of exotic material during magma crystallisation. Hydrothermal alteration of magmatic apatite is most varied in the dolerite where interaction with fluids is expressed as subtle changes in Cl- versus F- and REY-enrichment, and most importantly, S-enrichment in grains adjacent to crosscutting, carbonate–sulphide-bearing veins. Highly acidic fluids, which not only corroded apatite but also quartz, led to recycling of REY via subsequent crystallisation of discrete REY-bearing species, notably monazite. Hydrothermal apatite often occurs as interstitial aggregates and displays a wider range of textures indicating variability in local growth conditions and/or sustained interaction with evolving hydrothermal fluids. Apatite from the deep mineralisation is richer in Cl whereas increases in ΣREY and S correlate with higher Si in both deep and distal cases. The co-correlation between Na and S in apatite from distal mineralisation ties apatite crystallisation to replacement of albite by sericite + chlorite. The textural and chemical variation of apatite relative to magmatic to hydrothermal transition suggests that the mineral represents a petrogenetic tool to gain insights into mineralising processes at Olympic Dam. Apatite evolution clearly played a key contributing role in the elevated REY-concentrations seen at Olympic Dam. The marked differences in apatite chemistry between mineralised and non-mineralised lithologies show promise for potential application as a tool in mineral exploration, in which apatite chemistry represents a means for outlining spatial position within an alteration envelope, or identifying if a particular alteration system is barren or fertile with respect to Cu–Au mineralisation.

© 2016 Elsevier B.V. All rights reserved.

1. Introduction

Apatite is a ubiquitous accessory component in igneous rocks, as well as a common hydrothermal mineral. It generally hosts the majority of the whole rock P and a significant portion of the total budget of rare earth elements (REE) and Y (Piccoli and Candela, 2002).

Apatite chemistry is complex and can be defined by the formula $A_5(XO_4)_3Z$ (Pasero et al., 2010), where A is largely occupied by Ca^{2+} in two different positions. The 'A' site also hosts Sr^{2+}, Ba^{2+}, Mg^{2+}, Mn^{2+}, Fe^{2+}, Cd^{2+}, Na^{+}, Eu^{2+}, Y^{3+} and REE^{3+}. The X position is dominated by P^{5+}, as (PO_4), but can also host other small highly-

* Corresponding author.
E-mail address: Sasha.krneta@adelaide.edu.au (S. Krneta).

http://dx.doi.org/10.1016/j.lithos.2016.07.033
0024-4937/© 2016 Elsevier B.V. All rights reserved.

charged cations such as V^{5+}, As^{5+}, Si^{4+} and S^{6+}. Halogens (F and Cl) and OH^{-} occupy the Z position and define the three named minerals, fluorapatite, chlorapatite and hydroxyapatite; most natural apatite contains all three end-members in varying proportions (cf. Hughes and Rakovan, 2015).

Although many of the aforementioned elements substitute directly into apatite, others, such as $(Y,REE)^{3+}$ or S^{6+}, require charge compensation via coupled substitution in order to be incorporated into the apatite structure in Ca^{2+} and P^{5+} positions, respectively. The proposed relevant coupled substitutions (Rønsbo, 1989; Pan and Fleet, 2002):

$$REE^{3+} + Na^{+} = 2Ca^{2+}$$
$$REE^{3+} + SiO_4^{4-} = Ca^{2+} + PO_4^{3-}$$
$$SO_4^{2-} + Na^{+} = PO_4^{3-} + Ca^{2+}$$
$$SO_4^{2-} + SiO_4^{4-} = 2PO_4^{3-}$$

Elemental substitution in apatite is governed by parameters inherent to the apatite structure, as seen in the uptake of REE^{3+} whereby those elements with atomic radii closest to Ca^{2+} (i.e., Sm–Nd) are most readily substituted. However, variation in apatite chemistry can depend on external parameters such that apatite is considered an ideal mineral to fingerprint metasomatic processes and as a tool for tracking fluid interaction in igneous and metamorphic rocks (e.g., Harlov, 2015; Webster and Piccoli, 2015).

Numerous studies have focused on apatite as a petrogenetic indicator of metallogenic processes in different settings. Examples include Iron-oxide–Apatite (Harlov et al., 2002; Bonyadi et al., 2011; Jonsson et al., 2016), Iron-oxide–Copper–Gold (IOCG) (Belousova et al., 2001; Ismail et al., 2014; Kontonikas-Charos et al., 2014), reef-type PGE (Boudreau and Kruger, 1990), and magmatic–hydrothermal systems (Streck and Dilles, 1998; Cao et al., 2012).

In this contribution, the textural and geochemical evolution of apatite is described in the context of the magmatic-to-hydrothermal transition associated with metasomatism and early mineralisation in the Olympic Dam Cu–Au–U–Ag deposit, South Australia. Apatite is described in relation to the igneous chemistry, different types of alteration, and mineralisation types, as well as in the context of magmatic evolution and interaction with hydrothermal fluids. Particular emphasis is placed on the utility of apatite to track changes in fluids, its potential use as a petrogenetic tool, and as a mineralisation pathfinder in IOCG systems.

2. Deposit background

The Olympic Dam (OD) Cu–Au–U–Ag deposit (10,100 Mt tonnes @ 0.78% Cu, 0.25 kg/t U_3O_8, 0.3 g/t Au, 2 g/t Ag; BHP Billiton, 2015) is located on the eastern margin of the Archean to Mesoproterozoic Gawler Craton, South Australia. It is by far the largest deposit within the Olympic Cu–Au Province (Skirrow et al., 2007), which stretches some 700 km N–S, and also encompasses other IOCG deposits and prospects such as Prominent Hill, Carrapateena, Hillside, Cairn Hill, Wirrda Well, and Acropolis. All are temporally and spatially associated with a major tectonothermal event at 1.6 Ga (e.g., Hayward and Skirrow, 2010).

The oldest rocks in the OD area comprise deformed, syntectonic granitoids of the ~1.85 Ga Donington Suite (Jagodzinski, 2005), located SE of the deposit area. Regionally, although well outside the deposit perimeter, these are overlain by ~1.76–1.74 Ga meta-sedimentary sequences of the Wallaroo Group (Jagodzinski, 2005). During the ~1.6 Ga tectonothermal event, extensive emplacement of felsic through to mafic–ultramafic intrusive rocks (Hiltaba Intrusive Suite; HIS) occurred coevally with the eruption of the volumetrically large bimodal Gawler Range Volcanics (GRV; Blissett et al., 1993). HIS granitoids include the Roxby Downs Granite (RDG) and Horn Ridge Quartz Monzonite (HRQM) (Creaser, 1989; Fig. 1). Olympic Dam and other deposits in the province are covered by Neoproterozoic, Cambrian, and later sedimentary successions up to hundreds of metres in thickness.

The OD deposit is confined to the Olympic Dam Breccia Complex (ODBC; Reeve et al., 1990), and is hosted within the Roxby Downs Granite (RDG) (1588 ± 4 Ma; Creaser, 1989; Johnson and Cross, 1995). The ODBC is made up primarily of various hydrothermal breccias,

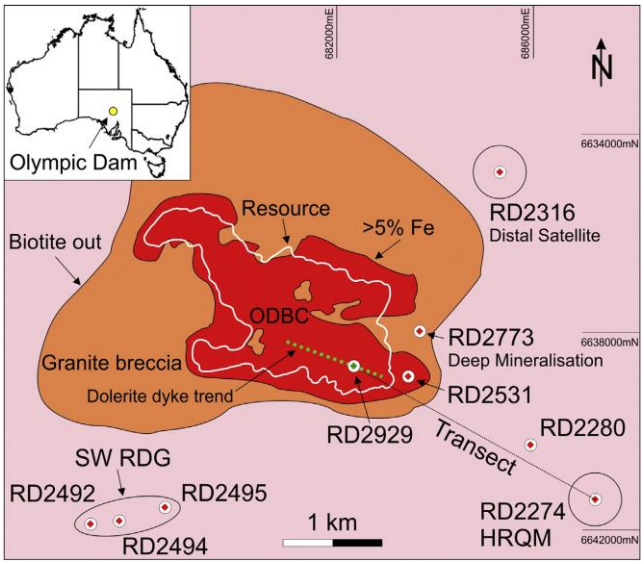

Fig. 1. Geological sketch map of the Olympic Dam deposit at RL-350 showing the location of the studied/sampled drillholes (modified from Ehrig et al., 2012). Insert shows the location of Olympic Dam.

variably altered RDG, coeval felsic through to mafic–ultramafic volcanics (Huang et al., 2016), and a series of bedded clastic facies rocks, all of which are enriched in Fe-oxides. Ehrig et al. (2012) define the boundary of the ODBC at >5% Fe (Fig. 1). Mafic dykes of 0.8 Ga age ('Gairdner dyke suite') crosscut the deposit (Huang et al., 2015; Apukhtina et al., 2016).

Ehrig et al. (2012) provide the most recent and comprehensive overview of the OD deposit, with particular emphasis on element and mineral zonation. Copper–Au–U mineralisation is associated with sericite- and iron-oxide alteration (hematite and subordinate magnetite at depth and at the deposit margins). The current resource broadly overlaps with the boundary of the ODBC (Fig. 1). Economic minerals are Cu–(Fe)-sulphides (chalcocite, bornite, and chalcopyrite), U-minerals (uraninite, brannerite, and coffinite), native gold, and electrum. The deposit also contains disseminations of pyrite and lesser but locally abundant galena, sphalerite, and molybdenite, and is also enriched in F, As, Ba, Bi, Cd, Co, Cr, In, Nb, Ni, Sb, Se, Sn, Sr, Te, V, W, Y, and REE. Deposit-scale zoning is defined by changes in the dominance of particular Cu- and Fe-species. Although apatite is not particularly abundant in the deposit itself (0.1029 wt.% based on 10,000-sample MLA dataset; Ehrig et al., 2012), it is a ubiquitous component of high-grade bornite ore from which the U-bearing hematite has been dated at 1577 ± 5 Ma (Ciobanu et al., 2013).

3. Sampling approach and methodology

The present study describes apatite from samples of two fresh granitoids: RDG (beyond the biotite-out boundary) and HRQM, as well from an intensely-altered, coeval dolerite dyke (Fig. 1), which forms part of a mafic–ultramafic suite of dikes crosscutting the orebody. The study also encompasses variably-altered RDG, both within and outside the biotite-out boundary, samples of mineralised RDG from locations at depths exceeding 2.0 km (hereafter 'deep mineralisation', DM), and samples from distal mineralisation outside the main brecciated granite, hereafter called 'distal satellite mineralisation' (Table 1; Fig. 1).

In order to understand the textural and chemical variation in apatite from the freshest granitoid in the ODBC, as well as to compare this with apatite from coeval igneous lithologies, three drillcores southwest of the deposit, as well as along a 5.6 km-long NW–SE transect, were sampled (Fig. 2). Although considered some of the freshest within the mine perimeter, RDG in the three drillholes from the southwest location display different intensities of albitization (Kontonikas-Charos et al., 2015) from one drillcore to another. This alteration can be readily seen in terms of K/Na ratio (Fig. 2). Samples were taken from the least altered interval in drillholes RD2494 and RD2495, and from a moderately-altered interval in drillhole RD2492. Similarly, samples along the transect record an increase in Na/K and Fe towards the deposit, corresponding with a marked decrease in the abundance of apatite relative to other phosphates. RDG intersected in drillhole RD2280 features abundant, heavily sericitized mafic enclaves, which were also sampled.

'Deep mineralisation' is hosted by RDG and an intensely-altered felsic rock with porphyritic appearance ("felsic unit"). Fig. 3 shows the variation in P, Fe, and Cu in drillhole RD2773, all of which correlate with one another, and are always higher where coarse-grained apatite is abundant. In the 'distal satellite' (DS) within drillhole RD2316 (Fig. 3), Fe-metasomatism increases towards depth, coincident with a decrease in K. The lowest part of the drillhole displays albitization. Copper, Mo, U, and LREE all correlate with the Fe content.

3.1. Analytical technique

Samples were prepared as 1-inch polished blocks. Each was imaged using a FEI Quanta 450 FEG ESEM equipped a with a back-scattered electron detector prior to electron probe microanalysis (EPMA). Analysed grains were selected based on textures, compositional zonation, and relationships to co-existing minerals.

Quantitative compositional data for apatite were obtained using two electron microprobes: a CAMECA SX-Five instrument at Adelaide Microscopy (University of Adelaide) and a Cameca SX100 (University of Tasmania). These instruments were both operated at accelerating voltages of 15 kV, and beam currents of 20 nA. X-ray lines, standards, count times, and typical minimum limits of detection are given as Electronic Appendix A. A spot size of 4 μm was used for most analyses in order to target distinct domains within individual grains but a larger spot size (10 μm) was used whenever possible to obtain optimal sensitivity for minor elements. Grain-scale cathodoluminescence (CL)

Table 1
Overview of lithologies and samples discussed in this study.

Drillhole no.	Sample ID	Depth (m)	Sample category/rock type
RD2494	RX7860	588.2	*Roxby Downs Granite* — Equigranular, medium to coarse grained K-feldspar–quartz–plagioclase granite. Fresh to pervasively hematite–sericite–chlorite altered. Some samples contain spherical mafic enclaves. Fresh samples are characterised by the presence of biotite, edenite and ilmenite. Locally abundant apatite in association with other accessories such as magnetite, ilmenite and zircon.
RD2492	RX7864	756	
RD2495	RX7866	584	
RD2280	2280-1	413	
	-2	416.5	
	-3	416.9	
	-4	440	
	-5	466	
	-6	467.5	
	-7	475.7	
RD2274	2274-1	372.5	*Horn Ridge Quartz Monzonite* — Equigranular, medium-grained K-feldspar–quartz–plagioclase Quartz Monzonite. Lightly hematite–sericite–chlorite altered. Abundant biotite and hornblende have been altered to chlorite. Some ilmenite remains. Abundant apatite in association with accessory magnetite, ilmenite and zircon.
RD2929	RX7913	401.3	*Dolerite dyke* — intensely hematite–sericite–chlorite–carbonate altered dolerite. The majority of primary silicates are replaced by secondary minerals but accessory apatite and Fe–Ti-oxides (hemoilmenite) are largely preserved.
	RX7914	411.1	
RD2773	2773-1	2208.5	*Deep mineralisation* — magnetite–chlorite–carbonate to hematite–sericite altered Roxby Downs Granite and Felsic Unit. Apatite occurs in a number of morphologies ranging from small, unzoned to large, zoned and fractured grains, in isolation as well as large aggregates.
	-2	2261	
	-3	2289.5	
	-4	2309.5	
	-5	1998.1	
RD2316	RX6685	580.2	*Distal satellite* — magnetite–chlorite–sericite (minor) altered Roxby Downs Granite. Red-stained K-feldspar present, no plagioclase present. Apatite occurs in a wide range of sizes. Larger grains are commonly zoned and occur in aggregates in close association with magnetite. Feldspars replaced by chlorite and by an unusual assemblage of molybdenite–bastnäsite–synchysite.
	RX6687	588.2	
	RX6691	645.3	

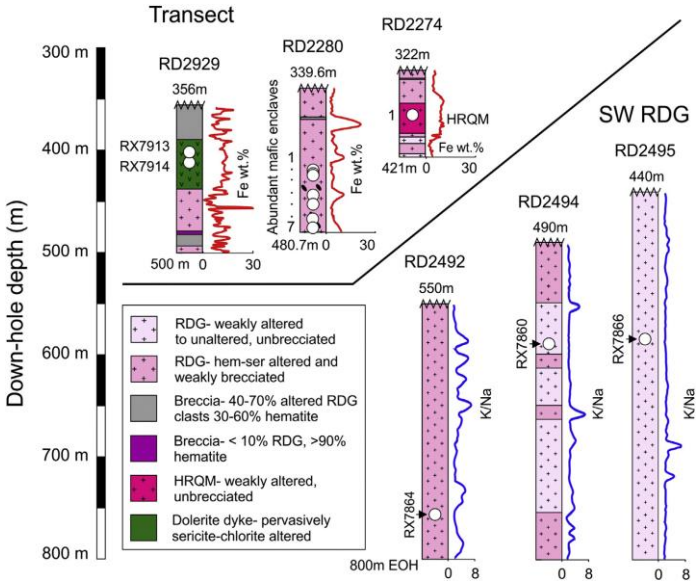

Fig. 2. Schematic representation of three drillholes southwest of the deposit, as well as along a 5.6 km-long NW–SE transect, sampled in this study. Variation in Fe content is indicated for the drillhole transect, and K/Na ratio for the drillholes southwest of the deposit.

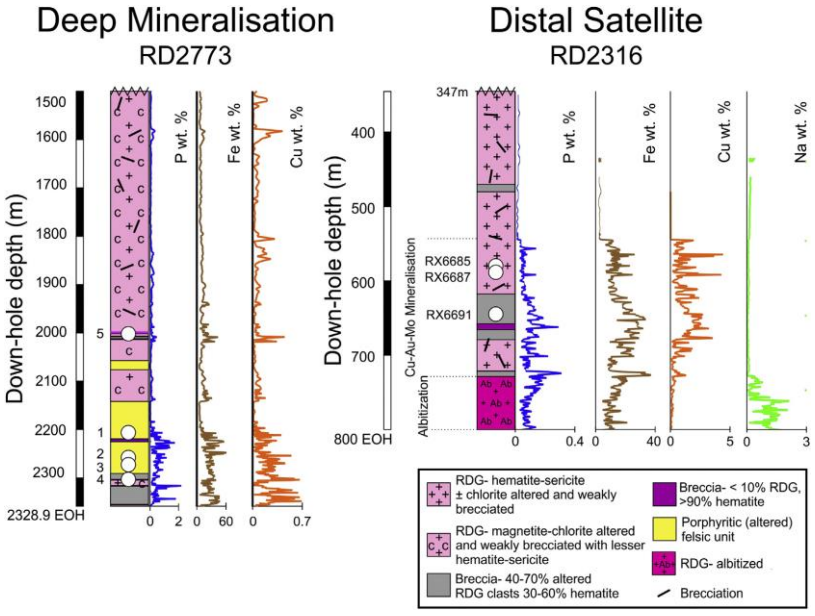

Fig. 3. Schematic representation of distal satellite mineralisation intersected in drillhole RD2316 and 'deep mineralisation' in drillhole RD2773. Variation in P, Fe, Cu, and Na across the sampled intervals.

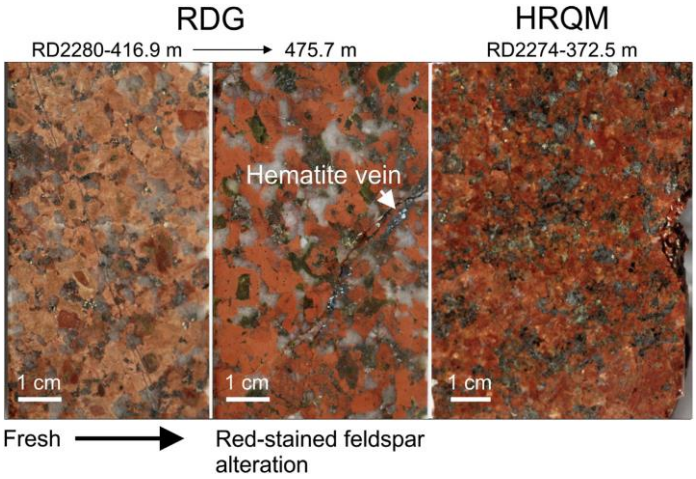

Fig. 4. Hand-specimen photographs showing the two granitoids from this study and variation in alteration in RDG as marked. Note the finer-grained and more mafic-rich character of the HRQM relative to RDG.

imaging was conducted using a Philips XL40 SEM fitted with a Gatan CL detector.

4. Petrography and apatite textural and chemical variation

Fig. 4 illustrates differences in hand-specimen appearance between granitoids. Differences in appearance can be seen even in the same drillhole (Fig. 4a, b), and are expressed as a reddening of feldspar and veining of hematite. Both are linked to hematite alteration. The HRQM is both fine-grained and richer in mafic minerals (Fig. 4c).

4.1. Roxby Downs Granite

Roxby Downs Granite (RDG) is a peraluminous, undeformed, equigranular granite (Kontonikas-Charos et al., 2015) and was sampled along the NW–SE transect and also from the SW locality (Fig. 1). This is a

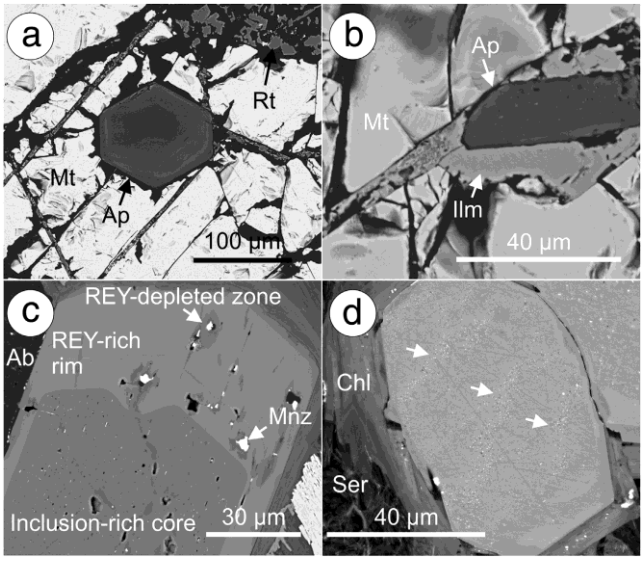

Fig. 5. Back-scatter electron (BSE) images showing the textural and morphological character of apatite in RDG. (a and b) Small, weakly zoned apatite hosted in Fe–Ti-oxides. (c) Dominant type of apatite with core–rim zonation expressed as a variation in REY. Note depletion in REY and monazite nucleation related to the fractures and pores. (d) Inclusion-rich apatite cores (arrowed) in apatite from RDG with mafic enclaves. Some of the coarser and brighter inclusions are monazite, the smaller are sulphides. Note the 'emulsion-like' texture of the bands with inclusions. Abbreviations: Ab — albite, Ap — apatite, Chl — chlorite, Ilm — ilmenite, Mnz — monazite, Mt — magnetite, Rt — rutile.

two-feldspar rapakivi granite that retains perthitic textures but with varying degrees of alteration at metre-scales, caused by deuteric coarsening, albitization, and formation of new, Ba-rich K-feldspar. Altered mafic enclaves, varying in size from mm- to dm-size are abundant in cores along the drillhole transect. The freshest samples preserve mafic minerals (edenite and biotite). Elsewhere, these are altered to chlorite, quartz, hematite, and rutile (Kontonikas-Charos et al., 2015). Mafic minerals in the enclaves are completely replaced by secondary chlorite + sericite. Iron–Ti-phases are abundant and preserved.

The RDG is rich in accessory minerals (zircon, apatite, Fe–Ti-phases), and in many instances, these occur together as clots up to mm-size. Apatite is enclosed within all Fe–Ti-phases (magnetite, Mn-bearing ilmenite, titanite), where it is typically small (tens of μm) and displays only weak zoning (Fig. 5a, b). The most abundant type of apatite in the RDG is, however, coarse single grains (reaching hundreds of μm in size) or aggregates with core-to-rim compositional zoning expressed as variation in REE + Y (hereafter REY), where the cores are REY-poor and the rims are REY-richer (Fig. 5c). Secondly, apatite shows distinct cores characterised by dense, sub-microscopic inclusions (hereafter 'inclusion-rich cores'; Fig. 5d), particularly in the granite with mafic enclaves from the transect location. Coarsening of these inclusions is observed along microfractures crosscutting the apatite. In this case, inclusions, a few μm in size, are identified as sulphides (pyrite, chalcopyrite and galena), and monazite using EDX–SEM. The smallest (<1 μm) inclusions, however, have elongate habit and show Fe:S ratios closer to pyrrhotite than pyrite. Some of the apatite grains feature a reshaping of the compositional zoning relative to the grain boundaries, sometimes with development of porosity and nucleation of monazite along microfractures (Fig. 5c). In the mafic enclaves, a greater proportion of the apatite grains display an elongate habit, and some have quartz cores (Krneta et al., 2015).

All aforementioned RDG apatites are end-member fluorapatite with negligible Cl content. However, apatite hosted within the mafic enclaves display slightly higher Cl concentrations. Compositional variation is expressed by differing REY concentrations (Electronic Appendix Table B1). All are considered magmatic apatite based on their association with Fe–Ti-phases, as well as the characteristic euhedral habit with REY zonation. In the most altered RDG, however, the apatite is corroded and replaced by either quartz (Fig. 6a), or sericite when hosted by altered feldspars (Fig. 6b). A final stage of apatite evolution, only seen in

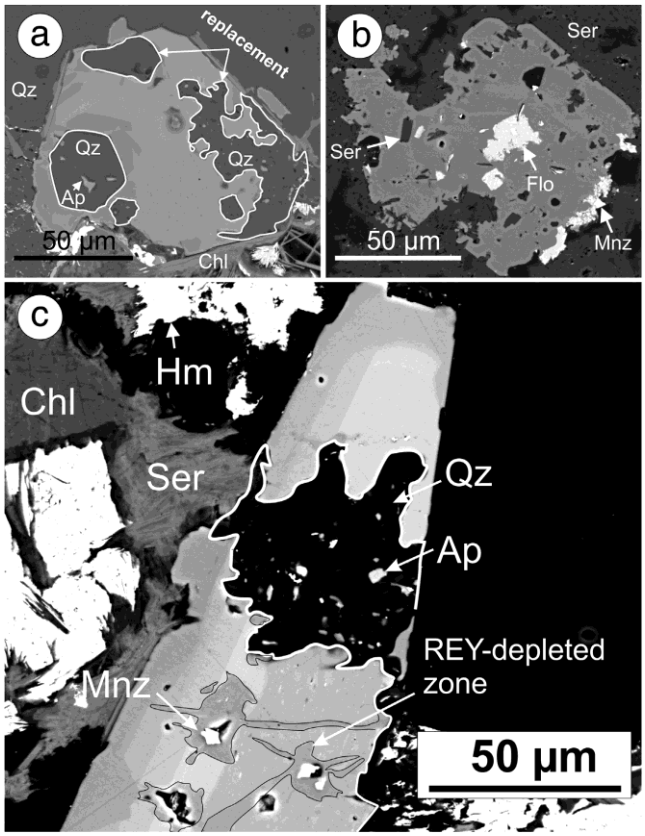

Fig. 6. BSE images showing the textural and morphological character of the hydrothermal alteration of apatite in RDG. (a) Quartz replacement of apatite. Changes in morphology of the replaced areas from pseudomorphic (hexagonal outline) to skeletal indicating a transition from coupled-dissolution reprecipitation to a fracture-porosity controlled replacement. (b) Unzoned apatite with atypical, hypidiomorphic morphology from intensively sericite-altered RDG along the drillhole transect. Coarse florencite and monazite are present. Although marginal replacement of apatite by sericite is observed, the irregular morphology of the sericite and florencite inclusions suggests late apatite crystallisation relative to these minerals. (c) Detail of apatite replacement by quartz accompanied by REY-depletion and monazite formation along fractures crosscutting patterns in apatite (REY-zonation and core–rim boundary). Abbreviations: Ap — apatite, Chl — chlorite, Flo — florencite, Hm — hematite, Mnz — monazite, Qz — quartz, Ser — sericite.

RDG displaying with more intense sericite–hematite alteration, is represented by replacement by quartz (containing monazite inclusions), and by fracture networks (also carrying inclusions of sericite and hematite) associated with the loss of REY from the apatite grains (Fig. 6c). In highly-altered RDG samples, containing base metal sulphides, hematite veinlets, and Nb-bearing rutile, magmatic apatite is largely obliterated and xenotime may be the dominant REE-phosphate. Samples from drillhole RD2513 at the margin of the ODBC along the transect (Fig. 1) do not contain apatite. The alteration assemblage is comprised of siderite, barite, fluorite, and sericite.

4.2. Horn Ridge Quartz Monzonite

The Horn Ridge Quartz Monzonite (HRQM) has been intersected in a drillhole ~4 km SE from the boundary between the altered and fresh RDG (biotite-out limit) and the outer limit of the ODBC (Fig. 1). The HRQM is similar in appearance to the RDG, although with greater proportions of both mafic minerals and accessory Fe–(Ti)-oxides, reflecting its less-evolved character (a QAP diagram is given by Kontonikas-Charos et al., 2015). At this location, mafic minerals in the HRQM are completely altered to chlorite, quartz, and rutile. Iron–Ti-oxides are abundant, and consist of magnetite and ilmenite, where the latter preserves domains of ulvöspinel, as well as more common decomposition to symplectites of hematite and rutile.

Apatite is an abundant component, occurring within the replaced mafic minerals, often together with clots of Fe–Ti-oxides, or at the boundaries of such clots (Fig. 7a). Some of the smallest apatite grains (down to ~5 μm) are un- or weakly-zoned, and are observed to be entirely enclosed within magnetite, either surrounded by coronas of decomposed ilmenite (Fig. 7b), or as euhedral grains oriented parallel to magnetite cleavage planes (Fig. 7c). In contrast with these, larger (up to a few hundred μm) individual, or aggregated apatite grains are seen outside Fe–Ti-oxides. Most such grains contain inclusion-rich cores, similar to those as described for the RDG above. The host apatite is zoned, either with preservation of core-to-rim geometry (Fig. 7d), or a more irregular outline between zones caused by reworking (Fig. 7e, f). Grains lacking inclusions are also seen outside the Fe–Ti-oxides. These vary in size from tens to hundreds of μm, and also show zoning, as well as reworking. The latter is expressed as pore-controlled nucleation of new apatite (Fig. 7g), overgrowths on rounded cores (Fig. 7h), and as patchy chemical zoning (Fig. 7i). The latter is associated with the nucleation of relatively coarse monazite and lesser xenotime.

Compositionally, all apatite grains are fluorapatite but with variable Cl and (inferred) OH content (Electronic Appendix Table B2). The smallest, magnetite-hosted grains are clearly magmatic because of their entrapment in magnetite during growth. They are the richest in Cl (up to 0.14 atoms per formula unit; apfu) but with variable REY content (ΣREY apfu 0.045–0.122). All other apatites contain zones with ~0.08–0.10 apfu Cl, but also zones that are Cl-depleted (<0.02 apfu).

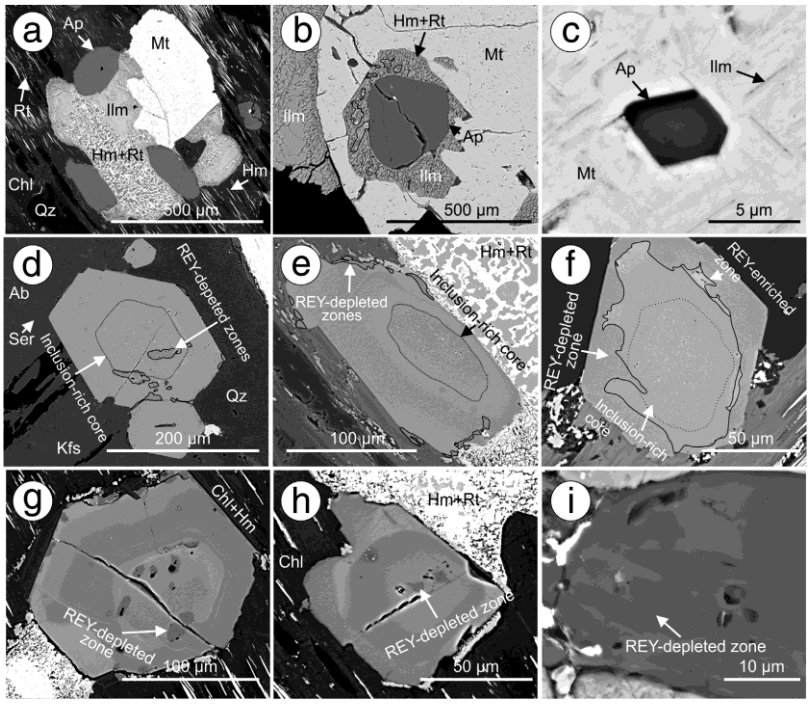

Fig. 7. BSE images showing the textural and morphological character of apatite in HRQM. (a) Apatite associated with Fe–Ti-oxides forming a clot within an altered mafic mineral. Note the decomposition of ilmenite into a rutile + hematite symplectite. (b and c) Fe–(Ti)-oxide hosted apatite. Note the lack of zoning and small size of apatite. In (c) see also the coherent orientation of the grains relative to the magnetite cleavages. (d, e and f) Inclusion-rich cores in dominant, coarse apatite with a euhedral morphology. Core–rim zoning (e) and core outline relative to margin (f), indicating superposed hydrothermal alteration expressed also as REY-depletion or local enrichment. (g and h) REY-zoned apatite with no obvious inclusion-rich cores. Further evidence for hydrothermal alteration is seen as pore-controlled nucleation of small, REY-depleted apatite. Rounding of the core with irregular overgrowth in apatite (h). (i) Detail of REY-depleted zones showing patchy morphology. Abbreviations: Ap — apatite, Chl — chlorite, Hm — hematite, Ilm — ilmenite, Kfs — K-feldspar, Mt — magnetite, Qz — quartz, Rt — rutile, Ser — sericite.

The Cl-rich zones in a given grain are associated with variable but generally higher REY, together accounting for the patterns seen on the BSE images.

4.3. Dolerite

The dolerite dyke from the mafic–ultramafic suite, coeval with RDG, has a dark-green to white-yellowish appearance in hand specimen due to intensive alteration to an assemblage of chlorite + sericite + carbonate + quartz. Carbonates, mainly siderite, occur as mm-scale veinlets throughout the rocks. Sulphides, such as pyrite and chalcopyrite, are found as scattered disseminations that increase in abundance along/within the veins. In most cases, chlorite + sericite ± carbonate assemblages occur as fine-grained intergrowths, with rhythmic layering within ovoid shapes.

The mafic–ultramafic origin of these rocks is evidenced by their Zr/Ti ratios and also by the high abundance of hemoilmenite as the main magmatic accessory phase. The latter occurs as aggregates or clots and preserves fields of dense ilmenite exsolutions. Rutile rather than titanite is the more abundant Ti-mineral, occurring either as acicular aggregates within hemoilmenite, or as tiny, abundant inclusions throughout the altered sericite–chlorite mass. Apatite is the other abundant accessory (Fig. 8). Zircon is present as rare grains, in some cases enveloped by sulphides. Although rare, K-feldspar is identified as small grains enclosed within both the Fe–Ti-oxides and apatite, indicating the presence of a potassic alteration stage that pre-dates carbonate–chlorite–sericite alteration.

Apatite ranges in size from 10 to 600 μm. It ranges in morphology from euhedral to subhedral (Fig. 8a, b), and rarely as acicular grains. The smallest grains, which are the least common, are compositionally homogenous, and have the highest Cl concentrations (up to 0.235 apfu; Electronic Appendix Table B3). The most common apatite grains are, however, larger and are characterised by either equant or corroded outlines. These are compositionally heterogeneous and display areas of patchiness (Fig. 8c). Abundant pores and μm-sized inclusions of monazite are often observed within the patchy zones.

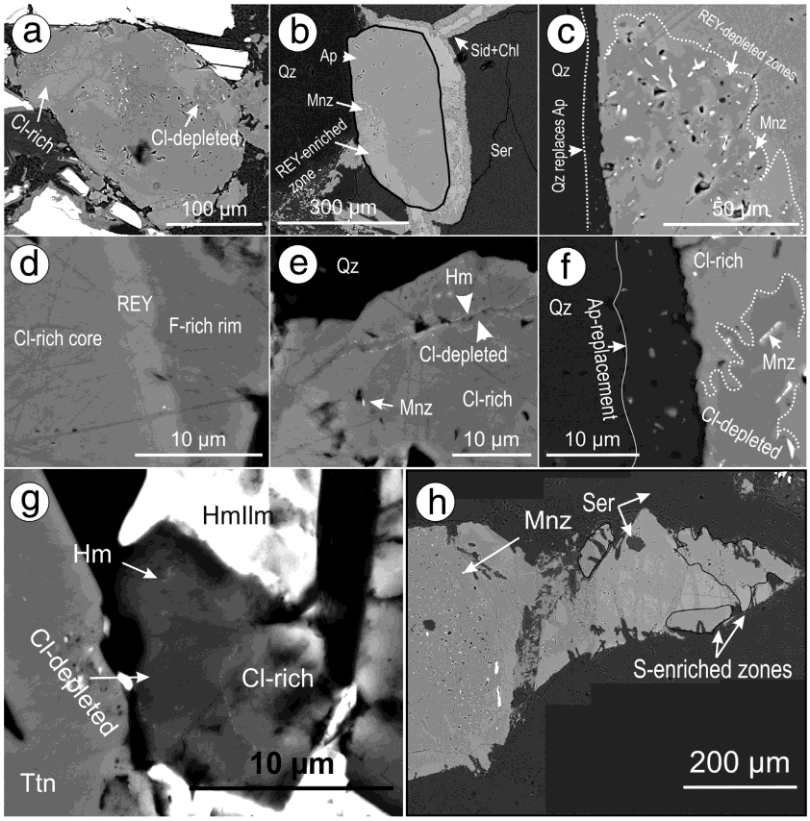

Fig. 8. BSE images showing apatite from the dolerite dyke (a–b). Coarse apatite with equant, slightly rounded morphology and with patchy Cl-rich, F-rich domains. In (b), carbonate partially envelopes a grain located at the junction of the fractures filled with secondary minerals. (c) Detail of a F-rich and Cl-REY-depleted zone showing the development of pores and monazite nucleation indicative of the superposed, hydrothermal alteration. (d–h) Various aspects of apatite alteration. In (d), a REY-rich band at the contact between the F-rich rim and a typical, Cl-rich apatite shows a reaction front with zonal development from margin to core. In (e), a Cl-depleted fracture is fringed by tiny platelets of hematite. Marginal replacement of apatite by quartz is marked by a scalloped outline — typical of a metasomatic reaction front. The adjacent zone in apatite with Cl-depletion and monazite inclusions has an irregular morphology indicating that the two alteration stages are distinct from one another. (g) Scalloped core morphology of a F-rich, Cl-depleted core marked by sub-μm hematite. (h) Sulphur-rich domains in apatite adjacent to a wide (cm-size) fracture filled by carbonate and sulphides. Note brittle fracturing of the apatite itself. Abbreviations: Ap — apatite, Chl — chlorite, Hm — hematite, Hmilm — hemoilmenite, Mnz — monazite, Qz — quartz, Ser — sericite, Sid — siderite, Ttn — titanite.

Zones of relative REY-enrichment (up to 0.087 apfu ΣREY in the bright areas on the BSE images; Electronic Appendix Table B3) are also present (Fig. 8b). The patchy zoning corresponds to the highest F (up to 0.998 apfu; Electronic Appendix Table B3). There are however, various relationships between the REY- and F-rich apatite zones. This can be seen either as a zonal arrangement of F- and REY-rich zones from the grain boundary inwards (Fig. 8d), or as patchy F-rich zones crosscutting the REY-rich zones (Fig. 8b). The F-rich zones are most varied texturally and clearly show association with microfractures fringed by hematite (Fig. 8e), or with apatite margins displaying scalloped morphologies against replacive quartz (Fig. 8f). The presence of tiny fragments of apatite within replacive quartz indicates the nature of this replacement as pseudomorphic. Cores of F-rich apatite are also observed within otherwise Cl-rich apatite (Fig. 8g). These cores have an irregular morphology and are sealed by dusty hematite inclusions, which suggests that they relate to an overprint event. The majority of apatite grains, however, display a combination of all the aforementioned textures.

A further category of apatite, observed in these rocks, is relatively SO_3-rich (up to 0.041 apfu S; Electronic Appendix Table B3) and occurs within angular terminations of larger, equant grains placed along the carbonate veins. In this case, textures clearly indicate an overlap of various categories of apatite as defined above. For example, the high-REE apatite zones are crosscut by F-rich veinlets, and only a few monazite inclusions occur within or adjacent to such veinlets (Fig. 8h). Areas of coarse pores and filling of the F-rich veinlets by sericite are also observed. The SO_3-rich zones are observed around the margins of, or adjacent to, crosscutting veins that occur at the boundaries between equant apatite and its angular edge.

4.4. Deep mineralisation

The deepest mineralisation is intersected in a 2.3 km-deep drillhole (RD2773) at the eastern boundary of the brecciated RDG (Fig. 1). Mineralisation is hosted by altered intrusive rocks (altered RDG and a felsic unit between 1500 and 2328 m), and intensifies over the lowermost ~300 m. The relationship between the RDG and felsic unit is, however, irregular with interfingering of one into the other over a 270 m-thick interval. Early emplacement of the 'felsic unit' relative to the RDG is suggested by contacts with fragments of the former incorporated within the latter. Mineralisation consists of sulphides (chalcopyrite + pyrite + sphalerite + galena) as disseminations and mm-size veinlets associated with a characteristic alteration assemblage comprising Fe-oxides (magnetite–hematite, with interconversion between the two), sericite, chlorite, carbonates, quartz, and locally abundant anhydrite. Carbonates are the most abundant within crosscutting late veins. Uranium minerals (uraninite, brannerite, and coffinite), as well as REE-minerals (monazite, synchysite, and bastnäsite), are also present. Alteration is patchy across the lower portion of the drillhole but zones of intense alteration, from mm up to as much as 4 m in size, are concentrated at the contacts between the RDG and felsic unit or along fractures.

Apatite is a ubiquitous component of the alteration irrespective of lithology, and displays a variety of grain sizes (up to cm-size), habits, and mineral associations. Although euhedral, REY-zoned grains comparable to those described from RDG are present (Fig. 9a). The majority and highest concentration of apatite occurs within cm-scale aggregates (Fig. 9b). Compositionally, apatite is close to end-member fluorapatite (Electronic Appendix Table B4) but with zones of higher Cl-content within any given grain (0.016–0.05 apfu Cl; i.e., higher than in RDG magmatic apatite). This variation in Cl-content is expressed as core-to-rim zoning (either with Cl in the cores or at the rims), as well as patchy zoning linked in some cases to microfractures (Fig. 9b–d). The Cl-rich zones also contain higher amounts of both REY and SO_3. Low-REY, F-rich zones are predominantly located along fractures and associated with inclusions of monazite (locally also hematite and chalcopyrite). When in contact with late quartz and calcite, apatite is typically brecciated and partially replaced. In contrast to magmatic apatite in RDG, F-enrichment clearly post-dates an early Cl-rich fluorapatite (Fig. 9c). Together with the close association with alteration, this indicates that apatite characteristic of deep levels, such as that intersected here, has a dominantly hydrothermal origin despite a similar equant habit in some cases. Although rare, potentially magmatic fluorapatite grains, characterised by very low Cl, but with relatively high $\sum$REY, are preserved as inclusions within Fe-oxides in altered RDG (Fig. 9e). Whereas monazite inclusions of varying size and density are common in all cases, in the deepest samples, bi-component (monazite + $ThSiO_4$) inclusions are conspicuous within F-rich, REE-poor zones in apatite, and also as splays crosscutting boundaries between the F- and Cl-rich domains (Fig. 9f). In detail, the $ThSiO_4$ (most likely huttonite) can be as abundant as the monazite (Fig. 9g). The inclusions may also be multi-component with hematite. Apatite may also contain inclusions of sulphides.

4.5. Distal satellite mineralisation

Mineralisation intersected in drillhole RD2316, 2.7 km NE from the ODBC, and 1 km from the biotite-out boundary within the RDG (Fig. 1), represents one of the distal satellite bodies in the OD area. The drillhole intersects 450 m of RDG below cover with zonation ranging from relatively fresh to mineralised and brecciated (below 543 m), with weakening of mineralisation towards the bottom of hole (800 m). Magmatic K-feldspar is partially preserved over the strongest mineralised interval and coexists with hydrothermal K-feldspar, whereas over the bottom 75 m, albitization is preserved (Fig. 3; Kontonikas-Charos et al., 2015). As in the DM, both magnetite and hematite (and their interconversion) are associated with pyrite, chalcopyrite, native gold, U-minerals, and an abundance of REE-minerals, particularly epitaxially intergrown REE fluoro-carbonates (e.g., bastnäsite, synchysite and parisite). In contrast to the DM, however, molybdenite is moderately abundant, and coexists, within lamellar intergrowths, with the REE-minerals. Alteration consists of chlorite (mostly associated with magnetite), sericite (with hematite), quartz, and rare carbonates.

In samples from the most intensely mineralised interval, apatite is abundant, occurring in close association with Fe-oxides (mostly martite), other alteration minerals, and sulphides. In this drillhole, the textures and chemistry of apatite differ markedly within individual samples, depending on the local association. Where closely associated with Fe-oxides and pyrite, apatite forms aggregates interstitial to other minerals, as in the uppermost sample (Fig. 10a). Such aggregates can either retain growth zoning and equilibrium textures, or display evidence of brecciation. Co-precipitation of apatite aggregates with a primary magnetite is suggested.

In contrast, in samples from deeper levels, apatite occurs as single grains that are brecciated and replaced by quartz, with REY-minerals or molybdenite marking the replacement front (Fig. 10b). A distinct, fine-grained apatite occurs within or at the margins of K-feldspar (Fig. 10c). The smallest apatite grains are seen in areas outside of the Fe-oxides and Cu-sulphides, and are characteristically unzoned and include fine-grained hematite in vugs and along trails (Fig. 10e). In some cases, apatite features more complex textures with both sectorial and oscillatory zonation (Fig. 10e). REY-depleted margins suggest hydrothermal overprinting on inherited magmatic grains.

All categories described here are end-member fluorapatite with negligible Cl content (Electronic Appendix Table B5). There is, however, variability with respect to the REY content, particularly core-enriched to margin-poor (Fig. 10e). All grains contain some S. Aggregates and large apatite grains are, however, markedly lower in S (0.01–0.02 apfu) than the smaller grains within and at the margins of K-feldspar (0.03–0.04 apfu). Although within each category, individual grains can contain domains that are completely depleted in S, the S-REE-rich domains also feature higher Na (up to 0.05 apfu) within the smaller grains that are located in and around K-feldspar (Fig. 10d).

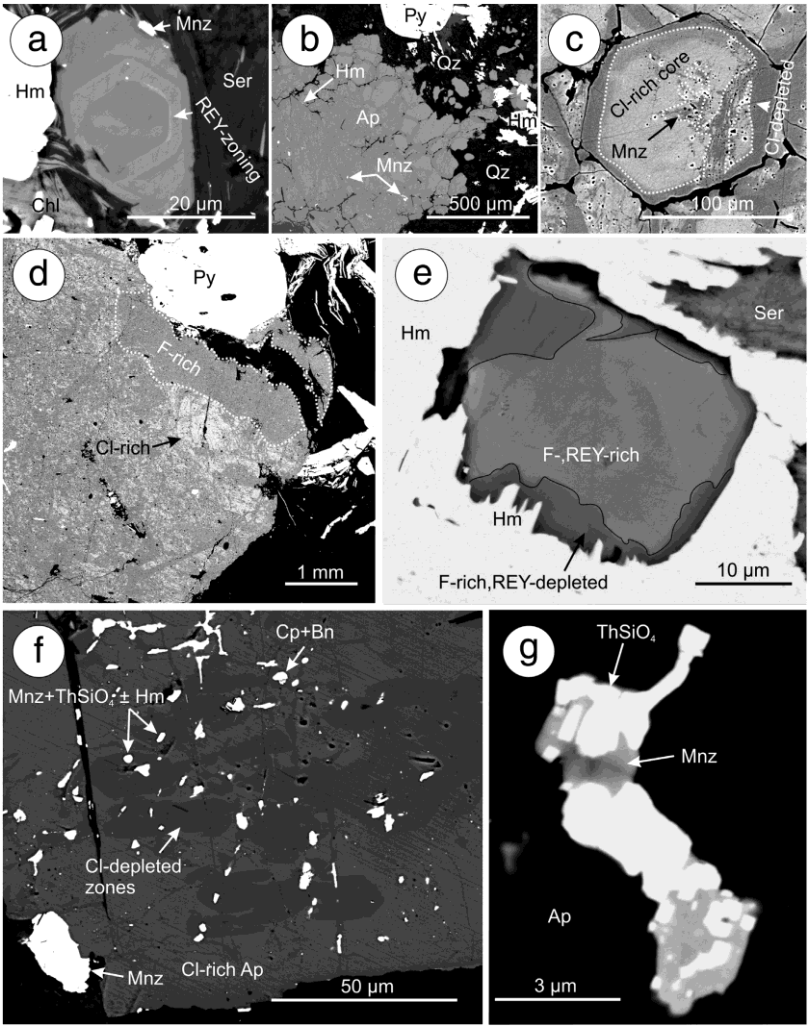

Fig. 9. BSE images showing apatite from the 'deep' mineralisation. (a) Rare, single grain of Cl-bearing hydrothermal apatite. (b) Typical large, Cl-rich apatite aggregate. (c) Detail of grains from (b) fractures and margins depleted in Cl and richer in F. (d) Detail of patchy Cl/F domains at the margin of an apatite where alteration is advanced (sulphides + hematite). (e) Marginal REY-depletion of a Cl-poor, REY-zoned fluorapatite embedded within hematite. This grain could be of magmatic origin. (f) Patchy Cl- and F-domains in apatite crosscut by trails of dominantly bi-component inclusions consisting of monazite-Th-rich silicate (huttonite?). Noteworthy is the presence of various sulphides and hematite. Such trails and inclusion variety indicate advanced hydrothermal alteration of apatite. (g) Detail of bi-component inclusions (monazite-huttonite?). Abbreviations: Ap — apatite, Bn — bornite, Cp — chalcopyrite, Hm — hematite, Mnz — monazite, Py — pyrite, Qz — quartz, Ser — sericite.

This can be attributed to a characteristic signature associated with the obliteration of albite in these samples during interaction with S-bearing fluids, particularly when such grains are formed.

5. Discussion

The ubiquitous character of apatite in igneous rocks and its ability to incorporate halogens, magmatic water, S, C, and trace elements, including Sr, REY, Th and U, are, if combined with careful textural and compositional analysis, considered important tools for understanding pluton building and associated mineralising systems (Webster and Piccoli, 2015). Magmatic apatite, the single mineral that accounts for the majority of the P content in melts, is of particular interest because both halogens (F, Cl) and OH are interdependent of one another since they are hosted in the same crystallographic site. The relative concentrations of these elements can therefore be linked to those of the parent melt.

Variation in the halogen content of magmatic apatite was initially considered predictive (Candela, 1986; Zhu and Sverjensky, 1991; Piccoli and Candela, 1994) and halogen variation, expressed as zonation

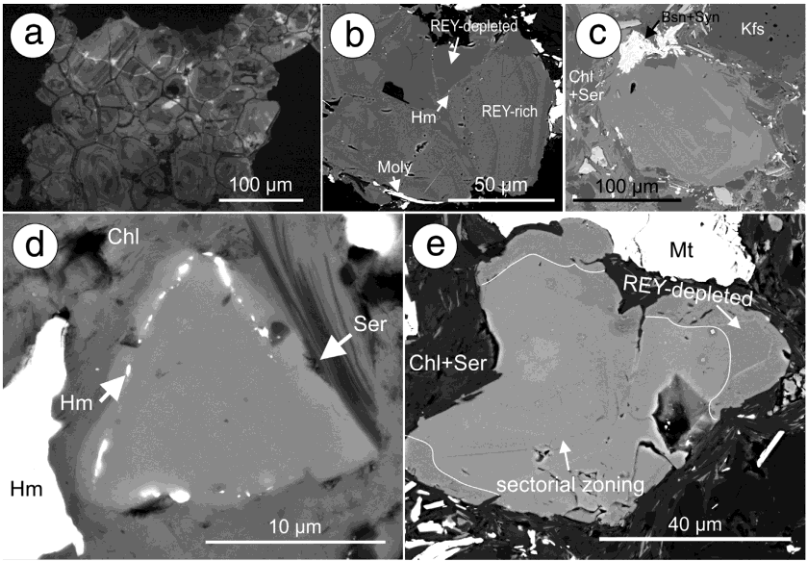

Fig. 10. Cathodoluminescence (a) and BSE (b–e) images showing apatite from the distal satellite mineralisation. (a) Aggregate of interstitial apatite with no obvious chemical zoning but with growth zones depicted in the CL image typical of the upper interval with lesser sulphides and more Fe-oxides. (b) Apatite aggregate with grain-boundaries marked by porosity and replacement by molybdenite. (c–d) Small, unzoned apatite formed within or along boundaries of K-feldspar with intense replacement by intergrown assemblage of bastnäsite, synchysite and molybdenite (c), and hematite trails (d). (e) Unusual sectorial zoning in apatite expressed as REY variation. Note that such grains (probably magmatic-inherited) are affected by marginal replacement (scalloped morphology) and overgrowth. Abbreviations: Chl — chlorite, Hm — hematite, Kfs — K-feldspar, Moly — molybdenite, Mt — magnetite, Ser — sericite.

within individual single grains or within an intrusion, was believed to be instructive for identifying igneous systems associated with ore generation. The predictability of halogen uptake into apatite has, however, been questioned (e.g., McCubbin and Jones, 2015). It is currently accepted that partitioning of halogen species into apatite is governed by fluid composition, the presence of other halogen-consuming species, P–T conditions, and other factors. Although all these factors can influence partitioning, plutonic apatite with >3.5 wt.% Cl is rare (Webster and Piccoli, 2015). Halogen partitioning within apatite can, however, be related to trends of magmatic evolution in a given orefield or region that share common magmatic reservoirs (e.g., Boudreau and Kruger, 1990).

Apatite composition in our samples can be expressed in terms of the following variables: halogens, REY, Si, Na, S, Sr, and Mn. Their variation correlates with specific textures observed in each of the five study cases described above. Collectively, the dataset shows a transition between magmatic to hydrothermal apatite recorded both as textures and as geochemical trends.

5.1. Magmatic apatite

Although the presence of almost-end-member fluorapatite in the RDG cannot be used to infer crystallisation from a F-rich magma, the relative concentration of halogens and other minor elements in apatite from igneous rocks at Olympic Dam shows systematic variation depending upon rock type and local context.

5.1.1. Magmatic differentiation and halogens in apatite

The most obvious compositional variable observed in magmatic apatite from the igneous rocks is the F/Cl ratio. This correlates with rock basicity, with the HRQM positioned midway between the RDG and the dolerite dyke, in agreement with the less-evolved character of the HRQM relative to the RDG (Fig. 11a). The Sr vs. Cl plot (Fig. 11b) is evidence for the control imposed by the fractionation character of the magma in determining the chemistry of igneous apatite (Belousova et al., 2001). In terms of the calculated OH component, the three rock types cannot be distinguished from one another. In all three lithologies, magmatic apatite displays a strong correlation between ΣREY and Si, although the absolute values of both variables are an order of magnitude lower in the dolerite dyke than in the granitoids. The highest ΣREY concentrations in granitoid apatites are observed in rims surrounding grain cores rich in mineral inclusions. In the granitoids, the smallest apatite grains, hosted by Fe–(Ti)-oxides, have ΣREY contents comparable to apatite from the inclusion-rich cores. Such apatite in the HRQM is also markedly enriched in Cl compared to the inclusion-rich cores.

Apatites from both RDG and HRQM plot in a similar region on a Sr vs. Mn plot (Fig. 11c), which is used as a measure of magmatic differentiation. They overlap with the granitoid field for occurrences elsewhere (Belousova et al., 2001, 2002) whereas apatites from the dolerite dyke plot astray, inferring that the dolerite dyke is a less-evolved magmatic phase.

5.1.2. Apatite crystallisation and Cl-concentration estimates in melt and volatile phase

Harrison and Watson (1984) considered P_2O_5 concentrations in the whole rock chemistry and the integral part they play in the cooling history of felsic melts. Taking the various parameters which affect apatite saturation into consideration, they conclude that, in the case of subaluminous granites, the greatest controls are exerted by silica concentrations and temperature. However, in the case of peraluminous granites, P_2O_5 solubility is enhanced, shifting apatite saturation to lower temperatures (Bea et al., 1992). Experimental work by Wolf and London (1995) provides further evidence of this phenomenon, observing that incongruent melting of apatite and the formation of monazite along grain margins can be achieved in peraluminous melts. Bea et al. (1992) incorporated the effects of Al_2O_3 concentrations into their

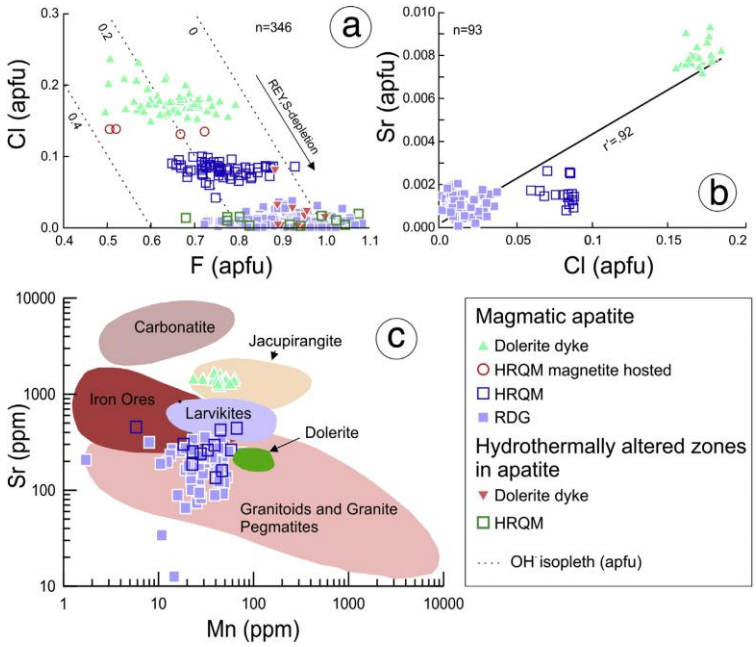

Fig. 11. Plots of (a) Cl vs. F, (b) Sr vs. Cl, and (c) Sr vs. Mn for magmatic apatite. Fields on (c) are from Belousova et al. (2002).

modified formula for calculating apatite saturation temperatures (AST) in peraluminous granites.

The presence of apatite with inclusion-rich cores, which are particularly abundant in RDG with mafic enclaves from the transect, raises the question of whether such apatite could be different relative to the majority of apatite in the RDG in terms of magma mixing and evolution, or it indicates the incorporation of exotic, compositionally-different material during magma crystallisation. Examples of such apatite with pyrrhotite-rich cores are reported from granitoids in the German Erzgebirge (Gottesmann and Wirth, 1997) and were interpreted to reflect assimilation of exotic material in the granite melt, possibly mafic material from the margins of the magma chamber. Attempts to definitively understand the identity of these inclusions are hampered by the fact that, in cores not affected by later fractures and coarsening of the inclusions, the inclusions are sub-μm size. Preliminary nanoscale studies, nevertheless, confirm that the enclave-hosted apatite from OD also includes pyrrhotite and fluorite (the latter as some of the smallest inclusions). This data will be published elsewhere.

Calculations of Cl in the melt relative to the volatile phase at AST were performed using whole rock assays from a limited number of samples from drillhole RD2495 (Fig. 1). These samples correspond to the freshest granites in which mafic minerals are still present. AST calculations were performed using formulae given by Harrison and Watson (1984) and Bea et al. (1992), using parameters such as the A/CNK ratio (Al/(Ca + Na + K) in molar terms) and the concentrations of SiO_2 and P_2O_5. Chlorine concentrations in melt and fluid were calculated following Piccoli and Candela (1994). Calculation details and formulae applied are described in Electronic Appendix C.

Calculated AST values overlap within error with temperatures obtained from feldspar–amphibole and two-feldspar geothermometric estimates on the same RDG samples (Kontonikas-Charos et al., 2015). Hovis and Harlov (2010) and Hovis et al. (2014) found, however, that F–Cl and F–OH mixing exhibits non-ideal characteristics thus reducing the accuracy with which F concentrations can be estimated. The calculations require the input of AST, pressure, and measured halogen concentrations in apatite (ideally also independently measured OH). We therefore calculated only Cl, because this is the parameter most sensitive to the distinct mafic vs. felsic categories of igneous rocks at OD.

The calculations are very sensitive to pressure (P) estimates. Here, we adopt the 2.2 kbar value derived from Al-in hornblende geobarometry (Creaser, 1989; Kontonikas-Charos (unpublished data)). Calculations were performed using average Cl concentrations

Table 2
Calculated Cl-concentrations (ppm) in coexisting melt and volatile phase at the time of AST in RDG.

Drillhole ID	Sample	Number of analyses	F (apfu)	Cl (apfu)	OH[a] (apfu)	Cl in volatile phase (ppm)	Error 2σ	Cl in melt (ppm)	Error 2σ
RD2492	RX7864	7	0.838	0.010	0.152	18,324	4396	29.0	10.7
RD2494	RX7860	21	0.913	0.011	0.076	42,744	10,255	67.8	25.0
RD2495	RX7866	1	0.840	0.005	0.154	9943	2385	15.8	5.8
RD2280	2280-2	19	0.919	0.005	0.077	17,079	4097	27.1	10.0
	2280-3	19	0.875	0.015	0.110	38,418	9217	60.9	22.5
	2280-5	41	0.917	0.014	0.069	59,600	14,299	94.5	34.8

[a] OH calculated.

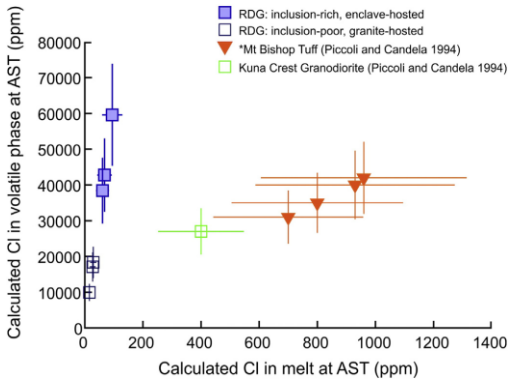

Fig. 12. Plot of calculated Cl (ppm) in volatile phase vs. calculated Cl (ppm) in melt at AST for magmatic apatite using grain core compositions. Note: Piccoli and Candela (1994) do not provide errors for their Mt. Bishop Tuff apatite halogen concentrations. Errors equivalent to those estimated for the Kuna Crest granodiorite have been used in the error calculations here.

from a number of grains and yield Cl values varying between 15 and 94 ppm (±6 to 35) Cl in the melt, and between 10,000 and 60,000 ppm (±2400 to ±14,300) Cl in the volatile phase (Table 2). Such values accord with the known behaviour of Cl to partition into the volatile phase over both apatite and the melt. Identical P and T values were used in calculations for all samples, and the variability in the calculated values can thus only be attributed to slight changes in Cl-concentration. The highest Cl-concentrations derive from apatite grains with inclusion-rich cores within samples dominated by mafic enclaves. The correlation of higher Cl in apatite, hosted by mafic enclaves within the RDG, is in agreement with observations made elsewhere (Piccoli and Candela, 2002). The dataset shows that the values for inclusion-bearing core apatite are statistically distinct from grains without such inclusions. For the sake of comparison, the plot (Fig. 12) also shows the fields for the un-mineralised Mt. Bishop Tuff and the Kuna Crest Granodiorite samples using values from Piccoli and Candela (1994). These latter two rocks show far higher Cl values in the melts than the RDG apatite, which is potentially a meaningful finding considering the very distinct tectonic settings of the Mt. Bishop Tuff and the Kuna Crest Granodiorite compared to the RDG, even if magma chemistry and pressure are the most important controls on apatite saturation temperatures and chemistry.

5.2. Hydrothermal apatite

Magmatic apatite shows textural and geochemical evidence of hydrothermal alteration in all cases. In addition, abundant hydrothermal apatite is recognisable in both mineralised granites, albeit with differences depending upon depth and alteration type.

5.2.1. Hydrothermal alteration of magmatic apatite

Apatite from the dolerite dike shows the most diverse range of alteration trends (Fig. 13). For example, in contrast to granitoids, the highest ΣREY values in apatites from the mafic dyke are observed in reaction zones on the margins of unaltered magmatic Cl-rich apatite grains often adjacent to REY-depleted zones in the same grains (e.g., Fig. 8e). Another important difference between the granitoids and the dolerite dyke is the measurable S content in the latter, with maximum concentrations in intensely altered grains in close proximity to the chlorite veins (Fig. 13). In apatite from all three igneous rocks, relatively F-rich zones, with negligible Cl, REY, Si, and S, crosscut pre-existing domains. Scattered coarse-grained monazite, and more rarely florencite (in the RDG), occur within such zones.

Common to all occurrences of magmatic apatite is the formation of monazite inclusions in areas affected by depletion in REY and enrichment in F relative to Cl (Fig. 6; see below).

5.2.2. Hydrothermal apatite in mineralised granitoids

Apatite in the mineralised RDG from the deep mineralisation contrasts markedly with igneous apatite from non-mineralised RDG in that it contains higher concentrations of Cl (Fig. 14a). Such Cl-rich apatite is less altered relative to F-rich zones in the same grain, which are characteristically superimposed onto the former. From this, it is clear that such apatite is typical of an early hydrothermal stage and distinct, both chemically and texturally from the magmatic apatite observed in the RDG. Inclusion-rich cores, diagnostic of magmatic apatite, are completely lacking in the hydrothermal grains. As in the RDG, the early hydrothermal apatite shows a strong correlation between REY and Si, in which the F-rich zones are REY-depleted (Fig. 14b). However, in contrast to the RDG, S also correlates with REY, Cl, and Si (Fig. 14c).

Apatite in the distal satellite contains negligible Cl but shows similar REY vs. Si and S vs. Si trends as the deep mineralisation (Fig. 14d, e). There is, however, a sub-population (the small unzoned grains), which plots with high S values, even higher than the apatite in the DM. This sub-population also shows the highest Na concentrations relative to other apatite populations in the DS (Fig. 14f). Noteworthy is the

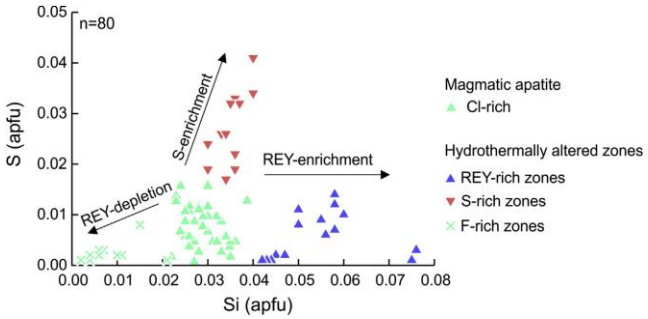

Fig. 13. Plot of S vs. Si illustrating compositional ranges of apatite from the dolerite dyke and key geochemical trends associated with hydrothermal alteration.

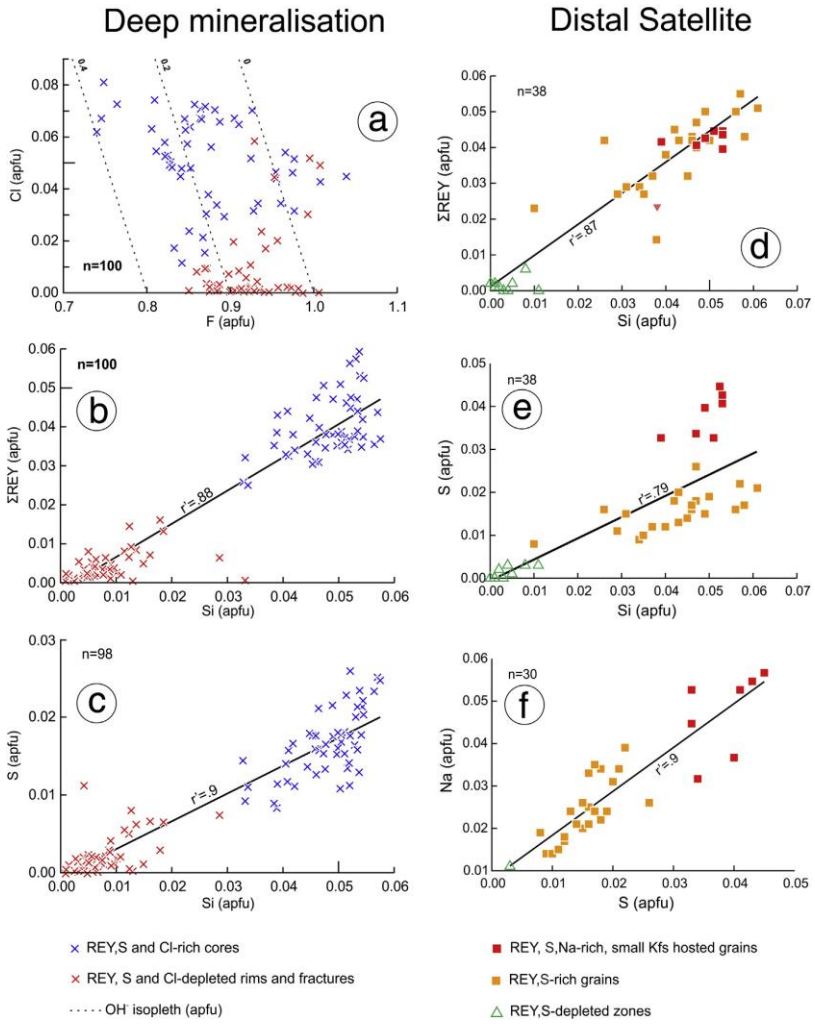

Fig. 14. (a–c) Compositional trends of apatite from Deep Mineralisation: (a) F vs. Cl; (b) ∑REY vs. Si; and (c) S vs. Si. (d–f) Compositional trends of apatite from distal satellite mineralisation: (d) ∑REY vs. Si; (e) S vs. Si; (f) Na vs. S.

excellent correlation between Na and S ($r^2 = 0.9$), which can be attributed to the obliteration of albite during apatite growth at the time of K-feldspar staining by Fe-oxides (Kontonikas-Charos et al., 2015). At this stage, Na can be assumed to be in the fluids (dissolution of albite), and will be readily incorporated in apatite particularly if S is also available. The latter can be also assumed since sulphides are formed at this stage. The strong correlation between S and Na (Fig. 14f) supports the idea that the two elements were incorporated at the same time in apatite via a coupled substitution mechanism (e.g., $SO_4^{2-} + Na^+ = PO_4^{3-} + Ca^{2+}$). Therefore the measured Na + S signature in this apatite, tied to areas around red-stained K-feldspar, can be related to progressive feldspar alteration in the RDG.

Despite the fact that the same style of mineralisation is observed in both locations, there are pronounced differences in the apatite compositions, i.e., Cl-rich in the DM, and Na-rich in the DS. These are features, which can be related to distinct stages of alteration. Similar to the non-mineralised granitoids, the F-rich, REY-poor, and S-poor zones crosscut earlier domains.

5.3. Apatite evolution at Olympic Dam

The evolution of apatite at Olympic Dam clearly spans both magmatic and hydrothermal stages. The composition of magmatic apatite reflects both the bulk rock chemistry of the host rock and its crystallisation history. Differences, both textural and geochemical, between apatite in the RDG and enclave-hosted apatite are indicative of the incorporation of exotic material into the RDG melt at the time of crystallisation. This interpretation rests on several lines of evidence: (i) the increased incidence

of pyrrhotite inclusions in apatite is closely tied to the presence of mafic enclaves in both RDG and HRQM; (ii) textural evidence for undercooling conditions during apatite crystallisation, e.g., abundance of acicular apatite in the enclaves, presence of small grains with quartz cores (Piccoli and Candela, 2002); (iii) neither RDG nor the HRQM granitoids contain pyrrhotite outside of the apatite cores; and (iv) whereas pyrrhotite inclusions are most likely to occur in apatite from mafic melts, the fluorite inclusions, present in the same cores, are likely be formed from felsic melts. All of these suggest that apatite co-crystallised with pyrrhotite + fluorite under conditions which were significantly different to those of each of the respective intrusive units, i.e., granitoids and mafic enclaves. Observations of pyrrhotite inclusions in apatite from granitic rocks elsewhere are also interpreted as 'foreign', possibly mafic material (Gottesmann and Wirth, 1997).

Hydrothermal apatite, hosted in early magnetite-dominant mineralisation in both mineralised locations, is interpreted to trace a high-temperature mineralising event in which the fluid is Cl-rich. The early generation is thus distinct from REY-, S-, and Cl-depleted apatite associated with later hematite–sericite alteration. Although not direct evidence, changes in the fluid salinities from early, hypersaline to late, diluted fluids spanning the magnetite dominant to hematite dominant alteration stages are put forward from fluid inclusion studies of various deposits and prospects in the Olympic Province; see summary and discussion in Bastrakov et al. (2007) and references therein. We can only speculate that the type of ligands for various metals and cations in fluids associated with alteration cycles would have also changed from Cl-dominant to others, e.g., fluoride, carbonate, and sulphate. Such changes are however far more complex considering the deposit scale variation in any given mineral association and geochemistry throughout the deposit area (Ehrig et al., 2012) but also the locally closed context that can form within a breccia environment.

Widespread, coarser, and generally irregular distribution of monazite inclusions in apatite is seen in all samples. These are readily identified and are interpreted as products of hydrothermal overprinting by their increased abundance in domains of intense hematite–sericite alteration, alteration of biotite to chlorite, breakdown of igneous ilmenite to hematite–rutile symplectites, an association with zones of hydrothermal interaction across grain margins and fractures, a close association with REY-depleted zones in apatite, and the presence of hydrothermal minerals along associated fractures and channels. Such monazite may be associated with what could be minor huttonite, i.e. monoclinic $ThSiO_4$ as opposed to tetragonal $ThSiO_4$ (thorite). The occurrence of monazite inclusions in apatite, and their interpretation as hydrothermal products, has been reported by Harlov (2015). These inclusions form from fluids of variable chemistry over a wide P–T range. REY-depletion and monazite formation are achieved by destabilisation of coupled substitution mechanisms involving Si^{4+} ($Si^{4+} + REE^{3+} = P^{5+} + Ca^{2+}$) and Na^+ ($Na^+ + REE^{3+} = 2Ca^{2+}$), which result in the inability of apatite to retain REY, in turn leading to monazite crystallisation via coupled dissolution–precipitation reactions (see Harlov, 2015, and references therein).

The rare presence of two-phase [monazite-$ThSiO_4$ (huttonite?)] inclusions (Fig. 9g) along distinct zones crosscutting earlier areas of REY depletion appears to indicate further reworking of apatite within the DM. Replacement of monazite by $ThSiO_4$ has been reproduced experimentally over a wide range of P–T conditions using Th-enriched fluids (Harlov et al., 2007).

Progressive hydrothermal overprinting modifies apatite-bearing assemblages, and ultimately leads to its obliteration. Direct textural observations suggest a two-stage process: (i) apatite replacement by quartz (Fig. 6), releasing Ca^{2+}, $(PO_4)^{2-}$, and F^- to hydrothermal fluid; and (ii) dissolution of that quartz, presumably under extremely acidic (HF-rich) conditions. Such sequential stages of alteration are clearly observed in RDG along the drillhole transect, where disappearance of apatite correlates with corrosion of quartz at the boundary to the orebody. We can only speculate that fluid changes that facilitated the precipitation of quartz that corrodes apatite, and the subsequent replacement of that quartz and ultimately, apatite dissolution, relate to changes in silica speciation and stabilities of dissolved species as a function of the availability of F (and, presumably, also other metals), e.g. Chemtob et al. (2015).

6. Implications and outlook

Previous studies of apatite have overwhelmingly focused on either gaining insights into magmatic processes (Streck and Dilles, 1998; Belousova et al., 2002; Cao et al., 2012), or on the evolution of apatite in response to hydrothermal processes (Bonyadi et al., 2011; Harlov, 2015). The advantage of combining these two approaches in the present study and examining magmatic apatite from distinct, yet related intrusives, has shown that the geochemical and textural responses of apatite to a particular mineralising fluid is largely independent of the magmatic heritage since they all show comparable alteration patterns. Such an observation is important in the study of apatite in magmatic–hydrothermal systems as mineralisation and associated alteration are superimposed onto multiple protoliths, and where the source and physicochemical nature of the hydrothermal fluid(s) are often poorly constrained relative to the sequence of magmatic events.

At OD, apatite evolution, from magmatic to early- and late-stage hydrothermal, is expressed both geochemically and texturally emphasising its potential as a petrogenetic tool. Whereas the petrography of RDG magmatic apatite points to the assimilation of exotic material, subtle changes in the mineral chemistry of hydrothermal apatite record transition in alteration stages. The replacement of apatite, to complete obliteration by highly acidic fluids, which not only corroded apatite but also quartz, led to recycling of REY via subsequent crystallisation of discrete REY-bearing species — notably monazite but also xenotime and florencite. As such, apatite evolution clearly played an important role and may have been integral in contributing to the elevated REY-concentrations seen at OD.

Future work would encompass accurate, independent measurements of OH in apatite, allowing for a more confident approach to fluid–melt–mineral partitioning, also considering the recent concept for an apatite-based hygrometer (McCubbin and Jones, 2015).

Given the marked differences between mineralised and non-mineralised lithologies at OD, apatite chemistry has potential application as a tool in mineral exploration. This rationale will be further explored by testing whether distinct chondrite-normalised REE-patterns in apatite may represent a means for outlining its spatial position within an alteration envelope, or identifying if a particular alteration system is barren or fertile with respect to Cu–Au mineralisation. Such an approach may be extended to include detrital apatite in the thick cover sequences that blanket much of the Olympic Cu–Au Province.

Work to ascertain whether the categories of apatite defined here can be fingerprinted with respect to trace element signatures is currently ongoing. In this, we will also include apatite hosted within high-grade Cu ore, as well as other IOCG systems and larger expressions of alteration yet without mineralisation within the Olympic Cu–Au Province.

Acknowledgements

This work is supported by BHP Billiton. We gratefully acknowledge microanalytical assistance from the staff at Adelaide Microscopy, notably Ben Wade, and from Karsten Goemann, Central Science Laboratory, University of Tasmania. N.J.C. and K.E. acknowledge support from the ARC Research Hub for Australian Copper–Uranium. CLC acknowledges support from the 'FOX' project (Trace elements in iron oxides), supported by BHP Billiton Olympic Dam and the South Australian Mining and Petroleum Services Centre of Excellence. We appreciate the helpful and insightful review comments received from Daniel Harlov and an anonymous reviewer, as well as editorial handling by *Lithos* Editor-in-Chief, Nelson Eby.

Appendix A. Supplementary data

Supplementary data to this article can be found online at http://dx.doi.org/10.1016/j.lithos.2016.07.033.

References

Apukhtina, O.B., Kamenetsky, V.S., Ehrig, K., Kamenetsky, M.B., McPhie, J., Maas, R., Meffre, S., Goemann, K., Rodemann, T., Cook, N.J., Ciobanu, C.L., 2016. Postmagmatic magnetite–apatite assemblage in mafic intrusions: a case study of dolerite at Olympic Dam, South Australia. Contributions to Mineralogy and Petrology 171 (2). http://dx.doi.org/10.1007/s00410-015-1215-7.

Bastrakov, E.N., Skirrow, R.G., Davidson, G.J., 2007. Fluid evolution and origins of iron oxide Cu–Au prospects in the Olympic Dam District, Gawler Craton, South Australia. Economic Geology 102, 1415–1440.

Bea, F., Fershater, G., Corretge, L.G., 1992. The geochemistry of phosphorus in granite rocks and the effect of aluminium. Lithos 29, 43–56.

Belousova, E.A., Walters, S., Griffin, W.L., O'Reilly, S.Y., 2001. Trace-element signatures of apatites in granitoids from the Mt Isa Inlier, northwestern Queensland. Australian Journal of Earth Sciences 48, 603–619.

Belousova, E.A., Griffin, W.L., O'Reilly, S.Y., Fisher, N.I., 2002. Apatite as an indicator mineral for mineral exploration: trace-element compositions and their relationship to host rock type. Journal of Geochemical Exploration 76, 45–69.

Billiton, B.H.P., 2015. http://www.bhpbilliton.com/~/media/bhp/documents/investors/annual-reports/2015/bhpbillitonannualreport2015.pdf.

Blissett, A.H., Creaser, R.A., Daly, S.J., Flint, D.J., Parker, A.J., 1993. Gawler Range Volcanics. In: Drexel, J.F., Preiss, W.V., Parker, A.J. (Eds.), The Geology of South Australia. The Precambrian: Adelaide, Geological Survey of South Australia, Bulletin 54 Vol. 1, pp. 107–131.

Bonyadi, Z., Davidson, G.J., Mehrabi, B., Meffre, S., Ghazban, F., 2011. Significance of apatite REE depletion and monazite inclusions in the brecciated Se–Chahun iron oxide–apatite deposit, Bafq district, Iran: insights from paragenesis and geochemistry. Chemical Geology 281, 253–269.

Boudreau, A., Kruger, F., 1990. Variation in the composition of apatite through the Merensky cyclic unit in the western Bushveld Complex. Economic Geology 85, 737–745.

Candela, P.A., 1986. Generalized mathematical models for the fractional evolution of vapor from magmas in terrestrial planetary crusts. In: Saxena, S.K. (Ed.), Advances in Physical GeochemistryPhysics and Chemistry of the Terrestrial Planets Vol. 6. Springer-Verlag, New York, pp. 362–398.

Cao, M., Li, G., Qin, K., Seitmuratova, E.Y., Liu, Y., 2012. Major and trace element characteristics of apatites in granitoids from Central Kazakhstan: implications for petrogenesis and mineralization. Resource Geology 62, 63–83.

Chemtob, S.M., Rossman, G.R., Young, E.D., Ziegler, K., Moynier, F., Eiler, J.M., Hurowitz, J.A., 2015. Silicon isotope systematics of acidic weathering of fresh basalts, Kilauea volcano, Hawai'i. Geochimica et Cosmochimica Acta 169, 63–81.

Ciobanu, C.L., Wade, B., Cook, N.J., Schmidt Mumm, A., Giles, D., 2013. Uranium-bearing hematite from the Olympic Dam Cu–U–Au deposit, South Australia; a geochemical tracer and reconnaissance Pb–Pb geochronometer. Precambrian Research 238, 129–147.

Creaser, R.A., 1989. The geology and petrology of Middle Proterozoic felsic magmatism of the Stuart Shelf, South Australia. Unpublished Ph.D. thesis, La Trobe University, Melbourne.

Ehrig, K., McPhie, J., Kamanetsky, V.S., 2012. Geology and mineralogical zonation of the Olympic Dam iron oxide Cu–U–Au–Ag deposit, South Australia. In: Hedenquist, J.W., Harris, M., Camus, F. (Eds.), Geology and Genesis of Major Copper Deposits and Districts of the World, a Tribute to Richard Sillitoe. Society of Economic Geologists Special Publication Vol. 16, pp. 237–268.

Gottesmann, B., Wirth, R., 1997. Pyrrhotite inclusions in dark pigmented apatite from granitic rocks. European Journal of Mineralogy 9, 491–500.

Harlov, D.E., 2015. Apatite: a fingerprint for metasomatic processes. Elements 11, 171–176.

Harlov, D.E., Andersson, U.B., Förster, H.-J., Nyström, J.O., Dulski, P., Broman, C., 2002. Apatite–monazite relations in the Kiirunavaara magnetite–apatite ore, northern Sweden. Chemical Geology 191, 47–72.

Harlov, D.E., Wirth, R., Hetherington, C.J., 2007. The relative stability of monazite and huttonite at 300–900 °C and 200–1000 MPa: metasomatism and the propagation of metastable mineral phases. American Mineralogist 92, 1652–1664.

Harrison, T.M., Watson, E.B., 1984. The behaviour of apatite during crustal anatexis: equilibrium and kinetic considerations. Geochimica et Cosmochimica Acta 48, 1467–1477.

Hayward, N., Skirrow, R.G., 2010. Geodynamic setting and controls on iron oxide Cu–Au (±U) ore in the Gawler Craton, South Australia. In: Porter, T.M. (Ed.)Hydrothermal Iron Oxide Copper–Gold & Related Deposits: A Global Perspective Vol. 3. PGC Publishing, Adelaide, pp. 1–27.

Hovis, G.L., Harlov, D.E., 2010. Solution calorimetric investigation of fluor-chlorapatite crystalline solutions. American Mineralogist 95, 946–952.

Hovis, G.L., McCubbin, F.M., Nekvasil, H., Ustunisik, G., Woerner, W.R., Lindsley, D.H., 2014. A novel technique for fluorapatite synthesis and the thermodynamic mixing behaviour of F–OH apatite crystalline solutions. American Mineralogist 99, 890–897.

Huang, Q., Kamenetsky, V.S., McPhie, J., Ehrig, K., Meffre, S., Maas, R., Thompson, J., Kamenetsky, M., Chambefort, I., Apukhtina, O., Hu, Y., 2015. Neoproterozoic (ca. 820–830 Ma) mafic dykes at Olympic Dam, South Australia: links with the Gairdner Large Igneous Province. Precambrian Research 271, 160–172.

Huang, Q., Kamenetsky, V.S., Ehrig, K., McPhie, J., Kamenetsky, M., Cross, K., Meffre, S., Agangi, A., Chambefort, I., Direen, N.G., Maas, R., Apukhtina, O., 2016. Olivine-phyric basalt in the Mesoproterozoic Gawler silicic large igneous province, South Australia: examples at the Olympic Dam Iron Oxide Cu–U–Au–Ag deposit and other localities. Precambrian Research 281, 185–199.

Hughes, J.M., Rakovan, J.F., 2015. Structurally robust, chemically diverse: apatite and apatite supergroup minerals. Elements 11, 165–170.

Ismail, R., Ciobanu, C.L., Cook, N.J., Teale, G.S., Giles, D., Schmidt Mumm, A., Wade, B., 2014. Rare earths and other trace elements in minerals from skarn assemblages, Hillside iron oxide–copper–gold deposit, Yorke Peninsula, South Australia. Lithos 184–187, 456–477.

Jagodzinski, E.A., 2005. Compilation of SHRIMP U–Pb Geochronological Data. Olympic Domain, Gawler Craton, South Australia, 2001–2003. Geoscience Australia, Record 2005/20.

Johnson, J.P., Cross, K.C., 1995. U–Pb geochronological constraints on the genesis of Olympic Dam Cu–U–Au–Ag deposit, South Australia. Economic Geology 88, 1046–1063.

Jonsson, E., Harlov, D.E., Majka, J., Högdahl, K., Persson-Nilsson, K., 2016. Fluorapatite-monazite-allanite relations in the Grängesberg apatite-iron oxide ore district, Bergslagen, Sweden. American Mineralogist 101, 1769–1782.

Kontonikas-Charos, A., Ciobanu, C.L., Cook, N.J., 2014. Albitization and redistribution of REE and Y in IOCG systems: insights from Moonta-Wallaroo, Yorke Peninsula, South Australia. Lithos 208, 178–201.

Kontonikas-Charos, A., Ciobanu, C.L., Cook, N.J., Ehrig, K., Kamenetsky, V.S., 2015. Deuteric coarsening and albitization in Hiltaba granites from the Olympic Dam IOCG deposit, South Australia. Proceedings, Mineral Resources in a Sustainable World, 13th Biennial SGA Meeting, Nancy, France, August 2015 Vol. 3, pp. 1099–1102.

Krneta, S., Ciobanu, C.L., Cook, N.J., Ehrig, K., Kamenetsky, V.S., 2015. Apatite in the Olympic Dam Cu–U–Au–Ag deposit. Proceedings, Mineral Resources in a Sustainable World, 13th Biennial SGA Meeting, Nancy, France, August 2015 Vol. 3, pp. 1103–1106.

McCubbin, F.M., Jones, R.H., 2015. Extraterrestrial apatite: planetary geochemistry to astrobiology. Elements 11, 183–188.

Pan, Y., Fleet, M.E., 2002. Compositions of the apatite-group minerals: substitution mechanisms and controlling factors. Reviews in Mineralogy and Geochemistry 48, 13–49.

Pasero, M., Kampf, A., Ferraris, C., Pekov, I.V., Rakovan, J., White, T., 2010. Nomenclature of the apatite supergroup minerals. European Journal of Mineralogy 22, 163–179.

Piccoli, P.M., Candela, P.A., 1994. Apatite in felsic rocks: a model for the estimation on initial halogen concentrations in the Bishop TuV (Long Valley) and Tuolumne Intrusive Suite (Sierra Nevada Batholith) magmas. American Journal of Science 294, 92–135.

Piccoli, M.P., Candela, P.A., 2002. Apatite in igneous systems. Reviews in Mineralogy and Geochemistry 48, 255–292.

Reeve, J.S., Cross, K.C., Smith, R.N., Oreskes, N., 1990. Olympic Dam copper–uranium–gold–silver deposit. In: Hughes, F.E. (Ed.), Geology of the Mineral Deposits of Australia and Papua New Guinea: Australasian Institute of Mining and Metallurgy. Monograph Vol. 14, pp. 1009–1035.

Rønsbo, J.G., 1989. Coupled substitutions involving REE's and Na and Si in apatites in alkaline rocks from Ilimaussaq, South Greenland, and the petrological implications. American Mineralogist 74, 896–901.

Skirrow, R.G., Bastrakov, E.N., Barovich, K., Fraser, G.L., Creaser, R., Fanning, M.C., Raymond, O.L., Davidson, G.J., 2007. Timing of iron oxide Cu–Au–(U) hydrothermal activity and Nd isotope constraints on metal sources in the Gawler craton, South Australia. Economic Geology 102, 1441–1470.

Streck, M.J., Dilles, J.H., 1998. Sulfur evolution of oxidized arc magmas as recorded in apatite from a porphyry copper batholith. Geology 26, 523–526.

Webster, J.D., Piccoli, P.M., 2015. Magmatic apatite: a powerful, yet deceptive, mineral. Elements 11, 177–182.

Wolf, M.B., London, D., 1995. Incongruent dissolution of REE- and Sr-rich apatite in peraluminous granitic liquids: differential apatite, monazite, and xenotime solubilities during anatexis. American Mineralogist 80, 765–775.

Zhu, C., Sverjensky, D.A., 1991. Partitioning of F–Cl–OH between minerals and hydrothermal fluids. Geochimica et Cosmochimica Acta 55, 1837–1858.

ADDITIONAL MATERIAL F

CONFERENCE ABSTRACT:

DEUTERIC COARSENING AND ALBITIZATION IN HILTABA SUITE GRANITES FROM THE OLYMPIC DAM IOCG DEPOSIT, SOUTH AUSTRALIA

Alkis Kontonikas-Charos[1], Cristiana L. Ciobanu[2], Nigel J. Cook[2], Kathy Ehrig[3], Vadim S. Kamenetsky[4]

[1]School of Physical Sciences, The University of Adelaide, Adelaide, SA, 5005, Australia

[2]School of Chemical Engineering, The University of Adelaide, Adelaide, SA, 5005, Australia

[3]BHP Billiton Olympic Dam, Adelaide, SA, 5000, Australia

[4]School of Physical Sciences, University of Tasmania, Hobart, TAS, 7001, Australia

Abstract and Presentation, Mineral Resources in a Sustainable World. Proceedings of the 13th SGA Biennial Meeting, Nancy, France, August 24-27th, 2015. ISBN: 978-2-85555-065-7, Volume 3, 1099-1102.

Deuteric coarsening and albitization in Hiltaba granites from the Olympic Dam IOCG deposit, South Australia

Alkis Kontonikas-Charos
School of Physical Sciences, University of Adelaide, Adelaide S.A. 5005, Australia

Cristiana L. Ciobanu, Nigel J. Cook
School of Chemical Engineering, University of Adelaide, Adelaide S.A. 5005, Australia

Kathy Ehrig
BHP Billiton Olympic Dam, Adelaide S.A. 5000, Australia

Vadim S. Kamenetsky
School of Physical Sciences, University of Tasmania, Hobart, TAS, 7001, Australia

Abstract. Feldspar replacement and re-equilibration reactions within the Roxby Downs Granite (RDG) and variably altered counterparts, host for the Olympic Dam IOCG deposit, are discussed. Feldspars in these rocks, and within a distinct quartz monzonite in the area (Horn Ridge Granite; HRG), preserve complex textural relationships. Alkali feldspars form intricate exsolution microtextures of microperthite and cryptoperthite which have recrystallized and subsequently coarsened to form patch perthite. Igneous plagioclase varies in composition; from oligoclase-andesine (~An_{11-39}) in the RDG to oligoclase (~An_{24}) in the HRG, and is pervasively replaced by albite ± sericite ± hematite. As hydrothermal alteration progresses, plagioclase and albite are almost completely removed, while sericite and red-stained K-feldspar are stable in altered RDG. Textural observations of both feldspar reactions are consistent with a replacement process governed by coupled dissolution-reprecipitation reaction. The evidence suggests a significant role for deuteric coarsening followed by albitization prior to mineralization in the RDG.

Keywords. Olympic Dam, IOCG, albitization, deuteric coarsening, feldspar

1 Introduction

The Olympic Dam iron-oxide copper-gold (IOCG)-U deposit, South Australia, is widely regarded as the archetype of the IOCG *sensu stricto* deposit class (e.g. Hitzman et al. 1992; Groves et al. 2010). However, many questions remain unanswered regarding the role and significance of early widespread alkali (sodic) metasomatism of the host rocks, as well as the apparent temporal and/or spatial relationship between IOCG deposits and magmatism. The Olympic Dam deposit is located within the ~1.6 Ga Roxby Downs Granite (RDG) (e.g. Reeve et al. 1990; Creaser and Cooper 1993), providing the opportunity to test the validity of the relationship between magmatism, metasomatism and mineralization by comparing the chemistry and sub-µm-scale textures in fresh granite and altered counterparts. Constraining the major mineralogical changes preserved in host rocks prior to mineralization may offer new insights into the earliest stages of IOCG genesis.

Feldspar reactions in granitic rocks have been studied in detail, particularly with respect to feldspar re-equilibration (e.g. Parsons and Lee 2009; Plümper and Putnis 2009). Deuteric coarsening, a process that takes place during the cooling of igneous rocks, results in recrystallization and subsequent coarsening of feldspars via the circulation of deuteric fluids (Worden et al. 1990). Albitization, which involves the replacement of plagioclase and/or alkali feldspar by albite, is one of the most common metasomatic aluminosilicate reactions in the Earth's upper crust (Perez and Boles 2005), and has been reported from various igneous-metamorphic terranes including the Bamble Sector, Norway (Engvik et al. 2008), Cloncurry District, Queensland, Australia (e.g. Oliver et al. 2004), and recently from the southern part of the Gawler Craton, South Australia (Conor et al. 2010; Ismail et al. 2014; Kontonikas-Charos et al. 2014). Such feldspar reactions are capable of altering the physical properties and chemistry of rocks by significantly enhancing rock permeability via the generation of interconnected porosity (e.g. Putnis 2002), and remobilization of minor/trace elements (e.g. Parsons et al. 2009; Hövelmann et al. 2010).

Given the apparent close association between sodic metasomatism and IOCG deposits (e.g. Hitzman et al. 1992), chemical and textural changes induced by reactions involving feldspars may carry implications for understanding processes associated with alteration and mineralization at Olympic Dam and elsewhere.

2 Geological background

The Olympic Dam deposit (9840 Mt @ 0.78% Cu, 0.25kg/t U_3O_8, 0.3g/t Au, 2g/t Ag (BHP Billiton 2014) is hosted within hydrothermal breccias of the Olympic Dam Breccia Complex (ODBC) contained within the Mid-Proterozoic RDG and unconformably overlain by sediments of the Stuart Shelf. The RDG is a coarse-grained, Hiltaba Suite, equigranular to porphyritic, relatively undeformed granite and is primarily composed of alkali feldspar (~45%), plagioclase (~20%), quartz (~30%), biotite, amphibole and accessories (<5%) (Ehrig et al. 2012).

The ODBC is characterized by a gradational continuum from granite breccias to hematite-granite breccias to hematite breccias from the edge to the center of the deposit (Reeve et al. 1990). It also comprises various felsic and mafic-ultramafic intrusives, attributed to the Gawler Range Volcanics (GRV), as well as bedded sedimentary rocks of disparate origin. Oreskes and Einaudi (1990) reported widespread sericite and hematite alteration of feldspars, and to a lesser extent chloritization of mafics, within the RDG. Sodic alteration (particularly albitization) was not considered to be significant at Olympic Dam despite its prominence elsewhere in the Olympic Cu-Au Province (e.g. Hayward and Skirrow 2010).

3 Approach and methodology

The study was undertaken on granite samples representing various parts of the Olympic Dam area (Fig. 1). Drillholes along a transect (from RD2274 to RD2511) were selected to understand feldspar modifications from relatively fresh to altered granite on the margin of the deposit. The sample suite also includes fresh granite from drillhole RD2494 and altered granites hosting weak sulfide mineralization (drillholes RD3554 and RD2316).

A mineralogical and petrological study was carried out on thin sections and polished blocks which were analyzed by optical microscopy, scanning electron microscopy in back-scatter electron (BSE) mode and electron probe microanalysis.

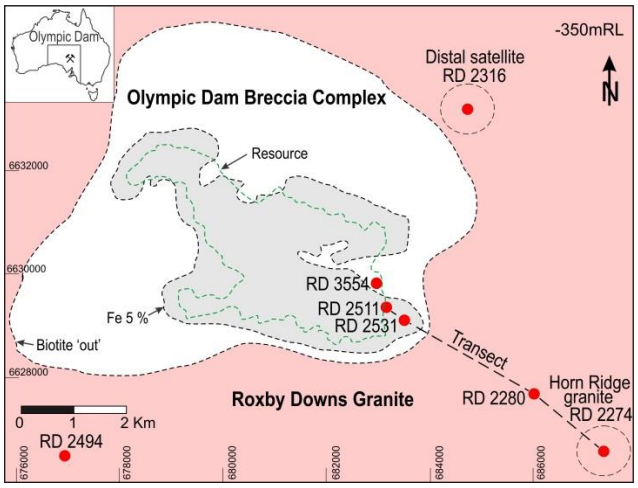

Figure 1. Sketch map showing sampled drillhole locations at Olympic Dam, modified from Ehrig et al. (2012).

4 Results

4.1 Samples and whole-rock chemistry

Fresh granite was recognized via a combination of macroscopic observations (including the presence of biotite) and a K_2O/Na_2O ratio of ~5.5:3.5 in whole-rock analyses (e.g. Ehrig et al. 2012). Samples of moderately-altered granite were obtained from drillholes proximal to the ODBC, and were identified by changes in feldspar coloration (pink to red) and a distinct drop in Na_2O content (<0.5 wt%). Intensely-altered samples, representative of the ODBC, were identified by Fe content and textural observations.

Results of whole-rock analyses of selected samples reveal 3 distinct clusters on a QAP diagram (Fig. 2) The RDG plots in the granite field, however sericite and hematite alteration, particularly of feldspars (Fig. 3a, b), skew the RDG towards the alkali feldspar granite field.

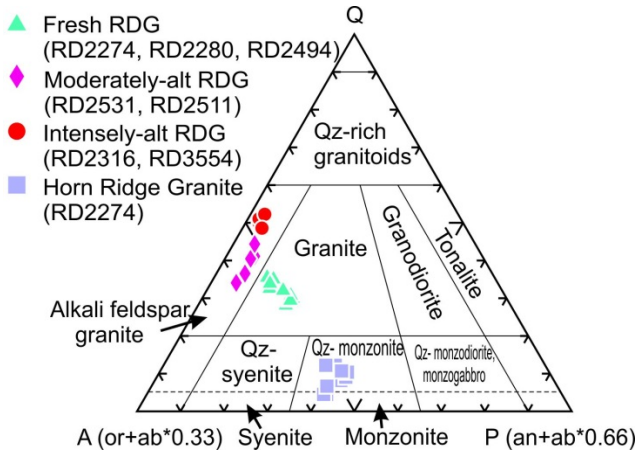

Figure 2. Modified QAP diagram based on CIPW normative compositions calculated from whole-rock analyses and IUGS classification of RDG and HRG granitoids. Q: quartz.

The Horn Ridge Granite (HRG) is interpreted as an early Hiltaba Suite granite intruded by the RDG (RD2274; Fig. 1) and has a SHRIMP U/Pb age of 1594.4 ± 3.4 Ma (Jagodzinski 2005). It plots in a tight cluster within the quartz monzonite field on Fig. 2. The HRG has a similar mineralogy to the RDG but can be distinguished by a greater proportion of mafic minerals (Fig. 3c). This observation, along with its silica deficiency, indicate it may be a primitive relative of the RDG - both granites form part of the Burgoyne Batholith (Creaser 1996).

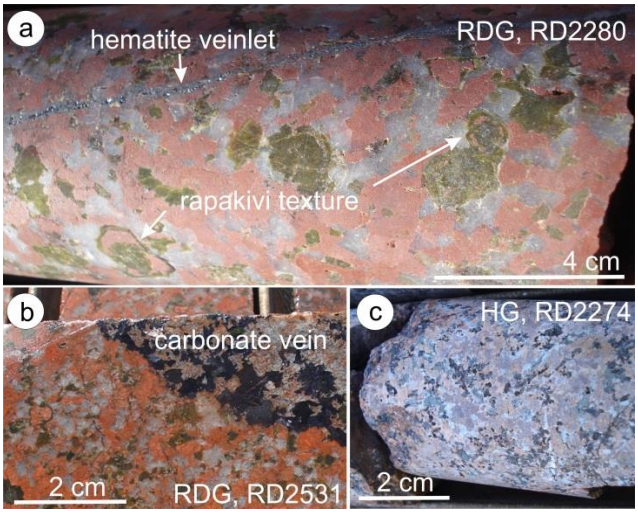

Figure 3. Hand specimen photographs showing characteristics of the granites discussed. Note the RDG micro-rapakivi texture in (a) as stated by Oreskes and Einaudi (1990), and transition from hematite (a) to carbonate (b) veins along the transect on Fig. 1.

4.2 Feldspar textures and mineralogy

Feldspars of the RDG and HRG display varying textures, morphologies and alteration. Three alkali feldspar micro-textures are identified (following nomenclature of Parsons et al. 2005): microperthite, cryptoperthite, and patch perthite. Microperthite and cryptoperthite consist of semi- to fully-coherent Ab-rich lamellae within an Or-rich feldspar. Patch perthite comprises coarse, incoherent Ab-rich and Or-rich subgrains (Fig. 4). It typically forms along lamellae of perthitic feldspar grains and may result in sets of intragranular anastomosing veins. Alkali feldspar microtextures are similar in the HRG; they are, however, all dominated by Or-rich phases.

Two compositions of igneous plagioclase are preserved in the RDG: andesine (~An_{35-39}); and oligoclase (~An_{11-18}), whereas only oligoclase (~An_{24}) has been identified in the HRG. The RDG micro-rapakivi texture (Fig. 3a) consists of oligoclase as coarse rims (>2 mm) around alkali feldspar. Similarly to the alkali feldspars, plagioclase commonly preserves complex, multistage overprints possibly related to feldspar re-equilibration. Subsequently, pervasive replacement of plagioclase by newly-formed albite is observed to various extents (Fig. 5a, b). This replacive albite is extremely porous and contains intergrown sericite ± hematite (Fig. 5c).

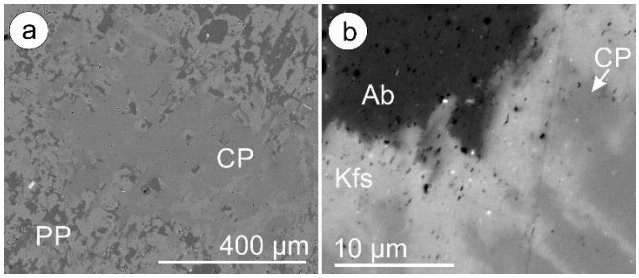

Figure 4. BSE images showing typical aspects of deuteric coarsening of alkali feldspar in the RDG. (a) Patch perthite (PP) consisting of albite-rich (Ab) and Or-rich (Kfs) phases forming irregular, crenulated boundaries with cryptoperthite (CP). (b) Micro-porosity in PP relative to CP.

Igneous plagioclase is absent from moderately- and intensely-altered RDG, however albite may be preserved at depth or at the peripheries of the ODBC. Perthitic K-feldspar grains may be preserved in altered RDG, however these are overprinted by highly porous, red-stained K-feldspar containing various disseminated inclusions (quartz, chlorite, sericite, siderite, fluorite, hematite and occasionally sulfides; Fig. 5d).

5 Discussion

Textural observations and relationships between alkali feldspar and plagioclase strongly suggest that post-magmatic processes operated within the RDG and HRG. The micro-rapakivi textures in the RDG likely relate to remobilization and redistribution of feldspar components following initial crystallization (Dempster et al. 1994). In addition, the recrystallization of alkali feldspar exsolution textures is suggestive of deuteric coarsening. In this case, patch perthite appears to form on behalf of microperthite and cryptoperthite; a process which may also promote subsequent feldspar-fluid interaction (Lee and Parsons 1997). The pervasive nature of this replacement, noticeable porosity in the product phase and the sharp interface at the reaction front, are consistent with a coupled dissolution-reprecipitation reaction (CDRR, e.g. Putnis 2002). CDRR has been proposed for numerous replacement reactions including deuteric coarsening of cryptoperthite to patch perthite (e.g. Worden et al. 1990; Norberg et al. 2013) and albitization (e.g. Lee and Parsons 1997; Plümper and Putnis 2009).

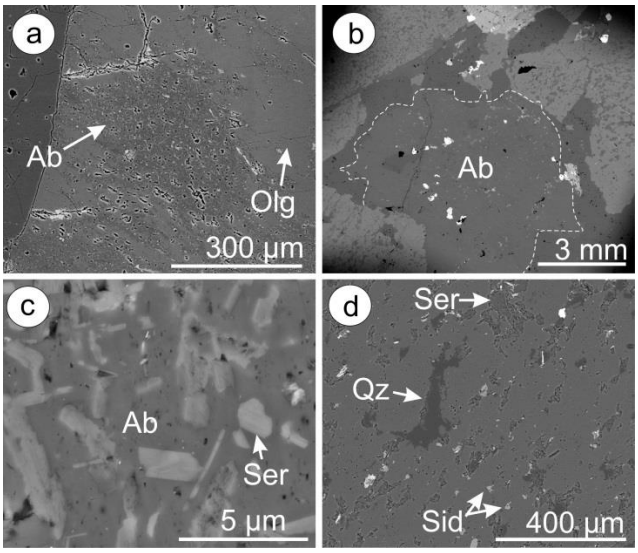

Figure 5. BSE images showing key albitization textures in the RDG (a-c) and altered K-feldspar in the ODBC (d). Ab: albite; Olg: oligoclase; Qz: quartz; Ser; sericite; Sid: siderite.

Albitization of igneous plagioclase is ubiquitous within the RDG and HRG, and also displays textural features suggestive of CDRR. This replacement tends to occur along cleavage planes of plagioclase, and may lead to the formation of isolated patches of albite. Given sustained fluid supply and continuous generation of porosity, these patches can eventually form large pseudomorphs of albitized plagioclase (e.g. Fig. 5b). A similar process was documented by Plümper and Putnis (2009). The presence of co-precipitates (e.g. sericite and hematite) within albite, may be attributed to the non-isochemical nature of the albitization reaction (Perez and Boles 2005). In addition, trace elements remobilized during albitization may be transported over long distances via reaction-enhanced permeability (Putnis 2002). This association between albitization and trace element remobilization has been documented in several studies of IOCG terranes (e.g. Oliver et al. 2004; Ismail et al. 2014; Kontonikas-Charos et al. 2014).

Textures observed within altered RDG and the ODBC indicate a physico-chemical change from albite-stable to sericite- and K-feldspar-stable conditions. This

hydrothermal K-feldspar overprint contains disseminated sub-μm-sized inclusions of hematite which likely account for the characteristic red-staining. Such features have been interpreted to represent large-scale subsolidus re-equilibration (e.g. Putnis et al. 2007). Moreover, given the extent of Fe-oxides at Olympic Dam, variable dusty hematite alteration of feldspars may relate to infiltration of Fe-rich hydrothermal fluid associated with mineralization (e.g. Haynes et al. 1995).

Further work will address trace element redistribution relating to deuteric coarsening and albitization. The primary focus is to understand whether these feldspar reactions are more important than previously thought, and to ascertain their impact on the anomalous enrichment of key trace elements such as REE and U at Olympic Dam.

6 Conclusions

Recognition of post-magmatic processes within the RDG prior to mineralization at Olympic Dam may have significant implications for deposit formation. Deuteric coarsening and albitization are clearly capable of enhancing porosity and permeability, and remobilizing major, minor and trace elements. Given the anomalous enrichment of many trace elements in the Olympic Dam deposit, albitization may represent an initial stage of leaching and redistribution of these trace elements, as a prerequisite for subsequent stages of mineralization. The recognition of albitization at Olympic Dam is noteworthy and supports a close association between sodic metasomatism and IOCG mineralization.

Acknowledgements

We thank BHP Billiton for financial support and access to Olympic Dam samples and facilities. We also thank Adelaide Microscopy for assistance with microanalysis.

References

BHP Billiton (2014) http://www.bhpbilliton.com/home/investors/reports/Documents/2014/BHPBillitonAnnualReport2014.pdf

Creaser RA, Cooper JA (1993) U-Pb Geochronology of Middle Proterozoic felsic magmatism surrounding the Olympic Dam Cu-U-Au-Ag and Moonta Cu-Au-Ag deposits, South Australia. Econ Geol. 88:186-197

Creaser RA (1996) Petrogenesis of a Mesoproterozoic quartz latite-granitoid suite from the Roxby Downs area, South Australia. Precambrian Research 79:371-394

Conor C, Raymond OL, Baker T, Teale G, Say P, Lowe G (2010) Alteration and mineralisation in the Moonta-Wallaroo Copper-Gold Mining Field Region, Olympic Domain, South Australia. Hydrothermal Iron Oxide Copper-Gold & Related Deposits: A Global Perspective. 3:1–24

Dempster T, Jenkin G, Rogers G (1994) The origin of rapakivi texture. J Petrol 35:963-981

Ehrig K, McPhie J, Kamenetsky V (2012) Geology and mineralogical zonation of the Olympic Dam iron oxide Cu-U-Au-Ag deposit, South Australia. SEG Spec Publ 16: 237-268

Engvik AK, Putnis A, Gerald JDF, Austrheim H (2008) Albitization of granitic rocks: the mechanism of replacement of oligoclase by albite. Can Mineral 46:1401-1415

Groves DI, Bierlein FP, Meinert LD, Hitzman MW (2010) Iron Oxide Copper-Gold (IOCG) Deposits through Earth History: Implications for Origin, Lithospheric Setting, and Distinction from Other Epigenetic Iron Oxide Deposits. Econ Geol 105:641-654

Haynes DW, Cross KC, Bills RT, Reed MH (1995) Olympic Dam ore genesis; a fluid-mixing model. Econ Geol 90:281-307

Hayward N, Skirrow RG (2010) Geodynamic Setting and Controls on Iron Oxide Cu-Au(±U) Ore in the Gawler Craton, South Australia. Hydrothermal Iron Oxide Copper-Gold & Related Deposits: A Global Perspective. 3:1-28

Hitzman MW, Oreskes N, Einaudi MT (1992) Geological characteristics and tectonic setting of Proterozoic iron oxide (Cu-U-Au-REE) deposits. Precambr Res 58:241-287

Hövelmann J, Putnis A, Geisler T, Schmidt BC, Golla-Schindler U (2010) The replacement of plagioclase feldspars by albite: observations from hydrothermal experiments. Contrib Mineral Petrol 159:43-59

Ismail R, Ciobanu CL, Cook NJ, Teale GS, Giles D, Mumm AS, Wade B (2014) Rare earths and other trace elements in minerals from skarn assemblages, Hillside iron oxide–copper–gold deposit, Yorke Peninsula, South Australia. Lithos 184–187:456-477

Jagodzinski EA (2005) Compilation of SHRIMP U-Pb geochronological data. Geoscience Australia Record 2005/20

Kontonikas-Charos A, Ciobanu CL, Cook NJ (2014) Albitization and redistribution of REE and Y in IOCG systems: Insights from Moonta-Wallaroo, Yorke Peninsula, South Australia. Lithos 208–209:178-201

Lee MR, Parsons I (1997) Dislocation formation and albitization in alkali feldspars from the Shap granite. Amer Mineral 82:557-570

Norberg N, Harlov D, Neusser G, Wirth R, Rhede D, Morales L (2013) Experimental development of patch perthite from synthetic cryptoperthite: Microstructural evolution and chemical re-equilibration. Amer Mineral 98:1429-1441

Oliver NH, Cleverley JS, Mark G, Pollard PJ, Fu B, Marshall LJ, Rubenach MJ, Williams PJ, Baker T (2004) Modeling the role of sodic alteration in the genesis of iron oxide-copper-gold deposits, Eastern Mount Isa block, Australia. Econ Geol 99:1145-1176

Oreskes N, Einaudi MT (1990) Origin of rare earth element-enriched hematite breccias at the Olympic Dam Cu-U-Au-Ag deposit, Roxby Downs, South Australia. Econ Geol 85:1-28

Parsons I, Lee MR (2009) Mutual replacement reactions in alkali feldspars I: microtextures and mechanisms. Contrib Mineral Petrol 157:641-661

Parsons I, Thompson P, Lee MR, Cayzer N (2005) Alkali feldspar microtextures as provenance indicators in siliciclastic rocks and their role in feldspar dissolution during transport and diagenesis. J Sed Res 75:921-942

Parsons I, Magee CW, Allen CM, Shelley J, Lee MR (2009) Mutual replacement reactions in alkali feldspars II: trace element partitioning and geothermometry. Contrib Min Pet 157: 663-687

Perez RJ, Boles JR (2005) An empirically derived kinetic model for albitization of detrital plagioclase. Amer J Sci 305:312-343

Plümper O, Putnis A (2009) The complex hydrothermal history of granitic rocks: multiple feldspar replacement reactions under subsolidus conditions. J Petrol 50:967-987

Putnis A (2002) Mineral replacement reactions: from macroscopic observations to microscopic mechanisms. Mineral Mag 66:689-708

Putnis A, Hinrichs R, Putnis CV, Golla-Schindler U, Collins LG (2007) Hematite in porous red-clouded feldspars: evidence of large-scale crustal fluid–rock interaction. Lithos 95:10-18

Reeve JS, Cross KC, Smith RN, Oreskes N (1990) Olympic Dam copper-uranium-gold-silver deposit. AusIMM Monogr 14: 1009-1035

Worden RH, Walker FDL, Parsons I, Brown WL (1990) Develop-ment of microporosity, diffusion channels and deuteric coarsening in perthitic alkali feldspars. Contrib Min Pet 104:507-515

ADDITIONAL MATERIAL G

CONFERENCE ABSTRACT AND POSTER:

FELDSPAR RE-EQUILIBRATION REACTIONS IN HILTABA SUITE GRANITE FROM THE OLYMPIC DAM IOCG-(U) DEPOSIT, SOUTH AUSTRALIA

Alkis Kontonikas-Charos[1], Cristiana L. Ciobanu[2], Nigel J. Cook[2], Kathy Ehrig[3], Sasha Krneta[1], Vadim S. Kamenetsky[4]

[1]*School of Physical Sciences, The University of Adelaide, Adelaide, SA, 5005, Australia*

[2]*School of Chemical Engineering, The University of Adelaide, Adelaide, SA, 5005, Australia*

[3]*BHP Billiton Olympic Dam, Adelaide, SA, 5000, Australia*

[4]*School of Physical Sciences, University of Tasmania, Hobart, TAS, 7001, Australia*

Abstract and Poster, Society of Economic Geologists Conference 2015, 'World-Class Ore Deposits: Discovery to Recovery', Hobart, TAS, Australia, September 27-30th.

Feldspar re-equilibration reactions in Hiltaba suite granites from the Olympic Dam IOCG-(U) deposit, South Australia

Alkis Kontonikas-Charos[1], Cristiana L. Ciobanu[2], Nigel J. Cook[2], Kathy Ehrig[3], Vadim S. Kamenetsky[4]

[1]School of Physical Sciences, University of Adelaide, Adelaide S.A. 5005, Australia

[2]School of Chemical Engineering, University of Adelaide, Adelaide S.A. 5005, Australia

[3]BHP Billiton Olympic Dam, Adelaide S.A. 5000, Australia

[4]School of Physical Sciences, University of Tasmania, Hobart, TAS, 7001, Australia

Our reconnaissance study investigates textural relationships and geochemical signatures of feldspars from 'fresh' to variably sericite-hematite-altered ~1.595 Ga Hiltaba suite granites at Olympic Dam. The sample suite is representative of the Horn Ridge Granite (HRG), a quartz monzonite, and the Roxby Downs Granite (RDG) distal and proximal to, as well as within, the Olympic Dam Breccia Complex (ODBC). Microscopic observations and quantitative analyses indicate the presence of feldspar re-equilibration and replacement reactions prior to deposition of mineralization within the RDG.

Alkali feldspars, at the earliest preserved stage, display characteristic fine-grained cryptoperthite and microperthite exsolution textures, which have been pervasively recrystallized by circulation of deuteric fluids in the form of patch perthite, consisting of Ab-rich and Or-rich subgrains. Igneous feldspar in both granites, oligoclase (An_{11} in RDG, An_{24} in HRG), is commonly observed as rims surrounding alkali feldspar phenocrysts (rapakivi texture), which are partially and completely replaced by albite ± sericite. While sericite commonly forms an intergrowth texture with replacive albite, other mineral inclusions also nucleate in association with feldspar replacement phases. Sub-µm sized hematite inclusions form within and, most commonly, near the reaction boundary of patch perthite and replacive albite, respectively, while fluorite is a frequent accessory in oligoclase. In addition, synchysite is occasionally observed in replacive albite. Irrespective of source, the presence of such inclusions indicates the remobilization of these elements during early feldspar re-equilibration reactions. Quantitative LA-ICP-MS analyses of the various feldspars can provide insight into the behaviour of such trace elements during fluid-rock interaction.

A sharp reaction-interface, the generation of pores (± inclusions) in the product phase and pseudomorphic textures associated with both deuteric coarsening and albitization are strongly supportive of coupled dissolution re-precipitation reaction. Electron microprobe mapping is in accordance with these textural observations. The rapakivi texture may have also formed via a similar dissolution re-precipitation mechanism.

Following early deuteric coarsening and incipient albitization, hydrothermal alteration progresses, particularly in the ODBC, and results in widespread sericitization at the expense of igneous plagioclase and albite. Red-stained K-feldspar (attributed to dusty sub-µm hematite inclusions) is the only persisting alkali feldspar, however, albite and rare alkali feldspar microtextures are preserved at depth or at the peripheries of the ODBC.

Given the abundance of alkali and plagioclase feldspars in the RDG (>65 vol.%), such textural features, in particular the generation of transient porosity, may have greatly increased the overall permeability of the rocks during fluid-rock interaction. Therefore, sustained flow of an oxidized (hematite-stable) fluid may have led to significant redistribution of major, minor and trace elements, including rare-earth elements and yttrium, within the RDG prior to subsequent mineralizing stages. Feldspar re-equilibration and replacement reactions would thus represent the circulation of fluid(s), at least locally, accounting for overlapping alteration styles during the initial stages of IOCG genesis.

Feldspar re-equilibration reactions in Hiltaba suite granite from the Olympic Dam IOCG-(U) deposit, South Australia

Alkis Kontonikas-Charos[1*], Cristiana L. Ciobanu[2], Nigel J. Cook[2], Kathy Ehrig[3], Sasha Krneta[1] and Vadim S. Kamenetsky[4]

[1]School of Physical Sciences, University of Adelaide, Adelaide, SA, 5000, Australia
[2] School of Chemical Engineering, University of Adelaide, Adelaide, SA, 5000, Australia
[3]BHP Billiton, Olympic Dam, Adelaide, SA, 5000, Australia
[4]School of Physical Sciences, University of Tasmania, Hobart, TAS, 7001, Australia

*alkiviadis.kontonikas-charos@adelaide.edu.au

Rationale: The presence of feldspar replacement reactions has long been recognised as a diagnostic property of iron-oxide copper-gold (IOCG) systems [1]; however the exact role they play in the genesis of such deposits remains poorly constrained. At Olympic Dam, all IOCG mineralisation is localised within the ~1.6 Ga Roxby Downs Granite (RDG) [2], therefore providing an outstanding opportunity to track changes in feldspar chemistry and textures from fresh granite to altered counterparts. Constraining major mineralogical changes preserved in host rocks prior to mineralisation offers new insights into the earliest stages of IOCG genesis.

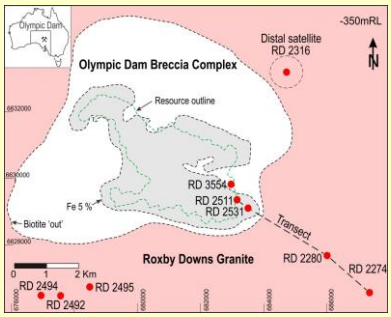

Figure 1: Sketch map of the Olympic Dam deposit and sampled drillhole locations. Modified after [3].

Samples and whole-rock geochemistry

Freshest RDG is abundant in drillholes >3 km outside the ODBC and is primarily recognised by the pink colouration of feldspars, preservation of mafic minerals and rapakivi textures (Fig. 2b). Red-staining and alteration of feldspars and mafic minerals are diagnostic of altered RDG (Fig. 2c), which is more intense in drillholes proximal to the ODBC. Low Na_2O content (<0.5 wt %) and elevated Fe (>7 wt. %) is also characteristic of altered RDG.

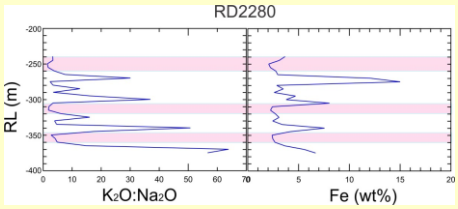

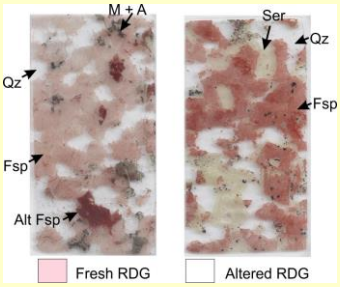

Figure 2: Binary plots of whole-rock analyses for drillhole RD2280 and scanned thin sections outlining differences in appearance between fresh and altered RDG. Sections shaded pink represent low K_2O:Na_2O ratios and low Fe content, likely corresponding to fresh RDG. Note the change from pink to red colouration of feldspars and abundance of sericite in altered RDG.
Abbreviations: Alt - altered, Fsp - feldspar, M + A - mafic and accessory minerals, Qz - quartz, RL - relative depth of drillhole, Ser - sericite.

Results: Feldspar relationships and compositions in fresh and altered Roxby Downs Granite

Fresh RDG

- Two generations of igneous plagioclase: (i) Andesine-oligoclase (~An_{27-34}) occurs as cores mantled by (ii) oligoclase (An_{12-20}) (Fig. 3a), which also forms rapakivi textures.
- Igneous alkali feldspar (micro– and cryptoperthite) has been extensively recrystallised to coarse, highly porous patch perthite (Fig. 3b).
- All plagioclase has been affected by pervasive albitisation, consisting of albite + sericite (Fig. 3c). Fine-grained Ba-rich K-feldspar (up to 15 wt. % BaO) is found in and restricted to previously albitised areas of plagioclase (Fig. 3d).

Altered RDG

- No igneous plagioclase or mafic minerals are preserved. Chlorite, sericite, hematite and quartz dominate. Albite still preserved at depth or to the periphery of the ODBC.
- Alkali feldspar overprinted by Fe-rich (up to 3 wt.% FeO), red-stained K-feldspar (Fig. 3e). Such feldspar is also locally associated with sulphides.
- The abundance of red-stained K-feldspar increases with proximity to the ODBC, while albite progressively disappears. At upper levels, sericite predominates, and no feldspars are preserved.

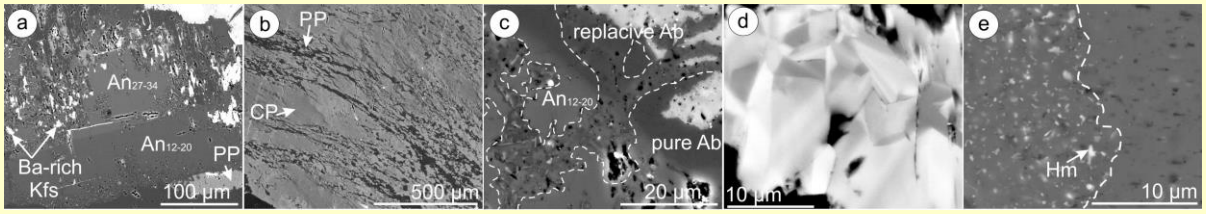

Figure 3: Images displaying important feldspar disequilibrium textures observed in the RDG. Sourced from [4]. (a) Discontinuous zonation of plagioclase. (b) Widespread recrystallization of igneous alkali feldspar to patch perthite. (c) Two generations of albite associated with plagioclase; pure and replacive. (d) Discrete Ba-rich K-feldspar, found in previously albitised areas. (e) Red-stained K-feldspar, abundant and characteristic of altered RDG. Abbreviations: Ab - albite, An - anorthite content, CP - cryptoperthite, Hm - hematite, PP - patch perthite.

Discussion

- Replacement of alkali feldspar by low-An oligoclase and discontinuous plagioclase rims is interpreted to be the result of late-stage magma mixing and/or ascent.
- The results collectively point to a cyclic process in which initial fluids exsolved from the melt and evolved through cooling and convection within the granitoid pluton leading to deuteric coarsening, albitisation and nucleation of hydrothermal K-feldspar (Fig. 4).
- Regardless of the feldspar disequilibrium textures in the fresh RDG samples, the rock still maintains its overall granitic composition, implying that hydrothermal albite and K-feldspar can form *in situ* within the granite.

Implications

- Textural and geochemical evidence from feldspars indicate late-stage magma mixing prior to complete crystallisation of the RDG at Olympic Dam.
- Feldspars record a transition from magmatic to hydrothermal processes (Fig. 4).
- Evidence of extensive feldspar re-equilibration reactions prior to IOCG mineralisation is significant and concordant with initial stages of IOCG genesis.
- Further work is still required to constrain the effects such feldspar re-equilibration reactions have on element remobilisation within the RDG.

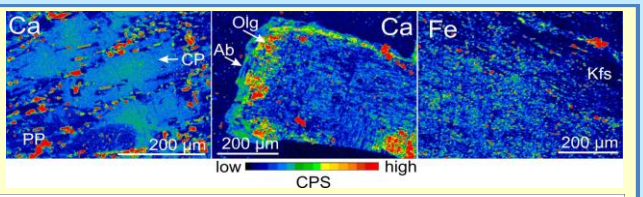

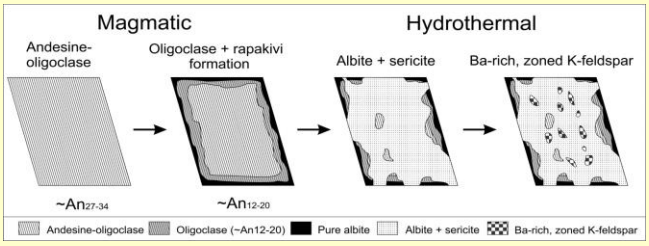

Figure 4: Top - EPMA element maps illustrating deuteric coarsening of alkali feldspar, albitisation of oligoclase and red-stained K-feldspar. CPS - counts per second. Bottom - Schematic detailing the magmatic-hydrothermal transition for plagioclase in the RDG.

References: [1] Groves *et al.* (2010) *Econ. Geol.* **105**, 641-654. [2] Johnson and Cross (1995) *Econ. Geol.* **90**, 1046-1063. [3] Ehrig *et al.* (2012) *SEG Spec. Pub.* **16**, 237-267. [4] Kontonikas-Charos et al. (in review) *J. Petrol.*

Acknowledgements: BHP Billiton, Adelaide Microscopy

ADDITIONAL MATERIAL H

CONFERENCE ABSTRACT AND POSTER:

FELDSPAR REPLACEMENT REACTIONS IN IOCG SYSTEMS: THE OLYMPIC CU-AU PROVINCE

Alkis Kontonikas-Charos[1], Cristiana L. Ciobanu[2], Nigel J. Cook[2], Kathy Ehrig[3], Vadim S. Kamenetsky[4]

[1]*School of Physical Sciences, The University of Adelaide, Adelaide, SA, 5005, Australia*

[2]*School of Chemical Engineering, The University of Adelaide, Adelaide, SA, 5005, Australia*

[3]*BHP Billiton Olympic Dam, Adelaide, SA, 5000, Australia*

[4]*School of Physical Sciences, University of Tasmania, Hobart, TAS, 7001, Australia*

Abstract and Poster, The Institute for Geoscience Research Conference 2015, 'Key issues in fluid-rock interaction: From the nano to the macroscale', Curtin University, Perth, WA, Australia, 23-25th September 2015.

Feldspar replacement reactions in IOCG systems: The Olympic Cu-Au Province

Alkis Kontonikas-Charos[1], Cristiana L. Ciobanu[2], Nigel J. Cook[2], Kathy Ehrig[3] and Vadim S. Kamenetsky[4]

[1]School of Physical Sciences, University of Adelaide, Adelaide, SA, 5000, Australia
[2] School of Chemical Engineering, University of Adelaide, Adelaide, SA, 5000, Australia
[3]BHP Billiton, Olympic Dam, Adelaide, SA, 5000, Australia
[4]School of Physical Sciences, University of Tasmania, Hobart, TAS, 7001, Australia

The presence of feldspar replacement reactions has long been recognized as a diagnostic property of iron-oxide copper-gold (IOCG) systems (e.g., Groves *et al*., 2010); however the exact role they play in the genesis of such deposits remains poorly constrained. Detailed studies of deuteric coarsening (e.g., Parsons and Lee, 2009) and albitization (e.g., Putnis, 2002; Plümper and Putnis, 2009) have highlighted the ability of such reactions to alter the physical and chemical properties of the host rocks during fluid-rock interaction at the micro- and nanoscale. This invokes the idea that feldspar replacement reactions might be more important than once thought, and may even be a prerequisite stage for the deposition of IOCG mineralization.

The Olympic Cu-Au Province, situated in the eastern Gawler Craton, South Australia, provides a unique opportunity to constrain the role feldspars play in IOCG genesis. Recent studies have combined microanalytical techniques with macroscopic observations to outline changes in textures and geochemistry of feldspars from fresh to altered host rocks in different settings within the province (e.g., Kontonikas-Charos *et al.*, 2014; in review; Ismail *et al.*, 2014). Such studies have highlighted the applicability of feldspars as geochemical tracers of the magmatic-to-hydrothermal evolution of a system, and for understanding the effects abundant *in-situ* feldspar replacement reactions have on the host rocks (e.g., increase in porosity and remobilization of trace elements).

Further work is still required to provide constraints that can explain and help interpret observations from IOCG systems at province, ore deposit, hand-specimen, and micro- and nanoscales. Transmission electron microscopy on foils prepared *in-situ* by FIB-SEM is particularly invaluable and can assist in determining the behaviour of trace elements in feldspars during fluid-rock interaction (e.g., the presence of Fe as Fe-oxide nanoparticles or incorporated in the crystal lattice of hydrothermal K-feldspar), as well as identifying high- and low-temperature structural modifications and degrees of ordering in feldspars (e.g., high and low albite). The overarching goal is to trace fluid-rock interaction using feldspars as a proxy for complex metasomatism involving Fe-REE-U during sequential alteration stages in an IOCG system.

References

Groves, D.I., Bierlein, F.P., Meinert, L.D., Hitzman, M.W. (2010) *Econ. Geol.* 105, 641-654.

Ismail, R., Ciobanu, C.L., Cook, N.J., Teale, G.S., Giles, D., Schmidt Mumm, A., Wade, B. (2014) *Lithos* 184–187, 456-477.

Kontonikas-Charos, A., Ciobanu, C.L., Cook, N.J. (2014) *Lithos* 208–209, 178-201.

Kontonikas-Charos, A., Ciobanu, C.L., Cook, N.J., Ehrig, K., Krneta, S., Kamenetsky, V.S. (in review). *J. Petrol.*

Parsons, I., Lee, M.R. (2009) *Contrib. Mineral. Petrol.* 157, 641-661.

Plümper, O., Putnis, A. (2009) *J. Petrol.* 50, 967-987

Putnis, A. (2002) *Mineral. Mag.* 66, 689-708.

Feldspar replacement reactions in IOCG systems: The Olympic Cu-Au Province

Alkis Kontonikas-Charos[1*], Cristiana L. Ciobanu[2], Nigel J. Cook[2], Kathy Ehrig[3] and Vadim S. Kamenetsky[4]

[1]School of Physical Sciences, University of Adelaide, Adelaide, SA, 5000, Australia
[2] School of Chemical Engineering, University of Adelaide, Adelaide, SA, 5000, Australia
[3]BHP Billiton, Olympic Dam, Adelaide, SA, 5000, Australia
[4]School of Physical Sciences, University of Tasmania, Hobart, TAS, 7001, Australia

*alkiviadis.kontonikas-charos@adelaide.edu.au

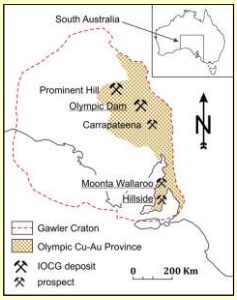

Rationale: The presence of feldspar replacement reactions has long been recognised as a diagnostic property of iron-oxide copper-gold (IOCG) systems [1]; however the exact role they play in the genesis of such deposits remains poorly constrained. Detailed studies of deuteric coarsening [2] and albitisation [3] have highlighted the ability of such reactions to alter the physical and chemical properties of the host rocks during fluid-rock interaction at the micro- and nanoscale. This invokes the idea that feldspar replacement reactions might be more important than once thought, and may even be a pre-requisite stage for the deposition of IOCG mineralisation.

Background: The Olympic Cu-Au Province, eastern Gawler Craton, South Australia (Fig. 1), is a large Mesoproterozoic metallogenic belt which extends for over 700 km and encompasses numerous prospects alongside the Olympic Dam and Prominent Hill deposits.

Alteration ranges from the 'end-member' sericite-hematite-breccia hosted type (e.g. Olympic Dam and Prominent Hill), to skarn-hosted mineralization in the Punt Hill district, and strongly potassic-altered and minor skarn-hosted mineralisation at Moonta-Wallaroo and Hillside [4].

Recent studies of the province (e.g. [4]; [5]; [6]) have highlighted the applicability of feldspars as geochemical tracers of the magmatic-to-hydrothermal evolution of a system, and for understanding the effects abundant *in-situ* feldspar replacement reactions have on the host rocks (e.g., increase in porosity and remobilisation of trace elements).

Figure 1: Sketch map of the Gawler Craton, Olympic Cu-Au Province and several IOCG deposits and prospects. Underlined areas are used here as case studies.

Feldspars as geochemical tracers of the magmatic-hydrothermal transition

- Both albitisation and subsequent nucleation of hydrothermal K-feldspar are prominent in Hiltaba suite granites of Olympic Dam (Roxby Downs Granite) and Moonta-Wallaroo (Arthurton and Tickera Granite) (Fig. 2)
- Feldspar textures and geochemistry record the magmatic-hydrothermal transition in the Roxby Downs Granite, from rapakivi formation to albitisation and hydrothermal K-feldspar nucleation (Fig. 3)
- Rare earth element fractionation trends in feldspars from Moonta-Wallaroo and Hillside (Fig. 4) also show evidence of the magmatic-hydrothermal transition, indicating remobilisation of trace elements within feldspars associated with albitisation.

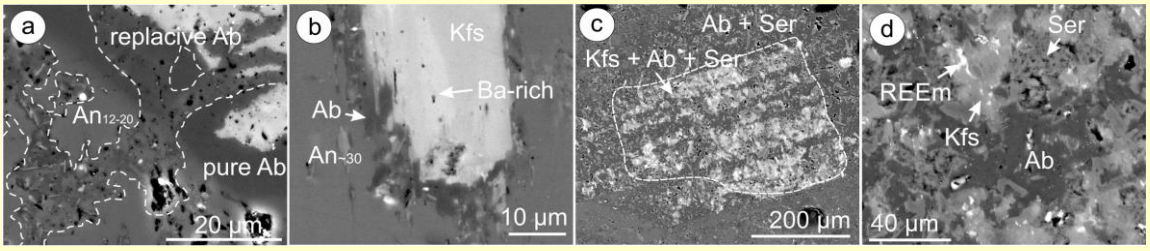

Figure 2: Images displaying important feldspar disequilibrium textures observed in Hiltaba Suite rocks from Olympic Dam (a) and Moonta-Wallaroo (b-d). (a) Two generations of albite associated with plagioclase; pure and replacive. (b) New, Ba-rich K-feldspar found in previously albitised areas of plagioclase. (c) Highly porous albitised area of plagioclase. Note the nucleation of new K-feldspar. (d) High magnification image of (c). Presence of REE minerals highlights the element remobilisation associated with albitisation. Abbreviations: Ab - albite, An - anorthite content, Kfs - K-feldspar, REEm - rare earth element mineral, Ser - sericite.

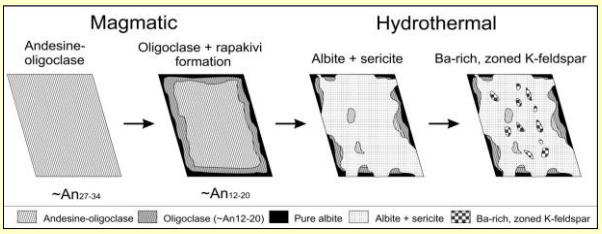

Figure 3: Schematic detailing the magmatic-hydrothermal transition for plagioclase in the Roxby Downs Granite.

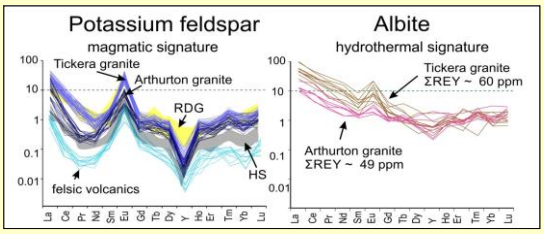

Figure 4: Chondrite-normalised REE fractionation trends for feldspars from the Moonta-Wallaroo and Hillside IOCG deposits.

Implications

- Evidence of extensive feldspar re-equilibration reactions prior to IOCG mineralisation.
- The ability for such reactions to alter physical and chemical properties of host rocks is significant and provides a platform for further alteration.
- Early alkali alteration is a prerequisite stage, and concordant with existing models for IOCG deposit genesis.

Future work

- Nanoscale investigation of trace element behaviour in feldspars during fluid-rock interaction.
- Are certain elements present as nanoparticles or are they incorporated into the feldspar crystal lattice? (Fig. 5)
- Are trace elements concentrated along twin planes or other structures within the feldspar crystal lattice? (Fig. 5)
- Speciation of albite, low or high? Implications for albitisation temperature and IOCG genesis.

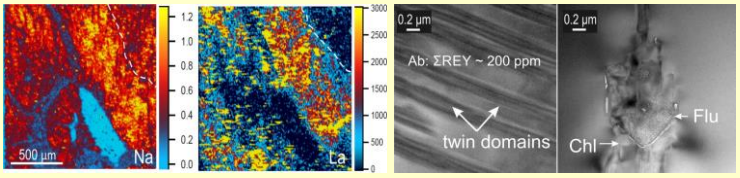

Figure 5: Left - EPMA elemental maps of partially albitised K-feldspar from the Arthurton Granite. Note the close association between Na and La, highlighting the mobility of LREE during albitisation. Scale for La in counts per second (cps); 10^6 cps for Na. Right - Transmission electron microscopy image of twinning domains in albite from the Moonta-Wallaroo region. Ab - albite, Chl - chlorite, Flu - fluorite.

References

[1] Groves *et al.* (2010) *Econ. Geol.* **105**, 641-654.
[2] Parsons & Lee (2009) *Contrib. Mineral. Petrol.* **157**, 641-661.
[3] Plümper & Putnis (2009) *J. Petrol.* **50**, 967-987.
[4] Ismail et al. (2014) *Lithos* **184-187**, 456-477.
[5] Kontonikas-Charos *et al.* (in review) *J. Petrol.*
[6] Kontonikas-Charos *et al.* (2014) *Lithos* **208-209**, 178-201.

Acknowledgements: BHP Billiton, Adelaide Microscopy

ADDITIONAL MATERIAL I

CONFERENCE ABSTRACT:

RARE EARTH ELEMENT REMOBILIZATION IN FELDSPARS: EXAMPLES FROM IOCG SYSTEMS IN THE OLYMPIC CU-AU PROVINCE

Alkis Kontonikas-Charos[1], Cristiana L. Ciobanu[2], Nigel J. Cook[2], Kathy Ehrig[3], Sasha Krneta[1]

[1]*School of Physical Sciences, The University of Adelaide, Adelaide, SA, 5005, Australia*

[2]*School of Chemical Engineering, The University of Adelaide, Adelaide, SA, 5005, Australia*

[3]*BHP Billiton Olympic Dam, Adelaide, SA, 5000, Australia*

Abstract (Oral presentation given by Cristiana L. Ciobanu), 2nd European Mineralogical Conference, 'Minerals, rocks and fluids: Alphabet and words of planet Earth', Rimini, Italy, 11-15th September, 2016.

RARE EARTH ELEMENT REMOBILIZATION IN FELDSPARS: EXAMPLES FROM IOCG SYSTEMS IN THE OLYMPIC CU-AU PROVINCE

Kontonikas-Charos, A.[1], Ciobanu, C. L.[2], Cook, N. J.[2], Ehrig, K.[3] & Krneta, S.[1]
[1] School of Physical Sciences, University of Adelaide, Adelaide, SA, 5000, Australia
[2] School of Chemical Engineering, University of Adelaide, Adelaide, SA, 5000, Australia
[3] BHP Billiton Olympic Dam, Adelaide, SA, 5000, Australia

Keywords: Trace elements, feldspars, remobilisation

Feldspars hosted by rocks that form part of, or are associated with, Fe-oxide Cu-Au systems in the Olympic Cu-Au Province, South Australia, contain significant concentrations of trace element, either within the feldspar lattice (REE, Ga), or as sub-microscopic-scale inclusions (Fe). Observed textures imply a strong link between fluid/rock interaction and remobilization of trace elements within individual feldspar grains, or away from the feldspar entirely. Reactions such as albitization (replacement of initial feldspar by albite) and deuteric coarsening (recrystallization of igneous alkali feldspars through interaction with deuteric fluids) are well constrained in terms of major element exchange. The behaviour of trace elements during fluid/rock interaction requires further constraints, however, in order to track their redistribution in the context of a mineralizing system.

Study of the Roxby Downs Granite (RDG), proximal to, and within, the Olympic Dam (OD) orebody, shows concentrations of ~1.5 wt% Fe within red-stained K-feldspar from altered RDG. These concentrations are attributed to disseminated μm-sized hematite inclusions within this K-feldspar, however LA-ICP-MS spot analyses on inclusion-free areas gave similar concentrations, suggestive of Fe within the feldspar lattice. The red-stained K-feldspar is overprinted by a complex fine-grained bastnäsite-synchysite-molybdenite intergrowth and sericite. Importantly, the K-feldspar grain outline is retained, implying pseudomorphic replacement resulting from coupled dissolution-reprecipitation reactions (CDRR). Moreover, there is a decrease in ∑REE in feldspars with proximity to the orebody, thus hinting at release and remobilisation of REE from feldspars during fluid/rock interaction and CDRR.

A study on rocks from the Moonta-Wallaroo region (Kontonikas-Charos et al. 2014) supports the applicability of REE-fractionation trends in feldspars as geochemical tracers of hydrothermal alteration. Similar to trends observed at OD, measured ∑REE in feldspars from non-mineralized host rocks were greater than those from mineralized host rocks. REE mobility is further supported by spot analyses from an albite-biotite schist which reveal (hydrothermal) albite contains up to ~200 ppm ∑REE. Nanoscale investigations found no sign of inclusions within the albite; REE are thus interpreted to be sited in the feldspar lattice. Whole-rock ∑REE concentrations were ~200 ppm, indicating that albite accounts for the majority of REE. This appears to contradict the initial trend observed in mineralized host rocks, however when considering that albite formed at high fluid/rock ratios and not via CDRR, as well as the lack of REE-accessories, it is expected that albite would be the main repository. Moreover, hundreds of ppm Ga were found within K-feldspars. Nanoscale studies can constrain trace element redistribution in minerals and track their behavior from host to newly-formed phases. Considering the crustal abundance of feldspars, their role in re-concentrating critical metals such as REE and Ga cannot be ignored.

References

Kontonikas-Charos, A., Ciobanu, C. L., Cook, N. J. (2014): Albitization and redistribution of REE and Y in IOCG systems: Insights from Moonta-Wallaroo, Yorke Peninsula, South Australia. *Lithos.,* **208–209**: 178-201.

ADDITIONAL MATERIAL J

CONFERENCE ABSTRACT:

REMOBILIZATION OF REE DURING FELDSPAR REPLACEMENT REACTIONS IN IOCG SYSTEMS: EXAMPLES FROM THE OLYMPIC CU-AU PROVINCE, SOUTH AUSTRALIA

Alkis Kontonikas-Charos[1], Cristiana L. Ciobanu[2], Nigel J. Cook[2], Kathy Ehrig[3], Vadim S. Kamenetsky[4]

[1]*School of Physical Sciences, The University of Adelaide, Adelaide, SA, 5005, Australia*

[2]*School of Chemical Engineering, The University of Adelaide, Adelaide, SA, 5005, Australia*

[3]*BHP Billiton Olympic Dam, Adelaide, SA, 5000, Australia*

[4]*School of Physical Sciences, University of Tasmania, Hobart, TAS, 7001, Australia*

Abstract and Presentation, Australian Earth Sciences Convention 2016 (On behalf of the Geological Society of Australia), 'Uncover Earth's past to discover our future', Adelaide Convention Centre, Adelaide SA, Australia, 26-30th June, 2016

Remobilization of REE during feldspar replacement reactions in IOCG systems: examples from the Olympic Cu-Au Province, South Australia

Kontonikas-Charos, Alkis[1], Ciobanu, Cristiana L.[2], Cook, Nigel J.[2], Ehrig, Kathy[3] and Kamenetsky, Vadim, S[4]

[1] *School of Physical Sciences, University of Adelaide, Adelaide, SA, 5000, Australia; alkiviadis.kontonikas-charos@adelaide.edu.au*
[2] *School of Chemical Engineering, University of Adelaide, Adelaide, SA, 5000, Australia*
[3] *BHP Billiton Olympic Dam, Adelaide, SA, 5000, Australia*
[4] *School of Physical Sciences, University of Tasmania, Hobart, TAS, 7001, Australia*

The presence of feldspar replacement reactions has long been recognized as a diagnostic property of iron-oxide copper-gold (IOCG) systems [1]; however the exact role they play in the genesis of such deposits remains poorly constrained. Detailed studies of deuteric coarsening and albitization have highlighted the ability of such reactions to alter the physical and chemical properties of the host rocks during fluid-rock interaction at the micro- to nanoscale. This invokes the idea that feldspar replacement reactions might be more important than once thought, and may even be a prerequisite for deposition of IOCG mineralization.

The Olympic Cu-Au Province, eastern Gawler Craton, South Australia, provides a unique opportunity to constrain the role feldspars play in IOCG genesis. Recent studies combining microanalysis with observations from the macro- to nanoscopic scales have outlined changes in the textures and geochemistry of feldspars in fresh to altered host rocks from different settings within the province [2]. Such studies have also highlighted the applicability of feldspars as geochemical tracers of the magmatic-to-hydrothermal evolution of a system, and for understanding the effects which abundant *in-situ* feldspar replacement reactions have on the host rocks.

The presence of REE-fluorocarbonate mineral inclusions within albite and other hydrothermal feldspars, together with chondrite-normalized REE+Y (REY) fractionation trends for feldspars supports local remobilization of such trace elements within the host rock, but importantly, out of feldspar crystal lattice itself. Significantly, this is observed in the unmineralized host rocks at depth or at the periphery of the IOCG orebody, likely representing the earliest stage of Fe-REY-U metasomatism in the nascent IOCG system. Comparison of REY fractionation trends between ~1.6 Ga Hiltaba suite granites and ~1.8 Ga Donington suite equivalents (Eyre Peninsula) highlights the enrichment of REY in the former. Given the physical dimensions of the Hiltaba suite granites (e.g. at least 7 x 9 x >2.5 km around the Olympic Dam orebody), and the abundance of feldspars in these rocks (~60% by mode), it is suggested that destruction of feldspars and leaching of REY contributed significantly to the 'enrichment' of REY in IOCG systems in the Olympic Cu-Au Province, notably at Olympic Dam.

Refractory magmatic mineral phases within the host rocks also display evidence of REE-U remobilization at this early stage (e.g. recrystallization of apatite coupled with a loss in REY + U). A common theme throughout is the leaching of REY and U from all mineral phases and re-deposition of these elements as discrete minerals, contributing to higher grades locally, and a marked 'enrichment' in mineralized rocks relative to background.

Further work is required to constrain certain textural and geochemical observations from IOCG systems at province, deposit/prospect, hand-specimen, and micro- and nanoscales. The overarching goal is to trace fluid-rock interaction using feldspars as a proxy for complex metasomatism involving Fe-REY-U during sequential alteration stages in an IOCG system.

References

[1] Groves D I, Bierlein F P, Meinert L D and Hitzman M W (2010) Econ. Geol. 105: 641-654
[2] Kontonikas-Charos A, Ciobanu C L and Cook N J (2014) Lithos 208–209: 178-201

ADDITIONAL MATERIAL K

CONFERENCE ABSTRACT:

THE IOCG-IOA ORE SYSTEM AT OLYMPIC DAM AND NEARBY PROSPECTS, SOUTH AUSTRALIA

Kathy Ehrig[1], Vadim S. Kamenetsky[2], Jocelyn McPhie[2], Olga Apukhtina[2], Cristiana L. Ciobanu[3], Nigel J. Cook[3], **Alkis Kontonikas-Charos**[4], Sasha Krneta[4]

[1]BHP Billiton Olympic Dam, Adelaide, SA, 5000, Australia

[2]School of Physical Sciences, University of Tasmania, Hobart, TAS, 7001, Australia

[3]School of Chemical Engineering, The University of Adelaide, Adelaide, SA, 5005, Australia

[4]School of Physical Sciences, The University of Adelaide, Adelaide, SA, 5005, Australia

Accepted abstract, 'Mineral Resources to Discover', Proceedings from the 14th Biennial SGA Meeting, Quebec City, Canada, August 20-23rd, 2017.

The IOCG-IOA ore system at Olympic Dam and nearby prospects, South Australia

Kathy Ehrig
BHP Billiton Olympic Dam, 55 Grenfell St, Adelaide, South Australia 5000, Australia

Vadim S Kamenetsky, Jocelyn McPhie, Olga Apukhinta
School of Physical Sciences, University of Tasmania, Hobart, Tasmania 7001, Australia

Cristiana L. Ciobanu, Nigel Cook
School of Chemical Engineering, The University of Adelaide, Adelaide 5001, Australia

Alkis Kontonikas-Charos, Sasha Krneta
School of Physical Sciences, The University of Adelaide, Adelaide 5001, Australia

Abstract. The Olympic Dam Cu-U-Au-Ag deposit remains the single largest iron oxide Cu-Au deposit, even after over forty years since its discovery. The deposit is part of the spectrum of IOA-IOCG deposits which are distinguished from other metalliferous deposit types (e.g. porphyry Cu, sediment hosted Cu, volcanogenic massive sulphides, etc) by the presence of iron oxide-alkali metasomatism (Na-Ca-Fe, high temperature Fe^{+2}-K, and low temperature Fe^{+3}-K-H_2O-CO_2 alteration facies). Hematite-sericite-chalcopyrite-bornite-chalcocite-fluorite-barite has overprinted, and largely obliterated, an earlier assemblage of magnetite-apatite-carbonates-chlorite-pyrite at Olympic Dam. Isochemical Na-Ca-Fe alteration occurs in the least altered parts of the host Roxby Downs Granite. Remnants of Fe^{+2}-K alteration are present in altered Roxby Downs Granite distal to texturally destructive hematite-sericite alteration. Similar to other IOA-IOCG ore systems, porosity generating albitisation also occurs in the region surrounding the Olympic Dam deposit.

1 Introduction

Iron oxide-alkali-alteration systems produce a wide spectrum of mineralization styles: iron oxide-apatite, iron oxide Cu-Au±U, polymetallic skarns, and epithermal deposits (Corriveau et al. 2016, Day et al. 2016, Porter 2010, and references therein). Regional clustering of these iron oxide-alkali alteration dominated systems include, but are not limited to, the Olympic Cu-Au Province (South Australia), Cloncurry district (Queensland), Great Bear Magmatic Zone (Canada), St. Francois Mountains Terrane (Missouri), Kiruna district (Sweden), etc. Alteration facies present in these districts systematically change from the regional to deposit scale. Four metasomatic types /alteration facies are recognized: 1) Na to Ca-Fe, 2) high temperature Fe^{+2}-K, 3) low temperature Fe^{+3}-K-H_2O-CO_2, and 4) quartz veins/silicification (e.g. Corriveau et al. 2016, Montreuil et al. 2016, Skirrow et al. 2007).

The importance of albitization as a prerequisite for formation of iron oxide copper gold (IOCG) deposits is mentioned by many authors (e.g. Haynes et al. 1995, Hitzman et al. 1992). Albitization within the Olympic Dam district was briefly mentioned by Creaser (1989) and Davidson et al. (2007). Even though magnetite is present on the peripheries of the Olympic Dam (OD) deposit, hematite-sericite-chlorite-carbonate is the dominant alteration assemblage. The presence of earlier high temperature alteration assemblages (such as Na-Ca-Fe or Fe^{+2}-K) was not documented until recently (Kontonikas-Charos et al. 2017, Mauger et al. 2016).

The present study uses whole rock Fe, K and Na assays from diamond drill core samples to demonstrate the presence of alteration styles other than hematite-sericite-chlorite-carbonate at OD and nearby prospects. Detailed petrographic studies (Apukhtina et al. 2017, Kontonikas-Charos et al. 2017, Krneta et al. 2016, and currently unpublished work) are briefly mentioned to show the widespread occurrence of paragenetically early IOA mineralization associated with OD and nearby IOCG prospects.

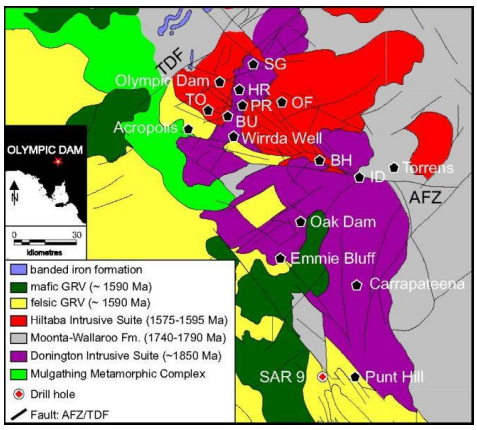

Figure 1. Basement geological map of part of the Olympic Cu-Au Province showing the location of the Olympic Dam deposit and surrounding prospects (diamonds) in the Olympic Dam district. SG-Snake Gully, HR-Horn Ridge, PR-Phillips Ridge, OF-Opal Fields, BU Burgoyne, TO-Town, BH- Burden Hill, ID-Island Dam. Map sourced from https://map.sarig.sa.gov.au/.

2 Geological Background

The Olympic Dam breccia hosted iron oxide Cu-U-Au-Ag deposit occurs in the central-northern part of the Olympic Cu-Au Province (e.g. Skirrow et al. 2007) which is located on the eastern margin of the Gawler Craton (Fig 1). Other deposits in the region include the Prominent Hill Cu-Au and Carrapateena iron oxide Cu-Au-Ag-U deposits. Numerous barren (Snake Gully, Horn Ridge, Phillips Ridge Opal Fields, Town, Burgoyne, Burden Hill) to subeconomic IOCG-related prospects (Acropolis, Wirrda Well, Oak Dam, Island Dam) are also present in the Olympic Dam district. Alteration and mineralization are linked to the ~1600 Ma Gawler Range Volcanics (GRV) and Hiltaba Intrusive Suite (HIS) event (e.g. Skirrow et al. 2007). All OD district prospects occur under a cover sequence of Neoproterozoic to Cambrian sediments varying in thickness from ~250 to >800 m.

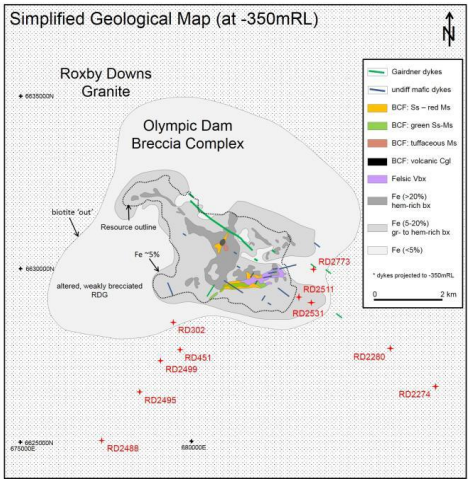

Figure 2. Simplified geological plan and cross-sections showing the basement (at -350 mRL) rock/alteration types. The outer limit of the Olympic Dam Breccia Complex (ODBC) is gradational with the Roxby Downs Granite (RDG) and is defined by the last occurrence of magmatic biotite, when progressing from the RDG into the ODBC (modified Ehrig et al 2012).

The OD deposit is hosted within the Roxby Downs Granite (RDG, a member of the HIS) and subordinate bedded clastic facies (Fig 2). Mafic-ultramafic dykes and lavas/sills are also present (Ehrig et al. 2012). The Acropolis prospect consists of magnetite-apatite±biotite±K-feldspar±quartz vein networks in sericite-hematite altered felsic GRV which overlies Donington (~1840 Ma) granitoids. Brecciation is weakly developed and occurs locally (Cross, 1993). The Wirrda Well prospect is hosted within sericite+chlorite altered Donington granitoids which are intruded by ~1840 Ma and GRV-aged mafic-ultramafic dykes. Hiltaba suite granites occur immediately to the NE and S of Wirrda Well. Brecciation is more extensive and widespread than at Acropolis. Magnetite-apatite±biotite±K-feldspar±calcite ±quartz is partly to completely replaced by hematite-sericite-chlorite. Pyrite and chalcopyrite are the principal sulphide minerals, while bornite-chalcocite are present but at low concentrations in both Acropolis and Wirrda Well. The Island Dam prospect is discussed by Keyser et al. (this volume). The barren prospects consist of either Donington and/or HIS granitoids and associated mafic-ultramafic dykes.

3 Approach and Results

To determine if the presence of Na-Ca-Fe or Fe^{+2}-K alteration facies could be detected in whole rock assay data of samples from diamond drill holes, nine drill holes along two traverses where selected from OD (Fig 2) which progress from the least altered Roxby Downs into economic mineralization. Four drill holes from the barren prospects (Phillips Ridge and Opal Fields), all drill holes from Acropolis, two Donington and four HIS drill holes from Wirrda Well were also selected for graphical analysis of Fe, K, Na. Alteration styles defined by whole rock K-Na-Fe assays for the selected drill holes are shown in Figures 3- 6 for OD, Phillips Ridge – Opal Fields, Acropolis, and Wirrda Well, respectively. K vs Na and K/Na ratio vs Fe are plotted in the upper and lower graphs in each figure.

Unaltered RDG granite (i.e. post-magmatic isochemical alteration or no net hydrothermal addition-subtraction of elements) plots within the dashed box outline at K ~4.6 wt% and Na ~2.6 wt% (Fig 3, upper graph). Progressive alteration of plagioclase to sericite forms a vector towards ~6.5 wt% K. Albitization forms a vector towards ~5-6 wt % Na. Rocks where hydrothermal K-feldspar is dominant plot >~6.5 wt% K. Weak to intense hematite-sericite and then hematite alteration vectors from ~6.5 wt% K towards the origin. Albite alteration is present in the RDG and is also indicated when K/Na ratios (Fig 3, lower graph) are < ~1.76. Weak to intense Fe-oxide metasomatism plots along the arc from > ~5 to > 60 wt% Fe.

Albitization (without significant Fe-oxide metasomatism overprinting) occurs in the unmineralized HIS granites at PR and OF (Figure 4).

At Acropolis, magnetite-apatite±K-feldspar±biotite (Fe^{+2}-K) alteration is extensively overprinted by an assemblage of hematite-sericite-chlorite-carbonate (Fe^{+3}-K-H_2O-CO_2). Minor albite alteration is present (Fig 5) in the felsic-mafic GRV and Donington granitoids.

The HIS granites (WRD3 and WRD6) located east of Wirrda Well are weakly albitized (Fig 6). Plagioclase in the Donington granitoids (WRD46 and WRD33) at Wirrda Well is partially to completely altered to sericite. Hydothermal K-feldspar occurs in HIS granites intruding Donington granitoids (WRD19) along the NE margin of the prospect.

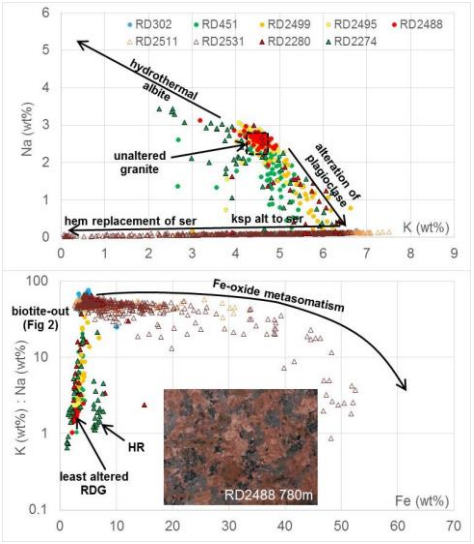

Figure 3. Whole rock analysis K vs Na (upper graph) and Fe vs K:Na ratio (lower graph) alteration trends for the RDG and ODBC. RD2274 is likely a hybrid of the RDG and HR granite which weak albite alteration is present. Inset is a photograph (image ~50 mm wide) of least altered RDG.

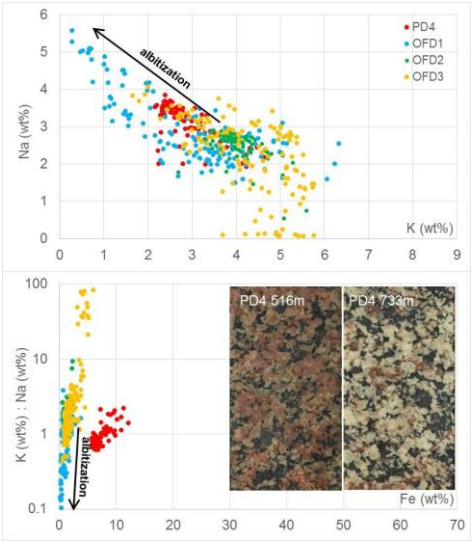

Figure 4. Whole rock analysis K vs Na and Fe vs K:Na ratio alteration trends for barren, albititized HIS felsic intrusions at PR (PD4) and OF (OFD1,2,3). Inset photos (width ~ 47 mm).

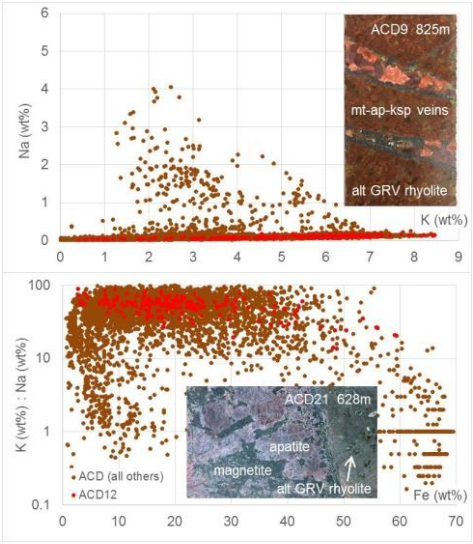

Figure 5. Whole rock analysis (n = 5075) K vs Na and Fe vs K:Na ratio alteration trends for all of the drilling within the Acropolis IOA-IOCG prospect. The red dots are the data from ACD12, a HIS. Inset photos (width = 47mm) magnetite+apatite±K-feldspar+quartz vein cutting intensely sericite altered felsic GRV lava.

4 Discussion and Implications

Albitization (Na-Ca-Fe alteration) creates porosity, enhances permeability, and can lead to element remobilization (e.g. Haynes 1972, Haynes et al. 1995, Hitzman et al. 1992, Kontonikas-Charos et al. 2017, and references therein). It is clearly a precursor alteration style required for the formation of IOCG-IOA deposits (e.g. Corriveau et al. 2016, Day et al. 2016, Porter 2010, Williams et al. 2005). Na-Ca-Fe alteration occurs in the Olympic Cu-Au Province (e.g. Skirrow et al. 2007), but, until recently, mentioned only rarely in the Olympic Dam district (e.g. Creaser 1989, Davidson et al. 2007). Kontonikas-Charos et al. (2017) detailed petrographic study of the RDG was the first to describe the isochemical formation of hydrothermal albite and K-feldspar within apparently geochemically unaltered RDG (Ehrig et al. 2012). During albitisation of the RDG, porosity was created and coarsening of minerals occurred due to the release of metals. Krneta et al. (2016) linked albitisation to the transition of magmatic apatite to hydrothermal apatite at OD. Remnants of early magnetite-apatite associated mineralization was described in the deepest drill hole distal to hematite-sericite dominated alteration at OD (Apukhtina et al. 2017).

Albitization (without significant Fe-oxide

metasomatism overprinting) occurs in the unmineralized HIS granites at PR and OF proscpects, as well as the subeconomic Acropolis and Wirrda Well prospects. High temperature Fe^{+2}-K followed by Fe^{+3}-K alteration at Acropolis and Wirrda Well partially overprints the Na-Ca-Fe alteration and early magnetite apatite vein networks.

Simple K-Na-Fe scatterplots supported by detailed petrography can be used to identify various iron oxide-alkali alteration types which are often difficult to recognize when logging and mapping.

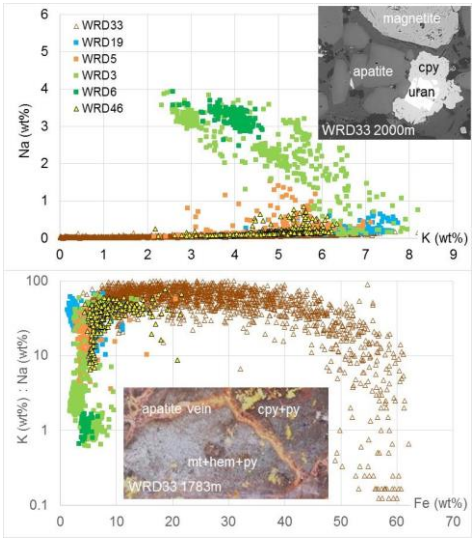

Figure 6. Whole rock analysis (n =3245) K vs Na and Fe vs K:Na ratio alteration trends for the Wirrda Well IOA-IOCG prospect. Drill holes WRD33 (mineralized) and WRD46 (unmineralized Donington megacrystic granitoids) are extensively altered and located within the prospect. The other drill holes (WRD3, 5, 6, 19) are HIS granitoids. WRD 3 and 6 are located ~22 km NE and ~14 km E of the prospect center, respectively. WRD 6 and 19 are on the SE and NE edges of the prospect. The upper inset is a BSE image (~200 µm wide) showing magnetite, apatite, chalcopyrite and uraninite. The lower photograph (height ~47 mm) shows and apatite-calcite veins which cuts chalcopyrite+pyrite-bearing magnetite+hematite+ apatite breccias.

Acknowledgements

This is a contribution to the Australian Research Council (Linkage Grant "The supergiant Olympic Dam U-Cu-Au-REE ore deposit: towards a new genetic model") and 'FOX' project, supported by BHP Billiton Olympic Dam and the South Australian Mining and Petroleum Services Centre of Excellence.

References

Apukhtina OB, Kamenetsky VS, Ehrig K, Kamenetsky MB, Mass R, McPhie, J Ciobanu, CL and Cook NJ (2017) Early magnetite-fluorapatite mineralization at the Olympic Dam Cu-U-Au-Ag deposit, South Australia. Economic Geology, *in press*.

Cross KC (1993) Acropolis and Wirrda Well, in: Drexel JF, Preiss WV, Parker AJ (Eds.), The geology of South Australia. Vol. 1, The Precambrian. Geological Survey of South Australia, South Australia, pp. 138

Corriveau L, Montreuil JF, Potter EG (2016) Alteration facies linkages among iron oxide copper-gold, iron oxide-apatite, and affiliated deposits in the Great Bear Magmatic Zone, Northwest Territories, Canada. Econ Geol 111:2045-2072

Creaser RA (1989) The geology and petrology of Middle Proterozoic felsic magmatism of the Stuart Shelf, South Australia. PhD thesis (unpublished), La Trobe University, Bundoora

Davidson GJ, Paterson H, Meffre S, Berry RF (2007) Characteristics and origin if the Oak Dam East breccia-hosted, iron oxide Cu-U-(Au) deposit: Olympic Dam region, Gawler Craton, South Australia. Econ Geol 102:1471-1498

Day WC, Slack JF, Ayuso RA, Seeger, CM (2016) Regional geologic and petrologic framework for iron oxide ± apatite ± rare earth element and iron oxide copper-gold deposits of the Mesoproterozoic St. Francois Mountains Terrane, Southeast Missouri, USA. Econ Geol 111:1825-1858

Ehrig K, McPhie J, Kamenetsky V (2012) Geology and mineralogical zonation of the Olympic Dam Iron Oxide Cu-U-Au-Ag deposit, South Australia. SEG Spec Publ 16:237-267

Haynes DW (1972) Geochemistry of altered basalts (continental tholeiites) and associated copper deposits. PhD thesis (unpublished), Australian National University, Canberra

Haynes DW, Cross KC, Bills RT, Reed MH (1995) Olympic Dam ore genesis: A fluid-mixing model. Econ Geol 90:281-307

Hitzman MW, Oreskes N and Einaudi MR (1992) Geological characteristics and tectonic setting of Proterozoic iron oxide (Cu-U-Au-LREE) deposits. Precambrian Research 58:241-287

Keyser, WH, Ciobanu CL, Cook, NJ, Courtney-Davies L, Ehrig K, Gilbert S, McPhie J (2017) Links between sedimentary protoliths and IOCG-skarn alteration, Island Dam, South Australia. *this volume*

Kontonikas-Charos A, Ciobanu CL, Cook NJ, Ehrig K, Krneta S, Kamenetsky VS (2017) Feldspar evolution in the Roxby Downs Granite, host to Fe-oxide Cu-Au-(U) mineralisation at Olympic Dam, South Australia. Ore Geol Rev 80:838-859

Krneta S, Ciobanu CL, Cook NJ, Ehrig K, Kontonikas-Charos A (2016) Apatite at Olympic Dam, South Australia: A petrogenetic tool. Lithos 262:470-485

Mauger AJ, Ehrig K, Kontonikas-Charos A, Ciobanu CL, Cook NJ, Kamenetsky VS (2016) Alteration at the Olympic Dam IOCG-U deposit: insights into distal to proximal feldspar and phyllosilicate chemistry from infrared reflectance spectroscopy. Aust Jour Earth Sci 63:959-972

Montreuil JF, Corriveau EG, Potter EG, De Toni AF (2016) On the relationship between alteration facies and metal endowment of iron oxide-alkali-altered systems, Southern Great Bear Magmatic Zone (Canada). Econ Geol 111:2139-2166

Porter TM (2010) Current understanding of iron oxide associated-alkali altered mineralised systems. Part 1. An overview. In: Porter TM (ed.), Hydrothermal Iron Oxide Copper-Gold & Related Deposits, vol. 3. PGC Publishing, Adelaide, p. 5-32

Skirrow RG, Bastrakov EN, Barovich K, Fraser GL, Creaser RA, Fanning CM, Raymond OL, Davidson GJ (2007) Timing of iron oxide Cu-Au-(U) hydrothermal activity and Nd isotope constraints on metal sources in the Gawler Craton, South Australia. Econ Geol 102:1441-1470

Williams PJ, Barton MD, Johnson DA, Fontboté L, de Haller A, Mark G, Oliver NS, Marschik R (2005) Iron oxide copper-gold deposits: Geology, space-time distribution, and possible modes of origin. Economic Geology 100th Anniversary Volume, p371-405

CHAPTER 9

REFERENCES

Agangi, A., Kamenetsky, V.S., McPhie, J., 2012. Evolution and emplacement of high fluorine rhyolites in the Mesoproterozoic Gawler silicic large igneous province, South Australia. Precambrian Research 208, 124-144.

Aigner-Torres, M., Blundy, J., Ulmer, P., Pettke, T., 2007. Laser ablation ICPMS study of trace element partitioning between plagioclase and basaltic melts: an experimental approach. Contributions to Mineralogy and Petrology 153, 647-667.

Allen, S., McPhie, J., Ferris, G., Simpson, C., 2008. Evolution and architecture of a large felsic igneous province in western Laurentia: the 1.6 Ga Gawler Range Volcanics, South Australia. Journal of Volcanology and Geothermal Research 172, 132-147.

Alt, J.C., 1999. Hydrothermal alteration and mineralization of oceanic crust: mineralogy, geochemistry and processes. Reviews in Economic Geology 8, 133–155.

Andersen, D.J., Lindsley, D.H., 1985. New (and final!) models for the Ti-magnetite/ilmenite geothermometer and oxygen barometer. American Geophysics Union Spring Meeting. Eos 66 (18), 416.

Anderson, A.T., 1968. The oxygen fugacity of alkaline basalt and related magmas. American Journal of Science 266, 704–727.

Anderson, J.L., Smith, D.R., 1995. The effects of temperature and fO_2 on the Al-in-hornblende barometer. American Mineralogist 80, 549-559.

Barker, F., 1979. Trondhjemite: definition, environment and hypotheses of origin. Trondhjemites, dacites and related rocks. 1-12, Elsevier, Amsterdam, p. 659.

Barnicoat, A., 1988. The mechanism of veining and retrograde alteration of Alpine eclogites. Journal of Metamorphic Geology 6, 545-558.

Barton, M., 2014. Iron oxide (–Cu–Au–REE–P–Ag–U–Co) systems. Treatise on Geochemistry (second edition, volume 13): Amsterdam, Elsevier, 515-541.

Barton, M.D., Johnson, D.A., 1996. Evaporitic-source model for igneous-related Fe oxide–(REE-Cu-Au-U) mineralisation. Geology 24, 259–262.

Barton, M.D., Johnson, D.A., 2000. Alternative brine sources for Fe-oxide (-Cu-Au) systems: implications for hydrothermal alteration and metals. Hydrothermal Iron Oxide Copper-Gold & Related Deposits: A Global Perspective. vol. 1, PGC Publishing, Adelaide, 43–60.

Barton, M.D., Johnson, D.A., 2004. Footprints of Fe-oxide (-Cu-Au) systems. University of Western Australia Special Publication 33, 112-116.

Bastrakov, E.N., Skirrow, R.G., Davidson, G.J., 2007. Fluid evolution and origins of iron oxide Cu-Au prospects in the Olympic Dam district, Gawler Craton, South Australia. Economic Geology 102, 1415-1440.

Bau, M., 1991. Rare-earth element mobility during hydrothermal and metamorphic fluid-rock interaction and the significance of the oxidation state of europium. Chemical Geology 93, 219-230.

Bau, M., Dulski, P., 1995. Comparative study of yttrium and rare-earth element behaviours in fluorine-rich hydrothermal fluids. Contributions to Mineralogy and Petrology 119, 213-223.

Bédard, J.H., 2006. Trace element partitioning in plagioclase feldspar. Geochimica et Cosmochimica Acta 70, 3717-3742.

Belousova, E.A., Griffin, W.L., O'Reilly, S.Y., Fisher, N.I., 2002a. Apatite as an indicator mineral for mineral exploration: trace-element compositions and their relationship to host rock type. Journal of Geochemical Exploration 76, 45–69.

Belousova, E.A., Griffin, W.L., O'Reilly, S.Y., Fisher, N.I., 2002b. Igneous zircon: trace element composition as an indicator of source rock type. Contributions to Mineralogy and Petrology 143, 602–622.

Belousova, E., Griffin, W., O'Reilly, S.Y., 2006. Zircon crystal morphology, trace element signatures and Hf isotope composition as a tool for petrogenetic modelling: examples from Eastern Australian granitoids. Journal of Petrology 47, 329-353.

Belperio, A., Flint, R., Freeman, H., 2007. Prominent Hill: A hematite-dominated, iron oxide copper-gold system. Economic Geology 102, 1499-1510.

Bertelli, M., Baker, T., 2010. A fluid inclusion study of the Suicide Ridge Breccia Pipe, Cloncurry district, Australia: Implication for Breccia Genesis and IOCG mineralization. Precambrian Research 179, 69-87.

Bernal, N. F., Gleeson, S. A., Smith, M. P., Barnes, J. D., Pan, Y., 2017. Evidence of multiple halogen sources in scapolites from iron oxide-copper-gold (IOCG) deposits and regional Na Cl metasomatic alteration, Norrbotten County, Sweden. Chemical Geology 451, 90-103.

BHP Billiton, 2015. http://www.bhpbilliton.com/home/investors/annualreporting2015.pdf

BHP Billiton, 2016. http://www.bhpbilliton.com/home/investors/annualreporting2016.pdf

Bindeman, I.N., Davis, A.M., 2000. Trace element partitioning between plagioclase and melt: investigation of dopant influence on partition behavior. Geochimica et Cosmochimica Acta 64, 2863-2878.

Bindeman, I.N., Davis, A.M., Drake, M.J., 1998. Ion microprobe study of plagioclase-basalt partition experiments at natural concentration levels of trace elements. Geochimica et Cosmochimica Acta 62, 1175-1193.

Blundy, J.D., Holland, T.J., 1990. Calcic amphibole equilibria and a new amphibole-plagioclase geothermometer. Contributions to Mineralogy and Petrology 104, 208-224.

Blundy, J.D., Wood, B.J., 1991. Crystal-chemical controls on the partitioning of Sr and Ba between plagioclase feldspar, silicate melts, and hydrothermal solutions. Geochimica et Cosmochimica Acta 55, 193-209.

Boles, J.R., 1982. Active albitization of plagioclase, gulf coast Tertiary. American Journal of Science 282, 165-180.

Brimhall, G.H., Agee, C., Stoffregen, R., 1985. The hydrothermal conversion of hornblende to biotite. Canadian Mineralogist 23, 369–379.

Brown,W., Parsons, I., 1984. Exsolution and coarsening mechanisms and kinetics in an ordered cryptoperthite series. Contributions to Mineralogy and Petrology 86, 3–18.

Brown, W.L., Parsons, I., 1989. Alkali feldspars: ordering rates, phase transformations and behaviour diagrams for igneous rocks. Mineralogical Magazine 53, 25–42.

Brugger, J., Etschmann, B., Pownceby, M., Liu, W., Grundler, P., Brewe, D., 2008. Oxidation state of europium in scheelite: tracking fluid–rock interaction in gold deposits. Chemical Geology 257, 26-33.

Bychkov, A., Kotelnikov, A., Romanenko, I., Senderov, E., 1989. Effect of isomorphic replacement of silicon by phosphorus on structural peculiarities of feldspars. Rossiiskaya Akademiya Nauk Savelevskii Per., Moscow, Russia, pp. 310-313.

Cao, M., Li, G., Qin, K., Seitmuratova, E.Y., Liu, Y., 2012. Major and trace element characteristics of apatites in granitoids from Central Kazakhstan: implications for petrogenesis and mineralization. Resource Geology 62, 63–83.

Carmichael, I.S.E., 1967. The iron-titanium oxides of salic volcanic rocks and their associated ferromagnesian silicates. Contributions to Mineralogy and Petrology 14, 36–64.

Chiaradia, M., Banks, D., Cliff, R., Marschik, R., De Haller, A., 2006. Origin of fluids in iron oxide–copper–gold deposits: constraints from $\delta^{37}Cl$, $^{87}Sr/^{86}Sr_i$ and Cl/Br. Mineralium Deposita 41, 565-573.

Ciobanu, C.L., Cook, N.J., Utsunomiya, S., Pring, A., Green, L., 2011. Focussed ion beam transmission electron microscopy applications in ore mineralogy: bridging micro and nanoscale observations. Ore Geology Reviews 42, 6–31.

Ciobanu, C.L., Wade, B.P., Cook, N.J., Mumm, A.S., Giles, D., 2013. Uranium-bearing hematite from the Olympic Dam Cu–U–Au deposit, South Australia: a geochemical tracer and reconnaissance Pb–Pb geochronometer. Precambrian Research 238, 129-147.

Ciobanu, C.L., Cook, N.J., Maunders, C., Wade, B.P., Ehrig, K., 2016. Focused ion beam and advanced electron microscopy for minerals: Insights and outlook from bismuth sulphosalts. Minerals, 6(4), 112.

Ciobanu, C.L., Cook, N.J., Ehrig, K., 2017. Ore minerals down to the nanoscale: Cu-(Fe)-sulphides from the iron oxide copper gold deposit at Olympic Dam, South Australia. Ore Geology Reviews, 81, 1218-1235.

Colville, A.A., Ribbe, P.H., 1968. The crystal structure of an adularia and a refinement of the structure of orthoclase. American Mineralogist 53, 25-37.

Conor, C., 1995. Moonta-Wallaroo region: an interpretation of the geology of the Maitland and Wallaroo 1: 100 000 sheet areas. Mines and Energy South Australia, Open File Envelope 8886.

Conor, C., Raymond, O., Baker, T., Teale, G., Say, P., Lowe, G., 2010. Alteration and Mineralisation in the Moonta-Wallaroo Cu-Au Mining Field Region, Olympic Domain, South Australia. In: Porter TM (Ed.), Hydrothermal Iron Oxide Copper-Gold & Related Deposits: A Global Perspective 3, PGC Publishing, Adelaide, 1-24.

Cook, N.J., Ciobanu, C.L., Meria, D., Silcock, D., Wade, B., 2013. Arsenopyrite-pyrite association in an orogenic gold ore: tracing mineralization history from textures and trace elements. Economic Geology, 108, 1273-1283.

Cook, N., Ciobanu, C.L., George, L., Zhu, Z.Y., Wade, B., Ehrig, K., 2016. Trace element analysis of minerals in magmatic-hydrothermal ores by laser ablation inductively-coupled plasma mass spectrometry: Approaches and opportunities. Minerals, 6(4), 111.

Corriveau, L., Montreuil, J.-F., Potter, E., 2016. Alteration facies linkages among iron oxide copper-gold, iron oxide-apatite, and affiliated deposits in the Great Bear magmatic zone, Northwest Territories, Canada. Economic Geology 111, 2045-2072.

Courtney-Davies, L., Zhu, Z., Ciobanu, C.L., Wade, B.P., Cook, N.J., Ehrig, K., Cabral, A.R., Kennedy, A., 2016. Matrix-matched iron-oxide laser ablation ICP-MS U–Pb geochronology using mixed solution standards. Minerals 6, 85.

Cowley, W., Conor, C., Zang, W., 2003. New and revised Proterozoic stratigraphic units on northern Yorke Peninsula. MESA Journal 29, 46-58.

Creaser, R.A., 1989. The geology and petrology of Middle Proterozoic felsic magmatism of the Stuart Shelf, South Australia. La Trobe University, Melbourne.

Creaser, R.A., 1996. Petrogenesis of a Mesoproterozoic quartz latite-granitoid suite from the Roxby Downs area, South Australia. Precambrian Research 79, 371-394.

Cuney, M., 2010. Evolution of uranium fractionation processes through time: driving the secular variation of uranium deposit types. Economic Geology 105, 553–569.

Cuney, M., Emetz, A., Mercadier, J., Mykchaylov, V., Shunko, V., Yuslenko, A., 2012. Uranium deposits associated with Na-metasomatism from central Ukraine: a review of some of the major deposits and genetic constraints. Ore Geology Reviews 44, 82-106.

D'Arco, P., Piriou, B., 1989. Fluorescence spectra of Eu^{3+} in synthetic polycrystalline anorthite: Distribution of Eu^{3+} in the structure. American Mineralogist 74, 191-199.

Davidson, G.J., Paterson, H., Meffre, S., Berry, R.F., 2007. Characteristics and origin of the Oak Dam East breccia-hosted, iron oxide Cu-U-(Au) deposit: Olympic Dam region, Gawler craton, South Australia. Economic Geology 102, 1471–1498.

Day, W.C., Slack, J.F., Ayuso, R.A., Seeger, C.M., 2016. Regional geologic and petrologic framework for iron oxide ± apatite ± rare earth element and iron oxide copper-gold deposits

of the Mesoproterozoic St. Francois Mountains terrane, southeast Missouri, USA. Economic Geology 111, 1825-1858.

Dempster, T., Jenkin, G., Rogers, G., 1994. The origin of rapakivi texture. Journal of Petrology 35, 963–981.

Donnay, G., Donnay, J.D.H., 1953. The crystallography of bastnaesite-(Ce), parisite, roentgenite-(Ce) and synchysite-(Ce). American Mineralogist 38, 932-963.

Donovan, J.J., 2014. Probe for EPMA: Acquisition, automation and analysis. Ver. 10.3.5 Xtreme Edition, Probe Software, Inc., Oregon, United States of America

Drake, H., Tullborg, E.-L., Annersten, H., 2008. Red-staining of the wall rock and its influence on the reducing capacity around water conducting fractures. Applied Geochemistry 23, 1898–1920.

Ehrig, K., 2013. Geology of the Wirrda Well IOCG deposit. Powerpoint presentation, 10th Annual SA Exploration and Mining Conference, Adelaide. http://www.saexplorers.com.au

Ehrig, K., McPhie, J., Kamenetsky, V., 2012. Geology and mineralogical zonation of the Olympic Dam Iron Oxide Cu-U-Au-Ag deposit, South Australia. In: Hedenquist J.W., Harris, M., Camus, F., (Eds.), Geology and Genesis of Major Copper Deposits and Districts of the World: A Tribute to Richard H. Sillitoe, 16. SEG Special Publication, 237–267.

Ehrig, K., Kamenetsky, V.S., McPhie, J., Apukhtina, O., Ciobanu, C.L., Cook, N.J., Kontonikas-Charos, A., Krneta, S., (in press). The IOCG-IOA ore system at Olympic Dam and nearby prospects, South Australia. Proceedings from the 14th Biennial SGA Meeting, Quebec City, Canada, 2017.

Elderfield, H., Greaves, M.J., 1982. The rare earth elements in seawater. Nature 296, 214-219.

Emslie, R., 1991. Granitoids of rapakivi granite-anorthosite and related associations. Precambrian Research 51, 173–192.

Engvik, A.K., Putnis, A., Gerald, J.D.F., Austrheim, H., 2008. Albitization of granitic rocks: the mechanism of replacement of oligoclase by albite. The Canadian Mineralogist 46, 1401-1415.

Fanning, C.M., 1997. Geochronological synthesis of southern Australia. Part II. The Gawler Craton. South Australian Department of Mines and Energy, Open file envelope 8918 (unpublished)

Fanning, C.M., 2002. Gawler Craton: synthesis of recent SHRIMP U–Pb geochronology. In: Gawler Craton 2002: State of Play. Department of Primary Industries and Resources Workshop Proceedings (CD). Office of Minerals and Energy Resources, South Australia.

Fanning, C., Flint, R., Parker, A., Ludwig, K., Blissett, A., 1988. Refined Proterozoic evolution of the Gawler craton, South Australia, through U-Pb zircon geochronology. Precambrian Research 40, 363-386.

Fanning, C.M., Reid, A.J., Teale, G.S., 2007. A geochronological framework for the Gawler craton, South Australia. Bulletin 55. Primary Industries and Resources South Australia, Adelaide.

Ferris, G.M., Schwarz, M.P., Heithersay, P., 2002. The geological framework, distribution, and controls of Fe-oxide Cu–Au mineralisation in the Gawler Craton, South Australia: Part 1—Geological and tectonic framework. In: Porter TM (Ed.), Hydrothermal Iron Oxide Copper-Gold & Related Deposits: A Global Perspective 2, PGC Publishing, Adelaide, 9-32.

FitzGerald, J.D., Parise, J.B., Mackinnon, I.D.R., 1986. Average structure of an An_{48} plagioclase from the Hogarth Ranges. American Mineralogist 71, 1399-1408.

Fleet, M.E., 1988. Tetrahedral-site occupancies in reedmergnerite and synthetic boron albite ($NaBSi_3O_8$). American Mineralogist 77, 76-84.

Fleet, M.E., Pan, Y., 1994. Site preference of Nd in fluorapatite [Ca_{10} $(PO_4)_6$ F_2]. Journal of Solid State Chemistry 112, 78–81.

Fleet, S., Ribbe, P., 1965. An electron-microscope study of peristerite plagioclases. Mineralogical Magazine 35, 165-176.

Flint, R., 1993. Hiltaba suite. In: Drexel, J.F., Priess, W.V., Parker, A.J. (Eds.), The Geology of South Austalia 1, The Precambrian, South Australia Geological Survey Bulletin 54, 127-131.

Forbes, C., 2012. Report on production of first version of top of basement solid geology map for the central Yorke Peninsula. Project 3.2/3.3: Yorke Peninsula Project. Unpublished internal report, DET CRC (http://detcrc.com.au/publications/research/)

Frost, B.R., Barnes, C.G., Collins,W.J., Arculus, R.J., Ellis, D.J., Frost, C.D., 2001. A geochemical classification for granitic rocks. Journal of Petrology 42, 2033–2048.

Fuhrman, M.L., Lindsley, D.H., 1988. Ternary-feldspar modeling and thermometry. American Mineralogist 73, 201–215.

Garcia, D., Pascal, M-L., Roux, J., 1996. Hydrothermal replacement of feldspars in igneous enclaves of the Velay granite and the genesis of myrmekites. European Journal of Mineralogy 8, 703-718.

Gast, P.W., 1968. Trace element fractionation and the origin of tholeiitic and alkaline magma types. Geochimica et Cosmochimica Acta 32, 1057-1086.

Gay, P., Smith, J., 1955. Phase relations in the plagioclase feldspars: composition range An_0 to An_{70}. Acta Crystallographica 8, 64-65.

Goldschmidt, V.M., 1937. The principles of distribution of chemical elements in minerals and rocks. The seventh Hugo Müller Lecture, delivered before the Chemical Society on March 17th, 1937. Journal of the Chemical Society (Resumed), 655-673.

Grant, J.A., 1986. The isocon diagram; a simple solution to Gresens' equation for metasomatic alteration. Economic Geology 81, 1976–1982.

Gresens, R.L., 1967. Composition–volume relationships of metasomatism. Chemical Geology 2, 47–65.

Grove, T.L., Ferry, J.M., Spear, F.S., 1983. Phase transitions and decomposition relations in calcic plagioclase. American Mineralogist 68, 41-59.

Groves, D.I., Bierlein, F.P., Meinert, L.D., Hitzman, M.W., 2010. Iron Oxide Copper-Gold (IOCG) Deposits through Earth History: Implications for Origin, Lithospheric Setting, and Distinction from Other Epigenetic Iron Oxide Deposits. Economic Geology 105, 641-654.

Haas, J.R., Shock, E.L., Sassani, D.C., 1995. Rare earth elements in hydrothermal systems: estimates of standard partial molal thermodynamic properties of aqueous complexes of the rare earth elements at high pressures and temperatures. Geochimica et Cosmochimica Acta 59, 4329-4350.

Hammarstrom, J.M., Zen, E., 1986. Aluminium in hornblende: an empirical geobarometer. American Mineralogist 71, 1297–1313.

Hand, M., Reid, A., Jagodzinski, L., 2007. Tectonic framework and evolution of the Gawler Craton, southern Australia. Economic Geology 102, 1377-1395.

Harlov, D.E., Andersson, U.B., Förster, H.-J., Nyström, J.O., Dulski, P., Broman, C., 2002. Apatite–monazite relations in the Kiirunavaara magnetite–apatite ore, northern Sweden. Chemical Geology 191, 47-72.

Harlov, D.E., Meighan, C.J., Kerr, I.D., Samson, I.M., 2016. Mineralogy, chemistry, and fluid-aided evolution of the Pea Ridge Fe oxide-(Y+ REE) deposit, southeast Missouri, USA. Economic Geology 111, 1963-1984.

Haynes, D.W., Cross, K.C., Bills, R.T., Reed, M.H., 1995. Olympic Dam ore genesis: a fluid-mixing model. Economic Geology 90, 281-307.

Hayward, N., Skirrow, R., 2010. Geodynamic setting and controls on iron oxide Cu-Au (±U) ore in the Gawler craton, South Australia. In: Porter TM (Ed.), Hydrothermal Iron Oxide

Copper-Gold & Related Deposits: A Global Perspective, 3-4, PGP Publishing, Adelaide, 105-131.

Henderson, P., 1984. General geochemical properties and abundances of the rare earth elements. In: Henderson P (Ed), rare earth Element Geochemistry, 1st ed, Elsevier

Hibbard, M.J., 1981. The magma mixing origin of mantled feldspars. Contributions to Mineralogy and Petrology 76, 158–170.

Hitzman, M.W., 2000. Iron oxide–Cu–Au deposit: what, where, when, and why? In: Porter, T.M. (Ed.), Hydrothermal iron oxide copper-gold and related deposits a global perspective. Australian Mineral Foundation, 9–26.

Hitzman, M.W., Valenta, R.K., 2005. Uranium in iron oxide-copper-gold (IOCG) systems. Economic Geology 100, 1657–1661.

Hitzman, M.W., Oreskes, N., Einaudi, M.T., 1992. Geological characteristics and tectonic setting of proterozoic iron oxide (Cu-U-Au-REE) deposits. Precambrian Research 58, 241-287.

Hollister, L.S., Grissom, G.C., Peters, E.K., Stowell, H.H., Sisson, V.B., 1987. Confirmation of the empirical correlation of aluminium in hornblende with pressure of solidification of calcalkaline plutons. American Mineralogist 72, 231–239.

Hövelmann, J., Putnis, A., Geisler, T., Schmidt, B.C., Golla-Schindler, U., 2010. The replacement of plagioclase feldspars by albite: observations from hydrothermal experiments. Contributions to Mineralogy and Petrology 159, 43-59.

Huang, Q., Kamenetsky, V.S., McPhie, J., Ehrig, K., Meffre, S., Maas, R., Thompson, J., Kamenetsky, M., Chambefort, I., Apukhtina, O., 2015. Neoproterozoic (ca. 820–830Ma) mafic dykes at Olympic Dam, South Australia: Links with the Gairdner Large Igneous Province. Precambrian Research 271, 160-172.

Huang, Q., Kamenetsky, V.S., Ehrig, K., McPhie, J., Kamenetsky, M., Cross, K., Meffre, S., Agangi, A., Chambefort, I., Direen, N.G., 2016. Olivine-phyric basalt in the Mesoproterozoic Gawler silicic large igneous province, South Australia: Examples at the Olympic Dam Iron Oxide Cu–U–Au–Ag deposit and other localities. Precambrian Research 281, 185-199.

Ismail, R., 2016. Spatial-Temporal Evolution of Skarn Alteration in IOCG Systems: Evidence from Petrography, Mineral Trace Element Signatures and Fluid Inclusion Studies at Hillside, Yorke Peninsula, South Australia. Unpublished Ph.D. thesis, The University of Adelaide.

Ismail, R., Ciobanu, C.L., Cook, N.J., Teale, G.S., Giles, D., Mumm, A.S., Wade, B., 2014. Rare earths and other trace elements in minerals from skarn assemblages, Hillside iron oxide–copper–gold deposit, Yorke Peninsula, South Australia. Lithos 184–187, 456-477.

Jagodzinski, E., 2005. Compilation of SHRIMP U-Pb geochronological data, Olympic Domain, Gawler Craton. South Australia, 2001-2003. Geoscience Australia Record 2005/020

Jagodzinski, E.A., 2014. The age of magmatic and hydrothermal zircon at Olympic Dam, Australian Earth Sciences Convention Proceedings, Geological Society of Australia Abstracts 110, 260.

Jagodzinski, E.A., Reid, A.J., Hand, M., 2012. SHRIMP U-Pb geochronology of Archaean to Palaeoproterozoic rocks from southern Eyre Peninsula. Report book 2012/00015, Department of Manufacturing, Trade, Innovation, Resources and Energy, South Australia, Adelaide.

Johnson, J.P., Cross, K.C., 1995. U-Pb geochronological constraints on the genesis of the Olympic Dam Cu-U-Au-Ag deposit, South Australia. Economic Geology 90, 1046-1063.

Johnson, J.P., McCulloch, M.T., 1995. Sources of mineralising fluids for the Olympic Dam deposit (South Australia): Sm–Nd isotopic constraints. Chemical Geology 121, 177–199.

Johnson, M.C., Rutherford,M.J., 1989. Experimental calibration of the aluminium-in-hornblende geobarometer with application to Long Valley caldera (California). Geology 17, 837–841.

Johnson, J.W., Oelkers, E.H., Helgeson, H.C., 1992. SUPCRT92: a software package for calculating the standard molal thermodynamic properties of minerals, gases, aqueous species, and reactions from1 to 5000 bar and 0 to 1000 °C. Computers and Geoscience 18, 899–947.

Kamenetsky, V.S., Ehrig, K., Maas, R., Meffre, S., Kamenetsky, M., McPhie, J., Apukhtina, O., Huang, Q., Thompson, J., Ciobanu, C.L., Cook, N.J., 2015. The supergiant Olympic Dam Cu-U-Au-Ag Ore Deposit: Toward a new genetic model. Society of Economic Geologists, SEG 2015: World Class Ore Deposits: Discovery to Recovery, Hobart, TAS, Australia; 09/2015.

Kimata, M., 1988. The crystal structure of non-stoichiometric Eu-anorthite: an explanation of the Eu-positive anomaly. Mineralogical Magazine 52, 257-265.

Kish, L., Cuney, M., 1981. Uraninite-albite veins from the Mistamisk Valley of the Labrador Trough, Quebec. Mineralogical Magazine 44, 471-483.

Kneip, H.-J., Liebau, F., 1994. Feldspars with trivalent non-tetrahedral cations: Experimental studies in the system $NaAlSi_3O_8$-$CaAl_2Si_2O_8$-$LaAl_3SiO_8$. European Journal of Mineralogy 6, 87-98.

Kontonikas-Charos, A., 2014. Albitization and REE-U enrichment in IOCG systems: Insights from Moonta-Wallaroo, Yorke Peninsula, South Australia. Unpublished Honours thesis, The University of Adelaide.

Kontonikas-Charos, A., Ciobanu, C.L., Cook, N.J., 2014. Albitization and redistribution of REE and Y in IOCG systems: Insights from Moonta-Wallaroo, Yorke Peninsula, South Australia. Lithos 208–209, 178-201.

Kontonikas-Charos, A., Ciobanu, C.L., Cook, N.J., Ehrig, K., Kamenetsky, V.S., 2015. Deuteric coarsening and albitization in Hiltaba granites from the Olympic Dam IOCG deposit, South Australia. Proceedings, Mineral Resources in a Sustainable World, 13th Biennial SGA Meeting, 3:1099–1102.

Kontonikas-Charos, A., Ciobanu, C.L., Cook, N.J., Ehrig, K., Krneta, S., Kamenetsky, V.S., 2017. Feldspar evolution in the Roxby Downs Granite, host to Fe-oxide Cu-Au-(U) mineralisation at Olympic Dam, South Australia. Ore Geology Reviews 80, 838-859.

Kontonikas-Charos, A., Ciobanu, C.L., Cook, N.J., Ehrig, K., Ismail, R., Krneta, S., Basak, A. (in press) Feldspar mineralogy and rare earth element (re)mobilization in iron-oxide copper gold systems from South Australia: a nanoscale study. Mineralogical Magazine. https://doi.org/10.1180/minmag.2017.081.040.

Kontonikas-Charos, A., Ciobanu, C.L., Cook, N.J., Ehrig, K., Krneta, S., Kamenetsky, V.S., (in review). Rare earth element geochemistry of feldspars: Examples from Fe-oxide Cu-Au systems in the Olympic Cu-Au Province, South Australia. Mineralogy and Petrology.

Krneta, S., Ciobanu, C.L., Cook, N.J., Ehrig, K., Kontonikas-Charos, A., 2016. Apatite at Olympic Dam, South Australia: a petrogenetic tool. Lithos 262, 470–485.

Lee, M.R., Parsons, I., 1997. Dislocation formation and albitization in alkali feldspars from the Shap granite. American Mineralogist 82, 557–570.

Lee, M.R., Brown, D.J., Smith, C.L., Hodson, M.E., MacKenzie, M., Hellmann, R., 2007. Characterization of mineral surfaces using FIB and TEM: A case study of naturally weathered alkali feldspars. American Mineralogist 92, 1383-1394.

LeMaitre, R.W., Streckeisen, A., Zanettin, B., Le Bas, M.J., Bonin, B., Bateman, P. (Eds.), 1989. A Classification of Igneous Rocks and Glossary of Terms: Recommendations of the International Union of Geological Sciences Subcommission on the Systematics of Igneous Rocks. Blackwell Scientific, Oxford (193 pp.).

Lepage, L.D., 2003. ILMAT: an Excel worksheet for ilmenite-magnetite geothermometry and geobarometry. Computers and Geoscience 29, 673–678.

Lindsley, D.H., Spencer, K.J., 1982. Fe-Ti oxide geothermometry: reducing analyses of coexisting Ti-magnetite (Mt) and ilmenite (Ilm). EOS Trans. American Geophysics Union 63, 471.

London, D., Černý, P., Loomis, J.L., Pan, J.J., 1990. Phosphorus in alkali feldspars of rare-element granitic pegmatites. Canadian Mineralogist 28, 771-786.

Lottermoser, B., 1992. Rare earth elements and hydrothermal ore formation processes. Ore Geology Reviews 7, 25-41.

Macmillan, E., Cook, N.J., Ehrig, K., Ciobanu, C.L., Pring, A., 2016a. Uraninite from the Olympic Dam IOCG-U-Ag deposit: Linking textural and compositional variation to temporal evolution. American Mineralogist 101, 1295–1320.

Macmillan, E., Ciobanu, C.L., Ehrig, K., Cook, N.J., Pring, A., 2016b. Chemical zoning and lattice distortion in uraninite from Olympic Dam, South Australia. American Mineralogist 101, 2351-2354.

Macmillan, E., Ciobanu, C.L., Ehrig, K., Cook, N.J., Pring, A., 2016c. Replacement of uraninite by bornite via coupled dissolution-reprecipitation: Evidence from texture and microstructure. The Canadian Mineralogist 54, 1369-1383.

Macmillan, E., Cook, N.J., Ehrig, K., Pring, A. Chemical and textural interpretation of late-stage coffinite and brannerite from the Olympic Dam IOCG-Ag-U deposit. Mineralogical Magazine (in press). https://doi.org/10.1180/minmag.2017.081.006

Manning, D., 1981. The effect of fluorine on liquidus phase relationships in the system Qz-Ab-Or with excess water at 1 kb. Contributions to Mineralogy and Petrology 76, 206–215.

Mark, G., 1998. Albitite formation by selective pervasive sodic alteration of tonalite plutons in the Cloncurry district, Queensland. Australian Journal of Earth Sciences 45, 765-774.

Mark, G., Oliver, N.H., Williams, P.J., 2006. Mineralogical and chemical evolution of the Ernest Henry Fe oxide–Cu–Au ore system, Cloncurry district, northwest Queensland, Australia. Mineralium Deposita 40, 769-801.

Mauger, A., Ehrig, K., Kontonikas-Charos, A., Ciobanu, C., Cook, N., Kamenetsky, V., 2016. Alteration at the Olympic Dam IOCG–U deposit: insights into distal to proximal feldspar and phyllosilicate chemistry from infrared reflectance spectroscopy. Australian Journal of Earth Sciences 63, 959-972.

McDonough, W.F., Sun, S-S., 1995. The composition of the Earth. Chemical Geology 120, 223-253.

McPhie, J., DellaPasqua, F., Allen, S., Lackie, M., 2008. Extreme effusive eruptions: palaeoflow data on an extensive felsic lava in the Mesoproterozoic Gawler Range Volcanics. Journal of Volcanology and Geothermal Research 172, 148-161.

McPhie, J., Kamenetsky, V.S., Chambefort, I., Ehrig, K., Green, N., 2011. Origin of the supergiant Olympic Dam Cu-U-Au-Ag deposit, South Australia: Was a sedimentary basin involved? Geology 39, 795-798.

Meinert, L.D., 1992. Skarns and skarn deposits. Geoscience Canada Reprint Series 6, 117–134.

Meng, D.W., Wu, X.L., Mou, T., Li, D.X., 2001. Determination of six new polytypes in parisite-(Ce) by means of high resolution electron microscopy. Mineralogical Magazine 65, 797-806.

Meng, D.W., Wu, X.L., Han, Y.J., Meng, X., 2002. Polytypism and microstructures of the mixed-layer member B_2S, $CaCe_3(CO_3)_4F_3$ in the bastnaesite-(Ce)-synchysite-(Ce) series. Earth and Planetary Science Letters 203, 817-828.

Merino, E., 1975. Diagenesis in Tertiary sandstones from Kettleman North Dome, California. I. Diagenetic mineralogy. Journal of Sedimentary Research 45, 320-336.

Migdisov, A.A., Williams-Jones, A., 2014. Hydrothermal transport and deposition of the rare earth elements by fluorine-bearing aqueous liquids. Mineralium Deposita 49, 987-997.

Migdisov, A., Williams-Jones, A., Brugger, J., Caporuscio, F., 2016. Hydrothermal transport, deposition, and fractionation of the REE: Experimental data and thermodynamic calculations. Chemical Geology 439, 13-42.

Montreuil, J.-F., Corriveau, L., Potter, E.G., 2015. Formation of albitite-hosted uranium within IOCG systems: the Southern Breccia, Great Bear magmatic zone, Northwest Territories, Canada. Mineralium Deposita 50 (3), 293-325.

Montreuil, J.-F., Corriveau, L., Potter, E., De Toni, A., 2016. On the relationship between alteration facies and metal endowment of iron oxide-alkali-altered systems, southern Great Bear magmatic zone (Canada). Economic Geology 111, 2139-2168.

Morad, S., El-Ghali, M., Caja, M., Sirat, M., Al-Ramadan, K., Mansurbeg, H., 2010. Hydrothermal alteration of plagioclase in granitic rocks from Proterozoic basement of SE Sweden. Geological Journal 45, 105-116.

Morales-Ruano, S., Both, R., Golding, S., 2002. A fluid inclusion and stable isotope study of the Moonta copper–gold deposits, South Australia: evidence for fluid immiscibility in a magmatic hydrothermal system. Chemical Geology 192, 211-226.

Mortimer, G.E., 1984. Early to middle Proterozoic granitoids, basaltic dykes and associated layered rocks of SE Eyre Peninsula, South Australia. Unpublished PhD thesis, University of Adelaide.

Müller, A., Seltmann, R., Kober, B., Eklund, O., Jeffries, T., Kronz, A., 2008. Compositional zoning of rapakivi feldspars and coexisting quartz phenocrysts. Canadian Mineralogist 46, 1417–1442.

Müller, W., Shelley, M., Miller, P., Broude, S., 2009. Initial performance metrics of a new custom-designed ArF excimer LA-ICPMS system coupled to a two-volume laser-ablation cell. Journal of Analytical Atomic Spectrometry 24, 209–214.

Navrotsky, A., 2011. Nanoscale Effects on Thermodynamics and Phase Equilibria in Oxide Systems. ChemPhysChem 12, 2207–2215.

Navrotsky, A., Mazeina, L., Majzlan, J., 2008. Size-Driven Structural and Thermodynamic Complexity in Iron Oxides. Science 319, 1635-1638.

Ni, Y.X., Hughes, J.M., Mariano, A.N., 1993. The atomic arrangement of bastnaesite-(Ce), $Ce(CO_3)F$, and structural elements of synchysite-(Ce), roentgenite-(Ce), and parisite-(Ce). American Mineralogist 78, 415-418.

Norberg, N., Harlov, D., Neusser, G., Wirth, R., Rhede, D., 2014. Element mobilization during feldspar metasomatism: an experimental study. European Journal of Mineralogy 26, 71–82.

Oliver, N.H., Cleverley, J.S., Mark, G., Pollard, P.J., Fu, B., Marshall, L.J., Rubenach, M.J., Williams, P.J., Baker, T., 2004. Modelling the role of sodic alteration in the genesis of iron oxide-copper-gold deposits, Eastern Mount Isa block, Australia. Economic Geology 99, 1145-1176.

O'Neil, J.R., Taylor, H.P., 1967. The oxygen isotope and cation exchange chemistry of feldspars. American Mineralogist 52, 1414-1437.

Oreskes, N., Einaudi, M.T., 1990. Origin of rare earth element-enriched hematite breccias at the Olympic Dam Cu-U-Au-Ag deposit, Roxby Downs, South Australia. Economic Geology 85, 1-28.

Oreskes, N., Einaudi, M.T., 1992. Origin of hydrothermal fluids at Olympic Dam; preliminary results from fluid inclusions and stable isotopes. Economic Geology 87, 64-90.

Orville, P.M., 1963. Alkali ion exchange between vapor and feldspar phases. American Journal of Science 261, 201-237.

Otake, T., Wesolowski, D.J., Anovitz, L.M., Allard, L.F., Ohmoto, H., 2010. Mechanisms of iron oxide transformations in hydrothermal systems. Geochimica et Cosmochimica Acta 74, 6141–6156.

Papike, J.J., 1988. Chemistry of the rock-forming silicates: Multiple-chain, sheet, and framework structures. Reviews of Geophysics 26, 407-444.

Parker, A., 1993. Gawler craton. Cleve and Moonta subdomains: South Australian Geological Survey Bulletin 54, 51-68.

Parry,W., Downey, L., 1982. Geochemistry of hydrothermal chlorite replacing igneous biotite. Clay and Clay Minerals 30, 81–90.

Parsons, I., 1978. Feldspars and fluids in cooling plutons. Mineralogical Magazine 42, 1–17.

Parsons, I., 2010. Feldspars defined and described: a pair of posters published by the Mineralogical Society. Sources and supporting information. Mineralogical Magazine 74, 529-551.

Parsons, I., Brown, W.L., 1984. Feldspars and the thermal history of igneous rocks, Feldspars and feldspathoids. Springer, 317-371.

Parsons, I., Thompson, P., Lee, M.R., Cayzer, N., 2005. Alkali feldspar microtextures as provenance indicators in siliciclastic rocks and their role in feldspar dissolution during transport and diagenesis. Journal of Sedimentary Research 75, 921-942.

Parsons, I., Lee, M.R., 2009. Mutual replacement reactions in alkali feldspars I: microtextures and mechanisms. Contributions to Mineralogy and Petrology 157, 641-661.

Parsons, I., Magee, C.W., Allen, C.M., Shelley, J., Lee, M.R., 2009. Mutual replacement reactions in alkali feldspars II: trace element partitioning and geothermometry. Contributions to Mineralogy and Petrology 157, 663-687.

Parsons, I., Fitz Gerald, J.D., Lee, J.K.W., Ivanic, T., Golla-Schindler, U., 2010. Time-temperature evolution of microtextures and contained fluids in a plutonic alkali feldspar during heating. Contributions to Mineralogy and Petrology 160, 155–180.

Parsons, I., Gerald, J.D.F., Lee, M.R., 2015. Review. Routine characterization and interpretation of complex alkali feldspar intergrowths. American Mineralogist 100, 1277-1303.

Pearce, N.J., Perkins, W.T., Westgate, J.A., Gorton, M.P., Jackson, S.E., Neal, C.R., Chenery, S.P., 1997. A compilation of new and published major and trace element data for NIST SRM 610 and NIST SRM 612 glass reference materials. Geostandards Geoanalytical Research 21, 115-144.

Perez, R.J., Boles, J.R., 2005. An empirically derived kinetic model for albitization of detrital plagioclase. American Journal of Science 305, 312-343.

Plümper, O., Putnis, A., 2009. The complex hydrothermal history of granitic rocks: multiple feldspar replacement reactions under subsolidus conditions. Journal of Petrology 50, 967–987.

Pollard, P.J., 2006. An intrusion-related origin for Cu–Au mineralization in iron oxide–copper–gold (IOCG) provinces. Mineralium Deposita 41, 179–187.

Pun, A., Papike, J., Layne, G., 1997. Subsolidus REE partitioning between pyroxene and plagioclase in cumulate eucrites: An ion microprobe investigation. Geochimica et Cosmochimica Acta 61, 5089-5097.

Putnis, A., 1992. An Introduction to Mineral Sciences. Cambridge University Press.

Putnis, A., 2002. Mineral replacement reactions: from macroscopic observations to microscopic mechanisms. Mineralogical Magazine 66, 689-708.

Putnis, A., 2009. Mineral replacement reactions. Reviews in Mineralogy and Geochemistry 70, 87-124.

Putnis, A., 2015. Transient porosity resulting from fluid–mineral interaction and its consequences. Reviews in Mineralogy and Geochemistry 80, 1-23.

Putnis, A., Hinrichs, R., Putnis, C.V., Golla-Schindler, U., Collins, L.G., 2007. Hematite in porous red-clouded feldspars: evidence of large-scale crustal fluid–rock interaction. Lithos 95, 10–18.

Que, M., Allen, A.R., 1996. Sericitization of plagioclase in the Rosses granite complex, Co. Donegal, Ireland. Mineralogical Magazine 60, 927–936.

Rämö, O., Haapala, I., 1995. One hundred years of rapakivi granite. Mineralogy and Petrology 52, 129–185.

Raymond, O., 2003, Yorke Peninsula (Moonta Subdomain), Geophysical Interpretation of Pre-Neo Proterozoic Basement Geology 1:250 000 scale map (2nd edition). Geoscience Australia, Canberra.

Reeve, J., Cross, K., Smith, R., Oreskes, N., 1990. Olympic Dam copper-uranium-gold-silver deposit. Geology of the Mineral Deposits of Australia and Papua New Guinea 2, 1009-1035. AusIMM, Melbourne.

Reich, M., Hough, R.M., Deditius, A., Utsunomiya, S., Ciobanu, C.L., Cook, N.J., 2011. Nanogeoscience in ore systems research: Principles, methods, and applications: Introduction and preface to the special issue. Ore Geology Reviews 42, 1-5.

Reid, A.J., Fabris, A., 2015. Influence of Preexisting Low Metamorphic Grade Sedimentary Successions on the Distribution of Iron Oxide Copper-Gold Mineralization in the Olympic Cu-Au Province, Gawler Craton. Economic Geology 110, 2147-2157.

Reid, A., Hand, M., 2012. Mesoarchean to Mesoproterozoic evolution of the southern Gawler Craton, South Australia. Episodes 35, 216–225.

Reid, A.J., Swain, G.S. Mason, D., Maas, R., 2011. Nature and timing of Cu-Au-Zn-Pb mineralisation at Punt Hill, eastern Gawler Craton. MESA Journal 60, 7–17.

Reid, A., Smith, R.N., Baker, T., Jagodzinski, E.A., Selby, D., Gregory, C.J., Skirrow, R.G., 2013. Re-Os dating of molybdenite within hematite breccias from the Vulcan Cu-Au prospect, Olympic Cu-Au province, South Australia. Economic Geology 108, 883-894.

Ren, M., 2004. Partitioning of Sr, Ba, Rb, Y, and LREE between alkali feldspar and peraluminous silicic magma. American Mineralogist 89, 1290-1303.

Roberts, D., Hudson, G., 1983. The Olympic Dam copper-uranium-gold deposit, Roxby Downs, South Australia. Economic Geology 78, 799-822.

Rong, J., Wang, F., 2016. Metasomatic Textures in Granites: Evidence from Petrographic Observation. Springer.

Ruiz-Agudo, E., Putnis, C., Putnis, A., 2014. Coupled dissolution and precipitation at mineral–fluid interfaces. Chemical Geology 383, 132-146.

Ryan, B., 1991. Makhavinekh Lake pluton, Labrador, Canada: geological setting, subdivisions, mode of emplacement, and a comparison with Finnish rapakivi granites. Precambrian Research 51, 193–225.

Schilling, J-G., Winchester, J., 1967 Rare-earth fractionation and magmatic processes. In: Runcorn S.K. (Ed.), Mantles of the Earth and Terrestrial Planets. Interscience Publishers, New York, 267-283.

Schmidt, M.W., 1992. Amphibole composition in tonalite as a function of pressure: an experimental calibration of the Al-in-hornblende barometer. Contributions to Mineralogy and Petrology 110, 304-310.

Shand, S.J., 1943. The Eruptive Rocks. 2nd edition. John Wiley, New York.

Sillitoe, R.H., 2003. Iron oxide-copper-gold deposits: an Andean view. Mineralium Deposita 38, 787-812.

Skirrow, R., 2008. "Hematite-group" IOCG±U ore systems: tectonic settings, hydrothermal characteristics, and Cu–Au and Umineralising processes. In: Corriveau, L.,Mumin, A.H. (Eds.), Exploring for Iron Oxide Copper-gold Deposits: Canada and Global Analogues. Geological Association of Canada, Short Course Notes vol. 20, 39–57.

Skirrow, R., Bastrakov, E., Davidson, G., Raymond, O., Heithersay, P., 2002. The geological framework, distribution and controls of Fe-oxide Cu-Au mineralisation in the Gawler Craton, South Australia. Part II-alteration and mineralisation. In Porter, T.M. (Ed.), Hydrothermal Iron Oxide Copper-Gold and Related Deposits: A Global Perspective 2, PGC Publishing, Adelaide, 33-47.

Skirrow, R.G., Bastrakov, E.N., Barovich, K., Fraser, G.L., Creaser, R.A., Fanning, C.M., Raymond, O.L., Davidson, G.J., 2007. Timing of iron oxide Cu-Au-(U) hydrothermal activity and Nd isotope constraints on metal sources in the Gawler craton, South Australia. Economic Geology 102, 1441–1470.

Słaby, E., 1995. TAS classification — how to overcome problems with post-magmatic feldspar formation in Permian volcanic rocks. Zentralblatt für Geologie und Paläontologie. 5, 541–552.

Słaby, E., Goetze, J., 2004. Feldspar crystallization under magma-mixing conditions shown by cathodoluminescence and geochemical modelling — a case study from the Karkonosze pluton (SW Poland). Mineralogical Magazine 68, 561–577.

Słaby, E., Śmigielski, M., Śmigielski, T., Domonik, A., Simon, K., Kronz, A., 2011. Chaotic three-dimensional distribution of Ba, Rb and Sr in feldspar megacrysts grown in an open magmatic system. Contributions to Mineralogy and Petrology 162, 909–927.

Smith, J.V., 1974a. Feldspar Minerals. Volume 1. Crystal structure and physical properties. Springer-Verlag.

Smith, J.V., 1974b. Feldspar Minerals. Volume 2. Chemical and Textural Properties. Springer-Verlag.

Smith, J.V., Brown, W.L., 1988. Feldspar Minerals, 2nd, Springer, New York, pp 828

Smith, M., Henderson, P., Jeffries, T., Long, J., Williams, C., 2004. The rare earth elements and uranium in garnets from the Beinn an Dubhaich Aureole, Skye, Scotland, UK: constraints on processes in a dynamic hydrothermal system. Journal of Petrology 45, 457-484.

Smith, M., Storey, C.D., Jeffries, T.E., Ryan, C., 2009. In situ U–Pb and trace element analysis of accessory minerals in the Kiruna district, Norrbotten, Sweden: new constraints on the timing and origin of mineralization. Journal of Petrology 50, 2063–2094.

Snow, E., Kidman, S., 1991. Effect of fluorine on solid-state alkali interdiffusion rates in feldspar. Nature 349, 231–233.

Stix, J., Gorton, M.P., 1990. Variations in trace element partition coefficients in sanidine in the Cerro Toledo Rhyolite, Jemez Mountains, New Mexico: Effects of composition, temperature, and volatiles. Geochimica et Cosmochimica Acta 54, 2697-2708.

Stormer, J.C., 1983. The effects of recalculation on estimates of temperature and oxygen fugacity from analyses of multicomponent iron-titanium oxides. American Mineralogist 68, 586–594.

Streckeisen, A.L., 1976. Classification and nomenclature of igneous rocks. Earth-Science Reviews 12, 1–35.

Towell, D.G., Winchester, J.W., Spirn, R.V., 1965. Rare-Earth distributions in some rocks and associated minerals of the batholith of southern California. Journal of Geophysical Research 70, 3485-3496.

Trail, D., Watson, E.B., Tailby, N.D., 2012. Ce and Eu anomalies in zircon as proxies for the oxidation state of magmas. Geochimica et Cosmochimica Acta 97, 70–87.

Troeng, B., 1982. Uranium-rich granites in the Olden Window, Sweden. Mineralogical Magazine 46, 217–226.

Van Achterbergh, E., Ryan, C.G., Jackson, S.E., Griffin, W.L., 2001. LA-ICP-MS in the Earth Sciences - Appendix 3, data reduction software for LA-ICP-MS. In: Sylvester, P.J. (Ed.), Mineralogical Association of Canada Short Course 29, 239-243.

Van Dongen M., Weinberg, R.F., Tomkins, A.G., 2010. REE-Y, Ti, and P remobilization in magmatic rocks by hydrothermal alteration during Cu-Au deposit formation. Economic Geology 105, 763-776.

Van Landuyt, J., Amelinckx, S., 1975. Multiple beam direct lattice imaging of new mixed-layer compound of the bastnaesite– synchysite series. American Mineralogist 60, 351-358.

Wade, C.E., Reid, A.J., Wingate, M.T., Jagodzinski, E.A., Barovich, K., 2012. Geochemistry and geochronology of the c. 1585Ma Benagerie Volcanic Suite, southern Australia: Relationship to the Gawler Range Volcanics and implications for the petrogenesis of a Mesoproterozoic silicic large igneous province. Precambrian Research 206, 17-35.

Walker, F.D.L., Lee, M.R., Parsons, I., 1995. Micropores and micropermeable texture in alkali feldspars: geochemical and geophysical implications. Mineralogical Magazine 59, 505-534.

Wang, Y., Wang, Y., Merino, E., 1995. Dynamic weathering model: constraints required by coupled dissolution and pseudomorphic replacement. Geochimica et Cosmochimica Acta 59, 1559-1570.

Wark, D.A., Stimac, J.A., 1992. Origin of mantle (rapakivi) feldspars: experimental evidence of a dissolution- and diffusion-controlled mechanism. Contributions to Mineralogy and Petrology 111, 345–361.

Williams, P.J., 2010. Classifying IOCG Deposits. Short Course Notes 20, pp. 23–38. Canada: Geological Association of Canada.

Williams, P.J., Barton, M.D., Johnson, D.A., Fontboté, L., De Haller, A., Mark, G., Oliver, N.H., Marschik, R., 2005. Iron oxide copper-gold deposits: Geology, space-time distribution, and possible modes of origin. Economic Geology 100, 371-405.

Wilson, M., Åkerblom, G., 1982. Geological setting and geochemistry of uranium-rich granites in the Proterozoic of Sweden. Mineralogical Magazine 46, 233–245.

Winderbaum, L., Ciobanu, C.L., Cook, N.J., Paul, M., Metcalfe, A., Gilbert, S., 2012. Multivariate analysis of an LA-ICP-MS trace element dataset for pyrite. Mathematical Geosciences 44, 823–842.

Wingate, M.T.D., Campbell, I.H., Compston, W., Gibson, G.M., 1998. Ion microprobe U–Pb ages for Neoproterozoic basaltic magmatism in south-central Australia and implications for the breakup of Rodinia. Precambrian Research 87, 135-159.

Woodhead, J.D., Hellstrom, J., Hergt, J.M., Greig, A., Maas, R., 2007. Isotopic and elemental imaging of geological materials by laser ablation inductively coupled plasma-mass spectrometry. Geostandards and Geoanalytical Research 31, 331–343

Worden, R.H., Walker, F.D.L., Parsons, I., Brown, W.L., 1990. Development of microporosity, diffusion channels and deuteric coarsening in perthitic alkali feldspars. Contributions to Mineralogy and Petrology 104, 507–515.

Wu, X.L., Meng, D.W., Pan, Z.L., Yang, G.M., 1998. Transmission electron microscopic study of new, regular, mixed-layer structures in calcium – rare earth fluorocarbonate minerals. Mineralogical Magazine 62, 55-64.

Xavier, R., Monteiro, L., Moreto, C., Pestilho, A., Melo, G., Silva, M.d., Aires, B., Ribeiro, C., Silva, F., 2010. The Iron Oxide Copper-Gold systems of the Carajás Mineral Province, Brazil: an Updated and Critical Review. In Porter T M, (Ed), Hydrothermal Iron Oxide

Copper-Gold and Related Deposits: A Global Perspective 3, PGC Publishing, Adelaide, 285-306.

Zang, W.L., Fanning, G.M., Purvis, A.C., Raymond, O.L., Both, R.A., 2007. Early Mesoproterozoic bimodal plutonism in the southeastern Gawler Craton, South Australia. Australian Journal of Earth Sciences 54, 661–674.